OCS Study
MMS 2008-058

Cumulative Increment Analysis for the Breton National Wilderness Area

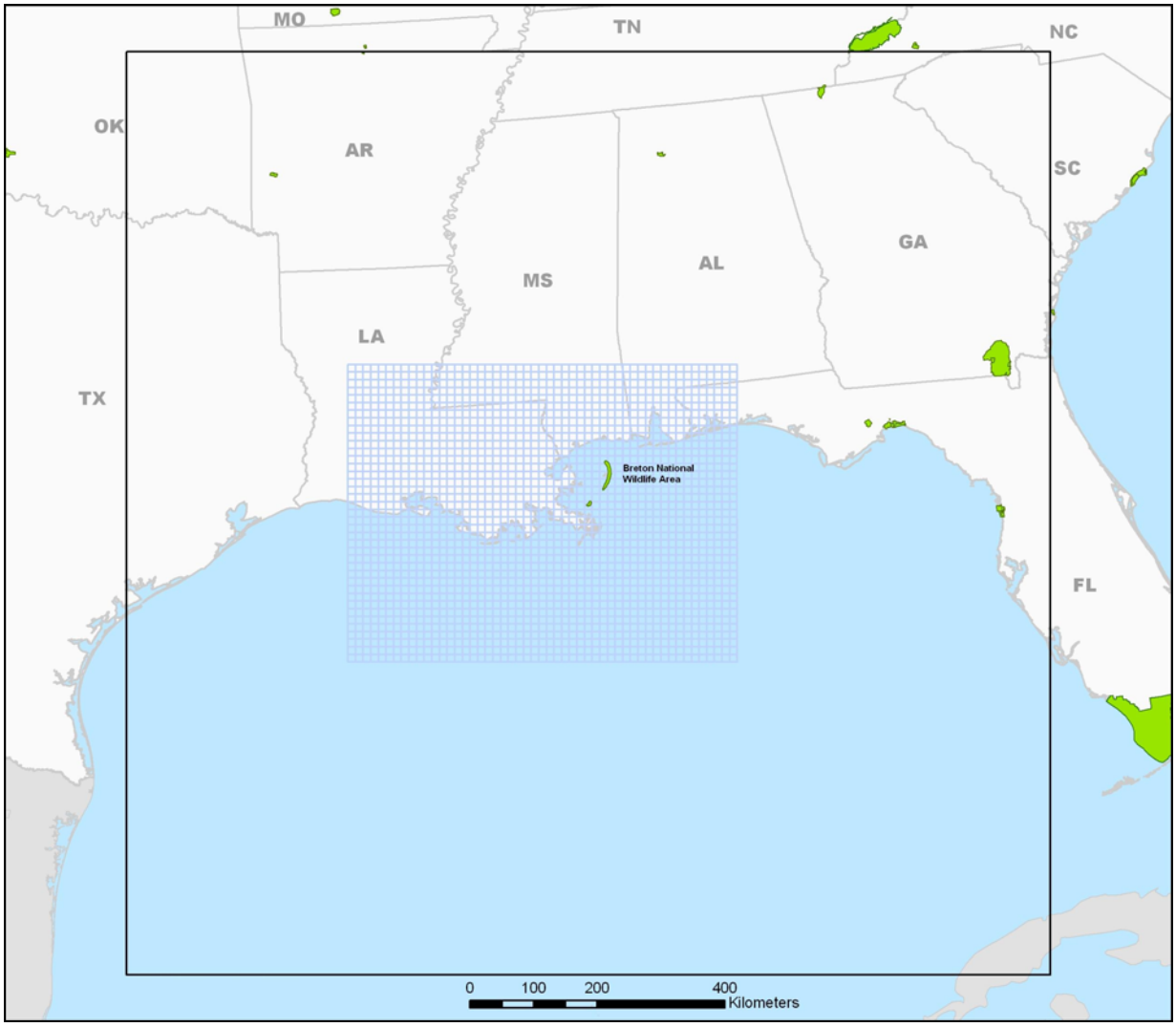

MMS U.S. Department of the Interior
Minerals Management Service
Gulf of Mexico OCS Region

OCS Study
MMS 2008-058

Cumulative Increment Analysis for the Breton National Wilderness Area

Authors

Neil J.M. Wheeler
Stephen B. Reid
Kenneth J. Craig
Sonoma Technology, Inc.
Petaluma, California

Jeffrey R. Zielonka
David R. Stauffer
Department of Meteorology
Pennsylvania State University
State College, Pennsylvania

Steven R. Hanna
Hanna Consultants
Kennebunkport, Maine

Prepared under MMS Contract
1435-01-01-CT-31065 (M07PC13316)
by
Sonoma Technology, Inc.
1455 N. McDowell Blvd, Suite D
Petaluma, CA 94954-6503

Published by

U.S. Department of the Interior
Minerals Management Service
Gulf of Mexico OCS Region

New Orleans
December 2008

DISCLAIMER

This report was prepared under contract between the Minerals Management Service (MMS) and Sonoma Technology, Inc. This report has been technically reviewed by the MMS, and it has been approved for publication. Approval does not signify that the contents necessarily reflect the views and policies of the MMS, nor does mention of trade names or commercial products constitute endorsement or recommendation for use. It is, however, exempt from review and compliance with the MMS editorial standards.

REPORT AVAILABILITY

Extra copies of this report may be obtained from the Public Information Office (Mail Stop 5034) at the following address:

U.S. Department of the Interior
Minerals Management Service
Gulf of Mexico OCS Region
Public Information Office (MS 5034)
1201 Elmwood Park Boulevard
New Orleans, Louisiana 70123-2394
Telephone: (504) 736-2419 or
1-800-200-GULF

CITATION

Suggested citation:

Wheeler, N.J.M., S.B. Reid, K.J. Craig, J.R. Zielonka, D.R. Stauffer, and S.R Hanna. 2008. Cumulative increment analysis for the Breton National Wilderness Area. U.S. Dept. of the Interior, Minerals Management Service, Gulf of Mexico OCS Region, New Orleans, LA. OCS Study MMS 2008-058. 343 pp.

ACKNOWLEDGMENTS

The authors wish to acknowledge contributions to this study from the Contracting Officer's Technical Representative (COTR), Dr. C. H. Huang; Robert Cameron; Dirk Herkhof; Dr. Ronald Lai; and Elizabeth Peuler of the Minerals Management Service; Dr. Nelson Seaman and Glenn Hunter of the Pennsylvania State University; and Dianne Miller and Bryan Penfold of Sonoma Technology, Inc. (STI). We also acknowledge former STI staff member, Dr. Patrick Ryan, who performed and documented much of the analysis on the historical representativeness of the periods being studied and selected cases for modeling. Finally, we thank Scientific Review Board members Dr. S.A. Hsu of Louisiana State University, Dr. Richard McNider of the University of Alabama at Huntsville, Dr. Steven Ziman formerly of Chevron, and Tim Allen of the Fish and Wildlife Service for their advice, suggestions, and guidance.

TABLE OF CONTENTS

Section **Page**

LIST OF FIGURES

LIST OF TABLES

1.0 INTRODUCTION

This document is the final report for U.S. Department of the Interior, Minerals Management Service (MMS), Gulf of Mexico Outer Continental Shelf (OCS) Region, contract number 1435-01-01-CT-31065, "The SO_2 and NO_2 Increment Analysis for the Breton National Wilderness Area (BNWA)". This section provides background information about the study, a discussion of increments for Class I areas, as defined in the Clean Air Act, a summary of objectives, and summaries of the methods and findings from the episode-type study.

1.1 STUDY BACKGROUND

The BNWA is surrounded by onshore sources of oxides of sulfur (SO_x) and oxides of nitrogen (NO_x) to the north and west and offshore sources to the south and east. The 1977 Clean Air Act limits the increases in concentrations of sulfur dioxide (SO_2), nitrogen dioxide (NO_2), and particulate matter less than 10 microns (PM_{10}) may increase in Class I areas such as the BNWA. These limits are referred to as increments. The magnitude and distribution of the sources introduce the possibility that SO_2 or NO_2 concentrations in the BNWA may exceed regulatory limits, which could result in regulatory consequences affecting several federal (U.S. Environmental Protection Agency [EPA], U.S. Fish and Wildlife Service [FWS], and MMS) and state agencies and the groups they regulate. As the federal land manager, the FWS expressed concerns that the SO_2 and NO_2 increments may be consumed on a cumulative basis and requested that a cumulative increment analysis be performed. However, no current information demonstrates whether the BNWA falls within mandated compliance limits.

The MMS has supported several studies to provide the emissions and meteorological databases needed to perform a modeling-based cumulative increment analysis for the BNWA. From October 2000 through September 2001 (the study year), meteorological and air quality data were collected under the sponsorship of the Offshore Operators Committee (OOC), an industry consortium, as part of the Breton Aerometric Monitoring Program (BAMP). The databases from these studies were used to perform and assess the meteorological and air quality modeling described in this report.

1.2 INCREMENTS FOR CLASS I AREAS

The 1977 Clean Air Act Amendments established the Prevention of Significant Deterioration (PSD) program for all attainment areas and set incremental limits for three categories, Class I, II, and III, with Class I being the most restrictive and Class III the least restrictive. There are no Class III areas. All areas that are not Class I are classified Class II.

Increments are the maximum increases in ambient pollutant concentrations allowed over baseline concentrations. Thus, increments should limit increases in ambient pollutant concentrations caused by new major sources or modification of existing major sources near areas subject to the PSD program. Increment consumption analyses for Class I areas should include not only emissions from a proposed source, but also increment-consuming emissions from other sources. The increments for Class I areas are shown in **Table 1-1**.

Table 1-1

Class I Increments ($\mu g/m^3$)

Pollutant	Annual Arithmetic Mean	24-hr Maximum	3-hr Maximum
Sulfur dioxide (SO_2)	2.0	5	25
Particulate matter < 10 μ (PM_{10})	4.0	8	N/A
Nitrogen dioxide (NO_2)	2.5	N/A	N/A

The amount of PSD increment that has been consumed in a PSD area is determined from the emissions increases and decreases that have occurred from sources since the applicable baseline date. Emission increases that consume a portion of the applicable increment are, in general, all those not accounted for in the baseline concentration and specifically include

- actual emission increases occurring after the major source baseline date (January 6, 1975, for SO_2 and PM_{10}, and February 8, 1988, for NO_2) that are associated with physical changes or changes in the method of operation (i.e., construction) at a major stationary source[1]; and
- actual emission increases at any stationary, area, or mobile source occurring after the minor source[2] baseline date (August 7, 1977, for SO_2 and February 8, 1988, for NO_2).

The amount of available increment may be added to, or "expanded," in two ways. The primary method is through the reduction of actual emissions from any source after the minor source baseline date. Any such emissions reduction would increase the amount of available increment to the extent that ambient concentrations would be reduced.

Increment expansion may also result from the reduction of actual emissions after the major source baseline date, but before the minor source baseline date, if the reduction results from a physical change or change in the method of operation (i.e., construction) at a major stationary source. Moreover, the reduction will add to the available increment only if the reduction is included in a federally enforceable permit or State Implementation Plan (SIP) provision. Thus, for major stationary sources, actual emissions reductions made prior to the minor source baseline date expand the available increment just as increases before the minor source baseline date consume increment.

Only the increments for SO_2 and NO_2 were considered in this study. PM_{10} increments were not considered because the PM_{10} emission inventories were inadequate and no monitoring of PM_{10} concentrations suitable for model evaluation was undertaken during the BAMP.

[1] Term used to determine the applicability of PSD and new source regulations. In a nonattainment area, any stationary pollutant source with potential to emit more than 100 tons per year is considered a major stationary source. In PSD areas the cutoff level may be either 100 or 250 tons, depending on the source.

[2] New emissions sources or modifications to existing emissions sources, which do not exceed major source emission levels.

1.3 OBJECTIVES

The overall objective of this study was to evaluate through modeling the contribution of OCS (both platform and non-platform) and onshore emission sources to SO_2 and NO_2 levels over the BNWA and access the relative trends in these concentrations in the BNWA with respect to the appropriate baseline values.

This study was conceived as a scientific investigation of the processes affecting trends in SO_2 and NO_2 concentrations near the BNWA and the models used to simulate those processes. While it was an objective of this study to compare the concentration trends with the PSD Class I increments, the analysis was not intended to take the place of a regulatory PSD increment analysis for the BNWA. This study consists of a best attempt to evaluate the relative magnitude of the changes with respect to the available PSD increments in the BNWA.

Other objectives addressed in the initial phases of the study included (1) assessing the representativeness of the year being analyzed, (2) identifying periods for episodic modeling and evaluation, and (3) selecting the meteorological and air quality models that would be used for annual simulations on which the analysis would be based.

1.4 SUMMARY OF APPROACH

To assess the representativeness of the year being analyzed (October 2000–September 2001), monthly mean surface temperatures, 850-mb temperatures, 500-mb heights, precipitation, and frequency of synoptic weather patterns for the study year were compared to historical records.

To identify periods for episodic modeling, days during the study year were percentile-ranked by SO_2 and NO_2 concentrations. Five periods of six days were selected from the highest concentrations so that the frequency of synoptic weather patterns for those periods would be representative of days with high SO_2 and NO_2 concentrations. One additional period was selected during which concentrations were at the 50^{th} percentile to provide more typical (non-episodic) conditions to evaluate the air quality models. Episodic meteorological and air quality modeling was performed to assist in selecting the air quality model that would be used for annual simulations on which the increment analysis would be based. Two models, the California Puff (CALPUFF) model and the Community Multiscale Air Quality (CMAQ) model were applied for the six periods selected for episodic modeling, the results of those applications were evaluated statistically and graphically, and the evaluations were compared to select the model that best replicated the SO_2 and NO_2 observed during those periods. CALPUFF was selected for the annual simulations.

CALPUFF was applied for the entire study year, the SO_2 baseline year (1977), and the NO_2 baseline year (1988). Concentration differences (annual for NO_2 and annual, 24-hr maximum, and 3-hr maximum for SO_2) between the study year and the baseline years (increments) were calculated and summarized.

1.5 SUMMARY OF FINDINGS

1.5.1 Meteorological Representativeness of the Study Year

The analysis of meteorological data for the period of October 2000 through September 2001 identified a number of deviations from climatological mean conditions:

- Sea surface temperatures were cooler than normal.
- From November 2000 to April 2001, surface land temperatures deviated by 2.3°F to 5.7°F from the climatological monthly means. However, only December 2000 was unusual in that its monthly mean temperature was among the five lowest on record.
- The distribution of synoptic weather patterns in October and December 2000 and in February and March 2001 showed moderate deviations from historical averages.
- June 2001 was the second wettest June on record and the ninth wettest month on record.

However, on an annual average basis, monthly surface temperatures and synoptic weather patterns closely match historical averages.

1.5.2 Episode-Type Modeling

The following six cases were selected for the episode-type modeling study:

1. December 1-6, 2000
2. March 2-8, 2001
3. July 9-14, 2001
4. August 8-13, 2001
5. November 8-13, 2000
6. December 30, 2000–January 4, 2001

High SO_2 concentrations were observed in five of these cases, and the synoptic weather pattern distribution during these cases closely matched the distribution of days with high SO_2 and NO_2 concentrations across the entire year. An additional case (August 8-13, 2001) was selected to test the models under average (non-episodic) conditions.

Episode-type modeling was performed with both the CMAQ model and the CALPUFF model. When observed and predicted concentrations were paired in time and space and compared, both models showed little skill. However, when the top 5% of observed and predicted concentrations, unpaired in time and space, were compared, we saw significant improvements in model performance. Both models met our performance goals for NO_2, but only CALPUFF met them for SO_2.

Because the SO_2 increment was the most likely to be exceeded based on a statistical analysis of ambient air quality data, the performance of the models for the highest SO_2

concentrations was of greatest importance. Based on the model performance evaluation for the top 5% of SO_2 concentrations, CALPUFF was recommended for increment analysis modeling because it replicated high SO_2 concentrations more reliably than CMAQ.

1.5.3 Annual Modeling and Increment Analysis

Annual modeling with CALPUFF of the study (2000-2001) and baseline (1977 for SO_2 and 1988 for NO_2) years revealed that none of the allowable SO_2 or NO_2 increments had been fully consumed.

- The maximum 3-hr SO_2 increment consumed within the BNWA was 1.70 $\mu g/m^3$. Increment consumption within the BNWA ranges from 0.42 to 1.70 μg/m3. The 3-hr maximum SO_2 increment of 25.0 $\mu g/m^3$ was not exceeded at any grid point within the BNWA, but a portion of the increment was consumed.
- The maximum 24-hr SO_2 increment consumed within the BNWA was 1.18 $\mu g/m^3$. Increment consumption within the BNWA ranges from 0.11 to 1.18 μg/m3. The 24-hr maximum SO_2 increment of 5.0 $\mu g/m^3$ was not exceeded at any grid point within the BNWA, but a portion of the increment was consumed.
- The maximum annual SO_2 increment consumed within the BNWA was -1.07 $\mu g/m^3$. Increment consumption within the BNWA ranged from -1.07 to -1.89 $\mu g/m^3$. The annual SO_2 increment of 2.0 $\mu g/m^3$ was not exceeded at any grid point within or around the BNWA.
- The maximum annual NO_2 increment consumed within the BNWA was 0.10 $\mu g/m^3$. The annual NO_2 increment of 2.5 $\mu g/m^3$ was not exceeded at any grid point within the BNWA, but a portion of the increment was consumed.

2.0 REPRESENTATIVENESS OF METEOROLOGY DURING THE STUDY PERIOD

Significant effort was expended in collecting meteorological, emissions, and air quality data for the year modeled in this study. This section describes the data sources and methods used to assess the historical meteorological representativeness of the study year and the results of that analysis. The purpose is not to determine whether the study year can be used for modeling but rather to describe the year in historical context.

2.1 APPROACH

Using available data, the surface temperatures, precipitation, sea surface temperatures, 500-mb geopotential heights, 850-mb temperatures, and synoptic weather patterns for October 2000 through September 2001 were compared to historical values. Sources of data used to determine representativeness included the NOAA-CIRES Climate Diagnostic Center and the Louisiana Office of State Climatology (LOSC). The NOAA-CIRES Climate Diagnostic Center (U.S. Dept. of Commerce, National Oceanic and Atmospheric Administration, 2003) reanalysis project uses a state-of-the-art analysis/forecast system to perform data assimilation using past data from 1948 to the present. A subset of these data was processed to create a time series of monthly means.[3] The LOSC monthly climate review (Louisiana Office of State Climatology, 2005) was used to obtain the monthly average surface temperature and monthly total precipitation for southeast Louisiana and the daily synoptic weather patterns for New Orleans, Louisiana.

2.2 RESULTS

2.2.1 Temperatures and Precipitation

A time series plot of the monthly mean surface sea temperatures since 1948 for the region surrounding the BNWA is shown in **Figure 2-1**. The minimum October 2000 through September 2001 monthly sea surface temperature of 13.5^{o}C appears to be close to the median value. However, the maximum October 2000 through September 2001 monthly sea surface temperature of 27.8^{o}C appears to be among the coolest maximum values on record.

[3] The reanalysis is a model itself that integrates observational data and, as such, may not compare exactly with actual observations. However, it is useful for placing the study year in historical context.

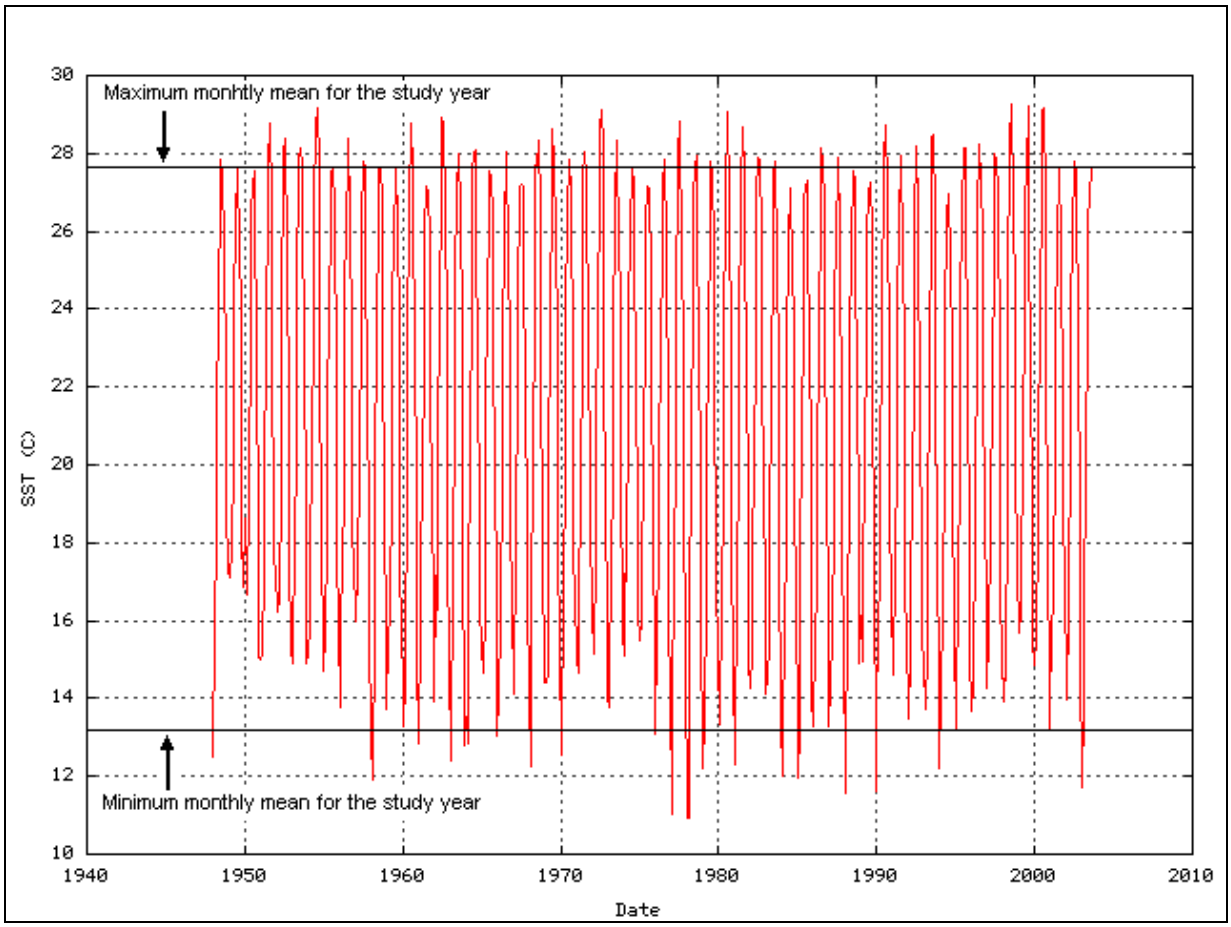

Figure 2-1. Monthly mean sea surface temperatures for the region surrounding the BNWA.

Monthly mean land surface temperatures in southeast Louisiana are shown in **Figure 2-2**. The data in Figure 2-2 reflect a 10-year period from 1981 to 1990 because monthly data were only available for that period. The LOSC monthly summaries were used to describe each month during the study year relative to the long-term historical record going back to 1889.

The surface temperature data indicate that monthly mean temperatures in October 2000 through September 2001 were comparable to monthly mean temperatures for 1981 through 1990. From November 2000 to April 2001, the monthly temperature deviated from the historical mean by a range of 2.0°F to 5.7°F. However, temperatures in November 2000 rank among the lowest 25% of all November temperatures dating back to 1889. Although January was a cool month by long-term standards, the –2°F departure from the historical mean is modest compared to extremes exhibited in some past Januarys. December 2000 and February 2001 were the most unusual months, when the average ambient temperatures in December and February were cooler and warmer than normal by 5°F or more. December's mean temperature ranked among the five lowest mean temperatures in December since 1889. February's mean temperatures, although notable, fell well short of record high February mean temperatures, but ranked among the top third of all February monthly averages over the past 100 years. The difference between temperatures from May to September 2001 and normal temperatures was 0.6°F or less.

The annual precipitation total from October 2000 through September 2001 was greater than the 1981 to 1990 average—precipitation totaling 70 inches in southeast Louisiana was eight inches more than normal (62 inches). **Figure 2-3** illustrates that precipitation from October 2000 through September 2001 would have been less than normal had it not been for Hurricane Allison. Because of Hurricane Allison, Louisiana's statewide rainfall made June 2001 the second wettest June, and the ninth wettest of any month, on record dating back to 1889. Before June 2001, Louisiana was suffering drought-like conditions for the fourth year in a row.

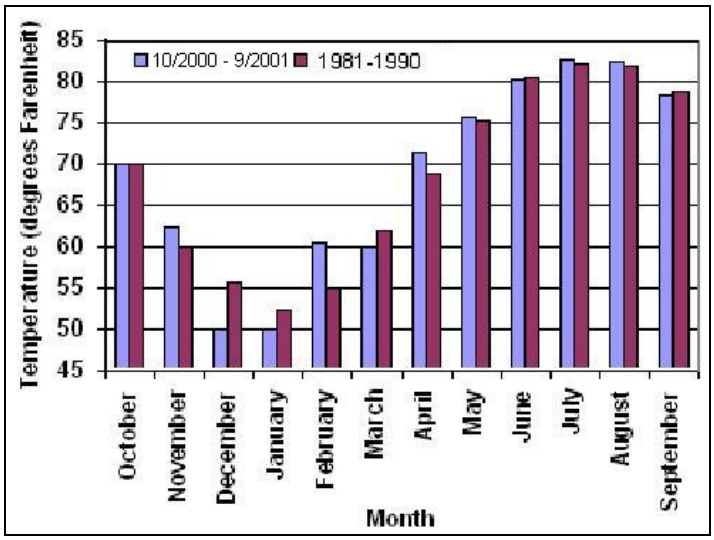

Figure 2-2. Monthly mean surface temperatures from October 2000 through September 2001 in southeast Louisiana compared with 1981 to 1990 averages.

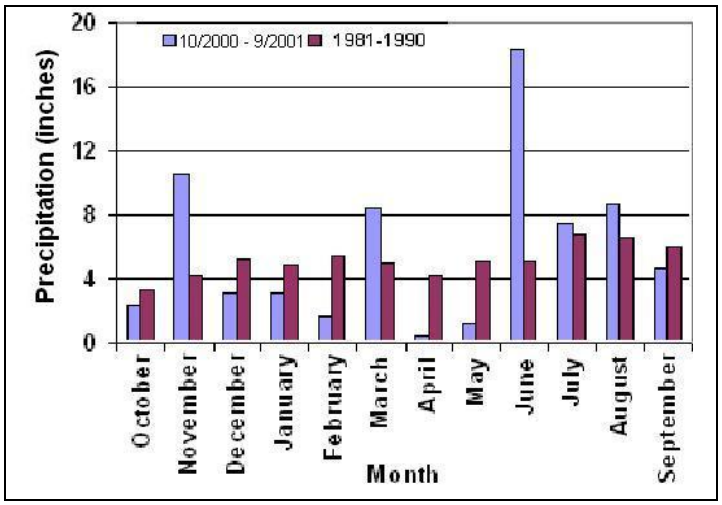

Figure 2-3. Monthly precipitation from October 2000 through September 2001 in southeast Louisiana compared with the 1981 to 1990 average monthly precipitation.

2.2.2 Upper-Air Data

A time series of monthly mean 500-mb geopotential heights is shown in **Figure 2-4**. From October 2000 to September 2001, the monthly minimum and maximum 500-mb geopotential heights (m) are among the lowest and highest observed from 1948 to 2003. A time series of monthly mean 850-mb temperatures is shown in **Figure 2-5**. The 850-mb minimum and maximum temperatures from October 2000 to September 2001 appear to be among the coolest and warmest observed between 1948 and 2003.

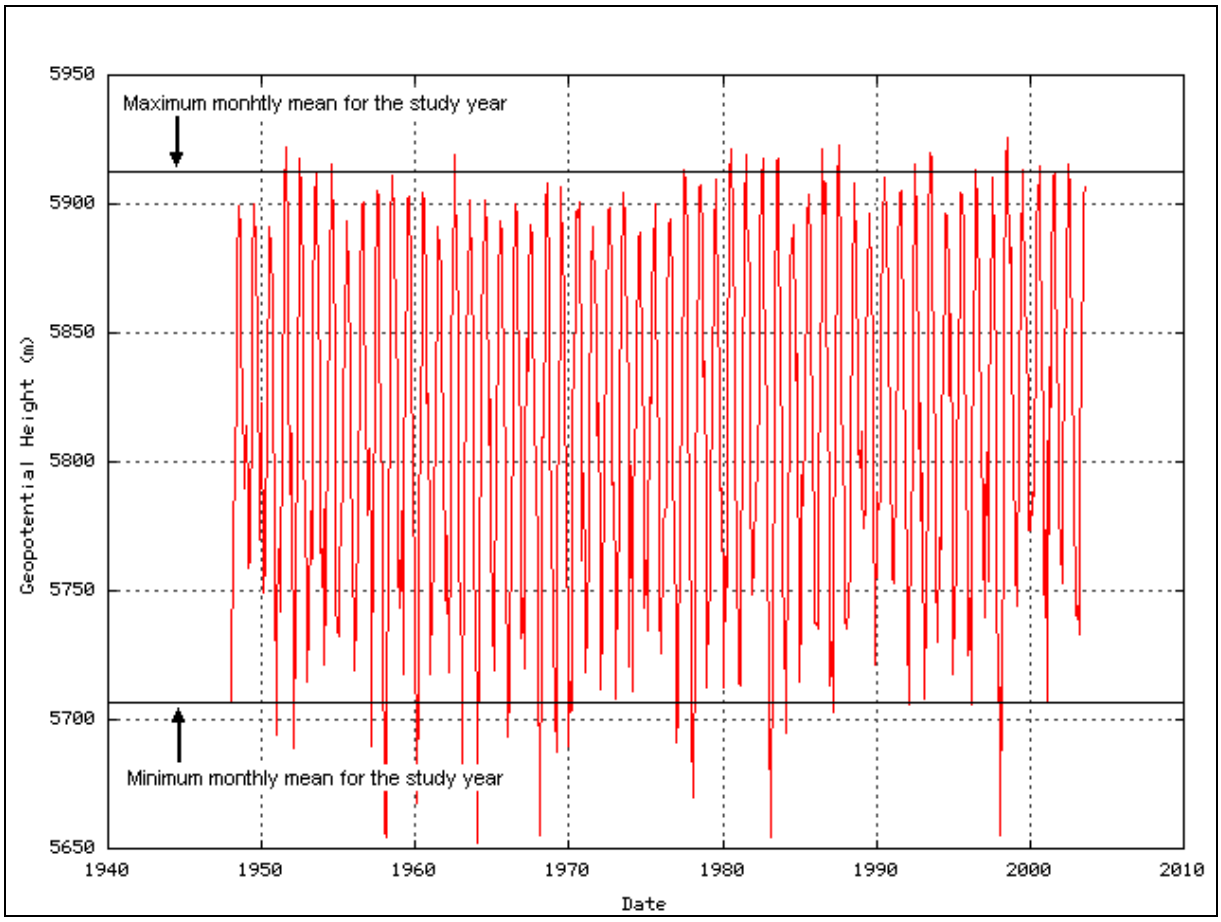

Figure 2-4. Monthly mean 500-mb geopotential heights for the region surrounding the BNWA.

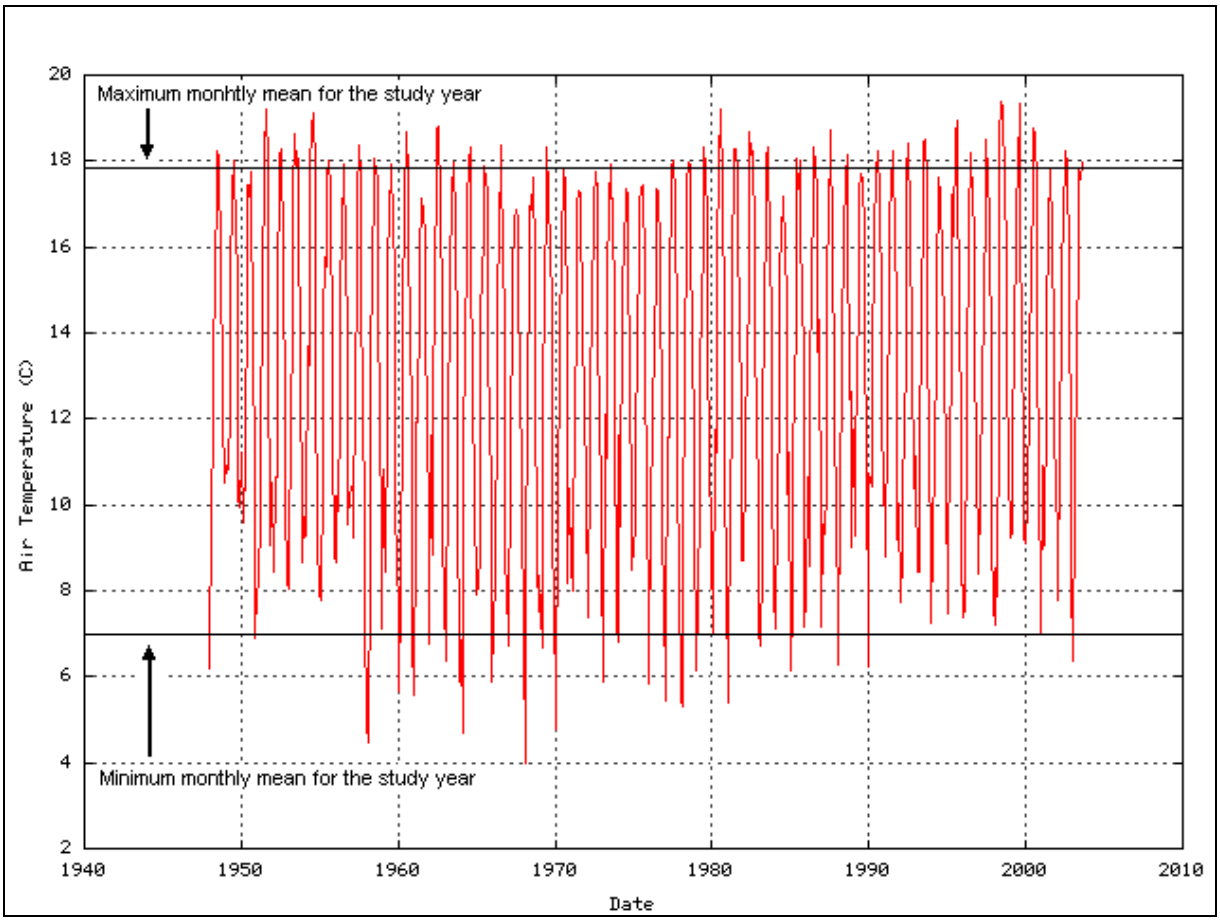

Figure 2-5. Monthly mean 850-mb temperatures for the region surrounding the BNWA.

2.2.3 Synoptic Weather Patterns

The LOSC (2005) classifies daily synoptic weather according to eight weather patterns: Pacific High (PH), Continental High (CH), Frontal Overrunning (FOR)[4], Coastal Return (CR), Gulf Return (GR), Frontal Gulf Return (FGR)[5], Gulf High (GH), and Gulf Tropical Disturbance (GTD). The LOSC also groups weather patterns into three index classifications: Continental Index (CI), which includes CH and FOR patterns, Tropical Index (TI), which includes GR, FGR, and GTD patterns, and Stormy Index (SI), which includes FOR, FGR, and GTD patterns.

Table 2-1 shows the percent of occurrence of each of these eight synoptic weather patterns (and three groups of patterns) over New Orleans for the months of October 2000

[4] Cold fronts that become stationary over the northern Gulf. "Wave development" along these stationary boundaries over the northwestern Gulf often brings spells of widespread cold rains to Louisiana.
[5] Upper-air troughs that introduce inflow of warmer and moister maritime tropical Gulf air over Louisiana and more frequent stormy frontal weather.

through September 2001 and the corresponding average synoptic weather pattern distribution for that month from 1981 to 1990.

The following points summarize the synoptic weather patterns for the study year:

- The CR frequency of 47% is the highest on record for October dating back to 1961, and the CH frequency of only 11% tied with 1984 as the lowest on record.
- The December CI of 82% is the second highest on record. The FOR frequency was ninth highest.
- The CI frequency of 38% tied for sixth lowest on record in February. At the same time, the GR and FGR weather—and the TI—were each about fifth highest on record in the historical series of Februarys.
- The March GR frequency of 2% was the lowest GR percentage on record for this month; the previous March low was 7% in 1979.
- The CI of 66% was the third highest recorded for any March, and the TI of 16% tied for third lowest on record.

Table 2-1

Percent Occurrence of Synoptic Weather Patterns over New Orleans by Month, October 2000-September 2001 and October-September 1981-1990

Synoptic Weather Types October 2000 – September 2001	**Oct**	**Nov**	**Dec**	**Jan**	**Feb**	**Mar**	**Apr**	**May**	**Jun**	**Jul**	**Aug**	**Sep**	**Average**
Pacific High (PH)	3	7	0	3	4	11	3	0	0	0	0	2	3
Continental High (CH)	11	23	40	29	13	32	12	18	18	5	2	38	20
Frontal Overrunning (FOR)	11	22	42	40	25	34	7	2	0	2	0	7	16
Coastal Return (CR)	47	8	3	2	7	0	18	6	3	37	32	10	14
Gulf Return (GR)	23	18	3	5	23	2	55	71	40	13	16	28	25
Frontal Gulf Return (FGR)	5	17	10	10	23	15	5	3	5	3	3	5	9
Gulf High (GH)	0	5	2	11	5	6	0	0	10	32	24	0	8
Gulf Tropical Disturbance (GTD)	0	0	0	0	0	0	0	0	23	8	23	10	5
Continental (CH+FOR)	23	45	82	69	38	66	18	19	18	6	2	45	36
Tropical (GR+FGR+GTD)	27	35	13	15	46	16	60	74	82	94	98	43	50
Storminess (FOR+FGR+GTD)	16	38	52	50	48	48	12	5	28	12	26	22	30
Synoptic Weather Types, 1981-1990	**Oct**	**Nov**	**Dec**	**Jan**	**Feb**	**Mar**	**Apr**	**May**	**Jun**	**Jul**	**Aug**	**Sep**	**Average**
Pacific High (PH)	1	6	3	5	5	6	7	2	0	0	0	0	3
Continental High (CH)	36	26	26	26	19	22	21	22	12	6	11	31	22
Frontal Overrunning (FOR)	15	19	32	34	40	24	13	12	7	5	6	11	18
Coastal Return (CR)	19	11	4	6	7	9	13	12	20	25	21	23	14
Gulf Return (GR)	14	22	15	11	12	24	27	33	31	20	17	15	20
Frontal Gulf Return (FGR)	10	14	15	11	13	11	14	15	11	9	8	7	12
Gulf High (GH)	2	2	5	7	6	5	8	3	12	27	23	6	9
Gulf Tropical Disturbance (GTD)	4	0	0	0	0	0	0	1	8	10	14	9	4
Continental (CH+FOR)	51	45	58	60	59	46	33	34	19	11	17	42	40
Tropical (GR+FGR+GTD)	27	37	31	22	25	34	40	52	81	89	83	36	46
Storminess (FOR+FGR+GTD)	29	34	47	45	52	34	26	27	25	24	28	26	33

2.2.4 El Niño-Southern Oscillation Conditions

El Niño-Southern Oscillation (ENSO) conditions seem to have occurred at every two to seven years for at least the past 300 years but most of them have been weak. Dr. S.A. Hsu of Louisiana State University reviewed Sea Surface Temperature (SST) analyses for the study year to identify ENSO conditions. His summary follows.

- October 2000 – SST remained weakly negative over portions of the central and eastern equatorial Pacific
- November 2000 – weak cold episode conditions redeveloped across the tropical Pacific
- December 2000 – cold episode conditions continued and strengthened
- January 2001 – mature cold episode conditions
- February 2001 – mature cold episode conditions
- March 2001 – mature cold episode conditions
- April 2001 – cold episode conditions weakened
- May 2001 – return to normal
- June 2001 – near normal
- July 2001 – near normal
- August 2001 – neutral
- September 2001 – neutral

On the basis of this review, it was concluded that near normal ENSO conditions occurred in most months.

2.2.5 Overall Meteorological Summary

The following points summarize the overall meteorology for the year, October 2000 through September 2001.

- The minimum winter sea surface temperature appears typical compared to all other years. The maximum summer sea surface temperature appears cooler than normal.
- Annual average land surface temperatures were neither warmer nor colder than normal.
- Excluding Hurricane Allison, precipitation was less than normal from October 2000 through September 2001.
- The 850-mb maximum summer temperatures appear to be among the coolest observed in the past 20 years. These cooler-than-normal temperatures may have been the result of Hurricane Allison.
- The frequency of monthly synoptic patterns deviated from historical frequency of occurrence. However, the annual average monthly synoptic weather patterns from

October 2000 to September 2001 agree well with the 1981 to 1990 averages. In other words, synoptic influences were typical.

Despite monthly extremes in temperatures and precipitation during the study year, the annual average values were typical compared to the historic record. Monthly weather patterns from October 2000 to September 2001 deviate from the 1981 to 1990 monthly averages, but the annual average of the monthly synoptic weather patterns from October 2000 to September 2001 agrees well with the 1981 to 1990 average. Overall, the meteorology of the study year is not atypical and should not significantly bias the results of the increment analysis.

3.0 INITIAL CASE SELECTION

Six five- to six-day cases were selected for initial modeling to test and evaluate the meteorological and air quality models used in this study. This section describes the analysis methods used to select cases for initial modeling, summarizes the results of the case selection process, and describes the selected cases.

3.1 CASE SELECTION

3.1.1 Data

Miller et al. (2003) described the collecting of hourly NO and NO_y (used to infer NO_2), and SO_2 data at three sites in the study area: Breton Island Platform (BIP), Fort Morgan (FTM), and West Delta Platform (WDP). The locations of these sites are shown in **Figure 3-1.** These data were available for our analysis.

Miller et al. (2003) also assigned a meteorological classification (Met Class) to each day of the study year. The LOSC issues a monthly climate review newsletter (Louisiana Office of State Climatology, 2005) that includes discussions of each month's weather and daily synoptic weather pattern (SWP) classifications for the Gulf region. The monthly weather discussions are provided in Appendix A. The Met Class and SWP for each day of the study year were entered into our analysis database. Descriptions of each Met Class and SWP are provided in **Table 3-1**.

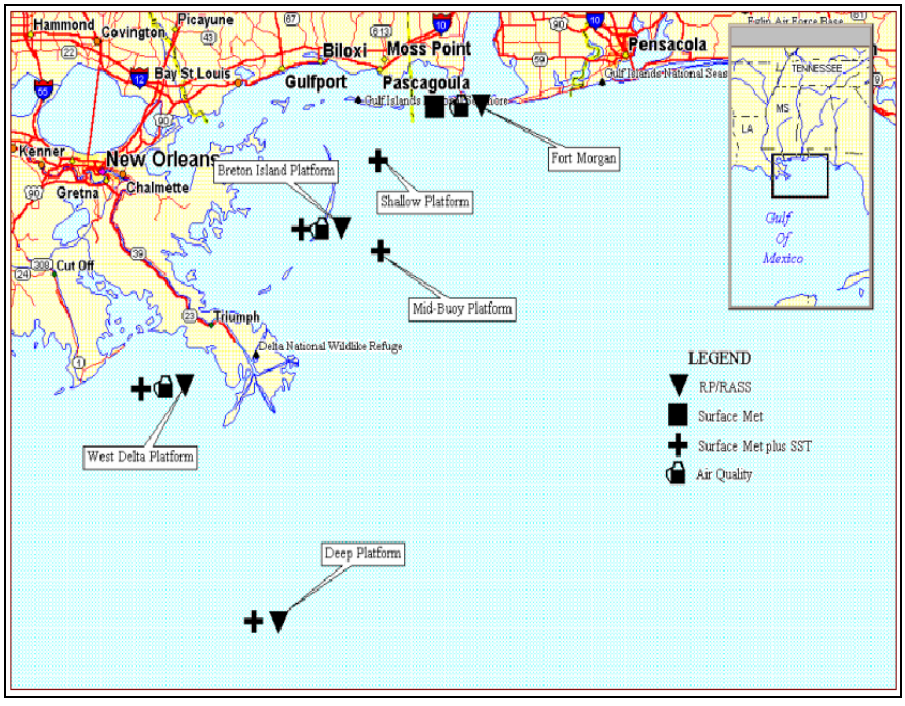

Figure 3-1. Ambient meteorology and air quality measurement in the study region.

Table 3-1

Description of Meteorological Classes and Synoptic Weather Patterns

Met Class	Description of Met Class		SWP Code	Description of SWP
1	Ridge		PH	Pacific High
2	Weak Ridge		CH	Continental High
3	Flat		FOR	Frontal Overrunning
4	Zonal		CR	Coastal Return
5	Post Trough		GR	Gulf Return
6	Weak Trough		FGR	Frontal Gulf Return
7	Trough		GH	Gulf High
8	Cut-off Low		GTD	Gulf Tropical Disturbance
9	Tropical Storm			

3.1.2 Approach

Because the increment for NO_2 is based on an annual average concentration, it is unlikely to be exceeded unless large, regional increases in NO_x emissions have occurred since 1988, which does not appear to be the case. Therefore, we focused on SO_2 concentrations in the episode selection. An analysis of SO_2 concentrations during the study year revealed that 24-hr SO_2 concentrations at BIP exceeded the 24-hr increment on 111 days and exceeded the 3-hr increment on 22 days. Thus, the 24-hr SO_2 concentrations were higher than the increment approximately five times (111/22) more often than 3-hr SO_2 concentrations. Therefore, the overall approach was to select five case periods with the highest 24-hr SO_2 concentrations that represented the range and frequency of synoptic weather patterns observed during the study year. We focused on days with the highest concentrations because we expected they would also be the days on which the increment would be exceeded. One additional case was selected to represent more typical (i.e., median) concentrations of SO_2 and NO_2 because such cases are important in modeling annual concentrations.

3.1.3 Analysis

An analysis of SO_2 and NO_2 concentrations by averaging time was performed to determine whether ambient concentrations by averaging time exceeded increment limits within the BNWA during the study year. The maximum NO_2 and SO_2 concentrations measured at BIP compared to Class I increments by averaging time are shown in **Table 3-2**.

The measured annual average NO_2 concentration of 6.1 $\mu g/m^3$ is a factor of 2.4 greater than the allowed increment of 2.5 $\mu g/m^3$. The highest and second-highest 3-hr and 24-hr SO_2 concentrations of 52 $\mu g/m^3$ and 25 $\mu g/m^3$ are factors of 2.1 and 5 greater than the allowed increments for these averaging times of 25 $\mu g/m^3$ and 5 $\mu g/m^3$, respectively. The annual SO_2 concentration of 4.1 $\mu g/m^3$ is a factor of 2 greater than the allowed increment of 2 $\mu g/m^3$. This comparison shows that exceedance of the SO_2 and NO_2 increments for all averaging times could occur.

Table 3-2

Comparison of Maximum Measured NO_2 and SO_2 Concentrations to Class I Increments ($\mu g/m^3$)

Pollutant	Averaging Time	Maximum Measurement ($\mu g/m^3$)	Increment ($\mu g/m^3$)	Ratio of Maximum To Increment
NO_2	Annual	6.1	2.5	2.4
SO_2	3-hr	52[a]	25[b]	2.1
	24-hr	25[a]	5[b]	5.0
	Annual	4.1	2	2.0

[a] Highest, second-highest
[b] Not to be exceeded more than once per year

Daily values of daily peak 3-hr SO_2, 24-hr average SO_2, 24-hr average NO_2, and the percentile rank of these concentrations within the study year were calculated. These results were tabulated, along with Met Class and SWP, and summarized in a table where concentrations at the 90^{th}, 95^{th}, and 98^{th} percentiles were color-coded. This table (see Appendix B) was visually reviewed to identify clusters of days when high SO_2 and NO_2 concentrations occurred.

Time series plots of SO_2 and NO_2 concentrations at BIP were prepared to visually compare the increment levels of interest and identify whether the likelihood of exceeding the increment was greater in some months compared to others. This analysis was designed to further clarify which cases to select. These plots are provided in Appendix C.

Plots of 3-hr SO_2, 24-hr SO_2, and 24-hr NO_2 concentration distributions by site (BIP, FTM, and WDP), and for the three sites combined, were prepared and are provided in Appendix D. Results show that three times as many high 3-hr SO_2 concentrations (greater than 20 $\mu g/m^3$) and 2.5 times as many high 24-hr SO_2 concentrations (greater than 10 $\mu g/m^3$) occurred at BIP and FTM relative to WDP. Approximately the same percentage of 24-hr NO_2 concentrations above 12 $\mu g/m^3$ occurred at each of the three sites.

The following statistical features were used to develop the objective scoring criteria for episode selection. On days when 24-hr SO_2 concentrations were greater than the 5 $\mu g/m^3$ increment, the average concentration was a factor of 1.9 times greater than the increment. When the 3-hr SO_2 concentrations were greater than the 25 $\mu g/m^3$ increment, the average concentration was a factor of 1.3 greater than the increment. Therefore, the probability of exceeding the 24-hr SO_2 the increment is higher by at least a factor of 1.5 than the probability of exceeding the 3-hr SO_2 increment. Additionally, 24-hr SO_2 exceeded the increment on five times more days (30%) than did 3-hr SO_2 (6%). For these reasons, the probability of a short-term exceedance is estimated at least 7.5 times more likely for 24-hr SO_2 compared to 3-hr SO_2. Therefore, five modeling episodes were selected based on 24-hr SO_2 using the following scoring criteria:

- 6 points were assigned to each day when 24-hr SO_2 exceeded the increment at BIP.
- 2 points were assigned to each day when 24-hr SO_2 exceeded the increment at BIP and either FTM or WDP.

- 2 points were assigned to each day when 24-hr SO_2 at BIP, FTM, and WDP exceeded the increment.

The total point score for each day determined its ranking. The maximum daily score possible is 10 points. **Table 3-3** illustrates this scoring technique; 49 days scored 10, the maximum score possible.

In addition to objective scoring criteria, other criteria were established to ensure the representativeness of the cases selected:

- The five cases selected had to have shown the following weather pattern distribution: CH, 40%; FOR, 25%; GH, 15%; and CR, 10%. These percentages are the occurrence of these weather patterns on all days in the study year when 24-hr SO_2 was above the increment. This criterion ensures that the meteorological phenomena in the cases selected are typical for days when SO_2 concentrations are highest.
- One of the cases selected had to have occurred in April, May, or July 2001. Both SO_2 and NO_2 monthly concentrations were low during these months, and the ratio of SO_2 to NO_2 was also low during these months. June was not considered because the effect of Hurricane Allison on emissions in June is not known.

Table 3-3

High Ranking 24-hr SO_2 Events. 3-hr and 24-hr SO_2 and 24-hr NO and NO_2 Concentrations are in Units of $\mu g/m^3$.

Synoptic Weather	Date	BIP				FTM				WDP				Score
		SO_2_3hr	SO_2_24hr	NO	NO_2	SO_2_3hr	SO_2_24hr	NO	NO_2	SO_2_3hr	SO_2_24hr	NO	NO_2	
PH	10/18/2000	26.33	10.33			21.07	10.10	1.05	14.38	13.38	8.19	9.32	8.71	10
CH	10/19/2000	10.41	6.28	17.45	12.25	11.71	7.68	0.05	10.75	10.56	8.72	4.82	15.07	10
FOR	**11/11/2000**	**34.88**	**11.51**	**1.33**	**5.05**	**24.34**	**11.95**	**0.90**	**8.30**	**8.08**	**6.20**	**37.23**	**0.05**	**10**
CR	**11/12/2000**	**38.90**	**15.35**	**1.08**	**5.63**	**11.06**	**9.41**	**0.14**	**9.27**	**6.92**	**5.41**	**36.15**	**2.26**	**10**
CR	11/22/2000	29.75	14.46	0.39	4.89	12.94	7.71	0.05	3.78	8.13	5.11	42.43	2.70	10
GH	11/27/2000	81.81	24.77	20.75	14.70	23.36	9.80	0.60	10.00	10.06	7.29	8.68	8.48	10
FGR	**12/1/2000**	**13.92**	**6.43**	**0.17**	**3.92**	**17.11**	**8.15**	**0.22**	**5.66**	**13.80**	**11.05**	**63.24**	**16.94**	**10**
FOR	**12/2/2000**	**14.09**	**8.25**	**1.02**	**6.99**	**44.69**	**10.91**	**0.67**	**12.89**	**16.46**	**9.90**	**4.72**	**10.03**	**10**
CH	**12/3/2000**	**22.98**	**15.54**	**0.66**	**7.76**	**18.24**	**14.27**	**0.91**	**13.66**	**20.72**	**13.72**	**3.49**	**8.11**	**10**
CH	**12/4/2000**	**31.69**	**15.05**	**0.71**	**7.94**	**30.02**	**17.20**	**0.83**	**17.34**	**25.49**	**13.28**	**3.94**	**6.90**	**10**
CH	**12/5/2000**	**20.96**	**15.62**	**1.41**	**8.11**	**32.43**	**18.37**	**1.26**	**19.48**	**24.74**	**13.81**	**22.90**	**9.56**	**10**
FOR	**12/6/2000**	**17.70**	**12.17**	**0.56**	**7.61**	**15.20**	**8.79**	**0.45**	**21.04**	**12.67**	**9.45**	**22.14**	**10.22**	**10**
GH	12/7/2000	25.33	14.45	0.35	7.49	29.73	13.48	0.37	19.33	25.97	14.64	6.10	14.50	10
CH	12/8/2000	24.38	11.58	2.15	13.58	10.85	6.58	0.83	18.55	15.41	9.26	14.07	17.23	10
CH	12/9/2000	17.39	14.11	5.88	9.04	6.79	5.42	1.67	15.20	12.44	8.06	1.68	8.30	10
CR	12/10/2000	20.35	13.97	3.07	8.15	20.83	8.87	0.21	11.02	15.57	8.97	16.36	16.69	10
CH	12/12/2000	19.36	9.00	2.52	10.62	12.83	5.89	1.68	11.15	10.26	5.98	3.33	8.25	10
FOR	12/14/2000	22.76	10.59	4.80	9.06	50.25	14.51	6.75	16.85	11.52	6.53	7.71	12.46	10
FOR	12/15/2000	11.24	5.11	1.81	11.22	12.84	5.24	2.49	10.66	8.79	6.03	16.48	11.16	10
CR	12/20/2000	12.09	6.91	1.08	4.75	14.46	5.78	0.09	2.78	8.19	6.59	12.27	4.78	10
CH	12/22/2000	14.37	7.42	0.60	6.30	10.63	5.14	0.14	2.83	12.87	7.80	2.35	4.41	10
FOR	12/23/2000	21.35	8.13	1.53	7.12	23.98	10.79	0.46	7.35	9.32	6.17	14.42	13.33	10
FOR	12/24/2000	14.02	8.70	1.03	6.99	18.24	8.05	0.42	6.20	10.89	5.85	9.58	10.85	10
CH	12/29/2000	10.28	5.32	12.72	8.16	16.04	6.42	0.39	5.46	12.89	7.87	1.08	6.64	10
FOR	**12/31/2000**	**16.02**	**6.47**	**0.88**	**5.47**	**16.83**	**6.36**	**0.03**	**3.21**	**9.06**	**6.11**	**11.52**	**11.35**	**10**
CH	**1/1/2001**	**22.94**	**8.97**	**0.76**	**5.74**	**36.49**	**17.38**	**0.12**	**5.19**	**15.15**	**8.15**	**1.14**	**5.21**	**10**
FOR	**1/2/2001**	**23.75**	**14.08**	**0.72**	**6.63**	**22.75**	**13.86**	**0.07**	**2.45**	**16.75**	**10.05**	**0.94**	**5.34**	**10**
CH	**1/3/2001**	**33.98**	**20.92**	**4.83**	**12.53**	**31.13**	**22.24**	**0.34**	**10.61**	**26.76**	**20.35**	**1.32**	**14.11**	**10**
CH	**1/4/2001**	**27.94**	**12.27**	**5.92**	**8.06**	**27.25**	**16.30**	**0.99**	**13.50**	**27.72**	**19.17**	**2.05**	**13.93**	**10**
GH	1/5/2001	18.31	11.12	30.15	23.74	23.61	14.01	1.84	35.66	23.44	10.96	2.38	9.96	10
GH	1/6/2001	19.33	10.64	3.72	8.00	12.34	10.23	3.98	29.17	16.47	10.07	13.50	28.33	10
FOR	1/10/2001	15.49	8.65	1.00	5.54	33.25	18.07	0.80	10.68	12.03	8.20	7.15	8.80	10
FOR	1/13/2001	7.98	5.08	0.53	4.27	17.54	12.33	0.25	6.37	7.28	5.27	15.45	16.82	10

Table 3-3

High Ranking 24-hr SO_2 Events. 3-hr and 24-hr SO_2 and 24-hr NO and NO_2 Concentrations are in Units of $\mu g/m^3$

Synoptic Weather	Date	BIP				FTM				WDP				Score
		SO_2_3hr	SO_2_24hr	NO	NO_2	SO_2_3hr	SO_2_24hr	NO	NO_2	SO_2_3hr	SO_2_24hr	NO	NO_2	
CH	1/20/2001	11.61	5.98	1.60	4.94	10.76	7.45	0.01	3.63	10.39	6.59	1.47	6.64	10
CH	1/21/2001	15.26	12.37	0.03	4.22	19.96	11.70	0.10	5.07	11.01	6.51	12.67	10.69	10
FOR	1/31/2001	12.60	10.24	22.35	24.78	33.69	18.53	1.83	22.79	12.74	7.00	22.56	14.38	10
FOR	2/2/2001	20.28	6.60	0.00	9.01	49.50	17.17	1.31	17.38	7.00	5.42	6.50	8.36	10
FOR	2/3/2001	11.24	6.87	0.04	8.65	10.66	5.41	0.06	6.16	9.22	6.80	44.33	7.76	10
PH	2/4/2001	16.15	9.43	14.15	24.13	15.17	8.02	0.71	11.51	21.10	11.93	5.77	14.06	10
GH	2/5/2001	13.38	6.60	13.51	14.88	14.19	5.63	0.84	12.68	14.74	10.40	5.50	16.94	10
CR	2/11/2001	13.49	9.33	0.57	8.69	13.26	7.37	0.34	6.10	11.89	7.45	23.94	15.71	10
CH	2/18/2001	18.42	10.63	0.46	8.89	17.79	5.76	0.10	5.29	14.79	8.67	32.91		10
CH	**3/7/2001**	**12.33**	**7.24**	**20.05**	**10.91**	**18.45**	**8.95**	**0.43**	**4.31**	**12.74**	**6.08**	**18.13**	**9.62**	**10**
GR	**3/8/2001**	**19.43**	**12.14**	**24.38**	**20.14**	**17.18**	**6.34**	**1.60**	**8.85**	**14.90**	**6.96**	**3.64**	**10.51**	**10**
CH	3/10/2001	23.40	10.99	0.31	12.41	18.19	10.68	0.27	6.82	17.01	9.29	50.98	19.49	10
CH	5/14/2001	22.90	8.24	2.91	10.43	10.24	5.60	0.00	4.89	51.43	12.51	29.10	5.35	10
GH	**7/10/2001**	**11.66**	**5.42**			**12.95**	**7.46**	**0.01**	**2.63**	**6.65**	**5.83**	**1.65**	**2.63**	**10**
GH	**7/12/2001**	**14.75**	**7.83**			**20.11**	**11.38**	**0.02**	**4.22**	**6.87**	**5.53**	**5.67**	**3.31**	**10**
CH	**7/14/2001**	**17.08**	**9.07**	**2.56**	**13.83**	**30.39**	**15.96**	**0.00**	**3.60**	**16.40**	**9.75**	**3.39**	**12.25**	**10**

3.1.4 Results

The cases selected for episodic modeling are listed in **Table 3-4**. In all cases, except Case 4, either the 3-hr or 24-hr SO_2 concentrations at BIP were higher than the corresponding increment, meaning that it was possible the increment could be exceeded. The sixth case was selected to represent average (non-episodic) conditions. Because 3-hr SO_2 concentrations above the increment often contribute to 24-hr SO_2 concentrations above the increment, the cases selected for evaluating 24-hr SO_2 model performance are also useful for evaluating 3-hr SO_2 model performance. Transport from various onshore source locations to the BNWA was evident in four cases (1, 2, 4, and 5). Two of the cases are thought to have had impacts from regional sources because the 24-hr SO_2 concentrations at BIP, FTM, and WDP are within a factor of two.

Table 3-4

Cases Selected for Modeling

Case	Dates
1	December 1-6, 2000
2	March 2-8, 2001
3	July 9-14, 2001
4	August 8-13, 2001
5	November 8-13, 2000
6	December 30, 2000–January 4, 2001

In two cases, emissions transported from onshore regions appear to be regional events.

- December 1-6, 2000. The BIP 24-hr SO_2 concentration for each day was within a factor of 1.4 of 24-hr SO_2 concentrations at WDP and FTM, excluding the start day. This episode included a monitored 3-hr SO_2 concentration at BIP that was 25% greater than the 3-hr increment.
- December 30, 2000 through January 4, 2001. The BIP 24-hr SO_2 concentration was within a factor of 2 of 24-hr SO_2 concentrations at WDP and FTM. The BIP 24-hr SO_2 concentration exceeded the increment on December 31-January 4. The maximum 24-hr SO_2 concentration was four times the increment. This case included a 3-hr SO_2 concentration at BIP that was 35% greater than the increment.

In three cases, emissions transported from onshore regions appear to be isolated events, that is, high concentrations were not observed at all three sites.

- November 8-13, 2000. The maximum 3-hr and 24-hr SO_2 concentrations in this time period are factors of 1.6 and 3 greater than their respective increments and 3 and 6 times greater than the 3-hr and 24-hr SO_2 start-day concentration, respectively. An isolated SO_2 event occurred on November 12, 2000 — the maximum BIP 24-hr SO_2 concentration was 1.5 times that at FTM and nearly 3 times that at WDP. A monitored 3-hr SO_2 concentration occurred at BIP during this episode that was 55% greater than the 3-hr increment.

- March 2-8, 2001. The start-day 24-hr SO_2 concentration was five times less than the peak value measure at BIP during this period. The peak 24-hr SO_2 concentration was twice the increment. There were no 3-hr SO_2 concentrations above the increment. On four of these six-days, the SO_2 24-hr concentration was less than 8 $\mu g/m^3$. Twenty-four-hour SO_2 concentrations less than 8 $\mu g/m^3$ contributed to half the annual SO_2 concentration.
- July 9-14, 2001. Emissions were transported from offshore to the BNWA on the first five days of this episode, followed by a flow reversal when emissions were transported from onshore. A sea breeze was present during this period. The month of July was unique because (1) the monthly average SO_2 concentrations relative to NO_2 concentrations were low in summer, and 24-hr SO_2 concentrations less than 8 $\mu g/m^3$ occurred on five of these six days; and (2) 24-hr SO_2 concentrations less than 8 $\mu g/m^3$ contributed to half the annual SO_2 concentration.

The five cases were also characterized by the following features:

- Days on which 24-hr NO_2 concentrations occurred were almost equally split, both greater than and less than 7 $\mu g/m^3$; 24-hr NO_2 concentrations greater than 7 $\mu g/m^3$ contributed to half the annual average NO_2 concentration.
- A synoptic weather pattern distribution (CH, 44%; FOR, 28%; CH, 11%; and CR, 5%) closely matched the distribution for all days in the study year when 24-hr SO_2 concentrations were above the increment (CH, 40%; FOR, 25%; GH, 15%; and CR, 10%).

3.2 METEOROLOGICAL CONDITIONS DURING THE SELECTED CASES

To assist in understanding the meteorology associated with each case selected for episode-type modeling and providing context for the air quality model performance evaluations, we characterized meteorological conditions for each case by reviewing surface and upper-air weather maps and calculating 72-hr backward trajectories from BIP, WDP, and FTM at three elevations (50, 300, and 600 m) using the HYbrid Single-Particle Lagrangian Integrated Trajectory (HYSPLIT) model (Draxler and Hess, 1997). HYSPLIT trajectories were obtained from the NOAA HYSPLIT web site (http://www.arl.noaa.gov/ready/hysplit4.html) and surface and upper-air weather maps were obtained from the NOAA Daily Weather Maps web site (http://www.hpc.ncep.noaa.gov/dailywxmap). Case period summaries are provided in the following subsections.

3.2.1 Case 1: December 1-6, 2000

On December 1, much of the central United States was under the influence of strengthening 1038 mb Canadian high pressure centered near the border of North Dakota and Canada (**Figure 3-2a**). A rapidly advancing cold front located northwest of Louisiana was associated with a low pressure region in Missouri. As the cold front moved through Louisiana on December 1, it produced overcast conditions and scattered precipitation. By the morning of December 2, the high pressure center had advanced across Minnesota, and the cold front had passed through the BNWA (**Figure 3-2b)**. This frontal passage started an extended period of synoptically driven northerly offshore flow over the BNWA that persisted through out the remainder of the episode.

(a) (b)

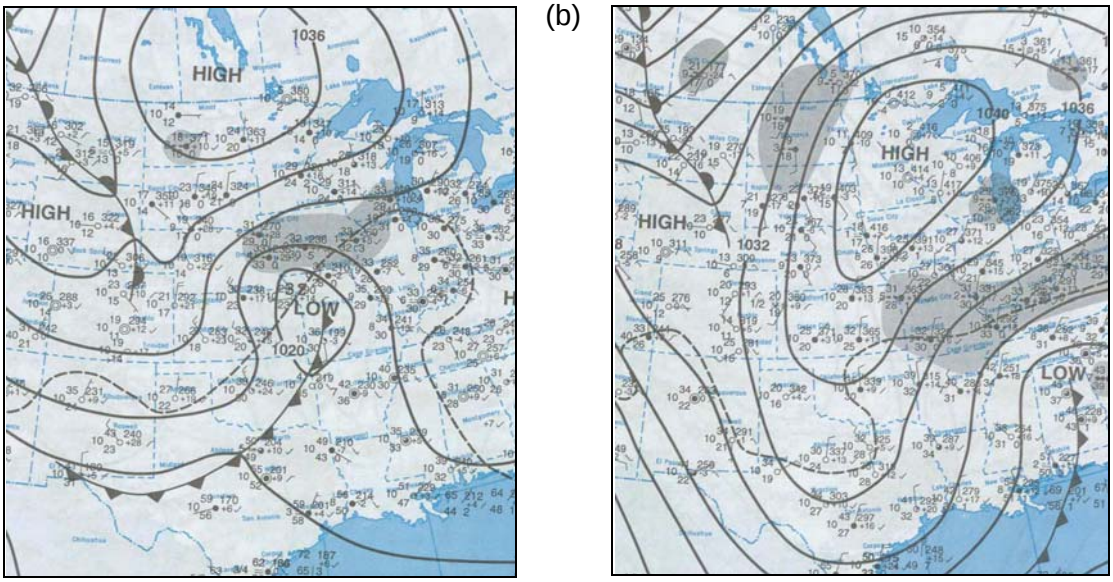

Figure 3-2. Surface weather map at 700 LST for (a) December 1 and (b) December 2, 2000.

As this large high pressure area moved southeast across the Upper Midwest and into Tennessee by December 4, the clockwise flow around the high maintained northerly and northeasterly offshore flow at BNWA (**Figure 3-3**). Another strong Canadian high pressure system and cold front located in North Dakota on December 4 quickly moved south through the Plains and then through Louisiana on December 5 and 6, reinforcing the northerly flow regime at BNWA. HYSPLIT backward trajectories indicated deep (through 600 m) southward transport from onshore areas to the BNWA monitoring sites during this episode.

(a) (b)

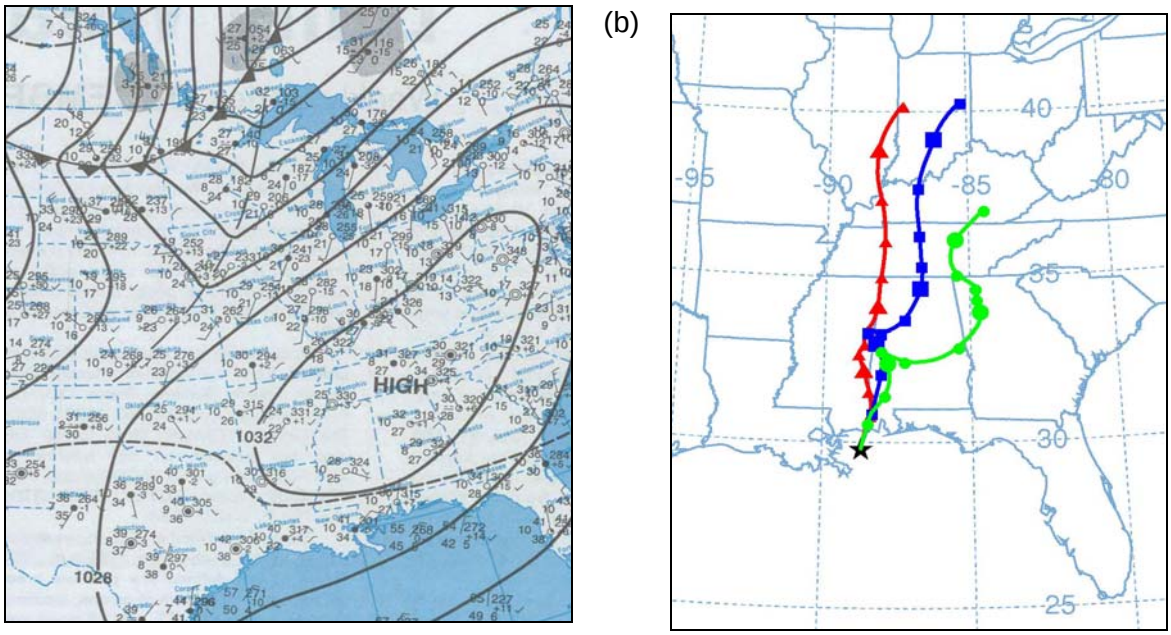

Figure 3-3. Surface weather map for December 4, 2000, at 0700 LST (a), and 72-hr backward trajectories from the NOAA-HYSPLIT model ending on December 5, 2000, at 1200 LST (b) from BIP at 50 m (red triangles), 300 m (blue squares), and 600 m (green circles).

3.2.2 Case 2: March 2-8, 2001

In the days leading up to this case, a quasi-stationary frontal zone was located over the Gulf Coast. In response to an approaching upper-level disturbance from the west, a wave developed along the front on the Texas Gulf Coast on March 2, resulting in a significant overrunning precipitation event over southern Louisiana on March 2 and 3. The BWNA was on the southern side of the frontal zone, and counter-clockwise flow around the developing low pressure system produced southerly and southwesterly onshore winds over the BNWA, as indicated by HYSPLIT backward trajectories (**Figure 3-4**).

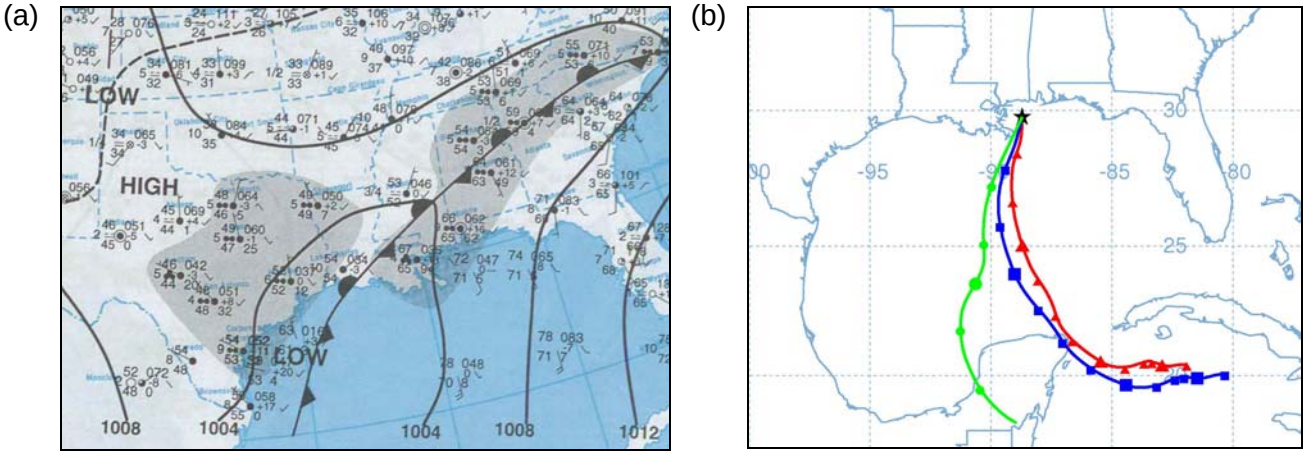

Figure 3-4. Surface weather map from March 3, 2001, at 0700 LST (a), and 72-hr backward trajectories from the NOAA-HYSPLIT model ending on March 3, 2001, at 1200 LST (b) from BIP at 50 m (red triangles), 300 m (blue squares), and 600 m (green circles). The 600-m trajectory is shorter than 72 hours because it reached the edge of the HYSPLIT model domain.

As the low pressure system moved northeast into the Appalachians on March 3, the quasi-stationary frontal zone transitioned into a cold front, which passed through Louisiana and the BNWA and brought moderate westerly winds and fair weather conditions. Under the influence of weak continental high pressure on March 4-7, surface winds weakened, and transitioned from northwesterly flow on March 5, to northerly flow on March 7. HYSPLIT trajectories (**Figure 3-5**) highlight this transition and also indicate transport from onshore sources.

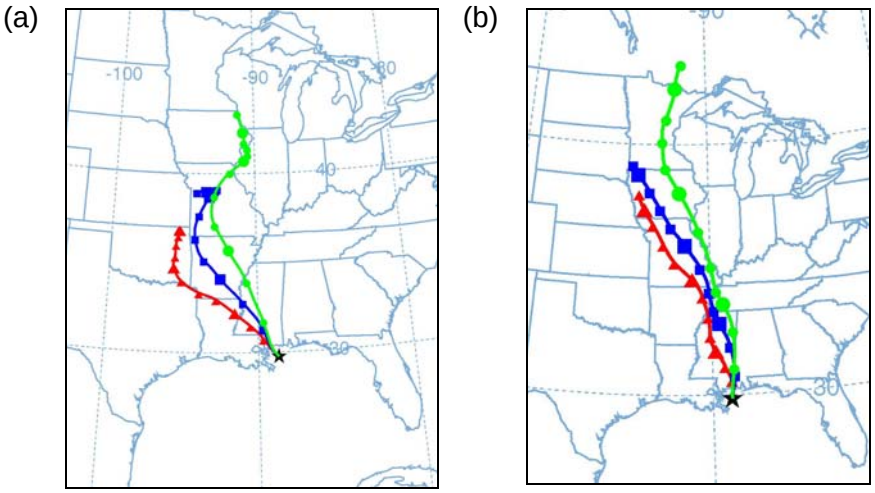

Figure 3-5. Seventy-two-hour backward trajectories from the NOAA-HYSPLIT model ending on March 5 (a) and March 7 (b), 2001, at 0700 LST at BIP at 50 m (red triangles), 300 m (blue squares), and 600 m (green circles).

3.2.3 Case 3: July 9-14, 2001

For the first five days of this case, the Gulf Coast region was under the influence of a hot and humid maritime tropical air mass, with high pressure and weak wind flow conditions at the surface and aloft. HYSPLIT trajectories, as well as surface weather maps, indicated weak westerly winds at the surface over the Gulf Coast during this time (**Figures 3-6 and 3-7**). Note that, unlike northerly flow conditions where transport is from the land at all three BNWA monitoring sites, westerly flow conditions result in transport primarily from the land (southern Louisiana) at FTM, and primarily from the water at WDP.

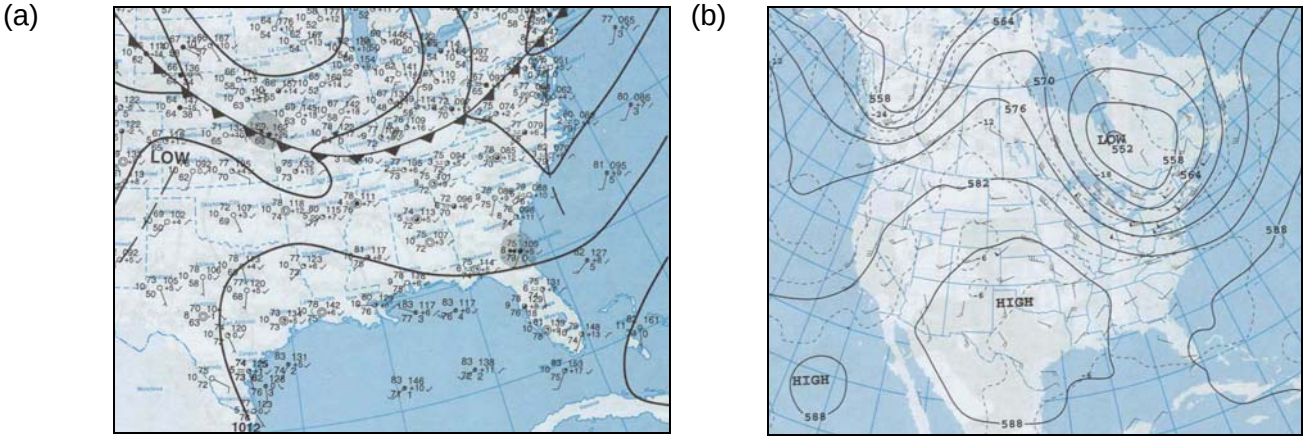

Figure 3-6. Surface (a) and 500 mb (b) weather map from July 11, 2001, at 0700 LST.

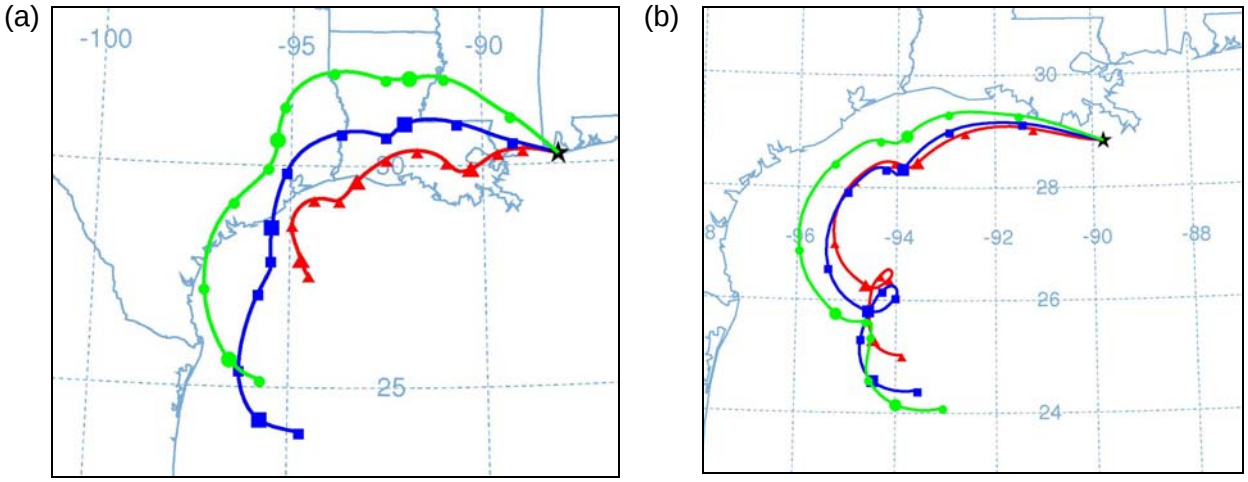

Figure 3-7. Seventy-two-hour backward trajectories from the NOAA-HYSPLIT model ending on July 11, 2001, at 1200 LST at FTM (a) and WDP (b) at 50 m (red triangles), 300 m (blue squares), and 600 m (green circles).

A 500 mb low pressure system initially located over the Hudson Bay on July 9 moved southeast and slowly expanded its influence into the United States during the episode. This

allowed a cooler and drier continental high pressure system and a cold front to move southward out of Canada and into the central Plains. This slow-moving cold front was located in south-central Missouri at 0700 LST on July 11, and it began passing through the Gulf Coast region the afternoon of July 13, triggering showers and thunderstorms. By the morning of July 14, the front had passed through the Gulf Coast (**Figure 3-8a**), and the surface wind direction, which was predominately from the west for the first five days of this episode, became northerly. July 14 is the only day of this episode where HYSPLIT trajectories (**Figure 3-8b**) indicated northerly surface flow from onshore source regions.

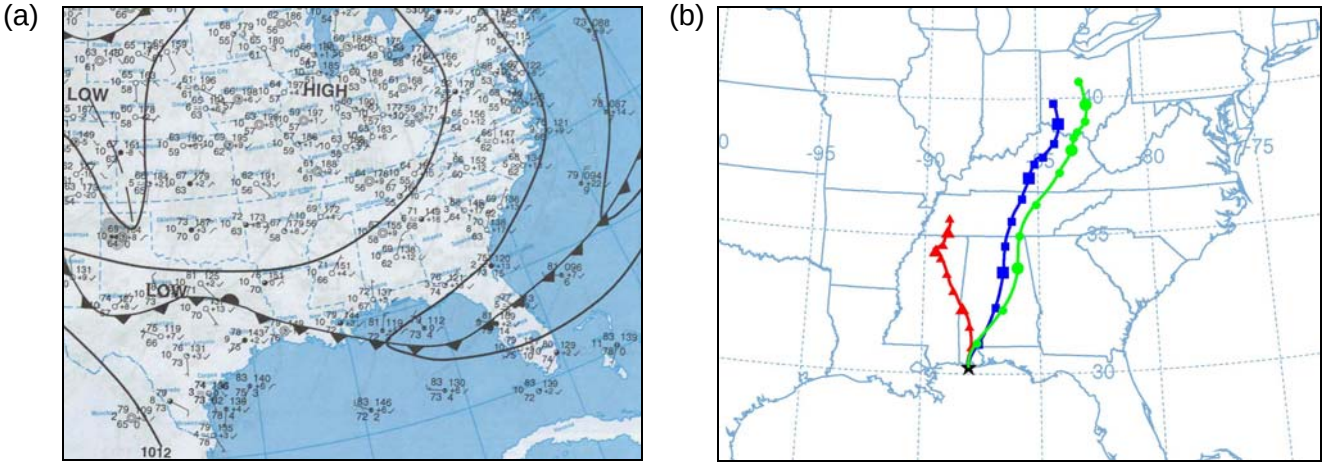

Figure 3-8. Surface weather map from July 14, 2001, at 0700 LST (a), and 72-hr backward trajectories from the NOAA-HYSPLIT model ending on July 14, 2001, at 1200 LST (b) at FTM at 50 m (red triangles), 300 m (blue squares), and 600 m (green circles).

3.2.4 Case 4: August 8-13, 2001

On all days during this case, the Gulf Coast region was under the influence of a typical mid-summer hot and humid air mass, with persistent high pressure and weak winds at the surface and aloft, and daily afternoon thunderstorms. The BNWA was on the western periphery of the Bermuda high pressure system located over the eastern Atlantic Ocean (**Figure 3-9a**). The clockwise flow around the Bermuda high directed moist southerly and southwesterly onshore winds though the BNWA during the entire episode. HYSPLIT trajectories on all days of this episode show persistent southerly and southwesterly transport from the Gulf of Mexico (GOM) (**Figure 3-9b**). Disturbances rotating around an upper-level high pressure ridge centered over the Southern Plains (not shown) contributed to strong thunderstorms on August 10-13. A weak cold front approaching from the north stalled over Arkansas, leaving the large-scale weather pattern over the BNWA unchanged during the episode.

(a) (b)

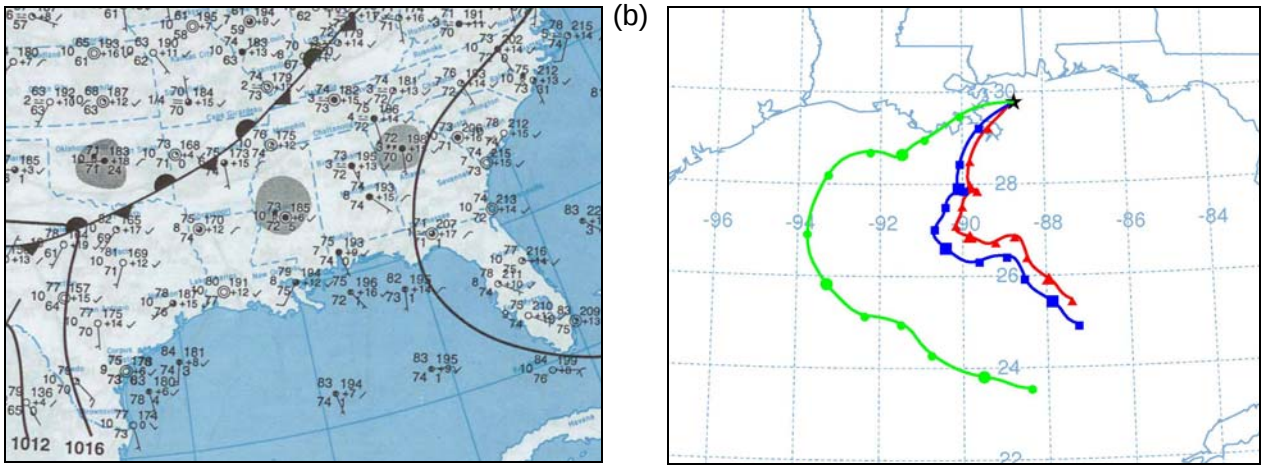

Figure 3-9. Surface weather map from August 12, 2001, at 0700 LST (a), and 72-hr backward trajectories from the NOAA-HYSPLIT model ending on August 12, 2001, at 1200 LST (b) at BIP at 50 m (red triangles), 300 m (blue squares), and 600 m (green circles).

3.2.5 Case 5: November 8-13, 2000

On November 7, a strong cold front associated with a storm system over the Upper Midwest approached the Gulf Coast. Ahead of this front, winds over the BNWA were from the south and southeast. In response to an approaching upper-level disturbance from the west, a wave developed along this front on the Texas coast on November 8 (**Figure 3-10**). This new low pressure system strengthened the southerly flow and produced significant precipitation over the Gulf Coast. The storm moved rapidly to the northeast, and by the morning of November 9, a cold front had passed through the BNWA (**Figure 3-11a**), bringing westerly and northwesterly winds to the region (**Figure 3-11b**).

(a) (b)

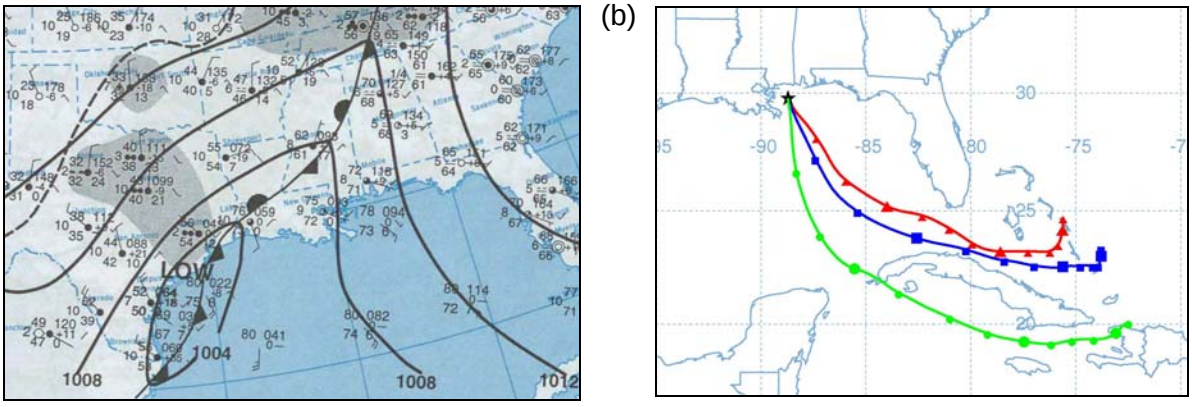

Figure 3-10. Surface weather map at 700 LST for November 8, 2000 (a), and a 72-hr backward trajectories from the NOAA-HYSPLIT model ending on November 8, 2000, at 1200 LST (b) at BIP at 50 m (red triangles), 300 m (blue squares), and 600 m (green circles).

(a) (b)

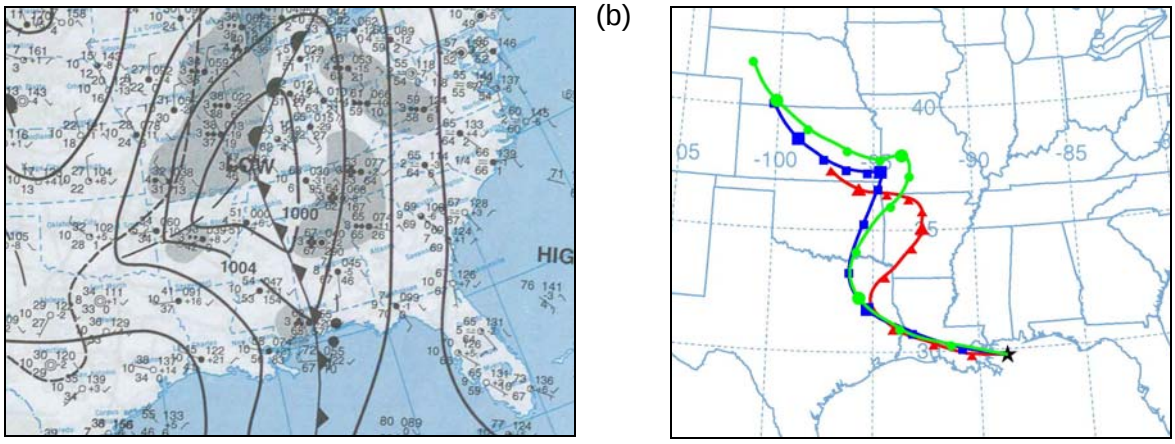

Figure 3-11. Surface weather map at 700 LST for November 9, 2000 (a), and 72-hr backward trajectories from the NOAA-HYSPLIT model ending on November 9, 2000, at 1200 LST (b) at BIP at 50 m (red triangles), 300 m (blue squares), and 600 m (green circles).

As the storm continued northeast on November 9, Canadian high pressure brought colder air and onshore northerly winds to BNWA by the morning of November 10 (**Figure 3-12**). As the high pressure area weakened and moved southeast across the Plains and into the Appalachians on November 10-11, winds in the BNWA weakened, but remained northerly and offshore.

(a) (b)

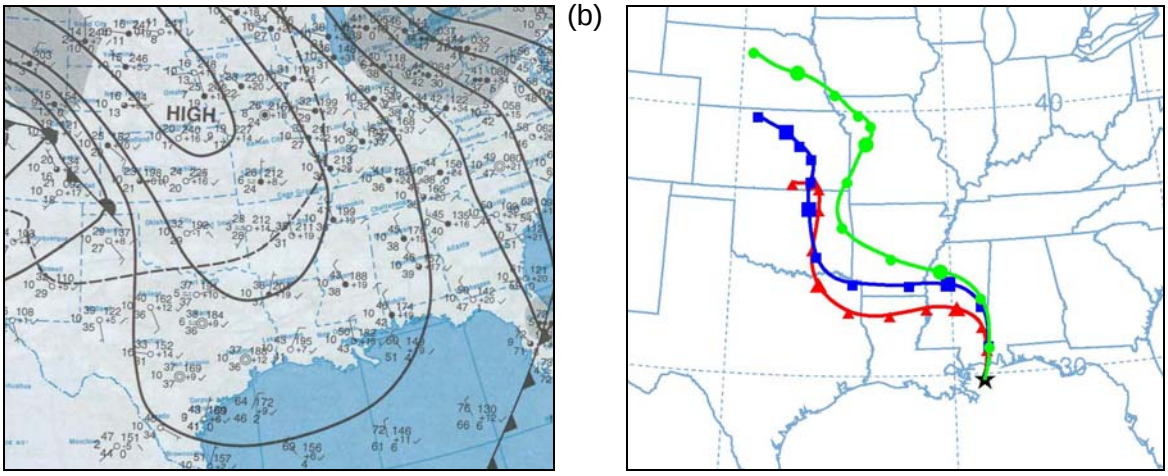

Figure 3-12. Surface weather map at 700 LST for November 10, 2000 (a), and 72-hr backward trajectories from the NOAA-HYSPLIT model ending on November 10, 2000, at 1200 LST (b) at BIP at 50 m (red triangles), 300 m (blue squares), and 600 m (green circles).

By the afternoon of November 11, high pressure had dissipated over the Appalachians, leading to nearly stagnant wind conditions over the Gulf Coast through the morning of November 12 (**Figure 3-13a**). While many stations across the Southeast reported calm winds the morning of November 12, HYSPLIT trajectories at BIP (**Figure 3-13b**) indicated a continuation of very light, offshore northerly winds. These near-stagnation conditions only lasted 12-18 hours as light easterly winds increased the afternoon of November 12 in advance of another cold front approaching from the northwest. The front passed through the BNWA the morning of November 13, along with additional precipitation, and a return to northerly flow conditions at BNWA.

(a) (b)

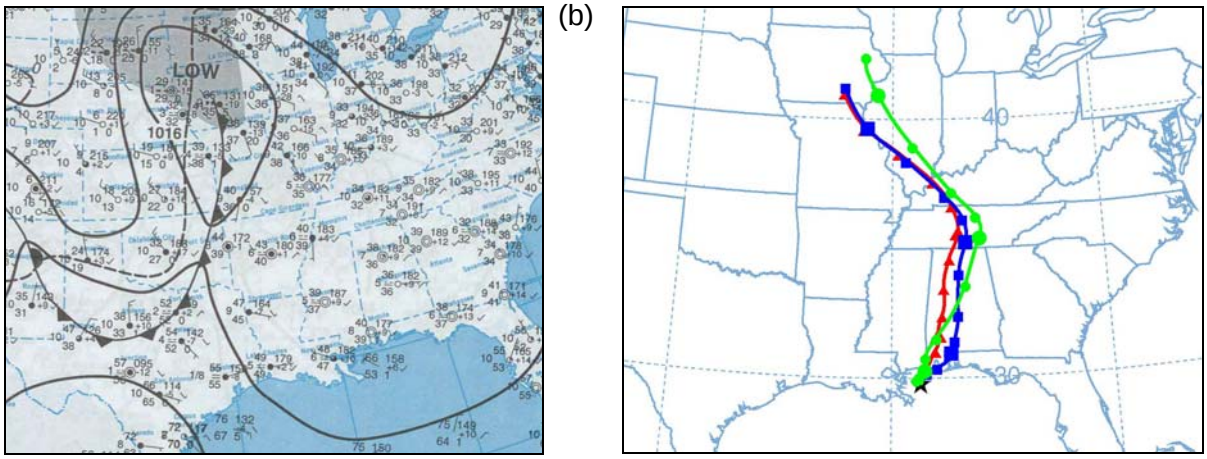

Figure 3-13. Surface weather map at 700 LST for November 12, 2000 (a), and 72-hr backward trajectories from the NOAA-HYSPLIT model ending on November 12, 2000, at 1200 LST (b) at BIP at 50 m (red triangles), 300 m (blue squares), and 600 m (green circles).

3.2.6 Case 6: December 30, 2000 – January 4, 2001

Several strong arctic high pressure systems advanced south from Canada toward the Gulf Coast during this episode, resulting in persistent northerly offshore winds at BNWA. On January 1, a weak disturbance embedded in strong northwesterly flow aloft produced scattered precipitation across Louisiana. This was followed by a reinforcement of arctic air and strong high pressure from the north. This high pressure center was over Arkansas on January 2 and over Houston on January 3 (**Figure 3-14**). Clockwise flow around the high resulted in continued northerly winds at BNWA. HYSPLIT backward trajectories on all days of this episode indicated transport from onshore areas to the BNWA (**Figure 3-15**).

(a) (b)

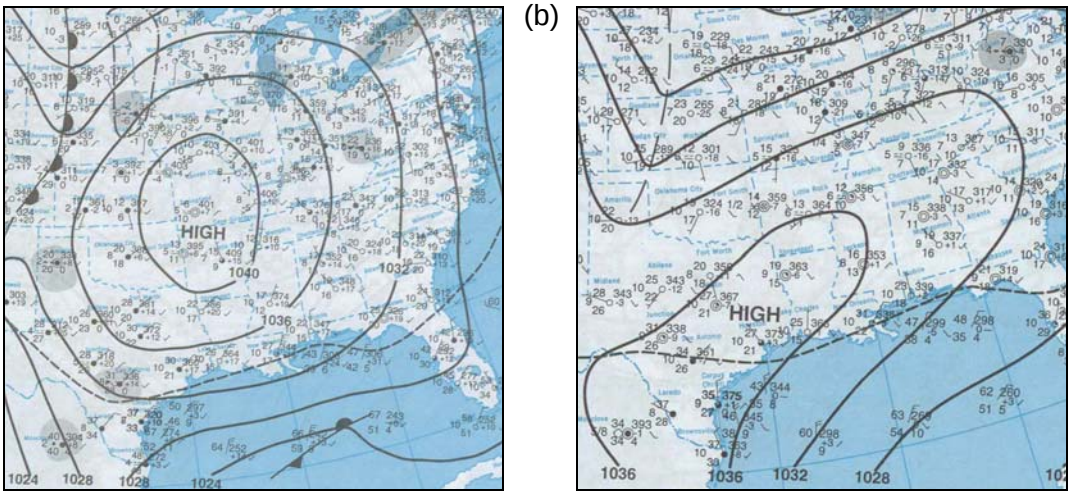

Figure 3-14. Surface weather map at 700 LST for (a) January 2 and (b) January 3, 2001.

(a) (b)

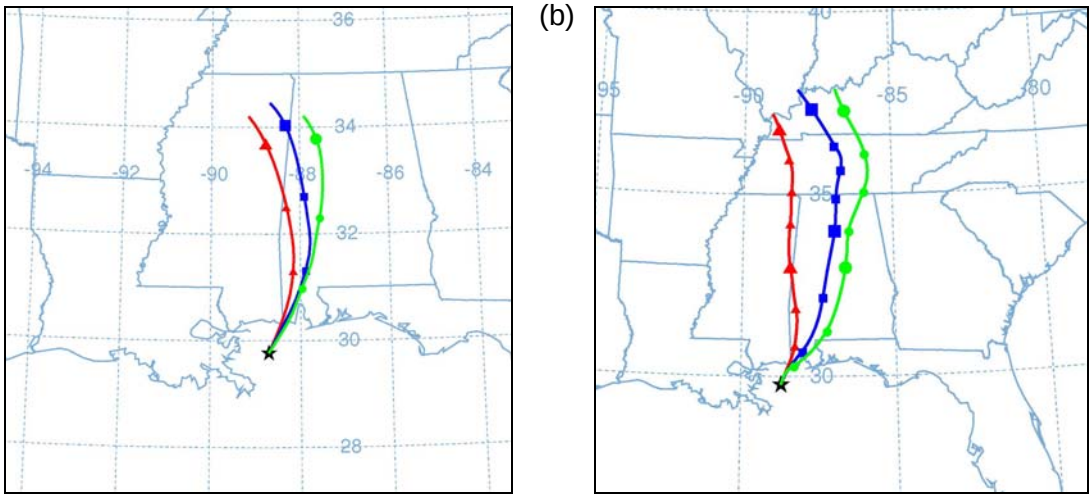

Figure 3-15. Backward trajectories from the NOAA-HYSPLIT model ending on (a) January 2, 2001, and (b) January 3, 2001, at 1200 LST at BIP at 50 m (red triangles), 300 m (blue squares), and 600 m (green circles).

4.0 METEOROLOGICAL MODELING

The Fifth-Generation Pennsylvania State University (PSU)/National Center for Atmospheric Research (NCAR) Mesoscale Model (MM5), Version 3.6.1, released August 1, 2003, was used in this study. This section describes the model, data sources, and processes used to perform meteorological modeling for the study.

4.1 THE PSU/NCAR MESOSCALE MODEL

4.1.1 Model Description

The MM5, described in detail by Grell et al. (1995) and Dudhia (1993), is a nonhydrostatic prognostic meteorological model that utilizes a terrain-following sigma vertical coordinate, such that

$$\sigma = \frac{p_r - p_{top}}{p_{sr} - p_{top}}, \qquad \textbf{(4-1)}$$

where σ is the vertical coordinate, ranging from 1 at the surface to 0 at the predefined model top, p_r is the reference pressure at a given point in the vertical, p_{top} is the pressure at the top of the model (defined to be 50 mb in this modeling study), and p_{sr} is the reference surface pressure. The non-hydrostatic model variables are perturbations to this hydrostatic reference or base state. This study uses 45 vertical sigma levels, defined in Section 4.2.3, with 16 full levels in the lowest kilometer and the first half-layer representing the surface layer at 15 m above ground level (AGL).

The MM5 prognostic variables α (u, v, T, q_v, p', etc.) are represented in the model in flux form, i.e. p*α, where p* is equal to $p_{sr} - p_{top}$. For example, the total pressure p is obtained by solving Equation 4.1 for the base-state, time-invariant value, p_r, and adding the tendency for the non-hydrostatic pressure perturbation p', derived from the model equation for $\partial p^* p'/\partial t$ (see Grell et al., 1995, for details). All prognostic variables, excluding the momentum variables p*u and p*v, are calculated on the cross points of the mesoscale model grid, and the momentum variables are calculated on the dot points (Grell et al., 1995). This grid configuration is referred to as a staggered B grid, as described by Arakawa and Lamb (1977). The vertical grid is also staggered with all calculations made on the sigma half-levels, except for vertical velocity, which is calculated on the full sigma levels.

To represent the moist physics in the model, the Dudhia simple-ice explicit (grid-resolved) moisture scheme is used on all the domains (36 km, 12 km and 4 km). This scheme predicts either cloud water or cloud ice or rain water or snow, depending if the temperature is above or below freezing, and thus does not include any mixed-phase moisture processes, as described in detail by Dudhia (1989) and Grell et al. (1995).

The 36-km and 12-km domains also use the newest Kain-Fritsch convective scheme (KF2) described by Kain (2004) for subgrid-scale cumulus parameterization. This scheme uses θ_e, or equivalent potential temperature, which is a conserved variable for both dry and moist processes. The updates within KF2 include a parameterization for shallow, non-precipitating convection, a minimum entrainment rate to suppress convection in marginally unstable conditions, variable cloud radius, and a minimum cloud depth for deep convection. Even though the assumptions within the parameterization are not really valid at 4-km resolution, Deng and Stauffer (2006) state that the application of the KF2 scheme on the 4-km domain can reduce the tendency for "grid-point storms", i.e. over-predicted precipitation and anomalous flow fields that may result from the application of the explicit moisture scheme alone.

Turbulence processes are represented on all model domains by the PSU Gayno-Seaman Planetary Boundary Layer (PBL) scheme (Gayno et al., 1994; Shafran et al., 2000; Stauffer et al., 1999). Subgrid-scale turbulence is parameterized using a 1.5-order closure turbulence scheme, meaning that all equations are considered first-order, except for the second-order predictive equation for turbulent kinetic energy (TKE). Shafran et al. (2000) have shown that the TKE predictive scheme outperforms other turbulence schemes by more accurately predicting the structure of the PBL in an air quality case under unstable conditions. This version of the model uses an updated version of this scheme, appropriate for saturated conditions and including ice, as described by Stauffer et al. (1999).

The atmospheric radiation forcing is computed using the shortwave parameterization of Dudhia (1989) and longwave parameterization of Mlawer et al. (1997). Radiative fluxes are affected by vapor and cloud and also contribute to the surface energy balance, which is computed here using a force-restore (slab) scheme (Grell et al., 1995). Sea-surface temperature is held constant in time and specified over space from the Moderate Resolution Imaging Spectroradiometer (MODIS) or Eta products described in Section 4.2.4.

4.1.2 Multi-Scale, Four-Dimensional Data Assimilation

The use of Four-Dimensional Data Assimilation (FDDA) programs dates back to Charney et al. (1969) for global-scale atmospheric measurement. Anthes (1974) used nudging FDDA techniques to gradually alter the state of a numerical weather prediction (NWP) model on a time-continuous basis for a hurricane simulation. Since the early 1990's, the idea of using FDDA techniques for meteorological modeling in support of air quality modeling has become relatively standard, e.g., Stauffer and Seaman (1990) and Stauffer et al. (1991). The multi-scale FDDA technique (Stauffer and Seaman, 1994) that is employed in most air quality applications involves a combination of two types of nudging: analysis nudging and observational nudging. Analysis nudging is an excellent way to incorporate synoptic-scale observational data into the model, because the meteorological data exist at the same time and are interpolated over the entire domain to a regular grid, and observation nudging is especially attractive for asynoptic data.

Stauffer and Seaman (1990)assimilated synoptic-scale data in an 80-km resolution NWP model using the analysis nudging technique, combined with individual observation nudging. This method produced favorable results in both the mass fields and the wind fields for conditions where synoptic-scale precipitation was important (e.g., an acid rain study). Conversely, the

technique provided little improvement in situations where precipitation was primarily convective. These results made theoretical sense because synoptic data are very coarse. These data resolved the large, weather-making systems, but did not represent well the convective scales, which were generally much smaller than the model grid cells. Synoptic-scale weather systems last several days, while convective systems exist on a time scale of several minutes to several hours. Upper-air radiosonde data are typically available every 12 hours, so long-lasting weather/precipitation patterns will be better resolved than convective weather/precipitation systems. Stauffer et al (1991) utilized surface data, once every three hours, within the planetary boundary layer (PBL) and obtained improved results for case days with weak large-scale forcing and convection.

Stauffer and Seaman (1994) again used these techniques, but in combination with observations and model resolutions on the mesoscale (30 km and 10 km). The use of a higher-resolution model and observations in a grid-nesting approach was called multi-scale FDDA. It was shown that assimilating gridded analyses of synoptic-scale data on a fine-resolution model grid can have negative effects on the model simulation. Use of individual observation nudging of mesoscale observations on the finer grids, in combination with the synoptic-scale analyses on the coarser grids, was essential to obtain an accurate model simulation on the fine scale.

More positive results were obtained using a one-dimensional (1D) model by Alapaty et al. (2001), who further examined the assimilation of surface data and its effect on the boundary layer. By assimilating surface temperature and moisture observations and adjusting the ground temperature to preserve the surface fluxes, the resulting PBL simulations had significantly lower errors than simulations without surface data assimilation, while minimizing change to the PBL structure. Although difficult to apply to general three-dimensional problems, this work emphasized the attention that needed to be given to the boundary layer in atmospheric dispersion. Pollutants that directly affect the areas studied in air quality projects may never leave the turbulent boundary layer, and concentrations are very dependent on PBL height and wind speeds.

Although effective, assimilation of mass-field (temperature and moisture) data within the PBL is an active area of research. It is more common and less problematic to assimilate surface and radiosonde wind observations throughout the depth of the PBL. Several studies have shown that nudging using radar wind profiler (RWP) data generally reduces the biases in the wind fields (e.g., Kuo and Guo, 1989; Seaman et al., 1995; Michelson and Seaman, 2000). Accurate winds and PBL height are essential in air quality modeling, because they control the ventilation of chemical and particulate concentrations near the earth's surface.

The PBL structure largely depends on the surface energy budget over land and the sea surface temperature (SST) over water. Coastal zone studies rely heavily on accurate low-level temperature fields, so the impact of higher-resolution SST data was also investigated in this Gulf Coast study.

As discussed, the use of the Newtonian Relaxation technique, otherwise known as "nudging," is especially attractive for air quality studies and has been implemented routinely because of the increasing availability of synoptic and asynoptic data from a number of sources including radiosonde, surface mesonets, profilers and satellites. Stauffer and Seaman (1990)

outline the two primary techniques for the assimilation of such data. The first technique is commonly referred to as analysis nudging, where synoptic data are analyzed to a grid, and the model state is then "relaxed" towards the gridded data. The second technique is commonly known as observation nudging. Observation nudging does not require the gridded analysis of data, but instead relaxes the model to an observation under certain temporal and spatial constraints. Both methods were used in this study and can be applied independently or together simultaneously on each grid during a simulation. Data available for this study included standard World Meteorological Organization (WMO) surface and radiosonde measurements, special asynoptic surface data from surface mesonets and oil platforms in the Gulf of Mexico, and RWP data from a number of oil platforms. WMO data were obtained from the National Climatic Data Center (NCDC) accessible at http://www.ncdc.noaa.gov. The sources of special data are described in Section 4.2.6.

Analysis Nudging

Analysis nudging is used on the 36-km and 12-km domains, using 12-hourly analyses based on WMO radiosonde observations, and 3-hourly surface analyses. These analyses are then interpolated to each model timestep, so that the data assimilation forcing is continuous. The analysis nudging equation is represented in the following form:

$$\frac{\partial p^* \alpha}{\partial t} = F(\alpha, \mathbf{x}, t) + G_\alpha W(\mathbf{x}, t) \varepsilon(\chi) p^* \left(\hat{\alpha}_0 - \alpha \right) \qquad \textbf{(4-2)}$$

In this equation, α is the model-dependent variable. The first term, the function F, represents all standard physical forcing terms in the model, with **x** as the spatial dimensions, and t is time. The second term is the analysis nudging term, where G_α determines the relative magnitude of the nudging, and W is a four-dimensional weighting term, which determines how heavily the analysis will be weighted in the horizontal and vertical and in time. The ε term is a confidence factor that can be based on the locations and density of observations that are contained in the analysis. Finally, $p^* \left(\hat{\alpha}_0 - \alpha \right)$ represents the innovation or the difference between the analyzed value of a variable and what the model has determined the value to be at that timestep. This nudging term is used for three-dimensional analysis nudging above the PBL, and for surface-analysis nudging of 3-hourly gridded surface data, which may be assimilated throughout the model-predicted PBL (Stauffer et al., 1991).

In the boundary layer, the model is nudged only to the wind analyses, based on the findings of Stauffer et al. (1991). Stauffer et al. showed that boundary layer structure and development were best represented when standard coarse-temporal resolution (i.e. 12-hourly) temperature and moisture were not nudged within the boundary layer. Surface heat and moisture fluxes can also be adversely influenced by nudging coarse mass fields. Above the PBL, however, wind, temperature and moisture variables are all nudged toward their respective analysis.

Observation Nudging

Observation nudging is used on the 36-km and 12-km domains, as well as the 4-km fine resolution domain. This scheme does not require the observational data to be analyzed to a grid, but instead relaxes the model to observations based on a predetermined time window and radius of influence (Stauffer and Seaman, 1994). The horizontal weighting function w_{xy} is a Cressman function given by

$$w_{xy} = \frac{R^2 - D^2}{R^2 + D^2} \tag{4-3}$$

where, R is the radius of influence of the observation, and D is the distance between the model grid point and the observation. If an observation lies outside the radius of influence, it carries zero weight at the given grid point. Observations are generally interpolated along constant pressure or height levels (except at the surface where sigma is used) to account for complex terrain conditions. A modified weighting scheme (Stauffer and Seaman, 1994) is used to adjust the influence regions to reflect the terrain details. This interpolation minimizes the risk of having an observation influence an area that would not be physically reasonable, for example a valley observation applied to the top of a mountain.

If any observations exist within the confines of the desired spatial and temporal constraints, the model will be relaxed toward these observations as follows:

$$\frac{\partial p^* \alpha}{\partial t} = F(\alpha, \mathbf{x}, t) + G_\alpha p^* \frac{\left[\sum_{i=i}^{N} W_i^2(\mathbf{x}, t) \gamma_i \left(\alpha_0 - \hat{\alpha} \right)_i \right]}{\sum_{i=1}^{N} W_i(\mathbf{x}, t)} \tag{4-4}$$

In this Newtonian relaxation equation all the variables are defined as before, and the weighting factors W contain components representing the horizontal, vertical and time separations of each observation from the model. Each observation located within the current time window and the radius of influence from a given grid cell is weighted in the correction as indicated within the summations over all observations. The variable γ_i is a confidence factor based on the usability or accuracy of the observations.

4.1.3 MODIS Sea-Surface Temperature

The MODIS is a sensor on the National Aeronautics and Space Administration (NASA) Terra and Aqua satellites. This sensor contains infrared bands that are designed specifically for acquiring SST measurements. The MODIS sensor was designed to be comparable to, or to outperform, the Advanced Very High Resolution Radiometer (AVHRR), by containing the conventional infrared wavelengths — 10-12 μm — in addition to three additional bands in the 3.5-4.2 μm, mid-infrared range (Minnett et al., 2002).

Minnett et al. (2002) determined that a direct comparison of the 10-12 μm bands of MODIS and AVHRR shows that the MODIS is at least comparable to the best AVHRR measurements. This result is favorable because the AVHRR is one of the most commonly used SST products in many disciplines.

The MODIS SST product also has several advantages over other commonly used SST products for numerical modeling. The National Centers for Environmental Prediction (NCEP) produces daily SST fields (available at http://wwwt.emc.ncep.noaa.gov/mmb/rreanl/index.html) based primarily on buoy and ship data. One of the major limitations to this data set is its coarse resolution of approximately 0.5 degrees, since it is derived primarily from ocean buoy and ship observations. Furthermore, the product is smoothed significantly. For these reasons, this NCEP Reanalysis SST product does not provide a model with detailed SST structure. A typical NCEP Reanalysis SST sample is given in **Figure 4-1**.

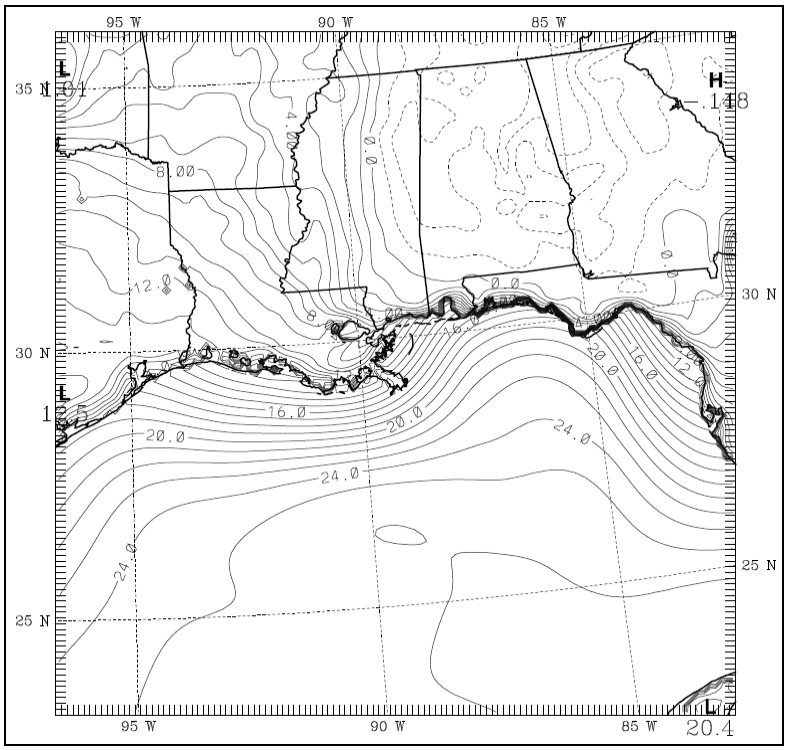

Figure 4-1. Surface skin temperature (°C) using the NCEP Reanalysis SST product for 1200 UTC, December 1, 2000. Isotherms are drawn every 1°C.

An alternative to the 0.5 degree resolution NCEP SST is the Eta model-derived SST. As the name implies, this product is based on output from the NCEP Eta model. This SST analysis is a more detailed product, as it is typically available at approximately 40-km resolution. This higher resolution is evident in **Figure 4-2**, which shows the surface skin temperature at 1200 UTC, as in Figure 4-1.

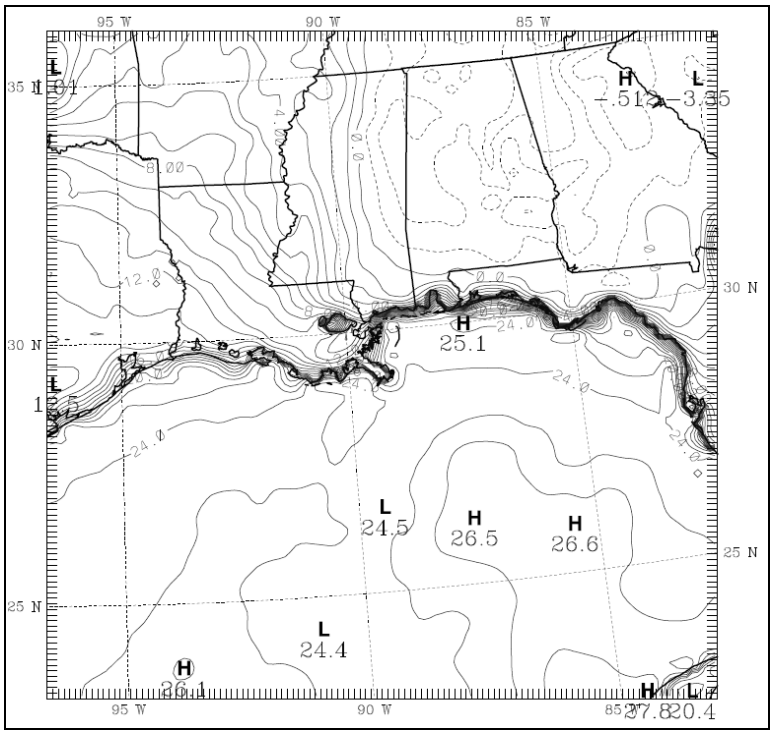

Figure 4-2. Surface skin temperature (°C) using the 40-km resolution Eta SST product for 1200 UTC, December 1, 2000. Isotherms are drawn every 1°C.

The MODIS product is available in a number of resolutions. This study employs both a 36-km resolution product, which is comparable to the Eta SST product, and a finer, 4-km resolution product provided by the MMS. This higher-resolution product should provide finer-scale SST structure in the coastal zone where its effects on Gulf Coast sea breeze circulations can be assessed. **Figure 4-3** shows the structure of the 36-km MODIS SST, and **Figure 4-4** shows the structure of the 4-km MODIS SST product for the same time, 1200 UTC as in Figures 4-1 and 4-2. Note the greater detail in the SST gradients near the coastline.

Typically, numerical modeling studies use archived SST products provided by NCAR, such as the NCEP Reanalysis SST, which is a 0.5-degree, coarse resolution SST product, or the Eta 212-grid SST, which is a 40-km resolution SST product. For modeling studies that are highly influenced by the surface fluxes from water bodies, the NCEP product is too coarse to provide an accurate representation of the SST.

For this project, the effect of the Eta SST product is compared to that based on the MODIS SST product. MODIS SST data can be provided in resolutions as fine as 1-km, but two coarser products (36-km and 4-km) were supplied for this study. Most primary modeling was performed with the 36-km resolution product, which is similar in resolution to the Eta SST product. The MODIS data set was provided in the GRIB format, so no preprocessing of the data set was necessary prior to model input.

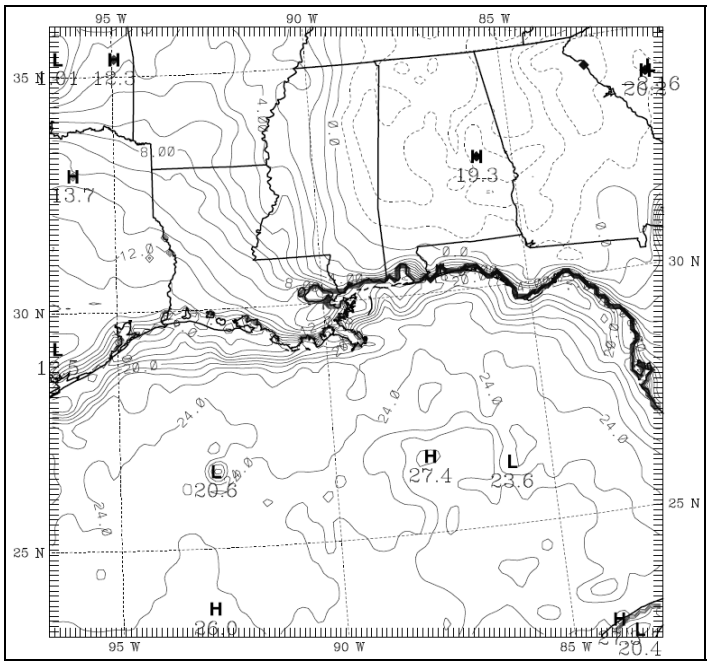

Figure 4-3. Surface skin temperature (°C) using the 36-km resolution MODIS SST product for 1200 UTC, December 1, 2000. Isotherms are drawn every 1°C.

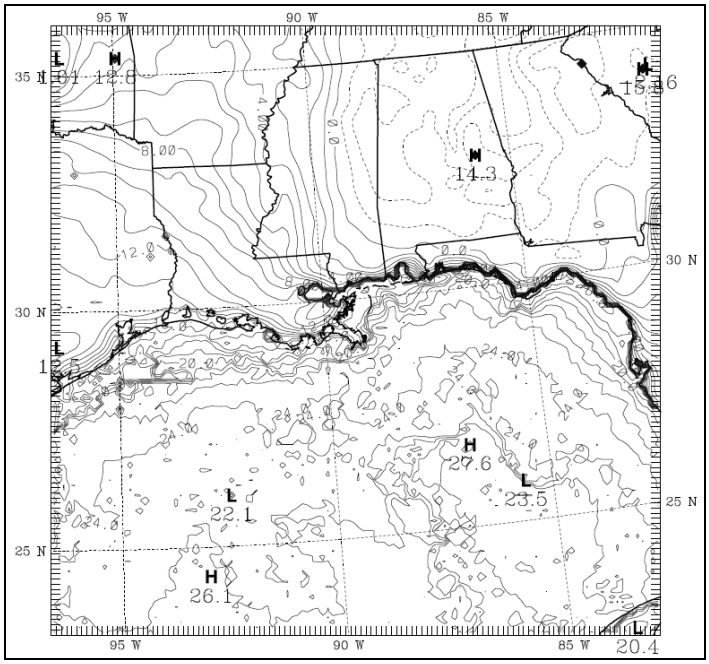

Figure 4-4. Surface skin temperature (°C) using the 4-km resolution MODIS SST product at 1200 UTC, December 1, 2000. Isotherms are drawn every 1°C.

To use the MODIS product, a few simple settings needed to be made to the REGRID MM5 preprocessing program, which is described in the PSU/NCAR Mesoscale Modeling System Tutorial Class Notes and User's Guide (Dudhia et al., 2005) and maps data on to the MM5 domain grid points. First, the SRCSST variable had to be changed from the default NCEP choice to the GRIB choice. Second, the VTSST variable was determined to reflect the appropriate Vtable for the MODIS data. In the Vtable files, the single difference between the two methods is the REGRID Name entry, which is denoted as "SKINTEMP" in the NCEP Vtable, and "SST" in the MODIS Vtable.

The MODIS SST product is a satellite-derived data set based on five channels of the MODIS sensor that "see" in the long-infrared and the mid-infrared, within the confines of two atmospheric "windows." The two long-infrared bands (between 10 μm and 12 μm) correspond directly with the bands of AVHRR. Where MODIS differs from the AVHRR is in the 3.5 μm to 4.2 μm wavelength range. In this wavelength range, AVHRR has one band and MODIS uses three.

Using the two sensor bands in the long-infrared, the MODIS algorithm includes an atmospheric correction algorithm based on past experiences of deriving SST fields from AVHRR (Minnett et al., 2002). Minnett et al. (2002) show that the atmospheric correction algorithm is

$$SST = a + bT_{31} + c(T_{31} - T_{32})T_{sfc} + d(T_{31} - T_{32})(\sec(\theta) - 1) \quad \textbf{(4-5)}$$

where T_{31} and T_{32} are the brightness temperatures from the two long-wave infrared bands, bands 31 and 32 on the MODIS sensor respectively, T_{sfc} is a first guess temperature, based on NCEP reanalysis data, and θ is the satellite zenith angle. The coefficients a, b, c, and were determined through experiments and theory. These equations were used, along with a strategy to fill holes in the analysis caused by clouds and rain, by EarthTech and provided to us by the MMS.

4.2 METHODOLOGY

In this section, the specific configuration of the MM5 used in the experimental design of this study is discussed, including the domain details, the vertical sigma layer distribution, FDDA parameters and special data sources. Additionally, experiments are defined to determine the best possible combination of model options and data to produce the most accurate meteorological fields using 36-km and 12-km model resolutions for a year-long air quality study. Experiments are also designed to assess the added value of 4-km resolution, 4-km SST data, and modified physics options for moist convection at 4-km resolution.

4.2.1 Model Configuration and Initialization

The configuration of domains in a modeling study is chosen carefully. The domain boundaries must be located far enough from the area of interest and where there is little interference with complex terrain, while encompassing a large enough area in the coarsest domain so that meaningful lateral boundary conditions can be supplied to the inner nested

domains. The nested domains should include a sufficient area away from the lateral boundaries, and cover the area of interest.

Gridded data for model initial conditions, lateral boundary conditions, and FDDA analyses must also be considered. Ideally, a data source (e.g., NCEP Reanalysis, Eta Data Assimilation System, and Global Data Assimilation System) should be chosen so that it has comparable resolution and minimal interpolation is needed between the data set and the model grid points. Preprocessing programs then use this data to create initial and lateral boundary conditions for the coarsest domain, which is then used for interpolation to the next successive model grid. These data fields are also used to create the FDDA gridded analyses, for analysis nudging, by enhancing them with the standard observations that have already undergone quality control (QC).

4.2.2 Horizontal Nest Configuration

This study uses three domains, with resolutions of 36 km, 12 km, and 4 km. The coarse (36-km) domain, covers the contiguous United States and is primarily used to provide lateral boundary conditions for the 12-km domain. Since the focus area of this study is in the area of Louisiana and the nearby coast of the GOM, a large amount of both landmass and water had to be covered, as shown in **Figure 4-5**. **Table 4-1** lists the details of the three model domains.

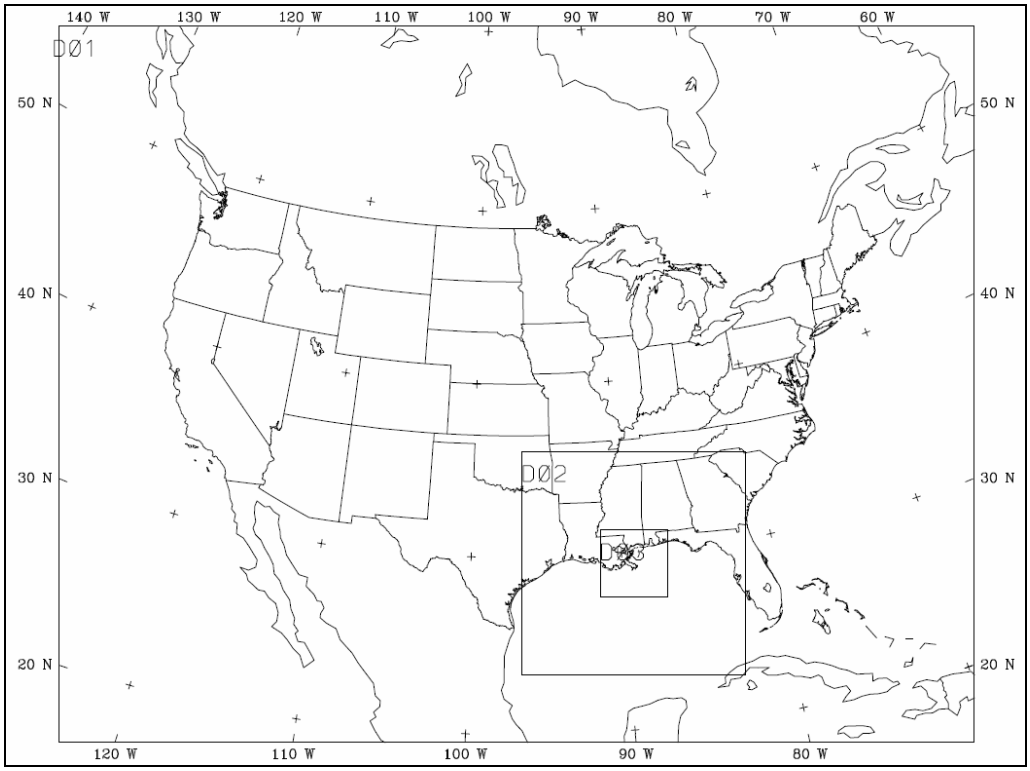

Figure 4-5. Configuration of the three MM5 domains. D01 (domain 1) has a horizontal resolution of 36 km, D02 has a resolution of 12 km, and D03 has a resolution of 4 km.

Table 4-1

Model Domain Configuration

Domain	Resolution (km)	E-W Gridpoints	N-S Gridpoints	Center Latitude	Center Longitude
1	36	165	129	40.00	-97.00
2	12	121	121	29.38	-89.19
3	4	109	109	29.35	-89.23

4.2.3 Vertical Sigma Layer Distribution

The resolution of the vertical sigma layers in the mesoscale model is just as important as the horizontal resolution of the model. To properly represent the intricate upward and downward motions and vertical mixing — especially in the atmospheric boundary layer — it is necessary to have sufficient resolution in the vertical. In this study, 45 vertical sigma layers are used (**Table 4-2**), with the vertical distribution and layer thicknesses shown in **Figure 4-6**. In this case, approximately 22 sigma levels are included within 1,500 m of the surface, which is a typical height for the top of a warm season atmospheric boundary layer. With this resolution, the first sigma layer has a total thickness of approximately 24 m, and the calculation level for this first sigma level of 0.997 is around 12 m agl, with increasing thickness between layers with increasing height. The highest resolution is thus created closest to the surface, where the meteorological processes are the most difficult to resolve. The surface layer, represented by the first calculation layer (half-layer) is 12 m agl.

Table 4-2

Model Sigma Levels

k	Sigma	k	Sigma	k	Sigma
1	0	16	0.668	31	0.892
2	0.046	17	0.692	32	0.902
3	0.092	18	0.714	33	0.910
4	0.138	19	0.734	34	0.918
5	0.184	20	0.752	35	0.926
6	0.230	21	0.769	36	0.934
7	0.276	22	0.785	37	0.942
8	0.322	23	0.800	38	0.950
9	0.368	24	0.814	39	0.958
10	0.414	25	0.827	40	0.966
11	0.464	26	0.840	41	0.973
12	0.508	27	0.853	42	0.980
13	0.552	28	0.866	43	0.986
14	0.601	29	0.874	44	0.992
15	0.640	30	0.882	45	0.997

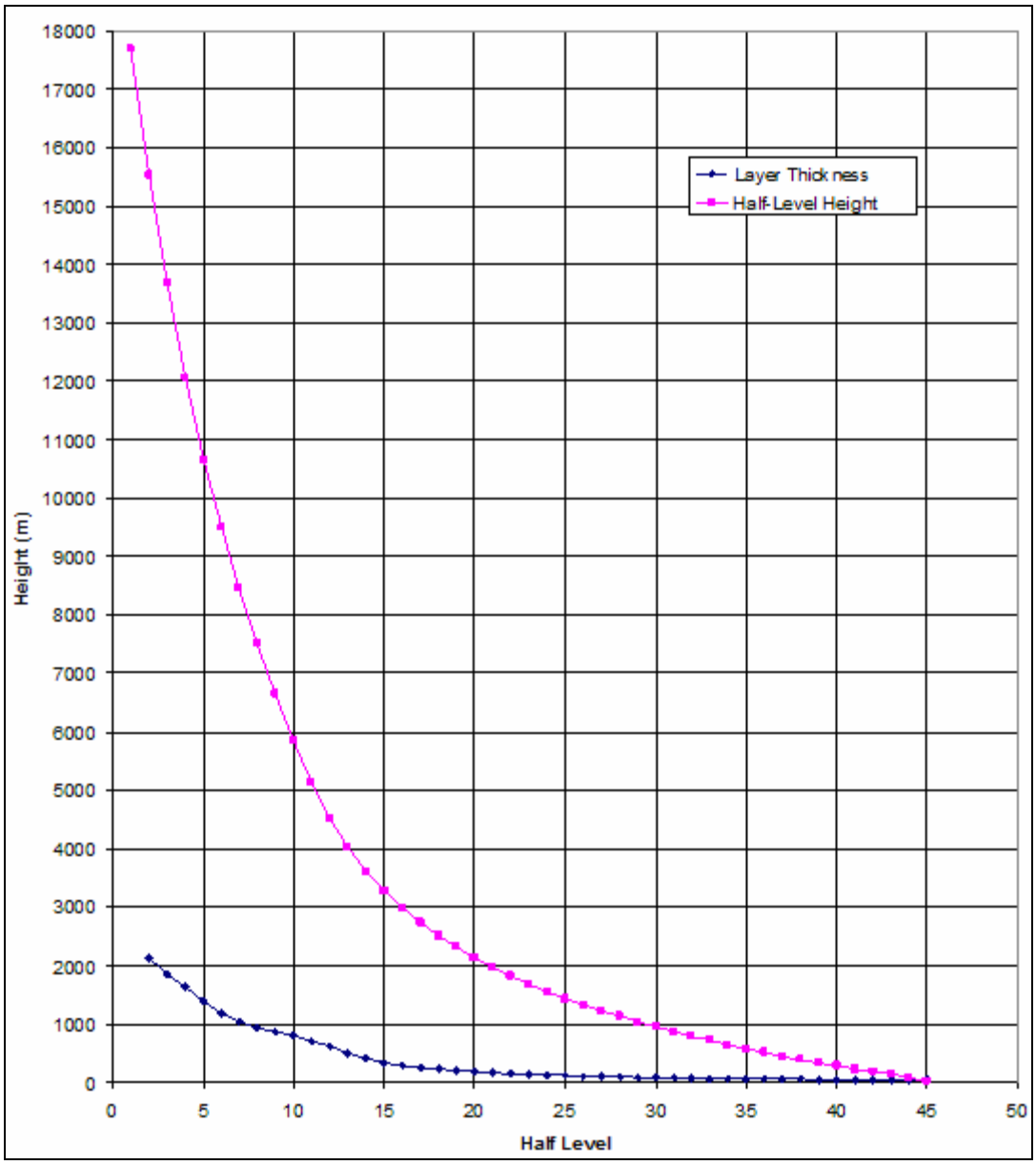

Figure 4-6. Graphical representation of the 45 vertical sigma layer distribution. The thickness of the sigma layers is represented by Series 1 (diamonds), and the approximate mean height of the individual sigma levels is represented by Series 2 (squares).

4.2.4 Model Initialization

The initial and lateral boundary conditions for this study are derived from the 0000 and 1200 UTC Eta-212 grid analyses. Temperature, horizontal winds, and relative humidity are acquired at approximately 40-km resolution at the mandatory and supplemental pressure levels (1000, 975, 950, 925, 900, 875, 850, 800, 750, 700, 650, 600, 550, 500, 400, 300, 250, 200, 150 100 mb), plus sea-level pressure, and ground temperature. These fields are projected first onto

the coarsest, 36-km resolution model domain grid, and used as "first guess" fields. The next step involves an objective analysis, in which the "first guess" fields are enhanced by standard observational data, i.e. radiosonde and standard surface observations. These observations are applied using the objective analysis technique outlined in Benjamin and Seaman (1985). In this technique, elliptical and "banana-shaped" weighting functions are used, which perform better than circular weighting functions, especially in strong flows and curved flows. The objectively analyzed fields are then interpolated from the given pressure levels to the model sigma levels and subsequently used for the model initial conditions. The initial conditions for the 12-km domain and 4-km domain are created the same way using "first guess" fields interpolated to each domain and enhanced by standard WMO observations.

The lateral boundary conditions (LBC) are created differently for each domain, depending on the nesting strategy that is used. For all model experiments, the LBC for the 36-km domain are created in the same way as the initial conditions, at 12-hour intervals starting at 1200 UTC for both upper-air and surface. The 12-km domain LBC for the year-long study are created by interpolating the 36-km domain model output onto the 12-km boundaries, at 1-hour intervals.

The LBC for the experimental 4-km model domain were created using three different methods. The first method is identical to the creation of the 12-km domain LBC, via interpolation from the 12-km model output at 1-hour intervals to the 4-km boundaries. The second and third methods involve tighter coupling of the nesting of the 12-km and 4-km model domains. The second method is also a one-way nesting approach, but it provides LBC for the 4-km domain every time step rather than hourly, based on the 12-km fields that are computed simultaneously. This method allows the modeler to use both the 12-km domain and the 4-km domain outputs. The third nesting technique is two-way nesting with one-point feedback with light smoothing. In this technique, the LBC are created every time step, the same as one-way nesting. The difference here is that the 4-km domain feeds back information to the 12-km domain, which theoretically produces better LBC for the 4-km domain. The drawback to this method, however, is that the 12-km domain model output typically cannot be used over the 4-km nest, because there are surface flux inconsistencies between the two domains after the feedback.

4.2.5 FDDA Parameters

The successful design of an FDDA scheme also depends on the choice of weighting factors for both analysis nudging and observation nudging. Analysis-nudging weighting coefficients that are too small do not allow the model state to be effectively relaxed toward the analysis, and the nudging would not have a very large impact on the model output. Conversely, a weighting coefficient that is too large will cause the model to look too much like the gridded analyses. In this situation, the model would not be allowed to produce its own mesoscale structures. The same logic applies to individual observation nudging, but more factors also apply. For example, considerations must be made regarding the length of time that an observation actually influences the model output, as well as the spatial extent of influence in the horizontal and vertical. Additionally, these observations must be applied differently at different heights. The model must also be nudged to individual surface observations for less time and

over a smaller area than an upper air observation, primarily due to the higher variability of surface conditions compared with upper air conditions.

All of the weighting coefficients are summarized in **Table 4-3**, which contains all FDDA design parameters. For this study, the analysis-nudging weighting coefficients only need to be chosen for the two coarsest domains, since analysis nudging is not used on the 4-km domain. For the 36-km and 12-km model runs, the nudging coefficients, G, which determine the strength of the analysis nudging, are different depending on domain resolution and the model variable that is being nudged. For the 36-km resolution model runs, where observational nudging is not used, analysis nudging is weighted more heavily. For example, the upper-air analysis-nudging weighting coefficients for both the wind fields and the temperature fields on the 36-km domain (G_{u36}) are 2.5×10^{-4} s^{-1}, compared to 1.0×10^{-4} s^{-1} for the 12-km domain (G_{u12}). Moisture fields above the surface are based on coarse radiosonde spacing, and are weighted less heavily, and we used a nudging coefficient of 1.0×10^{-5} s^{-1} on each domain. Either the PBL depth or a prescribed "ZFAC" setting determines the vertical distribution of the three-dimensional (3-D) analysis nudging. This setting allows the user to apply the upper-air analysis nudging only above a certain sigma level, usually to allow the model-derived PBL to evolve naturally when data for assimilation have limited spatial resolution. For this study, ZFAC zeroes out the analysis nudging below $\sigma = 0.8$, which includes 23 sigma levels, and an approximate depth of 1,700 m. Above this height, analysis nudging is applied normally.

In addition to upper-air analysis nudging, surface analysis nudging is also applied on both the 36-km and 12-km resolution domains, which applies surface analyses throughout the PBL (Stauffer et al., 1991). There are differences between upper-air and surface analysis nudging in the temporal resolution of the analyses, a confidence factor used in the spatial weighting of the analyses, and the variables that are nudged. In this study, only 3-hourly wind fields are nudged in the PBL, but with the same weights as the upper-air analysis nudging, i.e. 2.5×10^{-4} s^{-1} on the 36-km domain (G_{s36}), and 1.0×10^{-4} s^{-1} on the 12-km domain (G_{s12}). While the upper-air analyses assume a confidence factor of 1.0, the surface analyses are applied with a confidence factor based on a radius of influence (RINBLW) and the surface data density. In this study, RINBLW is set to 250 km. For grid cells outside of the 250-km radius of influence from the nearest surface observation, the weight of the analysis is dropped to 20%, because of decreased confidence in the applicability of the analysis in areas that far from an observation.

Table 4-3

FDDA Design, Including the Variables That are Assimilated, Nudging Coefficients (x 10^{-4}), and Where the Observations are Assimilated in the Vertical. Weighting Coefficients are Labeled According to the Data Source and Type of FDDA

3-D analysis nudging with upper-air data for FDDA every 12 hours (UFDA) design					
3D 12-hr Sondes			**G_{u36}/G_{u12}**		
u^1, v^1, T^2			2.5/1.0		
q_v^2			0.1/0.1		
UFDA plus surface analysis nudging using 3-hourly data (USFDA) design					
3D 12-hr Sondes	**G_{u36}/G_{u12}**		**2D 3-hr SFC Anal.**	**G_{s36}/G_{s12}**	
u^1, v^1, T^2	2.5/1.0		u^3, v^3	2.5/1.0	
q_v^2	0.1/0.1				
USFDA plus standard observation nudging (USFDA SOB) design					
12-hr Sondes	**G_{uo}**		**1-hr SFC Obs**	**G_{sto}**	
u^a, v^a, T^b, q_v^b	4.0		u^a, v^a	4.0	
USFDA SOB plus special observations, or all observations (USFDA AOB) design					
12-hr Sondes	**G_{uo}**	**1-hr SFC Obs**	**G_{sto}**	**Special Data**	**G_{spo}**
u^a, v^a, T^b, q_v^b	4.0	u^a, v^a	4.0	u^a, v^a	4.0

[1] Assimilate data only above $\sigma = 0.8$ (approximately 1700 m AGL).
[2] Assimilate data only above $\sigma = 0.8$ or the model PBL top, whichever is higher.
[3] Assimilate data in the PBL only (Stauffer et al., 1991)
[a] Assimilate data at all levels where data is available
[b] Assimilate data above the model PBL top only

Observation nudging is applied to winds, temperatures, and vapor mixing ratios on the finest two domains, where on the 12-km domain, analysis nudging is weighted less heavily than observations, and on the 4-km domain, analysis nudging is not used at all. At these grid lengths, observations can have more influence on the evolution of smaller-scale meteorological phenomena. Temporally, all observations are weighted equally, as wind, temperature, and mixing ratio observations all carry a weight of 4.0×10^{-4} s^{-1} on both the 12-km and 4-km domains. In the same manner, all observation types also carry identical weights, including 12-hourly sondes, or upper-air observations (G_{uo}), 1-hourly standard surface observations (G_{sto}) and all special observations (G_{spo}). Along with the analysis-nudging weights, the observation nudging weights are also summarized in the FDDA designs in Table 4-3.

As discussed above, this observation nudging methodology (Stauffer and Seaman, 1994) varies the spatial weighting of the observations in the horizontal and vertical to account for error covariances over a volume of influence for each observation. A radius of influence is set to 100 km for both the 12-km and 4-km domains, which is the radius of horizontal influence of an observation on a quasi-horizontal surface directly above the surface. At the surface, the minimum radius of influence is encountered, which is approximately two-thirds of the value directly above it. In this study, the surface radius of influence on the 12-km domain, for example, is limited to 67 km, or approximately 5.6 grid-lengths. Above the surface, the radius of

influence of the observations increases linearly to 200 km at 500 mb. Above 500 mb, the radius of influence for an observation remains at 200 km. As for the analysis nudging, there are also limitations to where the observational data is assimilated. As the default setting in the MM5 observation nudging technique, wind and mass (temperature and moisture) observations are handled differently. Wind observations are applied throughout the depth of the model, independent of the model-derived boundary layer. Nudging of mass observations, however, is dependent upon the height of the model-derived boundary layer, as temperature and moisture observations are only applied above the boundary layer.

Observation nudging also varies temporally. This study uses a 120-minute half-window. During the first 60 minutes of the half-window, the time weighting of the observation is linearly ramped up from 0.0 (no influence) to 1.0 (full influence). The maximum time weight of 1.0 is then applied at model times within one hour of the observation time, and ramped down to 0.0 again by two hours after observation time. As there are different spatial influences for the surface observation, there are also different temporal limitations for the surface observation. An observation at the surface is only applied for 0.5 times the time window, so the full weight (1.0) of a surface observation is only felt within a half-hour of the observation time. Outside the half-hour time window, the influence is ramped down to no influence (0.0) during the next half-hour period.

4.2.6 Special Data Sources

Many FDDA modeling studies use the widely available WMO surface and radiosonde observational data for purposes of nudging and model verification. Statistics show, however, that the larger the observation sample, the more effective the FDDA and more reliable the statistical results. In this study, both WMO and special observational data were used for FDDA input and model verification. These special data consisted of surface observations across the Gulf Coast region, surface observations from meteorological towers and oil platforms in the GOM, as well as upper-air wind observations from RWPs. The coverage of both WMO and special data is shown in **Figure 4-7**.

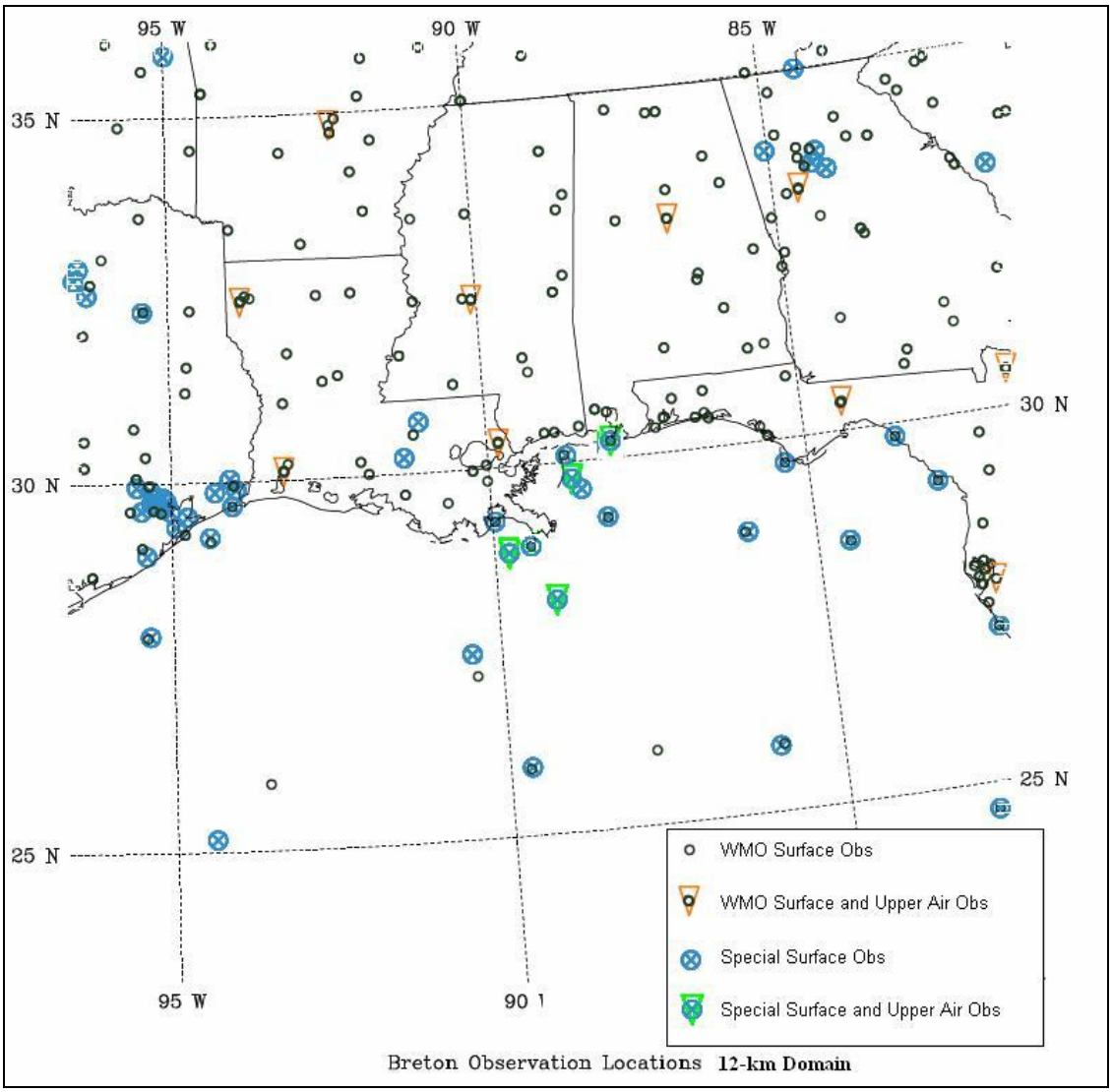

Figure 4-7. Observation locations within the 12-km resolution model domain. Observation symbols are broken into four categories, as detailed in the figure key.

Special Surface Data

The additional surface data were retrieved from four primary sources. Most surface data was obtained from the archives of the NCDC. These NCDC data consist of onshore data only, and cover many regions of the 12-km resolution model domain. Several clusters of data are shown in Figure 4-7, which correspond with the metropolitan areas of Houston, Texas, and Atlanta, Georgia.

Surface data were acquired from Coastal-Marine Automated Network (C-MAN) stations, which are operated by NOAA's National Data Buoy Center (NBDC). NBDC data are available at http://www.ndbc.noaa.gov. C-MAN stations are moored buoys — mostly in the GOM — that

monitor the standard meteorological variables, as well as SST and wave data. For our study, we used only the standard meteorological data.

Surface meteorological data were also available for some air quality monitoring sites in the EPA Air Quality System (AQS) (http://www.epa.gov/ttn/airs/airsaqs). MMS acquired both air quality and meteorological data for the study year from EPA and provided these data to the study team.

The final source of surface data is a series of six meteorological instrument platforms in the GOM. These platforms are part of the BAMP. Instruments on BAMP platforms were used to collect standard meteorological data, as well as SO_2, ozone, and NO_x measurements that helped researchers determine whether pollutant levels were much higher than federally mandated levels over a particular period of time. Due to the height of some of the instrumentation on the BAMP platforms, some observations had to be input into the FDDA scheme as upper air observations, because an observation can be considered a surface observation only if it is located below the first sigma half layer, or 15 meters above ground level.

Special Upper Air Data

In addition to the 12-hourly upper-air data collected by the National Weather Service, upper air data were also collected from RWPs at four of the six BAMP locations. RWPs are typically co-located with a Radio Acoustic Sounding Systems (RASS), and are capable of measuring both wind profiles and virtual temperature profiles. For this study, only the wind profiles were used for data assimilation. Even though the vertical extent of data collection from an RWP is not as large as with a conventional radiosonde, the wind profiles can represent the majority of the boundary layer.

4.2.7 Year-Long Modeling Study

The purpose of this modeling study is to produce an entire year of FDDA-assisted MM5 meteorological fields for use with an air quality model. This study also includes six episode-type cases, which were chosen to explore conditions that might typical contribute to increment consumption. The year-long modeling study presented an opportunity to examine the performance of the mesoscale model in dynamic-analysis mode when presented with widely varying weather conditions. The accuracy of the model was determined both subjectively — through examination of individual cases with typical weather charts — and statistically.

Model Development Experiments

The development of the best model setup to be used for a year-long study was determined by a set of experiments that explored the different levels of FDDA and two separate SST fields, the Eta model-derived SST and the MODIS SST. A control run (i.e., no FDDA) was performed using both SST fields. From that point, an additional level of FDDA was added for each SST product. **Table 4-4** summarizes the experiments in a systematic approach using the following techniques in sequence; 3-D analysis nudging with upper-air data for FDDA every 12 hours (UFDA), UFDA plus surface analysis nudging using 3-hourly data (USFDA), USFDA plus

standard observation nudging (USFDA SOB), and USFDA SOB plus special observations, or all observations (USFDA AOB). Table 4.4 offers a condensed version of this information useful for reviewing experimental results; Table 4-4 also summarizes the names of the experiments for the development case and details the individual differences for each simulation.

Table 4-4

Summary of the 12-km Resolution Development Case Experiments. CNTL Implies no FDDA. UFDA Implies Upper-Air Analysis Nudging, and USFDA implies Upper-Air Analysis Nudging Plus Surface Level Analysis Nudging

Experiment Name	Analysis FDDA	Observation FDDA	SST
CNTLETA	None	None	Eta
CNTLMOD	None	None	MODIS
UFDAETA	Upper	None	Eta
UFDAMOD	Upper	None	MODIS
USFDAETA	Upper+Surface	None	Eta
USFDAMOD	Upper+Surface	None	MODIS
USFDASOBETA	Upper+Surface	Standard	Eta
USFDASOBMOD	Upper+Surface	Standard	MODIS
USFDAAOBETA	Upper+Surface	Standard+Special	Eta
USFDAAOBMOD	Upper+Surface	Standard+Special	MODIS

Statistics

The statistics are calculated using the VEROBS software package, developed by David Stauffer and Anthony Schroeder at PSU. This software includes graphical tools that are capable of calculating statistics for any given user-defined layer, as well as vertical statistical profiles and all-layer averages, based on the accuracy of the model at every sigma level. The accuracy of the model is determined by interpolating the model result to the observation location within a given time window. Statistics are computed for five model output variables: vector wind difference, temperature, mixing ratio, wind speed, and wind direction. While all meteorological layers are important to some degree, the surface layer, the PBL (defined here for statistical purposes as 30 – 1000 m agl, and the all-layers-above-surface (ALAS) average are the focus of attention for the year-long study. All statistics are computed using the complete set of observations (standard WMO and special data) over the 12-km domain; when statistically comparing the 12-km and 4-km model results for the three cases, the statistics are computed over the 4-km domain area for direct comparison of the two model resolutions.

The year of model runs was broken into 5.5-day segments, with one-half day for model spin-up and one-half day of overlap between model runs. The length of the individual model runs makes it convenient to examine the statistical accuracy of the model over many timescales. Here, the statistical results will be time-averaged for each of the following timescales: individual 5.5-day case, monthly, seasonally, and annually.

The benefit of a case-long statistical average is twofold. First, the length of the pollutant episodes was generally between five and six days. Performing a statistical analysis of each case allows us to examine whether the episodes in question were also meteorological challenges for the numerical model. If this is true, then the complexities of the meteorological situation would have to be examined more closely. Second, the length of the model runs coincides with the typical synoptic timescale, that is, three to six days. It is possible that several synoptic conditions could occur during the course of a particular model run, or one synoptic condition persists through more than one model run. In general, however, the agreement between the synoptic timescale and the desired model simulation length is a convenient way to separate the statistics of individual meteorological events.

Throughout the research community, the expected performance of a mesoscale model during any particular month is generally unknown. For this reason, statistics are also calculated on a monthly basis, as a composite of the individual cases occurring during that month. Because this study occurred over only one calendar year, the monthly statistics may not be representative of the particular month in a given year, that is, the statistics are not climatological values.

Weather patterns clearly demonstrate seasonal variations, especially when the differences between summer and winter patterns on a continental scale are examined. During the winter months, synoptic patterns are stronger across the contiguous United States — with the main branch of the jet stream meandering across much of the country — causing a general increase in wind speed, less variability in wind directions, and well-defined frontal systems. During the summer months, however, the jet stream is located much farther north, which considerably weakens the synoptic patterns and results in generally lighter wind speeds, higher variability in wind direction, and less temperature definition between air masses.

From these seasonal differences, it can be inferred that the mesoscale model skill will vary throughout the year. A seasonal statistic is useful to understand how the meteorological uncertainty varies throughout the year-long study. Because seasonal variability has a large range across the country, it is most appropriate to perform these statistical evaluations based on the calendar seasons. In the Gulf Coast region, this assumption is relatively valid. **Figure 4-8** shows the average monthly surface temperatures in New Orleans, Louisiana. Note, however, that the seasonal differences in temperature and temperature error will also vary with location. More seasonal variation is likely at locations farther inland and locations at higher latitudes.

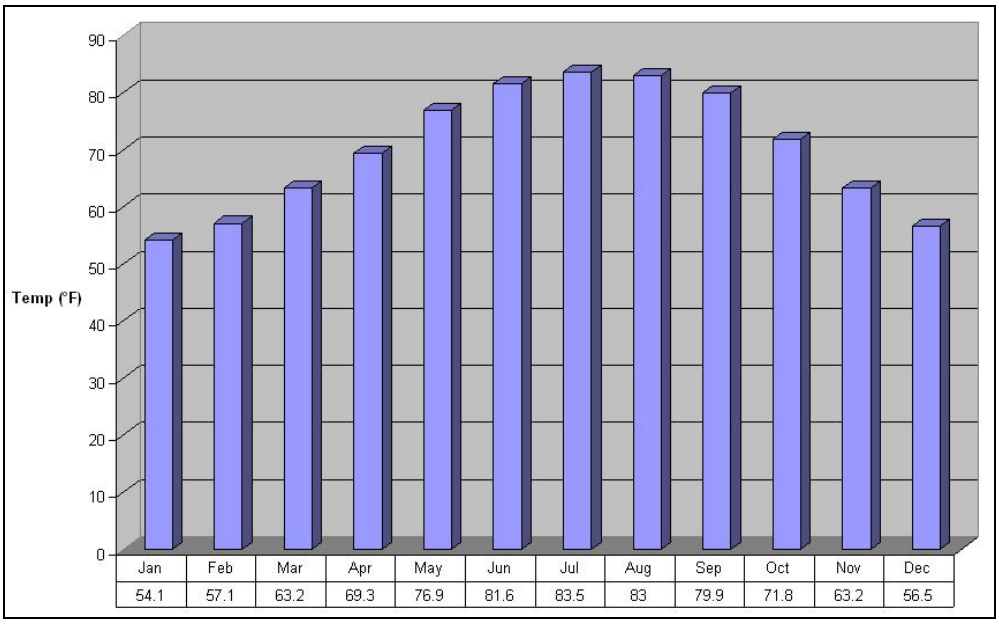

Figure 4-8. Monthly mean temperatures (°F) for New Orleans.

Finally, to understand the overall performance of the mesoscale model, it is essential to examine the average statistics for an entire calendar year. This statistic is a combination of the performance of the model during nearly every feasible synoptic situation. Strong flows are considered, as well as weak flows and subsequent mesoscale coastal circulations. Weak thermal gradients are likely to be observed, as well as strong baroclinic areas corresponding to frontal passage or the naturally baroclinic coastline. With the variety of meteorology considered during this year-long study, a statistic of this sort should give a good overall representation of the model performance for this area.

Subjective Analysis

Statistics are an excellent way to objectively assess the performance of the model system, but it is also necessary to perform a subjective analysis. With more than 70 individual cases, closely examining every case would be a very arduous task. Instead, a limited number of cases were chosen to analyze subjectively. To insure accuracy of the cases that mattered most to the study, all six cases were analyzed. In addition to the episodic cases, one case was chosen from each month, based on the statistical analysis. The case with the worst statistical results in either the wind or mass fields was analyzed to make sure there were no numerical difficulties causing the higher model errors for the particular case.

Once the cases were chosen, the following fields were analyzed: sea level pressure, fronts, surface temperature, precipitation, 500 mb heights and winds, and 300 mb winds. If the meteorological fields were in the proper location and the corresponding magnitudes were reasonable, and the timing of frontal passage was close to observation, the case was deemed to be accurate based on the subjective analysis, along with the statistical analysis results.

4.2.8 Grid Resolution Analysis

In addition to the year-long modeling study at 12-km resolution, a modeling study at 4-km resolution was also conducted. MMS requested that the study team determine whether it would be reasonable or necessary to conduct the year-long modeling study at 4-km resolution. Depending upon the results of the 12-km versus 4-km analysis, it may have been determined that the finer, 4-km resolution model runs provided enough additional benefit to warrant the extra computing time needed to simulate the entire year at that resolution.

There are three focus points for this higher-resolution investigation. First is simply the added value of a 4-km resolution model simulation over a 12-km resolution model simulation. It is crucial to determine if a 4-km model simulation predicts the state of the atmosphere more accurately than a 12-km model simulation in the area of interest. Greater accuracy in the meteorological fields should lead directly to greater accuracy of the atmospheric chemistry models that are driven by the meteorological model output. The resolution of the SST field may affect 4-km model results in this Gulf Coast region. Two resolutions of the MODIS SST product (36 km and 4 km) were used over the waters of the GOM. This study tested justification for using a higher-resolution SST field, since such fields are not always readily available.

As summarized in **Table 4-5**, nine experiments were performed. The experiments include two control runs for each of the three cases: a 12-km control run based on the configuration used for the year-long study (DEC12, MAR12, and JUL12), and a 4-km control run, with the default 36-km resolution MODIS (DEC4, MAR4, and JUL4). Table 4-5 also indicates whether or not the Kain-Fritch 2 (KF2) convective parameterization was used. The 12-km control runs were not modified during the process, but acted as a baseline for comparison with the 4-km simulations. Options on the 4-km simulations were changed one at a time, until the suite of experiments for each case was completed.

Table 4-5

Summary of the Nine Experiments Conducted for the 4-km Analysis. Experiment Names are Denoted by a Three-Letter Abbreviation of the Case Month, Grid Resolution (4 or 12 km), and Whether 4-km MODIS SST Data Were Used

Experiment Name	Grid Length (km)	SST Resolution (km)	KF2
DEC12	12	36	Yes
DEC4	4	36	No
DEC4M4	4	4	No
MAR12	12	36	Yes
MAR4	4	36	No
MAR4M4	4	4	No
JUL12	12	36	Yes
JUL4	4	36	No
JUL4M4	4	4	No

4-km Resolution Simulations

Studies by Schroeder et al. (2006) and Mass et al. (2002) have shown that fine-scale model simulations generally produce more realistic results, especially in complex terrain or coastal situations. These studies concluded that while the benefits of the 4-km resolution were nominal from an objective, statistical standpoint, there was more mesoscale structure, especially when dealing with complex terrain and coastal circulations.

The meteorological scenarios of this study include local, mesoscale features that are not typically resolved in coarser-resolution (e.g., 36-km) models. While the Louisiana Gulf Coast does not include terrain conventionally considered complex, i.e. mountain/valley topography, the coastline plays a major role in some cases. This complexity is directly related to the coastal baroclinity and the strength of the larger-scale flow.

Higher-Resolution MODIS SST Sensitivity

This test involves the comparison of model results using different resolution SST fields. Two MODIS SST products were provided by MMS for this study. The first product was a standard 36-km resolution product, which is comparable in resolution to the Eta model-derived SST product available from NCAR. The second product has a resolution of 4 km. Because atmospheric dispersion is so highly dependent on local-scale or mesoscale features, the interest in this test is to determine whether a high resolution SST field can play a substantial role in improving the meteorological fields around a complex coastline such as the Louisiana Gulf Coast.

These two SST products are used during the creation of the lower boundary conditions in INTERPF (Dudhia et al., 2005). To use the SST data, INTERPF determines if a grid cell is

water or land by referencing the terrain file. If the land-use is determined to be water, INTERPF substitutes the SST field for which a ground (surface skin) temperature field would typically exist. From that point on, the value of the SST is stored as a ground temperature value. Each 4-km experiment above, run with default 36-km MODIS SST, is rerun with 4-km MODIS SST. This allows for the comparison of the SST products both with and without use of convective parameterization.

Domain Nesting Strategy

The MM5 model enables the user to pick a number of strategies to produce multiple domains with increasing resolutions. The standard method used to make the initial and lateral boundary conditions for the 12-km resolution runs for the year-long study involves running the coarse model domain separately and interpolating the coarse grid model results onto the next higher-resolution model domain, here the 12-km domain. This is commonly referred to as a 1-way nest, with lower and lateral boundary conditions that are updated once per hour (1W1H).

Alternatively, the MM5 has the ability to run more than one domain at the same time. The simplest option is also referred to as 1-way nesting, but unlike 1W1H, the coarser-resolution model domain provides boundary conditions to the finer-resolution domains every time step (1W). In this strategy, using the data from both the coarse and fine model domains over the nest region is still advisable. A second nested domain strategy is referred to as 2-way nesting (2W). Like 1W, the coarser domain provides lateral boundary conditions for the finer domain every time step. In addition, the finer domain feeds back information to the coarser domain, which is a process that theoretically produces better scale interaction. However, there is a possibility that the communication from the finer domain back to the coarser model domain can cause the coarser domain to have inconsistent and erroneous surface fluxes. (One should simply discard the coarser mesh output in a 2-way nesting modeling strategy, and use the nested model output over the nest region.) Using the coarse mesh output from a 2-way nested run may create problems for a particular application: if the coarser resolution model results from a nested set of model runs are also needed, the 1-way nesting strategy should be used.

Several test runs were simulated, but no considerable differences were found between the model outputs using different nesting strategies. For this reason, the simplest 1-way nesting method, 1W1H, which places no restrictions on the use of the model data, was chosen to create the lower and lateral boundary conditions for all the 4-km resolution model experiments.

4.3 RESULTS

4.3.1 Development Case

The episode chosen by MMS for initial testing was defined as Case 1, which began at 1200 UTC, December 1, 2000, and ended at 0000 UTC, December 7, 2000. Efforts were focused on two primary objectives: development of the most appropriate data assimilation strategy on the 12-km domain, including standard WMO and the special observational data, and implementation of the MODIS SST product provided by MMS into the model runs. In order to find the best possible combination of FDDA strategy and SST product, all combinations were

examined (see overview of experiments in Table 4-4). A control run, that is, with no FDDA, was run using both the Eta SST (CNTLETA) and the MODIS SST (CNTLMOD). From here, both SST products were tested with additional levels of data assimilation. The addition of 3D analysis nudging (UFDA) to the control configuration was followed by 3D analysis nudging plus surface analysis nudging (USFDA), then the addition of observational nudging of standard observations (SOB), and then observational nudging of standard observations plus special observations (AOB). All standard WMO and special observational data were used to compute the statistics in the 12-km domain.

Table 4-6 is a comparison of the mean absolute error (MAE) statistic for all 10 model experiments conducted during the development stage. Comparison of the first two sets of model statistics, which illustrate the performance of the two control simulations, indicates that statistically the CNTLMOD simulation performed equally as well or better than the CNTLETA simulation. The improvements over all layers including the surface are about 0.2 m/s, 0.3°C, 0.1 g/kg, and 0.1 degrees for wind direction, and there are no instances when the model performs more poorly when using the MODIS SST. This is a typical winter season case, where the flow is dictated by a predominant flow from the northwest. Under these conditions, there is little influence from the GOM, even though the water temperatures are warmer than the bordering land temperatures, and it is unlikely that there would be a large difference between the model runs just by using a different SST product.

The statistics in Table 4-6 indicate that with the addition of more refined data assimilation techniques, the 12-km domain model simulations show subsequent decreases in model error, since more observed and analyzed data are being used to nudge the model state. Detailed descriptions of the 10 experiments performed on the development case are provided in Appendix F.

Based on the subjective and statistical results of this development case, it was decided that the best possible FDDA strategy to use for the year-long study was the USFDAAOB strategy with the MODIS SST product. Not only does this USFDAAOBMOD strategy provide the best statistical results, it also successfully utilizes the additional special observation data sources that were provided by MMS.

Table 4-6

Summary Mean Absolute Error (MAE) Statistics for Each Step of the FDDA Strategy Development Experiments

Experiment	Layers	MAE TEMP (°C)	MAE MIXR (g/kg)	MAE WSPD (m/s)	MAE WDIR (degrees)	MAE VWD (m/s)
CNTL ETA	SURFACE	3.1	2.1	1.4	2.2	28.8
	ALL-LAYERS	5.3	2.1	1.4	3.1	36.9
CNTL MOD	SURFACE	2.9	2.1	1.2	2.1	28.3
	ALL-LAYERS	5.0	2.0	1.2	3.0	36.0
UFDA ETA	SURFACE	2.9	2.0	1.4	2.1	26.0
	ALL-LAYERS	4.3	1.8	1.4	2.7	28.5
UFDA MOD	SURFACE	2.7	1.7	1.3	2.0	25.4
	ALL-LAYERS	4.1	1.6	1.2	2.6	26.4
USFDA ETA	SURFACE	2.6	1.9	1.4	1.8	23.9
	ALL-LAYERS	4.0	1.8	1.4	2.5	27.8
USFDA MOD	SURFACE	2.5	1.7	1.3	1.8	23.6
	ALL-LAYERS	3.9	1.6	1.2	2.5	26.2
USFDA SOB ETA	SURFACE	2.4	1.9	1.4	1.8	21.5
	ALL-LAYERS	3.9	1.8	1.4	2.5	26.7
USFDA SOB MOD	SURFACE	2.3	1.7	1.2	1.7	20.9
	ALL-LAYERS	3.8	1.6	1.2	2.5	25.5
USFDA AOB ETA	SURFACE	2.1	1.9	1.5	1.6	19.4
	ALL-LAYERS	1.9	1.8	1.4	1.2	15.5
USFDA AOB MOD	SURFACE	2.0	1.7	1.3	1.6	18.5
	ALL-LAYERS	1.9	1.6	1.2	1.1	14.8

4.3.2 Cases

After the completion of the development case, the next most important concern was the simulation of five additional cases. These cases are described in Section 3 and are summarized in **Table 4-7**. It is interesting to note that the meteorology in the episode cases is not confined to one or two synoptic types. Instead, every type of synoptic regime is represented in the six cases. For this reason, the entire year of model simulations is further justified, because it is necessary to examine all types of flows for the purposes of an air quality study. High pollution concentrations could possibly occur during any type of synoptic regime.

Table 4-7

Descriptions of the Six Initial Cases Modeled

Case	Date	Synoptic Regimes
1	1200 UTC, 1 DEC 2000 to 0000 UTC, 7 DEC 2000	FGR, FOR, CH
2	1200 UTC, 1 MAR 2001 to 0000 UTC, 7 MAR 2001	FGR, FOR, PH, CH
3	1200 UTC, 8 JUL 2001 to 0000 UTC, 14 JUL 2001	GH, FGR
4	1200 UTC, 7 AUG 2001 to 0000 UTC, 13 AUG 2001	GH, GR
5	1200 UTC, 7 NOV 2000 to 0000 UTC, 13 NOV 2000	FGR, FOR, CH, CR
6	1200 UTC, 29 DEC 2000 to 0000 UTC, 4 JAN 2001	CH, FOR

The statistical histograms presented in **Figures 4-9 to 4-13** summarize the results from the six cases, broken into three layers: surface (SFC), approximate PBL (30-1000m), and all-layers above surface (ALAS). These statistics distinguish between the surface layer and upper-air statistics, which are based on observations that are available at different time intervals. This strategy separates the hourly surface statistics from the upper-air statistics that are based on observation intervals that range from one to 12 hours.

Even though all classified types of synoptic regimes are represented in the six cases, some characteristics stand out. In the surface layer, VWD errors are as large as 2.5 m/s (Figure 4-9), while WSPD errors are generally 1.8 m/s or less (Figure 4-10). The ALAS errors

are the same or smaller than those in the PBL. In the PBL, the mean absolute error (MAE) values are only slightly lower than the surface layer statistics for the cold season cases (Cases 1, 2, 5 and 6). The warm season cases (Cases 3 and 4), however, when the wind speeds are generally weaker, have VWD MAE values that are lower by approximately 0.7 m/s in the PBL. The ALAS statistic shows a similar pattern, where the cold season cases have lower errors than the surface counterparts, but only by differences ranging from 0.3 m/s in Cases 1 and 2, to 0.2 m/s in Cases 5 and 6. The warm season cases have larger VWD differences between the SFC and ALAS, with a 0.9 m/s lower error above the surface for Case 3, and a 0.8 m/s difference for Case 4 (**Figure 4-9**). The pattern of WSPD errors (**Figure 4-10**) is generally similar to that for the VWD errors — the warm-season cases exhibit the lowest errors and the largest differences between the SFC, PBL and ALAS.

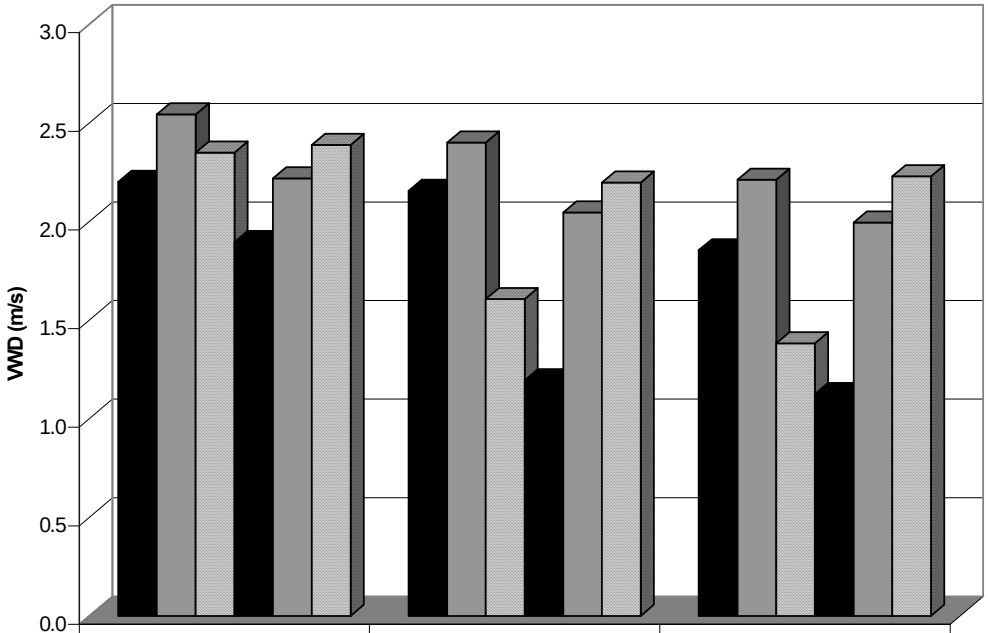

	SFC	30-1000m	ALAS
Ep. 1 - DEC	2.2	2.2	1.9
Ep. 2 - MAR	2.5	2.4	2.2
Ep. 3 - JUL	2.3	1.6	1.4
Ep. 4 - AUG	1.9	1.2	1.1
Ep. 5 - NOV	2.2	2.0	2.0
Ep. 6 - JAN	2.4	2.2	2.2

Figure 4-9. MAE histograms of VWD (m/s) statistics for each of the six cases. Statistics are broken into three layers: surface (SFC), 30-1000 m, and all layers above the surface (ALAS).

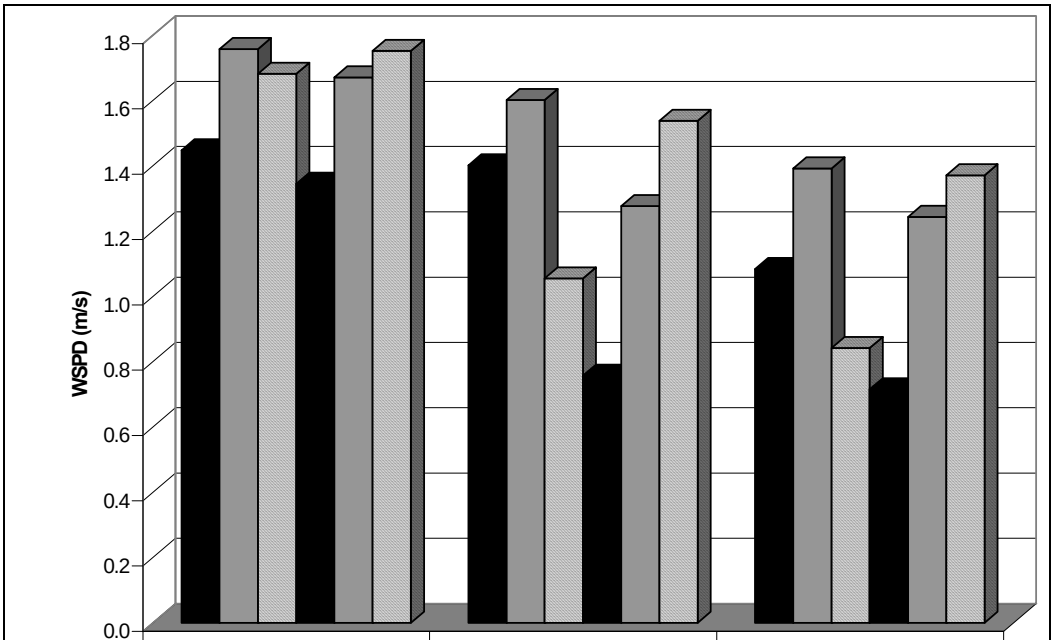

	SFC	30-1000m	ALAS
Ep. 1 - DEC	1.4	1.4	1.1
Ep. 2 - MAR	1.8	1.6	1.4
Ep. 3 - JUL	1.7	1.1	0.8
Ep. 4 - AUG	1.3	0.8	0.7
Ep. 5 - NOV	1.7	1.3	1.2
Ep. 6 - JAN	1.8	1.5	1.4

Figure 4-10. MAE histograms of WSPD (m/s) statistics for each of the six cases. Statistics are broken into three layers: surface (SFC), 30-1000 m, and all layers above the surface (ALAS).

The errors for WDIR in **Figure 4-11** have a pattern that is generally opposite to the WSPD errors, which is expected. For the SFC, the two warm-season cases have expectedly higher MAE WDIR values than Cases 2, 5 and 6. The December case (Case 1), however, has a SFC WDIR error of 21.8 degrees, which is larger than the 20.2 degree error posted by Case 3 in July. The lowest directional error in the surface layer occurs in Case 2 in March (17.5 degrees). In the PBL, the WDIR errors range from 12.2 degrees in Case 2 to 18.3 degrees in Case 1 (Figure 4-11). The ALAS statistic is a more expected result, as the largest errors occur during both of the warm-season cases, with 12.7 and 12.2 degree errors for Case 3 and Case 4, respectively. Both cases occur during the summer months of July and August, respectively, and are characterized (at least partially) by the GH synoptic regime, when weaker winds, combined with daytime convection, are inherently more difficult to predict at a point in space. Wind direction errors above the surface in the four other cold-season cases are two-thirds to one-half the summer values due to the stronger flow regimes during the cold-season cases as expected.

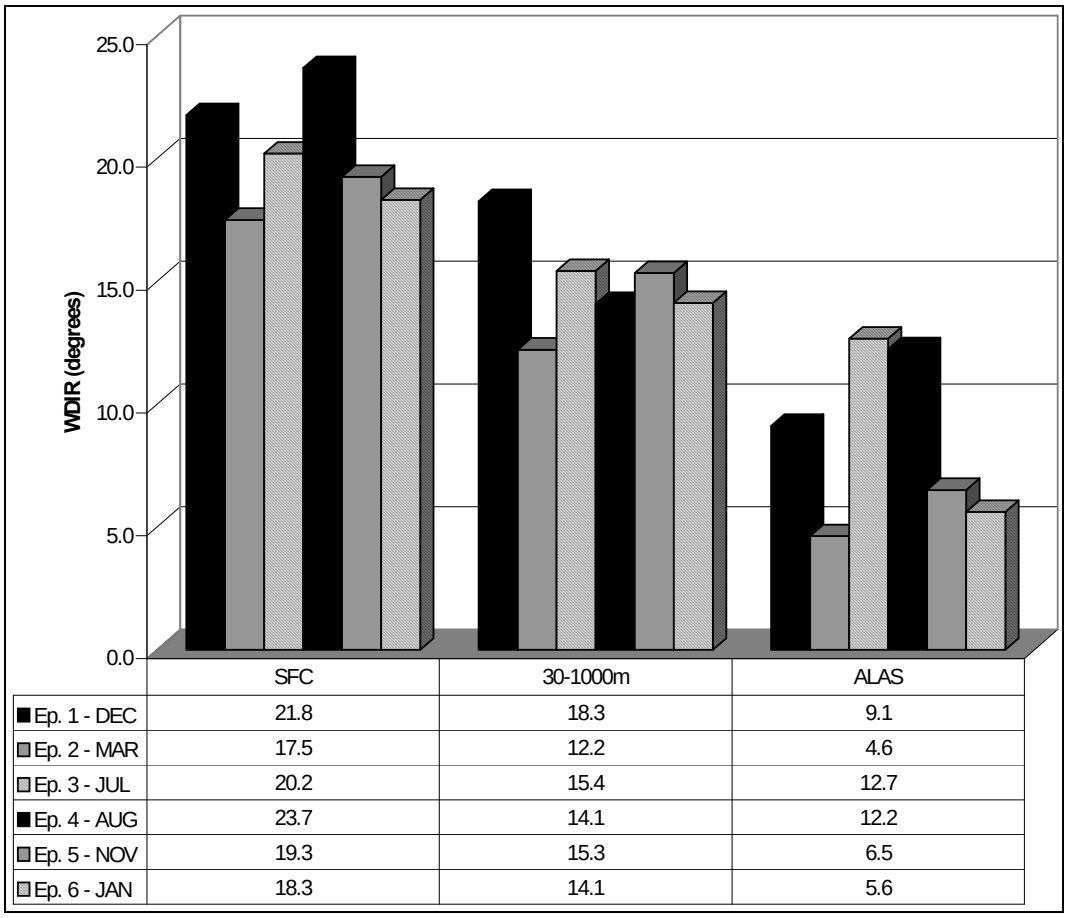

	SFC	30-1000m	ALAS
Ep. 1 - DEC	21.8	18.3	9.1
Ep. 2 - MAR	17.5	12.2	4.6
Ep. 3 - JUL	20.2	15.4	12.7
Ep. 4 - AUG	23.7	14.1	12.2
Ep. 5 - NOV	19.3	15.3	6.5
Ep. 6 - JAN	18.3	14.1	5.6

Figure 4-11. MAE histograms of WDIR (degrees) statistics for each of the six cases. Statistics are broken into three layers: surface (SFC), 30-1000 m, and all layers above the surface (ALAS).

MAE statistics of TEMP are harder to generalize, especially in the PBL. In the SFC, the smallest errors occur in Case 1 (1.7°C) and Case 2 (1.4°C). The other two cold-season Cases (Cases 5 and 6) have two of the three largest errors at this level (2.1°C and 2.3°C, respectively). In the PBL and ALAS the largest errors occurring during the warm-season (**Figure 4-12**), when there is less variation between air masses but convective activity can produce large spatial anomalies. The MAE values for MIXR (**Figure 4-13**) follow the expected pattern, with the largest surface values (1.6 to 1.7 g/kg) occurring during the warm-season cases and the November case (Case 5), when diurnal effects and land-sea interaction with the GOM are present. In November, the effects of the GOM interactions are still important, since the peak in ocean temperatures is generally in mid to late September, so the residual effects of the oceanic "summer" are still in effect. As expected, MIXR errors decrease in the cold season and with height due to colder-temperature air not holding as much water vapor (saturation mixing ratio decreases as temperature decreases).

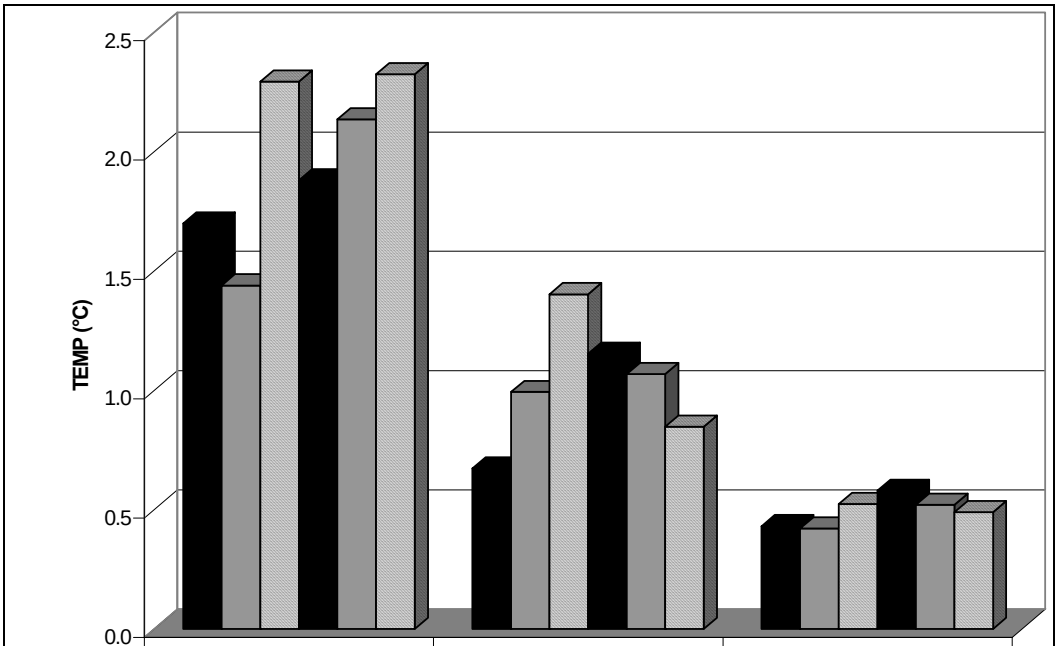

	SFC	30-1000m	ALAS
Ep. 1 - DEC	1.7	0.7	0.4
Ep. 2 - MAR	1.4	1.0	0.4
Ep. 3 - JUL	2.3	1.4	0.5
Ep. 4 - AUG	1.9	1.2	0.6
Ep. 5 - NOV	2.1	1.1	0.5
Ep. 6 - JAN	2.3	0.8	0.5

Figure 4-12. MAE histograms of TEMP (°C) statistics for each of the six cases. Statistics are broken into three layers: surface (SFC), 30-1000 m, and all layers above the surface (ALAS).

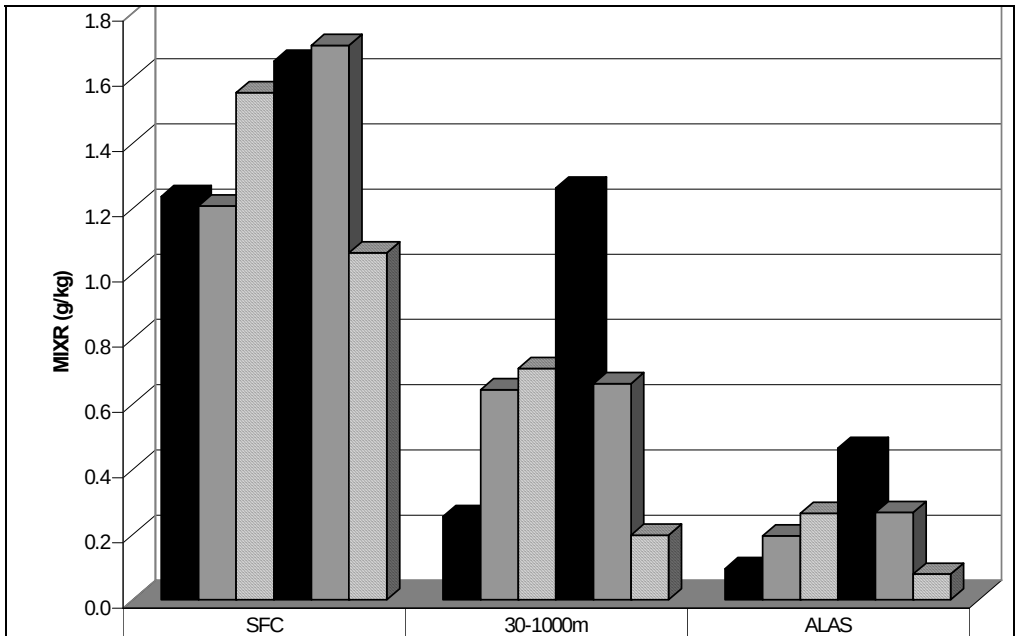

	SFC	30-1000m	ALAS
Ep. 1 - DEC	1.2	0.3	0.1
Ep. 2 - MAR	1.2	0.6	0.2
Ep. 3 - JUL	1.6	0.7	0.3
Ep. 4 - AUG	1.7	1.3	0.5
Ep. 5 - NOV	1.7	0.7	0.3
Ep. 6 - JAN	1.1	0.2	0.1

Figure 4-13. MAE histograms of MIXR (g/kg) statistics for each of the six cases. Statistics are broken into three layers: surface (SFC), 30-1000m, and all layers above the surface (ALAS).

4.3.3 Monthly Statistical Averages

A benefit of a full year of model simulations is the ability to calculate averaged model error statistics for other periods of time that may be of interest to other meteorological and chemistry modelers in the future. Calculating statistical averages for every month provides an approximate magnitude of error to expect for this Gulf Coast region during this study year. By no means is this a general measure for other years and locations due to the spatial limitations of the specific domain, and the fact that one year of FDDA-assisted model runs does not necessarily produce "climatological model errors." Nevertheless, it gives some indication of how model results may vary from one month to another.

Summary histograms of the mean monthly MAE statistics are given in **Figures 4-14 to 4-17**. Similar patterns to those in the episodic statistics are apparent in the histograms for each variable. In all three layers, the surface, the approximate PBL and all layers above surface, the largest MAE values for VWD occur in the cold-season months, from November to April, where the errors are nearly identical (2.2 m/s) throughout that period (Figure 4-14). None of the individual months appear to have average errors that are substantially different from the rest, however, as the MAE values only range from 1.8 m/s during July, to 2.2 m/s in the November to April period mentioned previously. The trend is also evident in the ALAS statistic, which ranges

from 1.2 m/s in July and August, to 2.5 m/s in January. Monthly average trends for WSPD are nearly identical to VWD trends, as cold-season monthly statistics are between 1.7 and 1.8 m/s, with the maximum in April, and the warm-season monthly averages producing a minimum of 1.3 m/s in August. Above the surface, the MAE values are once again smallest in July and August (0.7 m/s) and largest in January (1.5 m/s).

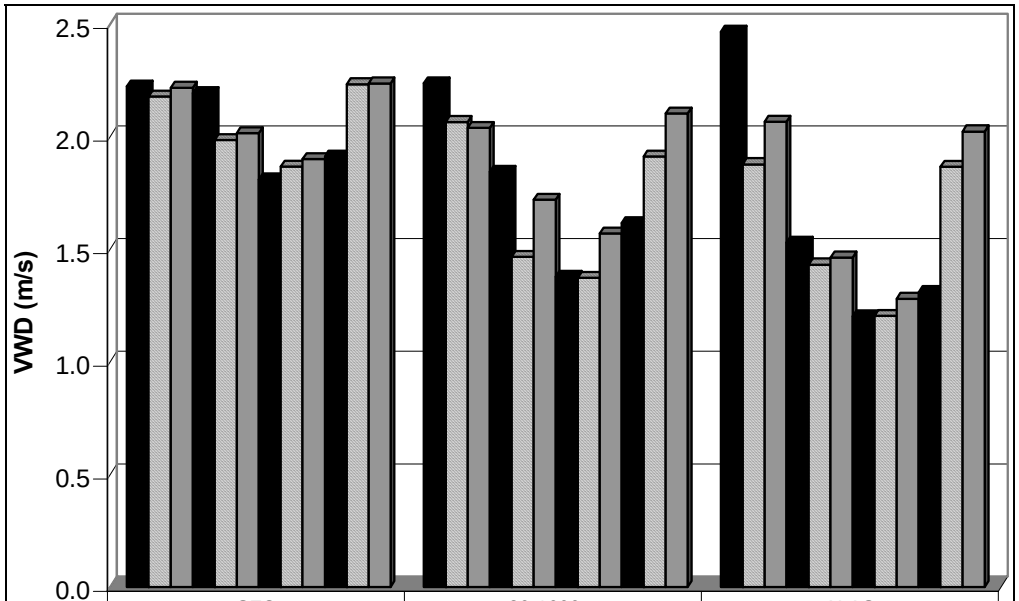

	SFC	30-1000m	ALAS
Jan	2.2	2.2	2.5
Feb	2.2	2.1	1.9
Mar	2.2	2.0	2.1
Apr	2.2	1.8	1.5
May	2.0	1.5	1.4
Jun	2.0	1.7	1.5
Jul	1.8	1.4	1.2
Aug	1.9	1.4	1.2
Sep	1.9	1.6	1.3
Oct	1.9	1.6	1.3
Nov	2.2	1.9	1.9
Dec	2.2	2.1	2.0

Figure 4-14. MAE histograms of VWD (m/s), with monthly statistical averages plotted for three layers: surface layer (SFC), the approximate PBL (30-1000 m) and "all layers above the surface" (ALAS).

The monthly WDIR statistics (Figure 4-15) have somewhat different monthly patterns. Average values for the MAE of WDIR for the SFC have the largest range, from 16.2 degrees in April to 25.5 degrees in August. As expected, the largest errors (from 22.1 degrees to 25.5 degrees) occur during the summer months, when much of the weather is dominated by high

pressure systems and relatively weak flows, in which wind directions are more difficult to predict. In the PBL, the statistics do not have as large of a range and have no obvious pattern from month to month, or cold-season to warm-season. Here, the largest WDIR errors occur during the cold-season months, ranging from 16.7 degrees in January to 18.3 degrees in November. A secondary peak in the error histograms is evident during June, July and August, which range from 16.0 to 16.2 degrees. The lowest calculated model errors, with a minimum of 14.4 degrees occur in both April and May. These differences are likely not significant. The ALAS average, however, again follows the expected pattern, with the largest monthly directional errors of 10.2 and 10.3 degrees occurring during July and August, and the lowest error of 5.9 degrees occurring in March. Other cool-season monthly averages (October to April) range from 6.5 to 7.6 degrees. As discussed previously, wind directions are generally easier to predict when speeds are greater, which is an explanation for the lower errors during the cool season. In summary, modeled above-surface wind directions are generally between 5 and 10 degrees, which is fairly impressive since radiosondes report wind direction to the nearest 10 degrees.

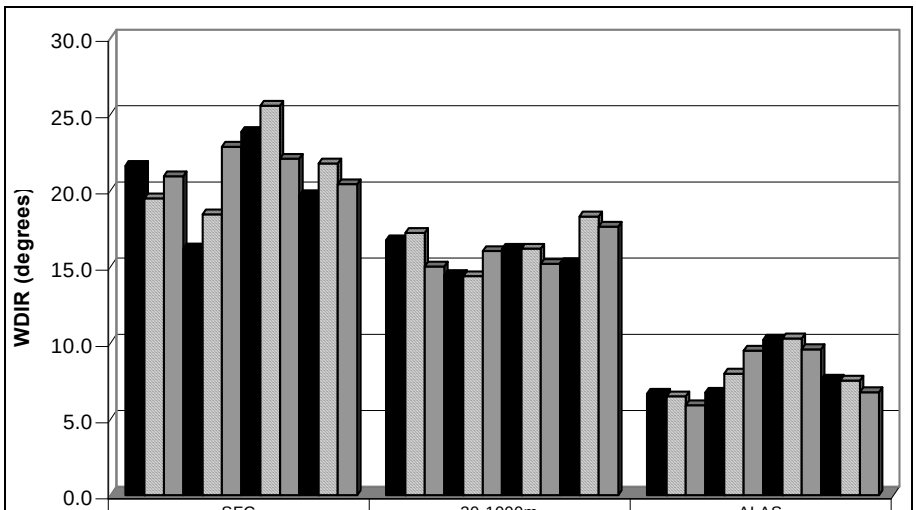

	SFC	30-1000m	ALAS
Jan	21.6	16.7	6.7
Feb	19.5	17.2	6.5
Mar	20.9	15.0	5.9
Apr	16.2	14.4	6.7
May	18.4	14.4	8.0
Jun	22.9	16.0	9.5
Jul	23.8	16.2	10.2
Aug	25.5	16.2	10.3
Sep	22.1	15.2	9.6
Oct	19.7	15.2	7.6
Nov	21.8	18.3	7.5
Dec	20.4	17.6	6.8

Figure 4-15. MAE histograms of WDIR (degrees), with monthly statistical averages plotted for three layers: surface layer (SFC), the approximate PBL (30-1000 m) and "all layers above the surface" (ALAS).

Monthly SFC and PBL averages of MAE for TEMP (Figure 4-16) appear to show the largest errors occurring during the cold season months, ranging from 2.0°C in October and November, to 2.2°C in December and January. Between March and October, the TEMP errors range from 1.6°C to 1.9°C. The most notable difference between the episodic results and the monthly results is in the PBL. The July and August Cases had the worst TEMP errors in the PBL. In the monthly statistics, July and August have the second lowest errors, as both have 0.9°C MAE values (the lowest error is 0.7°C in September). This trend is reasonable with the lowest errors occurring during the warm-season months, when few air masses have distinct characteristics and corresponding large horizontal temperature gradients. Convection can indeed cause isolated large temperature contrasts in the warm season, but the largest temperature errors occur during the cold-season months when air masses change at a higher frequency and strong frontal zones with large temperature gradients are more frequent. A small miscalculation in the timing of frontal passage can lead to large errors that would not typically occur during the warmer months when there is less weather system variability.

Errors for MIXR (Figure 4-17) generally follow the expected pattern, as is also the case in the episodic averages. The largest MAE errors occur during the summer months for each of the three layers, when mixing ratio values are largest and there is much more air-sea and land-sea interaction. During the cold season, when the flow is predominantly offshore and the water temperatures in the GOM are relatively cold, the amount of water vapor in the air and the role of land-sea interaction are decreased drastically.

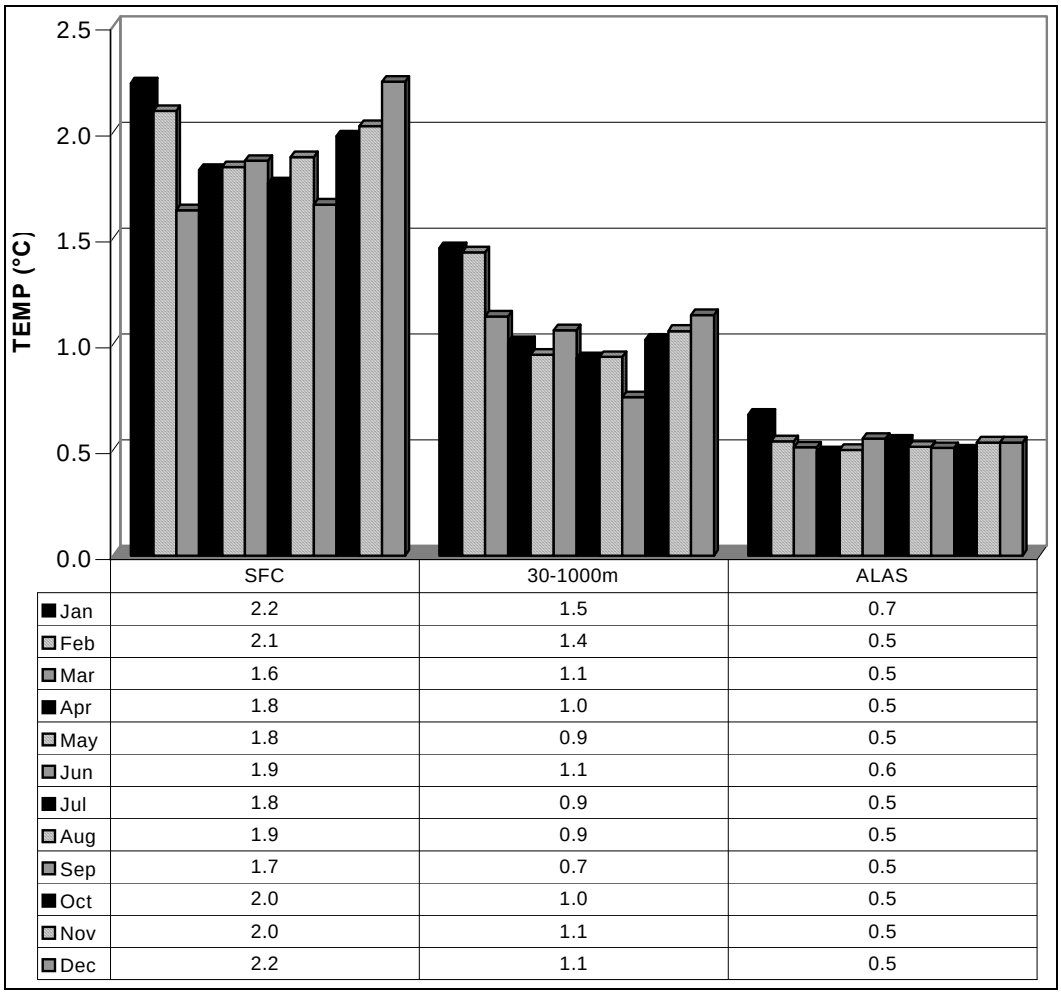

	SFC	30-1000m	ALAS
Jan	2.2	1.5	0.7
Feb	2.1	1.4	0.5
Mar	1.6	1.1	0.5
Apr	1.8	1.0	0.5
May	1.8	0.9	0.5
Jun	1.9	1.1	0.6
Jul	1.8	0.9	0.5
Aug	1.9	0.9	0.5
Sep	1.7	0.7	0.5
Oct	2.0	1.0	0.5
Nov	2.0	1.1	0.5
Dec	2.2	1.1	0.5

Figure 4-16. MAE histograms of TEMP (°C) with monthly statistical averages plotted for three layers: surface layer (SFC), the approximate boundary layer (30-1000 m) and "all layers above the surface" (ALAS).

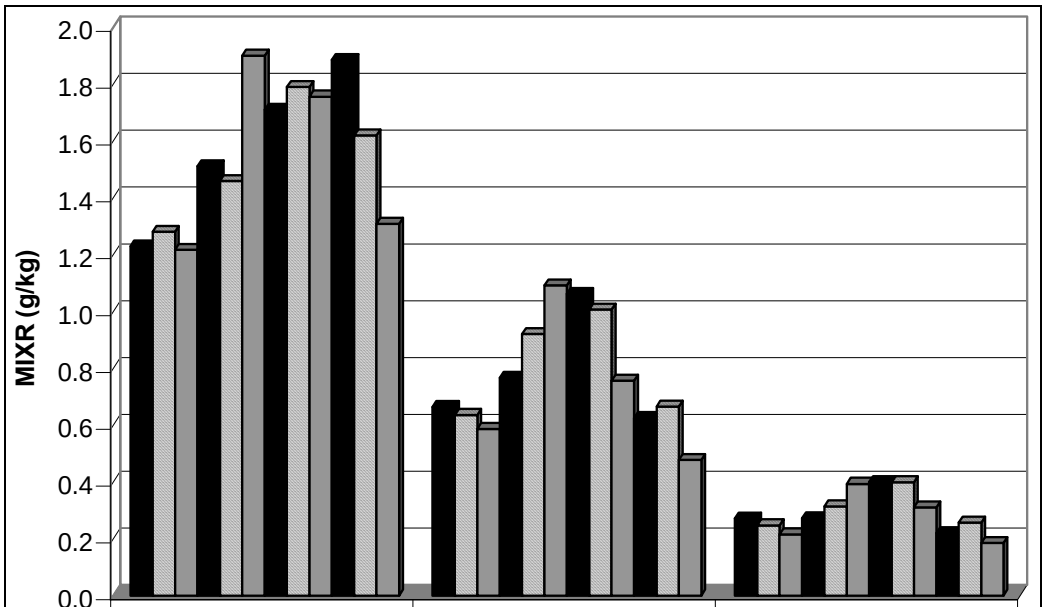

	SFC	30-1000m	ALAS
Jan	1.2	0.7	0.3
Feb	1.3	0.6	0.2
Mar	1.2	0.6	0.2
Apr	1.5	0.8	0.3
May	1.5	0.9	0.3
Jun	1.9	1.1	0.4
Jul	1.7	1.1	0.4
Aug	1.8	1.0	0.4
Sep	1.8	0.8	0.3
Oct	1.9	0.6	0.2
Nov	1.6	0.7	0.3
Dec	1.3	0.5	0.2

Figure 4-17. MAE histograms of MIXR (g/kg) with monthly statistical averages plotted for three layers: surface layer (SFC), the approximate boundary layer (30-1000 m) and "all layers above the surface" (ALAS).

4.3.4 Annual Statistical Averages

The statistics in this section are also calculated over the entire year of simulations, which serves as a good estimate of overall model performance, and are summarized by the annual mean statistical histograms in **Figure 4-18**. For this entire one-year period, the model simulations produce average VWD MAE values of 2.1 m/s for the SFC, 1.8 m/s for the PBL, and 1.6 m/s for the ALAS average. Errors of WSPD were approximately 1.6 m/s for the SFC, 1.2 m/s for the PBL, and 1.0 m/s for the ALAS average. Directional errors for the SFC average to 20.9 degrees for the year, compared to 16.0 degrees in the PBL, and 8.2 degrees for ALAS. An MAE of 20.9 degrees is actually very good for the surface, where direction errors are typically much larger. For example, the surface layer wind direction MAE statistics calculated for an

automated, high-resolution (12-km) FDDA-assisted MM5 system in Schroeder et al. (2006) ranged from approximately 29 degrees during an August simulation in Oklahoma, to approximately 35 degrees in an April simulation in the Chesapeake Bay area. The nature of the coastline and the land-sea interactions can also have a dominant effect on the winds in this study region, which reinforces the quality of the meteorological output.

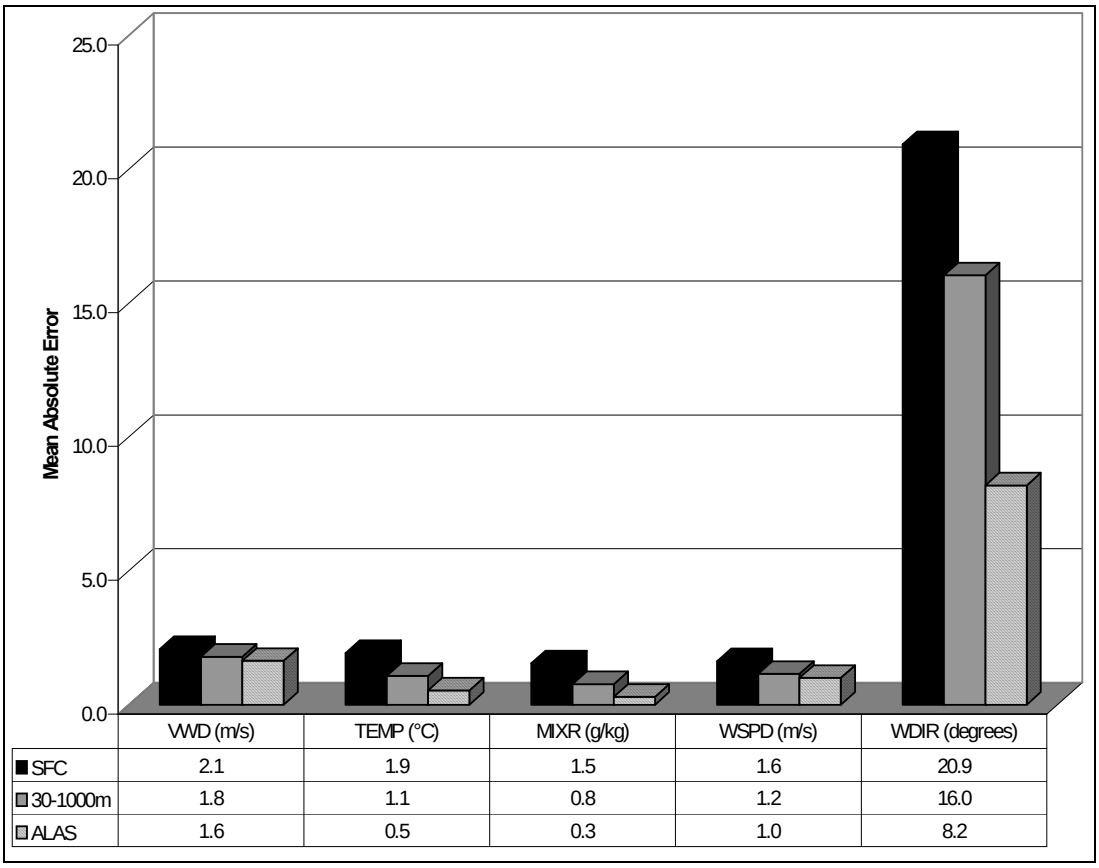

	VWD (m/s)	TEMP (°C)	MIXR (g/kg)	WSPD (m/s)	WDIR (degrees)
SFC	2.1	1.9	1.5	1.6	20.9
30-1000m	1.8	1.1	0.8	1.2	16.0
ALAS	1.6	0.5	0.3	1.0	8.2

Figure 4-18. MAE for all variables, averaged over the entire year of model simulations.

Over the entire year, the mass statistics had the greatest range of error between the surface and the upper levels (compared to VWD and WSPD). The mean annual TEMP error is 1.9°C for the SFC layer, while the ALAS average is calculated to be 0.5°C for the same period. Similarly, the MIXR errors range from 1.5 g/kg for the SFC layer, to 0.3 g/kg for ALAS. These error ranges are quite reasonable, and further indicate the high quality of this year-long meteorological data set.

4.3.5 4-km Resolution Simulations

It is hypothesized that the 4-km model-simulated meteorological fields will exhibit more detailed mesoscale structure that could enhance the performance of air-chemistry/pollutant

transport models in this Gulf Coast area. Three cases were modeled at 4-km resolution to explore the effect of grid resolution on model performance.

- Case 1: 1200 UTC, December 1, 2000 to 0000 UTC, December 7, 2000
- Case 2: 1200 UTC, 1 March 2001 to 0000 UTC, March 7, 2001
- Case 3: 1200 UTC, 8 July 2001 to 0000 UTC, July 14, 2001

Model results for the 12-km simulations were mapped to the 4-km domain area for direct comparison with the 4-km simulation results. Statistically, it is not clear whether there is any significant advantage or disadvantage of one model resolution over another, based on the control simulations in each case for each resolution. **Figures 4-19 and 4-20** summarize the WSPD and WDIR statistics for the three 12-km vs. 4-km resolution case experiments. The difference in WSPD statistics between the two resolutions is never greater than 0.1 m/s for the surface layer in any of the three cases, and 0.2 m/s for the ALAS average, with all statistics slightly favoring the 12-km simulations (Figure 4-18). The histograms indicate that the 4-km resolution simulation only has some statistical advantage for wind speeds in the PBL for the December case, but only by a very slight margin. The largest differences in model statistics are found in the MAE values for WDIR. The largest direction error differences occur during Case 3, which has the weakest flow through the entire period, so this result is expected. The largest difference between the two resolutions in the surface layer, however, was still only 3.0 degrees, averaged over the five-day length of the model simulations. In the PBL, the largest difference decreases to 2.1 degrees, and the difference in ALAS averages is a only 0.8 degrees (Figure 4-19). The mass statistics (not shown) also generally give some small objective advantage to the 12-km simulation, with a few exceptions. The 4-km resolution temperature output for Case 3 has a very slight advantage in the surface-layer, as well as a 0.2 °C advantage in the PBL. The only advantage for the 4-km simulations in terms of MIXR occurs in the surface layer of Case 1, where a very small difference is noticeable in the statistical histograms (not shown). From these statistical results between the control runs for the three cases, a clear advantage related to model resolution cannot be determined.

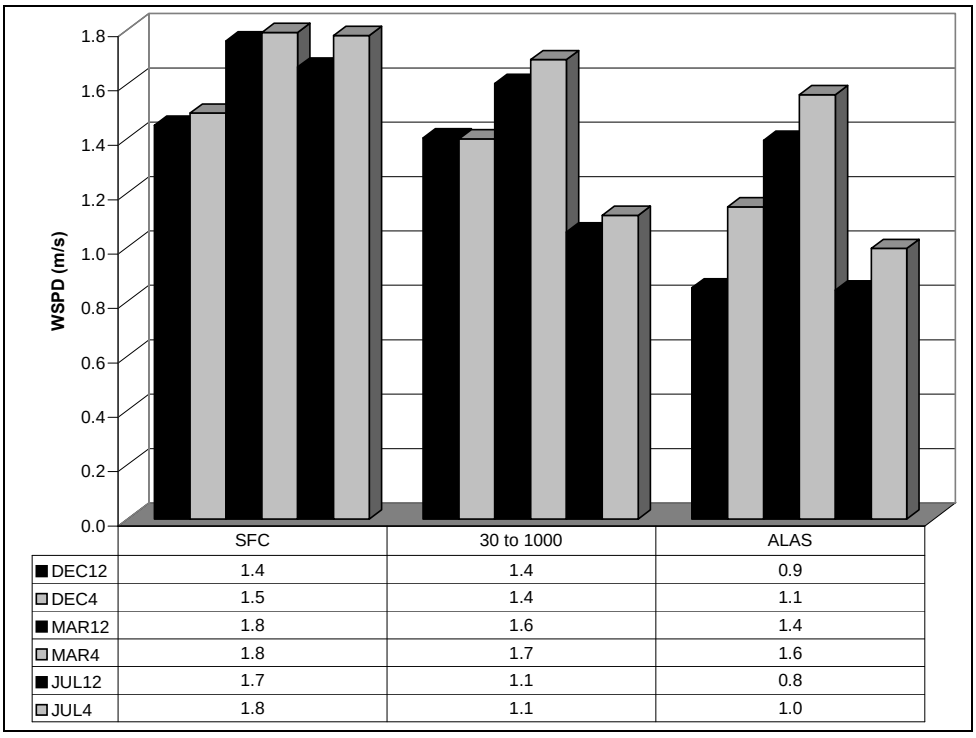

	SFC	30 to 1000	ALAS
DEC12	1.4	1.4	0.9
DEC4	1.5	1.4	1.1
MAR12	1.8	1.6	1.4
MAR4	1.8	1.7	1.6
JUL12	1.7	1.1	0.8
JUL4	1.8	1.1	1.0

Figure 4-19. Summary of MAE values for WSPD (m/s) for all three 12-km vs. 4-km case experiments.

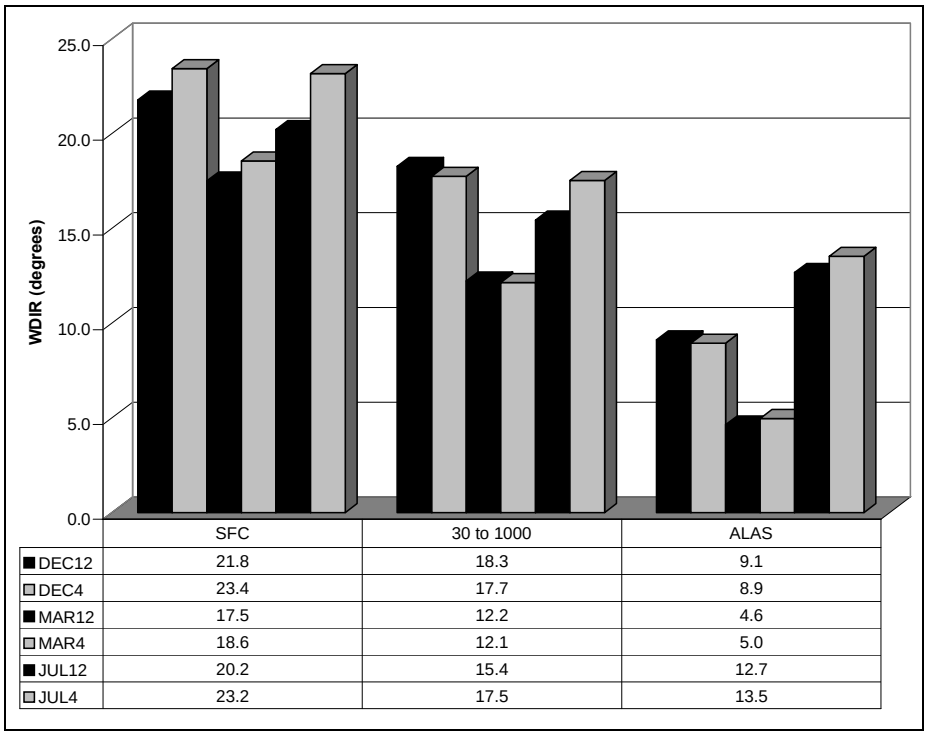

	SFC	30 to 1000	ALAS
DEC12	21.8	18.3	9.1
DEC4	23.4	17.7	8.9
MAR12	17.5	12.2	4.6
MAR4	18.6	12.1	5.0
JUL12	20.2	15.4	12.7
JUL4	23.2	17.5	13.5

Figure 4-20. Summary of MAE values for WDIR (degrees) for all three 12-km vs. 4-km case experiments.

The combination of the statistical results with the subjective analysis gives a little more information regarding which resolution performs "better." The greatest advantage of the 4-km simulations is the added detail in the model-derived wind fields, including frontal wind shifts, stronger sea breezes with tighter isotach gradients, and other small-scale circulations around the area of interest, especially over the waters of the GOM. Both resolutions tend to forecast the general wind fields well, including the timing and positioning of fronts. The largest errors in the surface wind fields during the two cases where frontal zones are involved are due to a misplacement of a front by a few grid-lengths. In Case 2, the frontal boundary remains relatively stationary throughout the first few days of the run, but shifts position slightly, which is probably the cause of many directional errors in that case. The possible benefits to an air-quality study can be seen most easily in Case 3, where the flow is weak, and local-scale, thermally driven circulations, including convective activity, are generally less resolved by the coarser resolution model. In situations such as these, it is clear how the transport of pollutants can change drastically with an increase or decrease of model resolution. In the following section, the 4-km resolution experiments are expanded to determine if other factors, such as use of a convective parameterization on a 4-km resolution domain or higher-resolution SST fields, can provide any additional benefits to a mesoscale modeling study at 4-km resolution.

4.3.6 4-km MODIS SST

The next part of this expanded 4-km experimental design involves the comparison of the 4-km resolution control simulations using different resolution SST fields. In Section 4.1.3, different SST products are discussed, including the Eta model-derived SST, the NCEP reanalysis SST, and the MODIS SST. The control simulations for this study, based on the results of the development case, use the 36-km MODIS SST product, equal in resolution to the model coarse domain used in this study. In addition to the 36-km SST product, there is a 4-km resolution MODIS SST product that the MMS also provided, which has more detailed structure in the SST field.

Figure 4-21 is a comparison of the ground temperature/SST field for each of the three cases, using both MODIS SST resolutions: 36-km resolution SST on the left and 4-km resolution SST on the right. These side-by-side comparisons make the differences easily apparent, as the 4-km MODIS SST contains much more detailed information than the 36-km MODIS SST at the same contour interval. With lower boundary conditions that are as different as the two SST fields, it is possible that using either product would make noticeable changes in the model output fields, especially near the surface. The actual model simulations do show some differences that may warrant the use of a 4-km resolution SST.

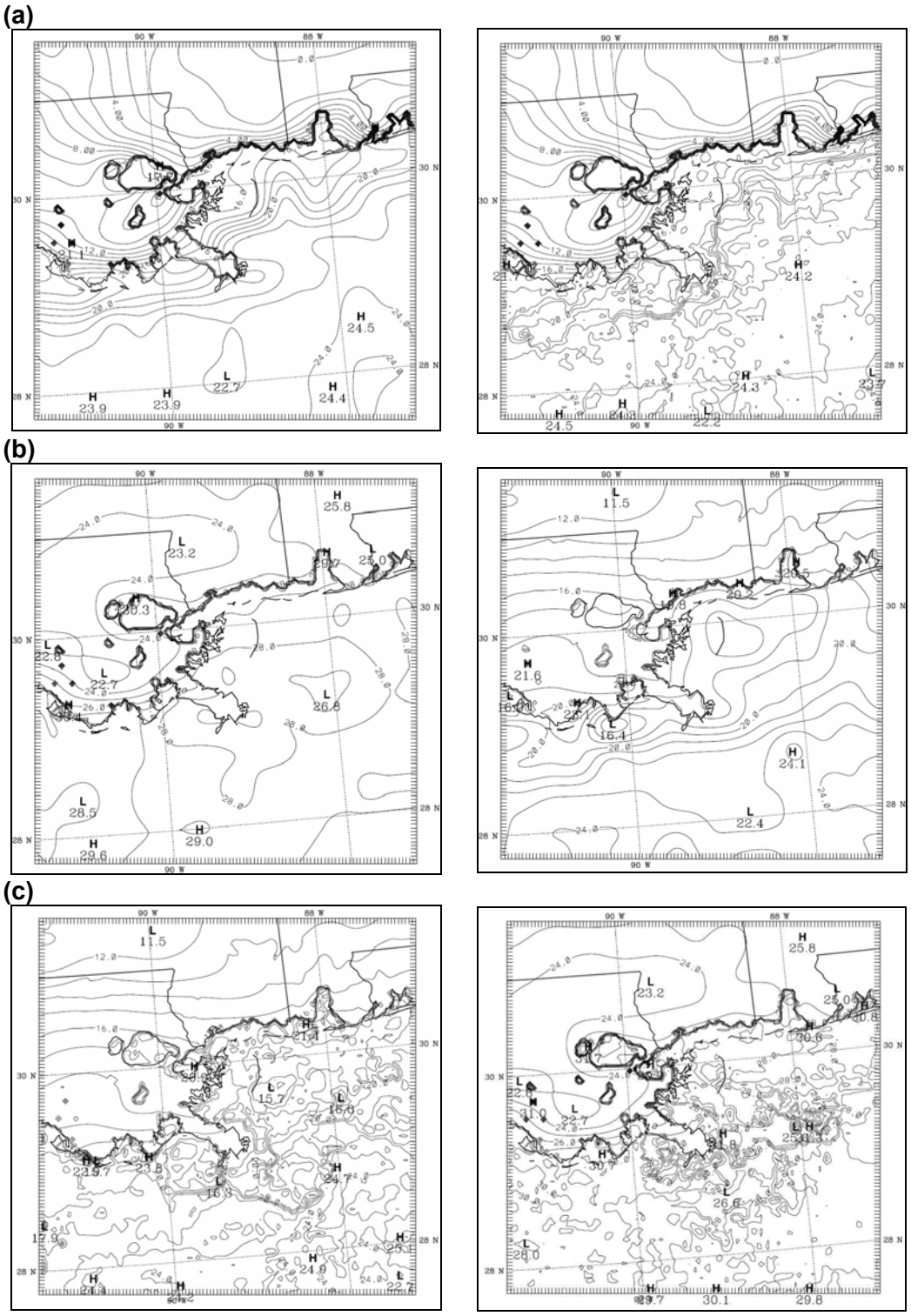

Figure 4-21. Comparison of model-derived ground temperature fields for the 36-km MODIS (left) and 4-km MODIS (right) at the initialization times for each case; (a) 12 UTC, 1 December 2000, (b) 12 UTC, 1 March 2001, and (c) 12 UTC, 8 July 2001. Isotherms are drawn every 1°C.

From the objective and subjective analyses of the wind fields in all three cases, it appears that the 4-km resolution MODIS SST has little effect, when averaged over a five-day period. In general, the statistical results (not shown) demonstrate relatively equal performances for wind speeds. The wind directions also do not have many differences that seem to be significant. The largest difference between the control simulations and the 4-km resolution MODIS SST simulations occurs in the surface layers for Case 1 and Case 3. For these two cases, there is a 1.0 degree and 1.2 degree detriment to the statistics, respectively, when the 4-km MODIS SST is used. Statistics for the temperature fields, however, suggest that the 4-km MODIS SST may be beneficial. In both Case 2 and Case 3, when the role of the air-sea interaction is more critical, there is a decrease in surface-layer TEMP errors. For Case 2, there is a 0.1 °C decrease in model error from the control simulation, and for Case 3 there is a 0.2 °C decrease in error (not shown). These errors appear to be minimal on average, but local differences in the temperature fields may be much larger and have an impact on photochemical reactions in an air-quality study.

The subjective analysis of the wind fields shows very few differences between the SST resolutions. Each model output is quite similar over the land areas, except when the winds are highly variable. The greatest differences in the wind fields are in Case 3 over the GOM, where the placement and intensity of convective activity seems to play the largest role in determining the direction of the winds. One of the biggest surprises in the results is the apparent lack of difference in the strength and positioning of the sea breeze fronts. A subjective comparison of the sea breezes simulated in both experiments shows few, if any, differences through most of the period. The largest noticeable difference between the simulated sea breeze fronts occurs at 2100 UTC, 12 July 2001. In the surface wind fields at this time (**Figure 4-22**), there is a slight, noticeable difference between the two model experiments in terms of the inland distance of the sea breeze penetration. In the JUL4M4 model output (**Figure 4-22b**), the sea breeze front has not penetrated as far inland as it has by the same time in the JUL4 output (**Figure 4-22a**). This difference is noticeable both on the Mississippi and Alabama coastlines, as well as the southern Louisiana coastline, but no observational data are available at this time that can help subjectively analyze which product may have the more accurate result. It is clear, however, that this difference in inland penetration is not very substantial, as the placement of the sea breeze front in the JUL4 output is only about one grid cell farther inland, so it would be difficult to determine the actual penetration of the sea breeze without high resolution observations.

Even though there is a lack of significant difference in the wind statistics and subjective analysis, the mass statistics (not shown) and the subjectively analyzed precipitation fields comparing the control and 4-km SST simulations suggest that there may be some advantage to using higher resolution SST fields. For the wind fields, it appears that incorporating a higher-resolution SST may not be necessary, but if the data are available for use, it should be used since it does not appear to adversely affect the model performance over the course of the simulation. Higher resolution SST may have a positive impact on the mass (temperature and moisture) and precipitation fields, which are both important in many air-chemistry applications, and improved precipitation fields may be related to improved sea-breeze front convergence but we do not have sufficient wind observations in the coastal zone to resolve it.

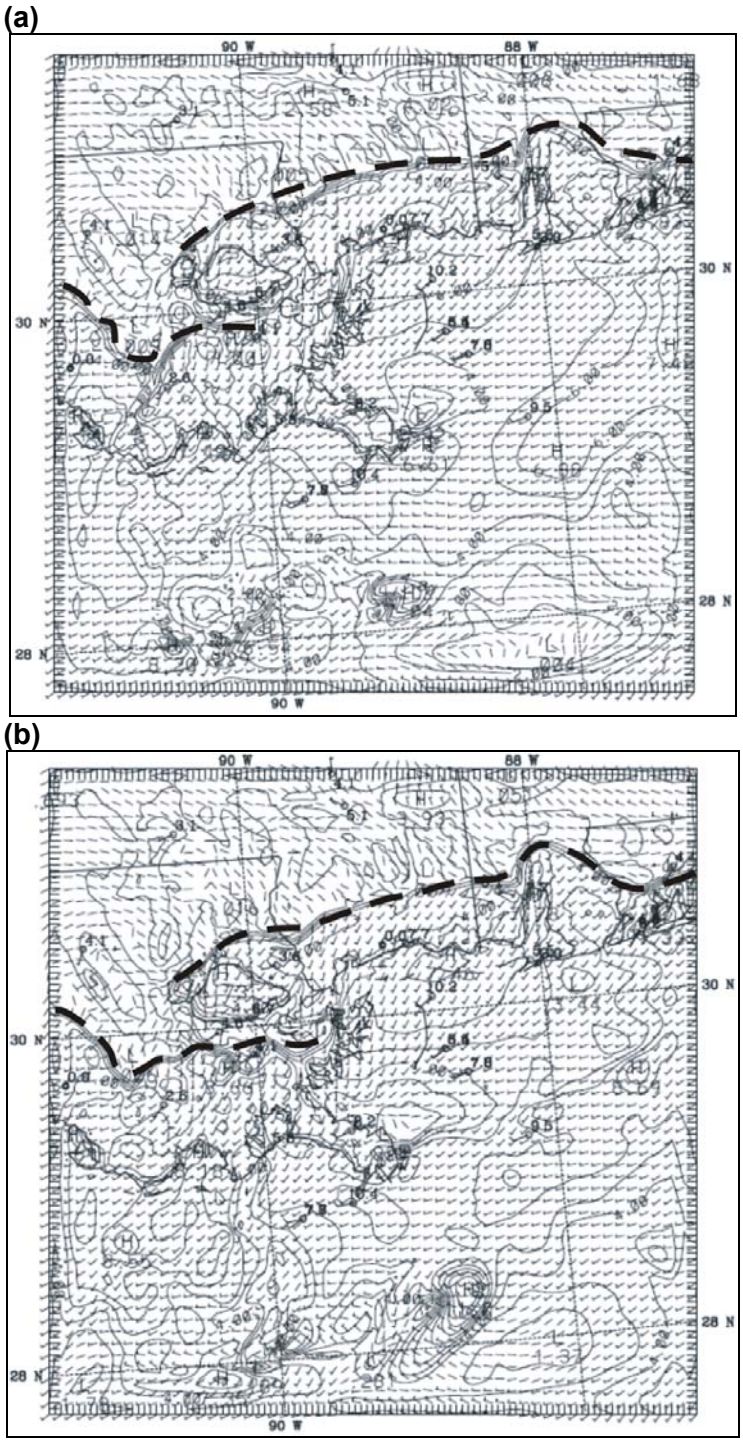

Figure 4-22. Comparison of the model-derived surface wind fields for (a) JUL4 and (b) JUL4M4, at 21 UTC, 12 July 2001. Modeled wind barbs are plotted every other grid cell. Wind speeds are plotted in m/s, and isotachs are drawn every 1 m/s.

4.3.7 Summary of the Additional 4-km Experiments

Among the 4-km resolution experiments, the statistical results for the wind variables were surprisingly close, even closer than the differences between the control 12-km and 4-km experiments with few exceptions. The temperature statistics do, however, show some slight benefits of using the 4-km MODIS SST. While the statistical differences among the four 4-km experiments may be small, the subjective analyses add some insight into the value of the various 4-km experiments.

The addition of the 4-km resolution MODIS SST had a lesser effect on the wind fields than the addition of the convective parameterization. Subjectively comparing the model results of the control simulation versus the 4-km MODIS simulations revealed very few differences, especially close to the area of interest. Some differences in the wind fields, and to a greater extent the precipitation fields, were present over the Gulf Coast and open waters of the GOM, where the circulations were slightly different, and local precipitation maxima were also different enough to warrant closer examination. A more detailed discussion of the 4-km experiments is provided in Appendix G.

5.0 EMISSION INVENTORY

This section describes the data sources and processes used to develop model-ready emissions inputs for the 2000-2001 study year and the SO_2 and NO_2 baseline years 1977 (SO_2) and 1988 (NO_2). For 2000-2001, emission inputs were developed for both the CMAQ and CALPUFF air quality modeling systems, while only CALPUFF emission inputs were developed for the 1977 and 1988 baseline years.

5.1 DATA SOURCES

The EPA's 1999 National Emission Inventory (NEI) (U.S. Environmental Protection Agency, 1999), version 3, was used to represent emissions from onshore sources in the Breton Island domain. This inventory has been made available in the Inventory Data Analyzer (IDA) format accepted by the Sparse Matrix Operator Kernel Emissions Modeling System (SMOKE), the tool used to prepare model-ready emission files for this study. The 1999 NEI contains annualized, county-level emissions estimates by source category for area sources, non-road mobile sources, and on-road mobile sources, as well as facility-specific emission estimates for individual point sources.

Projection from the 1999 NEI to the years modeled was performed using state-specific growth factors generated with the EPA's Economic Growth Analysis System (EGAS), version 5.0. EGAS generates growth factors by source category code (SCC) using forecasts of economic activity, population, and other variables and is capable of generating growth factors for any years between 1969 and 2035. Not all source categories in the 1999 NEI were addressed by EGAS for the 1977 and 1988 baseline years, including on-road mobile sources. In those cases, growth factors were derived from EPA national emission trends data, which are available on the Internet at http://www.epa.gov/ttn/chief/trends.

Emission estimates from biogenic sources were based on EPA's Biogenic Emission Landcover Database (BELD), emission factors contained in EPA's Biogenic Emissions Inventory System (BEIS), and gridded temperature data derived from MM5 runs. Biogenic emissions were held constant across all years of interest.

Emissions from offshore sources for the 2000-2001 study year were derived from a year-2000 emissions inventory developed by Eastern Research Group, Inc. (ERG) under contract with MMS[6]. This inventory contains estimates of all Outer Continental Shelf (OCS) oil and gas production-related sources in the Gulf of Mexico. Emissions from platform sources were based on monthly activity data collected through the Gulf Offshore Activities Data System (GOADS), and emission estimates were also developed for non-platform sources such as commercial marine vessels and helicopters. This emission inventory (October 6, 2004 version) was provided to STI in an Access Database and was converted to IDA format so that it could be processed through the SMOKE model. Commercial marine emissions covered by the offshore inventory were removed from the 1999 NEI to avoid double-counting (in-port emissions from these vessels in the 1999 NEI were retained).

[6] ERG has revised this inventory since the annual modeling was performed.

For the baseline years of 1977 and 1988, offshore emissions were derived from historical emissions estimates for oil and gas production activities in the Gulf of Mexico developed by STI under an earlier contract with MMS (Coe et al., 2003). During that project, STI developed 1977 and 1988 emission inventories for offshore stationary (e.g., platform-based equipment) and mobile (e.g., transitory equipment including crew and supply boats, drill and pipeline-laying vessels, etc.).

These 1977 and 1988 inventories were based on the gulf-wide emissions inventory (MOADS 3) that was developed as part of the Gulf of Mexico Air Quality Study (GMAQS) in 1993. The MOADS 3 inventory was used as a baseline from which historical emissions could be estimated by using economic scaling factors or extrapolated activity data (such as growth or decline in production rates and activity variations in platform equipment). For some sources, emissions modeling techniques were used to directly estimate emissions from emission factors and activity data. Historical emissions were distributed in space and time according to historical activity data or more recently developed Gulf-specific information by using spatial analysis techniques.

Finally, it should be noted that the 1977 and 1988 inventories previously developed by STI did not include emissions from commercial marine vessels not associated with oil and gas production, so emissions from these vessels were backcast from the 1999 NEI.

5.2 EMISSIONS PROCESSING

IDA-formatted emission files were processed through the SMOKE emissions modeling system, which transforms an annualized (or average day) emission inventory through temporal allocation, chemical speciation, and spatial allocation, to achieve the resolution required by an air quality model. Diurnal profiles developed for major offshore source categories by ERG were incorporated into the SMOKE temporal profile library, while SMOKE default profiles were used to temporalize onshore sources. All sources were speciated using SMOKE speciation profiles that are based on the Carbon Bond IV (CB-IV) chemical mechanism.

SMOKE has been designed to prepare model-ready emission files for CMAQ or UAM-based models such as CAM_x. To prepare emission files for CALPUFF, the merged, low-level emission file and the elevated point source file created by SMOKE had to be reformatted. For low-level sources, this was accomplished by altering SMOKE's SMK2EMIS module to write a CALPUFF-ready volume source emissions file. Volume sources were used for CALPUFF for consistency with CMAQ's treatment of emissions. Similarly, a CALPUFF-ready point source file was created by altering PTSRCE, a program designed to convert the ASCII elevated point source file output by SMOKE to UAM format. UAM format refers to the input file format used by the Urban Airshed Model (UAM) and the Comprehensive Air Quality Model with extensions (CAMx).

Day-specific emission files were generated for the 12-km air quality modeling domain, which is slightly smaller than the 12-km MM5 modeling domain (see Section 6.3.1), for the 2000-2001 study year and for the baseline years of 1977 and 1988.

5.3 SUMMARY OF EMISSIONS

The emissions for a sample date (December 1) are summarized in **Table 5-1** and displayed in emission density plots of low-level NO_x and SO_2 emissions in **Figures 5-1 through 5-6**. Changes in emission densities from the 2000-2001 study year to the 1977 and 1988 baseline years at 1200 CST on December 1 are shown in **Figures 5-7 through 5-10**. In change is positive when emissions increased and negative when emissions decreased since the baseline year.

Table 5-1

Emissions by Source Type and Year for December 1

Source Category	Emissions (tons/day)					
	CO	NO_x	VOC	SO_2	PM_{10}	$PM_{2.5}$
December 1, 2000						
Land-based Emissions						
Area	5,344.4	695.2	3,330.3	500.8	8,302.7	1,982.5
Non-road mobile	6,172.7	1,530.7	744.4	195.8	107.7	98.7
On-road mobile	29,810.1	3,302.2	2,292.1	121.2	95.5	74.2
Point	2,454.9	4,501.0	1,136.0	7,312.8	1,021.5	840.5
Biogenics	0.0	71.0	16,650.0	0.0	0.0	0.0
Offshore Emissions						
Non-platform (petroleum)	53.0	264.3	27.4	45.7	6.9	6.9
Non-platform (other)	12.1	66.4	40.8	12.2	1.7	1.7
Platform	241.9	200.8	177.1	8.4	2.0	2.0
Total	44,089.2	10,631.6	24,398.0	8,197.0	9,538.0	3,006.5
December 1, 1988						
Land-based Emissions						
Area	7,270.0	706.2	3,433.3	646.8	8,446.4	2,134.3
Non-road mobile	7,132.6	1,585.5	1,123.0	178.2	121.5	109.9
On-road mobile	53,300.0	3,925.4	4,661.2	258.6	165.4	134.3
Point	1,795.3	5,210.2	910.1	9,580.3	684.3	561.1
Biogenics	0.0	71.0	16,650.0	0.0	0.0	0.0
Offshore Emissions						
Non-platform (petroleum)	9.1	85.2	0.9	21.8	2.1	2.0
Non-platform (other)	5.2	39.7	1.2	29.6	2.2	2.0
Platform	246.2	203.4	92.9	7.4	1.5	1.4
Total	69,758.5	11,826.6	26,872.5	10,722.7	9,423.5	2,945.1
December 1, 1977						
Land-based Emissions						
Area	6,131.3	881.9	2,773.5	878.9	8,363.8	2,037.2
Non-road mobile	7,087.3	1,543.7	1,118.8	161.3	117.1	105.9
On-road mobile	63,313.6	4,350.6	6,152.0	176.7	174.3	126.3
Point	1,776.3	5,792.6	815.5	11,096.6	1,338.1	1,139.7
Biogenics	0.0	71.0	16,650.0	0.0	0.0	0.0
Offshore Emissions						
Non-platform (petroleum)	5.5	51.3	0.5	13.6	1.3	1.2
Non-platform (other)	4.5	34.5	1.1	25.7	1.9	1.8
Platform	224.0	197.7	127.6	18.4	3.4	3.3
Total	78,542.5	12,923.3	27,638.9	12,371.2	10,000.0	3,415.4

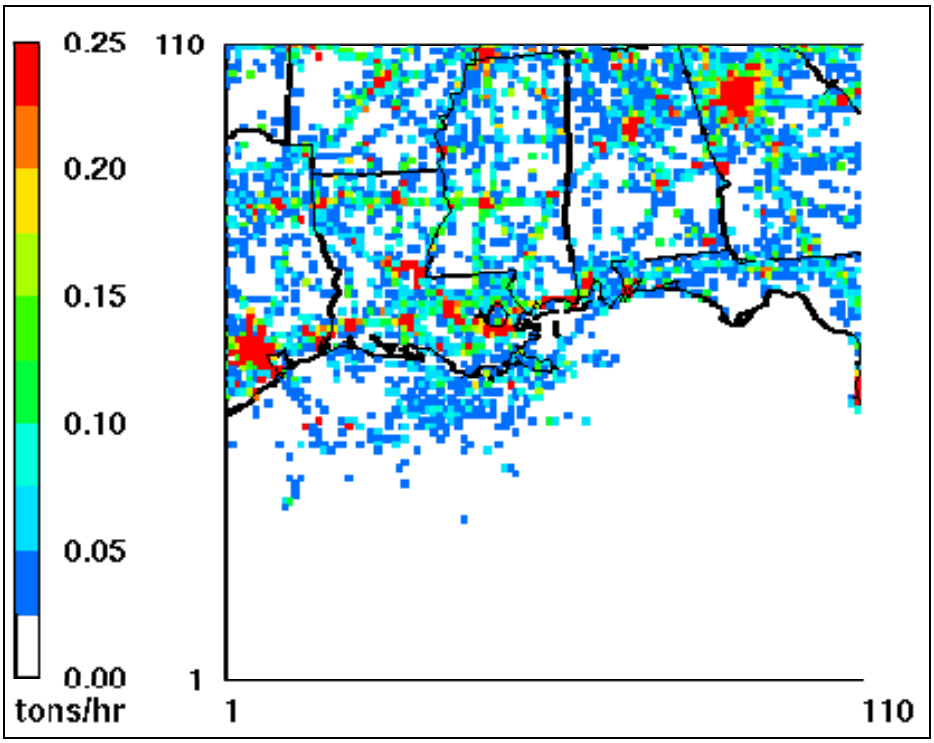

Figure 5-1. Low-level NO_x emissions for 1200 CST on December 1, 2000.

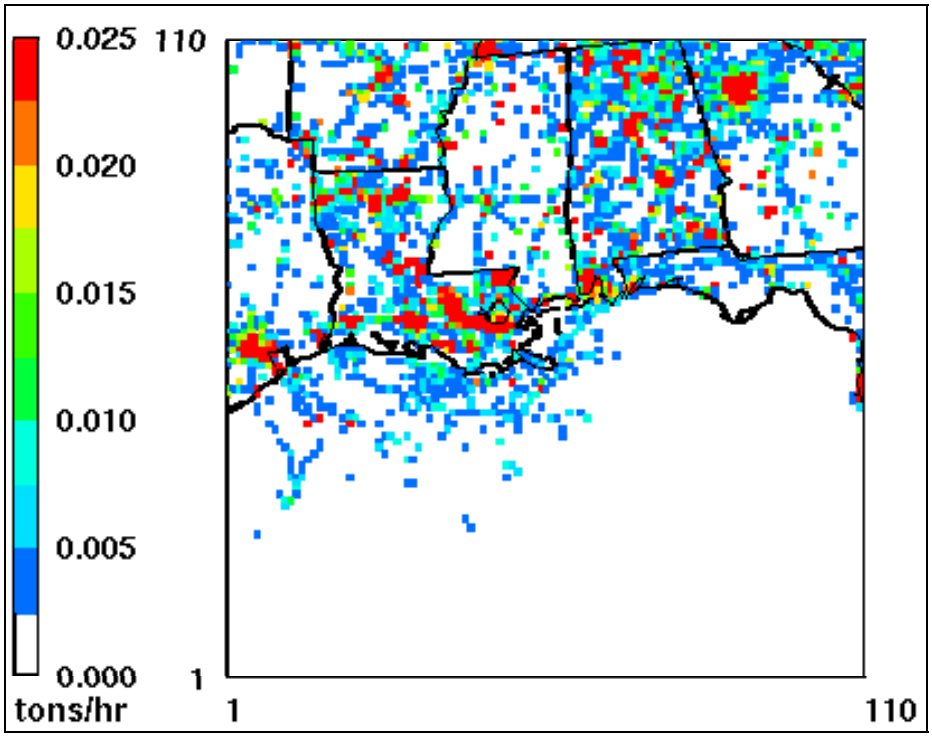

Figure 5-2. Low-level SO_2 emissions for 1200 CST on December 1, 2000.

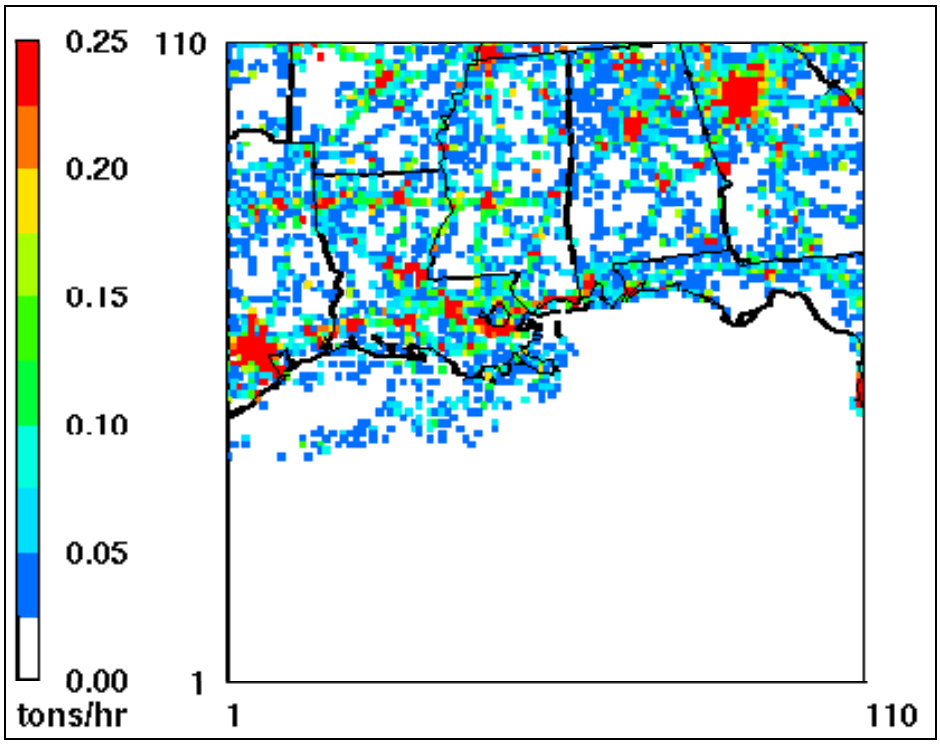

Figure 5-3. Low-level NO_x emissions for 1200 CST on December 1, 1988.

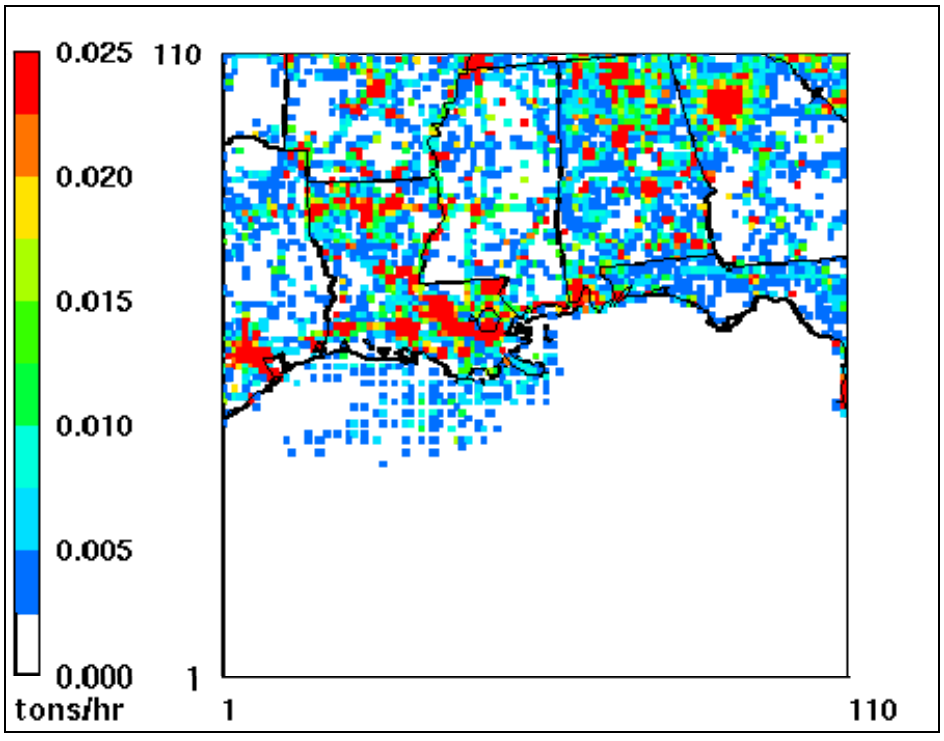

Figure 5-4. Low-level SO_2 emissions for 1200 CST on December 1, 1988.

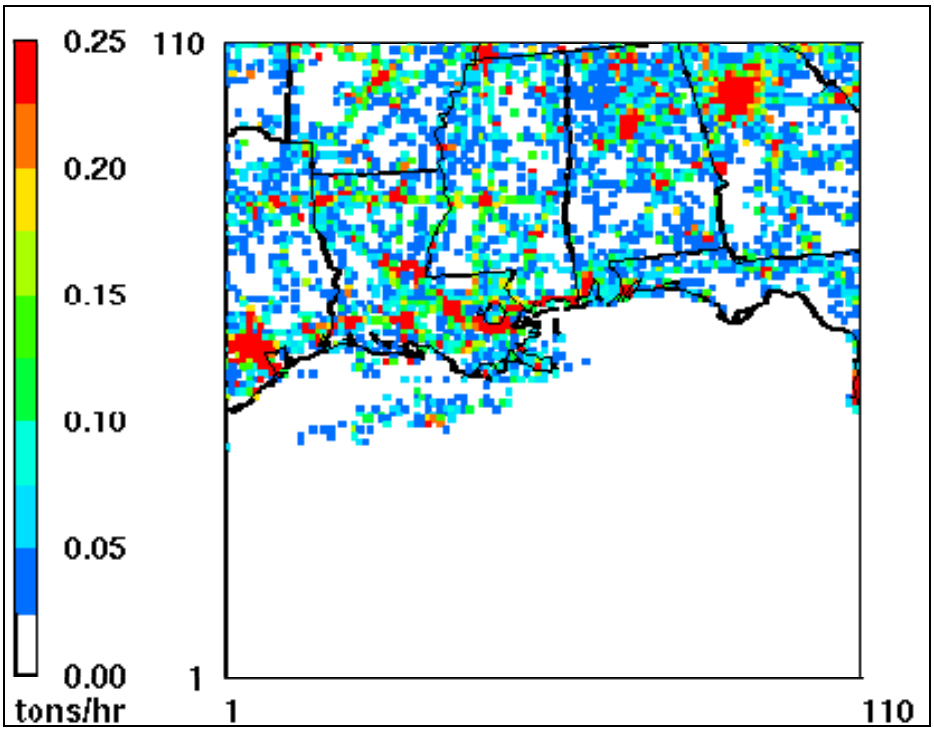

Figure 5-5. Low-level NO_x emissions for 1200 CST on December 1, 1977.

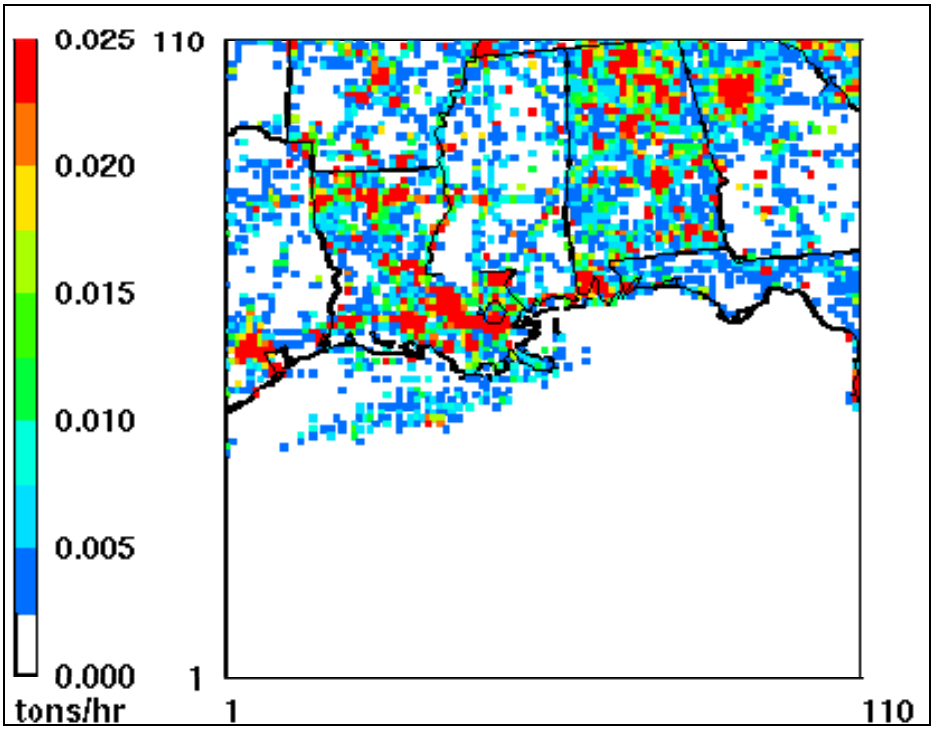

Figure 5-6. Low-level SO_2 emissions for 1200 CST on December 1, 1977.

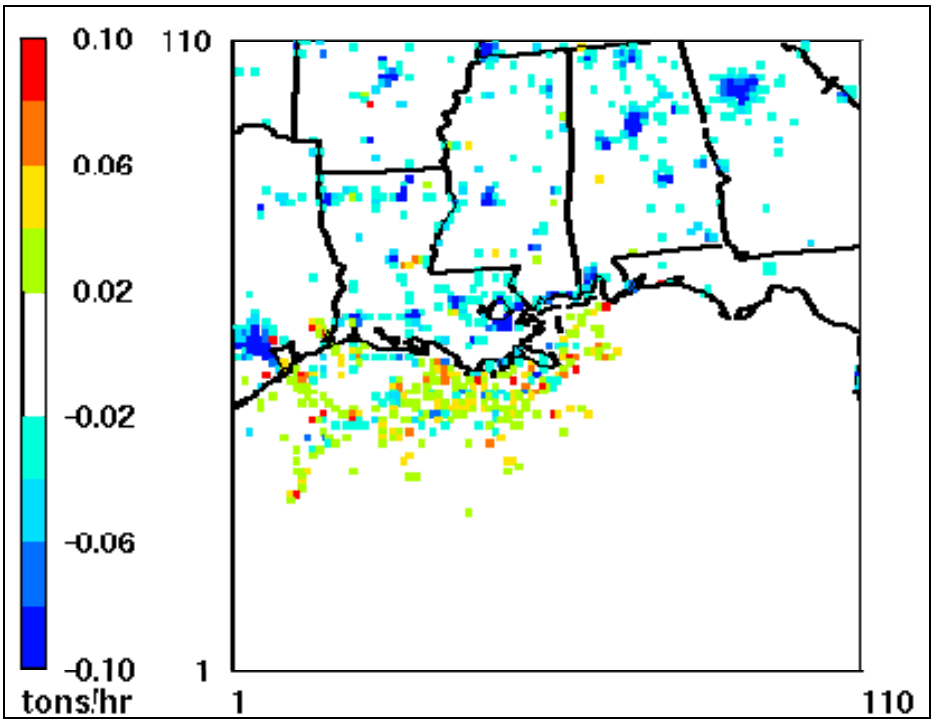

Figure 5-7. Changes in low-level NO_x emissions from 1988 to 2000 at 1200 CST on December 1.

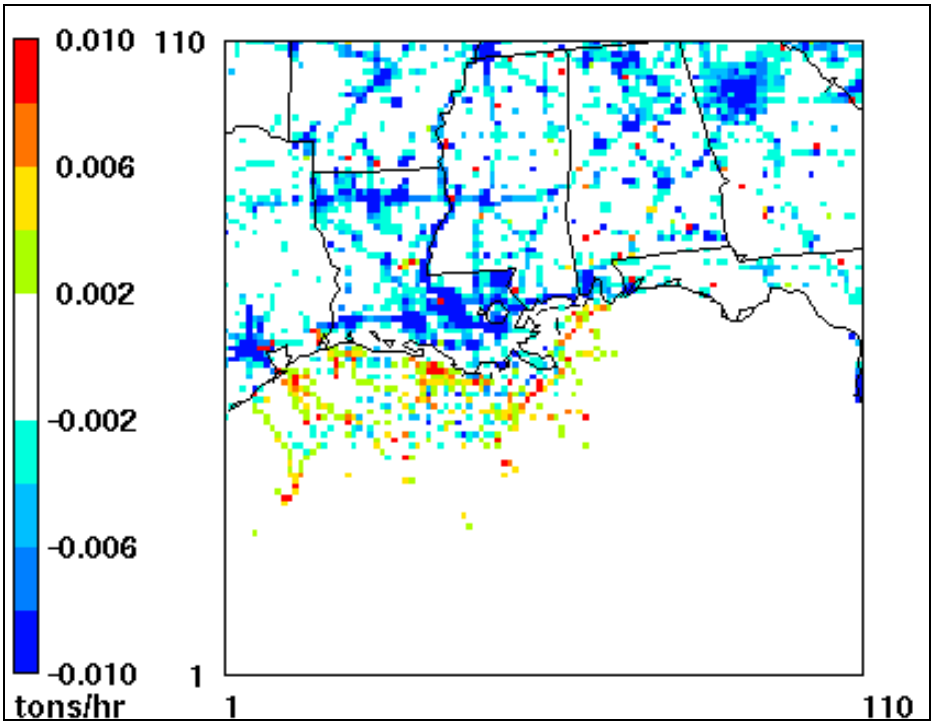

Figure 5-8. Changes in low-level SO_2 emissions from 1988 to 2000 at 1200 CST on December 1.

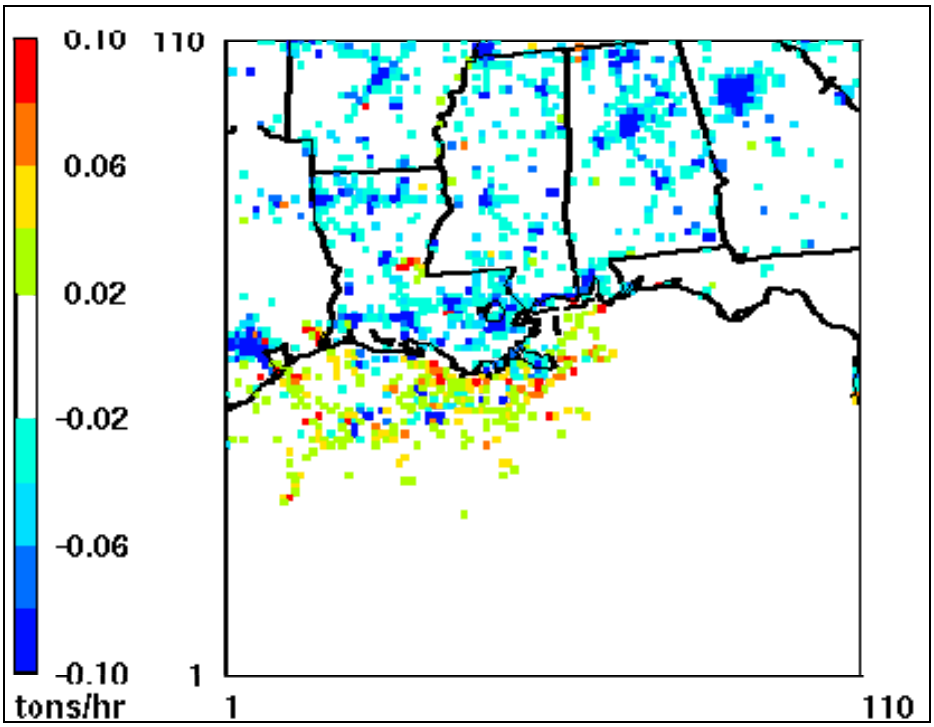

Figure 5-9. Changes in low-level NO_x emissions from 1977 to 2000 at 1200 CST on December 1.

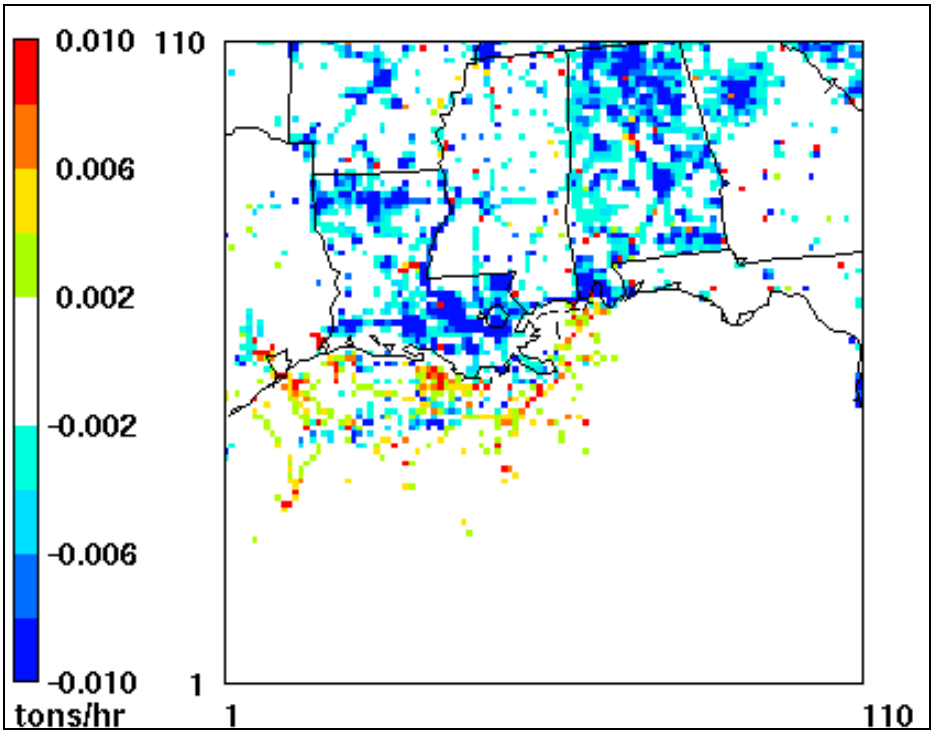

Figure 5-10. Changes in low-level SO_2 emissions from 1977 to 2000 at 1200 CST on December 1.

6.0 EPISODE-TYPE AIR QUALITY MODELING

This section describes the models and methods used to perform episode-type air quality modeling, and summarizes results of that modeling.

6.1 MODEL SELECTION

As part of the experimental design for this study, two air quality models were to be selected for initial evaluation: a Lagrangian puff model and an Eulerian photochemical grid model. Hanna and Chang (1995) documented the approach and results of the model selection process; they are described in this section. Models and modeling methods have evolved over the course of this study. While this section describes the state of air quality modeling when the model selection process began in 2003, it does not necessarily reflect the current state-of-the-science.

6.1.1 Overview

Guidance on modeling for PSD analysis requires that emissions within several hundred km of Class I areas be considered. Therefore, the models used should incorporate the meteorological model outputs and calculate the time-and-space dependent transport, dispersion, and chemical transformation of NO_2 and SO_2 emissions from the domain with a radius of 200 km or more. They should also account for background and other regional contributions to air quality. However, the maximum useful distance to which most steady-state Gaussian plume models (GPMs) are considered accurate for setting emission limits and performing increment analyses is 50 km.

For the BNWA, there are a mixture of both long-range and short-range source-receptor relationships in a large modeled domain. Historically, these applications have presented considerable difficulty to an analyst if impacts from sources having transport distances greater than 50 km significantly contributed to the design concentrations. To properly analyze applications of this type, a modeling approach is needed that has the capability of combining, in a consistent manner, impacts involving both short and long-range transport. The CALPUFF modeling system, listed in 40 CFR Ch. I (7–1–03 Edition), Appendix A to Part 51—Guideline on Air Quality Models, has been designed to accommodate both the Class I area long range transport situation and the large modeling domain situation. However, there are concerns about the adequacy of CALPUFF's treatment of chemical transformations, particularly for SO_2.

The chemical transformation of SO_2 emitted from point sources or single industrial plants in rural areas is generally assumed to be relatively unimportant to the estimation of maximum concentrations when travel time is limited to a few hours. In domains that include broader industrial and urban areas, where synergistic effects among pollutants are of considerable consequence, chemical transformation rates may be of concern. The EPA modeling guidelines suggest that the use of models that incorporate complex chemical mechanisms should be considered only on a case-by-case basis and with a proper demonstration of applicability. These are generally regional models not designed for the evaluation of individual sources but used

primarily for region-wide evaluations. Therefore, the model selection process will consider both Lagrangian and Eulerian models with varying levels treatment of chemical transformations.

To better identify candidate models, a critical review of available literature, model documents, examples of applications, and reviews by others was carried out. The team expanded on the reviews by Chang et al. (1998) and Tesche and McNally (1998) by considering model developments such as SCIPUFF and CMAQ. As part of the review of Eulerian photochemical grid models and Lagrangian puff models, a fundamental criterion is that the model is able to make use of mass-consistent wind distributions that satisfactorily account for space and time variations in meteorological parameters (e.g., fronts, sea breezes, and land breezes). Air quality models should be able to make use of accurate estimates of vertical stability, turbulence, and mixing depths. As shown by Sillman et al. (1993) and Hanna et al. (2006), boundary layer stabilities over water can persist with no diurnal variations and can lead to extended periods of very stable or very unstable conditions that must be accounted for in order to satisfactorily simulate vertical diffusion processes.

We also reviewed the literature to identify typical evaluation exercises of the models being considered. The focus was on NO_2 and SO_2 in coastal and over-water environments. The results of the limited evaluation exercises were used to develop preliminary estimates of the characteristics of acceptable model performance and to suggest some criteria. Conclusions about typical model performance and recommendations of model acceptance criteria are provided.

The following practical considerations for air quality models are also considered in the review.

Emissions Handling

- Many sources (onshore and offshore) need to be modeled, so the modeling system should be able to handle area and point sources numbering in the thousands.
- If the model includes more detailed chemistry, the modeling system needs to include tools/profiles to speciate volatile organic compounds (VOC) into model species.
- The model should handle arbitrarily varying emissions.

Meteorology Interface

- It would be desirable to select an air quality model (AQM) that can operate in the same coordinate system as MM5 to minimize re-gridding input data.
- The AQM should include a preprocessor that accepts MM5 as input. Otherwise, it would be necessary to develop one, which could be time-consuming and delay the project.

AQM System

- The AQM should be publicly available.
- The system should include post-processors to aid in data extraction and visualization.

- Eulerian models should meet the requirements proposed for 8-hr ozone and $PM_{2.5}$ modeling guidelines (MMS and the Scientific Review Board (SRB) have indicated interest in the utility of modeling beyond this study).
- Eulerian models should have state-of-the-science treatments of chemistry, advection, diffusion, deposition, and plume-in-grid formulation.

6.1.2 Air Quality Models Considered

Although there are dozens of Lagrangian puff and Eulerian grid models in the literature, the models listed below are the most widely used in the United States in general and in the Gulf of Mexico region particularly. We decided to focus on models already widely used because they have been thoroughly tested and they have a degree of acceptance by the community of researchers and regulatory agencies.

Lagrangian Puff Models:

- CALPUFF (California Puff) (Scire et al., 1995)
- SCIPUFF (Second-Order-Closure Integrated Puff) (Sykes et al., 1997)

Eulerian Grid Models:

- CAMx (Comprehensive Air quality Model with extensions) (ENVIRON International Corporation, 2002)
- CMAQ (Community Model for Air Quality) (National Exposure Research Laboratory, 1999)
- MAQSIP (Multiscale Air Quality Simulation Platform) (McHenry and Olerud, 2002)
- UAM-V (Urban Airshed Model with Variable grid) (Douglas et al., 2001).

In considering SCIPUFF, we also include the Second-Order-Closure Integrated Puff with Chemistry (Santos and Sykes, 2000 [SCHICHEM]) even though it is not publicly available and has not been applied widely. Note that several straight-line GPMs have been used in the Gulf of Mexico region and are mentioned later. However, these GPMs are not part of the MMS's plans for the current project, since the GPMs do not allow for changes in wind speed and direction, stability, or other meteorological parameters over the course of the plume trajectory, and are not recommended for modeling long range-transport.

6.1.3 Air Quality Model Applications and Contacts in Gulf of Mexico Area

The OCD (Offshore and Coastal Dispersion) model (DiCristofaro and Hanna, 1989, 1991) is used for modeling offshore sources, but OCD is a straight-line GPM that should not be used at distances beyond about 30 km to 50 km from the source. Since CALPUFF is a Lagrangian puff model that can account for changes in meteorological conditions over several hours, agencies and industry groups have used CALPUFF in some modeling exercises for offshore sources over larger domains.

There have been many Eulerian grid model applications for coastal urban ozone problems, but the emphasis of the runs has been primarily on the sources and receptors on the inland part of the domain. Concern about offshore sources and receptors is minimal, and no evaluations of the Eulerian grid models' performance for offshore sources have taken place.

The applications and evaluations of Eulerian grid models in coastal areas have been concerned mostly with ozone and its precursors. Few Eulerian grid model applications focus on NO_2 or SO_2 as the primary end product. The few available Lagrangian puff modeling studies in offshore domains have been related to permitting specific facilities and the studies do not include evaluations with field data.

Table 6-1 lists candidate models and the groups applying these models to the Gulf of Mexico area. Some of this information is available as publicly-distributed reports, journal articles, conference papers, and documents on EPA web sites. In addition, comprehensive sets of responses, including many reports and papers, were obtained from the persons and the organizations listed in the table and from others involved with modeling in the Gulf of Mexico area.

For specific permitting of offshore sources, states and industries primarily use the OCD model with a move toward the Lagrangian puff model, CALPUFF, if the source is more than 50 or 100 km from the receptor (as is the case with many sources that could impact Breton Island). CALPUFF/CALMET can be linked with the prognostic mesoscale meteorological model, MM5.

For coastal photochemical modeling, two Eulerian grid models have received the most use in the coastal areas of the Gulf of Mexico: (1) Texas uses CAMx linked with MM5, and (2) other states use UAM-V linked with MM5, as a result of experience with Gulf Coast Ozone Study (GCOS) and state implementation plan modeling in Florida.

CMAQ is a third Eulerian grid model increasingly used in the Gulf of Mexico. CMAQ was developed by the EPA (National Exposure Research Laboratory, 1999) and has been adopted by EPA regions and state agencies. A fourth Eulerian grid model is MAQSIP, which has been used for own operational runs in the Gulf Coast area but it is uncertain whether states and agencies use the information. CMAQ and MAQSIP are designed to link with MM5.

A drawback of MAQSIP is that it is unlikely to be widely adopted by agencies, since the version being used in the Gulf of Mexico is proprietary and the public version is not being actively maintained.

The Regional Planning Organizations (RPOs) established by EPA are inclined to use CMAQ for regional applications, which will eventually support State modeling programs. The Western Regional Air Planning (WRAP) group is using CMAQ, and the Central Regional Air Planning (CENRAP) group and the southeastern states are planning on using CMAQ. The Midwest RPO has been running both CMAQ and CAMx. EPA has been modeling extensively with CMAQ as well, and it is being used in several research programs at universities and by foreign governments. As an example, EPA supported a regional air pollution modeling study at the University of Houston, where MM5 and CMAQ were the models used.

Table 6-1

Lists of Models Used in the Gulf of Mexico Area with Emphasis on Regulatory Studies

Model	Area	Organization/Study	Contact
OCD, some use CALPUFF	Gulf of Mexico	Chevron	Steve Ziman sdzi@chevrontexaco.com
OCD	Gulf of Mexico	MMS	Dirk Herkhof dirk.herkhof@mms.gov
UAM-V; CAMx	Texas, Gulf, and Central US	TCEQ; MCNC; Environ; STI	Jim Smith JISMITH@tceq.state.tx.us
UAM-V	Gulf Coast, Florida	SAI/GCOS	Jay Haney JayHaney@icfconsulting.com http://gcos.saintl.com
MAQSIP-RT	Southeast US/ Texas nest	MCNC/Real-time modeling	John McHenry mchenry@emc.mcnc.org
CMAQ	Southeast Texas	Lamar University	Thomas C. Ho hotc@hal.lamar.edu
CAMx	Texas, Victoria, Austin	Univ. of Texas-Austin, has TexAQS web site	David Allen allen@che.utexas.edu
CMAQ	Texas	University of Houston	Daewon Byun dwbyun@math.uh.edu
N/A	Texas	TCEQ	Dom Ruggeri (512) 239-1463 druggeri@tceq.state.tx.us
UAM-V through GCOS	Louisiana	Louisiana Dept. of Environmental Quality, GCOS	Patrick Pakunpanya (225) 765-0240 patrickp@ldeg.org
CALPUFF	Mississippi	Department of Environmental Quality	Bruce Ferguson (601) 961-5742 bruce.ferguson@deq.state.ms.us
OCD, ISCST3, CALPUFF	Alabama	ADEM	Leigh Bacon lbb@adem.state.al.us
UAM-V	Florida	Florida DER; GCOS and subsequent FL study	Tom Rogers tom.rogers@dep.state.fl.us
OCD, CALPUFF	EPA Region IV	EPA Regional Modeler	Brenda Johnson (404) 562-9037 johnson.brenda@epa.gov
See state SIPs	EPA Region VI	EPA Regional Modeler	Quang Nguyen (214) 665-7238 nguyen.quang@epamail.epa.gov

Because the MMS and the project's SRB have said they are most interested in SO_2, the conversion to sulfate will be important for longer-range transport. Also, the MMS has suggested that it would be good if the chosen model could deal with PM for future applications. All the

models mentioned above have a PM version available that could be implemented for future studies.

Some pros and cons of the three primary candidate models are listed below:

- CMAQ can use MM5 output more directly (less manipulation), has more options for horizontal advection solvers, several options for chemistry solvers (including a new solver that is faster), and chemical mechanisms, and is supported by the EPA.
- CAMx has several options for horizontal advection solvers and chemical mechanisms, and has a chemistry solver that is significantly faster than the ones in CMAQ.
- UAM-V may have better treatment of deposition to water bodies. However, it is limited to the Smolarkiewicz advection scheme, which may produce large numerical diffusion.

We conclude that the most reasonable Eulerian grid (photochemical) model choices for the Gulf of Mexico are CMAQ, CAMx, and UAM-V, because they represent the state-of-the-science and are familiar to the modelers in the area. This statement is based on scientific formulation and peer reviews rather than applications since none have been evaluated overwater for the species of interest to this project (NO_2 and SO_2).

Some additional scientific aspects of the candidate Lagrangian puff models and Eulerian grid models are discussed below, as well as some conclusions concerning model performance standards.

6.1.4 Lagrangian Puff Models

The advantage of Lagrangian puff models over GPMs such as OCD (DiCristofaro and Hanna, 1991, 1989) is that Lagrangian puff models can treat changes in wind speed and direction and stability over the trajectory of the pollutant cloud. These changes are important if the cloud is transported at significant concentrations over distances exceeding 20 or 30 km or times exceeding several hours. Two Lagrangian puff models are currently widely used by federal agencies, are similar in scientific form, and produce similar performance measures when compared with observations (Chang et al., 1998). CALPUFF (Scire et al., 1995) is sponsored by the EPA and SCIPUFF (Sykes et al., 1997) is sponsored by the U.S. Department of Defense (DOD). Despite the fact that they are nearly equivalent, we recommend that CALPUFF be chosen as the representative Lagrangian puff model for the current study, since its applications are more in line with the needs of the MMS. Further, in a separate project, the MMS is sponsoring the modification of CALPUFF so it will be more appropriate for overwater applications.

Both CALPUFF and SCIPUFF make use of state-of-the-science boundary layer parameterizations involving surface energy balances, calculation of Monin-Obukhov length and use of the convective scaling velocity. Both models have detailed algorithms to combine puffs at large travel times when there is otherwise much overlap among puffs. Both models can incorporate wind outputs from either diagnostic or prognostic meteorological models; and, more importantly, both can incorporate outputs from the prognostic model, MM5, which is the model selected by the MMS for the current study.

CALPUFF and SCIPUFF differ in a few ways. However, it is important to note that few of the SCIPUFF scientific advantages are directly relevant to the current report, which concerns minimum averaging times of one hour, pollutants that are not highly reactive, and terrain that is not hilly.

CALPUFF has a minimum averaging time of one hour, because of its need to satisfy EPA regulatory requirements. In contrast, SCIPUFF can treat averaging times as small as a few seconds. Consequently, SCIPUFF can be used to accurately simulate the time variation of concentrations due to a single puff, whereas CALPUFF would average the single puff over an hour. For MMS purposes, however, the 1-hr averaging time is sufficient.

SCIPUFF is one of the few available models that include predictions of the variability in concentration. It assumes a clipped-normal distribution. Typically, the standard deviation of the concentration fluctuations has a magnitude approximately equal to the mean concentration. In contrast, CALPUFF predicts only the mean concentration. For current regulatory calculations for the MMS, the variability calculation is not needed.

SCIPUFF can treat dense gases and large concentrations of aerosols. However, SCIPUFF's plume rise algorithms are not as detailed as those of CALPUFF. Because the MMS applications do not include significant effects of dense gases and aerosols, but are more concerned with buoyant plume rise, CALPUFF has the advantage in this category.

CALPUFF has complex terrain algorithms for treating plumes in hill and valley situations, while SCIPUFF has only a rudimentary treatment of terrain. Even though the Gulf of Mexico region has no major hills or cliffs, CALPUFF's capability is still useful.

CALPUFF includes an option for parameterized chemical transformation effects using a five-species scheme (SO_2, SO_4, NO_x, HNO_3, and NO_3^-) that is employed in the MESOPUFF II (Scire et al., 1984) model. It requires a set of user-specified diurnally varying transformation rates. The model contains a linear, pseudo-first-order scheme to treat the chemistry. The other available option, the RIVAD/ARM3 method, treats the same species but considers NO_x as two species, NO and NO_2, and assumes an equilibrium between gaseous HNO_3 and NH_4NO_3 aerosol. In this scheme, sulfate and nitrate concentrations are calculated using steady-state expressions for OH and O(1D) (an electronically excited oxygen atom) concentrations. Area-specific photochemical flux is not calculated and is only considered indirectly in the calculation of the O(1D) concentration because the steady-state expression for O(1D) presented is proportional to the cosine of the solar zenith angle. The aqueous-phase oxidation of SO_2 to sulfates (SO_4^{-2}) is assumed to have a constant rate of 0.2 % per hour. User-specified diurnal concentration profiles are often used to evaluate transformation rates for the first order rate expressions. In particular, if the MESOPUFF II chemical scheme is used to simulate the following chemical transformations:

$$SO_2 \rightarrow SO_4^{-2} \qquad \textbf{(6-1)}$$

$$NO_x \rightarrow HNO_3 \rightarrow NO_3 \qquad \textbf{(6-2)}$$

Estimates of ambient ozone concentrations are required to compute the hourly conversion rates for these chemical transformations. CALPUFF provides two options for the ozone data. The first uses a single, typical value for the background ozone concentration, while the second option allows for use of hourly ozone data from one or more monitoring stations. Using the second option, a 24-hr cycle of transformation rates (1 per hour per each transformation) is derived that is based on ozone diurnal profiles. The transformation rate expressions were obtained by statistically analyzing hourly transformation rates determined from a photochemical model. The chemical model, the RHC/NO_x/SO_x model of Atkinson et al. (1982), was used to conduct box model calculations for a range of ambient conditions that were assumed to be representative of those spanned by a year. The results were used to determine daytime hourly conversion rates by numerical fitting. Variables considered were total solar radiation intensity, ozone concentration, an atmospheric stability index, and NO_x concentration.

The publicly available SCIPUFF treats chemical transformations by liner decay only. However, the EPRI sponsored SCICHEM version of the model does include a detailed gas and aerosol chemical mechanism typical of regional Eulerian photochemical models. Current implementations of SCICHEM include the Simulation Composition of Aerosol Particles at Equilibrium (SCAPE2) equilibrium scheme, which offers a comprehensive treatment of gas/particle chemical composition and thermodynamics, good accuracy, and reasonable computational efficiency. An application of the Reactive and Optics Model of Emissions (ROME) reactive plume model (Seigneur et al., 1997), which does include aqueous phase chemistry, to the Dallas-Fort Worth region showed that aqueous conversion played an important role in converting power plant SO_2 emissions to sulfate. As a result, work has also been done to include chemical transformations in the aqueous phase (Santos et al., 1999), since a significant amount of chemical conversion can occur in cloud or fog droplets. While the treatment of chemical transformations is greatly improved in SCICHEM, it is not clear whether its application for the large number of point and area sources in this increment analysis is viable.

CALPUFF treats building downwash, whereas SCIPUFF does not. Therefore CALPUFF is more useful than SCIPUFF for modeling near-field dispersion at industrial sites and oil platforms of interest to the MMS.

Both CALPUFF and SCIPUFF make use of gridded three-dimensional, time-dependent wind fields to move the puffs in the domain. SCIPUFF uses whatever vertical wind speed is provided. CALPUFF does not advect puffs vertically but instead uses the mean vertical gradient of vertical velocity across each puff to stretch the vertical distribution of mass in the puff. In the Gulf of Mexico region, there could be significant vertical speeds near frontal boundaries and sea and land breeze boundaries. However, strong vertical velocities are not expected during periods with high SO_2 and NO_2 concentrations and spurious positive vertical velocities could unrealistically advect a puff upward and out of the top of the mixing layer.

6.1.5 Eulerian Grid Models

Tesche and McNally (1998) surveyed models available for use in conjunction with the BAMP. However, there have been improvements in many of the Eulerian models since then. Another major change is that the CMAQ model developed by the EPA is gaining wider

acceptance. Furthermore, the TexAQS 2000 study (Allen and Durrenberger, 2002) and the Gulf Coast Ozone Study (GCOS) (Douglas et al., 2001) took place after the Tesche and McNally study, primarily making use of CAMx and UAM-V, respectively. As mentioned earlier, MAQSIP (McHenry and Olerud, 2002) was initially considered in our review but the version being applied in the Gulf of Mexico area is proprietary and therefore does not satisfy all of our criteria. Thus, the three candidate Eulerian grid models are CMAQ, UAM-V and CAMx.

All three candidate models can use MM5 prognostic meteorological predictions and have interfaces available for importing the MM5 predictions onto their respective 3-D grids. However, because the EPA developed the Models-3 system with the specific goal of linking MM5 and CMAQ, the CMAQ model can use MM5 outputs more directly with less manipulation necessary.

Both CMAQ and CAMx have several options for horizontal advection solvers, including newer solvers that are less diffusive than the old solvers.

All three models have updated their chemical mechanisms recently and have more than one chemical mechanism to choose from.

UAM-V may have better treatment of deposition to water bodies, although few data are available for evaluation.

Because they were used historically for simulating ozone in large urban regions, the three candidate Eulerian grid models have not been evaluated to determine the accuracy of their SO_2 or NO_2 predictions. Furthermore, none of these models has been evaluated with observations over water. In fact, there are often high concentrations of ozone and its precursors predicted over large water bodies such as Lake Michigan (Sillman et al., 1993), the Atlantic Ocean just to the east of New Jersey and New York, and the Gulf of Mexico just off the coast from Houston through Pensacola. These high predictions are often noted in project reports and are attributed to stable conditions over cool-water surfaces, which are common in the summer in Lake Michigan and in the Atlantic Ocean off the New England coast. However, no detailed study confirms the accuracy of these predictions. Furthermore, this effect is less likely over the Gulf of Mexico, where water temperatures are nearly always greater than air temperatures.

The CMAQ Eulerian grid model is recommended for further study as part of the current project. CMAQ has excellent scientific algorithms, was developed by the EPA specifically to be linked with MM5, and is receiving increasing acceptance by regulatory agencies. The major consideration in our decision is the acceptance factor. Since CMAQ was developed by the EPA and the EPA is training the regional offices and the state agencies in its use, CMAQ is likely to become the model of choice. CAMx is probably a reasonable second choice, but does not have the backing of the EPA development and maintenance teams. UAM-V is the third choice primarily because it does not easily link with MM5 and it is not being actively updated to the same extent as CMAQ.

6.1.6 Model Performance Standards

It would be helpful if the models discussed or recommended above had been evaluated with concentration observations offshore. Hanna et al. (1985) evaluated the currently approved MMS model, the OCD GPM, using several tracer experiments where the tracer gas was released a few km offshore and the concentrations were observed at the coastline and inland. In those evaluations, the OCD model was shown to have a relative mean bias of less than 30 or 40% and a relative scatter of about a factor of two. Subsequently, it has been shown that this is the typical performance expected of good models.

Neither CALPUFF nor SCIPUFF has been evaluated with offshore or coastal data. As shown by Chang et al. (1998), when the two models are evaluated side by side with mesoscale tracer data in two over-land experiments, they perform similarly, with relative biases and relative scatters similar to those of the OCD model mentioned above. However, the study also showed that the evaluation results were dependent on the diagnostic meteorological models that were linked with the Lagrangian puff dispersion models (CALMET is used as input for CALPUFF, and SWIFT is used as input for SCIPUFF)

None of the Eulerian grid models has been evaluated with offshore data. In contrast with the performance evaluation methods for OCD, CALPUFF and SCIPUFF mentioned above, a slightly different approach is recommended by the EPA to evaluate the Eulerian grid models in their many over-land evaluation exercises. In particular, the use of input adjustments is built into the EPA's evaluation process for Eulerian grid models. In other words, the modeler is allowed to adjust the initial and boundary conditions and other inputs and parameters (within reasonable bounds) so that the model predictions of ozone are within defined model acceptance bounds for the relative mean bias (e.g., +/- 15%) and relative absolute error (e.g., 35%). And even if the ozone predictions are within these bounds, the predictions of precursor concentrations, such as NO_2, NO and VOCs, are seldom as accurate. The Lake Michigan Ozone Study (LMOS) observed ozone and precursor concentrations by boat and aircraft over Lake Michigan, and showed layers of high concentrations in the shallow stable surface layer just above the cold lake surface and in several stable layers between the surface and the residual mixing depth at a height of about 1000 m (Hanna and Chang, 1995). The Eulerian grid model (an earlier version of UAM-V) was able to simulate the layering in LMOS but no quantitative comparisons were made.

We anticipate that the ongoing MMS-sponsored development project for a version of CALPUFF for use over water will eventually lead to comprehensive performance evaluations. However, performance evaluation is currently deficient for both Lagrangian puff and Eulerian grid models.

6.1.7 Discussion and Model Selection

Tables 6-2 and 6-3, respectively, contain summaries of the characteristics and pros and cons of the two primary Lagrangian puff models (CALPUFF and SCIPUFF) and the three primary Eulerian grid models (CMAQ, CAMx, and UAM-V) that were considered.

Table 6-2

Summary of Characteristics and Pros and Cons for Lagrangian Puff Models (CALPUFF and SCIPUFF) Considered

Lagrangian Puff Model	CALPUFF	SCIPUFF
Linked diagnostic met model	CALMET diagnostic model (only option)	SWIFT diagnostic model (only option other than simpler internal MCSCIPUFF)
Ability to link with prognostic met model	Many examples with MM5, possible with others	Many examples with MM5, RAMS, OMEGA, COAMPS, ARPS, Eta, and others
Uses vertical velocities	The mean vertical gradient of vertical velocity across each puff is used to stretch the vertical distribution of mass in the puff instead of transporting puff vertically	Yes, puffs can move vertically
Primary usage	EPA regulatory applications	Department of Defense applications
Boundary layer parameterizations	Monin-Obukhov similarity	Monin-Obukhov similarity
Complex terrain	Detailed approach for plume impacting hills	Approximate approach via diagnostic wind model, no plume impaction on hills
Building downwash	Yes, similar to other EPA models	No
Plume rise	Similar to other EPA models	Yes, for both buoyant and dense plumes. However, MMS plumes are not dense
Chemistry and aerosols	Has limited first-order chemistry for SO_2 and NO_2	Has a version (SCICHEM) with detailed in-plume chemistry and aerosol treatment
Averaging time	Minimum 1 hr, as required by regulatory agencies	Any, including as small as 1 sec (but anything less than 1 hr is not useful to EPA or MMS
Over-water applications	Some recent MMS applications to overwater scenarios with travel distances > 50 km. MMS is sponsoring upgrades to better treat overwater cases.	Some applications when hazardous releases are advected over water, such as at the Kennedy Space Center.

Table 6-3

Summary of Characteristics and Pros and Cons for Eulerian Grid Models (CMAQ, CAMx, and UAM-V) Considered

Eulerian Grid Model	CMAQ	CAMx	UAM-V
Link to prognostic met model	Efficient link with MM5 designed as part of Models-3	Links with MM5 and other met models but with more manipulation necessary	Links with met models but with fewer improvements than other models
Primary usage	Developed by EPA for regional and urban air quality applications	Developed by Environ for regional and urban ozone and PM studies	Longest history, developed by SAI as improvement to UAM-IV
Applications in Gulf of Mexico coastal area	EPA is training local regions and agencies; University of Houston is beginning extensive research study in Houston coastal area	Texas (TCEQ) uses CAMx linked with MM5	Most Gulf of Mexico states use UAM-V linked with MM5, as a result of GCOS and FL studies
Horizontal advection solvers	Has several options,	Has several options	Limited to Smolarkiewicz scheme, which produces numerical diffusion
Chemical mechanisms	Has several options with recent updates including a new fast solver	Has several options including a fast solver	Has several options
Deposition to water	Focus on land	Focus on land	Has specific deposition algorithm for water
Overwater applications	Nothing specific, although there are often water bodies in the domain, and concentrations are often higher over water	Nothing specific, although there are often water bodies in the domain, and concentrations are often higher over water	LMOS applications show increased ozone over Lake Michigan due to cool water and increased stability

In general, Lagrangian models are designed to model large point sources. While they can also be applied to aggregates of point sources (i.e., area sources), they are not as well suited for such applications as Eulerian models.

Eulerian photochemical models were designed and are applied to situations in which the treatment of gas-phase chemistry is a primary feature of the dynamic system in which pollutants are formed in the atmosphere. They address chemistry through simulation of dynamics using a detailed chemical mechanism. In contrast, CALPUFF is primarily a multi-source plume model that treats transport downwind and dispersion along the transport path. The representation of gas phase chemistry is highly simplified (linearization and parameterization) of the chemical relationships. These simplifications may be inadequate when applied to situations in which complex chemistry dominates the processes responsible for formation and destruction of the chemical species of interest. While SCICHEM (SCIPUFF with chemistry) provides a detailed treatment of chemistry in a Lagrangian modeling framework, it lacks some of the detailed treatment of near-source dispersion available in CALPUFF, has not been extensively evaluated, and has not been previously used in a cumulative increment analysis.

This study will entail the modeling of a large number of plumes, which inevitably will include many cases of overlap. The chemistry of overlapping plumes is not treated directly in CALPUFF or SCIPUFF/SCICHEM or in any other model. However, the plume orientation of CALPUFF and SCIPUFF do not confer any advantage over Eulerian models with respect of plume overlap.

While it is a goal of this project to apply scientifically rigorous methods to perform the increment analysis, we must also remember that this effort is part of regulatory analysis that has well-defined guidance. Therefore, it is recommended that at least one of the models applied be an EPA-preferred model for use in PSD analysis, i.e., the Lagrangian model, CALPUFF. This preferred model will provide a foundation for comparison of more complex and complete modeling methods. The second model should be either the CMAQ or CAMx photochemical model. These two models currently have more options, larger user communities, and greater potential for future development than UAM-V.

Each fall, the EPA-sponsored Community Modeling and Analysis System (CMAS) holds a users' workshop. The attendees represent many segments of the community: private, academic, industry, federal, state, and international. The workshop presentations discuss many aspects of CMAQ, covering topics such as model development, evaluation, decision making, risk assessment, and air quality impacts.

Discussions with participants at the Models-3 workshop indicate that both CMAQ and CAMx are considered to be state-of-the-science and yield similar model performance for gas-phase and aerosol species. The similarity in performance of the two models is confirmed recently in a study comparing the performance of CMAQ, CMAQ-MADRID, and CAMx by Knipping et al. (2004). CMAQ-MADRID is a new version of CMAQ funded by EPRI that includes a sectional approach to aerosol chemistry. CMAQ-MADRID has been transferred into the public domain and is now available through the CMAS. Another version of CMAQ with Advanced Plume Treatment (CMAQ-APT) is being developed with funding from EPRI. CMAQ-APT has integrated the SCICHEM model within CMAQ for plume-in-grid treatment.

The photochemical modeling community generally considers CMAQ to have better scientific documentation than CAMx but is more difficult to apply. The difficulties in applying CMAQ stem from its use of a complicated "model builder" program that enforces a structured approach to revision control and model programming, plus the use libraries for standardized input/output. While these make the model more difficult to use by novice users, they are a benefit to developers, researchers, and those working on collaborative modeling projects. The wide use of CMAQ by the research community has also led to the discovery of model errors that might not have been discovered if its use was primarily by the regulatory community.

Based on these considerations, it is recommended that the Lagrangian puff model, CALPUFF, and the Eulerian grid model, CMAQ, be considered for use in the Gulf of Mexico area for analyzing air quality impacts on the BNWA. CALPUFF is a well-established and tested model that is recommended by the EPA for use in this type of increment analysis. The technical advantages of SCIPUFF and SCICHEM do not appear to outweigh their disadvantages in the areas of near-field dispersion and experience in this type of integrated analysis. While CMAQ is somewhat more difficult apply, it is rapidly evolving as the academic, regulatory, and industrial communities apply and improve it. CMAQ's strong, well-documented science and the potential for improvements (e.g., CMAQ-APT) provide the best scientific basis for selecting it as an alternative to the EPA-preferred model.

6.2 DESCRIPTION OF AIR QUALITY MODELS

The following subsections summarize the features of the CMAQ and CALPUFF models used in this study.

6.2.1 CMAQ

The CMAQ modeling system was designed to approach air quality as a whole by including state-of-the-science capabilities for modeling multiple air quality issues, including tropospheric ozone, fine particles, toxics, acid deposition, and visibility degradation. CMAQ was also designed to have multi-scale capabilities so that separate models were not needed for urban- and regional-scale air quality modeling. The CMAQ chemical transport model (CCTM) includes the following processes:

- Horizontal advection
- Vertical advection
- Mass conservation adjustments for advection processes
- Horizontal diffusion
- Vertical diffusion
- Emissions injection
- Deposition
- Gas-phase chemical reactions
- Aqueous-phase reactions and cloud mixing
- Aerosol dynamics, thermodynamics, and chemistry
- Plume chemistry effects

- Photolytic rate computation
- Process analysis

Version 4.3 of CMAQ (September 12, 2003 release) was used in this study. This version includes updated science, corrected implementations, efficiency enhancements, and bug fixes. There are also model-to-model comparisons between the 2003 release and the 2002 release. The most significant changes involve aerosol modeling, particularly nitrate aerosols and secondary organic aerosols (SOA). Nitrate modeling was updated to be consistent with the most recent literature, and the SOA implementation was corrected to allow reversible semi-volatility. These changes resulted in substantially lower modeled concentrations of both aerosol nitrates and SOA. Minor changes were also made to aqueous processes and dry deposition.

Major modifications were made to improve model efficiency. A new fast gas-phase chemistry solver, known as the Euler Backward Iterative (EBI) scheme, was developed for the CB-IV mechanism. Also, some of the fastest reacting species were eliminated from the transport processors. The time step for operator splitting was revised to allow different advective time steps by vertical layer.

6.2.2 CALPUFF

CALPUFF is a multi-layer, multi-species, non-steady-state puff dispersion model that can simulate the effects of time- and space-varying meteorological conditions on pollutant transport, transformation, and removal. CALPUFF can use the three-dimensional meteorological fields developed by the CALMET model, or simple, single-station meteorology in a format consistent with the meteorological files used to drive the ISC or AUSPLUME steady-state Gaussian models. The model has been adopted by the EPA as the preferred model for assessing long-range transport of pollutants and their impacts on federal Class I areas and on a case-by-case basis for certain near-field applications involving complex meteorological conditions.

CALPUFF contains algorithms for near-source effects such as building downwash, transitional plume rise, partial plume penetration, and subgrid-scale terrain interactions as well as longer-range effects such as pollutant removal (wet scavenging and dry deposition), chemical transformation, vertical wind shear, over-water transport, and coastal interaction effects. It can accommodate arbitrarily varying point source and gridded area source emissions. Most of the algorithms contain options to treat the physical processes at different levels of detail depending on the model application.

Version 5.7 of CALPUFF, which was released in April 2003, was used in this study.

6.3 EPISODIC MODELING APPROACH

The following subsections describe how CMAQ and CALPUFF were configured and applied, including the preparation of input files.

6.3.1 Modeling Domains

The horizontal grid specifications for the CMAQ and CALPUFF modeling domains are listed in **Table 6-4**. The same horizontal domain definitions were used for CMAQ and CALPUFF. This domain is a subset of the 12-km MM5 domain: it is inset 5 grid cells (60 km) from the MM5 domain boundaries to minimize the effects of any instability that may exist at the MM5 domain interfaces. The vertical layer structure for CMAQ and CALPUFF is shown in **Table 6-5**. The CMAQ layers are aligned with the MM5 sigma layers although CMAQ layers may contain one or more MM5 layers. The CALPUFF layers generally match the CMAQ layers except there is no fifteenth layer, and the first layer is different because CALPUFF requires the first layer be 20-m deep. CMAQ's domain top matches the top of the MM5 domain, while CALPUFF was limited to 5005 m.

Table 6-4

Specifications for the CMAQ and CALPUFF Modeling Domains

Specification	Value
Cell size	12 km
Number of cells East-West	110
Number of cells North-South	110
Grid projection	Lambert Conformal
Center of projection	40° N Latitude, 97° W Longitude
First reference latitude	33° N
Second reference latitude	45° N
Southwest corner (X)[a]	+96000 m
Southwest corner (Y)[a]	-1812000 m

[a] Relative to center of projection

Table 6-5

Vertical Layer Structure for CMAQ and CALPUFF.

Layer	Top of CMAQ Layer (m)	Top of CALPUFF Layer (m)
15	20588	N/A
14	5005	5005
13	3080	3080
12	2394	2394
11	1883	1883
10	1485	1485
9	1131	1131
8	907	907
7	679	679
6	474	474
5	343	343
4	221	221
3	110	110
2	67	67
1	24	20

6.3.2 CMAQ Configuration

CMAQ was configured with the following options:

- Horizontal Advection – Piecewise parabolic method (PPM)
- Vertical Advection – PPM
- Horizontal Diffusion – Multiscale spatially varying eddy diffusion (K_v) coefficients
- Vertical Diffusion – Eddy diffusion (K_v)
- Photolysis – Temporally resolved three-dimensional gridded photolysis rates are interpolated from a lookup table
- Plume-in-Grid – Implemented for selected Major Elevated Point Source Emitters (MEPSEs)
- Gas-Phase Chemistry – Carbon Bond IV
- Aerosol Chemistry – AE3/ISORROPIA
- Chemistry Solver – Euler Backward Iterative (EBI)
- Cloud Processes –RADM

6.3.3 CALPUFF Configuration

CALPUFF was configured with the following options:

- Vertical distribution used in the near field – Gaussian
- Terrain adjustment method – partial-plume path adjustment
- Subgrid-scale complex terrain – not modeled
- Transitional plume rise – modeled
- Stack tip downwash – not modeled
- Vertical wind shear above stack top – modeled
- Puff splitting – yes
- Chemical mechanism – transformation rates computed internally (RIVAD/ARM3 scheme)
- Species modeled – SO_2, SO_4, NO, NO_2, HNO_3, NO_3
- Wet removal – modeled
- Dry deposition – modeled
- Dispersion coefficients – internally calculated using micrometeorological variables
- PG sigma-y,z adjusted for roughness – yes
- Partial plume penetration of elevated inversion – yes
- Probability density function (PDF) used for dispersion under convective conditions – no
- Boundary conditions – not modeled
- Background ozone concentrations – specified as the monthly mean measured at the BIP monitoring site
- Sub-grid thermal internal boundary layers (TIBL) module used for shore line – no

6.3.4 Preparation of Model-Specific Meteorological Input Files

Version 2.2 of the meteorology-chemistry interface processor (MCIP) was used to prepare the meteorological input files for CMAQ. The MCIP was run with options to use (1) PBL heights from input meteorology; (2) radiation fields from input meteorology; and (3) the RADM (Wesley) dry deposition routine to calculate deposition velocities. MCIP was configured to map the MM5 meteorological parameters into 15 vertical layers matching the MM5 layers at sigma values of 1.000, 0.997, 0.992, 0.986, 0.973, 0.958, 0.942, 0.918, 0.882, 0.866, 0.827, 0.785, 0.734, 0.668, 0.508, and 0.000. These sigma levels correspond to cell interfaces at 0, 24, 67, 110, 221, 343, 474, 679, 907, 1131, 1485, 1883, 2394, 3080, 5005 and 20558 m.

Version 5.5 (April 2003 release) of CALMET was used to prepare the meteorological input files for CALPUFF. CALMET was run in "no observations" mode using only data extracted from the MM5 output files with the program CALMM5. This mode is undocumented except in the CALMET source code. The publicly available version of CALMM5 (Version 1.0, February 2000) was designed to process MM5 Version 2 output data. Therefore, we modified

the program to process MM5 Version 3 output and made the following additional changes: (1) we corrected the hard-coded domain top for MM5 (100 mb) with the actual top in the MM5 output (50 mb in this case); and (2) we modified the program to pass through the MM5 estimates of PBL height to CALMET through the MM5.DAT file. The CALMET program was also modified to read the PBL heights in the MM5.DAT file and use them for the mixing heights under unstable conditions within CALMET. Thus, only the unstable mixing algorithm was bypassed. This approach resulted in improved estimates of overwater PBL height.

CALMET was configured to map the MM5 meteorological parameters into 14 vertical layers with cell interfaces at 0, 20, 67, 110, 221, 343, 474, 679, 907, 1131, 1485, 1883, 2394, 3080, and 5005 m. These layers approximate those used by MCIP, but the CMAQ modeling domain has one additional layer that extends to the top of the MM5 domain. Another difference is that the lowest MM5 layer is 25-m deep while CALMET requires the first layer be 20-m deep.

6.3.5 Initial and Boundary Conditions

No initial or boundary conditions, except for specifying a background ozone concentration, were used in CALPUFF. The monthly mean ozone concentration at BIP was used for the background ozone concentration. The default species profiles provided with CMAQ were used for initial and boundary conditions.

6.3.6 Photolysis Rates

Photolysis rates are required for the CMAQ chemistry. The J-value processor (JPROC) distributed with CMAQ was run to prepare the photolysis rate files specific to the CB-IV chemical mechanism.

6.3.7 Plume Dynamics Model

A plume-in-grid (PinG) technique was used to more realistically treat the dynamic and chemical processes impacting selected, major point source pollutant plumes in CMAQ. The principal science algorithms include a Plume Dynamics Model (PDM) and a Lagrangian reactive plume code. The PDM processor simulates plume rise, horizontal and vertical plume growth, and transport of each plume section during the subgrid-scale phase. It generates a data file of this information for use by the PinG module. In contrast to the traditional Eulerian grid modeling method of instantly mixing the emissions from each point source into an entire grid cell volume, the PinG module simulates the relevant physical and chemical processes during a subgrid-scale phase which allows each plume section to expand in a realistic manner and to evolve chemically. The PinG module is fully integrated into the CCTM in order to utilize the grid concentrations as boundary conditions and it provides a feedback of the plume pollutants to the grid model concentration field at the proper time and grid location.

The PDM was applied to elevated point sources processed for CMAQ that emitted 25 tons per day (tpd) or more of NO_x or 50 tpd or more of SO_2. The number of PDM sources varied by day and ranged from 32 to 41 for the cases modeled.

6.3.8 Model Performance Evaluation

Statistical and times series analyses were performed to compare observations and predictions. The model performance measures that were used are statistical measures applied to the evaluation of the MMS Offshore and Coastal Dispersion (OCD) model. Statistical measures that were calculated include

- Fractional bias (FB)
- Geometric mean bias (MG)
- Normalized mean square error (NMSE)
- Geometric mean variance (VG)
- Correlation coefficient (R)
- Fraction of predictions within a factor of two of observations (FAC2)

The calculation of these measures is as follows:

$$FB = \frac{(\overline{C_o} - \overline{C_p})}{0.5\,(\overline{C_o} + \overline{C_p})}$$

$$MG = \exp\left(\overline{\ln C_o} - \overline{\ln C_p}\right)$$

$$NMSE = \frac{\overline{(C_o - C_p)^2}}{\overline{C_o}\;\overline{C_p}}$$

$$VG = \exp\left[\overline{(\ln C_o - \ln C_p)^2}\right]$$

$$R = \frac{\overline{(C_o - \overline{C_o})(C_p - \overline{C_p})}}{\sigma_{C_p}\,\sigma_{C_o}}$$

$$FAC2 = \text{fraction which } 0.5 \le \frac{C_p}{C_o} \le 2.0$$

where C_p is model prediction, C_o is observation, and σ is standard deviation. An overbar indicates an average.

Modeled and observed pollutant concentrations are inherently incommensurable: observed concentrations are representative at a single point in space while predicted

concentrations may be representative of a vertical column or grid-cell average and are almost always available at a higher spatial resolution than observations. With only three permanent monitors in the modeling area, it is not possible to measure the impacts of all important pollutant plumes in the region. Conversely, small errors in modeled wind fields could result in a predicted pollutant plume to missing a monitoring location by an equally small distance. Thus, if observed and predicted concentrations are paired in time and space, model performance may appear worse than it actually is. This would not be true if concentrations were dominated by regional background concentrations rather than by large plumes or emissions areas; in such cases, both the model and monitors might adequately resolve the pollutant concentration. However, to address the problem of observation-prediction incommensurability, we also evaluated model performance for the top 5% of observations and predictions, unpaired in time and space.

Preliminary model acceptance criteria were proposed as a result of the literature review performed during the model selection phase of this study. A number of model evaluation exercises, including the previously mentioned OCD evaluation, were surveyed, and it was determined that a "good" model has the following characteristics when the highest 20 or 30 observed and predicted concentrations are considered:

- FB of magnitude less than about 50%
- NMSE less than about 1.0
- FAC2 greater than about 0.5

6.3.9 Sensitivity Simulation

A series of sensitivity simulations were performed during the episode-type study to aid in evaluating model performance, defining the final model configurations, assessing uncertainties in the modeling systems, and improving computational performance of the models. These simulations are described below.

- Ozone concentrations – Ozone concentrations are specified in CALPUFF and affect formation of NO_2 in the model. We explored a variety of options for specifying the ozone concentrations ranging from site-specific values to global values.
- Alternative MM5 configurations – During the initial MM5 development case, output from several configurations of MM5 were provided by PSU and simulations with both CMAQ and CALPUFF were performed.
- Plume-in-Grid – CMAQ modeling was performed both with and without PinG treatment for major point sources.
- Zero low-level emissions – Simulations were performed with CMAQ and CALPUFF using only point source emissions.
- PBL heights – CALPUFF simulations were performed using (a) the default CALMET estimates of over-water PBL heights and (b) MM5 estimates of over-water convective PBL heights.
- 4-km meteorology – CALPUFF was applied using 4-km MM5 meteorology for Case 3 and compared to the results for the same case using 12-km MM5 meteorology.

- Reduced emissions domain – Simulations were performed with CALPUFF using emissions from (a) the entire 12-km domain and (b) only sources within 200 km (north-south and east-west) of the BNWA.
- Puff splitting – CALPUFF simulations with and without the puff-splitting option were performed.
- Accelerated puff removal – CALPUFF was modified to remove a portion of the oldest puffs when a critical number of puffs was exceeded. Simulations were performed with this modified version of CALPUFF and compared to the original version.

6.4 AIR QUALITY MODELING RESULTS

This section describes the results of the model performance evaluations and, based on those results, discusses the relative merits of CMAQ and CALPUFF for use in the increment analysis.

6.4.1 Model Performance

The average observed and predicted SO_2 and NO_2 concentrations for each case modeled and all cases combined are compared in **Table 6-6**. While average concentrations are not a robust metric for model evaluation, some general tendencies of the models are illustrated. While CALPUFF predicts slightly higher average concentrations of SO_2 than CMAQ, both models underpredict SO_2 by a factor of two to three. For NO_2, the results are less clear — both models perform well in some cases but poorer in others; overall CMAQ tends to underpredict and CALPUFF tends to overpredict.

Table 6-6

Average Observed and Predicted Concentrations of SO_2 and NO_2

	SO_2 (ppb)				NO_2 (ppb)			
Case	N	Observed	CMAQ	CALPUFF	N	Observed	CMAQ	CALPUFF
1	411	4.7	2.0	2.1	552	6.2	6.1	6.8
2	484	2.1	0.9	1.0	648	5.0	4.2	5.3
3	414	2.8	1.1	1.6	552	4.4	2.5	4.3
4	414	0.5	0.2	0.2	552	3.6	1.6	3.2
5	414	2.6	1.5	1.8	552	3.0	5.8	6.3
6	412	4.6	2.0	2.0	552	5.2	4.8	4.9
All	2549	2.9	1.3	1.5	3408	4.6	4.2	5.1

Model performance statistics for both models are presented for SO_2 in **Table 6-7** and for NO_2 in **Table 6-8**. Note that a positive FB indicates underprediction while negative FB indicates overprediction. These statistics were calculated by pairing all observations and predictions in time and space. The comparison of the statistics for all cases is presented graphically for SO_2 in **Figure 6-1** and for NO_2 in **Figure 6-2**, along with means and standard deviations of the observations and predictions.

Both models significantly underpredict SO_2 with FB greater than 50%. Both models have an NMSE greater than 200%, and R ranges from 0.08 for CALPUFF to 0.16 for CMAQ. The standard deviations of the predictions (SDEV_pred) are less than the standard deviations of the observations (SDEV_obs), indicating the models predict less variability in concentrations than was observed. Overall, CMAQ performs slightly better than CALPUFF but neither model performs well.

Both models perform better for NO_2 than for SO_2 with FB less than 50% (CMAQ underpredicts by 16% while CALPUFF overpredicts by 11%). Both models have an NMSE of 50% or less and R ranges from 0.12 for CALPUFF to 0.21 for CMAQ. For both models, 42% of the predictions are within a factor of two of the observations. SDEV_pred is greater than SDEV_obs for NO_2, indicating the models predict greater variability in concentrations than was observed. With the exception of R, CALPUFF performs better than CMAQ for NO_2.

Table 6-7

Model Performance Statistics Paired in Space and Time for SO_2

	Fractional bias (FB)		Geometric mean bias (MG)		Normalized mean square error (NMSE)		Geometric mean variance (VG)		Correlation coefficient (R)		Predictions within a factor of two of observations (FAC2)	
Case	CMAQ	CALPUFF	CMAQ	CALPUFF	CMAQ	CALPUFF	CMAQ	CALPUFF	CMAQ	CALPUFF	CMAQ	CALPUFF
1	0.79	0.74	2.9	3.8	1.8	2.1	8.1	39.2	0.03	-0.06	0.33	0.30
2	0.75	0.67	2.4	3.0	2.8	2.7	10.2	24.0	0.28	0.26	0.31	0.29
3	0.89	0.53	2.7	2.8	2.0	1.7	6.8	17.8	0.36	0.22	0.30	0.29
4	0.75	0.83	3.7	3.5	3.8	3.8	25.1	15.4	-0.45	-0.22	0.14	0.13
5	0.50	0.35	2.4	2.7	1.5	1.5	8.8	36.9	0.39	0.27	0.41	0.41
6	0.78	0.81	2.2	3.3	1.6	2.3	3.4	19.9	0.34	0.02	0.38	0.21
All	0.74	0.65	2.7	3.2	2.2	2.4	10.4	25.5	0.16	0.08	0.31	0.27

Table 6-8

Model Performance Statistics Paired in Space and Time for NO_2

	Fractional bias (FB)		Geometric mean bias (MG)		Normalized mean square error (NMSE)		Geometric mean variance (VG)		Correlation coefficient (R)		Predictions within a factor of two of observations (FAC2)	
Case	CMAQ	CALPUFF	CMAQ	CALPUFF	CMAQ	CALPUFF	CMAQ	CALPUFF	CMAQ	CALPUFF	CMAQ	CALPUFF
1	0.02	-0.09	1.4	1.1	1.6	1.5	3.6	3.2	0.26	0.12	0.43	0.49
2	0.16	-0.06	1.6	1.1	2.1	2.2	6.2	4.9	0.39	0.27	0.37	0.45
3	0.56	0.03	1.9	0.9	3.5	2.2	6.6	5.8	0.02	-0.08	0.37	0.37
4	0.78	0.12	1.9	0.8	4.1	2.2	4.9	4.5	0.14	-0.06	0.44	0.43
5	-0.65	-0.72	0.8	0.6	4.7	3.5	6.0	6.1	0.32	0.28	0.38	0.32
6	0.08	0.07	1.1	1.0	2.0	1.6	3.3	3.3	0.12	0.17	0.50	0.47
All	0.16	-0.11	1.5	0.9	3.0	2.2	5.1	4.6	0.21	0.12	0.42	0.42

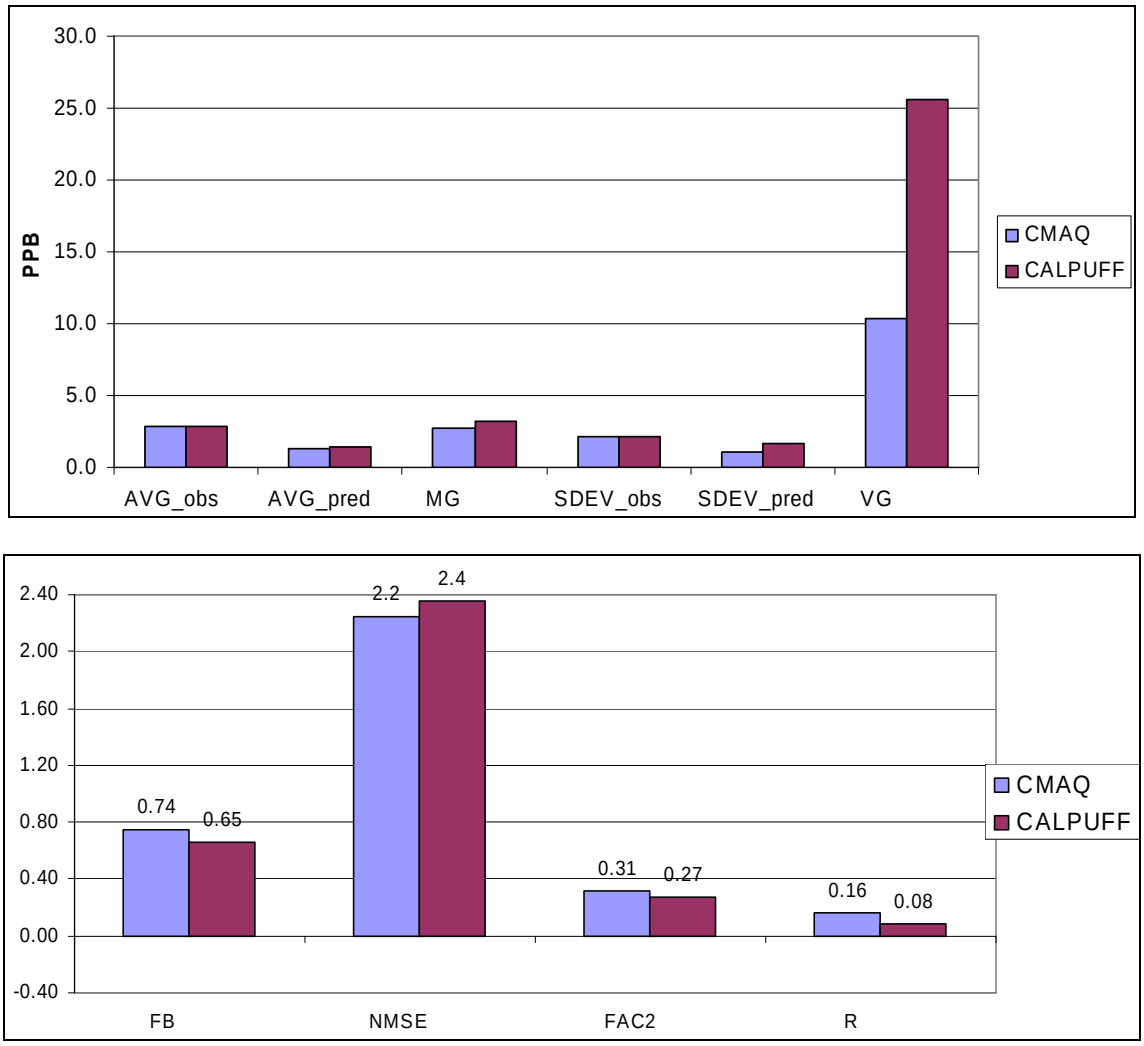

Figure 6-1. Model performance statistics for SO_2 concentrations paired in time and space: concentration-based statistics (top); non-dimensional statistics (bottom).

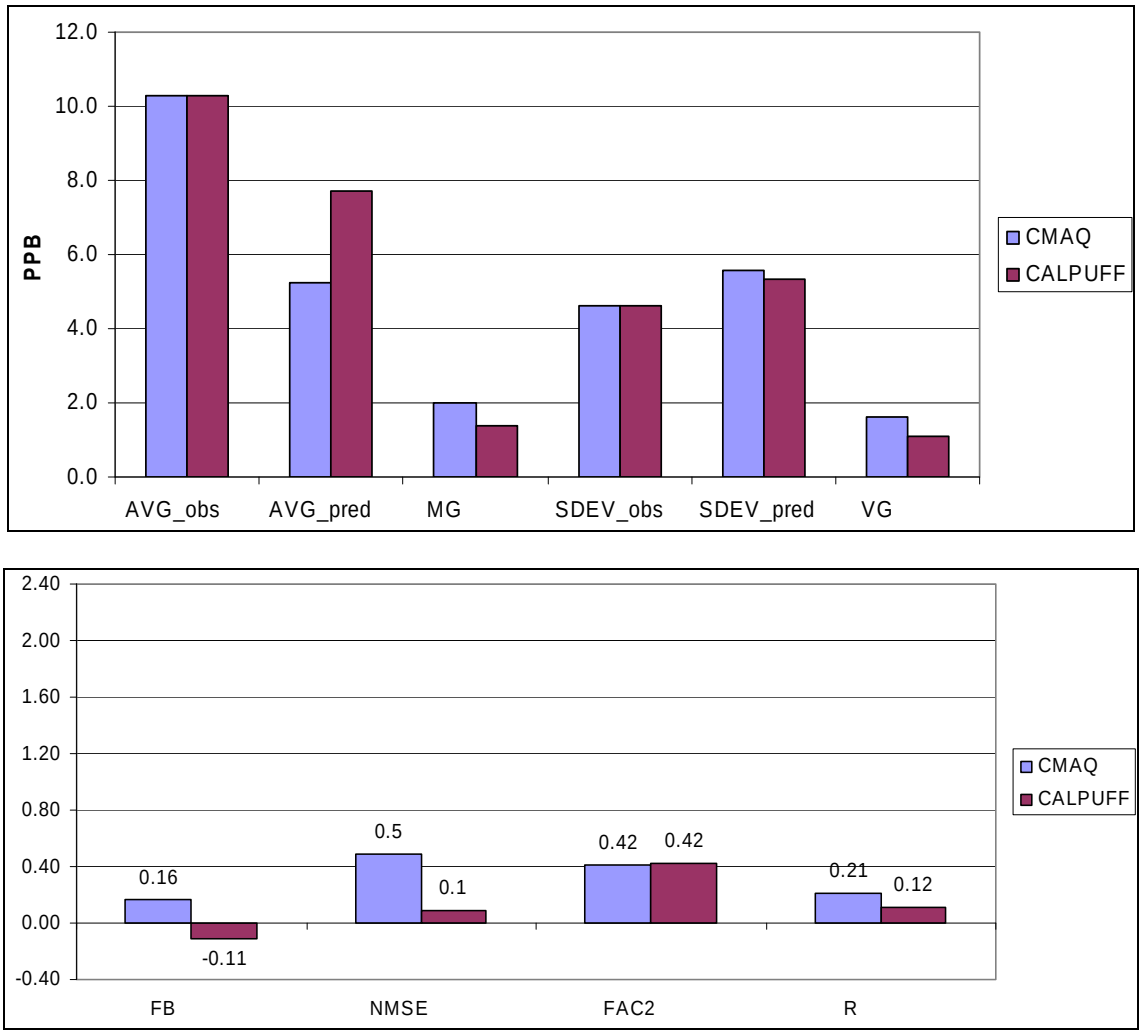

Figure 6-2. Model performance statistics for NO_2 concentrations paired in time and space: concentration-based statistics (top); non-dimensional statistics (bottom).

When the models are evaluated using the top 5% of observations and predictions, unpaired in time and space, their differences become clearer. The same comparison of the statistics for all cases is presented graphically for SO_2 in **Figure 6-3** and for NO_2 in **Figure 6-4** along with means and standard deviations of the observations and predictions.

Both models underpredict SO_2 concentrations although the FB for CMAQ remains high at 65% while the FB for CALPUFF is only 28%. The largest differences between models are in the NMSE and FAC2 statistics. The NMSE for CMAQ is 48% and only 9% for CALPUFF. All of CALPUFF's predictions are within a factor of two of observations while only 21% of CMAQ's are within a factor of two.

Both CMAQ and CALPUFF overpredict NO_2 concentrations although CMAQ more so with an FB of –30% compared to CALPUFF's –20%. Both models predict 100% of the concentrations within a factor of two of observations.

Many of the features identified in the statistical evaluations were also apparent in the hourly time series plots of observations and predictions. The plots for all six cases are presented in Appendix E.

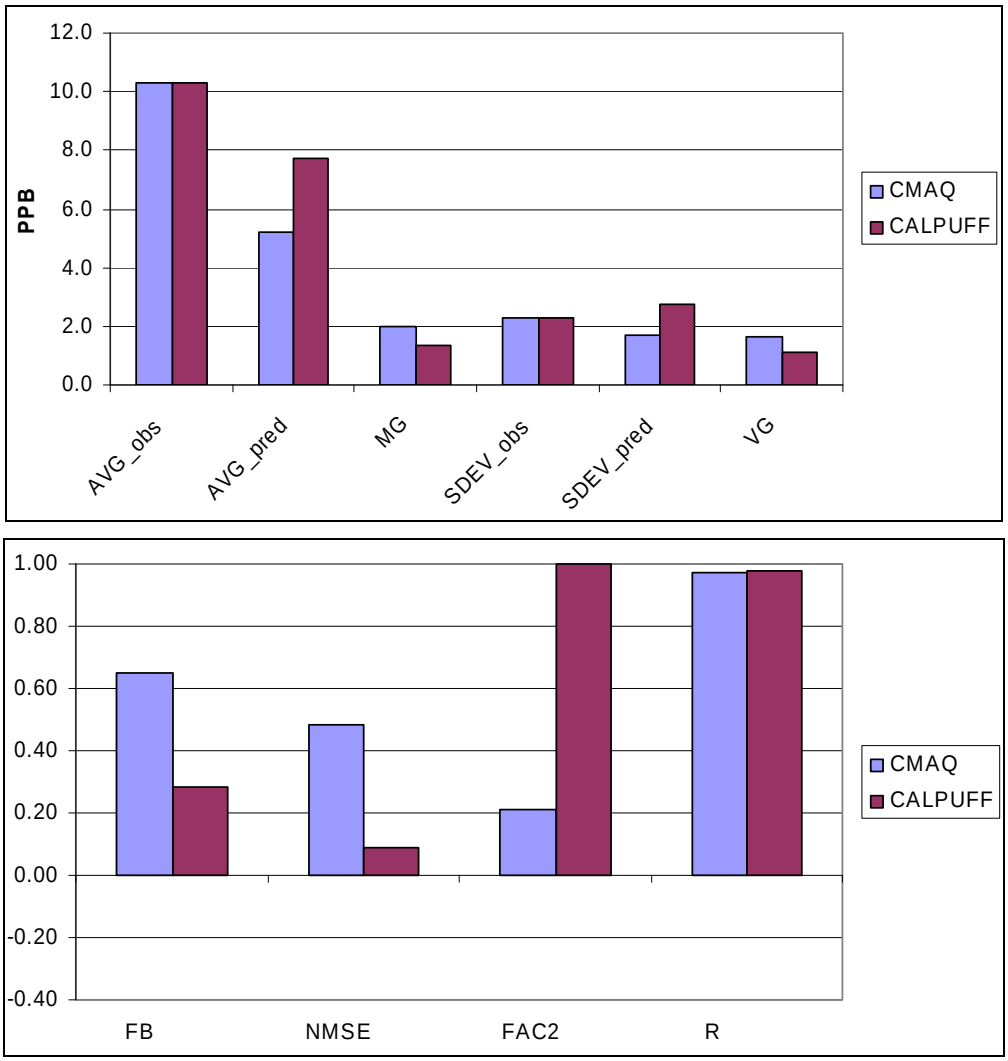

Figure 6-3. Model performance statistics for top 5% of SO_2 concentrations unpaired in time and space: concentration-based statistics (top); non-dimensional statistics (bottom).

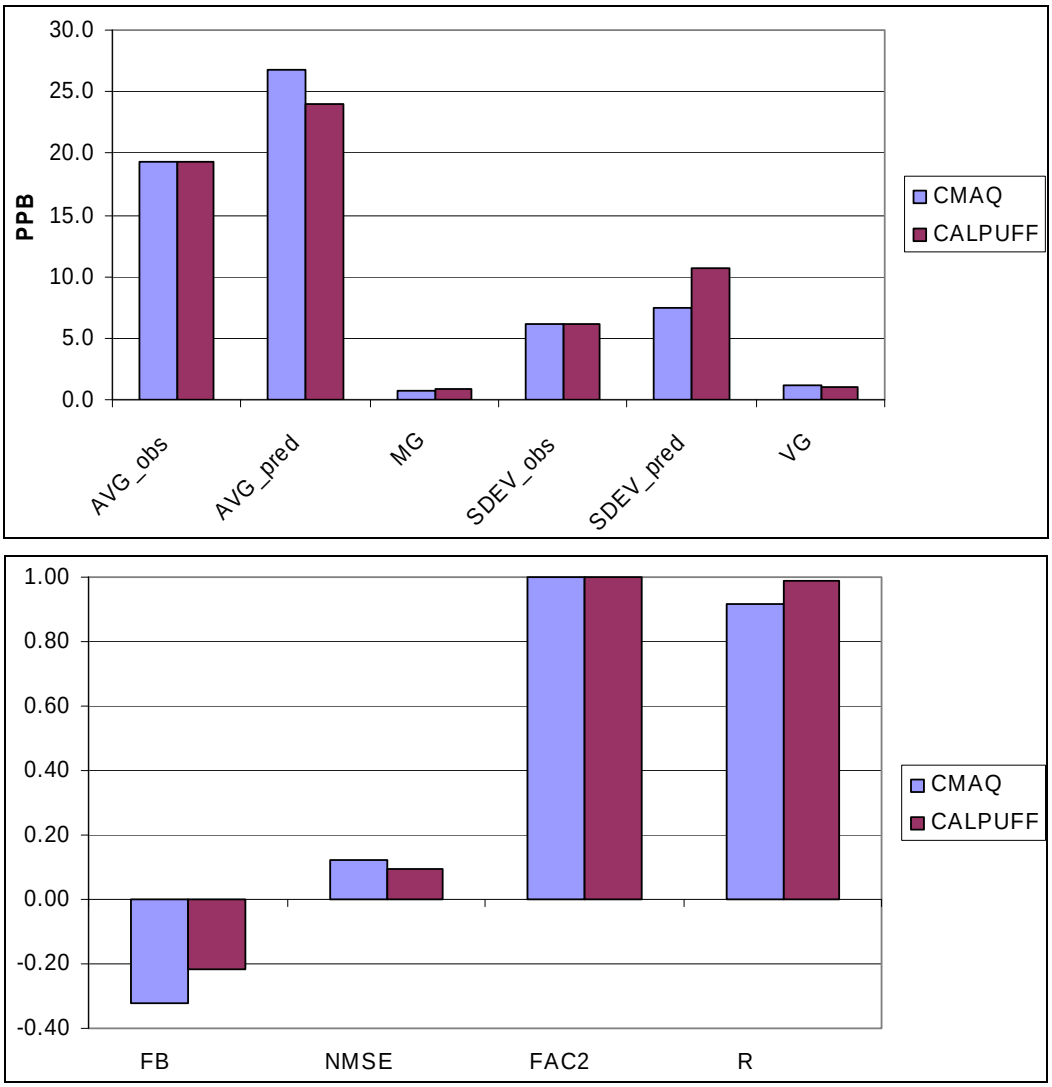

Figure 6-4. Model performance statistics for top 5% of NO_2 concentrations unpaired in time and space: concentration-based statistics (top); non-dimensional statistics (bottom).

6.4.2 Summary of Model Performance

When SO_2 and NO_2 observations and predictions are paired in time and space and compared, both CMAQ and CALPUFF show little skill. These results are not unexpected because the concentrations of species that are predominately associated with primary emissions (i.e., SO_2 and NO_2) can vary significantly depending on winds (i.e., source-receptor relationships), fluctuations in mixing depths, and variations in emissions from normal conditions. The fact that both models perform similarly under this rigorous evaluation indicates that variations in the observed concentrations are too subtle to resolve without higher resolution meteorological and emissions data that were unavailable for input to the models.

When only the top 5% of the observed and predicted SO_2 and NO_2 concentrations, unpaired in time and space, are compared, we see significant improvements in model performance. While both models meet performance goals for NO_2, only CALPUFF meets them for SO_2. Because of its detailed chemistry, we expected CMAQ to perform better than CALPUFF, particularly for NO_2, but that did not prove to be true. It appears that the highest measured SO_2 and NO_2 concentrations near the BNWA are a result of specific emissions plumes from individual or regional sources. The Eulerian formulation of CMAQ seems to result in over-dilution of emissions, even with the use of PinG. CALPUFF appears to represent these plumes more accurately, even without the detailed chemistry.

Because both models underpredict the highest SO_2 concentrations but overpredict NO_2 concentrations, we suspect the SO_2 underpredictions are not a result of meteorological biases and that the SO_2 emission inventory may be biased low.

Because, based on a statistical analysis of ambient air quality data, the 24-hr SO_2 increment is the most likely to be exceeded, the performance of the models for the highest SO_2 concentrations is of greatest importance. Based on the model performance evaluation for the top 5% of concentrations, CALPUFF appears to replicate high SO_2 concentrations more reliably and, therefore, will introduce the least bias when used to perform the increment analysis.

6.4.3 Summary of Sensitivity Simulation Results

Six sets of sensitivity simulations were performed to address model performance issues and assess uncertainties in the modeling. The results of the various sensitivity simulations performed during the episode-type study are described below.

1. Ozone Concentrations

Ozone concentrations are specified in CALPUFF and affect formation of NO_2 in the model. We explored a variety of options for specifying the ozone concentrations ranging from site-specific values to global values. Only a limited number of sites were available for specifying ozone concentrations outside the "ozone season". CALPUFF simulations using site-specific ozone data resulted in significantly lower NO_2 predictions because many of the so-called rural monitoring sites in the domain appear to be impacted by NO_x sources (probably roadways) and nighttime ozone concentrations typically fell to below 20 ppb at night. Ultimately the simulations that produced the most reasonable NO_2 predictions were based on using monthly average ozone concentrations from the BIP monitoring site.

2. Alternative MM5 Configurations

During the initial MM5 development case, outputs from several configurations of MM5 were provided by PSU and simulations with both CMAQ and CALPUFF were performed. While these produced some differences in the resulting CMAQ and CALPUFF concentration fields, the effect on model performance for SO_2 and NO_2 across a six day period was minimal.

3. Plume-in-Grid Treatment

CMAQ modeling was performed both with and without PinG treatment of major point sources. As noted in Section 6.3.7, major point sources were defined as having 50 tpd or more of SO_2 emissions or 25 tpd or more of NO_x emissions. While the concentrations fields were significantly changed within 4 or 5 grid cells of major sources, none of the major point sources treated with PinG were that close to the BNWA and the impacts in that region were on the order of a few percent.

4. Zero Low-level Emissions

Simulations were performed with CMAQ and CALPUFF using only point source emissions. Both models responded as expected to modeling only point sources. Both SO_2 and NO_2 were reduced throughout the region with the greatest impacts onshore.

5. PBL Heights

CALPUFF simulations were performed using (a) the default CALMET estimates of overwater PBL heights and (b) MM5 estimates of overwater convective PBL heights. Initial simulations with the default estimates of overwater PBL heights resulted in large (100–200%) overpredictions of SO_2 and NO_2. This was a result of underpredicted overwater mixing heights, which were 25% or less of expected. The use of MM5 convective boundary layer heights (which appeared more reasonable) instead of the CALMET defaults produced more reasonable estimates of SO_2 and NO_2 in the BNWA region, although there was a tendency for underprediction.

6. Fine Resolution (4-km) Meteorology

CALPUFF was applied using 4-km MM5 meteorology for Case 3 and compared to the results for the same case using 12-km MM5 meteorology. The results of this sensitivity simulation are discussed in further detail in Section 6.4.4.

Three sets of sensitivity simulations were performed with CALPUFF to test methods for reducing memory requirements for the annual simulations.

1. Reduced Emissions Domain

Simulations were performed with CALPUFF using emissions from (a) the entire 12-km domain and (b) only sources within 200 km (north-south and east-west) of the BNWA. Although the episode-type modeling was performed using emissions from the entire modeling domain, an increment analysis only requires that sources within 200 km be considered. Simulations using only sources within 200 km of the BNWA generally produced lower concentrations throughout the domain with the largest changes at receptors beyond 100 km of the BNWA. The maximum impacts at monitors near the BNWA were on the order of few percent.

2. Puff Splitting

CALPUFF simulations with and without the puff-splitting option were performed. Without puff splitting there were spatial variations in the concentrations near some of the larger

onshore point sources and concentrations tended generally to be slightly higher at ground level receptors. However, no significant changes in predicted concentrations were noted at the BAMP monitoring locations.

3. Accelerated Puff Removal

CALPUFF was modified to remove a portion of the oldest puffs when a critical number of puffs was exceeded. Simulations were performed with this modified version of CALPUFF and compared to the original version. As expected, concentrations throughout the modeling domain were reduced on some days (when wind speeds were low) with the maximum changes on the order of 5%. These impacts were mostly onshore and did not seem to impact the BNWA significantly. This modified version of CALPUFF was used later for the annual simulations.

6.4.4 Comparison of 4-km and 12-km CALPUFF Simulations

A 4-km CALPUFF air quality simulation (CPUF4) was performed for Case 3 using meteorology from the MM5 4-km nested grid simulation. The results of this simulation were compared to the results from the 12-km Case 3 CALPUFF simulation (CPUF12). On an hourly basis, when the MM5 12-km and 4-km wind fields were similar for several consecutive hours, both CALPUFF simulations tended to produce similar large-scale features of the SO_2 and NO_2 concentration fields, but differences at finer scales were common, in part due to differences in how dispersion within plumes is treated at different resolutions.

On July 13 at 1700 LST (**Figure 6-5**), several SO_2 plumes were evident in similar locations in both simulations. However, in CPUF4, the plumes were narrower and more distinct than in CPUF12, and the plumes maintained their identity at distances further downwind of their sources. Differences in predicted SO_2 concentration at a given site would depend on where the site is located with respect to the individual plumes. On July 11 at 2000 LST (**Figure 6-6**), both simulations resolve three distinct regions of enhanced SO_2 at the same locations. Differences in SO_2 concentrations between these two simulations occur between the major plumes, as gradients are sharper and better resolved in CPUF4. Concentrations also differ within the plumes.

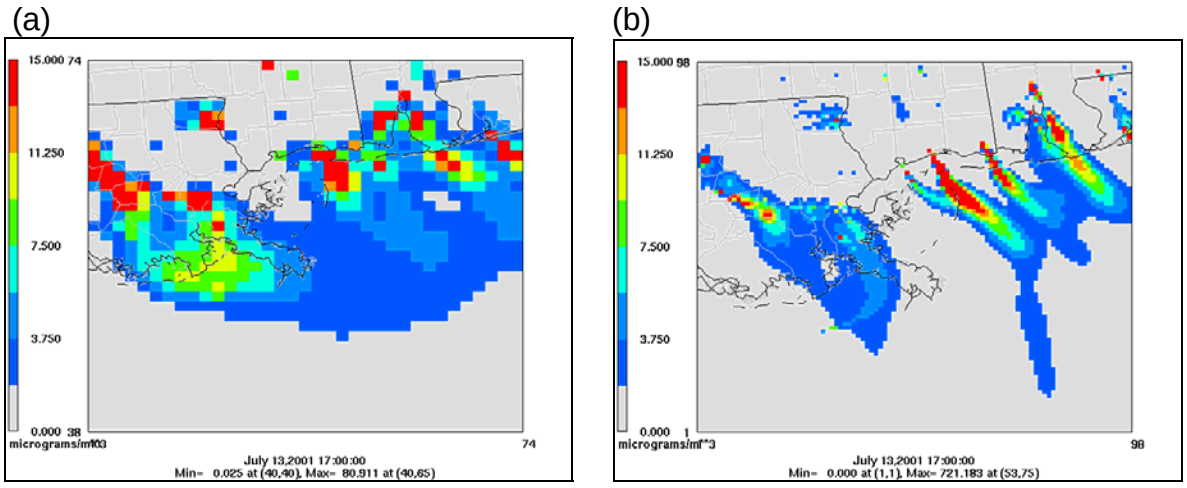

Figure 6-5. SO_2 concentrations ($\mu g/m^3$) from the Case 3 CALPUFF 12-km (a) and 4-km (b) simulations for July 13, 2001, at 1700 LST.

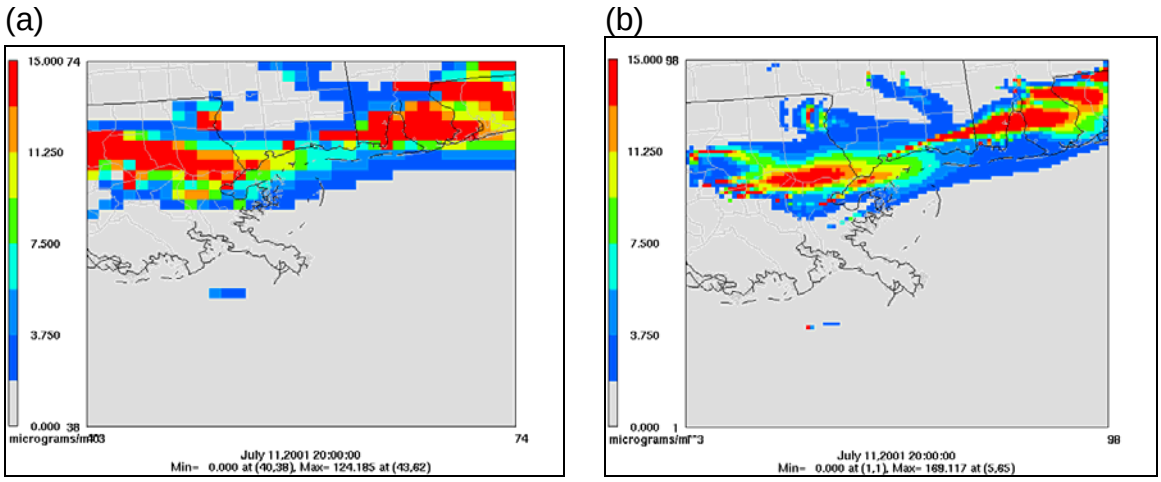

Figure 6-6. SO_2 concentrations ($\mu g/m^3$) from the Case 3 CALPUFF 12-km (a) and 4-km (b) simulations for July 11, 2001, at 2000 LST.

Significant differences in the large-scale spatial patterns of SO_2 occurred when the 4-km and 12-km MM5 wind fields differed substantially. **Figure 6-7** illustrates one such instance. Both MM5 simulations predicted winds over the Gulf Coast region to shift from westerly to northerly on July 13. In the 4-km MM5 simulation, the wind shift line passed through the Gulf Coast several hours earlier than in the 12-km simulation. As a result, CPUF4 predicted north-south-oriented SO_2 plumes over the Gulf of Mexico at 0600 LST, while CPUF12 predicted east-west-oriented SO_2 plumes along the Gulf Coast at the same time. It is unclear if this simulated wind shift was the result of a weak cold front that passed through the region earlier than observed, or if it was due to thunderstorm outflow boundaries. Regardless of the origin of the

predicted wind shifts, the difference in timing between the two MM5 simulations resulted in substantially different predictions of air quality in the BNWA.

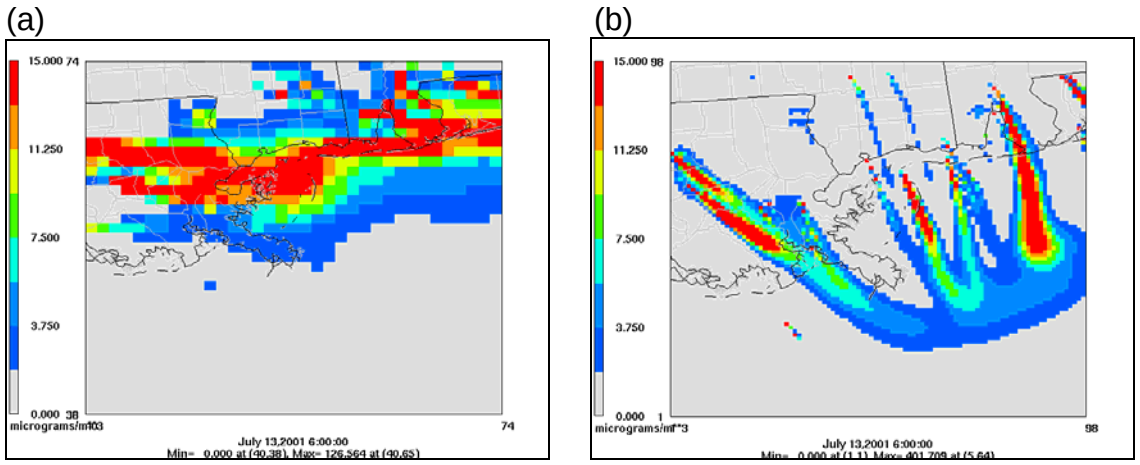

Figure 6-7. SO_2 concentrations ($\mu g/m^3$) from the Case 3 CALPUFF 12-km (a) and 4-km (b) simulations for July 13, 2001, at 0600 LST.

Differences in the predicted occurrence, strength, duration, and interaction of various mesoscale phenomena in MM5, such as coastal circulations, thunderstorms, and outflow boundaries also impacted CALPUFF SO_2 predictions on the timescale of several hours. As noted previously, the spatial distribution of SO_2 was similar for both CALPUFF simulations. On July 11 at 2000 LST (Figure 6-6) CALPUFF predicted high SO_2 concentrations over coastal Mississippi and Alabama. As the night progressed, an offshore flow developed in both MM5 simulations. It is unclear if this flow was the result of a nocturnal land breeze, outflow from thunderstorms, or some combination of both, but this offshore flow was stronger in the 4-km simulation. By 0700 LST the next morning (**Figure 6-8**), SO_2 was advected further away from the Alabama coast in CPUF4, while the SO_2 plume never made it this far offshore in CPUF12.

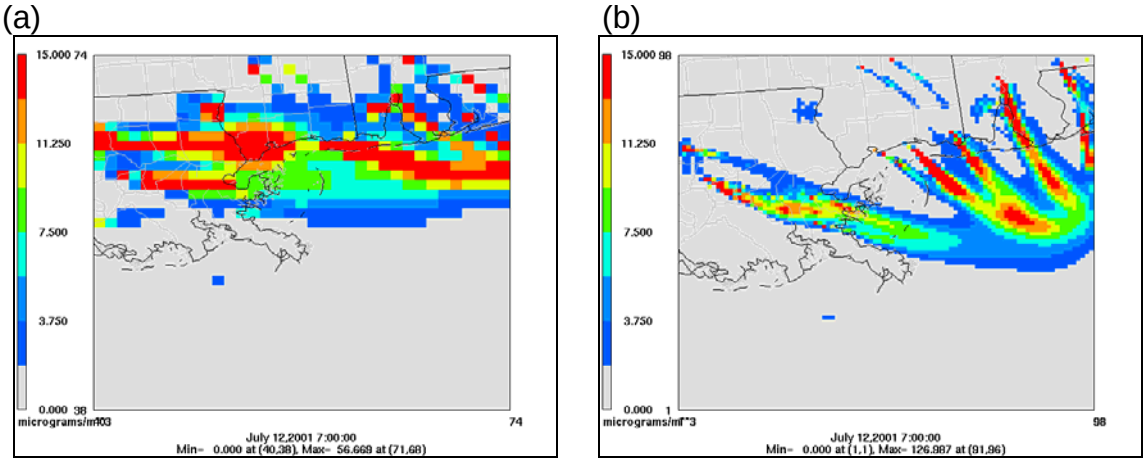

Figure 6-8. SO_2 concentrations ($\mu g/m^3$) from the Case 3 CALPUFF 12-km (a) and 4-km (b) simulations for July 12, 2001, at 0700 LST.

Differences in the hourly SO_2 concentration fields predicted by the CPUF4 and CPUF12 translated into differences in the predicted daily average 24-hr and peak 3-hr SO_2 concentration fields. On July 12 (**Figure 6-9**), the predicted average 24-hr SO_2 fields from both CALPUFF simulations are similar in that both predict higher concentrations along the Alabama and Mississippi coast. However, the 12-km simulation predicts a broad region of high (> 8 $\mu g/m^3$) SO_2 concentrations, whereas the 4-km simulation produces several smaller regions of high SO_2, probably associated with individual plumes that persisted in the same location for several hours during the day. These localized differences impacted predictions at BIP and FTM. Because the SO_2 plumes in the 4-km simulation missed FTM and BIP to the west, predicted 3-hr and 24-hr SO_2 concentrations at those locations were lower than predicted in the 12-km simulation.

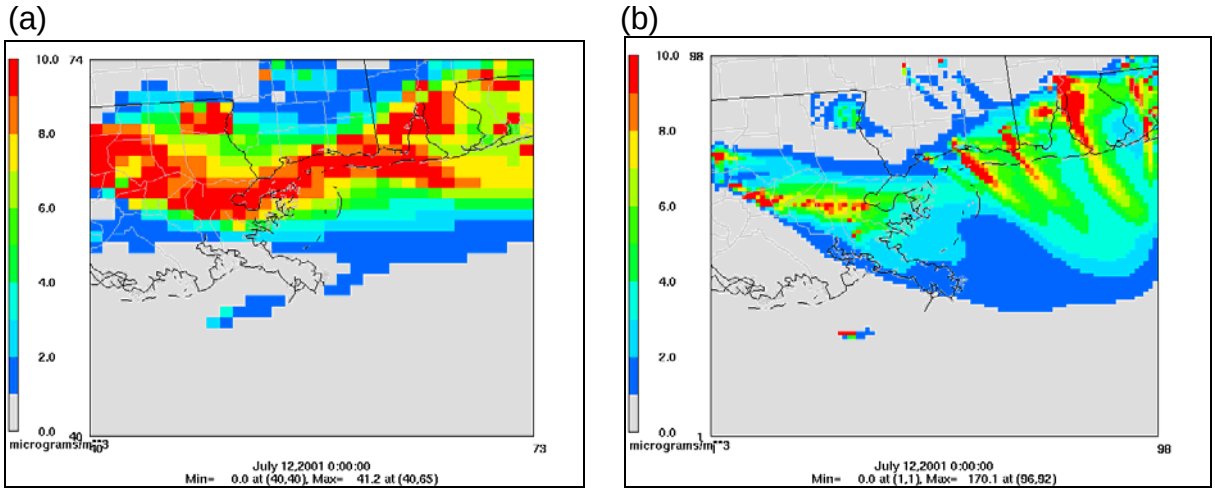

Figure 6-9. Average 24-hr SO_2 concentrations ($\mu g/m^3$) from the Case 3 CALPUFF 12-km (a) and 4-km (b) simulations for July 12, 2001, at 0700 LST.

Figures 6-10 through 6-12 illustrate comparisons of observed and predicted daily average (24-hr) and peak 3-hr SO_2 concentrations. Both CALPUFF simulations underpredicted daily average 24-hr and peak 3-hr SO_2 concentrations, but SO_2 concentrations from CPUF4 generally compared less favorably to observations than predictions from the 12-km simulation. On some days and at some sites, the 4-km simulation showed improvement over the 12-km prediction (e.g., July 9 at BIP and WDP). At WDP, both simulations still severely underpredicted SO_2, as they failed to properly capture the impact of localized offshore emissions. **Figure 6-13** shows the hourly observed and predicted SO_2 concentrations at BIP.

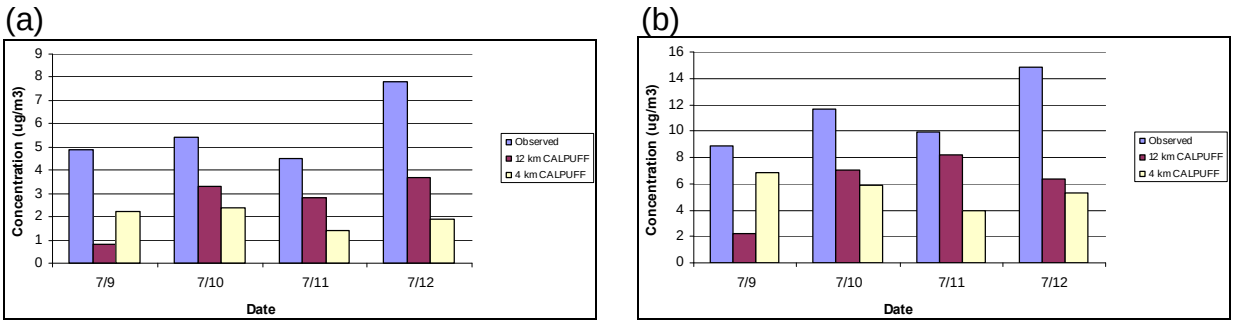

Figure 6-10. Daily average 24-hr SO_2 (a) and peak 3-hr SO_2 (b) concentrations observed and predicted at BIP during Case 3.

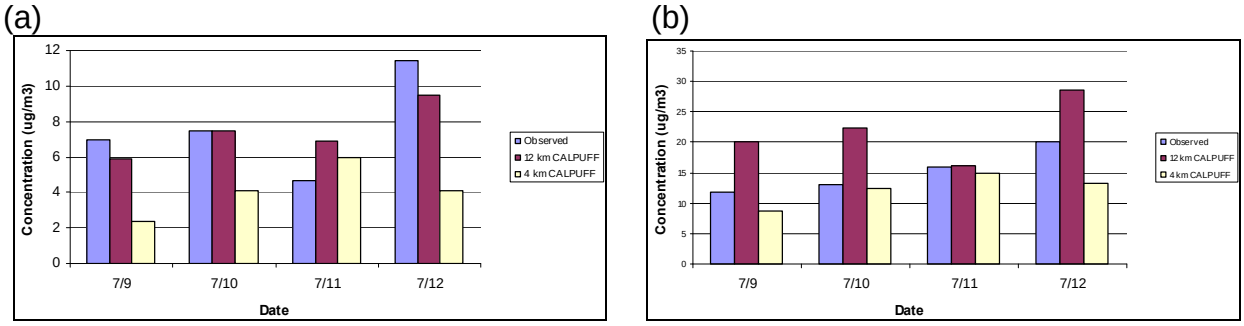

Figure 6-11. Daily average 24-hr SO_2 (a) and peak 3-hr SO_2 (b) concentrations observed and predicted at FTM during Case 3.

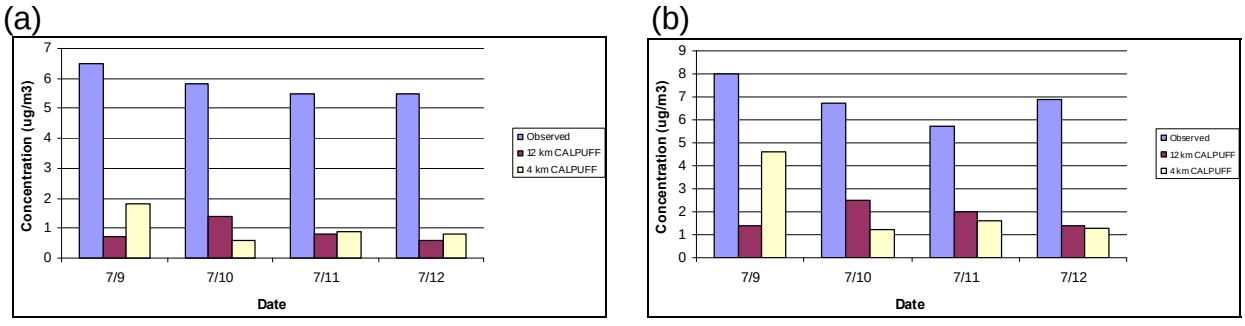

Figure 6-12. Daily average 24-hr SO2 (left) and peak 3-hr SO2 (right) concentrations observed and predicted at WDP during Case 3.

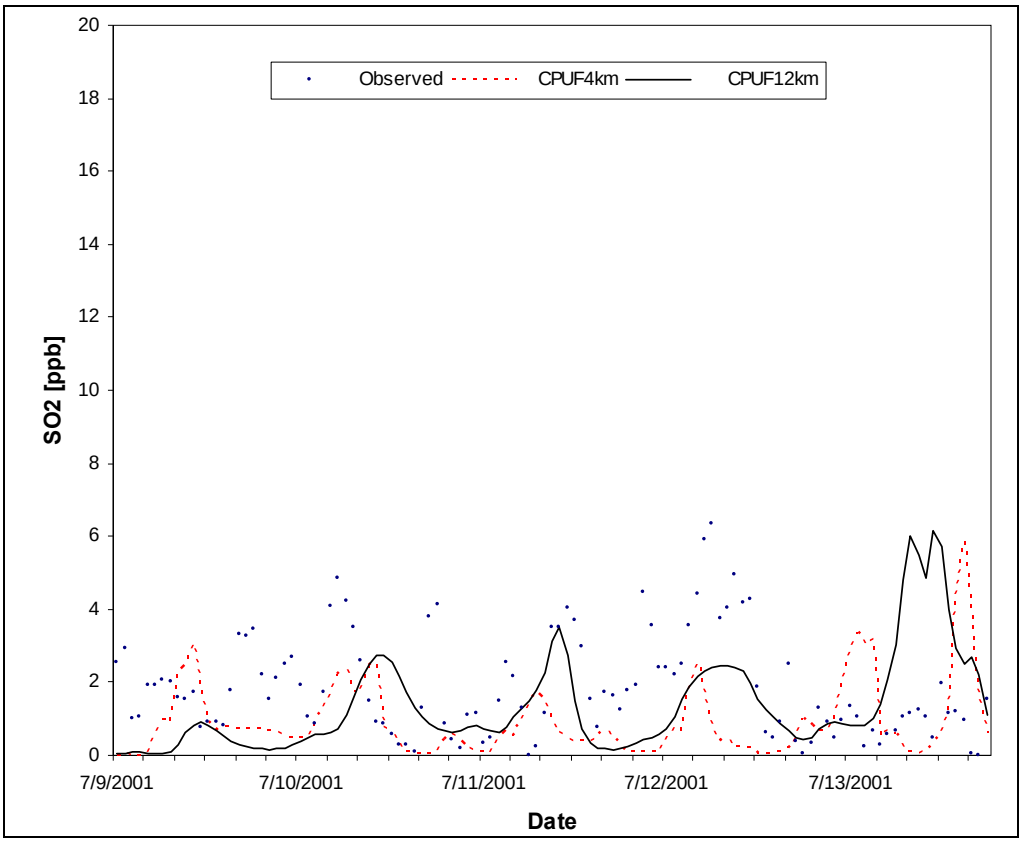

Figure 6-13. Observed and predicted SO_2 concentrations at BIP for Case 3.

Comparisons of observed and predicted daily average NO_2 concentrations (**Figure 6-14**) suggest that the CPUF4 simulation performed somewhat better than CPUF12 at FTM. At WDP, CPUF4 compared less favorably to observations on three out of four days. **Figure 6-15** shows the hourly observed and predicted NO_2 concentrations at BIP.

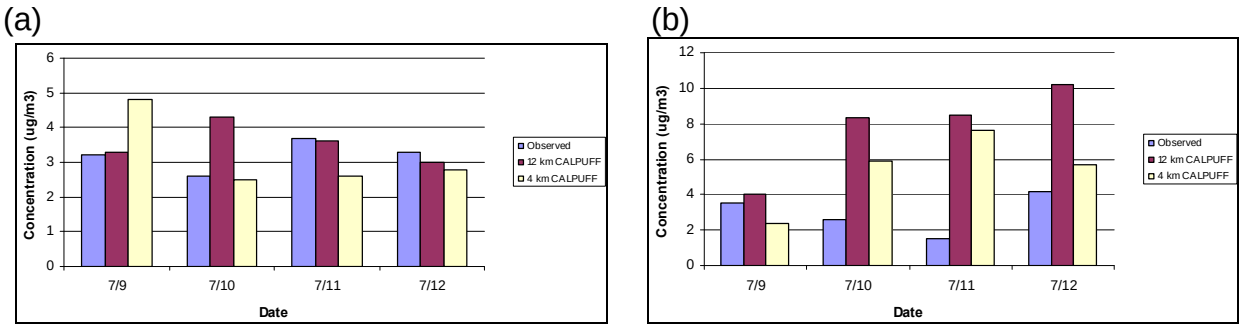

Figure 6-14. Daily average 24-hr NO_2 concentrations observed and predicted at WDP (a) and FTM (b) during Case 3.

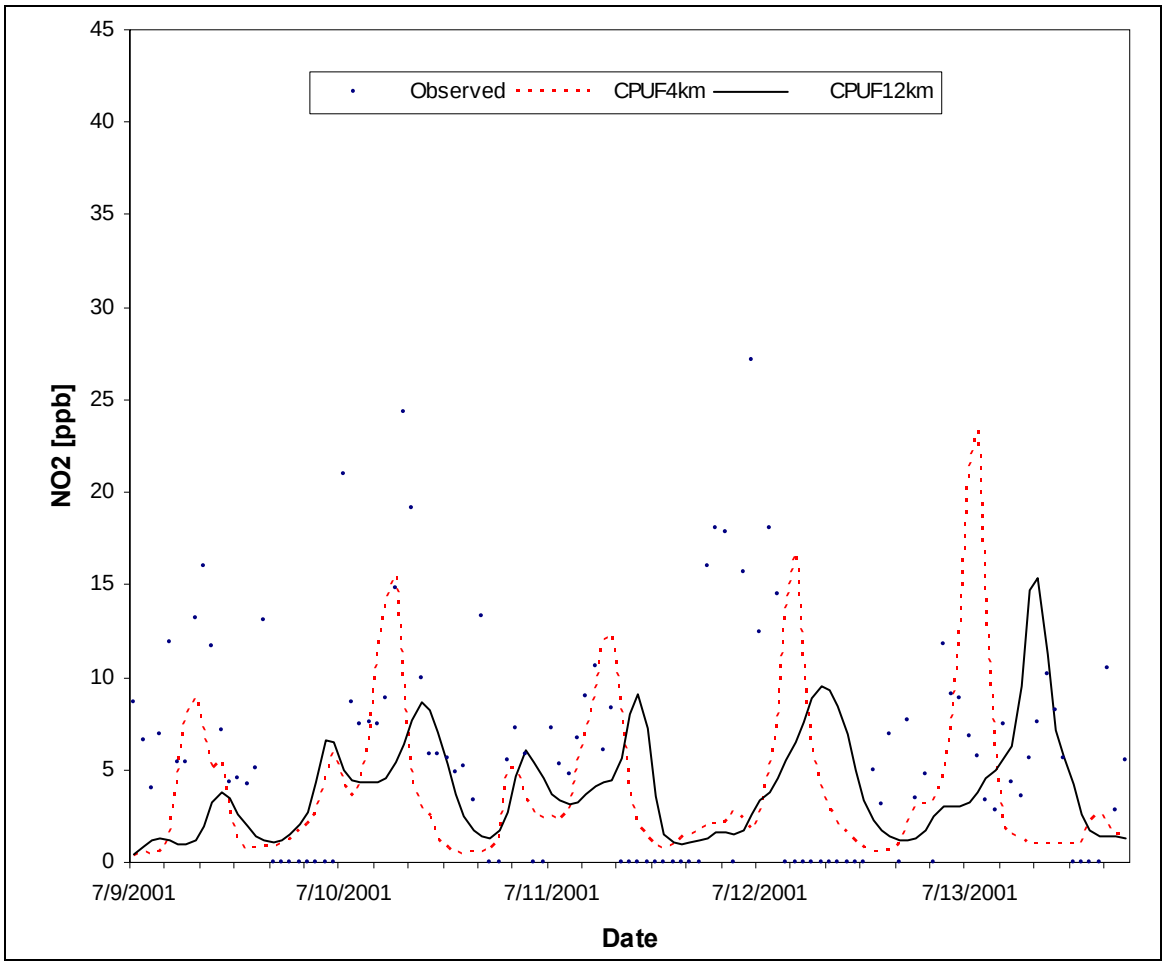

Figure 6-15. Observed and predicted NO_2 concentrations at BIP for Case 3

The average observed and predicted SO_2 and NO_2 concentrations at BIP, FTM, and WDP for CPUF4 and CPUF12 are compared in **Table 6-9**. While average concentrations are not a robust metric for model evaluation, some general tendencies of the simulations are illustrated. Both simulations underpredict SO_2 by about a factor of two, but the underprediction was more pronounced in CPUF4. The opposite is true for NO_2, however; while both simulations overpredicted the average NO_2 concentration, CPUF4 was actually closer to the observed average although at BIP (Figure 6-15) CPUF4 appears to match the observed concentrations closer.

Table 6-9

Average Observed and Predicted Concentrations of SO_2 and NO_2 at BIP, FTM, and WDP Combined

	SO_2 (ppb)				NO_2 (ppb)			
Case	N*	Observed	12 km	4 km	N	Observed	12 km	4 km
3	345	2.4	1.5	1.0	345	3.3	4.5	3.7

* Number of observation-prediction pairs.

Model performance statistics for both simulations are listed in **Table 6-10**. Note that a positive FB indicates underprediction while negative FB indicates overprediction. These statistics were calculated by pairing all observations and predictions in time and space.

Both simulations underpredict SO_2 with FB of 45% in CPUF12, and 86% in CPUF4. Both models simulations have an NMSE of at least 150%, and R is 0.18 in CPUF12 and 0.14 in CPUF4. The standard deviation of the predictions (SDEV_pred) is smaller in CPUF4 than in CPUF12 (1.3 versus 1.9), indicating the higher resolution simulation predicts less variability than CPUF12. All statistical indicators used in this analysis indicate that CPUF12 performs better than CPUF4 for SO_2, but overall both simulations perform poorly.

Both simulations perform better for NO_2 than for SO_2 with FB less than 50% (CPUF12 over predicts by 31% while CPUF4 overpredicts 10%). Correlation coefficients were quite low, however, with R values of -0.08 in CPUF12 and 0.11 in CPUF4. In CPUF12, 37% of the predictions were within a factor of two of the observations, compared to 42% for CPUF4. SDEV_pred in CPUF4 was close to that in CPUF12 (4.0 versus 3.9), and both were less than the standard deviation (SDEV_obs) of the observations (4.2), indicating the simulations predict less variability in concentrations than was observed. CPUF4 generally performs better than CPUF12 for NO_2.

Table 6-10

Model Performance Statistics Paired in Space and Time for SO_2 and NO_2 for the 4-km and 12-km CALPUFF Simulations.

	Fractional Bias (FB)		Geometric Mean Bias (MG)		Normalized Mean Square Error (NMSE)		Geometric Mean Variance (VG)		Correlation Coefficient (R)		Predictions Within a Factor of Two of Observations (FAC2)	
Species	12 km	4 km	12 km	4 km	12 km	4 km	12 km	4 km	12 km	4 km	12 km	4 km
SO_2	0.46	0.86	2.6	4.0	1.5	2.3	16.4	41.6	0.19	0.15	0.30	0.20
NO_2	-0.31	-0.10	0.6	0.9	2.5	2.5	8.2	6.2	-0.08	0.11	0.37	0.42

7.0 ANNUAL AIR QUALITY MODELING

7.1 MODELING APPROACH

7.1.1 Model Selection

Because the 24-hr SO_2 increment was the most likely to be exceeded, the performance of the models for the highest SO_2 concentrations is of greatest importance. Based on the episodic model performance evaluation for the top 5% of concentrations, CALPUFF was selected for annual increment analysis modeling because it replicated high SO_2 concentrations more reliably.

7.1.2 Model Configuration

Because of computer-memory issues and computational demands, the annual CALPUFF simulations were configured differently than the initial episode-type simulations. The initial simulations were typically 5 to 6 days in duration. However, while performing the annual simulations, we found that many periods of the year when puffs in the model accumulated in the modeling domain to the point that the computer-memory requirements exceeded the maximum allowed by CALPUFF. The following changes to the model configuration were made to reduce the memory and computational demands for the annual simulations.

- Puff splitting was turned off.
- Accelerated puff removal was implemented.
- A smaller receptor grid was used. While the annual CALPUFF simulations were performed on the full 12-km computational domain, only a subset of the domain was sampled to reduce computer-memory requirements and computational demands. The receptor grid for the annual simulations is shown in **Figure 7-1**.
- Only emissions within 200 km (north-south and east-west) of the BNWA were modeled. The initial case-specific CALPUFF simulations used all emissions within the 12-km modeling domain to provide the most accurate predictions possible. For the annual simulations, only sources within 200 km of the Class I area were modeled. Comparisons of results from the annual simulation and initial cases found that sources beyond 200 km contributed little to concentrations in the BNWA.

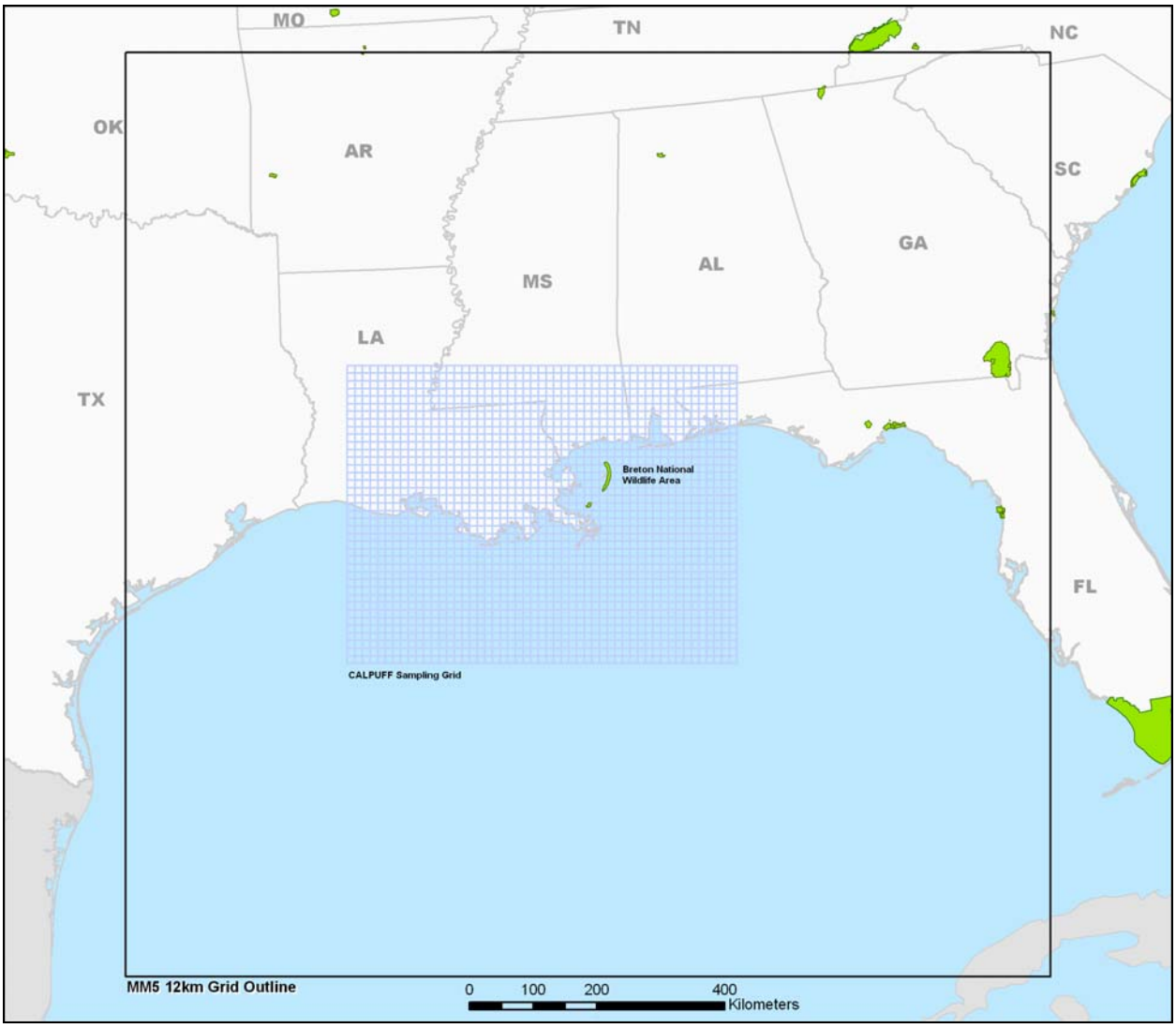

Figure 7-1. CALPUFF receptor (sampling) grid for the annual simulations.

7.2 STUDY-YEAR SIMULATION

The study-year simulation produced hourly concentrations for each day of the year. Post-processing was performed to calculate peak daily 3-hr SO_2, daily average SO_2 and NO_2, and annual average SO_2 and NO_2 concentrations for each receptor modeled.

7.2.1 Observational Data Quality and Completeness

The model performance evaluation was based on observational data from three sites: Breton Island (BIP), Fort Morgan (FTM), and West-Delta Platform (WDP). Maximum 3-hr and 24-hr SO_2, data completeness rates at the three sites were quite high, ranging from 95% to 100%. During periods when concentrations likely dropped below the instrument detection limit, small

negative concentrations were reported. These values were adjusted to 0.0 before evaluating model performance.

The 24-hr NO_2 data were less complete than the SO_2 data, as NO_2 data completeness was 84% at FTM and WDP, and 93% for BIP. Again, small negative concentrations were adjusted to 0.0, assuming they are the result of concentrations that fall below the instrument detection limit. At WDP, 14 large, negative (<-1.0) daily average NO_2 concentrations were reported. These large, negative values could not be attributed to instrument drift, and were therefore invalidated prior to evaluating model performance.

7.2.2 SO_2 Performance

For the annual simulation period starting October 1, 2000, and ending September 30, 2001, the annual SO_2 concentration predicted by CALPUFF was lower than the observed annual SO_2 concentration at all three sites (**Table 7-1**). At WDP, the CALPUFF predicted annual average SO_2 was under half of the observed averaged SO_2 concentration. The predicted annual average was closer to the observed average at FTM, but CALPUFF still underpredicted the annual average by 13%. At BIP, CALPUFF underpredicted the annual average by 33%. CALPUFF correctly predicted a higher annual average concentration at FTM than the other two sites, but it also predicted a larger difference between the annual averages at BIP and WDP.

Table 7-1

Predicted and Observed Annual Average SO_2 Concentrations ($\mu g/m^3$)

Site	Observation	CALPUFF
BIP	4.04	2.70
FTM	4.44	3.87
WDP	3.94	1.52

CALPUFF predictions of daily 24-hr average concentrations, in general, are also smaller than the observed values, especially at BIP and FTM, where the mean annual biases were -1.32 and -0.95 $\mu g/m^3$, respectively, while at WDP, the mean bias was -2.43 $\mu g/m^3$.

Time series analysis of observed and predicted daily average SO_2 concentrations illustrates the daily and seasonal variability of SO_2, and how CALPUFF predictions compare to observed values throughout the year. At all three sites, CALPUFF underpredicts daily average SO_2 on numerous days throughout the year. This is consistent with the low bias in the CALPUFF annual prediction. At WDP, the site with the largest SO_2 bias, CALPUFF tends to underpredict average SO_2 concentrations on most days during the year. At this site, CALPUFF frequently predicts small (< 1 $\mu g/m^3$) concentrations when observed concentrations are from 1 to 4 $\mu g/m^3$. Scatter plots of observed versus modeled 3-hr maximum and daily average SO_2 concentrations (**Figures 7-2 and 7-3**) show the tendency of CALPUFF to underestimate the highest SO_2 concentrations.

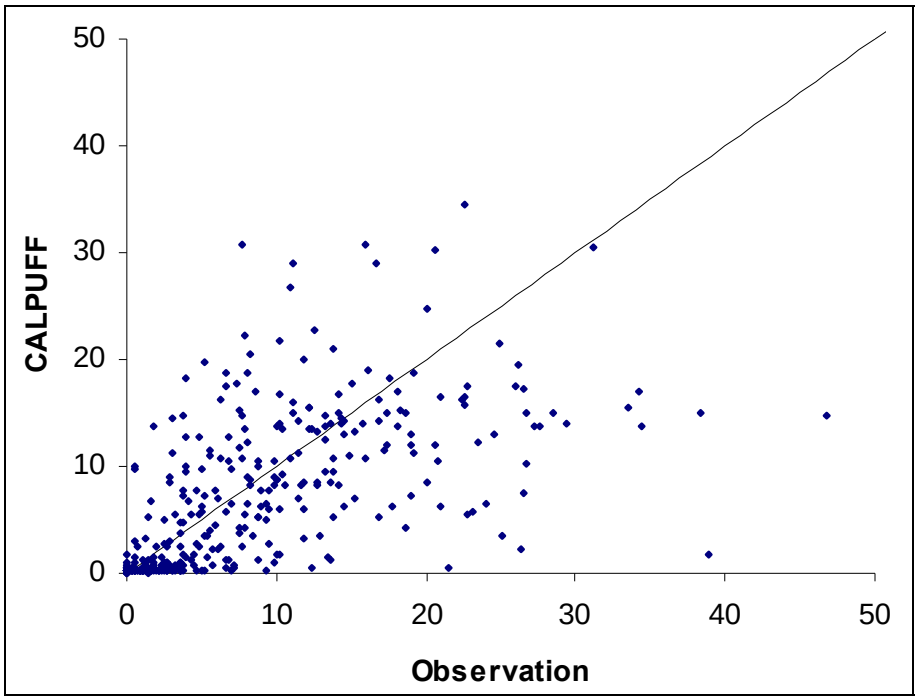

Figure 7-2. Scatter plot of observed vs. predicted 3-hr daily maximum SO_2 concentrations at BIP.

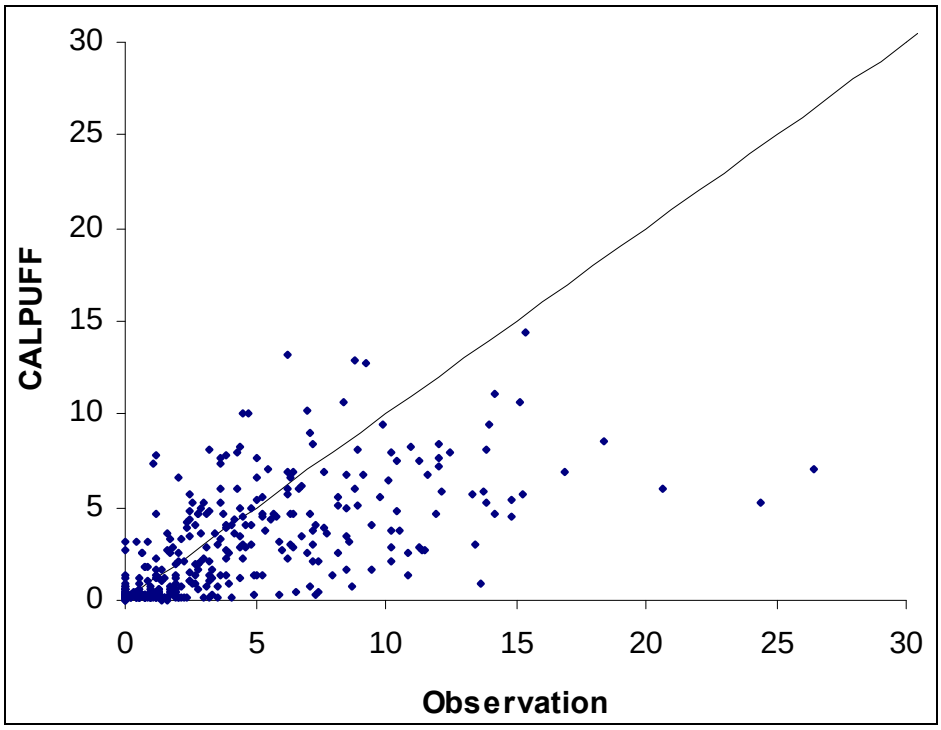

Figure 7-3. Scatter plot of observed vs. predicted 24-hr average SO_2 concentrations at BIP.

Higher concentrations of SO_2 are observed at all three sites during the winter months. This seasonal increase in SO_2 is due in part to the increased frequency of northerly (offshore) wind flow regimes that transport SO_2 from onshore sources. Regional and synoptic-scale atmospheric conditions that lead to air stagnation and recirculation are also more prevalent during the winter months. CALPUFF correctly reproduces the observed seasonal increase in SO_2 concentrations at the observation sites during the winter months. This indicates that MM5 reproduces the synoptic-scale flow patterns that are conducive to higher regional SO_2 concentrations, and that CALPUFF responds appropriately to seasonal variations in meteorological forcing.

From late spring until through early autumn (May through September), synoptic-scale southerly winds typically prevent SO_2 from onshore sources from reaching the observation sites over the Gulf of Mexico. High SO_2 episodes during the summer typically occur when the seasonal southerly flow temporarily reverses, bringing SO_2 from the land over the Gulf. CALPUFF often predicts the occurrence of these summertime SO_2 episodes at the observation sites, even though it does not always predict the correct peak concentrations during an episode.

The consistent underprediction of daily average SO_2 concentrations leads to negative mean biases of daily average and daily peak 3-hr average SO_2 (**Table 7-2**). The only exception is the positive bias in the peak 3-hr average SO_2 at FTM, where CALPUFF tends to overpredict SO_2 concentrations on an hourly basis during SO_2 episodes. We also calculated the mean bias for days when the 24-hour SO_2 concentration of 5 $\mu g/m^3$ was exceeded at the observation sites. Observations exceeded the 5 $\mu g/m^3$ level on 109 days at BIP, 124 days at FTM, and 101 days at WDP. CALPUFF predicted a daily average SO_2 concentration greater than 5 $\mu g/m^3$ on 137 out of the 334 total observed days at the three sites combined. It also predicted concentrations of greater than 5 $\mu g/m^3$ at the three sites on 62 additional total days when this level was not exceeded in the observations. Negative biases in predicted daily average SO_2 concentration increase when observations less than 5 $\mu g/m^3$ are filtered out of the calculation.

Table 7-2

Mean Bias for All Available Observations and When Observed Daily Average SO_2 Concentrations are Greater Than 5 $\mu g/m^3$

Mean Bias	BIP	FTM	WDP
Daily average SO_2	-1.32	-0.57	-2.43
Daily average NO_2	-1.91	-1.75	-1.78
Peak 3-hr average SO_2	-1.77	0.80	-3.70
SO_2 when the observation is above increment	-4.24	-2.93	-5.20

7.2.3 NO_2 Performance

The annual average NO_2 concentration is underpredicted at all three observation sites as shown in **Table 7-3**.

Table 7-3

Predicted and Observed Annual Average NO_2 Concentrations ($\mu g/m^3$)

Site	Observation	CALPUFF
BIP	6.01	4.04
FTM	6.31	4.16
WDP	6.34	4.37

CALPUFF also underpredicts NO_2 concentrations on a daily average basis. The mean bias at BIP, WDP, and FTM were -1.91, -1.75, and -1.78 $\mu g/m^3$, respectively. CALPUFF tended to significantly underpredict daily average NO_2 concentrations at all three sites during high NO_2 episodes. This tendency is shown for BIP in **Figure 7-4**. As with SO_2, the highest observed daily average NO_2 concentrations tend to occur during the winter months when northerly offshore winds are prevalent.

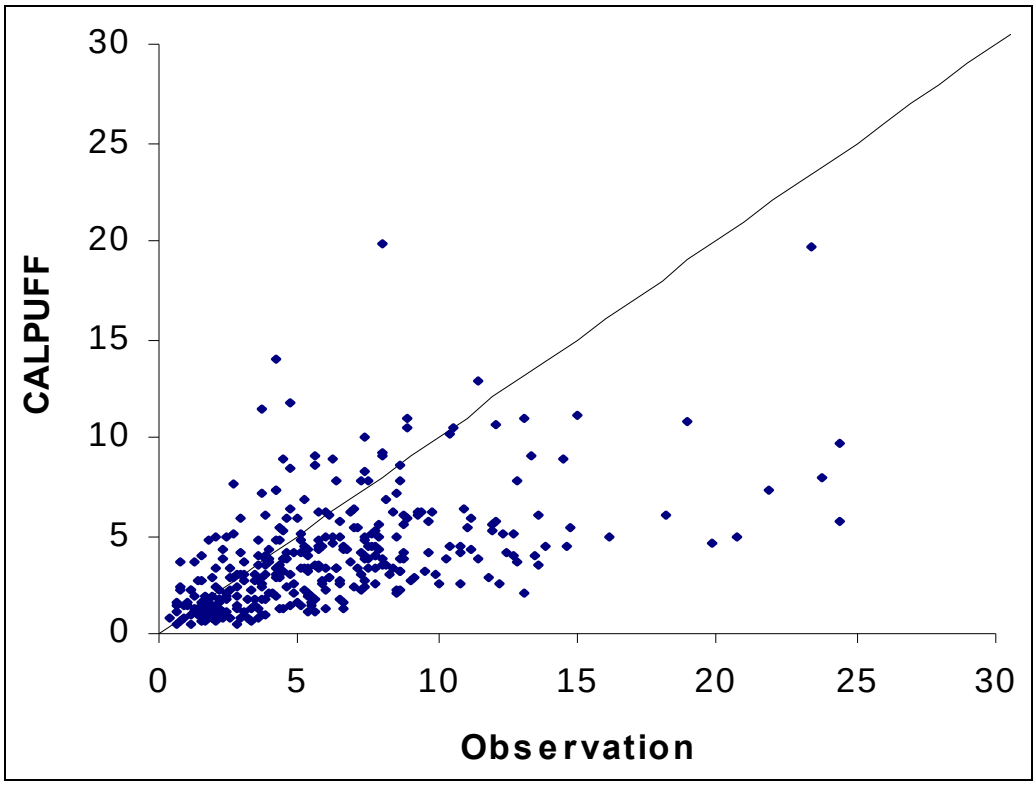

Figure 7-4. Scatter plot of observed vs. predicted 24-hr average NO_2 concentrations at BIP.

7.3 BASELINE-YEAR SIMULATIONS

The baseline years, 1977 for SO_2 and 1988 for NO_2, were simulated in CALPUFF using the same configuration and inputs as in the study-year simulation except for emissions. The preparation of model-ready emission inventories for 1977 and 1988 were described in Section 3.

Each simulation produced hourly concentrations for each day of the year. Post-processing was performed to calculate peak daily 3-hr SO_2, daily average NO_2, and annual average SO_2 and NO_2 concentrations for each receptor modeled.

7.4 RESULTS

Annual simulations of the study year and the baseline years (1977 and 1988) were successfully performed with CALPUFF, and the hourly results were averaged over the periods relevant for the increment analysis: 3-hr, 24-hr, and annual for SO_2 and annual for NO_2. **Figure 7-5** provides a comparison of 1977, 1988, and study-year annual average SO_2 concentrations and **Figure 7-6** provides the same comparison for annual average NO_2.

The effects of emission changes, between the baseline years and study year, on annual concentrations were evident. From 1977 to 2000/2001, the annual SO_2 concentrations declined throughout most of the modeling domain with only one onshore and six offshore receptors showing increases. The annual average domain peak SO_2 concentration declined from 60.7 $\mu g/m^3$ in 1977 to 50.9 $\mu g/m^3$ in the study year. From 1988 to 2000/2001, the annual NO_2 concentrations declined at most onshore receptors in the modeling domain with only four onshore receptors showing increases. However, there were widespread increases in NO_2 at offshore receptors. The annual average domain peak NO_2 concentration declined from 79.3 $\mu g/m^3$ in 1988 to 77.4 $\mu g/m^3$ in the study year.

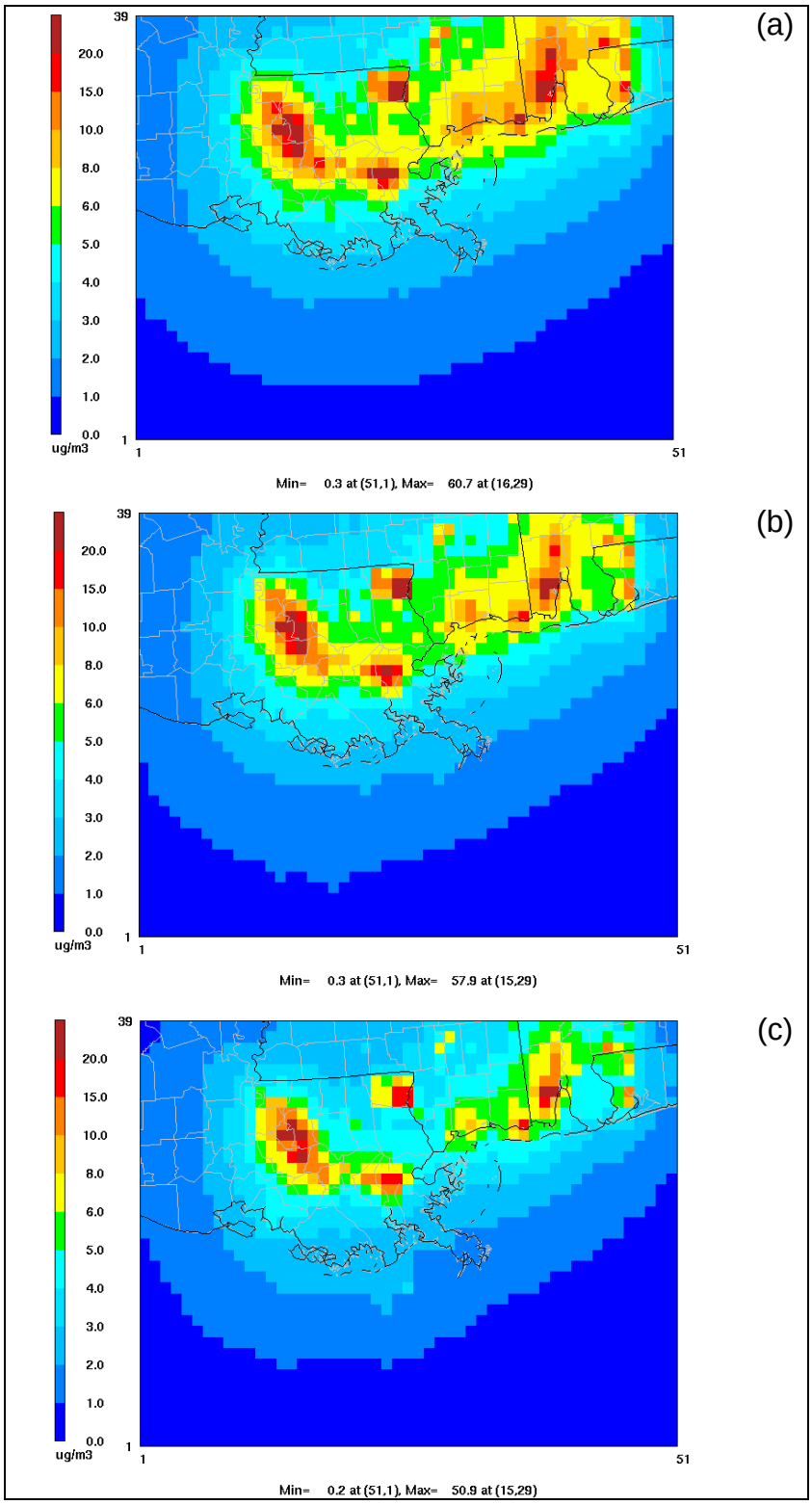

Figure 7-5. Annual SO_2 concentrations for (a) 1977, (b) 1988, and (c) the study year.

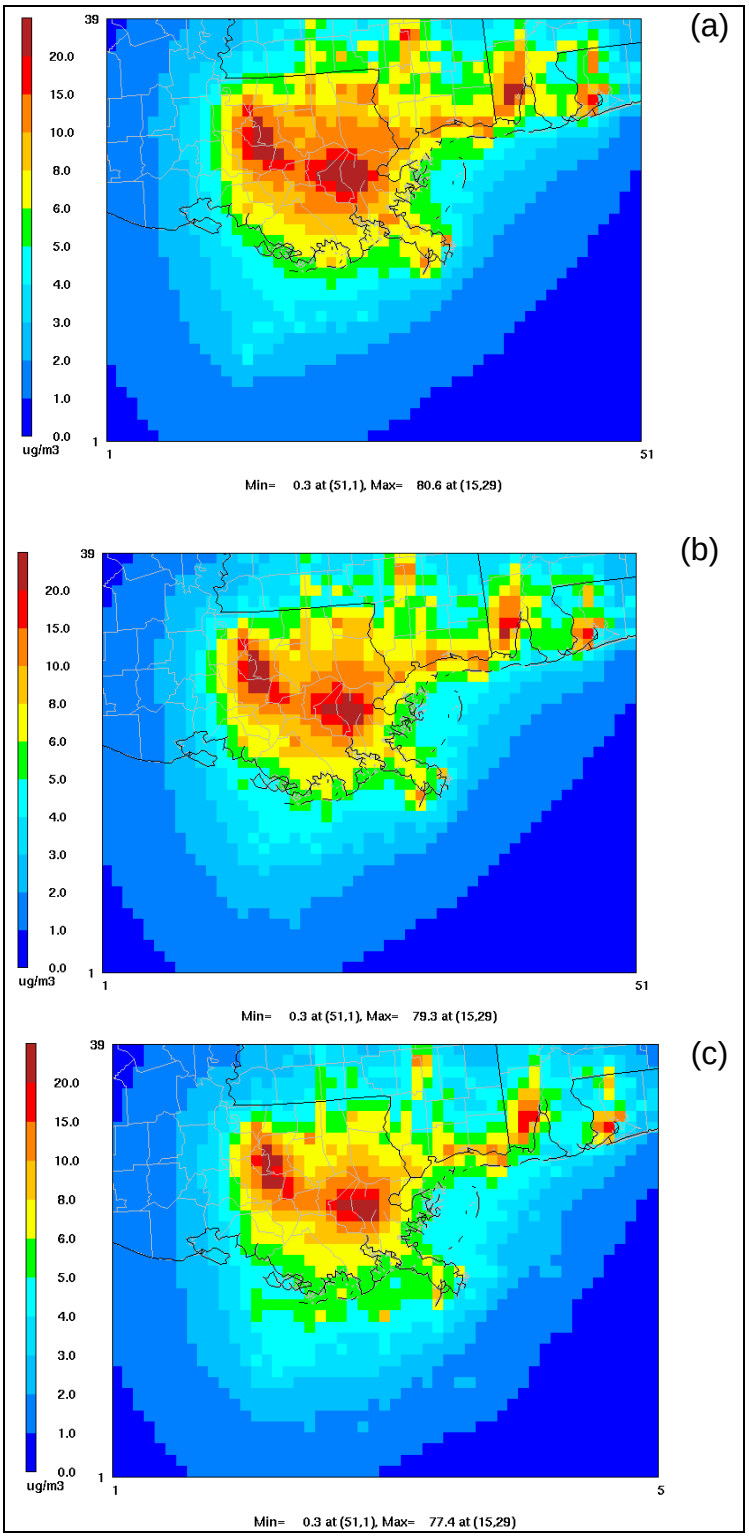

Figure 7-6. Annual NO_2 concentrations for (a) 1977, (b) 1988, and (c) the study year.

8.0 CUMULATIVE INCREMENT ANALYSIS

8.1 APPROACH

A geographical information system (GIS) analysis was performed to determine the intersection of the BNWA boundaries with the CALPUFF receptor grid. Based on this analysis, 11 grid cells were identified as intersecting with the BNWA as shown in **Figure 8-1**. Concentrations of SO_2 and NO_2 for the study year and the SO_2 and NO_2 baseline years (1977 and 1988, respectively) were extracted for each grid cell within the BNWA and the maximum values for each appropriate averaging tine were compared between the study and baseline years to estimate the amount of increment that may have been consumed.

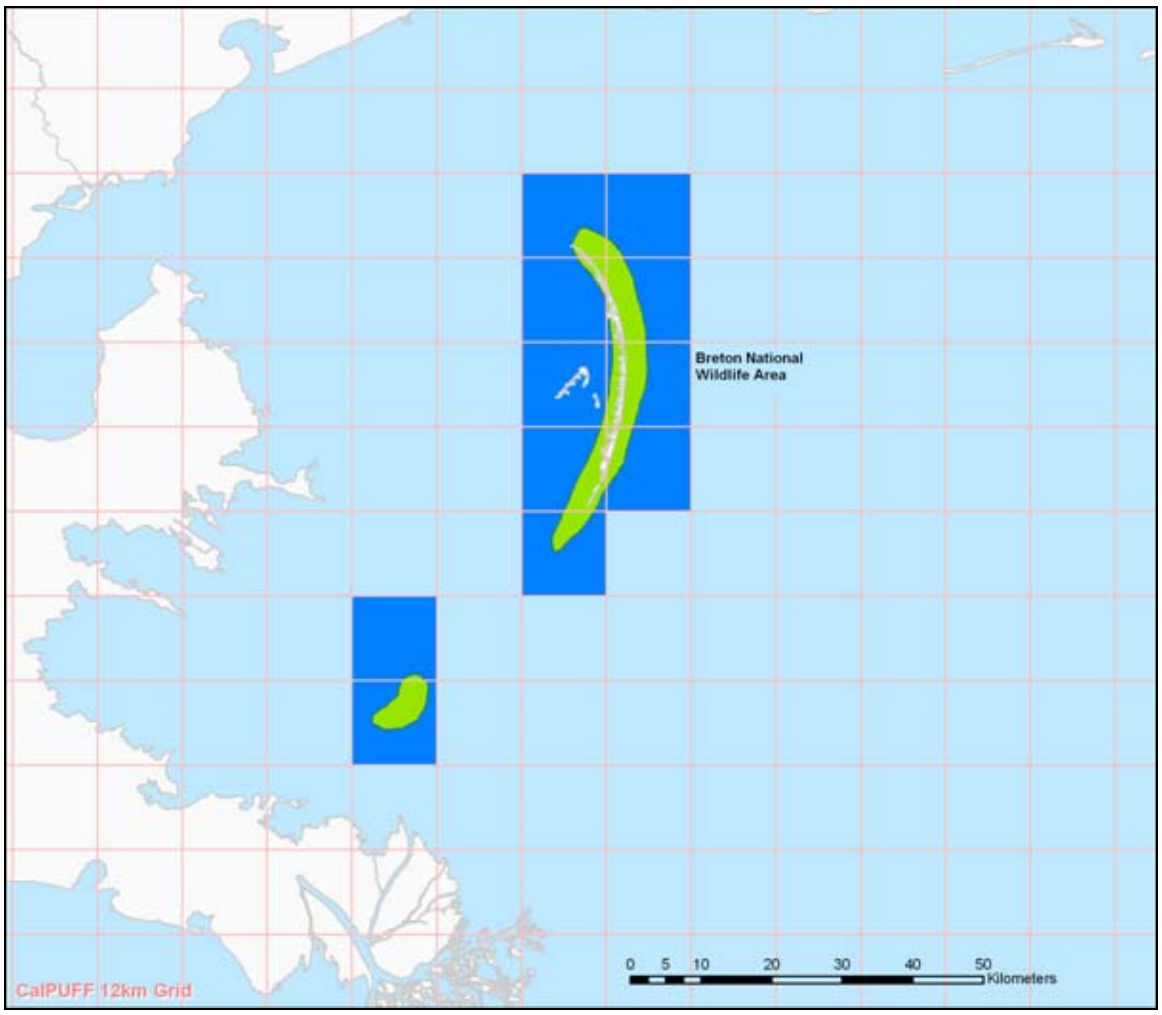

Figure 8-1. CALPUFF receptors within the BNWA.

Spatial displacements in modeled concentration patterns could lead to biases (high or low) in predicted SO_2 and NO_2 concentrations and the corresponding increments calculated for

the BNWA. If the predicted increments are biased high, we might argue that the increment analysis is conservative and protective of PSD. However, if the predicted increments are biased low, we might underestimate the amount of increment consumed in the BNWA. To address the uncertainties associated with model biases, we borrowed from an approach used when calculating relative reduction factors in ozone modeling for SIPs —calculate the increments for all cells in the domain (not just in the BNWA) and use the maximum increment consumption within a certain radius of the BNWA (e.g., 50 km) to account for spatial uncertainties in the model predictions.

8.2 UNCERTAINTIES

Many uncertainties can affect a model-based analysis. In both the episode-type and annual simulations, we found the models tend to underpredict NO_2 and SO_2, particularly when the observed concentrations are highest. These errors may be a result of uncertainties in model formulation, model inputs, and/or model configurations. The most likely uncertainties in this study include

- Emissions estimates – emission inventories are under constant revision and improvement. For example, the OCS emissions provided by ERG have been updated since the modeling was performed. There are also uncertainties in projecting emissions to the future and to the baseline years.
- Representation of transport – the difficulty of the models to replicate concentrations paired in time and space indicates uncertainties in the representation of transport. When modeling individual point sources, small errors in transport can result in a plume missing a given receptor that might in reality be impacted.
- Representation of vertical mixing – Our early sensitivity experiments found that CALPUFF predictions were very sensitive to mixing heights. While we believe the final mixing heights developed for this analysis are reasonable, they may be biased high during episodic conditions, which could explain the underpredictions of NO_2 and SO_2.
- Simple treatment of chemistry – CALPUFF has a fairly simplistic approach to the formation of NO_2, nitrate, and sulfate, and the chemical removal of NO_2 and SO_2. It is not clear whether the SO_2 loss via oxidation to sulfuric acid is realistic.

This last uncertainty warrants further discussion, particularly with respect to SO_2 losses. In an evaluation of CALPUFF chemistry algorithms (Morris et al., 2005), the authors found that the RIVAD chemistry scheme used in our simulation resulted in underpredictions of sulfate in both winter (fractional bias of -11%) and summer (fractional bias of -17%). Peak prediction accuracy for the RIVAD scheme was -10% in winter and -44% in summer. The tendency of this chemistry scheme to underestimate sulfate concentrations implies it would overestimate SO_2 concentrations. Considering that CALPUFF is underestimating SO_2, it is likely that some compensating errors exist in the simulations.

Fortunately, while the absolute predictions from even the best models and data bases have broad uncertainty, the incremental predictions derived from differences in two model simulations have a much narrower range of uncertainty. In a study of model uncertainties

(Hanna et al., 2000), it was found that the 95% confidence interval, the range on the residual distributions, was roughly one-fifth the range of the parent base case or control strategy distributions suggesting that uncertainties in ozone prediction differences between the base case and control case is about one-fifth of the total uncertainty in ozone predictions due to all model inputs. The study also found that the uncertainties in peak ozone prediction differences between a base case and an emissions control case (i.e., the incremental impacts) were about one-fifth of the total uncertainty in the base-case simulation.

These findings suggest that the incremental change in predicted concentrations between two simulations (i.e., the baseline and study year) may be better represented by the fractional change in concentrations relative to observed concentrations. EPA recommends the approach for modeled attainment demonstrations. Considering the model underpredictions of the highest SO_2 and NO_2 concentrations, the modeled increments may also be underestimated.

8.3 RESULTS

This section summarizes the results of the cumulative increment analysis.

8.3.1 3-hr Maximum SO_2

The maximum increase in the 3-hr SO_2 concentration within the BNWA is 1.70 µg/m^3. The increase in concentration ranges from 0.42 to 1.70 µg/m^3.

As shown in **Figure 8-2**, the 3-hr maximum SO_2 increment of 25.0 µg/m^3 is not exceeded in any grid point within the BNWA, but the results show that a small portion of the increment may have been consumed. Throughout most of the CALPUFF receptor grid, CALPUFF predicts an increase in the maximum 3-hr SO_2 concentration since 1977. The only exceptions are over New Orleans, Baton Rouge, Mobile, and a region of eastern Louisiana near the Mississippi border. In much of the BNWA, the concentration increase ranges from 0.5 to 1.5 µg/m^3. The largest change within a 50 km radius of the BNWA is 2.6 µg/m^3 and occurs to the south and east of Breton Island.

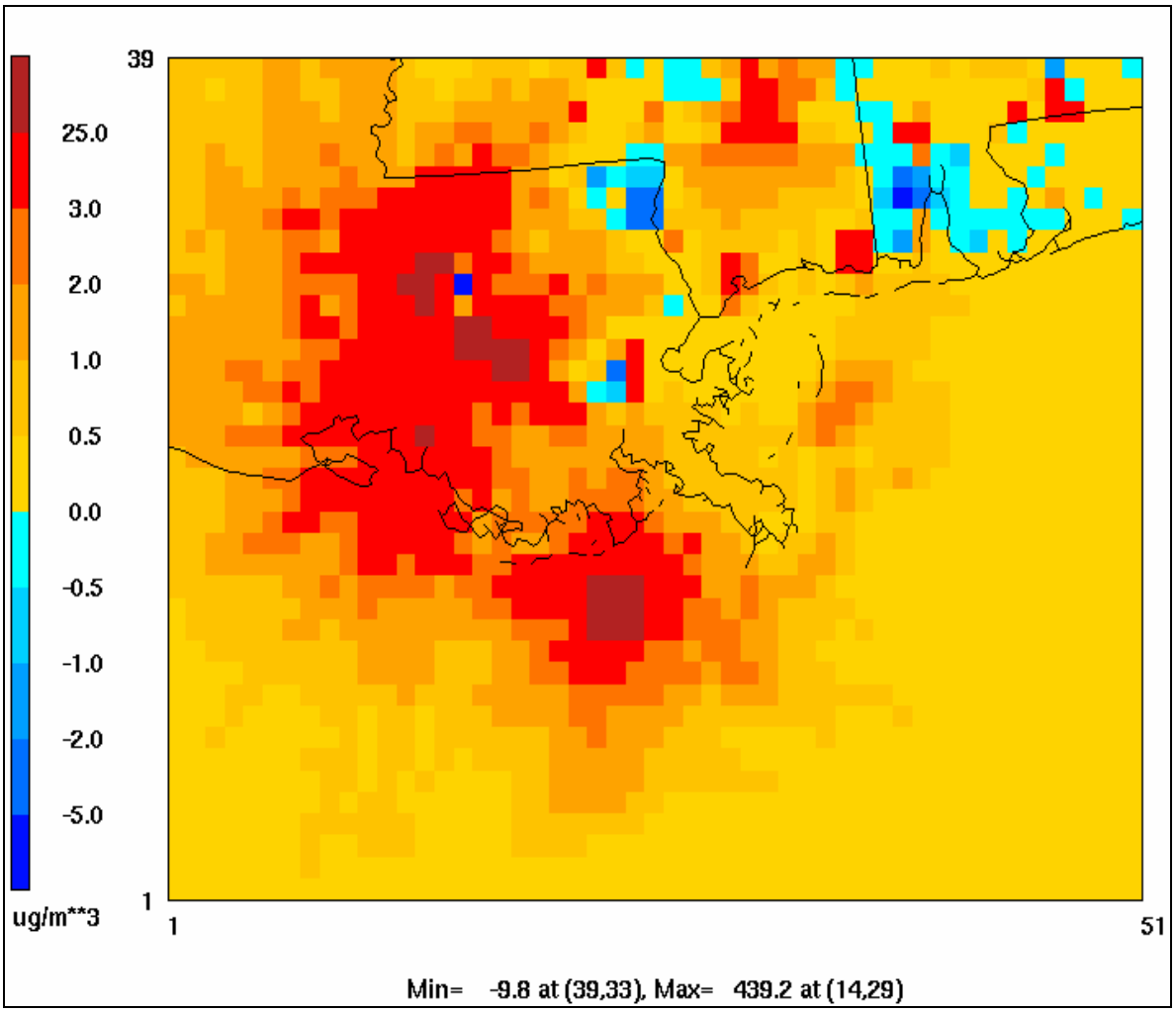

Figure 8-2. Model estimated maximum 3-hr SO_2 changes.

8.3.2 24-hr Maximum SO_2

The maximum increase in the 24-hr SO_2 concentration within the BNWA is 1.18 µg/m^3. The concentration increase ranges from 0.11 to 1.18 µg/m^3.

Figure 8-3 shows that the 24-hr maximum SO_2 increase in any grid point within the BNWA is less than the maximum allowable increment of 5.0 µg/m^3 but the values indicate that a portion of the increment may have been consumed. Over most of the Gulf of Mexico the maximum 24-hr average SO_2 concentration has increased since 1977. Over land, maximum 24-hr average SO_2 has increased or decreased, depending on location. Decreases as large as 7.7 µg/m^3 occur near Mobile, AL while smaller decreases are found over New Orleans and Baton Rouge. Within the BNWA, the increase in concentration ranges between 0.11 and 1.18 µg/m^3. In areas east of the Chandeleur Islands, and southeast of the Breton Islands, maximum 24-hr SO_2 concentration has increased between 1.0 and 1.64 µg/m^3. The largest concentration increase within a 50 km radius of the BNWA is 1.64 µg/m^3.

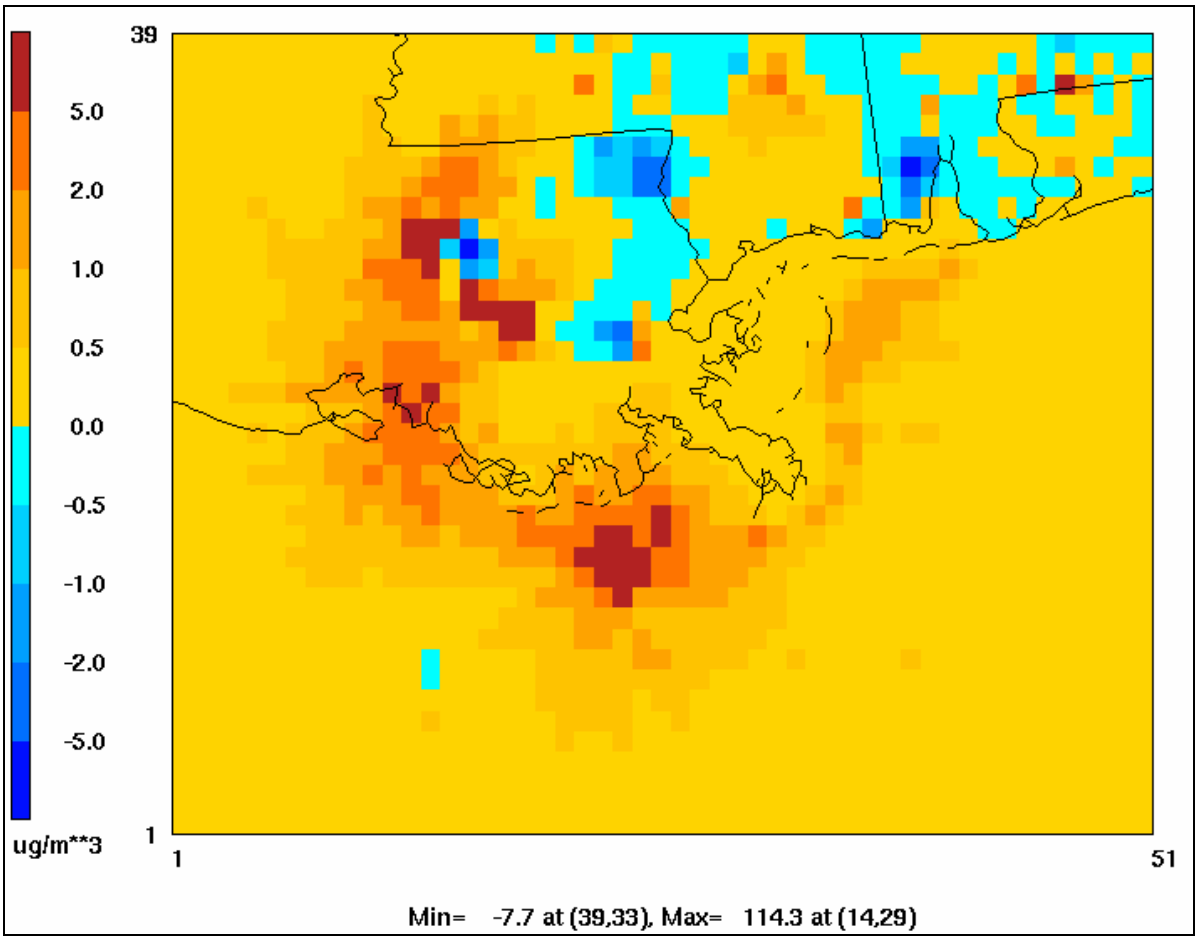

Figure 8-3. Model estimated maximum 24-hr SO_2 changes.

8.3.3 Annual SO_2

The annual SO_2 concentration within the BNWA decreased by 1.07 to 1.89 µg/m^3 since 1977.

Figure 8-4 shows that a decrease in annual SO_2 concentration is predicted almost everywhere within the CALPUFF receptor grid, as SO_2 emissions from on- and off-shore sources have generally decreased since 1977. Within the BNWA, the CALPUFF results indicate an expansion of the annual SO_2 increment in the range of 1-2 µg/m^3. The annual SO_2 concentration decreases more than 1.5 µg/m^3 near the Gulf Coast and inland over southern Mississippi and Alabama, and eastern Louisiana. Over much of the Gulf of Mexico, the decrease in annual SO_2 concentration is less than 0.5 µg/m^3. At one isolated grid point in Louisiana, and at five grid points in the Gulf of Mexico, CALPUFF indicates an increase in annual SO_2 concentrations from 1977 levels. These isolated increases are likely due to the local addition of SO_2 point sources since 1977.

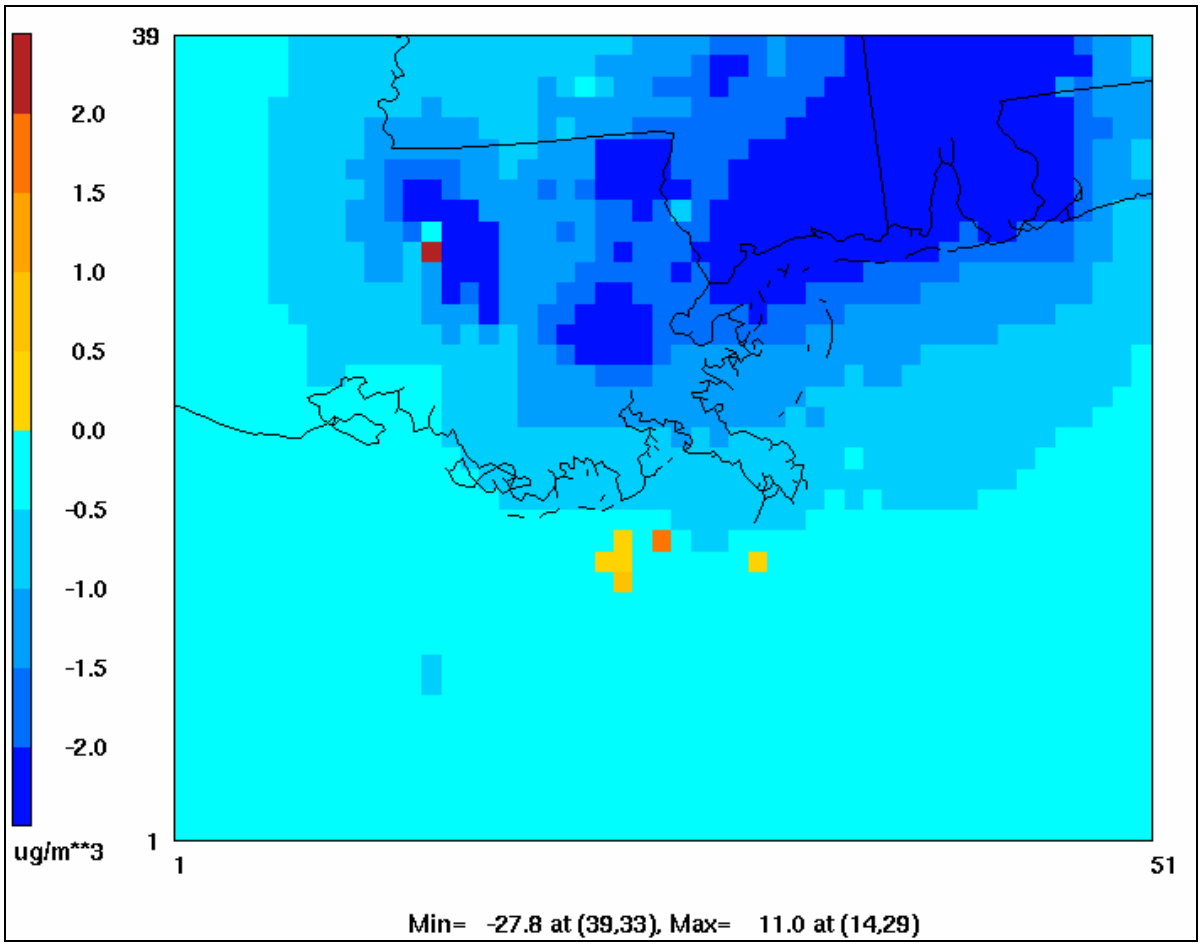

Figure 8-4. Model estimated annual SO_2 changes.

8.3.4 Annual NO_2

The maximum increase in annual NO_2 concentration within the BNWA is 0.10 µg/m^3.

Figure 8-5 shows the highest annual NO_2 increase in any grid point within the BNWA is well below the maximum allowable increment of 2.5 µg/m^3. The results indicate that a very small portion of the increment may have been consumed. CALPUFF suggests that annual NO_2 concentrations have decreased over land since the 1988 baseline year, where NO_x emission controls have been implemented. Over the Gulf of Mexico, the annual NO_2 concentrations have increased since 1988 due to the addition of off-shore NO_x emission sources. The competing effects of decreased onshore emissions and increased offshore emissions results in a boundary between increased annual NO_2 concentrations onshore to the north, and decreased annual NO_2 concentrations offshore to the south. This boundary follows the southern Louisiana coastline, then turns northeastward away from the Louisiana coast and over the Gulf of Mexico, where it crosses over the BNWA and then through the northern part of the Chandeleur Island chain. Part of the BNWA therefore lies within a region where NO_2 concentrations have increased since 1988.

While CALPUFF only suggests minor increases of annual NO_2 concentrations within the BNWA, it does suggest larger increases in areas within 75 km of the BNWA boundaries. One such region is located 20 - 40 km east of the Chandeleur Islands. Within that area, the maximum annual NO_2 increase is 0.93 $\mu g/m^3$. Another region can be seen 50 - 75 km south and east of the BNWA. Increases here range from 0.2 to 1.5 $\mu g/m^3$, but at one grid cell, CALPUFF predicted an increase of 2.1 $\mu g/m^3$.

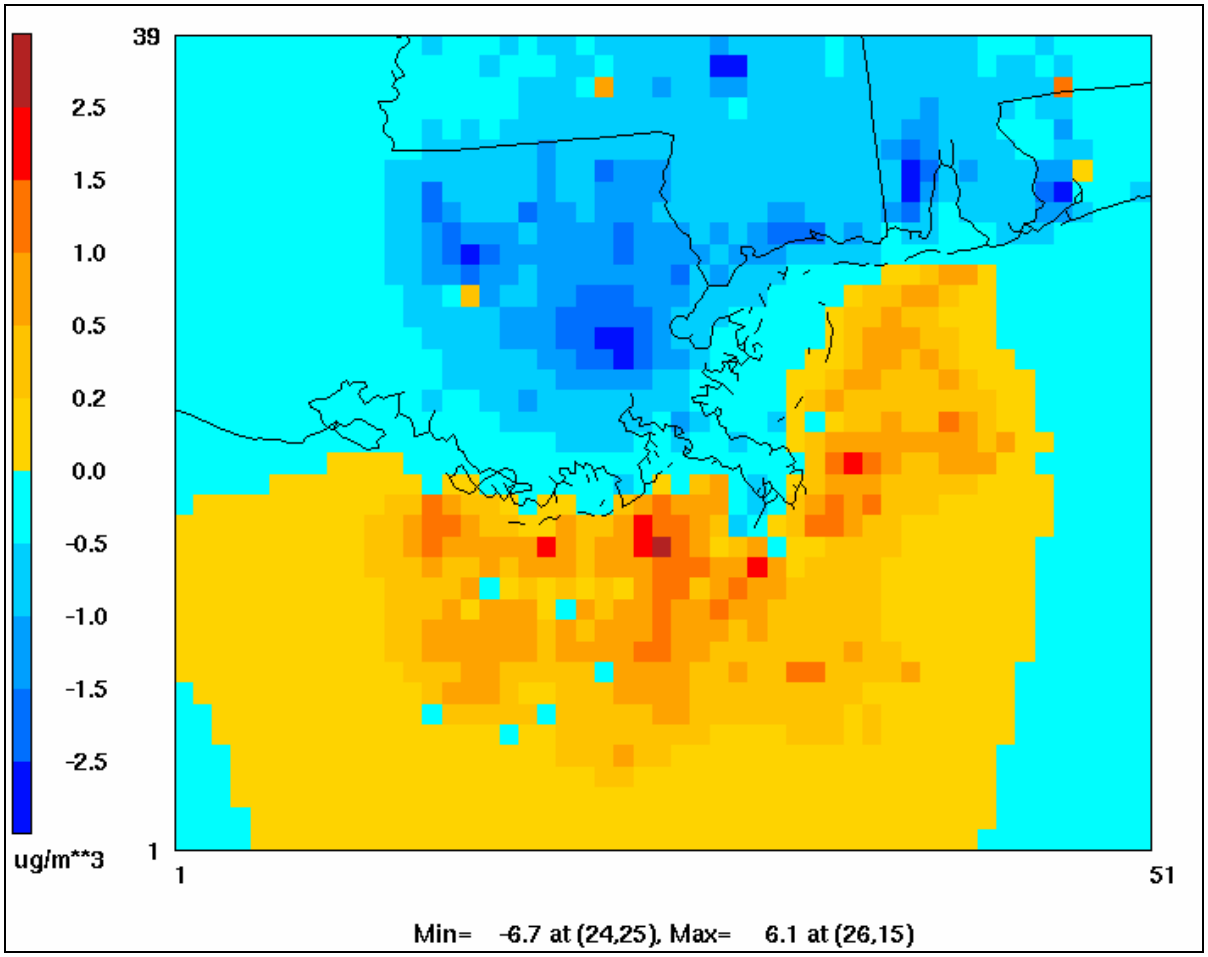

Figure 8-5. Model estimated annual NO_2 changes.

9.0 SUMMARY AND CONCLUSIONS

The section summarizes conclusions from the analyses described in this report.

9.1 METEOROLOGICAL REPRESENTATIVENESS

Our analysis of BNWA meteorology (Section 2) resulted in the following findings:

- The minimum sea surface temperature in winter 2000-2001 appears typical of other years. The maximum sea surface temperature in the summer appears cooler than normal.
- Annual average land surface temperatures were neither warmer nor colder than normal.
- Excluding Hurricane Allison, precipitation was less than normal from October 2000 through September 2001.
- The 850-mb maximum summer temperatures appear to be among the coolest observed in the past twenty years. This cooler-than-normal temperature may have been the result of Hurricane Allison.
- Monthly synoptic patterns deviated from historical monthly levels. However, the annual average of the monthly synoptic weather patterns from October 2000 to September 2001 agrees well with the 1981 to 1990 average. In summary, synoptic influences during the study year were typical.

9.2 EPISODE-TYPE MODELING

9.2.1 Case Selection

Five cases were selected based on the probability that they would represent days likely to contribute to an exceedance of the 24-hr SO_2 increment. An additional case (August 8-13, 2001) was selected to represent more "average" conditions with the highest SO_2 concentrations near the 50^{th} percentile.

- November 8-13, 2000
- December 1-6, 2000
- December 30, 2000–January 4, 2001
- March 2-8, 2001
- July 9-14, 2001
- August 8-13, 2001

Emissions were transported from onshore sources to the BNWA during four of these case periods. Conditions in two of the cases are thought to be the result of regional impacts because the 24-hr SO_2 concentrations at BIP, FTM, and WDP were within a factor of two. Selection of these five cases showed these results:

- Twenty-four-hour NO_2 concentration days were almost equally split, both greater than and less than 7 $\mu g/m^3$; 24-hr NO_2 concentrations greater than 7 $\mu g/m^3$ contributed to half of the annual NO_2 concentration.
- A synoptic weather pattern distribution (CH, FOR, GH, and CR at 44%, 28%, 11%, and 5%) closely matched the distribution for all days in the study year when 24-hr SO_2 concentrations were above the increment (CH, FOR, GH, and CR weather patterns present on 40%, nearly 25%, nearly 15%, and 10% of these events).

9.2.2 Air Quality Model Performance

Both CMAQ and CALPUFF had difficulty replicating observations when paired in time and space. However, when the top 5% of concentrations, unpaired in time and space, both models performed significantly better. While both models meet our performance goals for NO_2, only CALPUFF meets them for SO_2. Because of its detailed chemistry, we expected CMAQ to perform better than CALPUFF, particularly for NO_2, but that was not the case. The highest concentrations near the BNWA appear to be influenced by specific plumes of SO_2 or NO_2, whether from individual or regional sources. The Eulerian formulation of CMAQ seems to result in over-dilution of these plumes, even with the use of PinG. CALPUFF appears to represent these plumes more accurately even without the detailed chemistry.

From a regulatory standpoint, increment analysis is performed without regard for model performance. This lack of attention to model performance stems from the need to have a conservative uniform approach to increment analysis and the concept that the uncertainty in a model's response to emission changes is less than the uncertainty in a model's prediction of an absolute concentration. As was discussed at the project beginning and in subsequent progress meetings, we did not expect to obtain the same level of performance for SO_2 and NO_2 as that for ozone when comparing observations and predictions paired in time and space. The high end of the distribution is the most important because those concentrations are likely to dominate exceedances of the increments. That is why evaluating the high end of the concentration distribution (i.e., top 5%) unpaired in time and space was recommended.

When only the top 5% of the observed and predicted SO_2 and NO_2 concentrations, unpaired in time and space, are compared, we see significant improvements in model performance. While both models meet performance goals for NO_2, only CALPUFF meets them for SO_2. Because of its detailed chemistry, we expected CMAQ to perform better than CALPUFF, particularly for NO_2, but that did not prove to be true. It appears that the highest measured SO_2 and NO_2 concentrations near the BNWA are a result of specific emissions plumes from individual or regional sources. The Eulerian formulation of CMAQ seems to result in over-dilution of emissions, even with the use of PinG. CALPUFF appears to represent these plumes more accurately, even without the detailed chemistry.

Because the 24-hr SO_2 increment is the most likely to be exceeded (based on a statistical analysis of ambient air quality data), the performance of the models for the highest SO_2 concentrations is of greatest importance. Based on the model performance evaluation for the top 5% of concentrations, CALPUFF appears to replicate high SO_2 concentrations more reliably and, therefore, will introduce the least bias when used to perform the increment analysis.

9.3 ANNUAL MODELING

Three annual simulations were performed with CALPUFF: (1) with emissions for the study year, (2) with emissions for the SO_2 baseline year (1977), and (3) with emissions for the NO_2 baseline year (1988). Both SO_2 and NO_2 concentrations at the three BAMP air quality monitoring sites were generally under estimated.

The effects of emission changes, between the baseline years and study year, on annual concentrations were evident. From 1977 to 2000/2001 the annual SO_2 concentrations declined throughout most of the modeling domain with only one onshore and six offshore receptors showing increases. The peak annual average SO_2 concentration anywhere within the receptor grid (see Figure 7-1) declined from 60.7 $\mu g/m^3$ in 1977 to 50.9 $\mu g/m^3$ in the study year. From 1988 to 2000/2001 the annual NO_2 concentrations declined at most onshore receptors in the modeling domain with only four onshore receptors showing increases. However, there were widespread increases in NO_2 at offshore receptors. The peak annual average NO_2 concentration anywhere within the receptor grid declined from 79.3 $\mu g/m^3$ in 1988 to 77.4 $\mu g/m^3$ in the study year.

9.4 INCREMENT ANALYSIS

A modeling analysis was performed to assess changes in SO_2 concentrations between 1977 and the study year and NO_2 concentrations between 1988 and the study year. This analysis found the following.

- The maximum 3-hr SO_2 concentration within the BNWA increased by 0.42 to 1.70 $\mu g/m^3$. These values are well within the 3-hr maximum SO_2 increment of 25.0 $\mu g/m^3$. This increase suggests that any PSD increment consumption that may have occurred would be very small.
- The maximum 24-hr SO_2 concentration within the BNWA increased by 0.11 to 1.18 $\mu g/m^3$. These values are within the 24-hr maximum allowable SO_2 increment of 5.0 $\mu g/m^3$. This increase suggests a small amount of PSD increment consumption may have occurred.
- The maximum annual SO_2 concentration within the BNWA decreased by 1.07 to 1.89 $\mu g/m^3$. This decrease suggests there was an expansion of the available PSD increment.
- The annual NO_2 concentration within the BNWA increased by a maximum of 0.10 $\mu g/m^3$. This is well within the annual NO_2 increment of 2.5 $\mu g/m^3$. This increase suggests only a very small PSD increment consumption.

9.5 RECOMMENDATIONS

In this study we learned many things that will be useful in providing guidance on how to conduct improved regulatory analyses. However, there is much more to learn about air quality in the GOM region and how it is changing over time. The following additional research and investigations would be beneficial in expanding the MMS's understanding of air quality processes and issues in the GOM region and improve regulatory analyses and decisions.

- Trends Monitoring – While this study provides the baseline trends in air quality, the MMS could benefit from ongoing monitoring of air quality, meteorological, and emissions trends in the GOM region. Annual or bi-annual analysis and reporting of these trends collectively would provide insights into evolving air quality issues. New satellite platforms and measurement technologies are providing columnar and vertically resolved air quality measurements in the troposphere and may allow us to monitor regional and over water air quality trends without additional ground-based monitors.
- Additional Statistical Analyses – Additional non-paired in space and time statistics for evaluating model results such as frequency distributions, structure functions (in space and time), and spectral analyses could be examined.
- CALPUFF Modeling Reanalysis – The MMS has invested in an updated version of the CALMET-CALPUFF modeling system that was not available at the time the modeling in this study began. Remodeling the study year with the latest version of the system, analyzing model performance, and comparing to the results from this study would provide additional insight into model uncertainties and improvements.
- Particulate Matter Studies – The public's increasing awareness of the potential health risks of exposure to ambient particulate matter (PM) and recent regional monitoring and modeling analyses of PM and regional haze suggests PM will be a continuing air quality issue. The MMS may benefit from studies that investigate the contributions of OCS sources to secondary PM formation in the region.
- Investigations Local Scale Impacts – The ability of the models tested to properly represent local gradients and the impacts of nearby sources could not be adequately explored because of the grid resolution and receptor spacing used. Further, the Plume in Grid treatment in CMAQ was designed to address large regional sources, not smaller local sources. Therefore, the modeling in this may not have captured the impacts and trends due to smaller local sources. It is recommended that case study modeling analyses be performed to assess the potential of these smaller sources to influence air quality impacts and trends at selected receptors and that a variety grid resolutions, receptor spacing, and plume treatments be investigated.
- Lagrangian Particle Modeling – Lagrangian particle models release multiple particles and use subgrid scale turbulent parameterizations to replicate the scale and intensity of turbulent motions. These models have the capability to fully use the three-dimensional variation in winds and turbulence from models such as MM5 and may provide a better representation of physical plume spread and transport than either of the Lagrangian puff models or Eulerian models. While Lagrangian particle models do not include chemistry, they may have a role in future MMS analyses where accurate representation of turbulence and transport is critical.
- Expanded Investigations of Chemistry – It was difficult to fully examine the importance of SO_2 and NO_2 chemistry in the current study because of the domain size and grid resolutions. The benefits of CMAQ's more detailed chemistry may have been masked by compensating errors such as the dilution of emissions when introduced into CMAQ's grid cells. An expanded investigation of SO_2 and NO_2 chemistry based on case study analysis could address these issues. The case studies could include long range transport and near

source scenarios and would investigate the differences between modeled SO_2 and NO_2 concentrations when using simple chemistry and more detailed photochemistry, with the same emissions, meteorology, and plume treatment.

10.0 REFERENCES

Alapaty, K., N.L. Seaman, D.S. Niyogi, and A. Hanna. 2001. Assimilating surface data to improve the accuracy of atmospheric boundary layer simulations. J. Appl. Meteor. 40:2068-2082.

Allen, D. and C. Durrenberger. 2002. Accelerated science evaluation of ozone formation in the Houston-Galveston area: atmospheric chemistry. Prepared for Texas Natural Resource Conservation Commission, Technical Analysis Division, Austin, TX, by University of Texas, Austin, TX. Internet website: http://www.utexas.edu/research/ceer/texaqsarchive/pdfs/Chemistry05{I02.PDF.

Anthes, R.A. 1974. Data assimilation and initialization of hurricane prediction models. J. Atmos. Sci. 31:702-719.

Arakawa, A. and V.R. Lamb. 1977. Computational design of the basic dynamical process of the UCLA general circulation model. Methods in Comp. Physics 17: 173-265.

Atkinson, R., A.C. Lloyd, and L. Winges. 1982. An updated chemical mechanism for hydrocarbons/NO_x/SO_x photo oxidation suitable for inclusion in atmospheric simulation models. Atmos. Environ. 16:1341.

Benjamin, S.G. and N.L. Seaman. 1985. A simple scheme for objective analysis in a curved flow. Mon. Wea. Rev. 113:1184-1198.

Chang, J.C., M.E. Fernau, J.S. Scire, and D.G. Strimaitis. 1998. A critical review of four types of air quality models pertinent to MMS regulatory and environmental assessment missions. MMS Report No. 25194-58 prepared for the U.S. Department of the Interior, Minerals Management Service, Gulf of Mexico OCS Region, New Orleans, LA, by Earth Tech, Concord, MA.

Charney, J.G., M. Harlem, and R. Jastrow. 1969. Use of incomplete historical data to infer the present state of the atmosphere. J. Atmos. Sci. 26:1160-1163.

Deng, A. and D.R. Stauffer. 2006. On improving 4-km mesoscale model simulations. J. Appl. Meteor. 45:361-381.

DiCristofaro, D.C. and S.R. Hanna. 1989. OCD: The Offshore and Coastal Dispersion Model. Vol. I: Users Guide and Vol. II: Appendices. MMS Report No. A085-A prepared the U.S. Department of the Interior, Minerals Management Service, Herndon, VA, by Sigma Research Corp., Westford, MA.

DiCristofaro, D.C. and S.R. Hanna. 1991. The OCD model revisions and evaluations. In: Air Pollultion Modelling and Its Applications, VIII. New York:Plenum. Pp. 759-768

Douglas, S.G., Y.-H. Wei, and A.B. Hudischewskyj. 2001. Gulf Coast Ozone Study (GCOS) modeling analysis: Phase II: Methods and results. Prepared by SAI, San Francisco, CA.

Draxler, R.R. and G.D. Hess. 1997. Description of the HYSPLIT 4 modeling system. Technical memorandum prepared by the National Oceanic and Atmospheric Administration, Silver Spring, MD, ERL ARL-224, December 24.

Dudhia, J. 1989. Numerical study of convection observed during the winter monsoon experiment using a mesoscale two-dimensional model. J. Atmos. Sci. 46:3077-3107.

Dudhia, J. 1993. A non-hydrostatic version of the Penn State/NCAR mesoscale model: validation tests and simulation of an Atlantic cyclone and cold front. Mon. Wea. Rev. 121:1493-1513.

Dudhia, J., D. Gill, K. Manning, W. Wang, and C. Bruyere. 2005. Chapter 7: INTERPF. In: PSU/NCAR Mesoscale Modeling System Tutorial Class Notes and Users' Guide (MM5 Modeling System Version 3). 16pp.

ENVIRON International Corporation. 2002. User's guide, Comprehensive Air Quality Model with Extensions (CAMx). Prepared by ENVIRON International Corporation, Novato, CA.

Gayno, G.A., N.L. Seaman, A.M. Lario, and D.R. Stauffer. 1994. Forecasting visibility using a 1.5-order closure boundary layer scheme in a 12-km non-hydrostatic model. *10th American Meteorological Society Conference on Numerical Weather Prediction, July 18-22, Portland, Oregon, 18-20*.

Grell, G.A., J. Dudhia, and D.R. Stauffer. 1995. A description of the fifth generation Penn State mesoscale model (MM5). Available from NCAR Information Support Services, P.O. Box 3000, Boulder, CO 80397, NCAR Tech. Note NCAR/TN-398 + STR.

Hanna, S., Z. Lu, H.C. Frey, N.J.M. Wheeler, J. Vukovich, S. Arunachalam, M. Fernau, and J. Davis. 2000. Uncertainties in predicted ozone concentrations due to input uncertainties for the UAM-V photochemical grid model applied to the July 1995 OTAG domain. Report # 1000710 prepared by EPRI, Palo Alto, CA, and Ameren, St. Louis, MO.

Hanna, S.R., L.L. Schulman, R.J. Paine, J.E. Pleim, and M. Baer. 1985. Development and evaluation of the Offshore and Coastal Diffusion Model. J. Air Pollut. Control Assoc. 35:1039-1047.

Hanna, S.R. and J.C. Chang. 1995. Relations between meteorology and ozone in the Lake Michigan region. J. Appl. Meteorol. 34:670-678.

Kain, J.S. 2004. The Kain-Fritsch convective parameterization: An update. J. Appl. Meteor. 43:170-181.

Knipping, E.M., N. Kumar, Z.S. Wang, and G. Tonnessen. 2004. Comparison and diagnostic evaluation of three air quality models for PM: CAMx, CMAQ, CMAQ-MADRID. Presented at the *7th Electric Utilities Environmental Conference, Tucson, AZ, January 19-22*.

Kuo, Y.H. and Y.R. Guo. 1989. Dynamic initialization using observations from a hypothetical network of profilers. Mon. Wea. Rev. 117:1975-1998.

Louisiana Office of State Climatology. 2005. Monthly climate summaries indexed by month & year. Internet website: http://www.losc.lsu.edu/newsmonthly.html.

Mass, C.F., D. Owens, K. Westrick, and B.A. Colle. 2002. Does increasing the horizontal resolution produce more skillful forecasts? Bull. Amer. Meteor. Soc. (March 2002):407-430.

McHenry, J.N. and D. Olerud. 2002. MM5 and MAQSIP-RT refined forecast modeling of the August 2000 Houston-Galveston ozone episode. Prepared by MCNC EMC, Research Triangle Park, NC, MCNC-BCCA/MQ-2.

Michelson, S.A. and N.L. Seaman. 2000. Assimilation of NEXRAD-VAD winds in meteorological simulations over the northeast U.S. J. Appl. Meteorol. 39:367-383.

Miller, D.S., P.T. Roberts, and C.P. MacDonald. 2003. Breton Aerometric Monitoring Program data analysis. Executive summary prepared for Offshore Operators Committee and Minerals Management Service, Department of the Interior, New Orleans, LA, by Sonoma Technology, Inc., Petaluma, CA STI-999479-2267-ES2.

Minnett, P.J., R.H. Evans, E.J. Kearns, and O.B. Brown. 2002. Sea-surface temperature measured by the Moderate Resolution Imaging Spectroradiometer (MODIS). Presented at *IEEE International Geoscience and Remote Sensing Symposium, 24th Canadian Symposium on Remote-Sensing, Toronto, Ontario, Canada* by IEEE, Piscataway, NJ.

Mlawer, E.J., S.J. Taubman, P.D. Brown, M.J. Iacono, and S.A. Clough. 1997. Radiative transfer for inhomogeneous atmospheres: RRTM, a validated correlated-k model for the longwave. J. Geophys. Res. 102:4353-4356.

Morris, R.E., S. Lau, and B. Koo. 2005. Evaluation of the CALPUFF chemistry algorithms. Paper #1048 presented at *the Air and Waste Management Association's 98th Annual Conference, Minneapolis, MN, June*.

National Exposure Research Laboratory. 1999. Science algorithms of the EPA Models-3 Community Multiscale Air Quality (CMAQ) modeling system. Report prepared by the National Exposure Research Laboratory, Research Triangle Park, NC, EPA/600/R-99/030 (peer reviewed).

Santos, L., R.I. Sykes, P. Karamchandani, C. Seigneur, F.W. Lurmann, and R.L. Arndt. 1999. Second-order closure puff model with aqueous-phase chemistry and aerosols. Report prepared for EPRI, Palo Alto, CA, by ARAP Group, Titan Research & Technology, Atmospheric and Environmental Research, Inc., and Sonoma Technology, Inc., STI-999090-1901-FR.

Santos, L.P. and R.I. Sykes. 2000. SCICHEM Version 1.2 technical documentation. Prepared for EPRI by Titan Research & Technology Division, Titan Corp., Palo Alto, CA, EPRI Publication No. 1000713

Schroeder, A.J., D.R. Stauffer, N.L. Seaman, A. Deng, A.M. Gibbs, G.K. Hunter, and G.S. Young. 2006. An automated high resolution, rapidly relocatable meteorological nowcasting and prediction system. Mon. Wea. Rev. 134:1237-1265.

Scire, J.S., F.W. Lurmann, A. Bass, and S.R. Hanna. 1984. Development of the MESOPUFF II dispersion model. Final report prepared for the U.S. Environmental Protection Agency, Research Triangle Park, NC, by ERT Inc., Concord, MA. EPA Contract No. 68-02-3733; EPA-600/3/84-057.

Scire, J.S., D.G. Strimaitis, and R.J. Yamartino. 1995. User's guide for the CALPUFF dispersion model. Report prepared for the USDA Forest Service, Cadillac, MI by EARTH TECH, Concord, MA, No. 1406-01.

Seaman N.L. 2000. Meteorological modeling for air quality assessments. Atmos. Environ. 34:2231-2259.

Seaman, N.L., D.R. Stauffer, and A.M. Lario-Gibbs. 1995. A multi-scale four-dimensional data assimilation system applied in the San Joaquin Valley during SARMAP. Part I: modeling design and basic performance characteristics. J. Appl. Meteorol. 34:1739-1761.

Seigneur, C., X.A. Wu, E. Constantinou, P. Gillespie, R.W. Bergstrom, I. Sykes, A. Venkatram, and P. Karamchandani. 1997. Formulation of a second-generation reactive plume and visibility model. J. Air Waste Manage. Assoc. 47:176-184.

Shafran, P.C., N.L. Seaman, and G.A. Gayno. 2000. Evaluation of numerical predictions of boundary-layer structure during the Lake Michigan Ozone Study (LMOS). J. Appl. Meteorol. 39:412-426.

Sillman, S., P.J. Samson, and J.M. Masters. 1993. Ozone production in urban plumes transported over water: photochemical model and case studies in the northeastern and midwestern United States. J. Geophys. Res. 98:12,687-612,699.

Stauffer, D.R. and N.L. Seaman. 1990. Use of four dimensional data assimilation in a limited area mesoscale model. Part I. Experiments with synoptic data. Mon. Wea. Rev. 118:1250-1277.

Stauffer, D.R. and N.L. Seaman. 1994. On multi-scale four-dimensional data assimilation. J. Appl. Meteorol. 33:416-434.

Stauffer, D.R., N.L. Seaman, and F.S. Binkowski. 1991. Use of four dimensional data assimilation in a limited area mesoscale model. Part II. Effects of data assimilation within the planetary boundary layer. Mon. Wea. Rev. 119:734-754.

Stauffer, D.R., R.C. Munoz, and N.L. Seaman. 1999. In-cloud turbulence and explicit microphysics in the MM5. Preprints of the *Ninth PSU/NCAR MM5 Modeling System Users' Workshop, Boulder, Colorado, June 23-24*. Pp. 177-180.

Sykes, R.I. 1997. PC-SCIPUFF version 2.0, technical documentation. Prepared by Titan Research & Technology Division, Titan Corp., Princeton, NJ.

Tesche, T.W. and D.E. McNally. 1998. Recommendations for air quality dispersion models and related aerometric data sets in support of the Breton Aerometric Monitoring program (BAMP). Prepared by Alpine Geophysics, Covington, KY, AG-90/TS107.

U.S. Dept. of Commerce. 2003. The NCEP/NCAR Reanalysis Project. U.S. Dept. of Commerce, NOAA-CIRES Climate Diagnostics Center, Boulder, CO. Internet website: http://www.cdc.noaa.gov/cdc/reanalysis/.

U.S. Environmental Protection Agency. 1999. National emission inventory documentation and data. Internet website: http://www.epa.gov/ttn/chief/net/1999inventory.html.

APPENDIX A

SUMMARY OF MONTHLY SYNOPTIC WEATHER PATTERNS

Monthly synoptic information from October 2000 to September 2001 for the BNWA is summarized in this appendix and is derived from the Louisiana Office of State Climatology (2003) monthly newsletters.

October 2000

For most of October 2000, the day-to-day upper-air patterns—with one exception—kept the polar jet stream far to the north of Louisiana, near the Canadian border. Through the entire month only two cold fronts crossed the state, the first on October 6-7, and the second on October 16-17. The first, driven by a very strong deep upper-air trough, brought an extended run of Frontal Overrunning weather (FOR) on October 7-9, delivering the month's only significant rainfall. This front was followed by several Continental High (CH) days, with record cool temperatures. The continental air mass had characteristics similar to those of a mid-winter Arctic outbreak in terms of circulation patterns and weather—a bit surprising for so early in the fall season.

A four-day run of Coastal Return (CR) and Gulf Return (GR) weather preceded the second front on October 16-17. This cool front provided little or no rain, and was followed initially by a blend of Pacific High (PH) and CH weather, and then by about ten days of fair, dry and mild CR weather. The month closed with a run of GR weather. The weather types show that October was dominated by a nearly stalled upper-air circulation pattern, with only a few brief departures from otherwise fair, dry weather from day to day.

Over the long-term, atmospheric circulation patterns continue to be unusual. The Coastal Return (CR) frequency of 47% at New Orleans is the highest for October for the synoptic calendars dating back to 1961, and the CH frequency of only 11% tied with 1984 as the lowest of record. Continental Index (CI) frequencies continue to be below normal, and the extraordinary run of below normal Storminess Index (SI) continues. SI percentages have been at or below average for 19 consecutive months, with above average frequencies for only 5 of the last 41 months!

November 2000

The El Niño/Southern Oscillation (ENSO) regime over the tropical central Pacific has finally shifted from the La Niña pattern that persisted for more than two years to a "neutral" pattern — neither La Niña nor El Niño. In response, the upper-air patterns over the United States, and particularly, Louisiana, have shifted abruptly. Upper-air troughs controlled November weather over the eastern half of the nation most of the time after about Nov. 5, with seven cold fronts crossing Louisiana during the latter 25 days of the month. Five of these stormy (frontal) events—Nov 4-5, 8, 13, 16-19, and 24—were associated with "wave development" over the northwestern Gulf and southeast Texas, with these developing lows tracking towards the northeast or east. This storm-track pattern frequently brings significant and even heavy rains to Louisiana, but was all but absent during the La Niña period—hence the drought for our state.

The persistent eastern trough served to make for a cool month for the Bayou State, while the return of frontal weather resulted in substantial rains throughout Louisiana, with monthly rains running more than double the norm for most locations. At New Orleans, most of the weather-type frequencies were near the long-term averages for November. But most significant was that the Storminess Index (SI) was above the monthly average for the first time in 20 months, and the Continental Index (CI) at or above the average for only the fourth month since January 1998! These frequencies indicate that cold fronts were at the coast or offshore with air flow over the state from the north rather than from the Gulf much of the time during November.

December 2000

The abrupt upper-air circulation pattern change that began across the U.S. on or about November 10th continued through December. The main feature of this pattern was a deep and persistent upper-air trough over the central or eastern states, allowing very cold Canadian and Arctic air to overrun the eastern half of the country and penetrate all the way to the Gulf Coast. (This pattern continued through the first half of January, with a highly unusual total of about 60 days of persistence by mid-January.)

On ten different occasions fronts were over Louisiana. Unlike several of the previous winters, "wave development" over the northwestern Gulf resulted in four low-pressure systems sweeping east and northeast near the coast, bringing runs of cloudy—and frequently wet—weather to Louisiana. These Gulf lows passed southern Louisiana on December 6-8, 13-15, 18, 21, and 24-28.

At New Orleans, the Continental Index (CI) of 82% is the second highest of the 40-year data series; the highest was 85% in 1979, during a run of winters that were among the coldest of the 20th Century for Louisiana. Continental High (CH) weather—at 40%—tied for third highest for the month, and December's Frontal Overrunning (FOR) frequency was ninth highest, further evidence of the unusual climate during December.

At the opposite extreme, the Tropical Index (TI) of only 13% tied for third lowest of the month, and Gulf Return (GR) weather of only 3% tied for second lowest. A notable change was that the Storminess Index (SI) was above average for the second consecutive month, after 20 consecutive months of remaining below average.

January 2001

The very long-lived upper-air pattern that developed in mid-November finally began to change a bit about January 10. For Louisiana, the very winter-like cold pattern was controlled by a strong and persistent upper-air trough over the central and eastern United States, bringing wave after wave of cold Canadian air to the Gulf Coast. After January 10, the trough broke down several times, allowing brief incursions of warmer and more moist Gulf air over southern Louisiana.

January was much more like an average January than Louisiana has seen in recent years. For New Orleans, the Continental Index (CI) frequency of 69% is the highest since 1992, and the Tropical Index (TI) frequency of 15% is the lowest since 1992. The Storminess Index (SI) of 50% is the highest since 1995, with January being the third consecutive month with an above-average SI frequency—this following 20 consecutive months of below-average SI percentages!

February 2001

The colder-water La Niña pattern over the central Pacific continued to weaken during February. As a result, portions of Louisiana continued to experience a return to warmer and wetter conditions that began in mid-January. A major feature of this recent pattern is frequent upper-air troughs over the Southwest, encouraging inflow of warmer and more moist maritime tropical Gulf air over Louisiana, and more frequent stormy frontal weather. Indeed, for the last 8 days of February, fronts were positioned over or close enough to Louisiana to generate frontal weather over the state without significant breaks.

February was an unusual month weather-wise in New Orleans. The Continental High (CH) frequency was the lowest since 1987, and similar to the very mild winters of 1974-76. The Continental Index (CI) frequency of 38% tied for sixth lowest of the 41 year data set. At the same time, Gulf Return (GR) and Frontal Gulf Return (FGR) weather—and the Tropical Index (TI)—were each about the fifth highest in the historical series of Februarys. The Storminess Index (SI) continued its run of above-average frequencies for the fourth consecutive month, after a much longer run of 20 months below long-term averages.

March 2001

Weather wise, March 2001 was almost the opposite of March 2000. For Louisiana and the Gulf Coast, March 2000 was dominated by Tropical Index (TI) weather with few fronts, and weather which was warmer and drier than normal. By comparison, March 2001 was dominated by Continental Index (CI) weather, very infrequent TI weather, and more Storminess Index (SI) weather.

During most of March, upper-air troughs were positioned over the East and occasionally the Central States, allowing colder air from Canada or mildly-cool air from The West to move over Louisiana, with the only brief periods of maritime tropical air from the Gulf.

Only five fronts were positioned over the state during the month; the most notable included a nearly stationary front during March 1-3, and two polar—or Arctic—fronts and continental polar air on March 4-7 and again on March 25-26.

At New Orleans, March's Gulf Return (GR) frequency of 2% was the lowest GR percentage for this month during the entire synoptic weather-type assessment, which dates back to 1961; the previous March low was 7% in 1979. The Continental Index (CI) of 66% was the third highest recorded for any March over the 40-year series, and the Tropical Index (TI) of 16% tied for third lowest. The lowest TI for March is 11% in 1969.

April 2001

April opened with an upper-level ridge over the western U.S. and a trough in the East. The western ridge drifted to the east during the first days of April, where it remained through the first two weeks of the month. As a result, unusually-warm and relatively dry Gulf Return (GR) weather persisted over the Gulf Coast region for the first half of the month. At mid-month, the upper-level flow pattern shifted again, becoming more zonal, and allowing a quasi-stationary front to remain over the Gulf Coast states between Apr 13-15, generating areas of rain across the northern parishes.

A cold front pushed across Louisiana on Apr 16, delivering much-needed rains to parts of the state. The trailing Canadian air mass produced record and near-record lows for many Louisiana parishes on Apr 17 and 18; dewpoints associated with the "dry" air mass briefly dipped into the 30°s statewide.

A cold front on Apr 23-24 produced another round of showers and thunderstorms for the Bayou State, with a handful of stations recording event totals on the order of ¼" to 3" or more. Continental High (CH) weather briefly followed that front, but was quickly replaced by Coastal Return (CR). Persistent easterly-to-southeasterly flow through the remainder of April resulted in choppy-to-rough seas over coastal waters and minor coastal flooding along east-facing shorelines.

The persistent ridging over the eastern U.S. during the first half of April—and the resulting run of GR days along the coast—produced GR frequencies that were roughly double-the-norm statewide, with the Tropical Index (TI) frequencies running 15% to 20% above average. Not surprisingly, the "dry" month meant below normal frequencies of storm-related weather types, with the Storminess Index percentages for the five sites running roughly one-half to two-thirds of the monthly norms.

May 2001

The first six days of May were warm but generally free of "active" weather. May's first significant storms developed over the greater Shreveport area on the evening of the 7th. Thunderstorms ahead of a weak and slow-moving front produced locally-damaging winds, heavy downpours with street flooding, and up to 1" hail. The state's weather returned to a "quiet" pattern until the 12th, when an east-west oriented cold front sagged southward across the state, producing sufficient instability to fire a series of *Severe Thunderstorms* that afternoon over a

number of northeastern and east-central parishes. Localized rainfall totals topped 1½", but no significant damage was reported as a result of these storms. Warm and muggy—but generally "quiet"—weather was re-established through the next several days.

As a weak cold front slid southward through Arkansas, a localized outbreak of *Severe Thunderstorms* developed over the northeastern quarter of the state late on May 18 and into the early hours of the 19th, producing isolated reports of hail and damaging winds in West Carroll and Union parishes. That front dissipated quickly, as a much stronger cold front rapidly approached from the northwest. With that stronger front approaching, three *Severe Thunderstorm Watch* areas (issued on May 21) included all but a handful of north central and southeastern parishes. Damaging winds and up to ¾" hail were reported across several central Louisiana parishes during the afternoon and evening; hailstones up to 1½" were reported that afternoon in Shreveport. Behind the May 21 frontal passage, a dry continental air mass delivered the month's "coolest" weather, with several stations recording record and near-record lows on May 23rd. Early morning lows for many sites in the northern half of the state dipping into the upper 40°s and lower 50°s on the 23rd and 24th.

Two *Severe Thunderstorm Watches* included roughly half of the state on the afternoon and evening of May 24 and pre-dawn hours of the 25th, as strong thunderstorms developed ahead of yet another cold front approaching the state from the northwest. Hail of 1" diameter or greater was reported in a half-dozen central Louisiana parishes, marking the event as one of the most significant hailstorms in recent years. 2¾" hail was noted in Alexandria (Rapides P.) and Effie (Avoyelles P.), 4" stones fell in Pineville (Rapides P.), and 4½" hail were confirmed by the local sheriff's office in Wildsville (northwestern Concordia P.)

On May 26, the cold front that had just passed through the state reversed course and began drifting northward across Louisiana as a warm front. Storms developed during the afternoon and evening of the 26th across southern and central Louisiana, with hail up to 2¾", localized wind damage, and isolated *Severe Thunderstorms*. Storm reports extended from the Texas/Louisiana line to the Baton Rouge metro area and eastward through the Florida Parishes.

June 2001

Rainfall was the big weather story for the month, as T.S. Allison and her remnants dumped as much as 15" to 25" (and more!) of rain over sections of south central and southeastern Louisiana between June 4-11, causing widespread flooding. A few northernmost parishes recorded less than 5" for the month, but June's excessive rains across the southern half of the state pushed statewide averaged rainfall above 12". From a statewide perspective, June 2001 ranks as the second "wettest" June of record, and the ninth "wettest" month in the series dating back to 1889! Louisiana's cumulative statewide total through June stands at nearly 35", roughly 5" above the mean, putting an end to any drought threats around the state—at least for the time being.

July 2001

The first two weeks of July were relatively quiet for most of the state. A weak easterly wave slid across the southern parishes on July 1-3, producing showers but no severe weather.

Afternoon and evening storms on the 5th prompted the NWS to issue Severe Thunderstorm Warnings for a handful of eastern and southern parishes. Isolated wind damage—mainly to trees and power lines—was reported in Livingston and East Baton Rouge parishes that afternoon. Later that evening, powerful thunderstorms dumped 1¾" hail and produced high winds that severely damaged several mobile homes in Grand Lake (Cameron P.). Wind damage reports were also received that evening from Calcasieu and Avoyelles parishes.

A high-pressure ridge centered over the Southern Plains kept most of Louisiana hot and dry during the second week of the month, pushing Heat Indices into the 100°-110° range and prompting the NWS to issue Heat Advisories for portions of northern and central Louisiana. Only the state's eastern parishes received any relief from the persistent heat during the period, as upper-level disturbances rotating around the edge of the high-pressure dome delivered showers and thundershowers between July 11-13. A few of these thunderstorms became rather strong, with storms during the early evening of July 11th delivering winds up to 80 mph (est.) across sections of East Baton Rouge, Livingston and Ascension parishes.

The following evening (July 12), a series of Severe Thunderstorms pushed through northeastern Louisiana, with reports from several parishes indicating high winds and minor damage. At the same time, a weak frontal boundary slipped southward across the eastern half of the country. The boundary spawned some spotty showers across the state, but more importantly, "slightly cooler and drier" air behind the front provided a brief reprieve from the excessive heat between July 14-15.

Summertime heat and humidity quickly returned, however, with Heat Advisories once again issued for much of northern Louisiana on July 22-24. At the same time, instability enhanced by daytime heating produced afternoon showers over southern sections of the state, with 1" to 2" daily totals recorded across sections of south Louisiana.

Gulf moisture and a weak disturbance produced substantial rains for sections of the state on July 26-27, with a number of locations recording daily totals in excess of 3". In addition to the heavy rains, reports from the public noted isolated funnel clouds over several of the state's southern parishes during the period. After the rainy period, oppressive heat returned to many of the state's northern parishes, with another series of NWS Heat Advisories in effect at month's end.

August 2001

August opened with oppressive heat over much of the state. Heat Indices ('feels-like temperatures') reached the 105° to 110° range over many northern parishes, prompting the NWS to issue Heat Advisories for that portion of the state on Aug 1st. BARRY developed into a tropical storm over the east-central Gulf on Aug 2-3. A Tropical Storm Watch and Warning were in place for sections of the southeast Louisiana coast from the Pearl River to Morgan City between Aug 3-5, but advisories were cancelled on the 5th as T.S. BARRY pushed northward into the Florida Panhandle.

August's first outbreak of severe weather developed over and near St. Mary Parish on the evening of the 5th, as strong thunderstorms produced wind damage, power outages and localized

flooding in Morgan City. NWS radar estimates indicated as much as 3" of rain fell in one hour during the event. Between Aug 10-13, several thunderstorm complexes – linked to upper-level disturbances rotating around a Southern Plains high pressure ridge—passed through portions of eastern Louisiana.

Occasionally these complexes included storms which achieved 'severe' thresholds, as occurred over Ascension and southern Livingston parishes (and neighboring Lake Maurepas) on the afternoon of the 10th and over Tangipahoa Parish on the 11th. These storms produced locally-heavy rains, prompting a string of Flash Flood Watches for a number of east-central, south-central and southeastern parishes. River flooding occurred along the lower Pearl, Bogue Chitto and the Tangipahoa (in the EC Div), with sections of these rivers remaining in-flood for a period of a week or more.

Thunderstorms pounded sections of northern Louisiana on August 16-18. Storms on the afternoon of the 16th downed trees in Union and Ouachita parishes. Thunderstorms over northern Louisiana between 4:00-7:00 a.m. on the 18th resulted in reports of downed trees in a half-dozen parishes. Storms along the coast during the early evening of the 20th produced 1¾" hail in DelCambre and downed trees and damaged roofs to several homes near Abbeville (both towns in Vermilion P.).

Hot but "quiet" conditions prevailed from Aug 21-25 as high pressure settled over the region. Louisiana's next significant thunderstorm outbreak developed over the extreme northwestern parishes on the afternoon and evening of the 26th, with trees and powerlines reported down in Caddo, Bossier and Webster parishes.

Over the remaining days of August, a series of upper-level disturbances moving to the northeast from the Texas coast and the western Gulf spawned showers and thunderstorms across sections of Louisiana. By the afternoon of the 29th, the repetitive pattern of passing storms prompted the NWS to issue a Flood Watch for the southwestern quarter of the state, which had received rains of 2" to 4" or more. A Flash Flood Watch was posted for northeastern Louisiana the following morning, with both watches remaining in effect through the close of the month.

Flood Warnings were issued for Calcasieu and Jefferson parishes on the morning of the 31st, with NWS reports noting water entering several homes in the Lake Charles area. Locally-heavy rains continued to fall over several south Louisiana parishes on the 31st, with the NWS posting another Flash Flood Watch—for sections of central and southern Louisiana—on the evening of the 31st. (Additional rains of 2" to 4" continued to fall on Sep 1-3, resulting in more flood-related woes for many southern and central parishes.)

September 2001

The wet-weather pattern that became established during the last days of August continued through the first 10 days of September for much of the state. Upper-level disturbances in the northwestern Gulf tracked northward—fueled by a moist Gulf air mass—to trigger locally-heavy rains and isolated Severe Thunderstorms. As a result, virtually the entire state was included within a series of Flood Watches and Warnings during the month's first days, with several Watches remaining in effect through Sep 4th. More than two dozen locations across the southern

half of the state recorded 10" or more between Aug 26 and Sep 10 (in the SW Div, Moss Bluff topped 20" for the period), with one-day totals in excess of 3" to 4" for a number of locations during the period.

These heavy rains pushed several south Louisiana rivers into flood, including the Vermilion, the Calcasieu, the Mermentau and sections of the lower Pearl. NWS reports noted that a number of homes in Calcasieu Parish were inundated by floodwaters on the 2nd. In north Louisiana, health officials were dealing with an outbreak of encephalitis—a mosquito-borne disease. The recent run of wet weather, which apparently contributed to increased numbers of insects, was considered a contributing factor. As of Sep 30th, 66 cases had been diagnosed across Ouachita and Morehouse parishes, with at least three infections proving fatal.

A cold front moved through the state on the 9th and 10th, with much-needed dry weather settling over the state during the next several days. A Coastal Flood Warning was posted for sections of the southeast coast on Sep 14th as a strong pressure gradient—resulting from high-pressure over the mainland and T.S. Gabrielle (in the eastern Gulf)—produced tides of 3 to 4 feet above normal.

Scattered showers and thunderstorms developed across the state between Sep 17-22 as southerly flow pumped low-level moisture into the state. A few thunderstorms achieved 'severe' thresholds on the afternoon and evening of Sep 20 across nine western and southwestern parishes. Isolated reports of wind damage—mainly to trees and powerlines—extended from DeSoto Parish south to Jeff Davis Parish, with 1" hail reported in Jennings (Jeff Davis P.).

A series of Severe Thunderstorms developed over a number of central and south-central parishes the following afternoon. These storms were somewhat less-organized and long-lived, with little damage associated with them. However, storm reports did note ¾" hail in New Iberia (Iberia P.), and 1¾" hailstones just north of Simmesport (Avoyelles P.).

A strong cold front on Sep 23-24 was followed by the state's first real taste of autumn weather, as a 'cool-and-dry' air mass kept daytime highs down in the 70°s to low 80°s statewide through the remainder of the month. Morning lows dipped into the low to mid 40°s for several northern parishes, with minimums slipping into the 50°s all the way to the coast.

APPENDIX B

CONCENTRATION RANKINGS FOR SO_2 AND NO_2

Each day of the year between October 1, 2000, and September 30, 2001, was assigned an STI meteorological class and a Louisiana Office of State Climatology (LOSC) synoptic weather pattern (SWP). Descriptions of these classes and patterns are provided in **Table B-1.**

Table B-1

Description of STI Meteorological Classes and LOSC Synoptic Weather Patterns

STI Met Class	Description	SWP Code	Description of SWP
1	Ridge	PH	Pacific High
2	Weak Ridge	CH	Continental High
3	Flat	FOR	Frontal Overrunning
4	Zonal	CR	Coastal Return
5	Post Trough	GR	Gulf Return
6	Weak Trough	FGR	Frontal Gulf Return
7	Trough	GH	Gulf High
8	Cut-off Low	GTD	Gulf Tropical Disturbance
9	Tropical Storm		

Table B-2 lists STI meteorological class, LOSC synoptic weather pattern, 3-hr SO_2, 24-hr SO_2, and 24-hr NO_2 concentration and percentile rankings for Breton Island Platform (BIP), Fort Morgan (FTM) and West Delta Platform (WDP) for each day of the study period. Percentile rankings of 98.0 or greater are highlighted in **red**. Percentile rankings of 95 to 97.9 are highlighted in **orange** and percentile rankings of 90 to 94.9 are highlighted in **yellow**.

Table B-2

Summary of Daily Weather Patterns, Concentrations, and Concentration Rankings

Date	STI Met Class	Synoptic Weather Pattern	3-hr SO_2						24-hr SO_2						24-hr NO_2					
			BIP	Percentile	FTM	Percentile	WDP	Percentile	BIP	Percentile	FTM	Percentile	WDP	Percentile	BIP	Percentile	FTM	Percentile	WDP	Percentile
10/1/2000	3	CR	0.3	5.6	4.3	40.3	4.8	43.6	0.1	10.2	3.6	55.7	3.6	55.8	1.5	12	5.2	50.1	4.2	41.7
10/2/2000	1	CR	0.3	5.5	4.5	42.2	5.1	44.8	-0.4	6	3.7	56.9	3.7	57.5	0.4	3.9	5.0	47.9	7.3	65.8
10/3/2000	1	CR	1.0	12.3	5.4	47.4	3.9	38.2	0.2	11.1	4.3	63.3	3.4	54.1	1.1	8.5	6.3	58.2	9.1	78.1
10/4/2000	6	GR	0.5	6.8	5.3	46.7	3.4	32.9	0.0	8.5	3.7	57.1	2.8	45.9	1.8	15.4	6.6	61.3	3.2	30.4
10/5/2000	2	GR	-0.1	3.4	3.1	30.3	4.3	40.2	-0.4	5.1	2.7	45.3	3.4	53.7	0.9	7	5.2	49.6	-8.1	0.6
10/6/2000	6	FGR	9.1	65.7	8.7	64.2	5.2	46.3	2.9	47.6	3.6	55.2	4.1	61.2	4.3	43.1	6.0	56.6	-3.9	1.1
10/7/2000	2	FOR	7.2	56.4	27.4	96.9	8.0	61.3	3.1	49.6	13.0	95.4	4.8	67.2	5.3	50.8	8.8	76.2	5.3	50.5
10/8/2000	6	FOR	4.2	40	23.2	94	8.1	61.8	1.7	31.6	11.4	93.6	5.3	69.9	5.1	49.4	5.1	49.3	6.4	59.8
10/9/2000	5	FOR	6.4	52.7	10.4	71.2	9.0	65.4	2.6	42.4	8.2	85.5	7.2	80.9	6.9	63.8	3.7	36.2	6.6	61.7
10/10/2000	6	CH	5.3	46.4	23.3	94.1	9.6	67.5	3.1	50.4	10.9	92.6	7.0	80	6.0	56.5	8.2	72.2	7.8	69.4
10/11/2000	1	CH	11.6	74.6	9.8	68.5	10.2	69.9	4.3	63	7.3	81.5	7.4	81.9	7.7	68.8	12.4	89.8	11.2	87.4
10/12/2000	1	CR	4.8	43.8	15.7	85.5	8.6	63.7	1.2	25.9	8.3	85.9	6.1	75.6	6.6	62.3	14.8	93.9	15.7	95.2
10/13/2000	1	CR	1.6	17.8	6.6	53.8	5.8	49.4	1.2	25.8	4.9	67.9	2.9	47.4	3.7	36.5	9.9	82	11.2	87.6
10/14/2000	1	CR	1.8	20.3	5.6	48.5	3.7	36	1.3	27.2	4.4	64.1	3.0	49.3	4.1	41.3	8.3	73	8.7	75.3
10/15/2000	1	GR	2.4	24.4	12.1	75.8	6.2	51.1	-0.1	7.7	4.7	66.5	3.6	55.5	2.1	19	5.7	54.3	2.9	28.2
10/16/2000	1	GR	3.7	36.3	13.2	79.6	6.4	52.7	0.8	19.8	5.9	74	3.1	50.4	4.5	45.1	10.8	85.7	0.1	3.4
10/17/2000	1	FGR	7.0	55.3	8.0	61.2	6.4	52.4	2.4	40.1	4.6	65.5					8.0	70.6		
10/18/2000	1	PH	26.3	96	21.1	92.2	13.4	80	10.3	91.3	10.1	90.8	8.2	85.3			14.4	93.4	8.7	75.5
10/19/2000	6	CH	10.4	71.1	11.7	74.8	10.6	71.9	6.3	76.3	7.7	83.1	8.7	87.2	12.3	89.4	10.7	85.4	15.1	94.6
10/20/2000	2	CR	3.8	36.8	4.7	43.2	12.5	77.2	1.9	33.8	2.5	41	9.3	88.5	8.9	76.9	8.1	71.2	13.6	92.3
10/21/2000	1	CR	2.3	24.1	3.3	31.8	8.9	64.7	0.0	9	2.3	39.1	4.1	61.9	4.5	44.7	3.1	30.1	-1.2	1.6
10/22/2000	1	GR	-0.2	2.8	3.4	33.3	2.1	22.9	-0.9	2.2	2.3	38.8	1.2	25.7	0.7	5	3.8	38.9	1.4	11
10/23/2000	1	CR	3.1	29.6	5.8	49.4	3.4	33	0.8	19.3	3.7	56.6	1.8	33.3	2.4	21.4	7.8	69.1	9.9	81.9
10/24/2000	1	CR	2.9	28.5	6.4	52.6	3.0	29.1	0.5	14.1	4.0	59.9	1.4	29.2	2.2	19.6	9.8	81.4	17.1	96.5
10/25/2000	1	CR	2.6	26.3	3.5	33.8	1.2	14	1.8	32.8	2.6	43.9	0.4	13	2.0	17.2	9.0	77.5	12.3	89.7
10/26/2000	1	GR	3.2	31.6	5.2	45.5	3.7	36.3	1.7	32	2.9	47.2	1.7	32.4	1.4	11.1	6.9	64	5.5	53

Table B-2. Summary of Daily Weather Patterns, Concentrations, and Concentration Rankings

Date	STI Met Class	Synoptic Weather Pattern	3-hr SO_2						24-hr SO_2						24-hr NO_2					
			BIP	Percentile	FTM	Percentile	WDP	Percentile	BIP	Percentile	FTM	Percentile	WDP	Percentile	BIP	Percentile	FTM	Percentile	WDP	Percentile
10/27/2000	1	CR	19.0	90.3	11.4	73.9	8.5	63.5	7.8	83.5	5.6	72.2	3.2	51.7	3.8	38.4	11.0	86.2	6.5	61.2
10/28/2000	1	CR	6.7	54.3	13.5	80.6	14.7	83.4	2.5	41.6	8.6	86.5	9.6	89.6	6.1	57.3	17.5	97.1	8.2	72.3
10/29/2000	1	CR	9.7	67.9	18.3	89.6	13.3	79.8	3.9	59.1	8.1	84.5	9.6	89.5	6.6	62.7	15.0	94.4	7.4	66.3
10/30/2000	1	GR	25.4	95.7	30.2	97.7	4.9	44	7.1	80.5	15.2	97.7	3.3	52.6	10.1	83	13.4	92	6.8	63.3
10/31/2000	1	GR	26.7	96.2	21.3	92.6	8.0	60.6	5.4	70.6	10.4	91.3	4.1	61.3	5.1	49	12.7	90.5	10.4	84
11/1/2000	1	GR	6.1	50.8	12.1	75.9	6.7	54.2	5.1	68.7	5.9	74.5	4.1	61.8	2.5	24.2	8.9	77	2.6	25
11/2/2000	1	GR	4.7	43	5.4	47.1	4.1	39.2	3.6	55.9	4.0	60.5	2.9	48.5	1.7	13.7	4.5	45.2	4.1	40.7
11/3/2000	1	GR	5.2	46	5.9	49.9	4.5	41.9	4.0	61	4.3	62.9	3.9	58.7	2.1	19.1	3.6	34.8	2.5	23.7
11/4/2000	2	GR	4.9	44.3	5.8	49.2	3.4	33	3.7	57.2	4.3	63.8	3.1	50.9	2.5	23.1	3.6	35.4	-1.1	1.7
11/5/2000	2	GR	4.5	42	4.3	40.4	4.3	40.2	3.2	51.8	3.1	51	3.5	54.7	1.8	14.9	2.5	23.8	0.9	6.7
11/6/2000	7	FOR	2.2	23.2	2.6	26.3	3.5	33.9	1.2	26.9	2.3	38.9	2.3	39.2			1.4	10.9	-2.8	1.2
11/7/2000	7	FGR	1.7	19.9	2.4	24.6	2.7	26.8	1.4	29.9	2.1	36.5	2.4	39.8	1.2	9	1.9	15.6	-6.3	0.8
11/8/2000	7	FGR	1.4	16.1	3.8	37.3	2.3	24	1.0	23.1	2.5	40.8	2.1	37.5			2.1	18.5	-5.9	0.9
11/9/2000	7	CH	12.7	78	10.1	69.8	8.2	62.4	4.2	62.3	3.5	55	3.7	57.4			3.3	31.2	4.0	39.9
11/10/2000	1	CH	27.1	96.7	23.3	94.2	7.1	56.3	11.8	94.2	11.2	93.2	4.1	61.1	3.9	39.2	5.5	52.4	5.5	51.9
11/11/2000	1	FOR	34.9	98.8	24.3	95.1	8.1	61.6	11.5	93.7	12.0	94.4	6.2	75.9	5.0	48.5	8.3	72.7	0.1	3.2
11/12/2000	7	CR	38.9	98.9	11.1	73.3	6.9	55.1	15.4	97.8	9.4	89	5.4	70.9	5.6	53.6	9.3	79.2	2.3	20.2
11/13/2000	7	FOR	18.6	89.9	9.9	68.8	3.3	32.1	7.3	81.2	5.9	74.3	2.4	40	4.7	46.4	5.5	51.8	-4.0	1
11/14/2000	4	CH	6.1	50.7	13.7	80.8	6.4	53.3	2.5	40.9	5.2	69.6	4.0	60	2.1	18.7	5.2	50.2	7.4	66.8
11/15/2000	4	CR	12.9	78.8	19.1	90.4	8.2	62.3	6.5	78.1	9.4	89.1	4.1	61.5	2.7	25.7	5.8	55.6	4.6	45.4
11/16/2000	4	FGR	8.9	64.9	4.9	43.9	2.2	23.3	3.1	49.8	2.9	48.2	1.8	33.2	1.6	12.2	5.6	53.4	-7.7	0.7
11/17/2000	4	FOR	10.0	69.2	23.9	94.7	8.0	60.2	4.6	65.6	6.3	76.2	2.7	44	3.0	29	7.4	67	4.9	47.5
11/18/2000	2	FOR	6.2	51.4	5.9	50.1	2.0	21.8	2.9	47.8	3.1	50.3	0.3	12.4	2.3	21.2	3.7	37.1	3.2	30.8
11/19/2000	7	FOR	12.1	75.6	18.1	89.2	0.5	7.2	4.7	66.8	4.3	63.7	0.0	8.7	3.7	36.4	3.9	39	2.0	17
11/20/2000	7	CH	13.4	80.2	19.7	91.1	2.8	27.5	3.5	54.9	9.8	89.9	1.2	26.7	3.0	28.9	8.8	76.1	5.5	52.7
11/21/2000	5	CH	26.8	96.4	14.2	82.4	5.7	49	8.6	86.6	7.7	83.2	2.2	38.5	3.8	38.2	5.9	56.3	4.2	41.6
11/22/2000	5	CR	29.8	97.6	12.9	78.9	8.1	62	14.5	97.1	7.7	83.4	5.1	69.1	4.9	47.3	3.8	38	2.7	25.8
11/23/2000	4	GR	1.9	21	3.9	37.9	1.3	15	1.0	23.5	2.7	45.5	0.6	16.7	0.8	6.1	3.5	34.1	-2.2	1.3
11/24/2000	1	FGR	7.3	57.1	4.4	41.5	1.9	21	0.9	20.9	2.6	42.6	0.6	16	2.9	28.7	2.5	24.1	-10.3	0.5

Table B-2. Summary of Daily Weather Patterns, Concentrations, and Concentration Rankings

Date	STI Met Class	Synoptic Weather Pattern	3-hr SO_2						24-hr SO_2						24-hr NO_2					
			BIP	Percentile	FTM	Percentile	WDP	Percentile	BIP	Percentile	FTM	Percentile	WDP	Percentile	BIP	Percentile	FTM	Percentile	WDP	Percentile
11/25/2000	7	PH	9.0	65.6	6.3	51.9	4.6	42.5	7.3	81.1	4.6	65.8	2.6	42.9			6.5	60.7	-0.7	1.8
11/26/2000	7	PH	12.9	78.9	11.3	73.8	7.3	57.1	9.1	88.4	6.0	75	4.8	67	22.2	98.8	9.6	80.7	1.8	14.8
11/27/2000	7	GH	81.8	99.9	23.4	94.2	10.1	69.3	24.8	99.8	9.8	90.1	7.3	81.4	14.7	93.8	10.0	82.5	8.5	73.8
11/28/2000	7	CR	10.6	72	11.1	73.4	8.5	63.4	8.7	86.8	7.4	82.2	4.4	64.5	6.3	58.7	14.6	93.7	16.0	95.6
11/29/2000	7	FGR	10.4	71.2	13.8	81.2	6.3	51.8	5.6	72.5	5.2	69.7	2.9	48.3	8.3	72.5	13.8	92.6	1.0	7.2
11/30/2000	1	CH	16.9	87.4	20.0	91.3	6.3	52.1	5.1	69.3	8.1	84.7	1.9	34.7	4.8	47	7.5	68.1	8.2	72.1
12/1/2000	7	FGR	13.9	81.6	17.1	88	13.8	81.5	6.4	77.3	8.1	85.1	11.1	92.9	3.9	39.4	5.7	53.7	16.9	96.3
12/2/2000	7	FOR	14.1	82	44.7	99.2	16.5	86.8	8.2	85.6	10.9	92.4	9.9	90.3	7.0	64.3	12.9	90.9	10.0	82.7
12/3/2000	5	CH	23.0	93.7	18.2	89.4	20.7	91.9	15.5	97.9	14.3	96.9	13.7	95.9	7.8	69.2	13.7	92.4	8.1	71.4
12/4/2000	7	CH	31.7	98.1	30.0	97.7	25.5	95.8	15.1	97.5	17.2	98.6	13.3	95.5	7.9	70.5	17.3	96.9	6.9	63.9
12/5/2000	5	CH	21.0	92	32.4	98.2	24.7	95.4	15.6	98	18.4	99	13.8	96.1	8.1	71.6	19.5	98	9.6	80.3
12/6/2000	7	FOR	17.7	88.5	15.2	84.5	12.7	77.9	12.2	94.7	8.8	87.3	9.4	89.3	7.6	68.5	21.0	98.6	10.2	83.5
12/7/2000	7	GH	25.3	95.6	29.7	97.5	26.0	95.9	14.4	97	13.5	95.6	14.6	97.2	7.5	67.7	19.3	97.9	14.5	93.6
12/8/2000	4	CH	24.4	95.2	10.9	72.5	15.4	84.8	11.6	93.9	6.6	78.2	9.3	88.6	13.6	92.2	18.5	97.5	17.2	96.7
12/9/2000	4	CH	17.4	88.3	6.8	54.7	12.4	76.9	14.1	96.6	5.4	71.1	8.1	84.6	9.0	77.8	15.2	94.8	8.3	72.6
12/10/2000	4	CR	20.4	91.7	20.8	91.9	15.6	85.2	14.0	96.3	8.9	87.5	9.0	87.7	8.2	71.8	11.0	86.5	16.7	96
12/11/2000	6	FGR	5.8	49.7	2.9	28.4	8.0	60.9	3.3	52.5	2.2	38.1	5.8	73.5	3.6	35.6	14.4	93.5	14.9	94.3
12/12/2000	4	CH	19.4	90.7	12.8	78.3	10.3	70.4	9.0	88.3	5.9	74.4	6.0	74.8	10.6	84.8	11.1	86.8	8.2	72.4
12/13/2000	7	FGR	10.8	72.4	16.0	85.9	5.9	50	3.4	54	6.5	77.7	4.0	60.2	6.6	61.6	9.2	78.6	1.3	10.4
12/14/2000	6	FOR	22.8	93.3	50.2	99.6	11.5	74.1	10.6	91.9	14.5	97.1	6.5	78	9.1	77.9	16.9	96.2	12.5	90
12/15/2000	7	FOR	11.2	73.5	12.8	78.4	8.8	64.3	5.1	69.2	5.2	69.8	6.0	75.1	11.2	87.5	10.7	84.9	11.2	86.9
12/16/2000	7	FGR	5.1	45.1	3.6	34.7	7.0	56	2.7	44.9	1.9	34.1	5.0	68.2	3.8	38.5	3.5	33.8	1.5	11.7
12/17/2000	5	CH	14.8	83.7	9.8	68.3	9.8	68.3	6.8	79.2	2.7	45.1	8.0	84.3	5.8	55.1	2.3	20.4	4.4	44.1
12/18/2000	7	FGR	7.6	58.6	13.1	79.3	7.4	57.6	4.3	63.6	5.7	72.6	5.8	73.4	4.5	45	3.6	35	4.5	44.6
12/19/2000	7	CH	8.2	62.1	6.2	51.7	8.7	64.1	4.0	59.7	3.0	49.5	6.4	77	6.6	62.2	2.5	24.4	2.4	22.2
12/20/2000	6	CR	12.1	75.8	14.5	83	8.2	62.5	6.9	79.7	5.8	73.3	6.6	78.2	4.7	46.6	2.8	26.7	4.8	46.9
12/21/2000	7	FOR	7.8	59.4	20.4	91.8	5.2	45.6	2.5	42	5.7	72.8	4.4	64.6	4.0	39.6	8.0	70.7	2.3	20.1
12/22/2000	5	CH	14.4	82.8	10.6	72.1	12.9	78.6	7.4	82.1	5.1	69.4	7.8	83.6	6.3	59	2.8	27.3	4.4	44.2
12/23/2000	6	FOR	21.4	92.7	24.0	94.8	9.3	66.6	8.1	84.8	10.8	92.3	6.2	75.8	7.1	64.9	7.4	66.2	13.3	91.9

Table B-2. Summary of Daily Weather Patterns, Concentrations, and Concentration Rankings

Date	STI Met Class	Synoptic Weather Pattern	3-hr SO_2						24-hr SO_2						24-hr NO_2					
			BIP	Percentile	FTM	Percentile	WDP	Percentile	BIP	Percentile	FTM	Percentile	WDP	Percentile	BIP	Percentile	FTM	Percentile	WDP	Percentile
12/24/2000	3	FOR	14.0	81.9	18.2	89.4	10.9	72.8	8.7	87.1	8.1	84.4	5.9	73.9	7.0	64.2	6.2	57.8	10.8	85.8
12/25/2000	1	FOR	19.0	90.1	24.6	95.3	9.2	66.1	11.0	92.7	10.4	91.6			6.1	57.4	5.5	52.8		
12/26/2000	2	FOR	5.2	45.3	7.6	58.6	4.5	42.5	2.1	36.3	4.0	60.1			2.0	17.3	2.8	26.5		
12/27/2000	2	FOR	1.5	17.5	2.7	26.6	4.7	43.1	1.1	24.3	1.8	33	3.5	54.5	1.3	10.1	11.0	86.1	2.4	22
12/28/2000	8	FOR	8.2	62.7	14.0	81.7	7.4	57.7	3.7	56.4	3.2	52.2	5.2	69.5	11.6	88.1	8.5	74.3	9.2	79
12/29/2000	7	CH	10.3	70.5	16.0	86.1	12.9	78.7	5.3	70.3	6.4	77.2	7.9	83.9	8.2	71.9	5.5	52	6.6	62.5
12/30/2000	7	CH	5.6	48.6	3.3	31.8	12.4	76.9	3.9	59	2.5	40.5			5.3	50.4	2.4	22.5		
12/31/2000	7	FOR	16.0	86	16.8	87.3	9.1	65.7	6.5	77.5	6.4	76.9	6.1	75.5	5.5	52.2	3.2	30.7	11.3	87.8
1/1/2001	7	CH	22.9	93.6	36.5	98.8	15.2	84.3	9.0	87.8	17.4	98.7	8.1	85	5.7	54.6	5.2	49.7	5.2	49.9
1/2/2001	7	FOR	23.7	94.6	22.8	93.2	16.7	87.2	14.1	96.5	13.9	96.2	10.1	90.5	6.6	62.4	2.5	22.9	5.3	50.9
1/3/2001	4	CH	34.0	98.6	31.1	98	26.8	96.3	20.9	99.6	22.2	99.7	20.3	99.5	12.5	90.1	10.6	84.7	14.1	93.1
1/4/2001	5	CH	27.9	97.2	27.2	96.8	27.7	97.1	12.3	94.9	16.3	98.4	19.2	99.4	8.1	71.3	13.5	92.1	13.9	92.9
1/5/2001	5	GH	18.3	89.6	23.6	94.5	23.4	94.4	11.1	93.1	14.0	96.4	11.0	92.7	23.7	99.2	35.7	100	10.0	82.2
1/6/2001	4	GH	19.3	90.6	12.3	76.6	16.5	86.9	10.6	92.1	10.2	91	10.1	90.7	8.0	70.9	29.2	99.8	28.3	99.7
1/7/2001	4	FGR	6.0	50.6	9.7	67.8	4.5	42.4	2.7	45.6	7.4	82			6.6	61.5	11.8	88.5		
1/8/2001	7	CH	9.5	67.2	10.1	69.4	27.0	96.5	4.7	66.7	7.8	83.7			3.7	36.7	10.2	83.3		
1/9/2001	5	CH	17.9	89	22.9	93.5	12.8	78.4	5.3	70.5	16.0	98.3			3.6	34.9	9.7	80.9		
1/10/2001	1	FOR	15.5	85	33.2	98.4	12.0	75.5	8.7	86.7	18.1	98.9	8.2	85.4	5.5	52.9	10.7	85.1	8.8	76.5
1/11/2001	7	PH	4.0	38.7	11.6	74.3	9.9	68.9	2.0	35	9.0	88.2			5.8	55.3	12.7	90.6		
1/12/2001	5	FOR	15.6	85.1	29.7	97.4	10.9	72.6	4.5	65.2	13.6	95.7	5.8	73.2	2.7	26.3	9.2	78.9	10.4	83.8
1/13/2001	1	FOR	8.0	60.5	17.5	88.5	7.3	57.1	5.1	68.8	12.3	95	5.3	70	4.3	42.4	6.4	59.5	16.8	96.1
1/14/2001	7	FGR	2.7	27.2	8.8	64.4	4.0	38.9	0.5	15	6.7	78.9	3.6	56.1	6.7	63	2.2	19.9	0.6	4.5
1/15/2001	4	FOR	8.3	63.2	19.3	90.5	5.5	47.8	3.2	52	8.1	84.9	4.5	65.1	4.8	47.1	13.2	91.4	11.8	88.6
1/16/2001	4	FOR	6.7	54.5	14.2	82.2	5.3	46.7	3.9	59.5	9.0	88.1	4.2	62.5	4.3	43.3	6.8	63.2	11.6	88.3
1/17/2001	4	FGR	3.7	35.6	9.5	67	4.4	41.2	2.4	40.3	7.6	82.9	3.8	58.2	2.4	21.8	7.4	66.6	9.7	81.2
1/18/2001	4	FGR	2.5	25.2	8.4	63.2	3.7	35.4	2.2	38.4	6.8	79.4	3.4	53.4	1.6	12.4	8.6	74.4	3.5	33.4
1/19/2001	7	FOR	11.0	73.2	7.8	59.7	5.4	47.2	3.7	56.8	6.7	78.7	3.9	58.8	8.1	71.7	16.0	95.5	10.2	83.4
1/20/2001	7	CH	11.6	74.4	10.8	72.4	10.4	70.8	6.0	74.6	7.5	82.3	6.6	78.3	4.9	47.8	3.6	35.8	6.6	62.6
1/21/2001	7	CH	15.3	84.6	20.0	91.2	11.0	73	12.4	95.1	11.7	94.1	6.5	77.8	4.2	41.8	5.1	48.9	10.7	85.2

Table B-2. Summary of Daily Weather Patterns, Concentrations, and Concentration Rankings

Date	STI Met Class	Synoptic Weather Pattern	3-hr SO_2						24-hr SO_2						24-hr NO_2					
			BIP	Percentile	FTM	Percentile	WDP	Percentile	BIP	Percentile	FTM	Percentile	WDP	Percentile	BIP	Percentile	FTM	Percentile	WDP	Percentile
1/22/2001	8	CH	27.1	96.6	42.3	99.1	9.2	66.4	15.1	97.6	18.5	99.1			8.9	77.1	10.8	85.6		
1/23/2001	1	FOR	47.5	99.3	25.2	95.5			26.8	99.9	17.9	98.8			18.4	97.4	22.7	99		
1/24/2001	7	GH	17.7	88.6	21.6	93			12.6	95.3	14.2	96.8			24.8	99.4	22.3	98.9		
1/25/2001	5	CH	17.1	88.1	24.1	94.9			13.5	95.6	14.8	97.4			14.9	94.2	18.8	97.6		
1/26/2001	4	GR	16.1	86.2	15.3	84.7			8.6	86.4	12.2	94.6			4.7	46.3				
1/27/2001	6	FOR	12.0	75.3	24.2	95			9.7	89.8	14.8	97.3			13.0	91.1	15.6	95.1		
1/28/2001	1	GR	7.0	55.7	12.6	77.4	2.6	25.7	6.0	75.2	11.6	93.8			2.6	25.1	6.3	59.1		
1/29/2001	7	FOR	7.3	57	12.5	77	3.6	34.4	5.0	68.5	10.9	92.5	2.9	47.7	2.1	18.2	4.0	39.8	0.0	3.1
1/30/2001	7	GH	7.7	59.2	14.3	82.6	6.4	52.9	6.1	75.3	11.6	94	4.0	60.8	15.2	94.9	5.7	53.9	3.6	36
1/31/2001	4	FOR	12.6	77.6	33.7	98.5	12.7	78.1	10.2	91.1	18.5	99.2	7.0	80.1	24.8	99.5	22.8	99.1	14.4	93.3
2/1/2001	4	FOR	26.5	96.1	13.4	80.4	7.5	58.1	10.0	90.4	3.3	53.3	5.5	71.7	10.7	85.3	7.0	64.1	12.2	89.2
2/2/2001	7	FOR	20.3	91.6	49.5	99.5	7.0	55.6	6.6	78.5	17.2	98.5	5.4	71	9.0	77.6	17.4	97	8.4	73.3
2/3/2001	7	FOR	11.2	73.5	10.7	72.2	9.2	66.2	6.9	79.7	5.4	70.8	6.8	79.6	8.7	74.8	6.2	57.7	7.8	69
2/4/2001	7	PH	16.2	86.2	15.2	84.4	21.1	92.4	9.4	89.2	8.0	84.2	11.9	94.3	24.1	99.3	11.5	88	14.1	93
2/5/2001	5	GH	13.4	80	14.2	82.1	14.7	83.4	6.6	78.4	5.6	72.4	10.4	91.7	14.9	94.1	12.7	90.4	16.9	96.4
2/6/2001	4	GH	7.0	55.8	5.0	44.6	12.3	76.1	4.6	65.7	2.3	38.7	8.2	85.2	13.7	92.5	7.6	68.4	13.2	91.5
2/7/2001	2	GR	2.7	27.4	0.7	8.9	3.7	35.6	1.9	34.7	0.0	9.6	3.1	49.9	3.4	32.7	2.6	24.6	2.5	24.5
2/8/2001	1	GR	2.3	24.2	2.4	24.6	3.2	31.4	1.8	33.3	0.2	11.3			2.7	25.6	4.6	46		
2/9/2001	7	FGR	1.8	20.5	1.2	14.9	3.9	37.9	1.3	28.3	0.0	9.3			2.3	20.3	3.5	34.5		
2/10/2001	4	CH	12.1	75.7	15.1	84.1	6.3	52	4.4	64.7	6.6	78.6	3.6	55.6	4.3	42.3	6.4	60.1	5.6	53.3
2/11/2001	2	CR	13.5	80.4	13.3	79.7	11.9	75.2	9.3	88.9	7.4	81.7	7.5	82.4	8.7	75.1	6.1	57	15.7	95.3
2/12/2001	2	FGR	9.4	66.8	6.0	50.5	4.4	41.1	3.3	52.7	1.8	33.5	3.2	51.5	5.4	51.6	5.8	55	9.9	81.8
2/13/2001	4	GR	2.0	22.1	0.3	5.2	2.9	28.8	1.4	28.7	-0.3	6.4	2.5	41.7	1.6	12.8	4.2	42.1		
2/14/2001	2	GR	1.2	14.3	0.5	7.6	3.2	31	1.0	24	-0.3	6.5	2.6	42.8	1.6	12.5	7.1	64.7		
2/15/2001	1	FGR	1.3	15.7	0.1	4.4	3.4	33	1.1	24.6	-0.5	4.5	2.9	47.9	1.3	9.7	2.4	22.8	4.3	43.4
2/16/2001	7	FGR	4.8	43.6	1.0	12.6	5.0	44.5	2.0	35.2	-0.4	5.9	3.1	50.7	7.3	66.1	6.6	62		
2/17/2001	6	CH	8.1	61.5	16.0	85.8	5.5	47.6	3.9	59.3	7.2	80.8	4.3	62.7	7.4	66.7	10.0	82.4	-25.8	0
2/18/2001	4	CH	18.4	89.7	17.8	88.8	14.8	83.8	10.6	92	5.8	73.1	8.7	86.9	8.9	76.8	5.3	50.7	-16.7	0.2
2/19/2001	2	CR	9.5	67.2	16.4	86.6	8.7	63.9	3.2	52.3	4.4	64.3	6.0	74.9	5.5	52.1	8.5	74.1	-14.2	0.4

Table B-2. Summary of Daily Weather Patterns, Concentrations, and Concentration Rankings

Date	STI Met Class	Synoptic Weather Pattern	3-hr SO_2						24-hr SO_2						24-hr NO_2					
			BIP	Percentile	FTM	Percentile	WDP	Percentile	BIP	Percentile	FTM	Percentile	WDP	Percentile	BIP	Percentile	FTM	Percentile	WDP	Percentile
2/20/2001	4	GR	3.6	34.2	0.8	9.9	7.9	59.8	1.6	31.2	-0.1	8	5.3	70.2	3.6	35.7	11.2	87.2	-15.9	0.3
2/21/2001	4	FGR	1.1	13.4	0.0	4	7.1	56.2	0.8	19.4	-0.5	4.7	5.0	68.5	1.9	16.3	8.4	73.7	-20.5	0.1
2/22/2001	4	FOR	7.9	60	8.9	65	13.2	79.5	3.3	53.1	2.2	38.2	5.3	70.1	13.1	91.2	10.2	83.2	9.4	79.9
2/23/2001	6	FGR	10.6	71.8	2.8	27.7	6.3	51.7	3.3	53	0.6	17	4.4	64.2	5.8	55.5	4.1	41	15.1	94.7
2/24/2001	7	GR	2.5	25.2	-0.1	3.5	2.5	25.5	1.7	31.8	-0.4	5.4	2.2	38.6	2.1	18.4	2.7	26.2	0.6	4.4
2/25/2001	4	FGR	1.5	17.6	-0.4	2.1	3.3	31.8	1.4	29.3	-0.7	3	2.5	42.1	2.1	18	3.2	30.6	1.7	13.8
2/26/2001	1	FOR	4.3	40.6	14.4	82.9	5.5	48.1	2.1	36.7	2.3	39.1	3.5	54.6	4.0	39.7	9.8	81.6	8.4	73.5
2/27/2001	1	FGR	8.6	63.6	3.4	32.8	4.2	39.9	2.7	45	1.3	27.5	3.3	52.8	4.4	44	12.3	89.6	3.8	38.6
2/28/2001	6	FGR	5.4	47.5	5.5	47.6	5.2	45.2	2.9	48	0.3	12.1	3.3	52.9	9.1	78.4	6.6	61.9	1.3	9.8
3/1/2001	1	FGR	6.7	54.3	7.2	56.7	5.6	48.3	3.6	56	2.7	44.3	3.9	58.6	6.3	58.8	6.5	60.5	5.2	49.8
3/2/2001	1	FGR	2.6	25.6	-0.1	3.4	3.4	33	2.0	35.8	-0.4	5.7	3.0	49.2	6.5	60.8	5.3	50.6	1.3	9.5
3/3/2001	7	FOR	21.8	93.1	-0.4	2.1	3.7	36.3	3.4	53.5	-0.6	3.4	3.1	50.8	5.8	54.9	9.3	79.4	3.1	29.9
3/4/2001	7	PH	21.1	92.3	4.9	44.3	7.3	57.4	7.3	81.6	1.8	32.7	3.8	58.4					1.5	11.5
3/5/2001	5	CH	24.9	95.4	3.7	35	9.8	68.2	11.4	93.5	2.0	34.9	7.1	80.4	10.9	86			6.8	63.7
3/6/2001	5	CH	12.3	76.3	5.5	47.9	17.9	88.9	6.4	77.4	0.9	21.5	11.4	93.4	7.9	70.1			11.2	87.1
3/7/2001	5	CH	12.3	76.3	18.4	89.8	12.7	78.1	7.2	81	8.9	87.6	6.1	75.3	10.9	85.9	4.3	42.9	9.6	80.8
3/8/2001	2	GR	19.4	90.8	17.2	88.2	14.9	83.9	12.1	94.5	6.3	76.8	7.0	79.9	20.1	98.5	8.8	76.7	10.5	84.5
3/9/2001	7	FOR	13.8	81.3	19.5	90.9	5.5	48.1	5.9	74.2	3.3	53.2	2.9	47.3	7.9	69.9	6.4	60	3.5	33.9
3/10/2001	2	CH	23.4	94.3	18.2	89.3	17.0	87.6	11.0	92.8	10.7	92.2	9.3	88.8	12.4	89.9	6.8	63.5	19.5	98.1
3/11/2001	4	FOR	3.7	36.7	7.5	57.8	3.1	30.1	2.3	39.5	2.5	42	2.5	40.7	3.2	30.5	5.2	50	5.0	48
3/12/2001	7	FGR	1.7	19.8	-0.5	1.9	5.2	45.6	1.3	27.3	-0.7	3.1	2.6	43.4	2.1	18.5	5.9	55.7	4.8	46.8
3/13/2001	7	PH	8.3	63	15.6	85.4	14.9	83.9	4.8	67.1	4.0	60.4	8.4	86.1	19.3	97.8	15.5	95	17.2	96.8
3/14/2001	4	FGR	5.7	48.9	7.3	57.4	7.0	55.9	2.7	44.8	1.7	32.6	4.0	60.3	4.3	43.9	9.1	78.2	16.0	95.4
3/15/2001	7	PH	17.0	87.6	9.0	65.2	7.2	56.7	7.3	81.3	2.1	36.8	3.7	56.7	13.8	92.7	5.5	52.3	8.0	71
3/16/2001	7	CH	13.0	79.1	10.2	70	8.0	60.3	4.9	67.6	3.4	53.8	5.5	71.5	12.8	90.8	6.2	58	9.9	81.7
3/17/2001	4	FOR	13.5	80.5	5.3	46.6	5.6	48.4	7.2	80.6	1.4	29.8	2.3	39.6	8.5	74	1.8	15.3	7.2	65.5
3/18/2001	7	CH	10.2	70.1	13.4	79.9	6.5	53.4	8.3	85.7	6.7	79	4.3	63	6.1	57.5	1.6	12.3	7.1	64.6
3/19/2001	7	CH	19.5	91	6.9	55.1	16.2	86.3	6.3	76.4	2.2	37.9	6.0	74.7	6.3	59.3	2.3	21.1	12.7	90.3
3/20/2001	8	FOR	10.3	70.6	4.3	40.5	8.3	62.9	4.6	66	1.3	27.8	4.3	63.6	5.4	51.2	2.0	17.7	7.2	65.1

Table B-2. Summary of Daily Weather Patterns, Concentrations, and Concentration Rankings

Date	STI Met Class	Synoptic Weather Pattern	3-hr SO_2						24-hr SO_2						24-hr NO_2					
			BIP	Percentile	FTM	Percentile	WDP	Percentile	BIP	Percentile	FTM	Percentile	WDP	Percentile	BIP	Percentile	FTM	Percentile	WDP	Percentile
3/21/2001	8	CH	19.4	90.8	9.0	65.5	12.6	77.7	11.7	94.2	3.8	57.9	8.3	85.8	10.2	83.6	3.8	38.8	10.1	82.8
3/22/2001	5	GH	27.6	97	21.5	92.8	8.2	62.6	17.1	98.5	4.8	67.3	6.3	76.7	11.4	87.9	9.2	78.7	13.2	91.3
3/23/2001	6	GH	34.7	98.7	7.7	59.3	12.3	76.3	18.7	99.3	3.0	49	7.5	82.6	16.4	95.9	7.8	69.5	20.0	98.3
3/24/2001	6	FGR	39.5	99	2.2	23.5	2.4	25.1	13.8	96	0.7	18.4	1.2	26.8	13.3	91.7	8.7	75.2	6.7	62.8
3/25/2001	7	CH	23.1	93.8	17.7	88.7	4.9	44.1	12.2	94.8	5.0	68.1	2.4	39.9	7.5	67.3	5.9	55.9	9.6	80.5
3/26/2001	7	CH	21.2	92.5	9.1	65.9	11.7	74.7	14.2	96.7	3.8	57.9	5.7	72.9	9.4	79.8	2.4	21.9	6.5	61.1
3/27/2001	6	FOR	13.7	81	33.0	98.3	7.5	57.9	10.4	91.5	7.9	84	4.6	66.2	9.2	78.8	4.8	46.7	10.8	85.5
3/28/2001	6	FOR	10.3	70.6	5.8	49.3	3.6	34.4	7.4	81.8	1.9	33.6	1.0	23	5.6	53.2	5.7	53.8	9.3	79.5
3/29/2001	7	FOR	13.7	80.9	12.6	77.4	1.1	12.6	8.8	87.4	1.0	22.7	0.2	11	5.1	49	6.5	60.6	9.5	80.1
3/30/2001	7	FOR	17.9	89.1	6.0	50.3	4.5	42.3	10.4	91.4	0.9	21.8	1.7	31.7			10.7	85	8.6	74.6
3/31/2001	7	PH	12.4	76.7	13.4	80.3	11.8	75	9.9	90.2	3.2	51.9	7.6	83	11.0	86.3	8.7	75	17.1	96.6
4/1/2001	5	PH	7.6	58.3	2.1	22.4	12.3	76.2	3.7	56.5	0.3	11.5	6.4	77.1	13.3	91.6	6.8	63.6	19.0	97.7
4/2/2001	4	GR	2.1	22.5	0.0	4.2	4.4	41.8	1.3	28	-0.9	2.5	0.9	20.6	3.8	37.5	2.5	23.6	2.9	27.5
4/3/2001	1	GR	2.3	23.8	0.0	3.7	0.4	6.3	0.9	22.5	-1.0	1.8	0.0	8.6	2.3	20.5	4.3	43.5	1.6	12.9
4/4/2001	1	GR	1.2	13.8	-0.4	2	0.8	9.8	1.0	22.7	-1.3	0.7	0.2	11.4	3.6	35.3	2.2	19.5	3.3	31.1
4/5/2001	1	GR	0.8	10	-0.9	0.7	3.3	31.8	0.8	19.1	-1.3	0.6	1.1	25.3	2.9	28			6.3	58.9
4/6/2001	1	GR	0.9	11.2	-0.8	1.1	2.0	21.4	0.7	18.5	-1.3	0.8	1.4	29	1.7	14.6			4.0	40.2
4/7/2001	1	GR	0.6	8.2	-1.0	0.3	0.9	11.1	0.5	14.5	-1.4	0.5	0.6	16.8	3.1	30.2			1.3	9.4
4/8/2001	1	GR	0.7	8.6	-1.4	0	0.6	8.3	0.6	15.9	-1.6	0.1	0.3	11.9	4.3	43.7			0.5	4.2
4/9/2001	2	GR	0.9	11.2	-1.4	0	1.1	13			-1.6	0	0.6	17.4			0.8	5.9	1.6	12.7
4/10/2001	1	GR	1.7	19.3	-1.1	0.2	0.7	9.2	1.4	29.1	-1.6	0.2	0.5	14.4	2.8	26.6			1.2	8.7
4/11/2001	6	GR	1.5	17.1	-0.4	2.3	0.6	7.9	1.2	26.5	-1.2	1.1	0.4	13.6	1.7	14.7			2.0	16.9
4/12/2001	4	GR	1.3	15	-0.9	0.5	0.9	11.2	1.2	26	-1.2	1.3	0.6	16.4	1.3	10.3			3.1	29.2
4/13/2001	1	GR	6.7	54.1	-0.9	0.6	0.8	9.6	4.2	62	-1.1	1.6	0.4	13.1			3.3	31.4	1.0	7.7
4/14/2001	1	GR	12.5	77.3	-0.5	1.8	1.6	18.3	7.6	82.8	-1.0	2.1	0.4	13.2	7.4	66.4	2.1	18.3	0.7	5.2
4/15/2001	4	FGR	10.1	69.7	1.0	11.9	1.6	18.3	6.7	78.8	-0.3	6.6	0.9	22	5.2	50.3			1.4	10.7
4/16/2001	6	CH	5.1	44.8	8.6	63.7	7.6	58.3	3.8	58.1	1.9	34.8	3.1	50	7.4	66.9	2.9	28.5	8.1	71.1
4/17/2001	7	FOR	4.0	39.1	10.4	71	2.8	27.8	2.8	46.5	4.1	61.7	1.8	33.1	7.4	67.1	4.6	45.6	7.8	69.6
4/18/2001	5	CH	3.8	36.9	8.1	61.6	8.9	65.1	2.8	46.8	3.5	55	3.8	57.6	8.7	75.9	1.7	14.1	5.9	56.1

Table B-2. Summary of Daily Weather Patterns, Concentrations, and Concentration Rankings

Date	STI Met Class	Synoptic Weather Pattern	3-hr SO_2						24-hr SO_2						24-hr NO_2					
			BIP	Percentile	FTM	Percentile	WDP	Percentile	BIP	Percentile	FTM	Percentile	WDP	Percentile	BIP	Percentile	FTM	Percentile	WDP	Percentile
4/19/2001	5	CR	2.9	28.5	8.5	63.3	9.6	67.6	2.5	42.2	4.9	67.8	3.7	57	6.1	57.6			4.1	40.9
4/20/2001	2	GR	2.2	23.5	1.7	19.2	0.8	9.3	2.0	36.1	1.0	23.7	0.3	12.5	2.0	17.6			-0.5	2.3
4/21/2001	1	GR	1.7	19.5	0.7	8.8	0.4	5.9	1.6	31.4	0.0	8.6	0.0	8.8	2.3	20.7			-0.5	2.2
4/22/2001	1	GR	1.5	17.4	0.5	6.9	0.2	4.8	1.4	28.9	0.0	8.9	0.0	9.5	1.7	14.2			-0.4	2.4
4/23/2001	6	GR	1.4	16.2	0.5	6.6	2.0	22.3	1.3	27.9	0.0	9.1	0.8	20.1	1.5	11.9			3.4	33.2
4/24/2001	7	FOR	1.9	21.2	1.1	12.8	3.0	29	1.4	29.5	0.0	9.2	2.0	35.3	2.9	28.1			3.7	37.2
4/25/2001	7	CH	8.0	60.6	7.1	56.3	10.5	71.7	1.2	26.6	3.8	57.8	4.7	66.9	7.0	64.5	1.8	15	7.2	65.1
4/26/2001	2	CR	7.0	55.4	15.6	85.2	9.2	66.2	2.1	37.6	5.4	71.3	5.0	68.3	6.2	57.9	2.3	20.6	16.1	95.7
4/27/2001	6	CR	2.8	27.9	3.1	30.7	7.9	60.1	0.9	21.1	2.0	35.4	5.0	68	5.4	51.4	4.1	40.6	4.4	44.3
4/28/2001	6	CR	9.0	65.2	17.0	87.5	5.8	49.6	1.9	34.3	4.9	67.4	2.7	44.7	6.1	56.9	3.3	31.9	9.0	77.3
4/29/2001	6	CR	2.6	25.8	7.0	55.5	4.4	41.2	0.5	14.9	2.8	45.7	2.0	36.2	5.7	54.2			16.1	95.8
4/30/2001	6	GR	2.7	26.9	1.4	16.3	1.1	13.5	1.6	31.5	0.6	16.6	0.3	11.6	2.8	26.9	1.5	11.8	0.5	4.1
5/1/2001	6	GR	0.6	7.8	1.7	18.9	1.3	15.6	0.0	9.8	0.6	15.5	0.4	13	0.9	7.1			5.7	54.1
5/2/2001	8	GR	0.6	7.7	3.1	30.2	1.8	20.4	-0.6	3.9	0.9	21.3	0.4	12.7	1.4	11.2	12.8	90.7	3.3	32.3
5/3/2001	8	GR	-0.1	3.2	2.0	21.8	1.4	16.9	-1.0	2	0.8	19.9	0.3	12.6	3.7	36.8	12.1	89	3.6	35.9
5/4/2001	2	GR	-0.7	1.3	1.1	13.5	0.5	6.8	-1.2	1	0.5	14.4	0.2	10.9	2.8	27.1	10.4	84.1	-0.6	1.9
5/5/2001	1	GR	-0.9	0.4	9.5	67.1	2.3	24.2	-1.5	0.4	2.1	36.2	0.9	21.9	2.1	18.1	8.3	73.2	0.5	4.2
5/6/2001	2	GR	-0.8	0.9	2.7	26.6	1.4	16	-1.5	0.3	0.9	21	0.6	17.3	2.5	23.5	7.6	68.3	0.7	5.6
5/7/2001	2	GR	-0.3	2.5	6.4	52.8	1.4	16.3	-1.2	1.2	1.5	30.2	0.9	21.2	3.5	33.6	8.6	74.5	3.1	29.6
5/8/2001	6	GR	-1.4	0.1	0.6	8.1	3.9	37.8	-2.2	0	0.2	11.2	0.9	20.8	1.6	12.6	6.4	59.9	1.7	14
5/9/2001	6	GR	1.4	16.5	9.8	68	1.7	19.3	-0.6	3.6	5.0	68.1	1.0	23.3	2.0	16.6	7.0	64.4	0.9	6.6
5/10/2001	6	GR	1.0	12.5	2.0	22.1	1.6	17.9	0.5	15.1	1.1	25.2	0.7	18	0.6	4.7	6.3	59.2	5.6	53.1
5/11/2001	6	CR	0.4	6.2	1.7	19	1.4	16.5	-0.4	5.8	0.8	18.9	0.5	15.4	1.0	7.6	5.0	48.3	-0.6	2.1
5/12/2001	6	GR	0.6	8	11.4	74	9.2	66.4	-0.2	7.3	2.9	47.8	3.7	57.3	4.3	42.6	7.4	66.5	2.5	23.4
5/13/2001	1	CH	8.0	61.3	11.5	74.2	13.8	81.3	3.0	49.1	5.4	71.4	6.3	76.1	12.0	88.7	7.5	67.4	6.3	58.3
5/14/2001	1	CH	22.9	93.4	10.2	70.2	51.4	99.7	8.2	85.5	5.6	72.3	12.5	95.2	10.4	84.2	4.9	47.4	5.3	51
5/15/2001	1	GR	11.3	73.7	7.8	59.5	47.6	99.4	4.6	66.1	5.6	72.1	11.1	93	10.6	84.6	8.0	70.8	7.6	68.2
5/16/2001	2	GR	13.1	79.3	14.2	82.3	1.6	18.5	2.8	46.3	5.5	71.8	1.3	28.5	14.1	93.2	4.1	41.4	1.9	15.8
5/17/2001	6	GR	5.8	49.4	5.6	48.8	1.4	16.5	1.9	34.2	1.8	32.9	1.1	24.2	8.3	72.8	1.7	14.5	3.5	33.3

Table B-2. Summary of Daily Weather Patterns, Concentrations, and Concentration Rankings

Date	STI Met Class	Synoptic Weather Pattern	3-hr SO_2						24-hr SO_2						24-hr NO_2					
			BIP	Percentile	FTM	Percentile	WDP	Percentile	BIP	Percentile	FTM	Percentile	WDP	Percentile	BIP	Percentile	FTM	Percentile	WDP	Percentile
5/18/2001	3	GR	1.5	17.2	1.0	11.4	1.2	14.7	1.0	22.6	0.6	16.2	0.9	21.7	3.2	31			0.2	3.6
5/19/2001	6	GR	1.1	12.6	0.7	8.6	2.0	21.5	0.7	18.3	0.3	12	1.1	25	4.6	45.8			2.7	25.4
5/20/2001	2	GR	1.6	17.9	1.1	13.1	1.3	15	0.8	19	0.5	14.7	1.0	23.6	7.3	66			0.7	5.5
5/21/2001	7	FGR	1.2	14.3	0.2	5	1.6	18.2	0.5	14.2	0.0	9.7	1.0	23.8	3.7	37			0.3	3.7
5/22/2001	7	CH	5.2	46	16.3	86.4	4.4	41.7	1.1	25.5	4.3	64	2.4	40.5	5.9	56	2.7	25.5	6.1	56.8
5/23/2001	8	CH	23.1	93.9	9.1	66	7.7	59.1	7.5	82.6	3.8	58	3.4	54.3	7.4	67.2	1.1	7.8	4.3	42.8
5/24/2001	8	CH	13.8	81.6	10.4	71.3	4.3	40.9	7.3	81.1	3.2	51.6	2.6	43.5	7.2	65.4	3.3	31.6	4.3	42.7
5/25/2001	8	CH	8.2	62.2	15.7	85.6	7.3	56.9	4.0	60.8	3.6	55.4	3.2	51.1	9.2	79.1	4.5	44.8	2.8	27.2
5/26/2001	8	CR	7.8	59.6	8.1	62	10.1	69.4	2.8	46.4	2.8	46.2	3.3	52.4	7.5	67.9	5.1	48.7	4.9	47.6
5/27/2001	7	GR	1.1	12.9	1.0	11.7	1.4	17	-0.4	5.6	0.3	12.3	1.1	24.4	5.7	54.5			1.1	8.2
5/28/2001	6	GR	-0.8	1.1	0.4	6.4	1.2	14	-1.1	1.4	0.0	10	0.9	20.5	2.9	27.9			0.0	3
5/29/2001	2	GR	1.2	13.9	4.4	41.2	1.3	15	-0.5	4.6	1.1	24.8	0.8	20.2	7.6	68.7	1.9	15.5	0.0	2.9
5/30/2001	2	GR	1.0	12.3	1.7	19.1	1.2	14	-0.7	2.8	0.3	12.2	0.9	20.4	4.6	46.1			-0.3	2.6
5/31/2001	6	GR	-0.5	1.5	0.9	10.9	1.0	11.9	-1.1	1.4	0.1	10.3	0.8	20.2	1.9	15.9			1.9	16.5
6/1/2001	7	GR	3.9	37.9	2.1	22.7	1.0	11.4	0.4	12.8	0.5	14.8	0.8	20	7.5	67.8			1.3	9.3
6/2/2001	7	GR	0.0	3.8	7.9	59.8	1.1	13.5	-0.8	2.7	2.5	41.1	0.9	20.7	5.7	54.7	2.7	25.9		
6/3/2001	2	GR	-0.2	3	0.0	3.9	1.4	16.5	-0.7	2.9	-0.1	7.5	1.2	26	2.6	24.8				
6/4/2001	6	GR	-0.6	1.4	0.3	5.3	0.9	10.9	-0.9	2.4	-0.2	7.2	0.8	19.6						
6/5/2001	6	GR	-0.5	1.7	8.0	60.8	0.8	9.7	-0.9	2.3	2.1	37.6	0.5	15.2						
6/6/2001	6	GTD	-0.5	1.6	3.9	38.4	0.7	8.4	-1.1	1.5	3.2	52.1	0.6	15.6						
6/7/2001	6	GTD	-0.8	0.8	4.0	39	1.2	14.5	-1.0	1.9	3.1	50.6	0.9	22.4	1.1	8.6				
6/8/2001	6	GTD	1.0	11.8	4.0	39	1.2	14.7	-0.6	4.2	2.8	45.9	1.0	23.9	1.7	13.6	0.6	4.8		
6/9/2001	6	GTD	0.5	7.2	3.6	34.8	1.5	17.2	-0.8	2.6	2.3	39.4	1.2	26.2	3.9	39.5	0.9	6.9	3.3	31.5
6/10/2001	6	GTD	-0.7	1.2	2.8	27.5	1.3	15.5	-1.1	1.7	1.7	32.5	1.1	24.9	3.1	29.4				
6/11/2001	6	GH	2.8	27.6	5.6	48.2	1.4	15.8	0.3	11.5	1.9	34.3	1.1	24.7	8.6	74.7			2.4	21.7
6/12/2001	6	GR	3.7	36.6	30.4	97.8	2.0	21.5	1.3	27.5	10.2	90.9	1.5	31	8.4	73.4	3.8	38.1	2.5	23.3
6/13/2001	2	GR	0.9	10.3	3.8	37.1	1.8	20.2	-0.6	3.5	2.8	45.8	1.5	30.5	3.4	32.8	0.8	6.2		
6/14/2001	2	GR	2.6	26.5	3.7	35.5	1.9	21.3	1.4	28.8	2.7	44.2	1.5	30.6	2.0	17.1				
6/15/2001	2	FGR	1.8	20.7	3.8	37.1	2.2	23	1.0	23.1	2.7	44.9	1.9	33.9	3.7	36.9				

Table B-2. Summary of Daily Weather Patterns, Concentrations, and Concentration Rankings

Date	STI Met Class	Synoptic Weather Pattern	3-hr SO_2						24-hr SO_2						24-hr NO_2					
			BIP	Percentile	FTM	Percentile	WDP	Percentile	BIP	Percentile	FTM	Percentile	WDP	Percentile	BIP	Percentile	FTM	Percentile	WDP	Percentile
6/16/2001	1	CH	3.9	38.4	17.1	87.8	3.1	30.4	1.1	24.5	8.0	84.1	2.6	43.3	8.8	76.4	4.1	41.1	6.6	61.8
6/17/2001	1	CH	6.4	52.5	10.9	72.9	6.2	51.1	5.1	68.9	6.8	79.5	4.4	64.4	11.0	86.6	2.5	24	9.3	79.3
6/18/2001	1	GTD	3.9	38.3	6.6	53.7	3.7	36.7	1.7	32.1	4.7	66.6	3.0	48.6	4.5	44.5	2.2	19.8	7.8	69.3
6/19/2001	2	GTD	4.6	42.6	3.7	36	2.7	26.9	1.2	26.1	2.4	40.2	2.5	41.5	4.6	45.3			5.1	48.8
6/20/2001	1	GH	2.9	28.8	4.2	39.6	3.7	35.6	0.9	22.1	3.4	53.6	2.4	39.7	4.3	42.5			3.8	37.7
6/21/2001	6	GH	2.7	27.1	6.2	51.5	10.4	70.8	1.2	26.3	3.9	59.4			4.0	40.3				
6/22/2001	7	CH	8.3	63	4.2	40	4.5	42	3.1	50.1	2.9	46.9	2.1	37.8	12.1	88.9	1.9	16	2.0	17.8
6/23/2001	7	CH	29.0	97.3	12.7	77.8	5.2	45.3	8.5	86.2	3.9	58.9	3.6	56.2	8.7	75.7	2.1	19.3	7.3	65.6
6/24/2001	1	CH	52.0	99.8	10.5	71.5	6.0	50.3	10.4	91.8	6.5	77.9	3.6	55.1	8.8	76.6	4.0	40	9.5	80
6/25/2001	5	CR	11.8	74.9	8.0	60.3	6.5	53.5	4.0	59.8	5.1	69	3.4	53.9	8.8	76	6.6	61.4	3.8	38.7
6/26/2001	8	GR	1.4	15.8	4.7	43.3	1.1	13.1	0.6	17.3	2.6	43.6	0.7	18.8	5.7	54.4	2.9	27.7	1.1	8.3
6/27/2001	8	GR	0.1	4.5	2.1	22.5	2.6	26.1	-0.3	6.3	0.7	18.2	0.7	17.7	2.4	22.3	2.9	28.3	4.2	41.5
6/28/2001	8	GR	0.5	7.2	3.7	35.2	3.9	37.6	0.0	8.3	1.9	33.7	1.0	22.9	3.8	37.3	3.3	31.3	3.4	33
6/29/2001	7	GR	1.5	17.7	3.3	32.3	12.0	75.4	0.7	17.5	2.1	37.4			6.4	59.6	2.2	19.7		
6/30/2001	6	GR	0.5	7.2	4.6	42.8	12.5	77.1	0.0	9.4	2.0	36	10.1	90.6	2.1	19.2	2.7	26.1		
7/1/2001	6	GTD	8.9	64.5	3.6	34.4	13.5	80.7	2.4	40.4	2.1	37	9.8	90	3.1	29.5			7.3	65.7
7/2/2001	3	GTD	0.3	5.4	1.8	20	12.7	78.1	-0.2	7	1.2	27.1	9.3	88.7					3.7	36.6
7/3/2001	3	GR	0.2	5	1.8	20.5	8.8	64.3	-0.2	7.1	1.3	27.7	7.0	79.8						
7/4/2001	3	GR	1.3	14.9	8.0	60.9	6.2	50.9	0.0	8.4	2.9	47.1	5.9	74.1	4.3	42.2			3.3	31.8
7/5/2001	3	GH	3.9	37.5	5.2	45.6	6.2	51	1.5	30.4	3.2	51.3	5.8	73.6	6.7	63.1	1.3	10.5	2.8	26.8
7/6/2001	1	GH	3.7	35.6	21.5	92.9	6.8	54.6	2.0	35.9	8.4	86	5.9	73.9	11.3	87.7	2.4	22.7	3.3	31.7
7/7/2001	1	GH	1.5	17.3	4.4	41.4	6.8	54.7	0.5	14.6	3.5	54.8	6.1	75.4	6.1	57.1	0.7	5.7	4.5	44.9
7/8/2001	1	GH	4.3	40.7	19.0	90.2	10.5	71.4	2.6	43	7.2	80.7	7.5	82.7	9.7	81.1	2.1	17.9	2.9	28.4
7/9/2001	1	GH	8.9	64.7	11.8	75.1	8.0	60.9	4.9	67.7	7.0	80.2	6.5	77.6			3.5	33.5	3.2	30.9
7/10/2001	1	GH	11.7	74.7	13.0	79.2	6.7	53.9	5.4	71	7.5	82.5	5.8	73.7			2.6	25.3	2.6	25.2
7/11/2001	1	GH	9.9	68.9	15.9	85.7	5.7	49.1	4.5	65.4	4.7	66.3	5.5	71.6			1.5	11.4	3.7	36.1
7/12/2001	1	GH	14.8	83.6	20.1	91.4	6.9	54.9	7.8	83.8	11.4	93.3	5.5	72			4.2	41.9	3.3	32.1
7/13/2001	5	FGR	3.8	37.3	16.5	87	10.9	72.6	2.1	37.2	10.3	91.2	6.8	79.3	12.3	89.5	3.1	29.8	9.4	79.6
7/14/2001	1	CH	17.1	87.8	30.4	97.9	16.4	86.5	9.1	88.4	16.0	98.2	9.8	89.8	13.8	92.8	3.6	35.5	12.2	89.3

Table B-2. Summary of Daily Weather Patterns, Concentrations, and Concentration Rankings

Date	STI Met Class	Synoptic Weather Pattern	3-hr SO_2						24-hr SO_2						24-hr NO_2					
			BIP	Percentile	FTM	Percentile	WDP	Percentile	BIP	Percentile	FTM	Percentile	WDP	Percentile	BIP	Percentile	FTM	Percentile	WDP	Percentile
7/15/2001	1	CH	14.0	81.8	9.4	66.6	20.2	91.5	3.8	57.7	5.2	69.5	15.7	98.1	9.4	79.7			10.4	84.3
7/16/2001	1	CR	0.5	7	6.3	52.1	6.9	55	-0.2	6.9	4.3	63.4	6.2	75.7	3.3	32.5			6.5	60.9
7/17/2001	1	CR	7.5	58.2	5.2	45.6	14.3	82.7	1.4	29.7	4.2	62.2	9.5	89.4	5.6	53.5				
7/18/2001	1	CR	3.0	29.4	5.4	47.3	9.5	66.9	0.4	13.3	4.0	59.6	6.8	79.1	3.9	39.3			9.2	78.5
7/19/2001	1	CR	3.7	36	6.4	53.2	6.0	50.2	0.6	17.1	4.2	62.6	5.6	72.4	4.7	46.5	1.2	8.9	6.5	60.4
7/20/2001	1	CR	3.7	35.2	6.0	50.5	8.0	60.9	2.0	35.7	4.3	63.9	6.2	76	7.9	70.3	2.5	23.9	1.5	11.6
7/21/2001	1	CR	8.1	61.9	4.4	41.6	5.2	46	2.7	44.4	3.1	50.7	3.1	49.7	12.9	91	3.3	32	5.0	48.2
7/22/2001	1	CR	3.0	29.3	6.4	52.9	3.6	34.4	-0.1	8.1	4.0	60.8	2.9	48.1	4.3	43.8	2.7	26		
7/23/2001	1	CR	3.3	32.1	9.8	68	5.3	46.9	0.9	21.6	5.3	70.4	3.4	54.2	4.1	40.4	2.9	27.6	19.8	98.2
7/24/2001	3	CR	5.6	48.6	9.5	67.4	5.4	47.1	0.7	18.6	4.7	66.4	3.1	50.2	6.0	56.4	3.5	33.9		
7/25/2001	2	CR	1.1	13.5	2.2	23.1	2.4	25	-0.6	3.7	2.0	35.5	2.1	36.4	1.3	9.6	-0.2	2.8		
7/26/2001	3	GTD	-0.2	2.6	3.0	29.2	4.4	41	-0.7	3.3	2.3	38.9	2.6	43.2	2.0	17.4	0.4	3.8		
7/27/2001	3	CR	0.3	5.7	3.9	37.7	3.1	29.8	-0.4	5.7	2.5	40.6	2.6	43.1	1.3	10.6	1.0	7.3		
7/28/2001	2	GR	0.1	4.3	2.3	23.7	2.9	28.5	-0.4	5.5	2.1	36.6	2.6	43.7	1.8	15.1	-0.3	2.5		
7/29/2001	3	GR	0.4	6.1	3.3	32.3	3.1	29.8	-0.3	6.8	2.5	41.2	2.6	43.8	3.5	34.3	0.2	3.5	1.6	13.1
7/30/2001	1	GH	2.6	26	10.7	72.3	3.2	30.9	0.8	19.5	5.0	68.4	2.7	45.2	5.5	52.5	1.3	10.2		
7/31/2001	1	FGR	8.9	64.6	10.0	69	3.7	35	3.4	53.6	4.2	62	3.0	48.9	8.5	74.2	3.9	39.1	2.0	16.7
8/1/2001	1	CR	16.5	86.7	9.0	65.5	6.2	51.6	3.2	51.4	4.0	60.6	3.4	54.4	4.4	44.4	2.3	21.3		
8/2/2001	1	CR	0.9	10.5	4.1	39.5	2.8	28.2	-0.1	7.9	1.5	30.8	2.6	42.5	1.7	13.4	1.5	12.1	28.2	99.6
8/3/2001	1	CR	0.1	4.5	12.4	76.8	2.9	28.3			2.1	36.9	2.7	44.6			2.4	21.5	18.0	97.3
8/4/2001	1	CR			7.7	58.9	3.1	29.7			1.9	34	2.7	44.5			2.4	22.1	9.0	77.7
8/5/2001	9	GTD			7.4	57.5	3.9	37.9			1.3	28.2	3.0	49.2					14.9	94
8/6/2001	9	GTD	0.6	8	6.2	51.1	3.1	30.4			2.2	38.3	2.5	41.8			2.8	26.4	9.9	82.1
8/7/2001	2	GH	2.5	25.3	0.2	4.9	2.8	28	1.5	30.4	-0.6	3.8	2.6	42.7	5.0	48.1			1.9	16.1
8/8/2001	3	GH	2.4	24.6	-0.2	2.9	4.9	44.2	0.1	10.1	-0.6	4.2	2.9	46.9	8.1	71.5	0.9	6.8	5.4	51.7
8/9/2001	3	GR	1.8	20.5	3.6	34.2	3.6	34	0.3	11.8	0.6	15.7	3.0	49.4	5.2	49.5	2.3	20.8	9.5	80.2
8/10/2001	3	GH	3.7	35.6	2.2	23.3	3.2	31.2	1.3	28.4	0.8	18.8	2.9	48.4	7.9	69.8	3.1	30	2.2	20
8/11/2001	3	GR	1.3	15.4	0.7	9.1	3.1	29.8	-0.3	6.1	-0.5	4.9	2.8	46.1	4.7	46.2	1.7	13.3	5.7	54.8
8/12/2001	3	GR	2.4	24.5	0.9	10.6	2.9	28.7	0.4	12.9	-0.4	5.3	2.7	44	7.9	70	1.7	13.2	3.3	32.2

Table B-2. Summary of Daily Weather Patterns, Concentrations, and Concentration Rankings

Date	STI Met Class	Synoptic Weather Pattern	3-hr SO_2						24-hr SO_2						24-hr NO_2					
			BIP	Percentile	FTM	Percentile	WDP	Percentile	BIP	Percentile	FTM	Percentile	WDP	Percentile	BIP	Percentile	FTM	Percentile	WDP	Percentile
8/13/2001	6	GR	2.6	25.8	0.0	3.6	2.8	28	0.6	16.3	-0.5	4.4	2.6	43.4	10.0	82.3	1.2	8.8	5.0	48.4
8/14/2001	5	FGR	9.6	67.7	5.9	49.8	3.0	29.4	4.5	65.2	1.5	30.9	2.5	41.9	21.1	98.7	3.8	37.9	11.2	87
8/15/2001	2	CR	3.8	37	11.6	74.5	3.2	31	1.7	32.1	3.9	58.5	3.0	48.8	9.8	81.5	2.9	28.6	1.9	16.4
8/16/2001	2	GR	3.2	31.5	0.7	8.4	3.1	30.7	1.3	28.1	-0.6	4.1	3.0	48.7			1.2	9.2	8.7	75.4
8/17/2001	4	GH	6.4	53.1	6.4	52.3	13.8	81.1	2.5	42.3	2.1	37.7	5.4	71.2	8.8	76.3	5.8	55.2	10.4	84.4
8/18/2001	6	GH	5.1	45	4.1	39.3	3.3	31.7	2.1	37.1	1.5	30.1	2.5	41.4	12.1	88.8	6.3	58.1	4.3	43
8/19/2001	7	GH	9.9	68.7	11.3	73.6	1.7	19.5	2.9	47.5	2.7	45.4	1.5	31.1	12.6	90.2	4.3	43.6	3.4	33.1
8/20/2001	7	GH	4.6	42.7	7.2	56.6	2.4	24.6	2.5	41.3	1.6	31.3	1.4	28.9	7.6	68.6	3.0	29.1	10.2	83.1
8/21/2001	5	CR	14.5	83	22.0	93.1	4.0	38.7	7.7	83.3	9.0	88	2.0	35.1	7.8	69.7	10.0	82.6	20.1	98.4
8/22/2001	1	CR	14.6	83.2	12.2	76	4.8	43.7	6.3	76.5	4.2	62.4			5.1	49.2	3.8	37.6		
8/23/2001	3	CR	6.9	55.2	9.9	68.6	6.5	53.6	3.6	55.3	2.8	46.3	3.7	56.3	4.8	47.2	4.1	41.2	9.1	78
8/24/2001	3	CR	5.3	46.5	1.7	18.7	4.2	39.7	1.9	34.5	0.9	22.2	3.9	59.4	6.7	62.9			4.0	40.1
8/25/2001	3	CR	3.2	31.2	2.0	21.7	4.1	39.4	1.1	25	1.1	24.6	3.8	58.3	3.5	34.2			1.3	10
8/26/2001	3	CR	1.8	20.8	1.7	19.7	4.3	40.7	0.6	16.9	0.4	13.5	4.1	61.4	1.1	8	1.3	9.9	-1.4	1.5
8/27/2001	3	GTD	6.7	54	2.3	23.9	4.8	43.4	2.2	38	0.6	15.8	4.2	62.3	5.8	55.4	2.6	24.9	-0.6	2
8/28/2001	2	GTD	5.5	48	2.3	24	7.7	59	1.8	33.4	0.9	22.3	4.5	65.3	2.5	23.2	4.2	42	0.5	4
8/29/2001	3	GTD	2.1	22.9	0.8	10.1	169.3	100	0.8	19.2	0.1	10.1	26.9	100	2.5	23	1.7	13.9	3.4	32.6
8/30/2001	3	GTD	0.5	6.5	-0.1	3.3	1.9	20.9	0.2	10.8	-0.3	6.7	1.5	30.3	2.0	16.8			3.5	33.7
8/31/2001	3	GTD	1.4	15.8	-0.4	2.4	1.1	13.1	0.0	9.9	-0.6	4.3	0.9	21.4	0.8	6.4			0.1	3.3
9/1/2001	3	GTD	0.5	6.6	0.1	4.5	1.2	14.6	0.1	10.6	-0.4	5.2	0.8	19.7	0.7	5.3	2.1	18.8	0.7	4.9
9/2/2001	3	GTD	0.3	5.7	0.3	5.7	0.9	10.8	-0.1	7.8	-0.2	7.2	0.7	17.8	0.7	5.1	1.7	14.3	0.6	4.6
9/3/2001	3	GR	0.9	10.2	-0.2	3	1.0	11.4	-0.2	7.4	-0.6	4	0.7	18.1	1.1	8.4	1.9	15.7	0.8	6.3
9/4/2001	2	GR	1.6	18.1	5.4	47	1.0	12.2	0.0	8.2	1.0	23.2	0.7	17.9	0.8	6	3.6	34.7	1.4	11.3
9/5/2001	2	GR	3.9	38.4	15.5	84.9	1.6	18.5	0.8	20.3	4.1	61.6	0.7	17.6	3.0	28.8	5.9	55.8	0.8	6.5
9/6/2001	1	GR	0.7	8.9	3.1	30.6	0.9	10.3	-0.3	6.2	0.6	16.1	0.5	15.2			2.8	27.4	5.9	56.2
9/7/2001	2	GR	-0.4	2.1	-0.2	2.7	0.9	10.3	-0.8	2.8	-0.5	4.8	0.4	13.8			2.4	22.6		
9/8/2001	2	GR	3.6	34.1	5.2	45.6	4.7	42.9	0.6	16.5	0.5	14.3	1.4	30	2.2	19.4	4.9	47.7	1.0	7.4
9/9/2001	2	FGR	2.6	26.1	3.4	32.7	1.8	20	0.5	14	0.5	13.9	1.0	23.4			3.8	37.4	3.1	29.3
9/10/2001	1	CH	26.9	96.5	7.7	58.7	15.5	85	13.7	95.8	2.8	46.5	4.6	65.9	5.4	51.5	8.4	73.6	2.9	27.8

Table B-2. Summary of Daily Weather Patterns, Concentrations, and Concentration Rankings

Date	STI Met Class	Synoptic Weather Pattern	3-hr SO_2						24-hr SO_2						24-hr NO_2					
			BIP	Percentile	FTM	Percentile	WDP	Percentile	BIP	Percentile	FTM	Percentile	WDP	Percentile	BIP	Percentile	FTM	Percentile	WDP	Percentile
9/11/2001	1	CH	14.7	83.3	3.5	33.6	6.7	53.9	5.4	70.7	1.4	29.4	3.2	52.1	5.4	51.1	3.7	36.3	4.6	45.7
9/12/2001	1	GTD	0.5	7.1	5.1	44.8	2.1	22.8	0.1	10.5	0.9	21.7	1.1	25.4	0.7	5.8	4.1	40.7	6.3	58.5
9/13/2001	1	CH	3.6	34.9	3.4	33.5	2.0	21.8	1.1	25.6	1.9	34.6	0.7	18.7	1.6	13	3.6	35.2	7.5	67.6
9/14/2001	9	CH	11.0	73.1	7.6	58.5	2.0	22	4.3	63.2	4.0	60.7	1.4	28.6	3.5	34.4	6.8	63.4	6.5	61
9/15/2001	1	CH	10.0	69.1	7.8	59.7	10.1	69.4	4.5	65	4.5	64.9	4.3	62.8	3.1	30.3	6.4	59.7	6.4	60.2
9/16/2001	3	CR	3.1	29.8	2.7	27.3	4.2	39.7	0.4	13.7	1.7	32.3	2.1	37.3	2.6	24.7	3.8	38.3	6.3	58.6
9/17/2001	6	GR	1.7	18.7	1.0	11.9	0.8	9.5	-0.1	7.6	0.1	10.4	0.6	17.2	1.8	15.2	2.3	20.9	2.4	22.4
9/18/2001	6	GR	0.0	4	0.9	10.6	0.7	9.1	-0.5	5	0.3	11.7	0.6	15.9	1.7	14.4	2.3	21	2.0	17.5
9/19/2001	6	FGR	-0.8	1	0.1	4.5	0.4	6	-1.3	0.9	-0.7	3.2	0.1	10.7	1.1	7.9	1.0	7.5	1.2	9.1
9/20/2001	2	CH	14.3	82.7	17.5	88.4	3.3	32.6	5.8	73.8	5.7	73	1.1	24.1	9.0	77.4	10.4	83.9	8.2	72
9/21/2001	6	FOR	7.5	58	13.1	79.4	3.3	32.5	4.4	64.8	7.9	84	1.4	29.5	6.1	57.2	8.9	77.2	11.7	88.4
9/22/2001	2	CR	10.2	70.1	15.0	84	3.2	31.1	6.3	76.6	8.7	87	1.7	31.8	7.7	68.9	8.7	75.8	8.3	73.1
9/23/2001	6	CR	9.6	67.8	16.7	87.1	2.5	25.4	6.3	76.8	9.0	87.9	1.2	26.4	9.8	81.3	7.9	70.4	3.5	34.6
9/24/2001	7	FOR	15.1	84.2	4.8	43.5	10.5	71.6	4.9	67.5	2.8	46.7	3.2	51.2	7.2	65.3	3.4	32.9	-1.4	1.4
9/25/2001	5	CH	14.3	82.5	7.1	56.1	0.8	9.4	7.1	80.3	4.3	63.5	0.4	13.4	7.1	65	4.6	45.5	7.5	68
9/26/2001	7	CH	10.3	70.3	8.2	62.7	3.4	33.4	3.7	56.5	4.7	66.6	1.5	30.6	7.3	65.9	5.5	52.6	6.3	58.4
9/27/2001	5	CH	8.7	64	18.8	90	3.5	33.7	5.5	71.9	8.6	86.3	2.0	35.6	9.6	80.4	8.5	73.9	9.6	80.6
9/28/2001	7	CH	21.0	92.1	16.8	87.3	1.6	18.4	9.6	89.7	8.7	86.9	1.3	27.4	11.6	88.2			11.2	87.3
9/29/2001	7	CH	7.7	58.8	9.4	66.6	1.7	19.5	2.3	39.3	5.7	72.7	1.2	27	8.7	74.9			11.1	86.7
9/30/2001	5	CH	5.0	44.7	7.2	56.5	2.6	26.4	1.7	31.9	3.9	59.2	1.3	27.6	6.5	60.3			10.1	82.9

APPENDIX C

CONCENTRATION TIME SERIES PLOTS

Time series plots of the BIP SO_2 and NO_2 data are presented with increment levels of interest to visually identify whether there is a greater likelihood of exceeding the increment in some months compared to others. This analysis is designed to help identify cases for episode-type modeling. The daily maximum 3-hr BIP SO_2 concentrations are shown in **Figure C-1**. The daily average BIP SO_2 concentrations are shown in **Figure C-2**. In Figures C-1 and C-2, the corresponding SO_2 increment for the averaging time is also shown. The daily average SO_2 concentrations and the annual SO_2 increment are shown in **Figure C-3**. The daily average 24-hr NO_2 concentrations and the annual NO_2 increment are shown in **Figure C-4**.

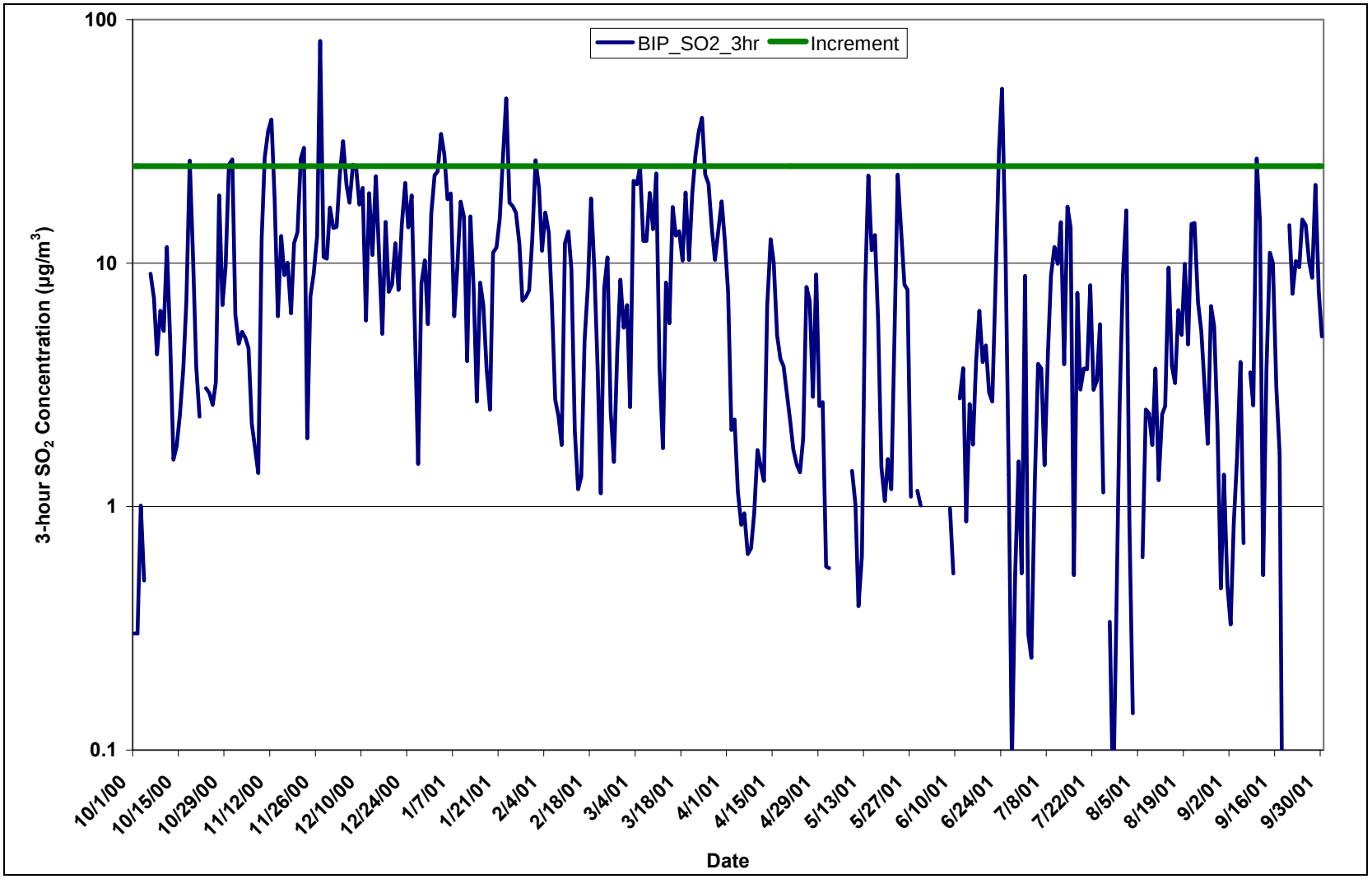

Figure C-1. Daily 3-hr maximum SO_2 concentrations ($\mu g/m^3$) at BIP compared with the 3-hr SO_2 increment.

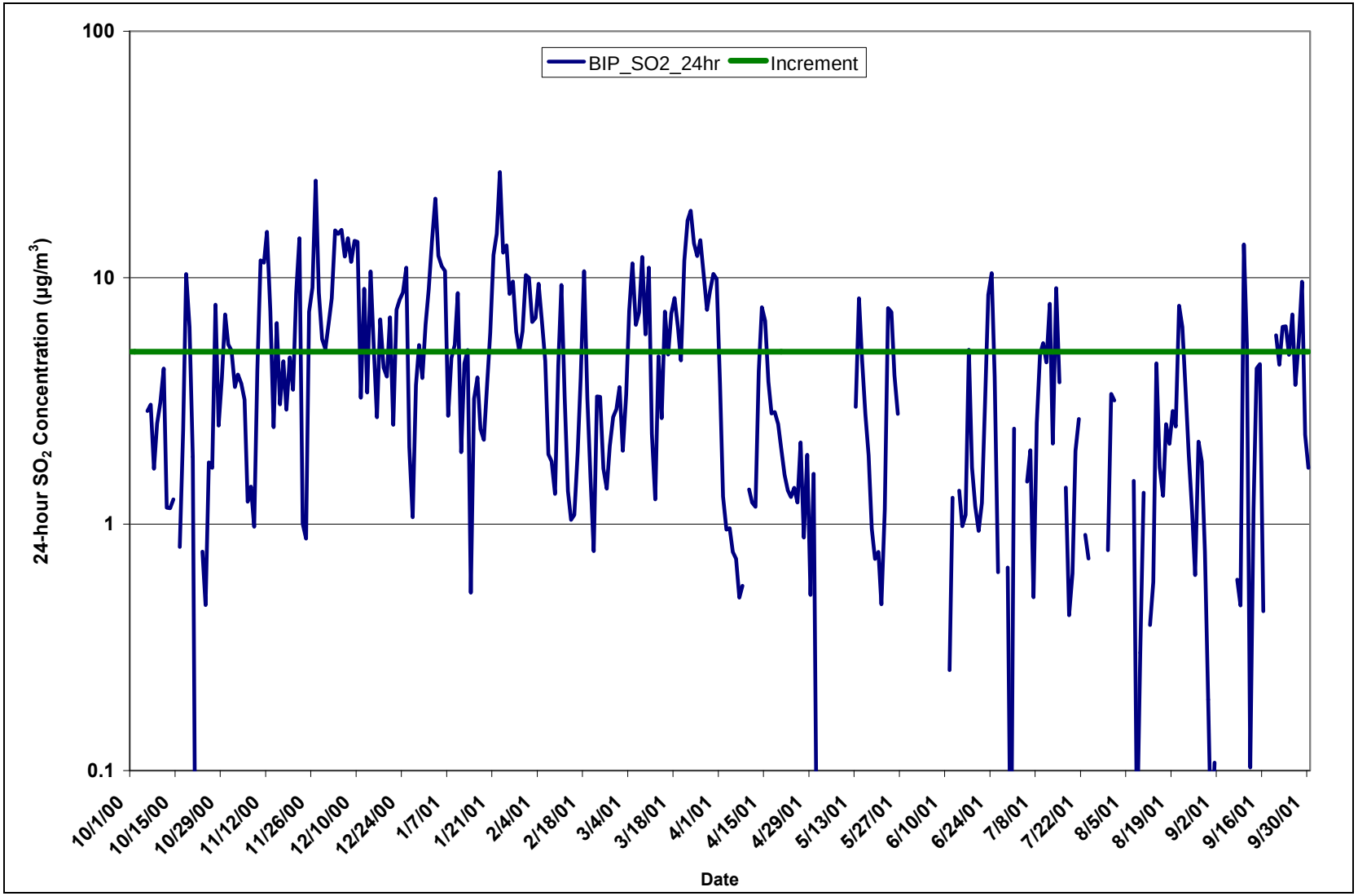

Figure C-2. Daily 24-hr average SO_2 concentrations ($\mu g/m^3$) at BIP compared with the 24-hr SO_2 increment.

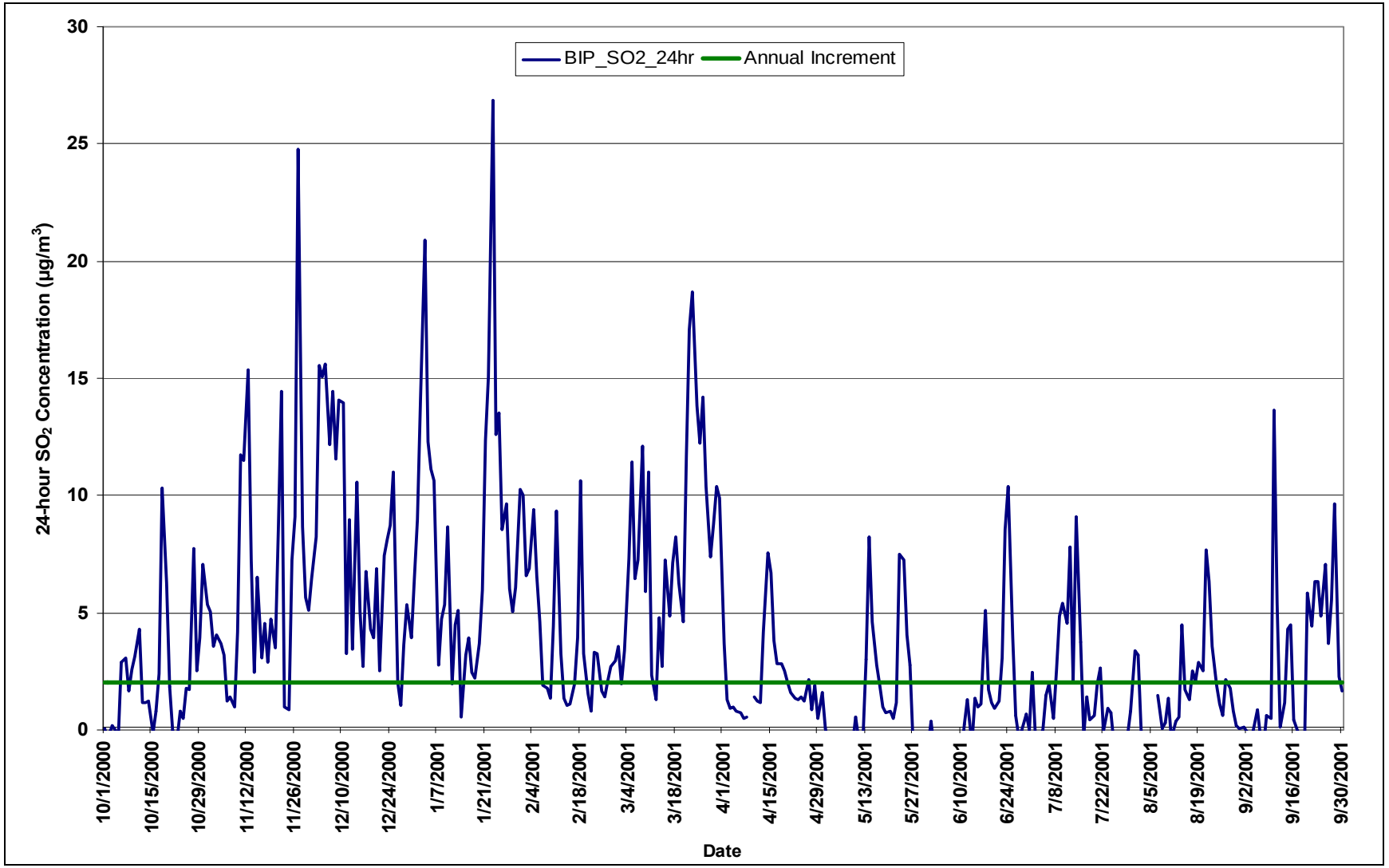

Figure C-3. Daily 24-hr average SO_2 concentrations ($\mu g/m^3$) at BIP compared with the annual SO_2 increment.

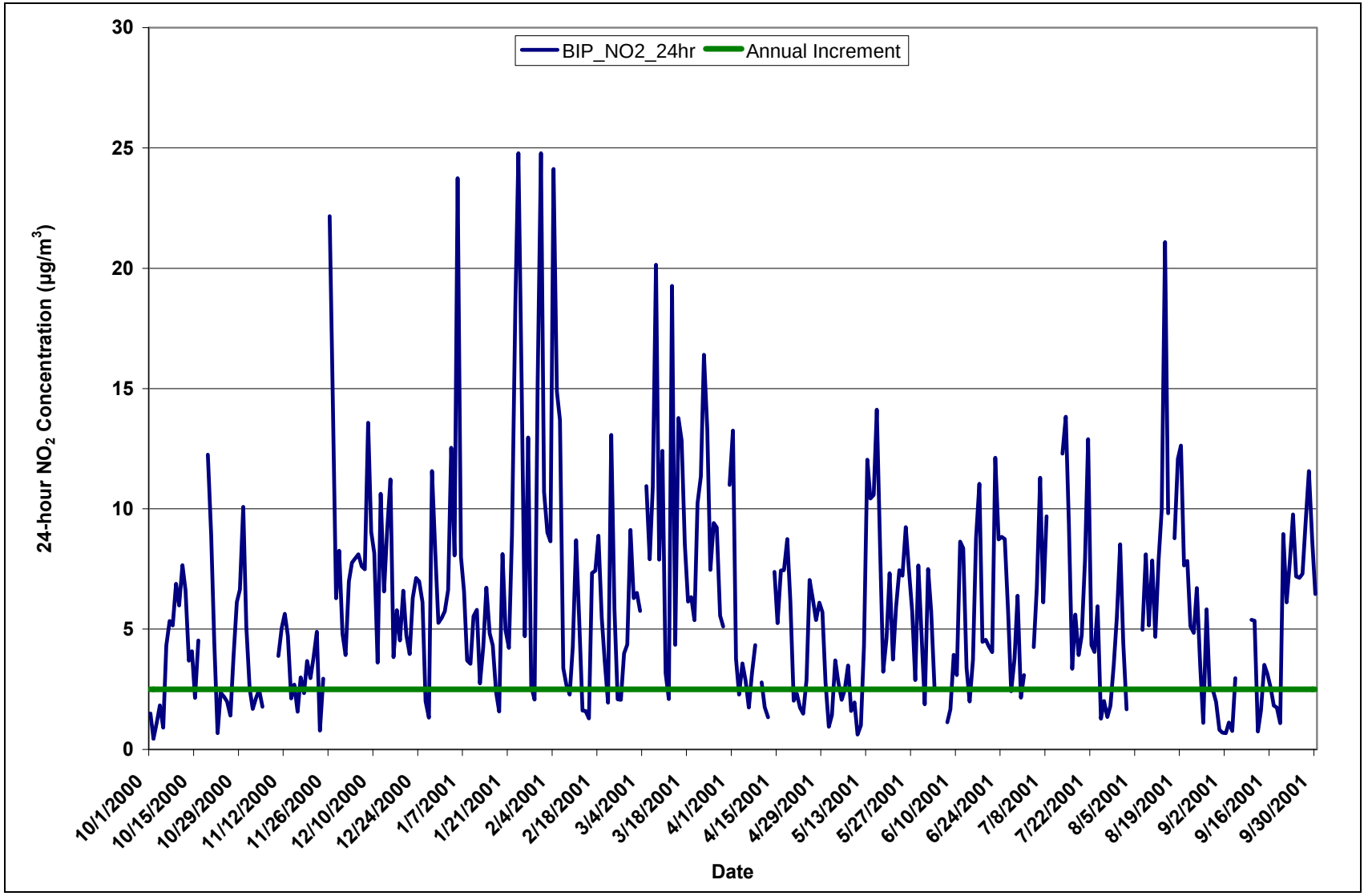

Figure C-4. Daily 24-hr average NO_2 concentrations ($\mu g/m^3$) at BIP compared with the annual NO_2 increment.

APPENDIX D

CONCENTRATION DISTRIBUTION PLOTS

Plots of 3-hr SO_2, 24-hr SO_2, and 24-hr NO_2 concentration distributions for each site (BIP, FTM, and WDP) individually and for the three sites combined are provided in this appendix. Results show that three times as many high 3-hr SO_2 concentrations (greater than 20 $\mu g/m^3$) and 2.5 times as many high 24-hr SO_2 concentrations (greater than 10 $\mu g/m^3$) occurred at BIP and FTM relative to WDP (see **Figures D-1 and D-2**). Roughly the same percentage of 24-hr NO_2 concentrations above 12 $\mu g/m^3$ occurs at each of the three sites (see **Figure D-3**).

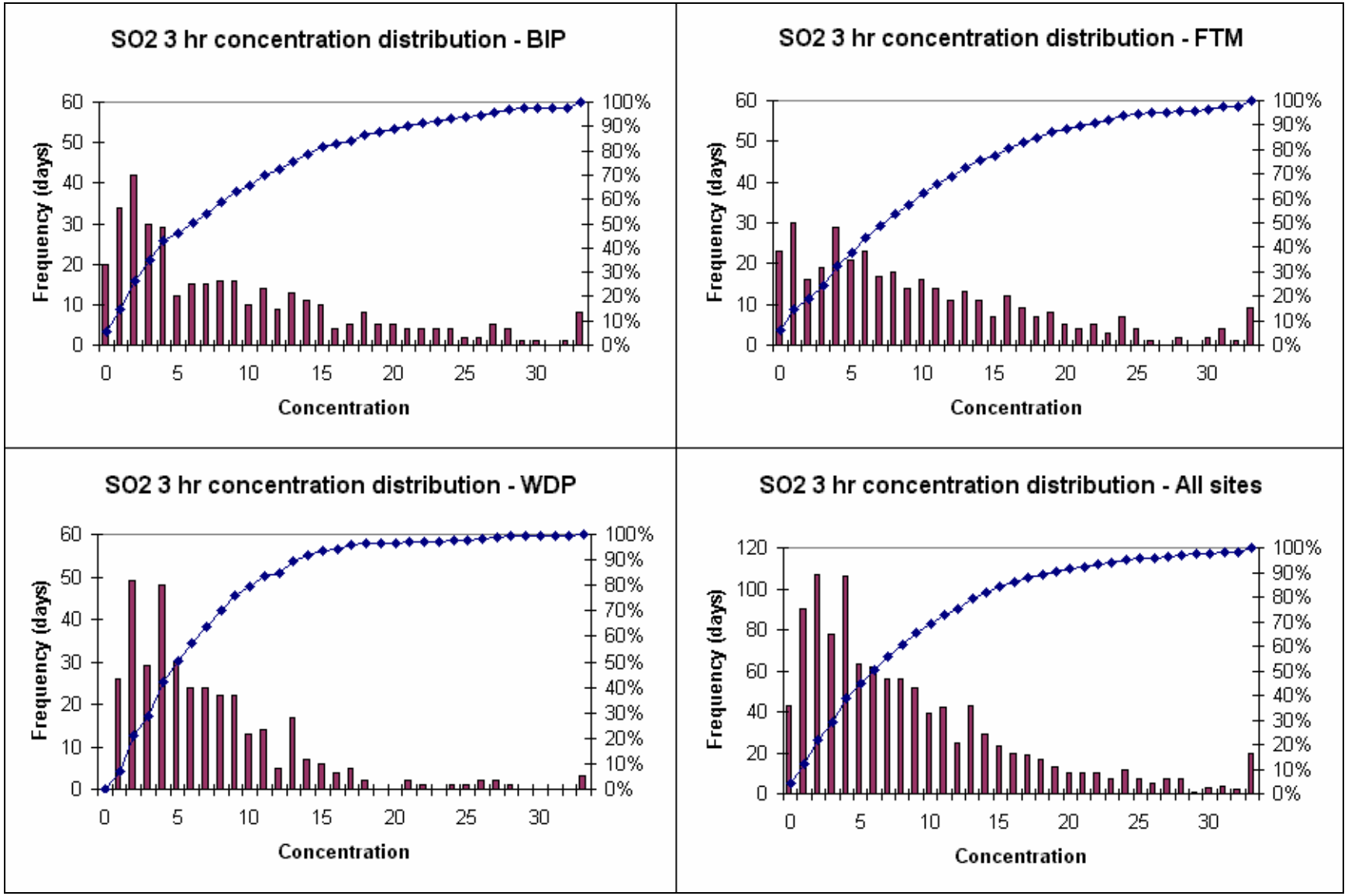

Figure D-1. SO_2 3-hr concentration ($\mu g/m^3$) distribution by site and for all sites combined.

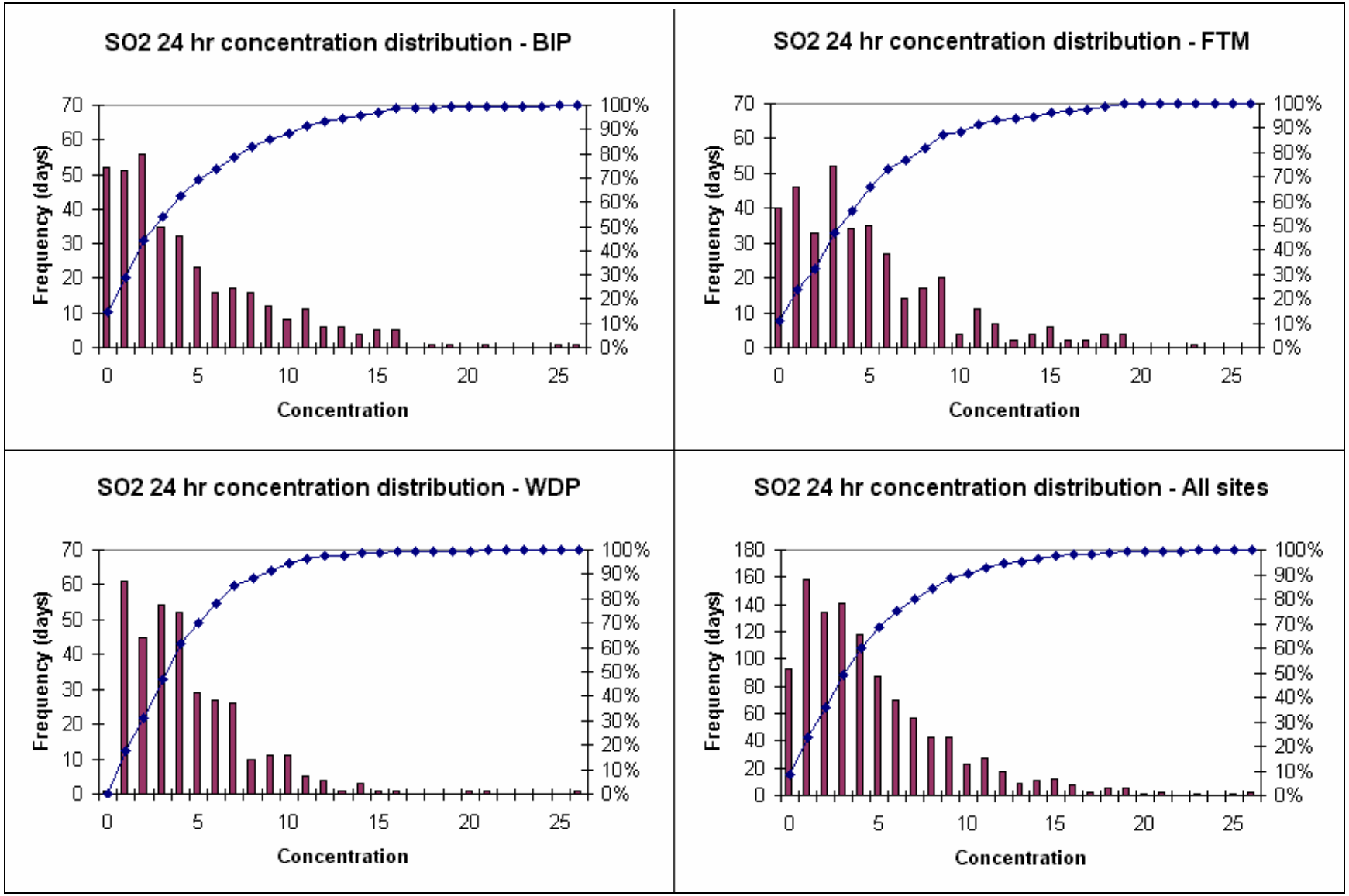

Figure D-2. SO_2 24-hr concentration ($\mu g/m^3$) distribution by site and for all sites combined.

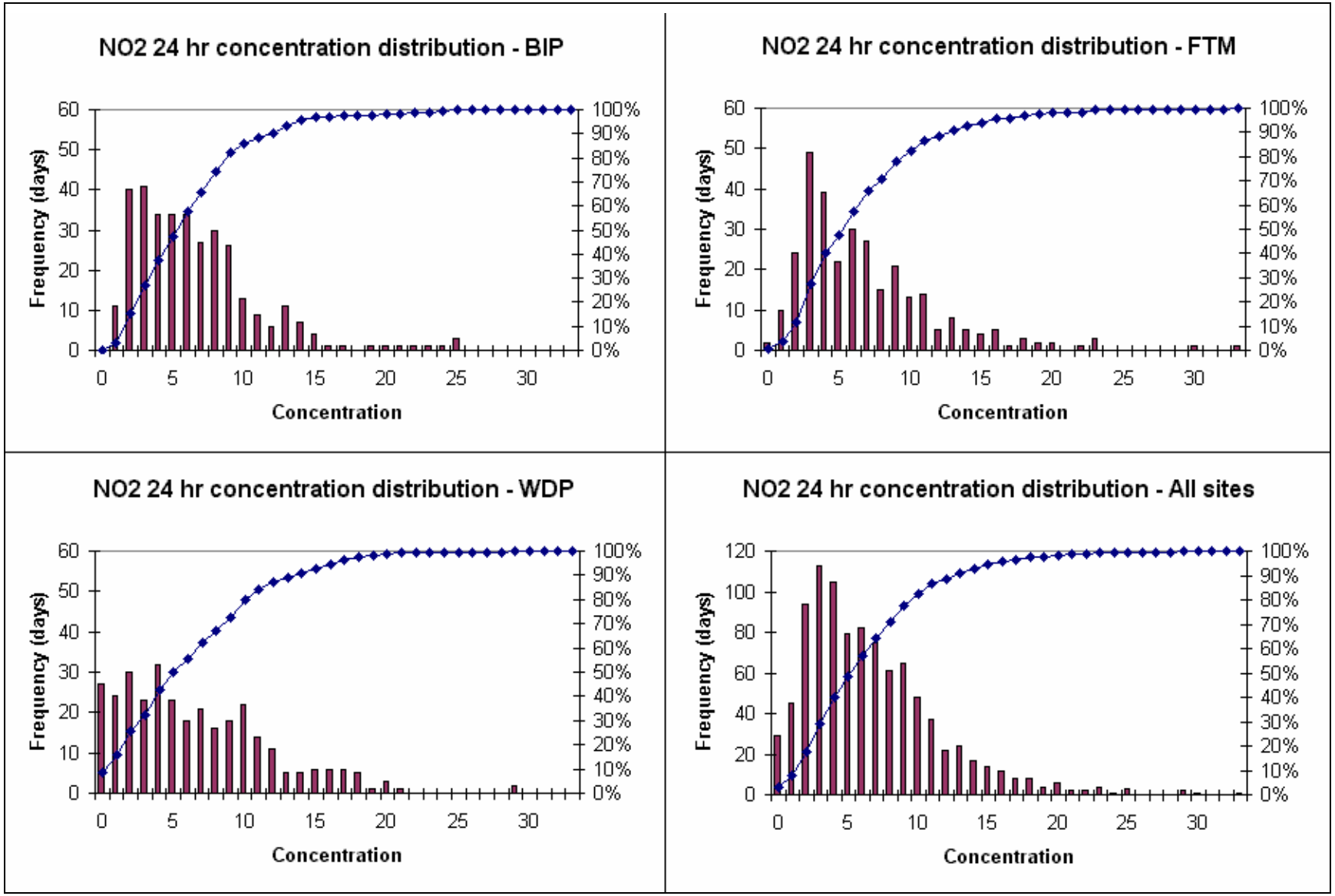

Figure D-3. NO_2 24-hr concentration ($\mu g/m^3$) distribution by site and for all sites combined.

APPENDIX E

TIME SERIES PLOTS

Time series plots of hourly SO_2 and NO_2 concentrations observed and predicted by CMAQ and CALPUFF for each site and case are provided in this Appendix.

Case 1. December 1-6, 2000

Case 2. March 2-8, 2001

Case 3. July 9-14, 2001

Case 4. August 8-13, 2001

Case 5. November 8-13, 2000

Case 6. December 30, 2000–January 4, 2001

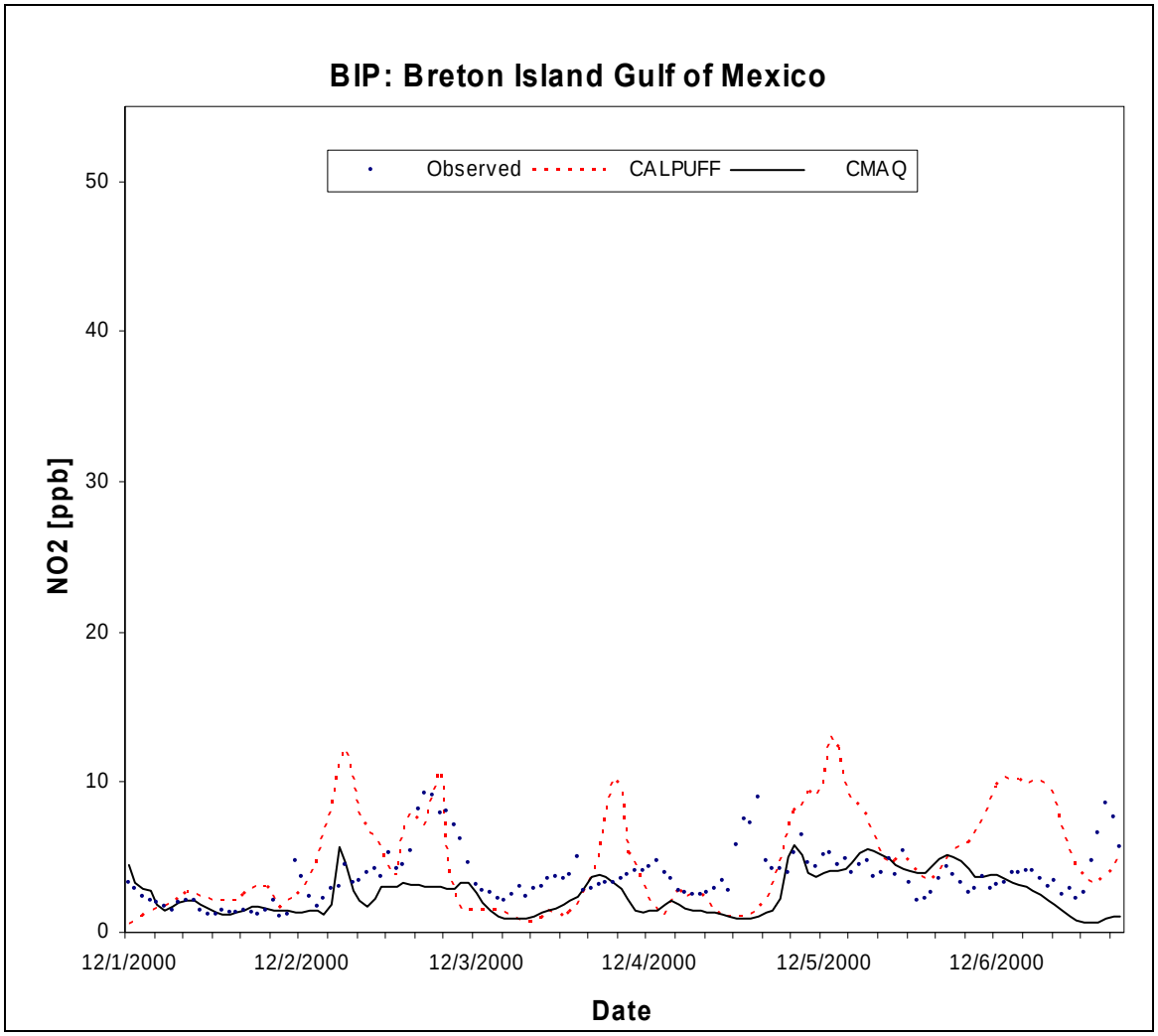

Figure E-1. Observed and predicted NO_2 concentrations at BIP for Case 1.

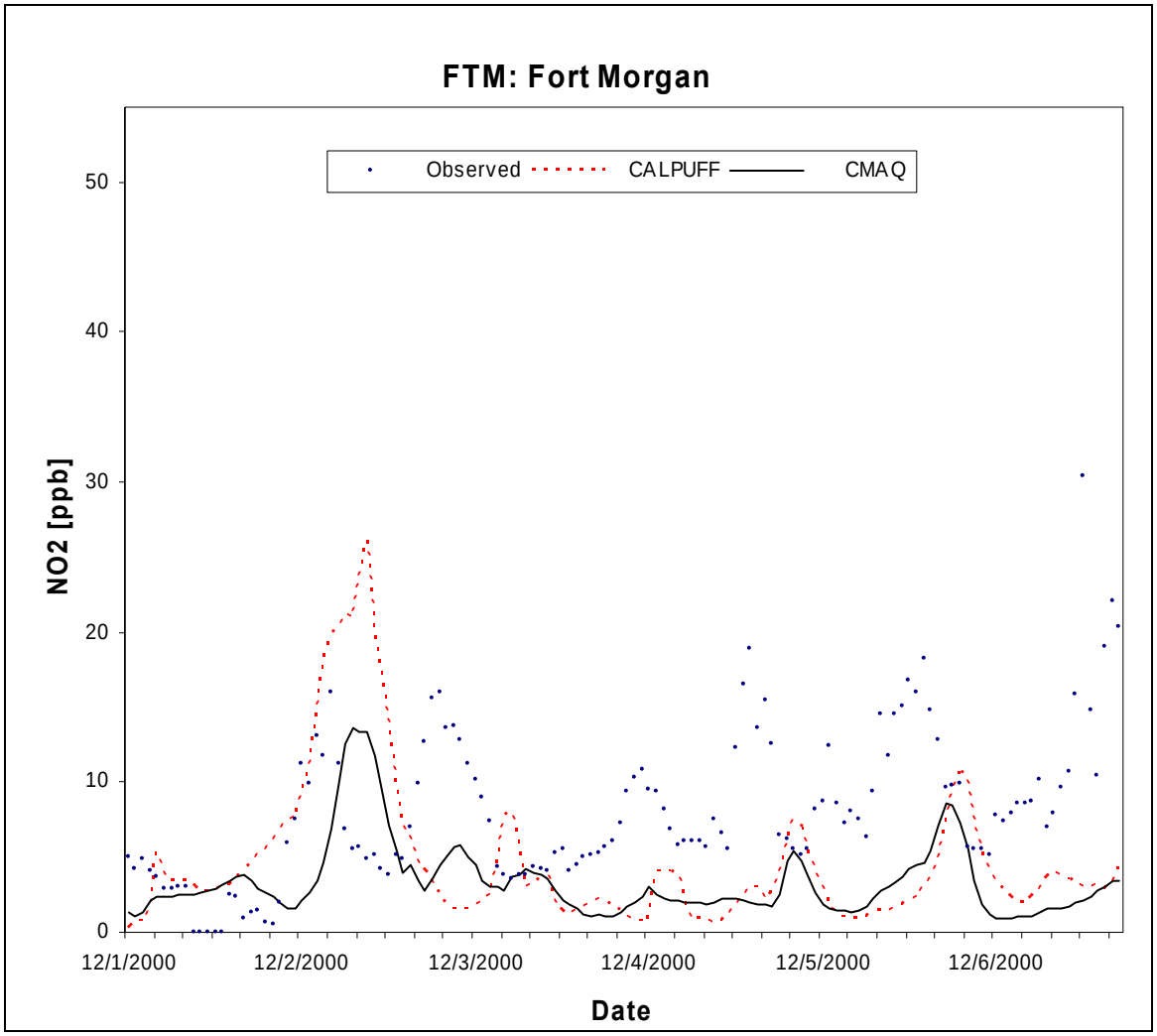

Figure E-2. Observed and predicted NO_2 concentrations at FTM for Case 1.

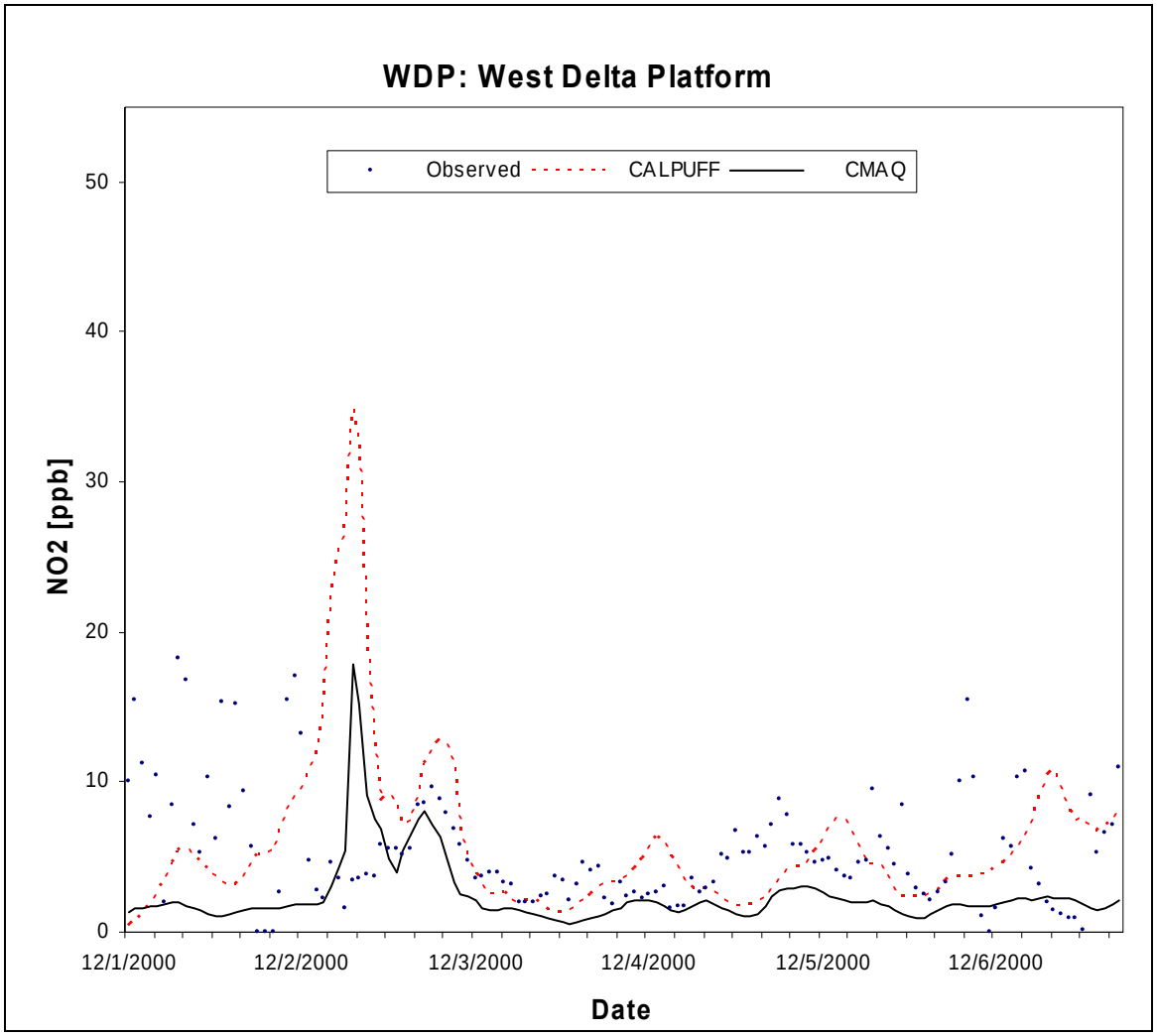

Figure E-3. Observed and predicted NO_2 concentrations at WDP for Case 1.

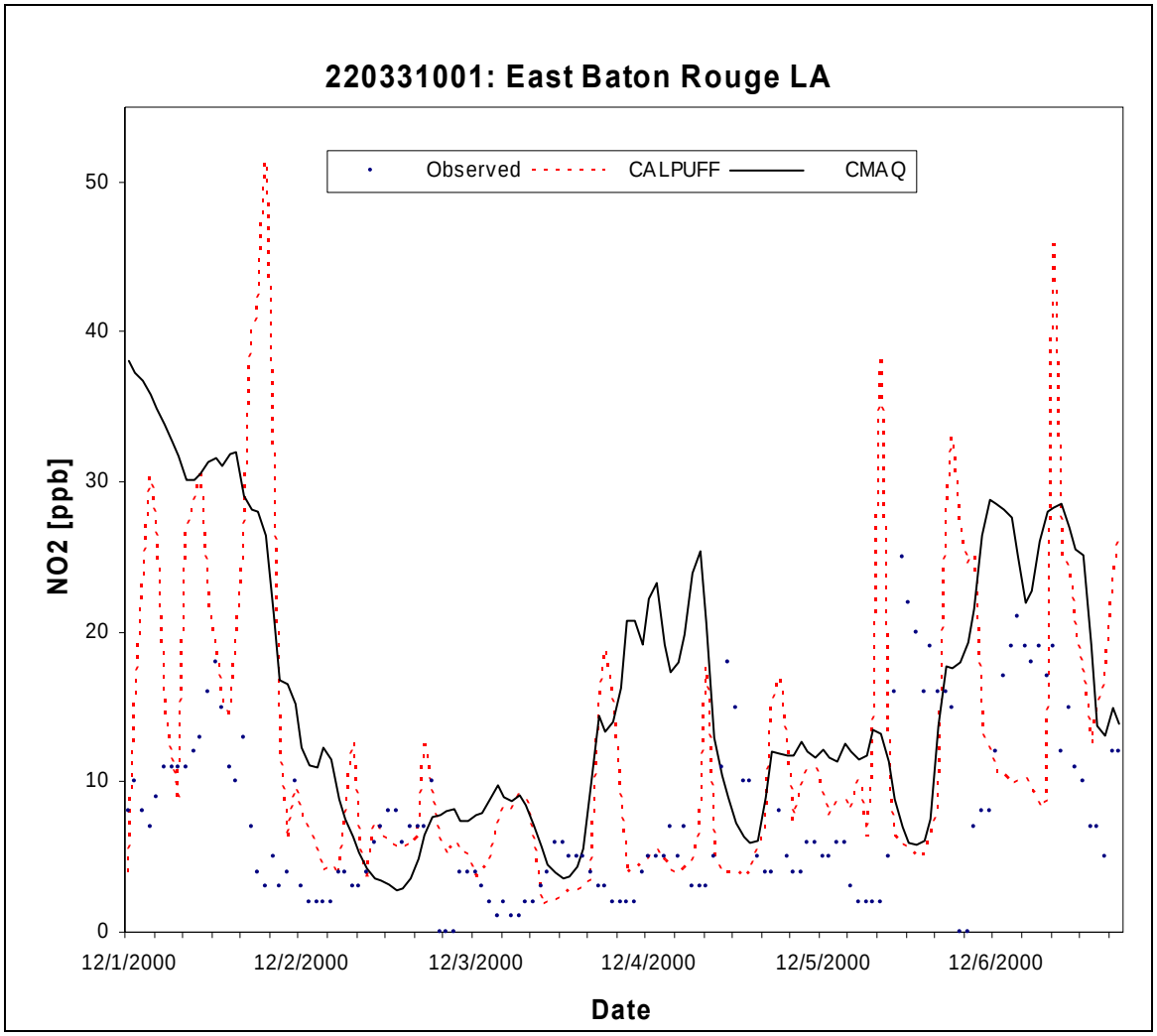

Figure E-4. Observed and predicted NO_2 concentrations at East Baton Rouge for Case 1.

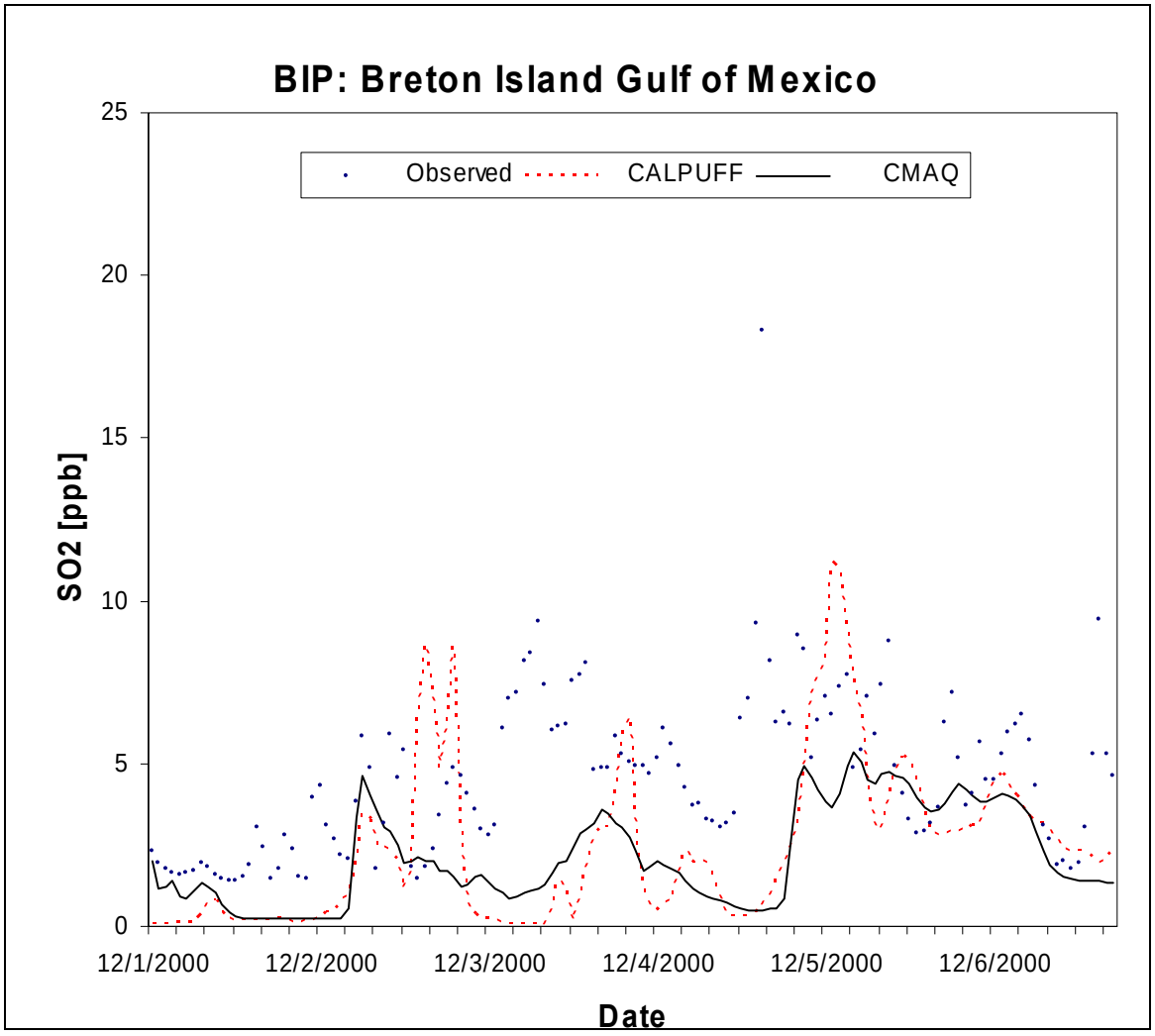

Figure E-5. Observed and predicted SO_2 concentrations at BIP for Case 1.

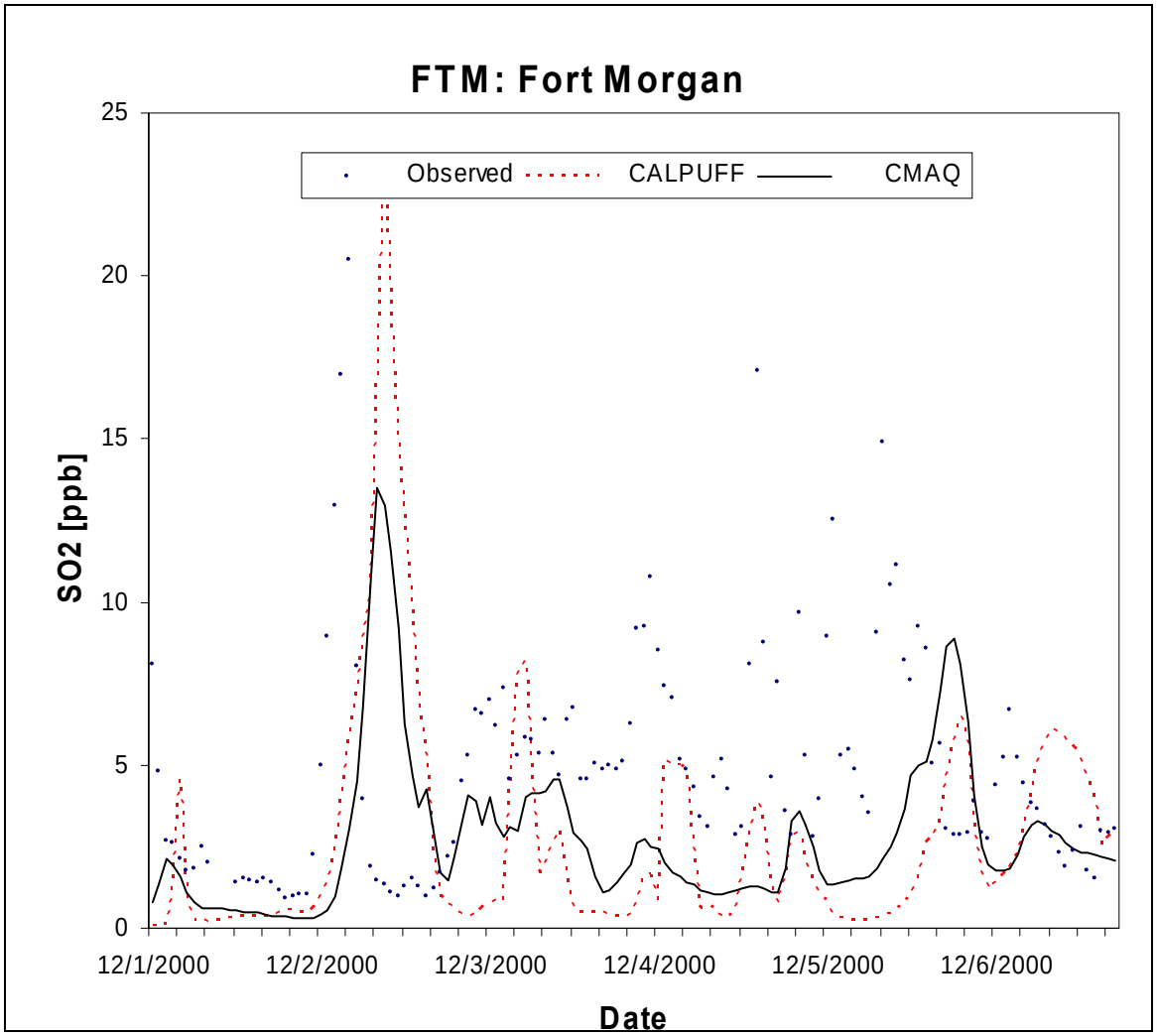

Figure E-6. Observed and predicted SO_2 concentrations at FTM for Case 1.

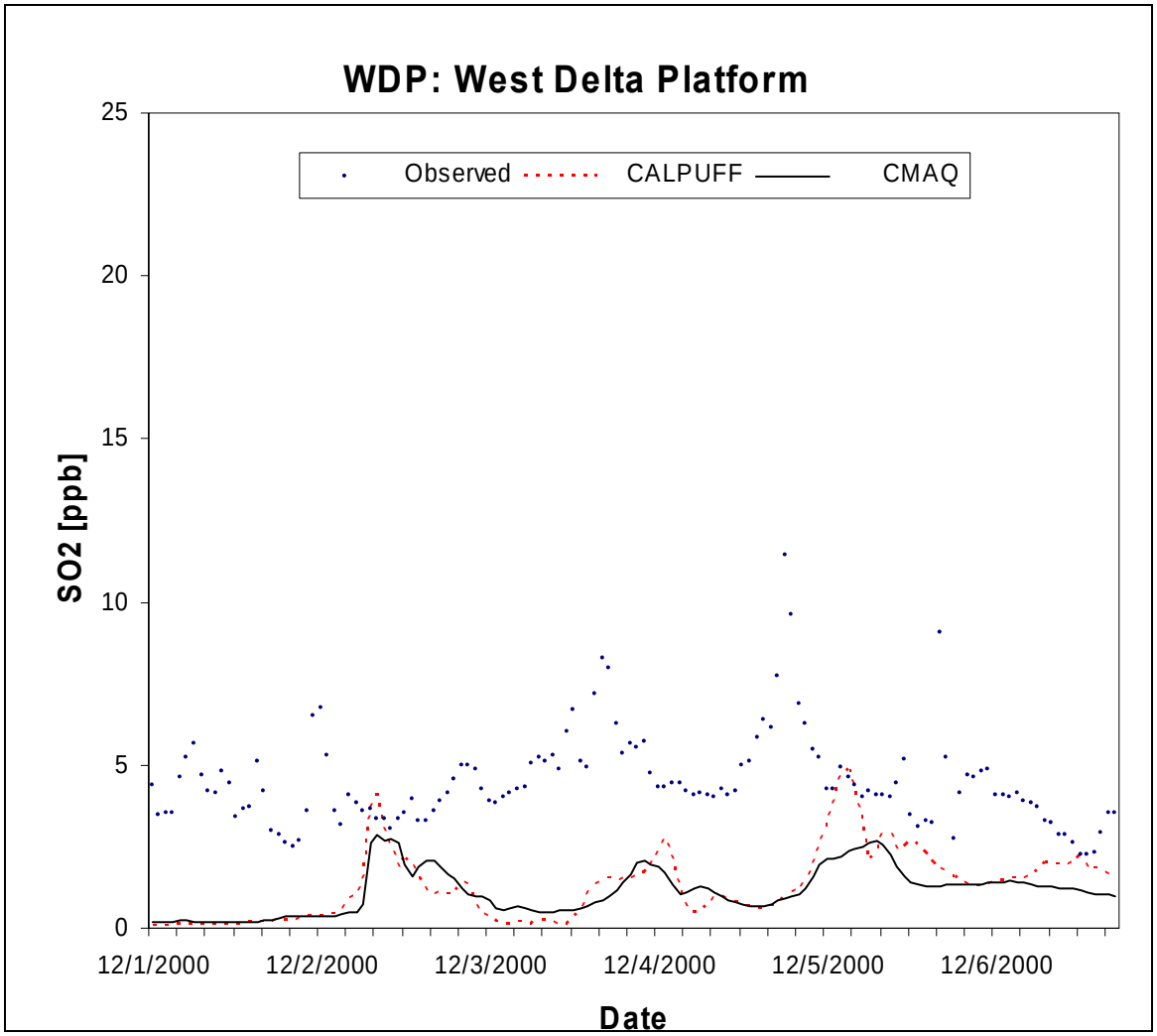

Figure E-7. Observed and predicted SO_2 concentrations at WDP for Case 1.

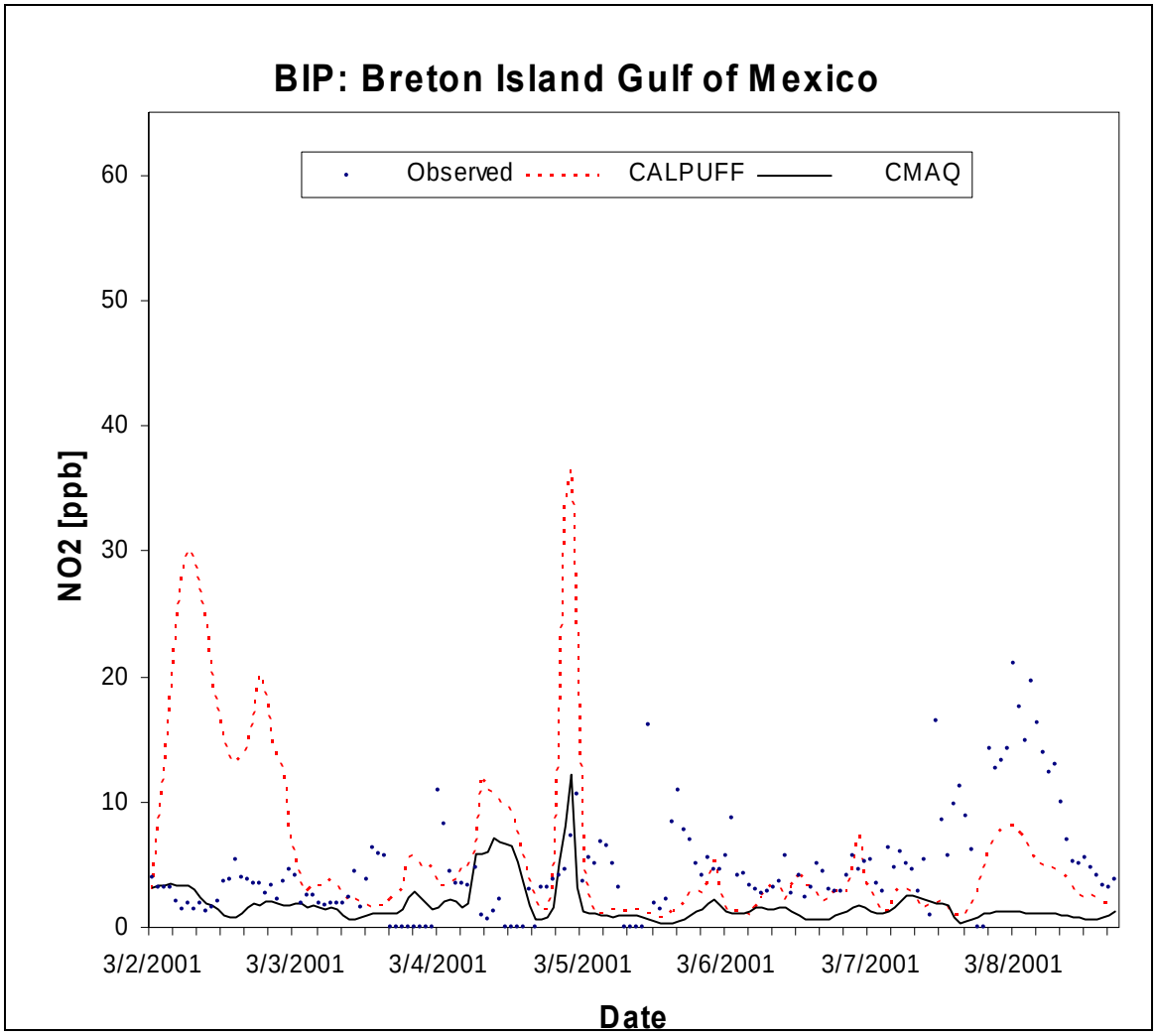

Figure E-8. Observed and predicted NO_2 concentrations at BIP for Case 2.

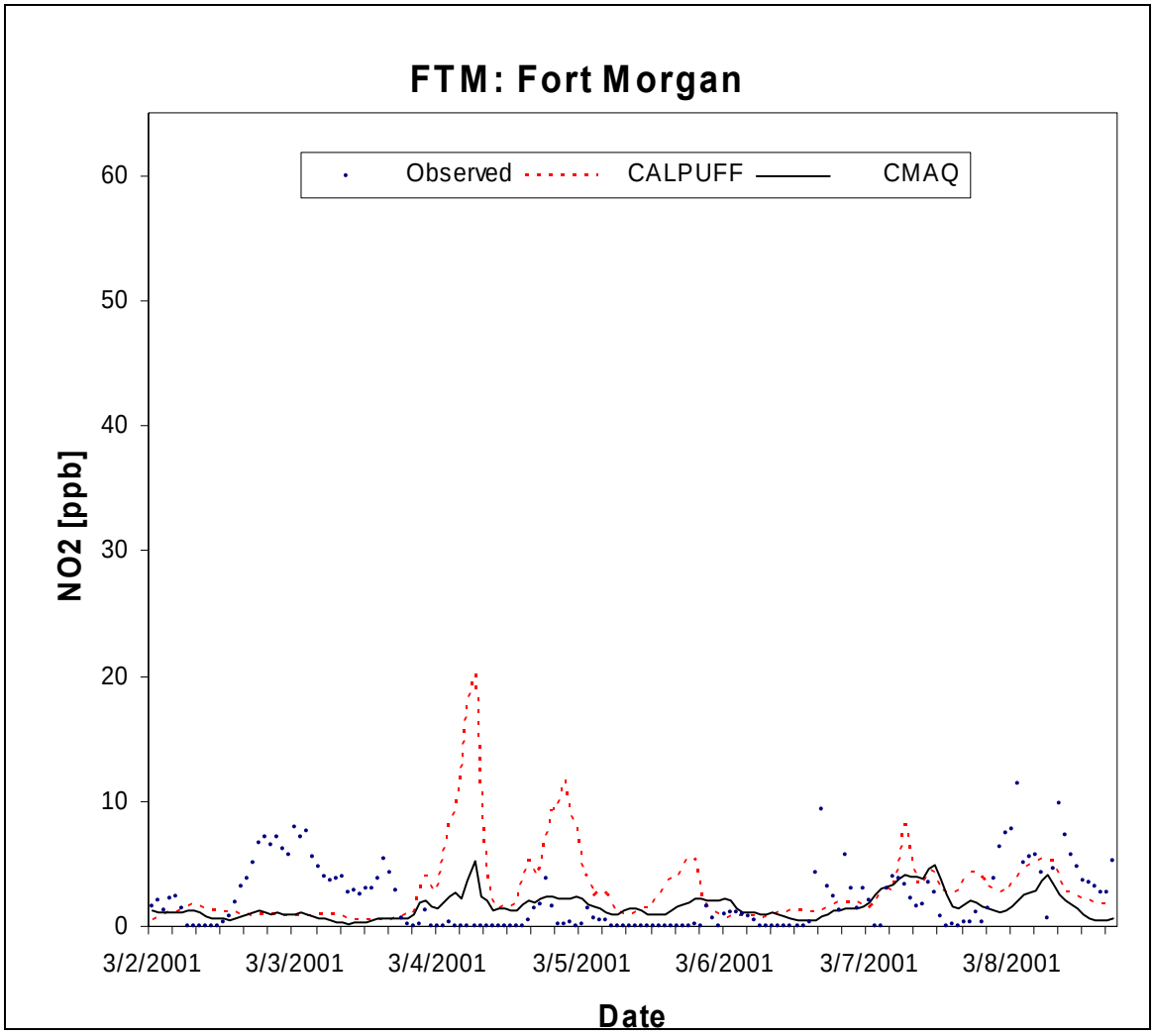

Figure E-9. Observed and predicted NO_2 concentrations at FTM for Case 2.

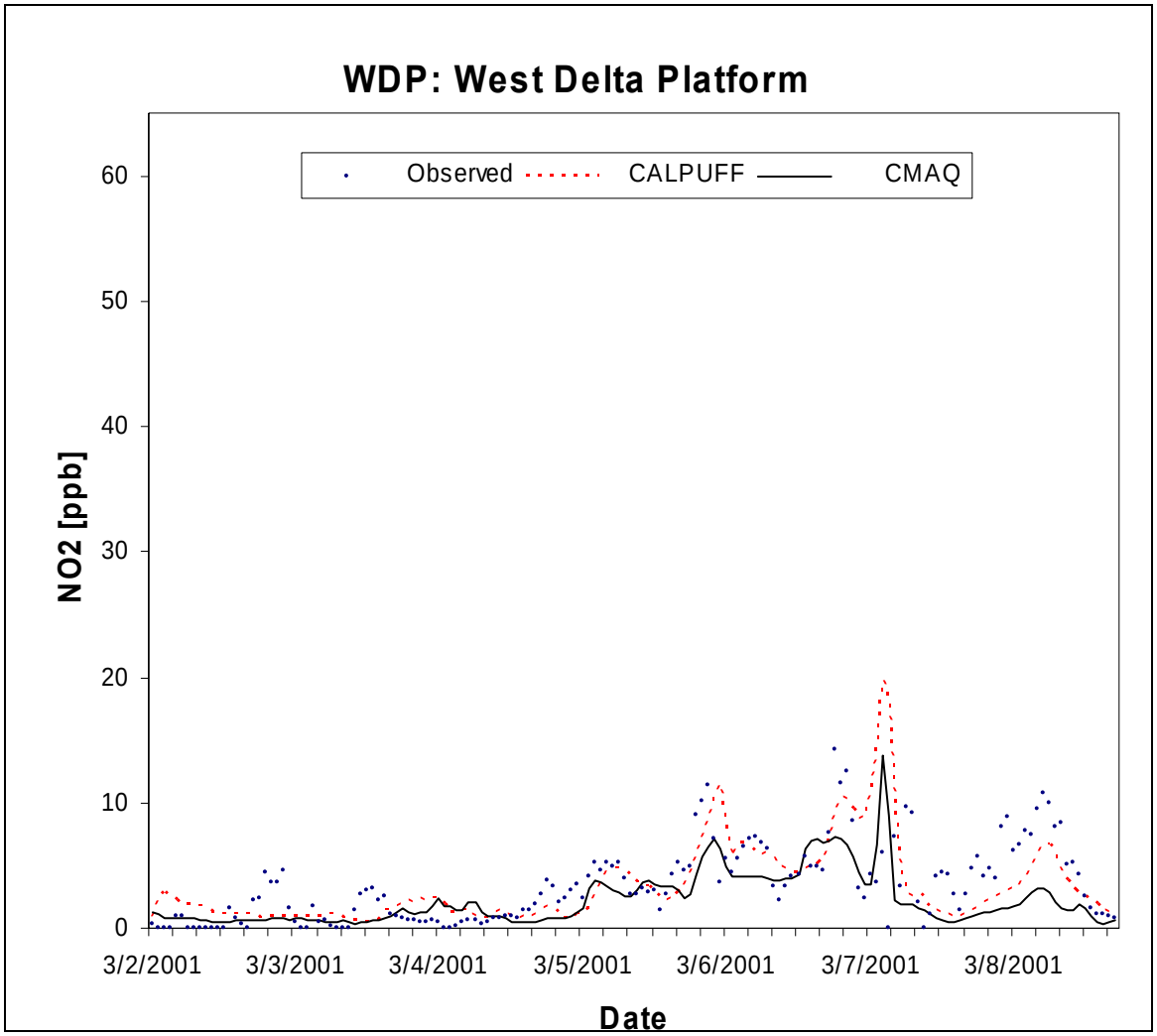

Figure E-10. Observed and predicted NO_2 concentrations at WDP for Case 2.

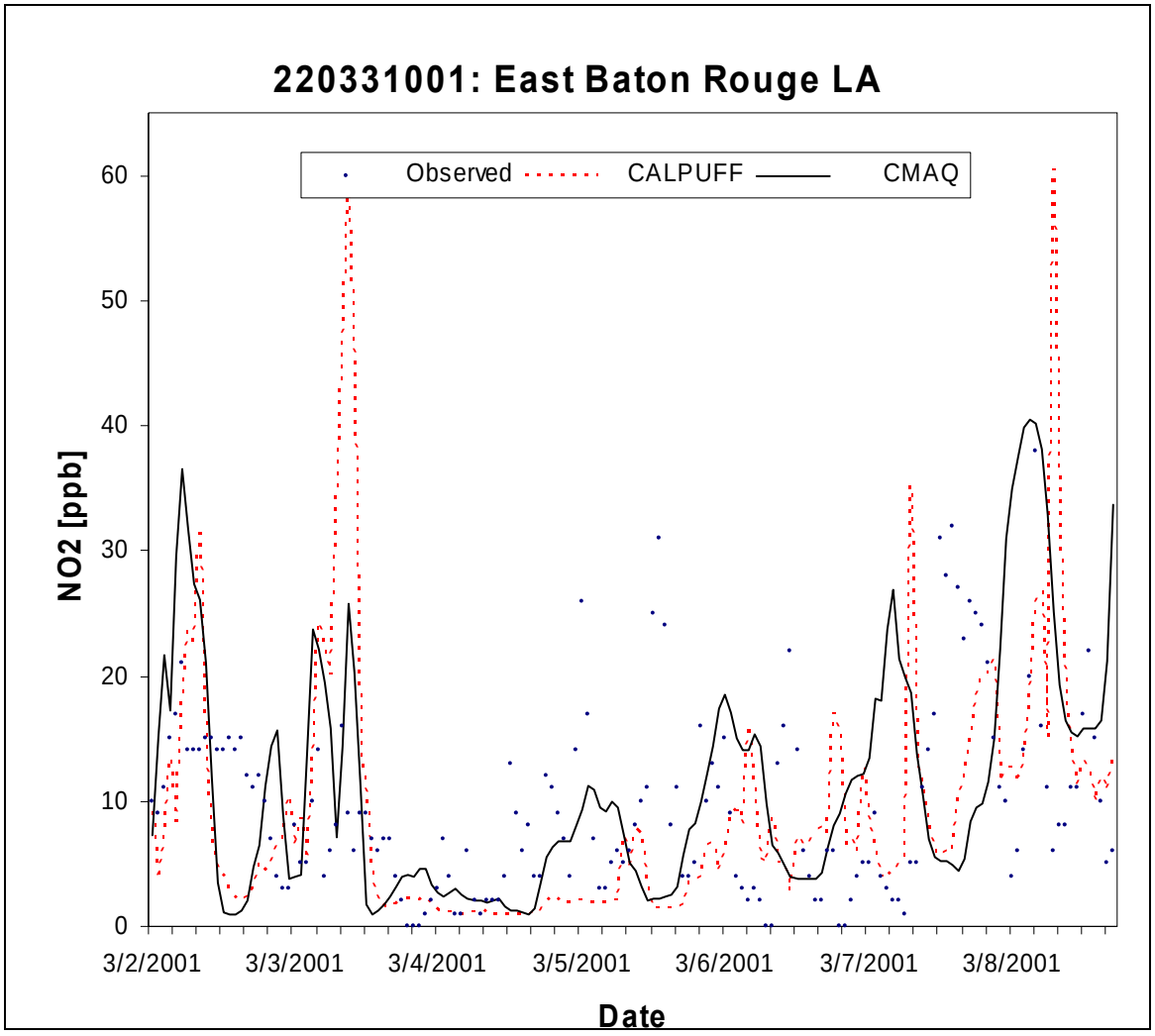

Figure E-11. Observed and predicted NO_2 concentrations at East Baton Rouge for Case 2.

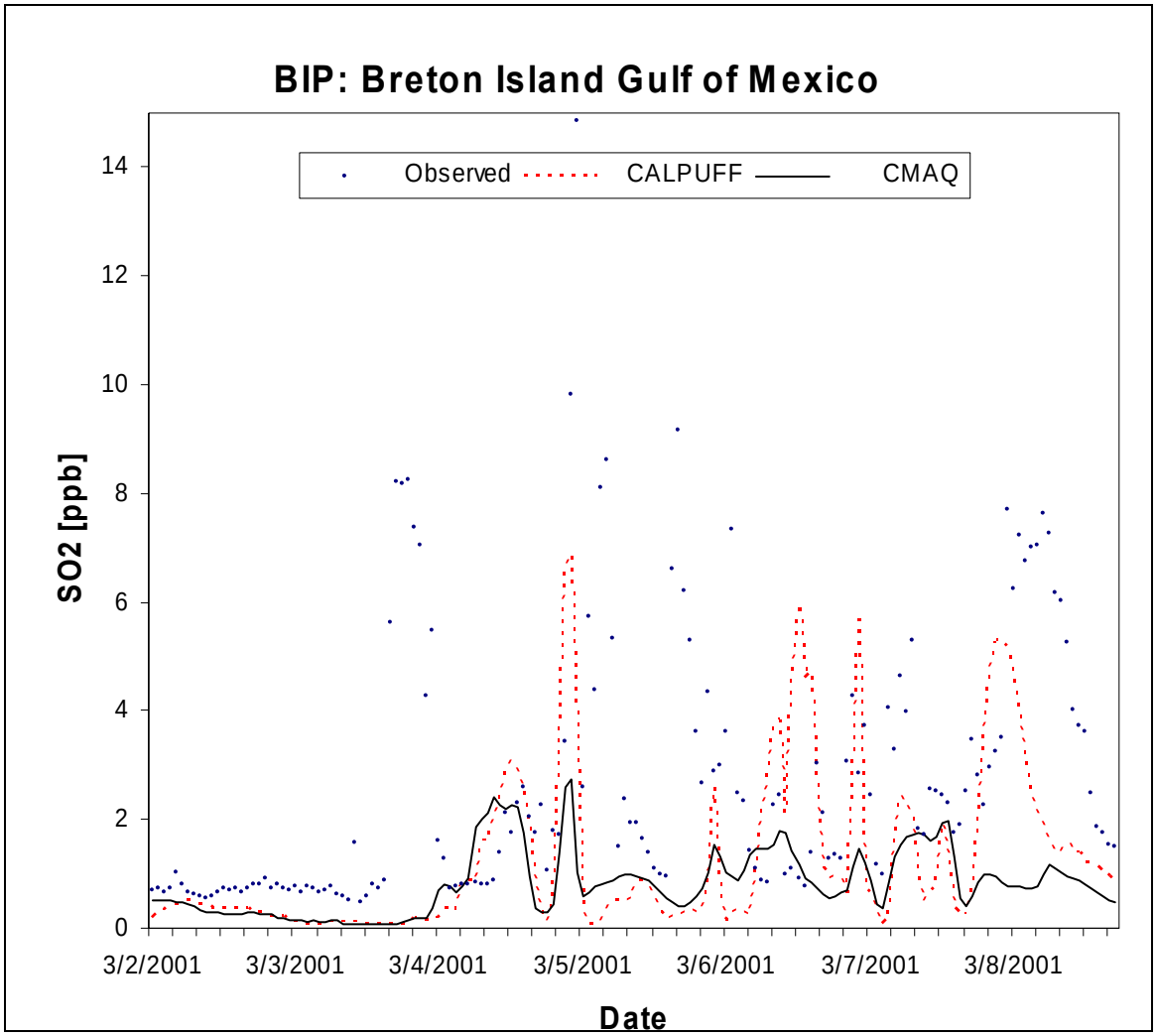

Figure E-12. Observed and predicted SO_2 concentrations at BIP for Case 2.

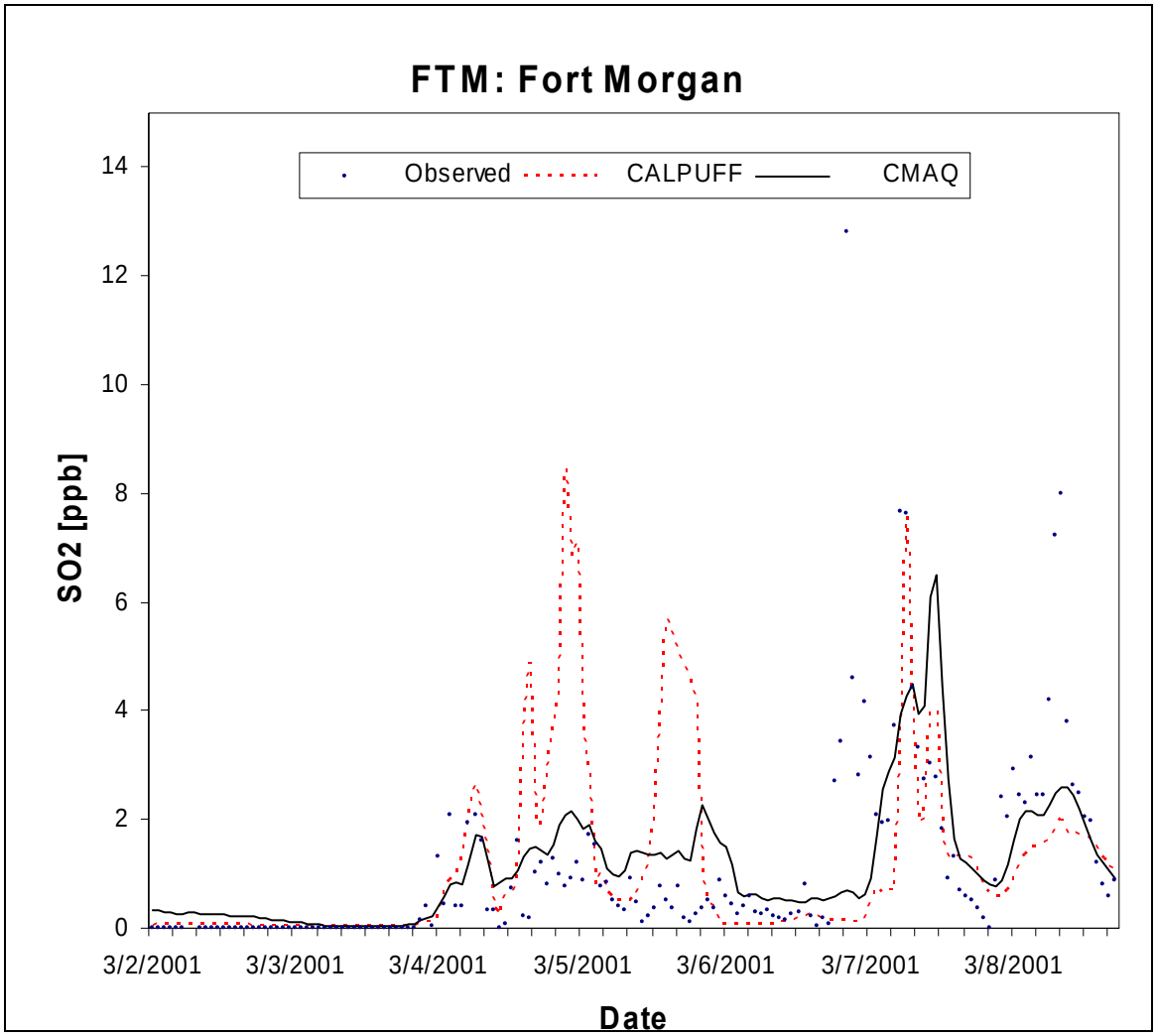

Figure E-13. Observed and predicted SO_2 concentrations at FTM for Case 2.

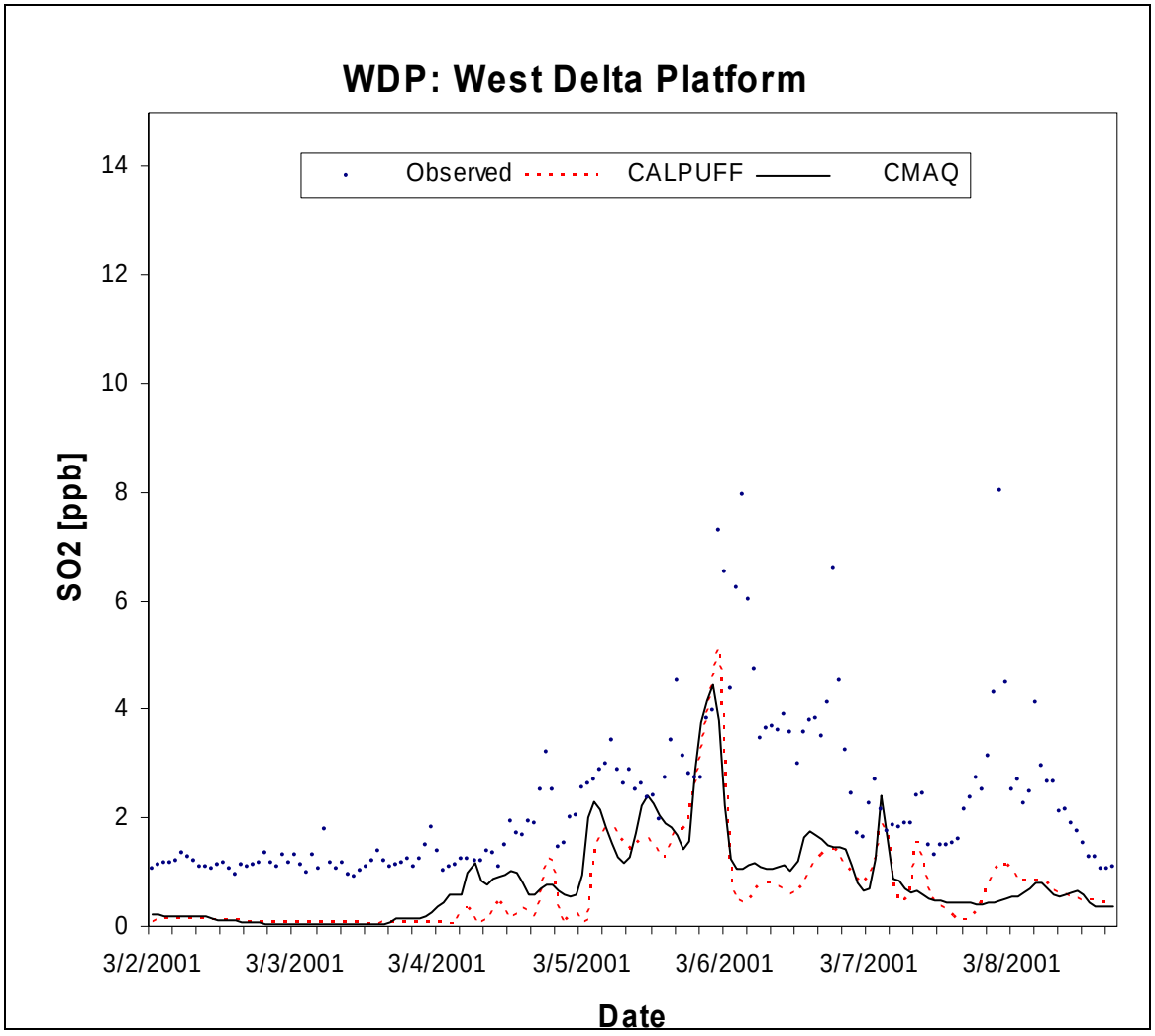

Figure E-14. Observed and predicted SO_2 concentrations at WDP for Case 2.

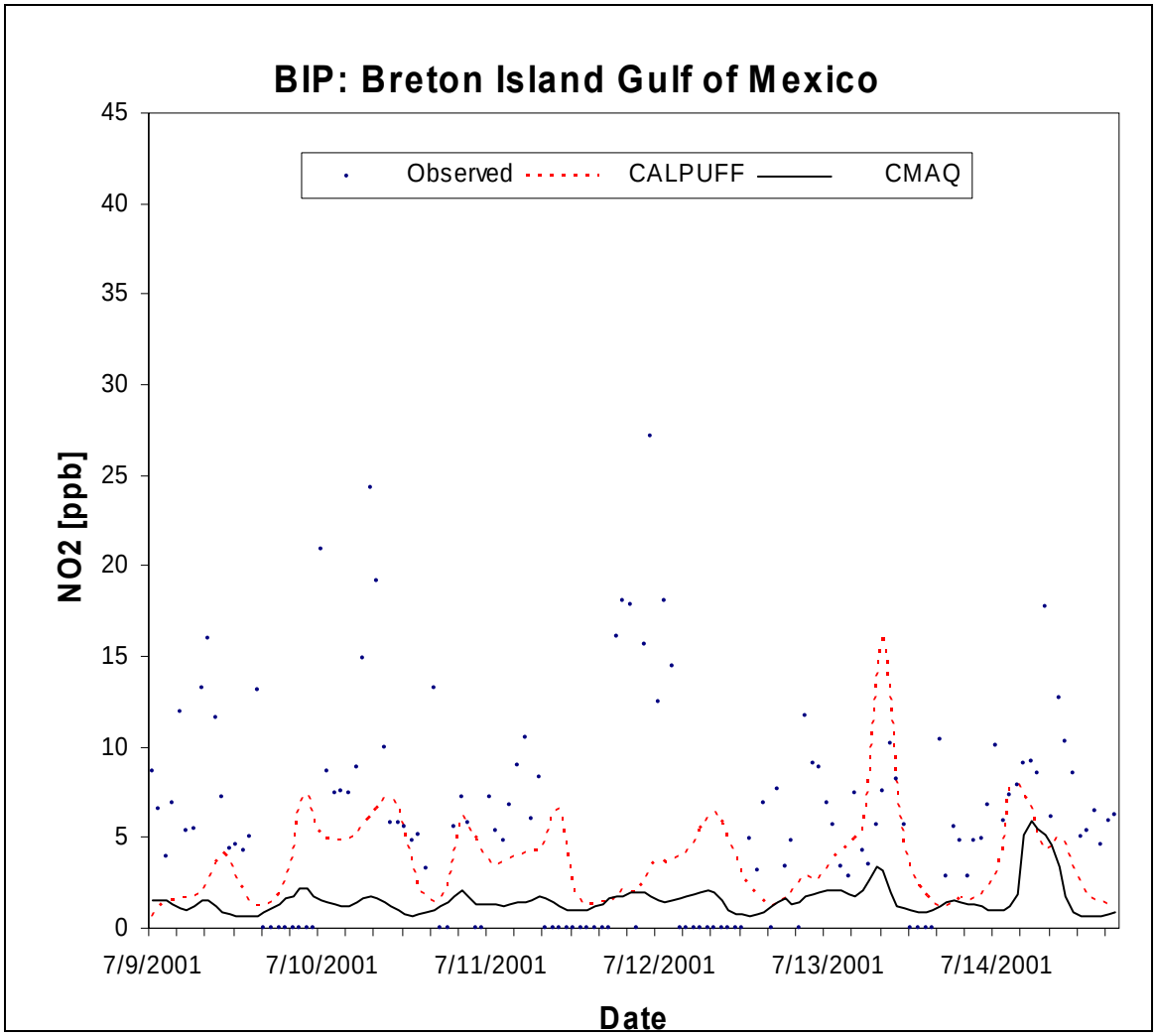

Figure E-15. Observed and predicted NO_2 concentrations at BIP for Case 3.

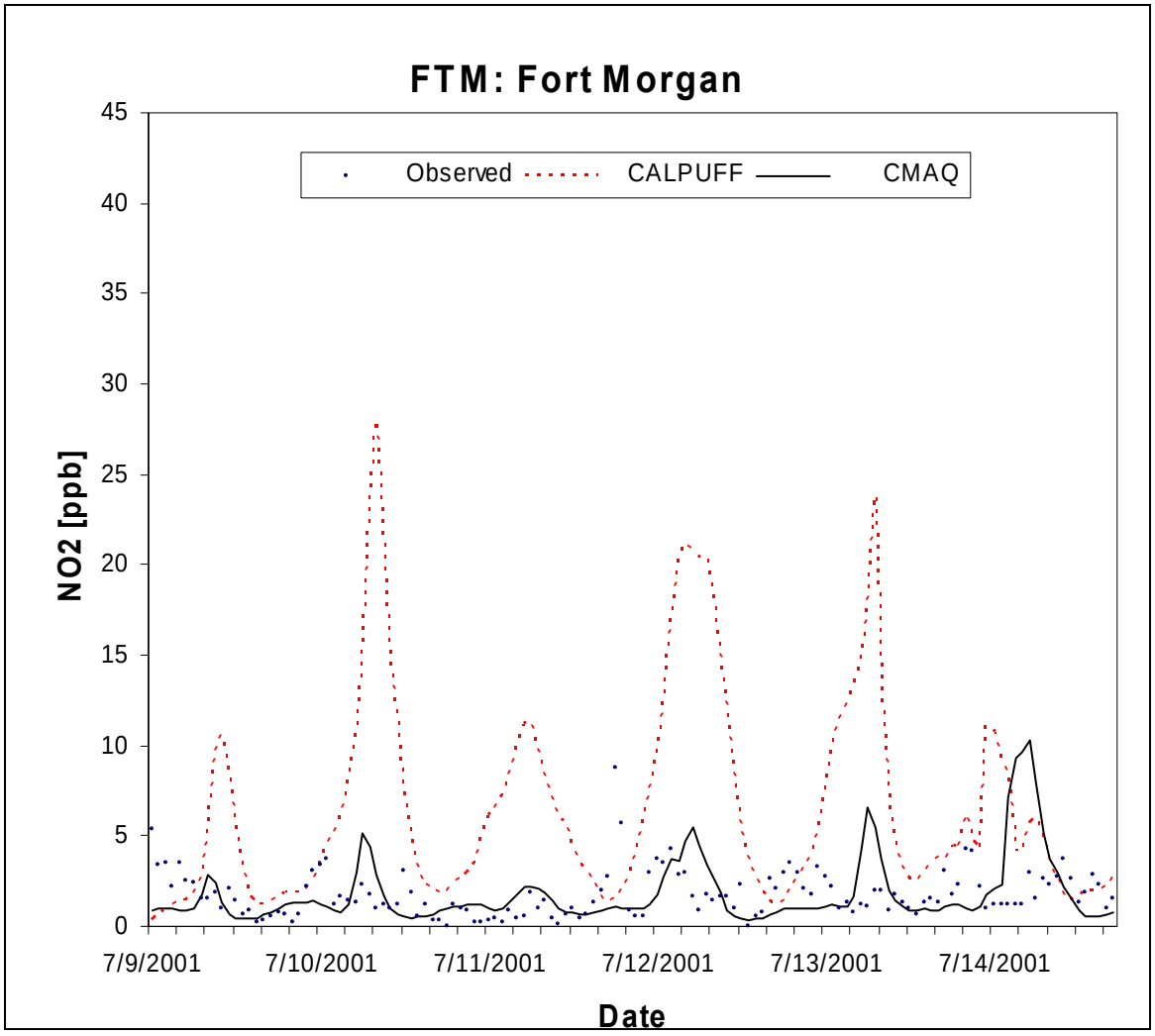

Figure E-16. Observed and predicted NO_2 concentrations at FTM for Case 3.

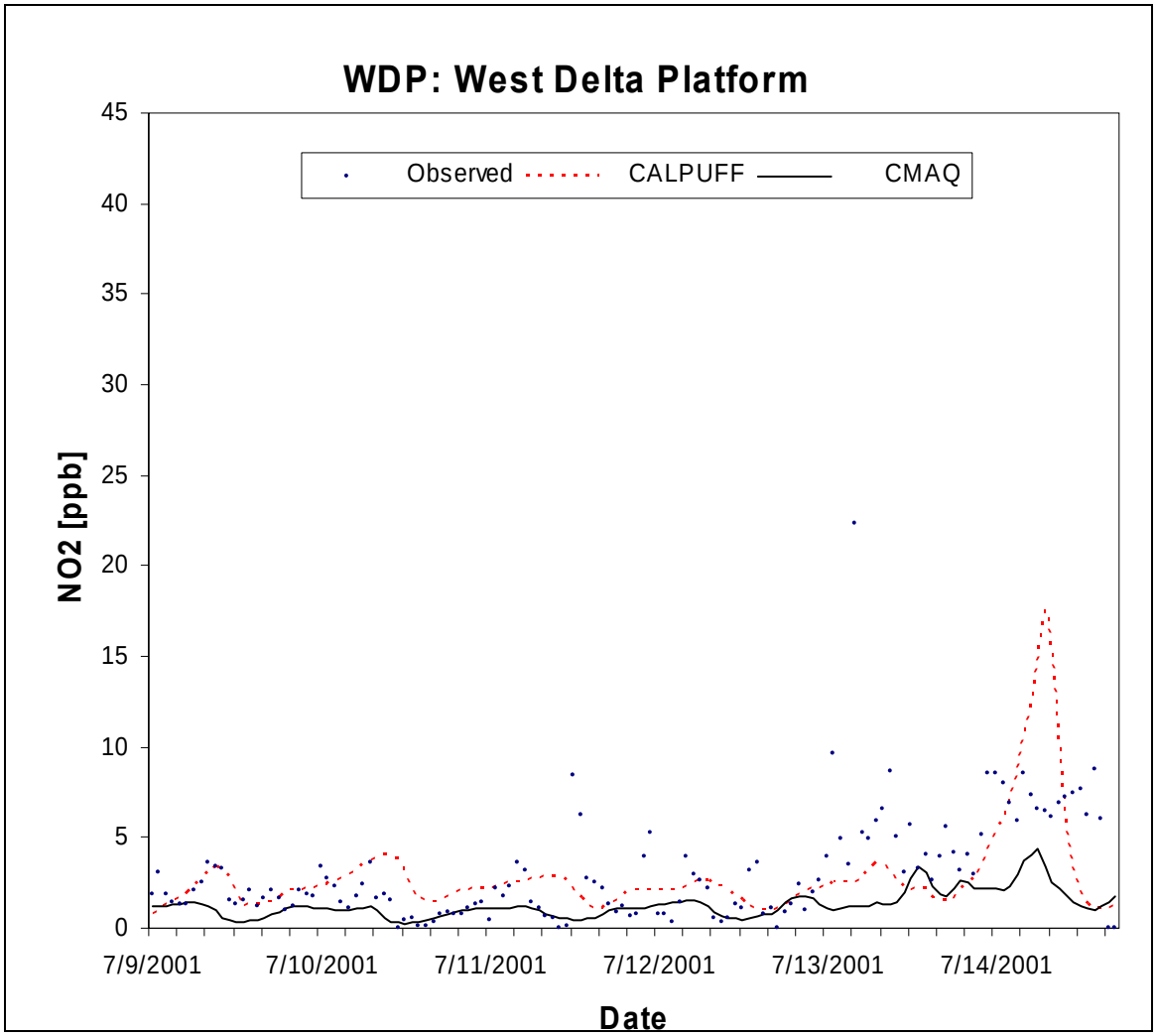

Figure E-17. Observed and predicted NO_2 concentrations at WDP for Case 3.

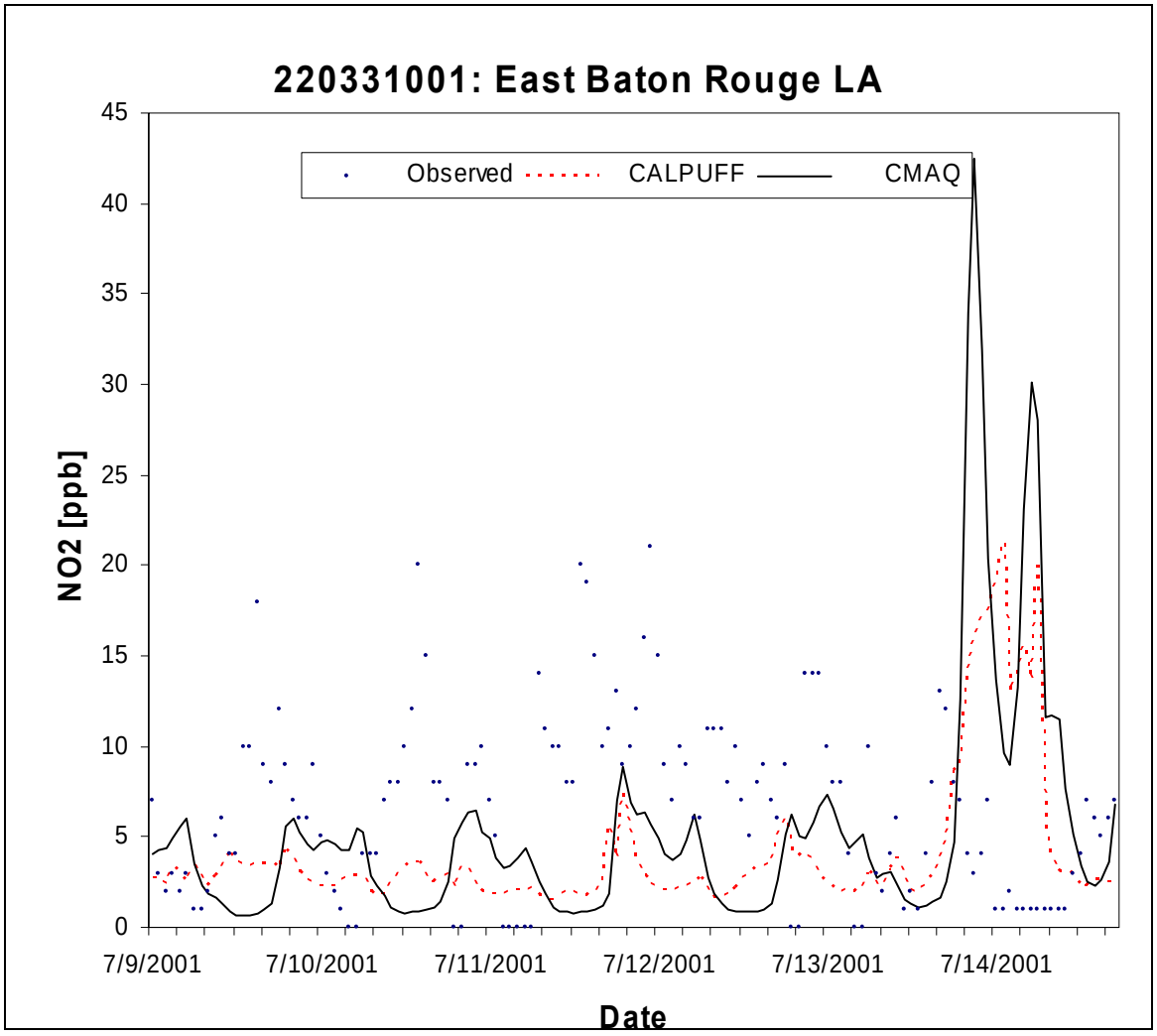

Figure E-18. Observed and predicted NO_2 concentrations at East Baton Rouge for Case 3.

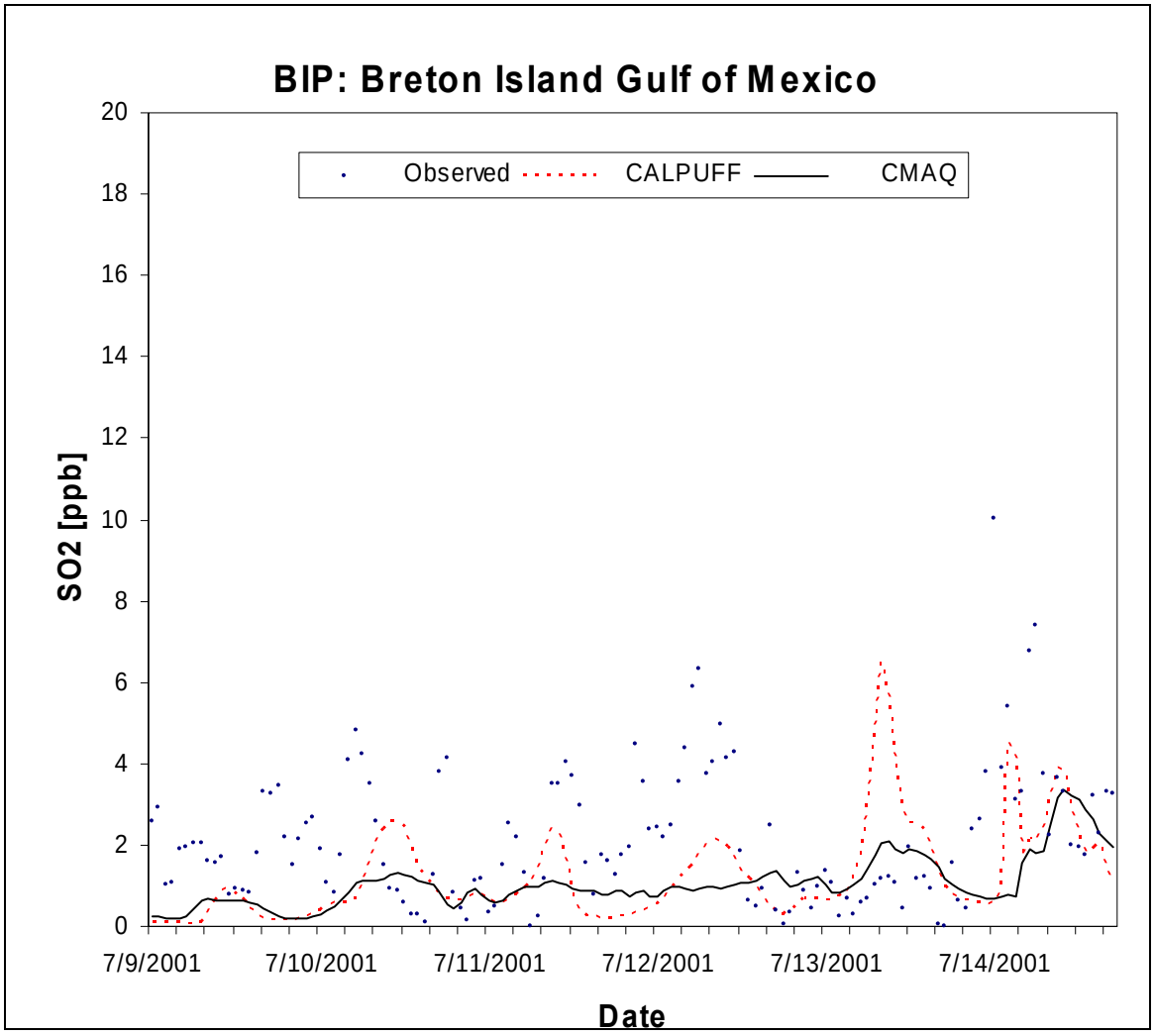

Figure E-19. Observed and predicted SO_2 concentrations at BIP for Case 3.

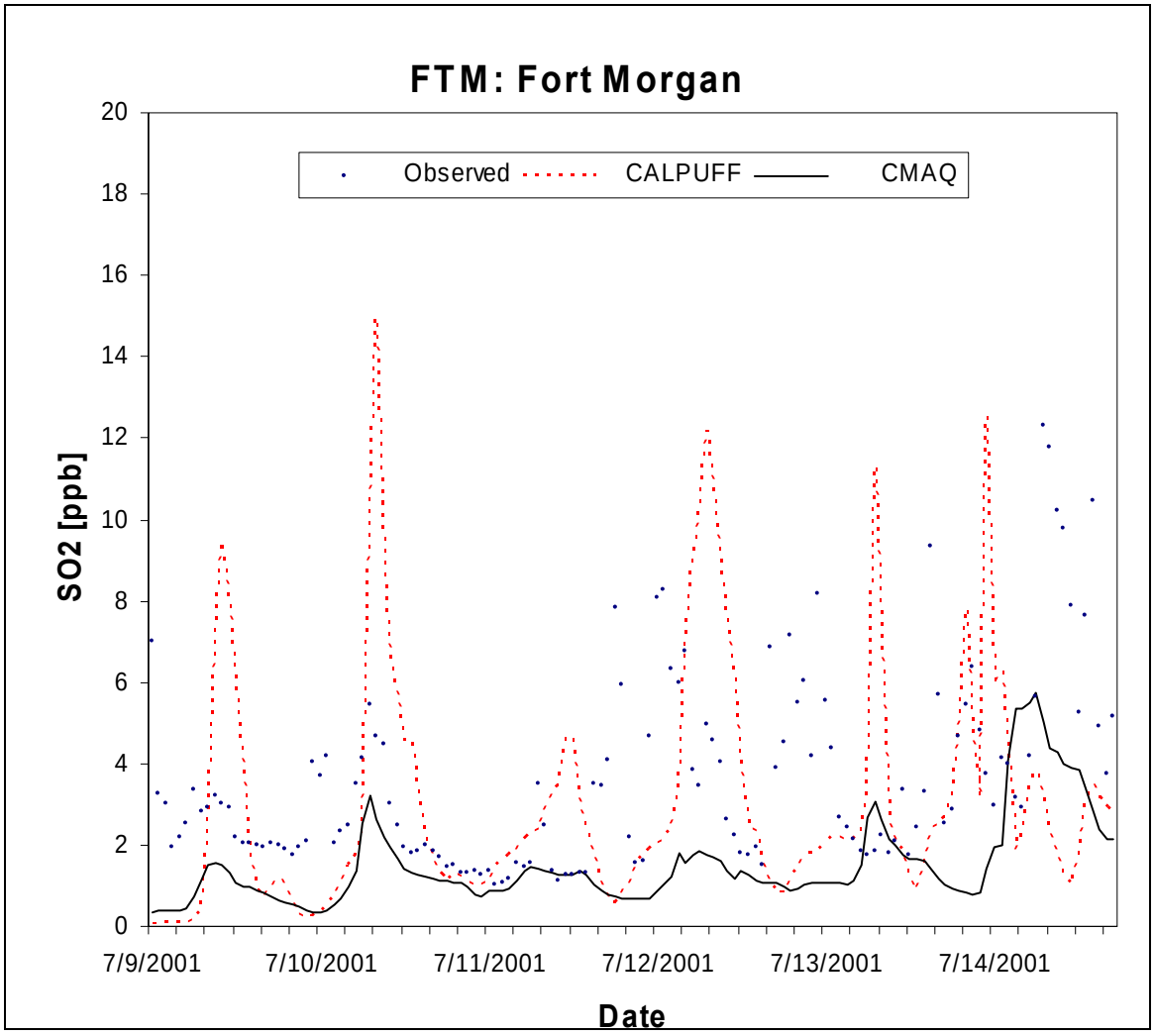

Figure E-20. Observed and predicted SO_2 concentrations at FTM for Case 3.

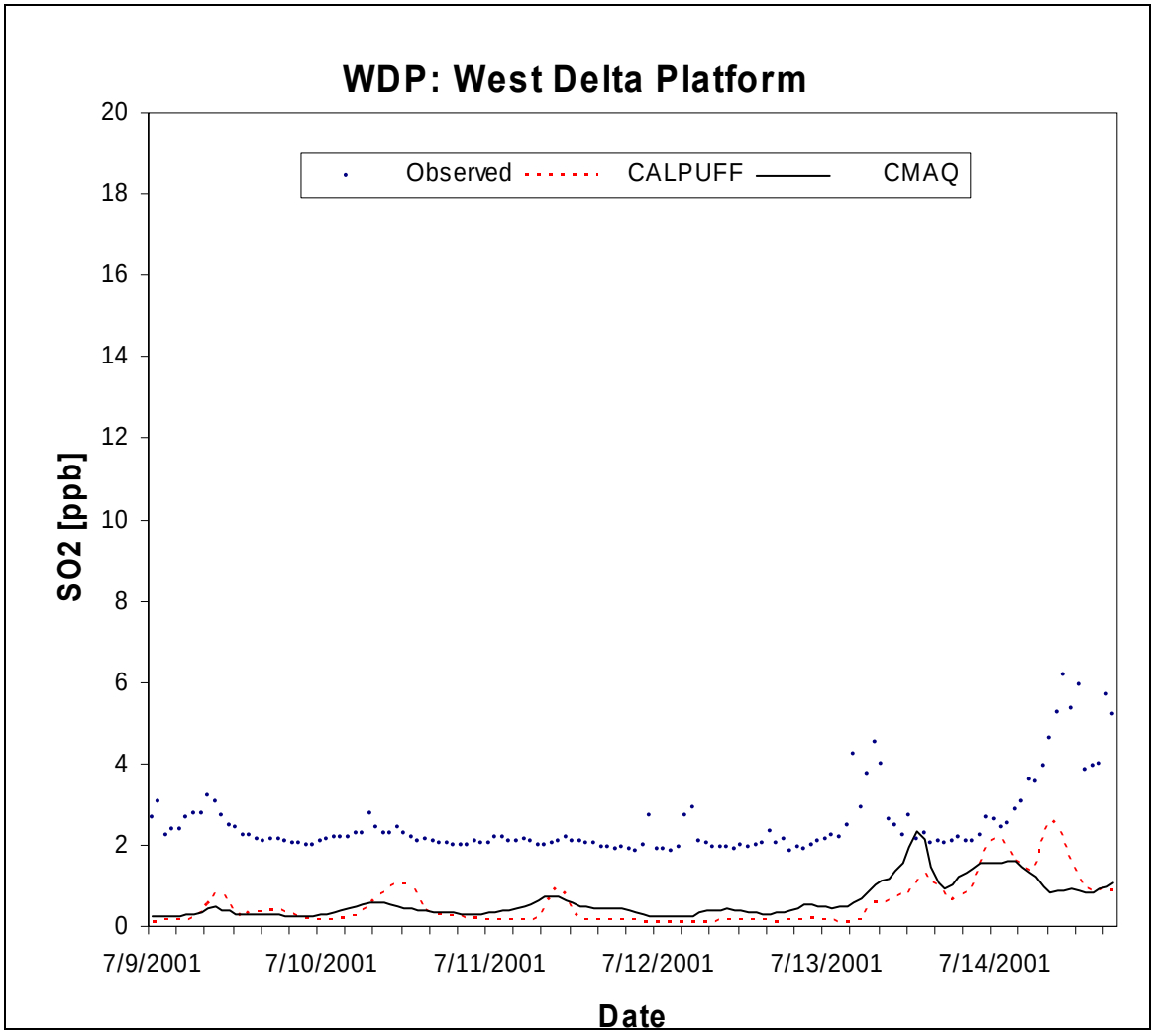

Figure E-21. Observed and predicted SO_2 concentrations at WDP for Case 3.

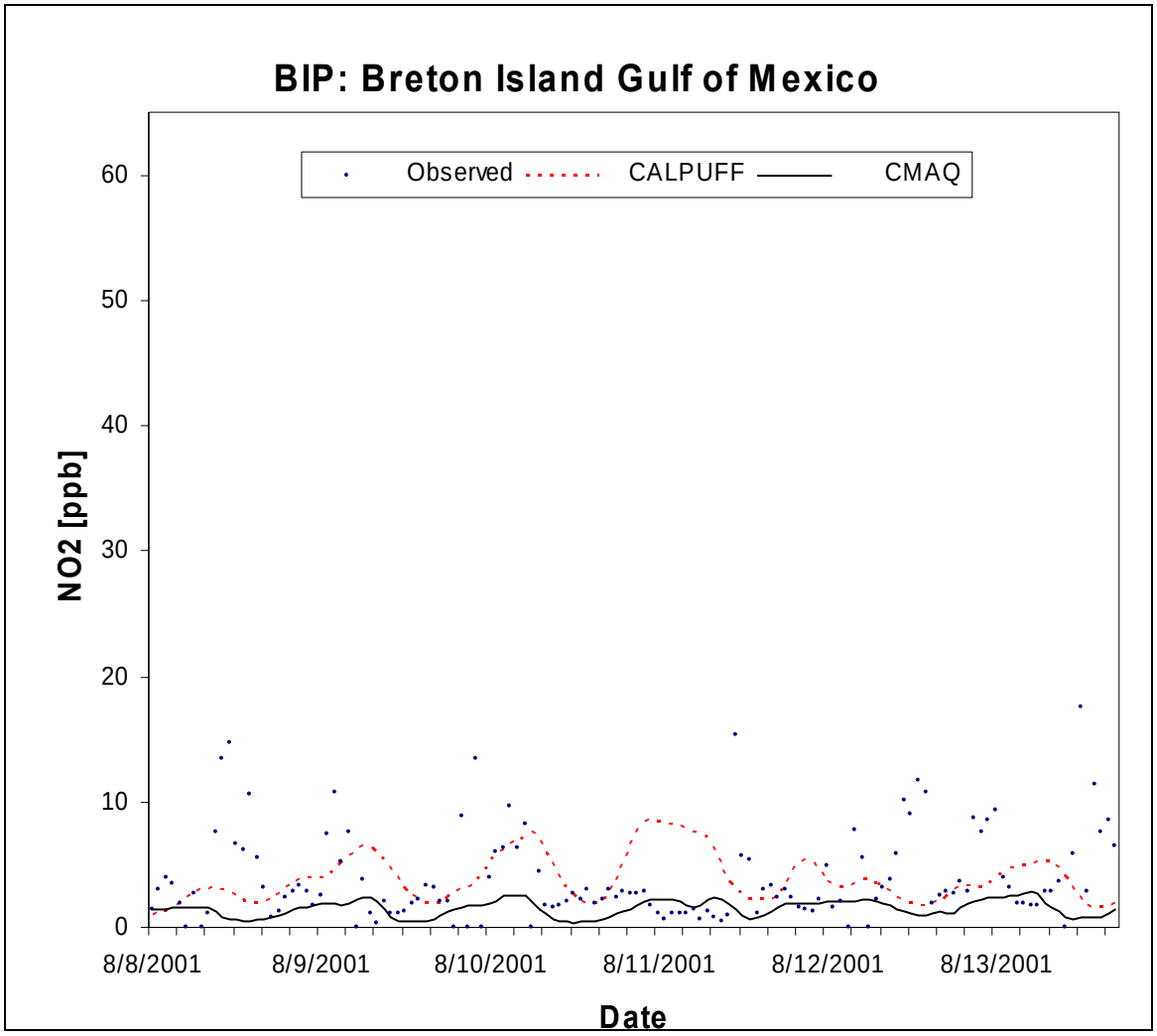

Figure E-22. Observed and predicted NO_2 concentrations at BIP for Case 4.

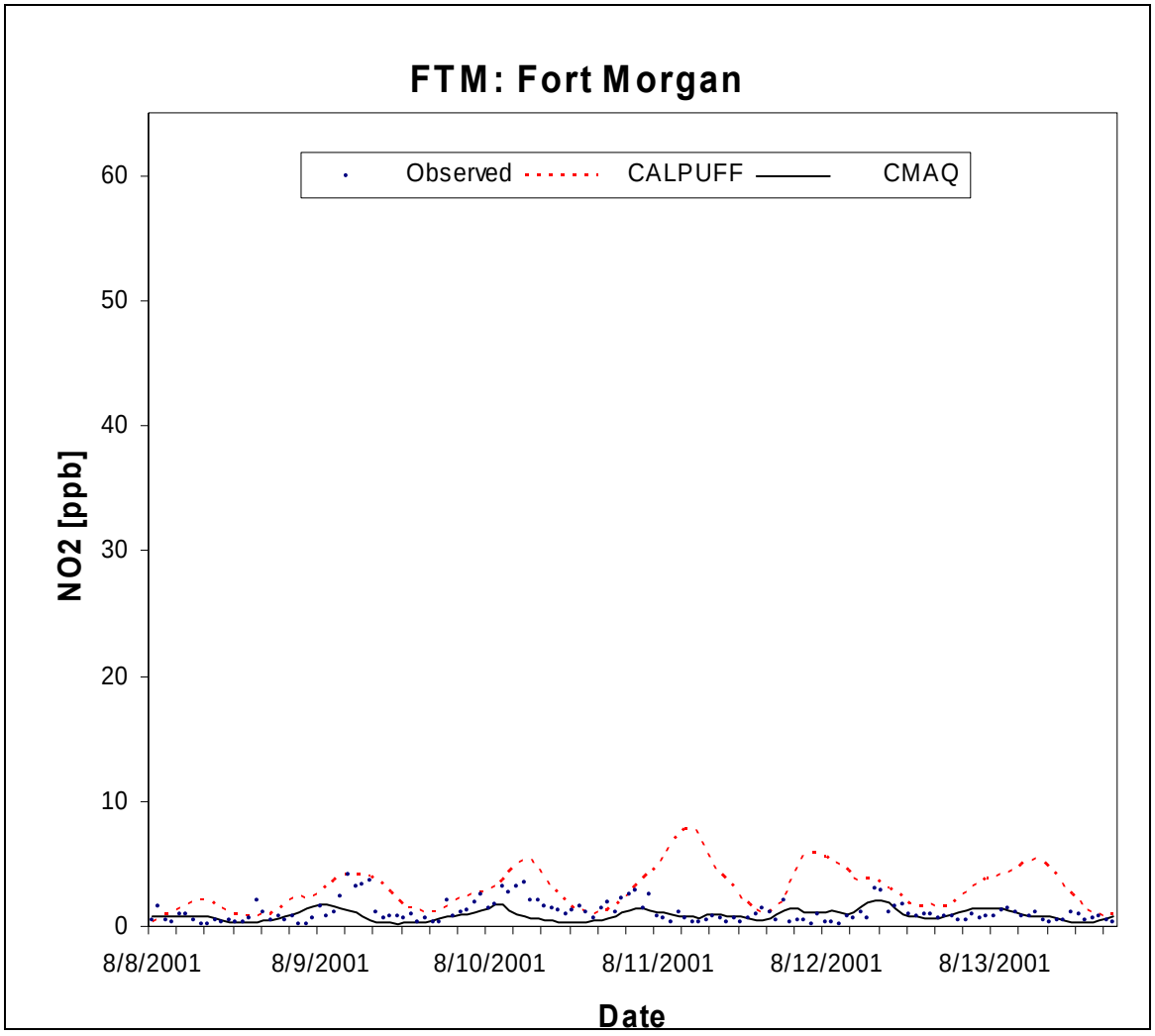

Figure E-23. Observed and predicted NO_2 concentrations at FTM for Case 4.

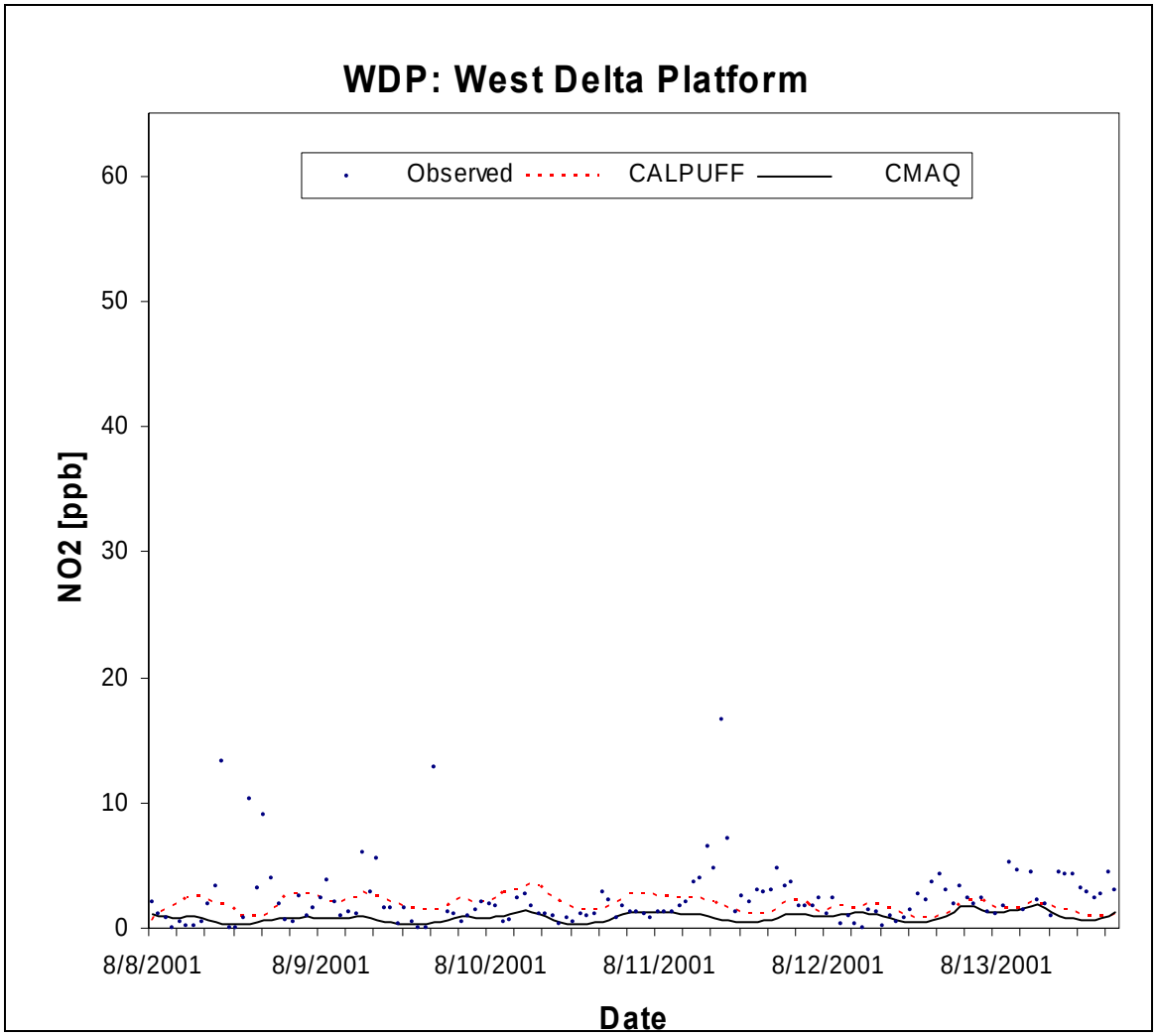

Figure E-24. Observed and predicted NO_2 concentrations at WDP for Case 4.

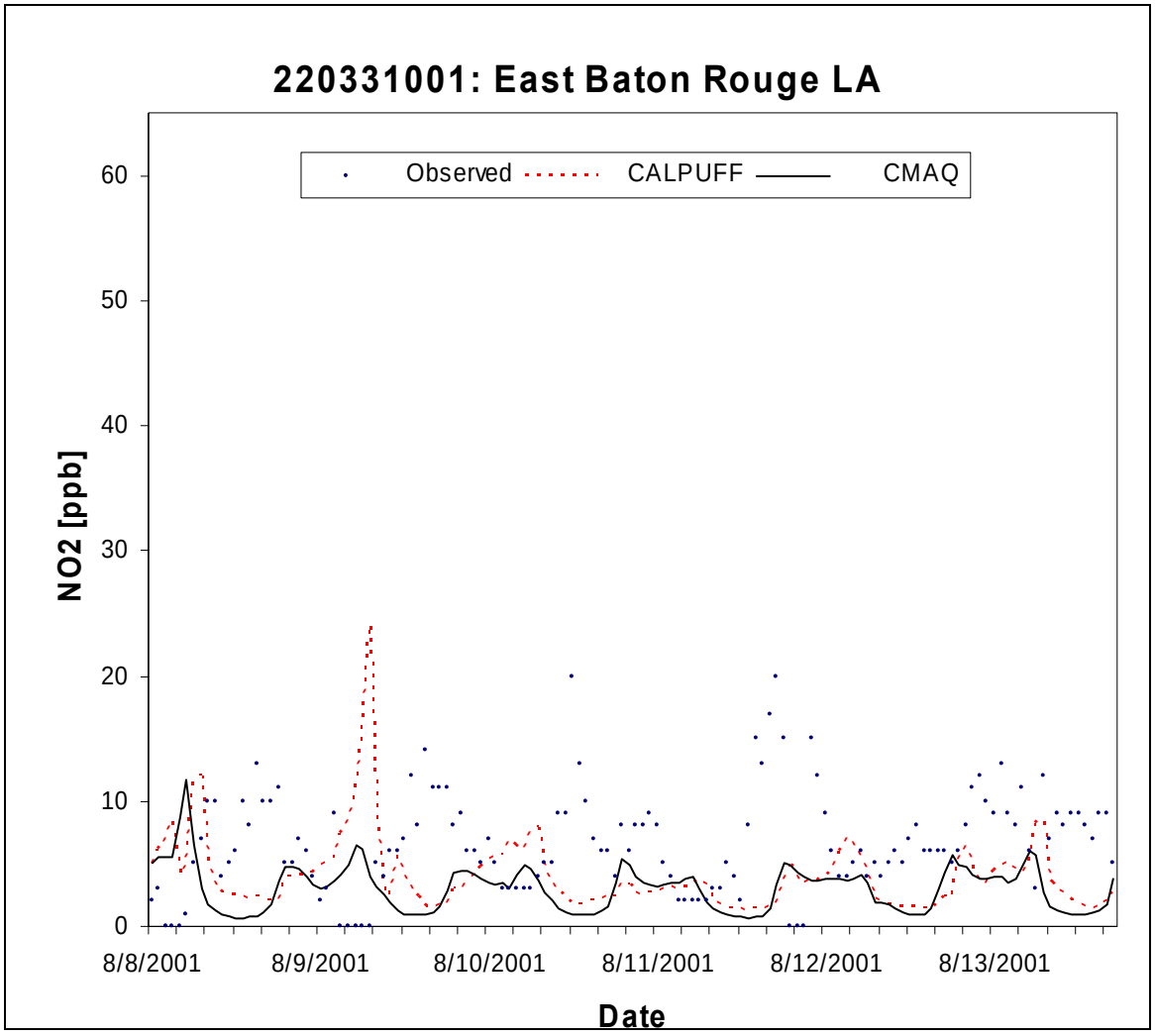

Figure E-25. Observed and predicted NO_2 concentrations at East Baton Rouge for Case 4.

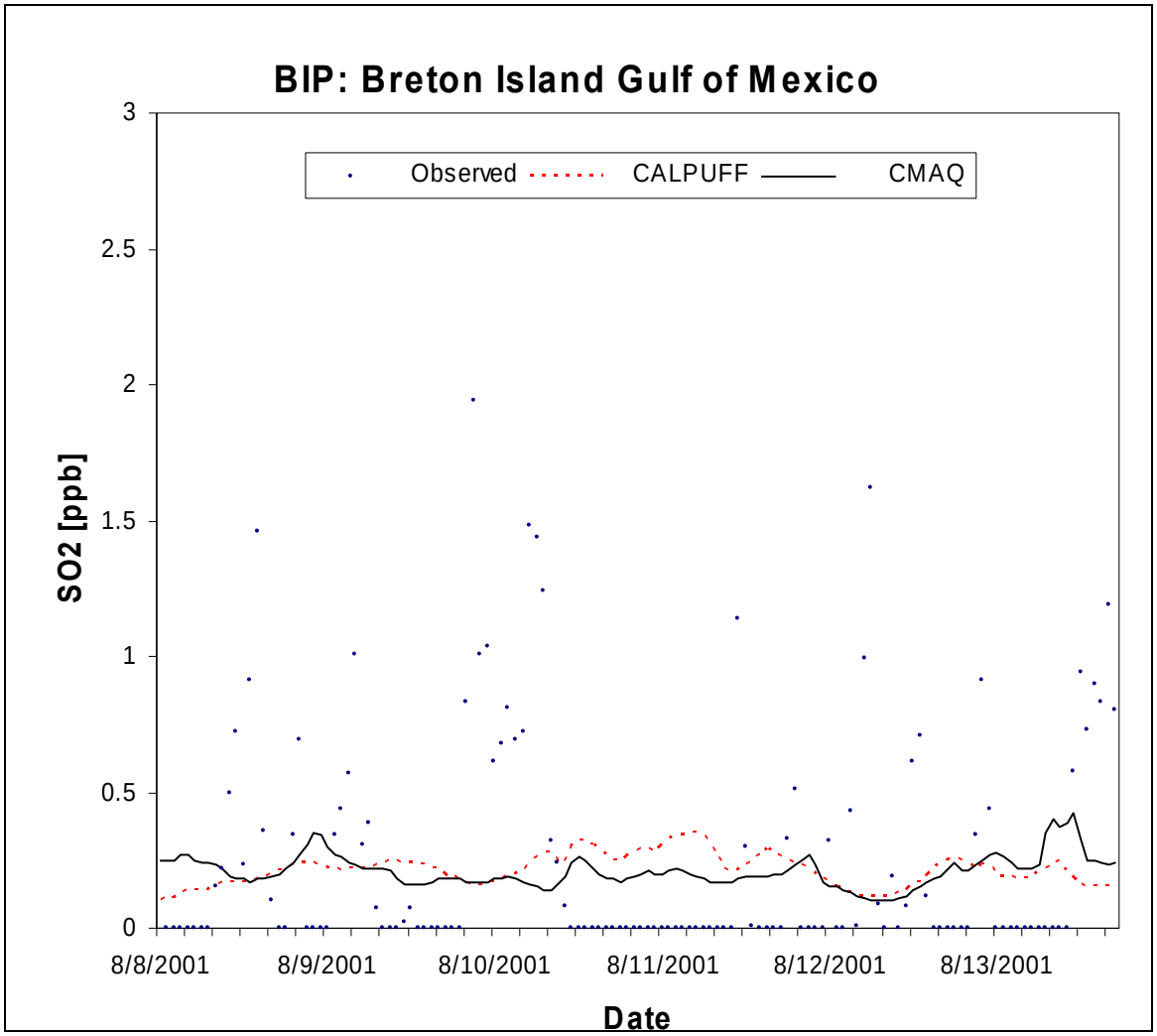

Figure E-26. Observed and predicted SO_2 concentrations at BIP for Case 4.

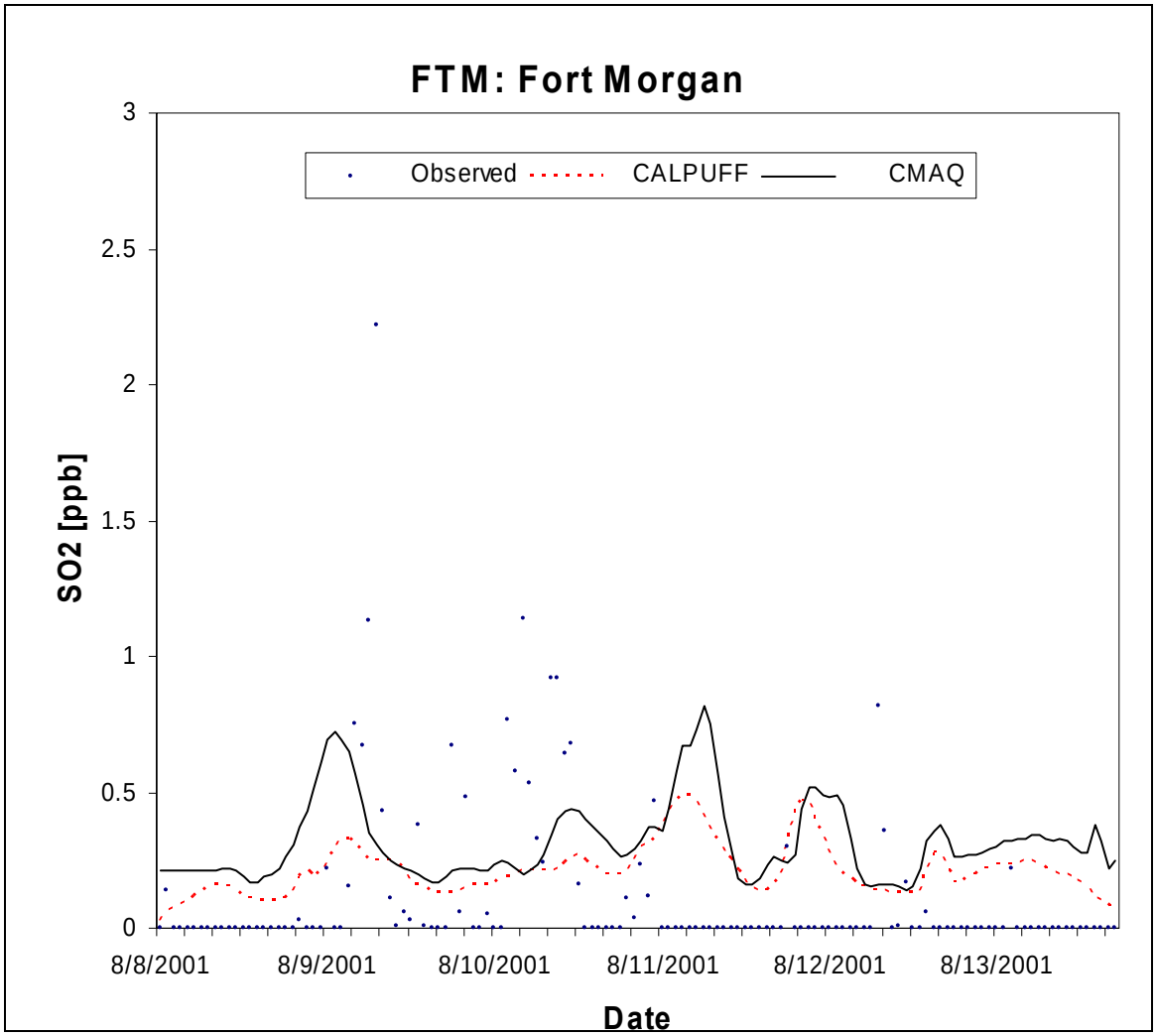

Figure E-27. Observed and predicted SO_2 concentrations at FTM for Case 4.

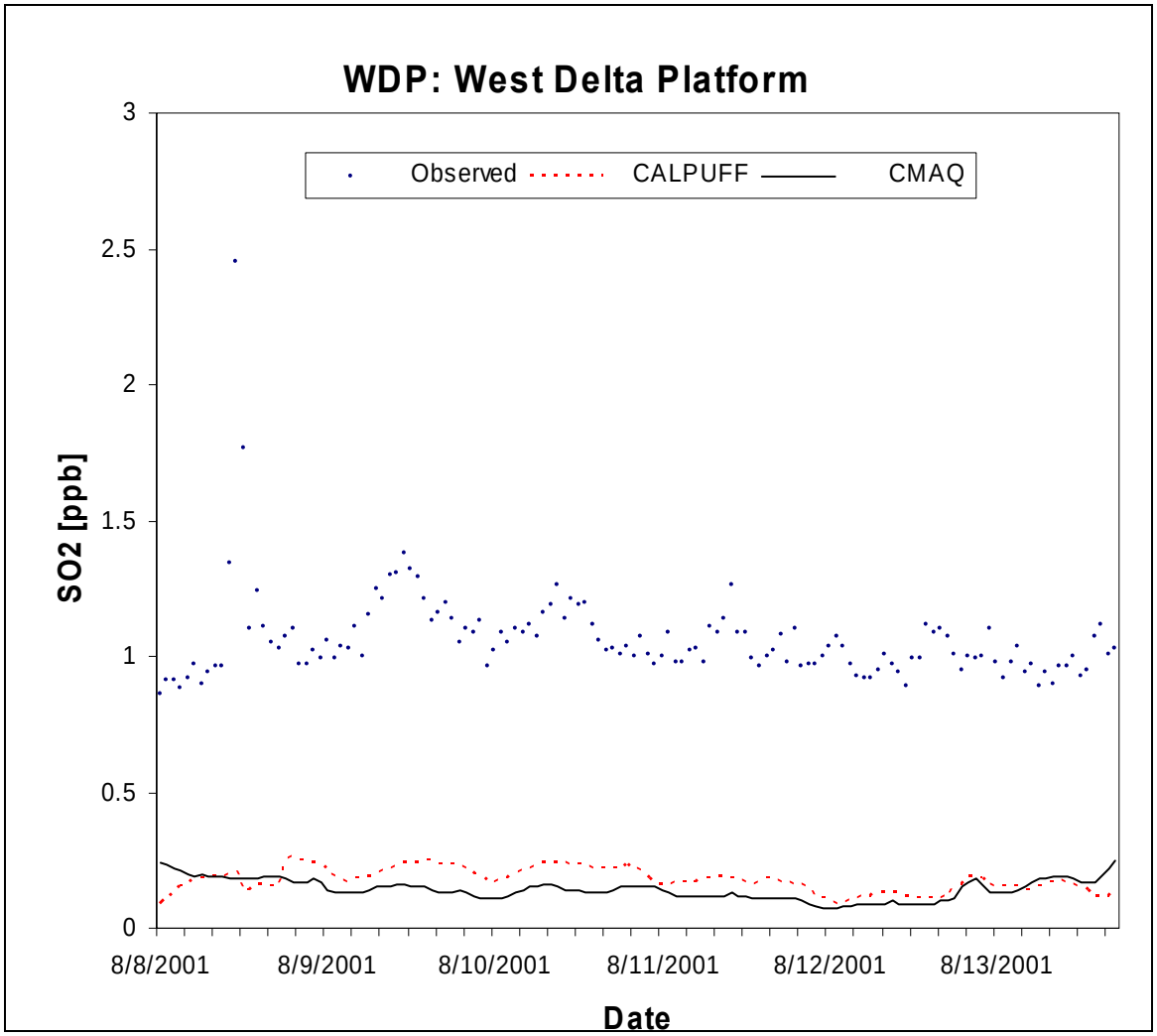

Figure E-28. Observed and predicted SO_2 concentrations at WDP for Case 4.

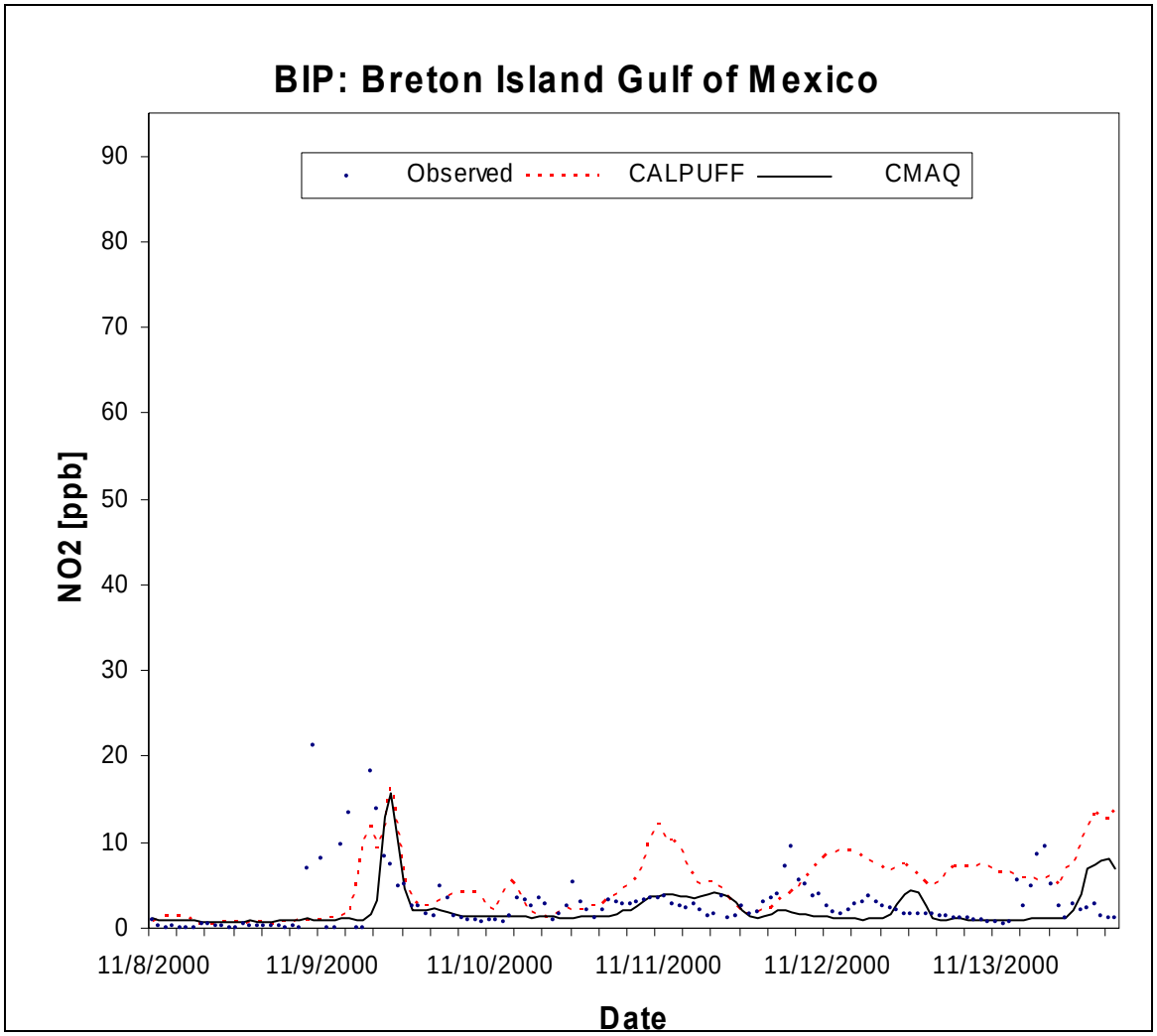

Figure E-29. Observed and predicted NO_2 concentrations at BIP for Case 5.

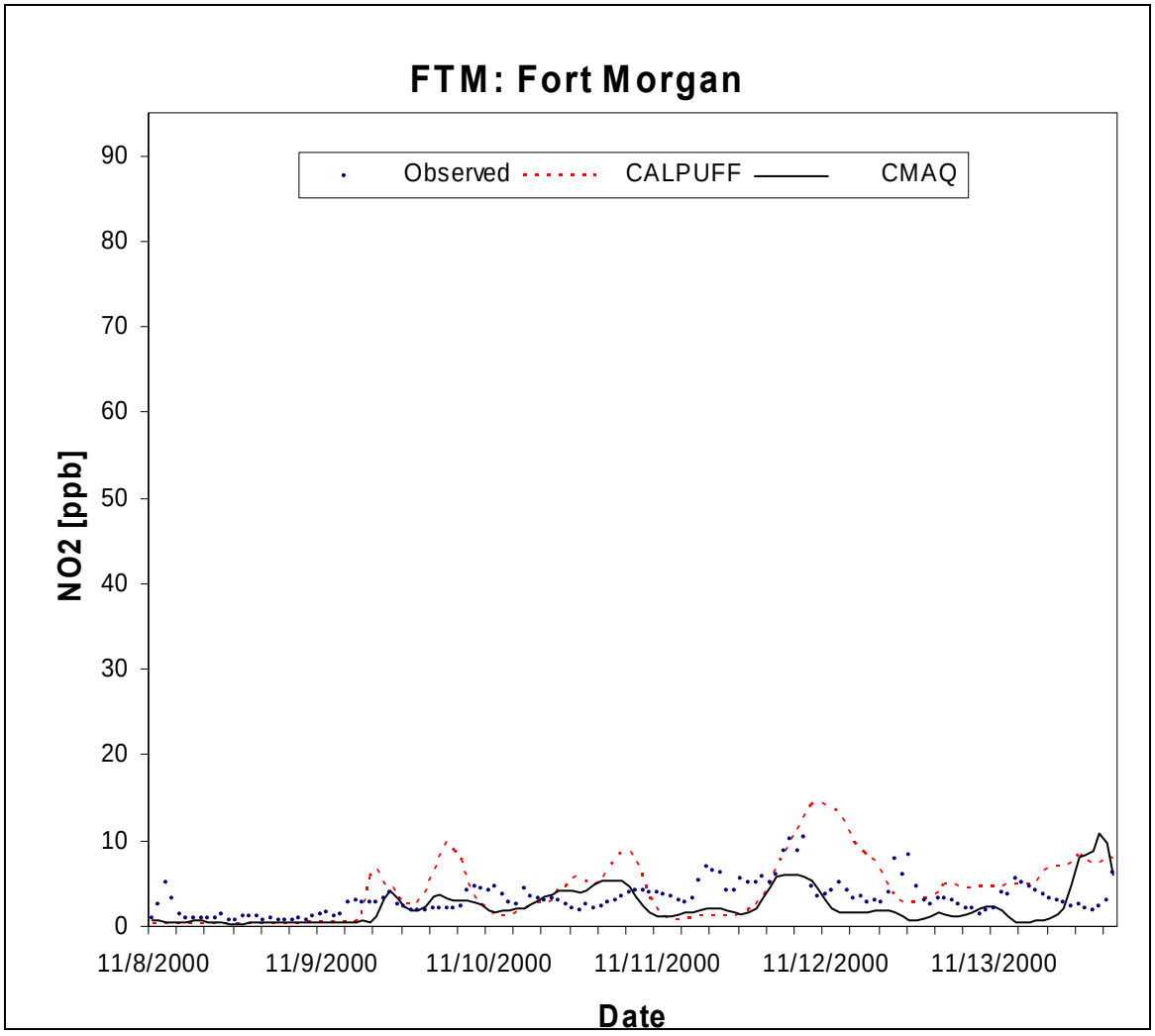

Figure E-30. Observed and predicted NO_2 concentrations at FTM for Case 5.

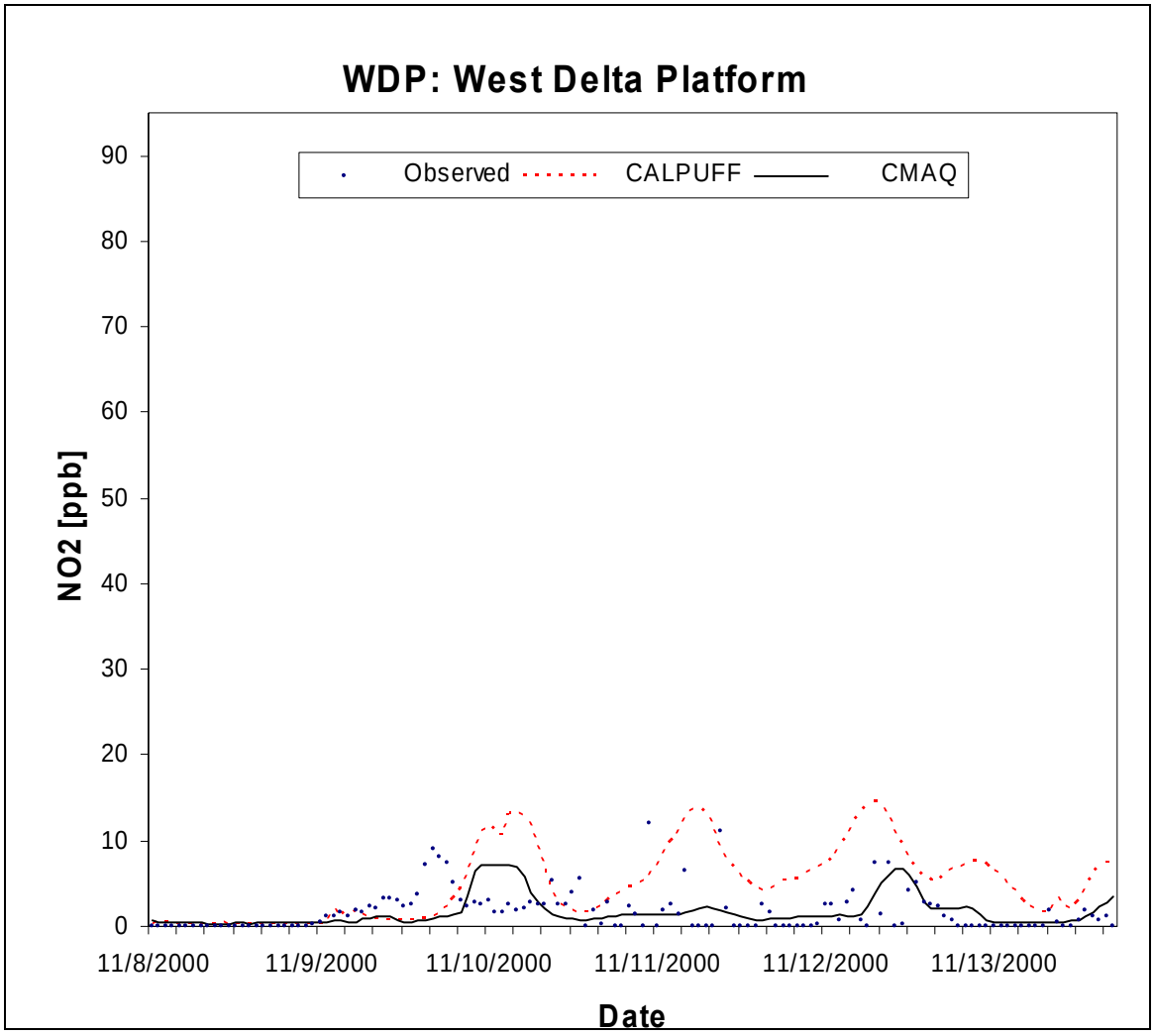

Figure E-31. Observed and predicted NO_2 concentrations at WDP for Case 5.

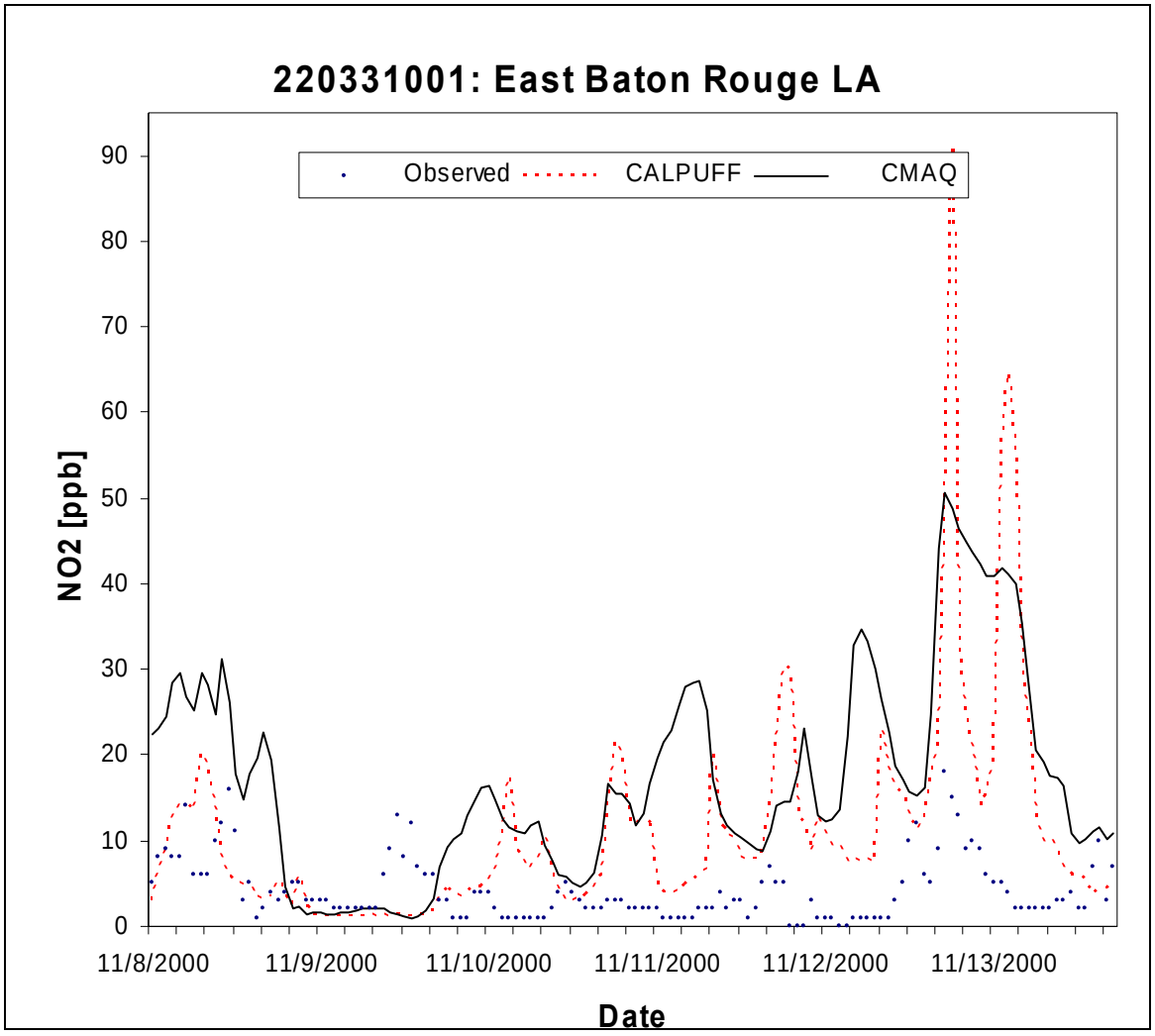

Figure E-32. Observed and predicted NO_2 concentrations at East Baton Rouge for Case 5.

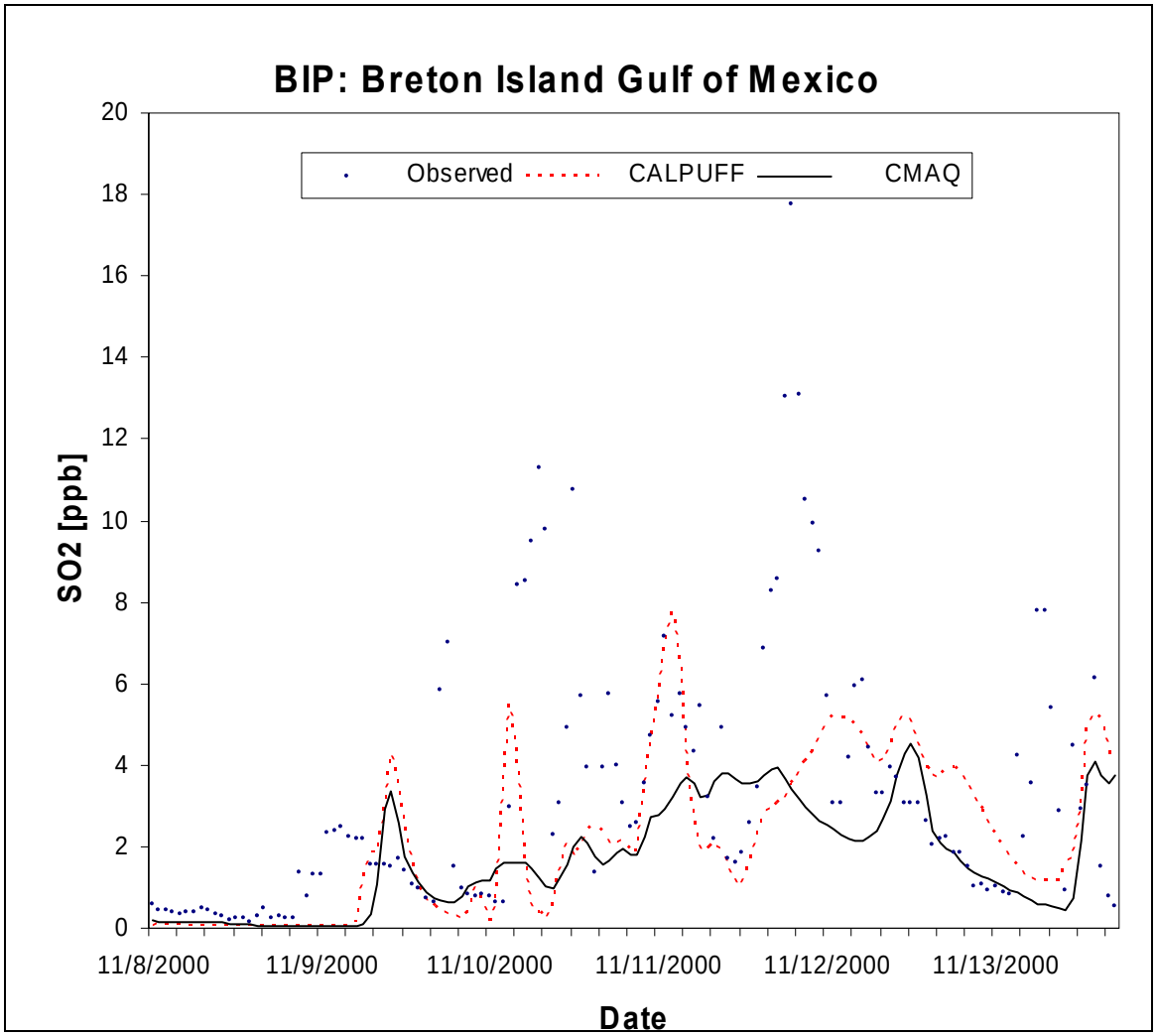

Figure E-33. Observed and predicted SO_2 concentrations at BIP for Case 5.

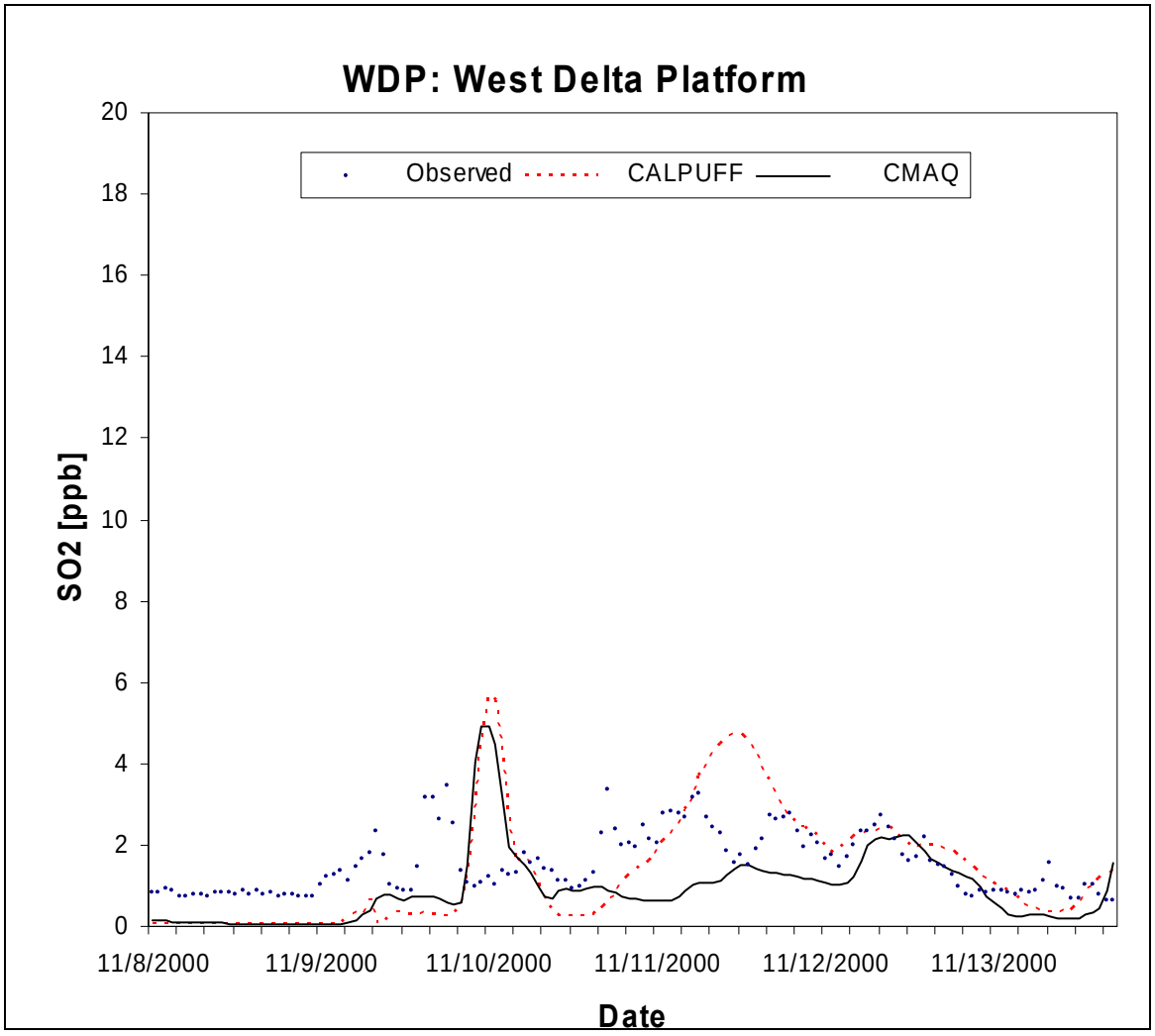

Figure E-34. Observed and predicted SO_2 concentrations at WDP for Case 5.

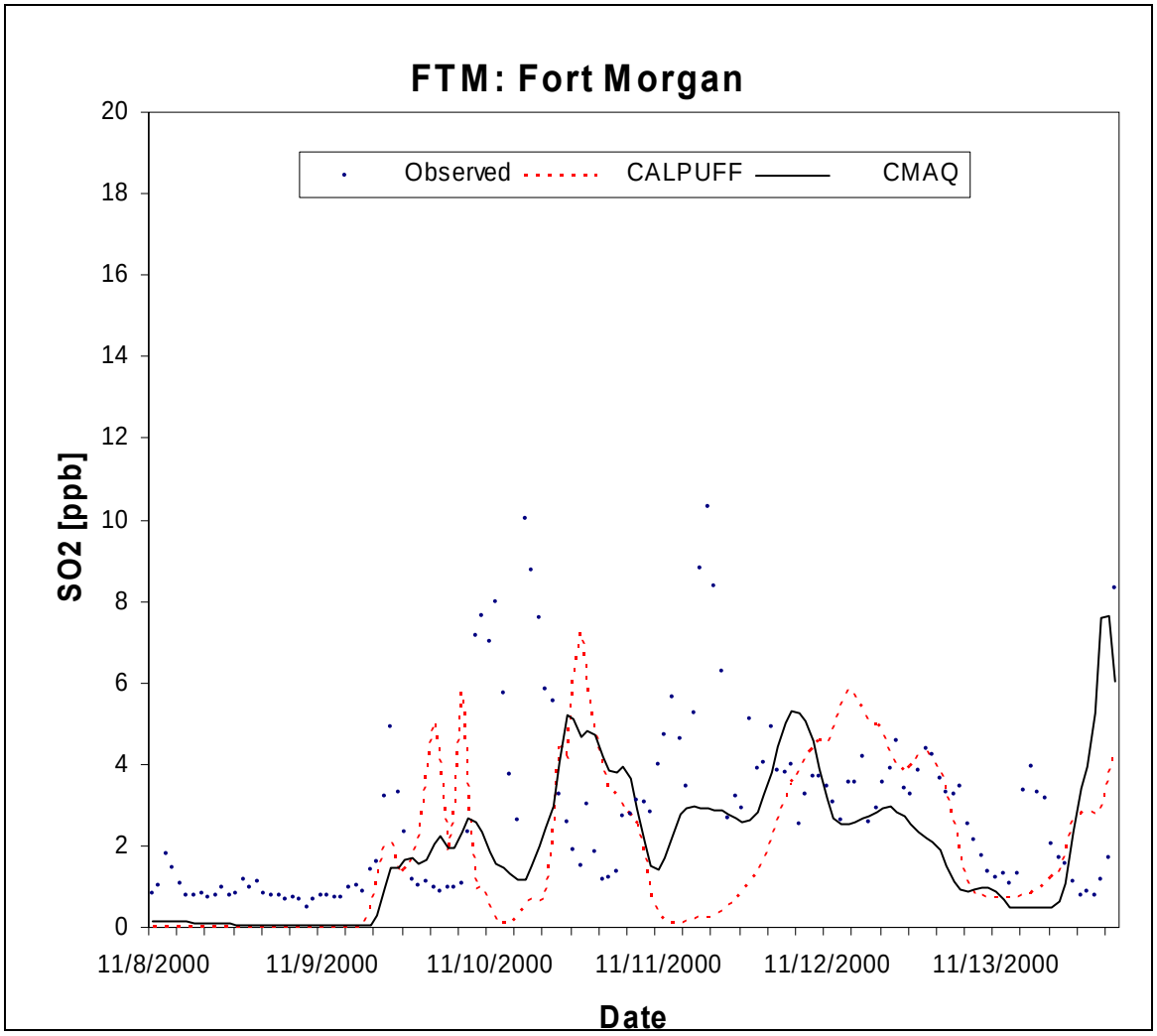

Figure E-35. Observed and predicted SO_2 concentrations at FTM for Case 5.

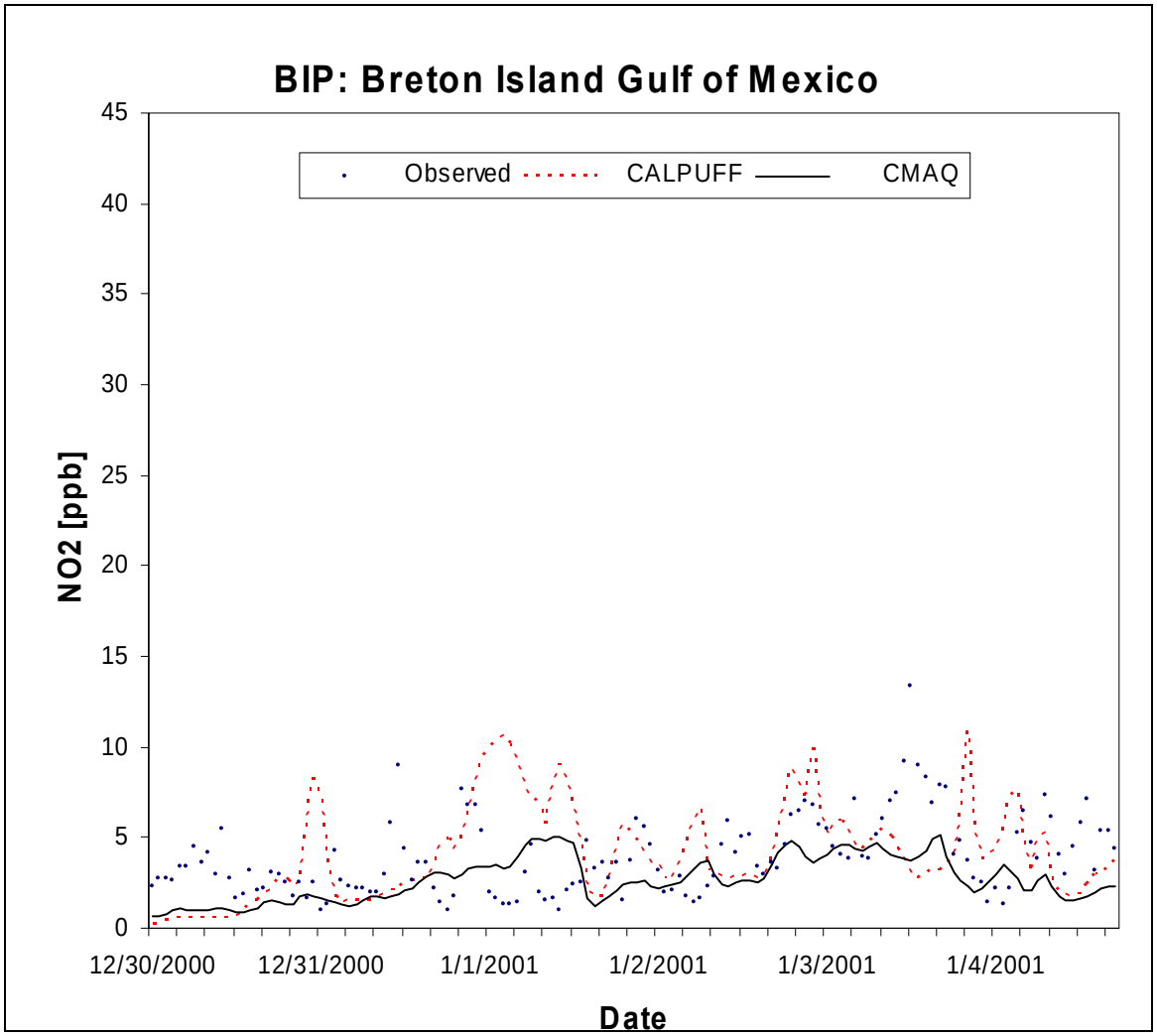

Figure E-36. Observed and predicted NO_2 concentrations at BIP for Case 6.

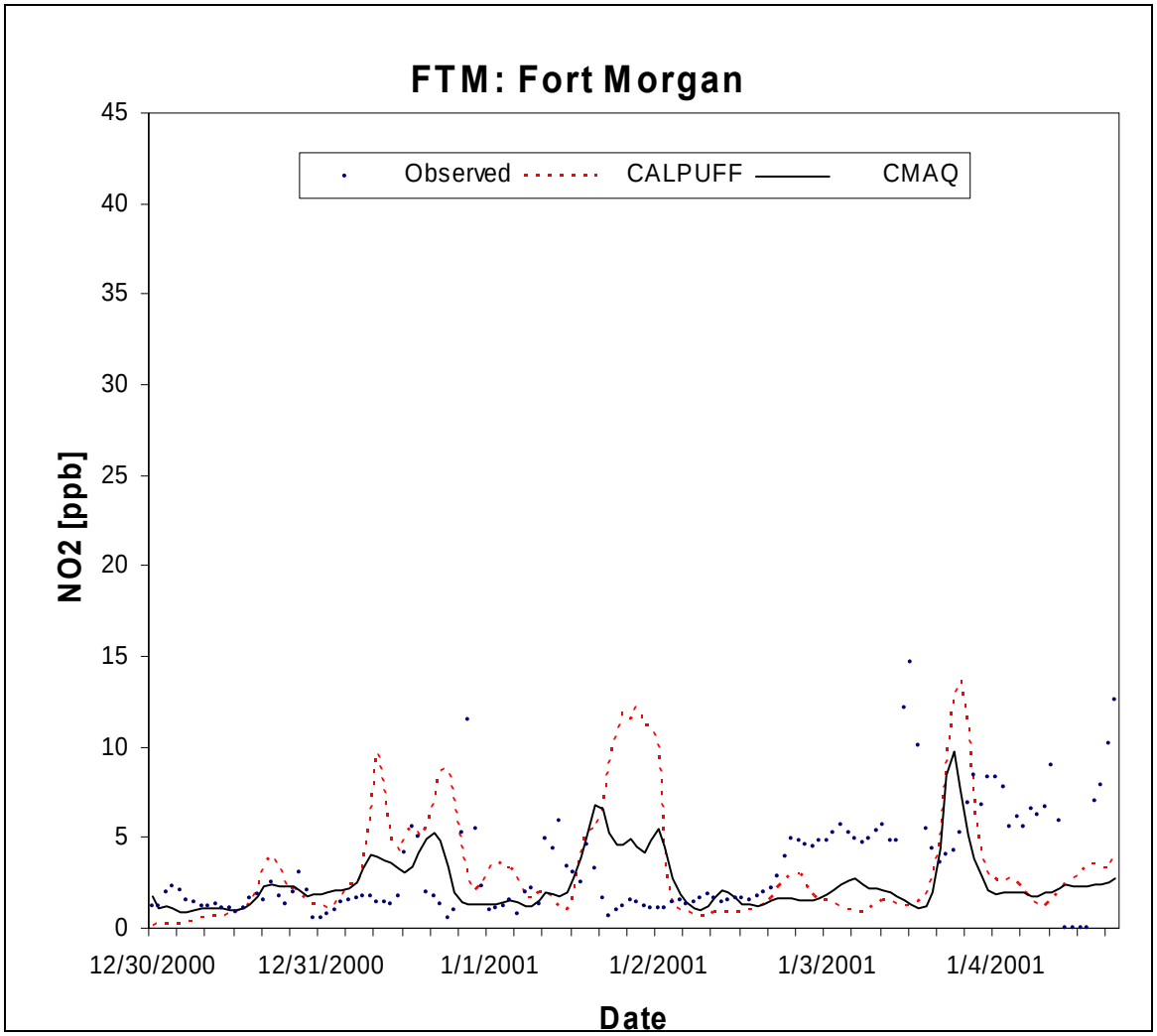

Figure E-37. Observed and predicted NO_2 concentrations at FTM for Case 6.

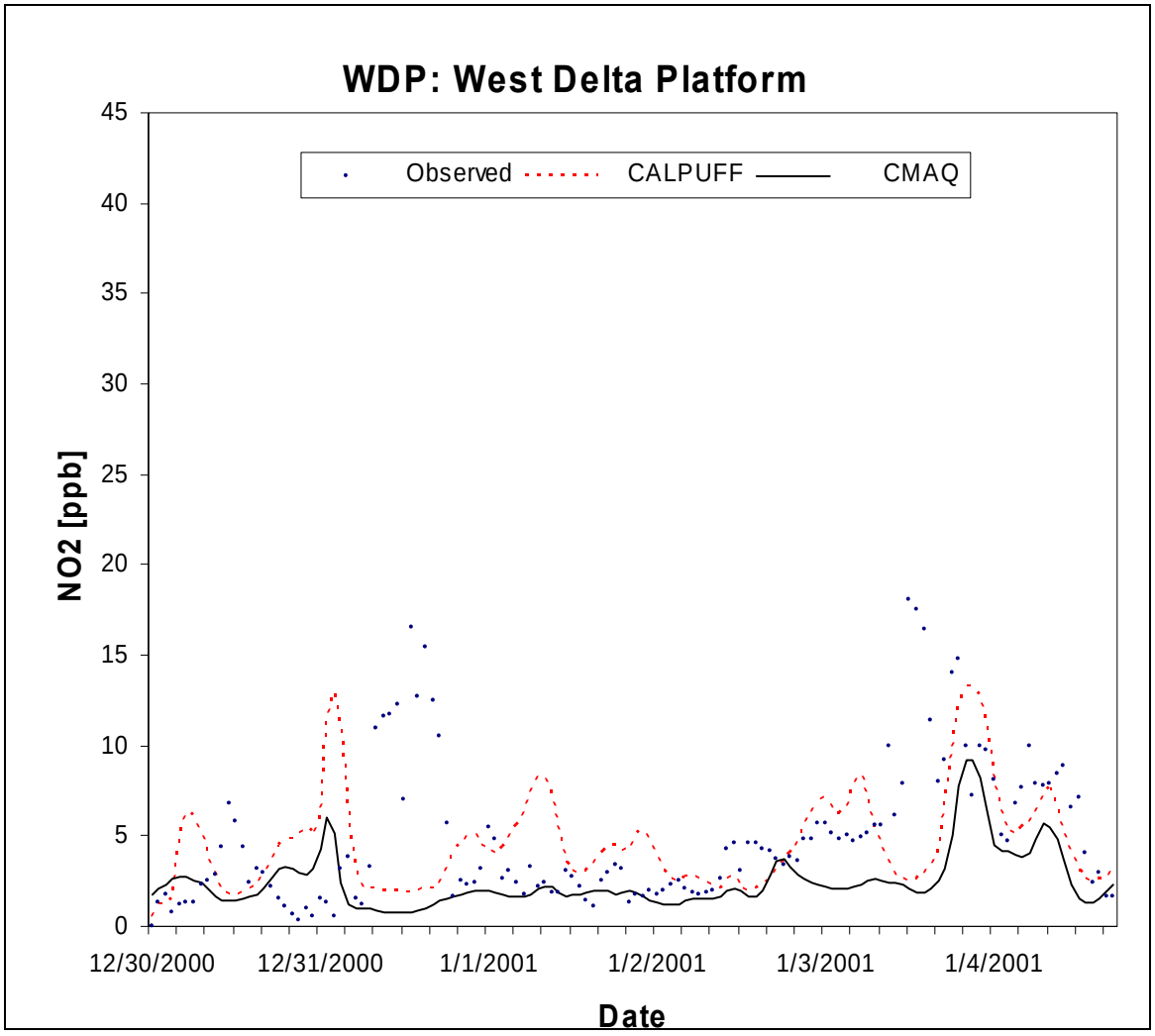

Figure E-38. Observed and predicted NO_2 concentrations at WDP for Case 6.

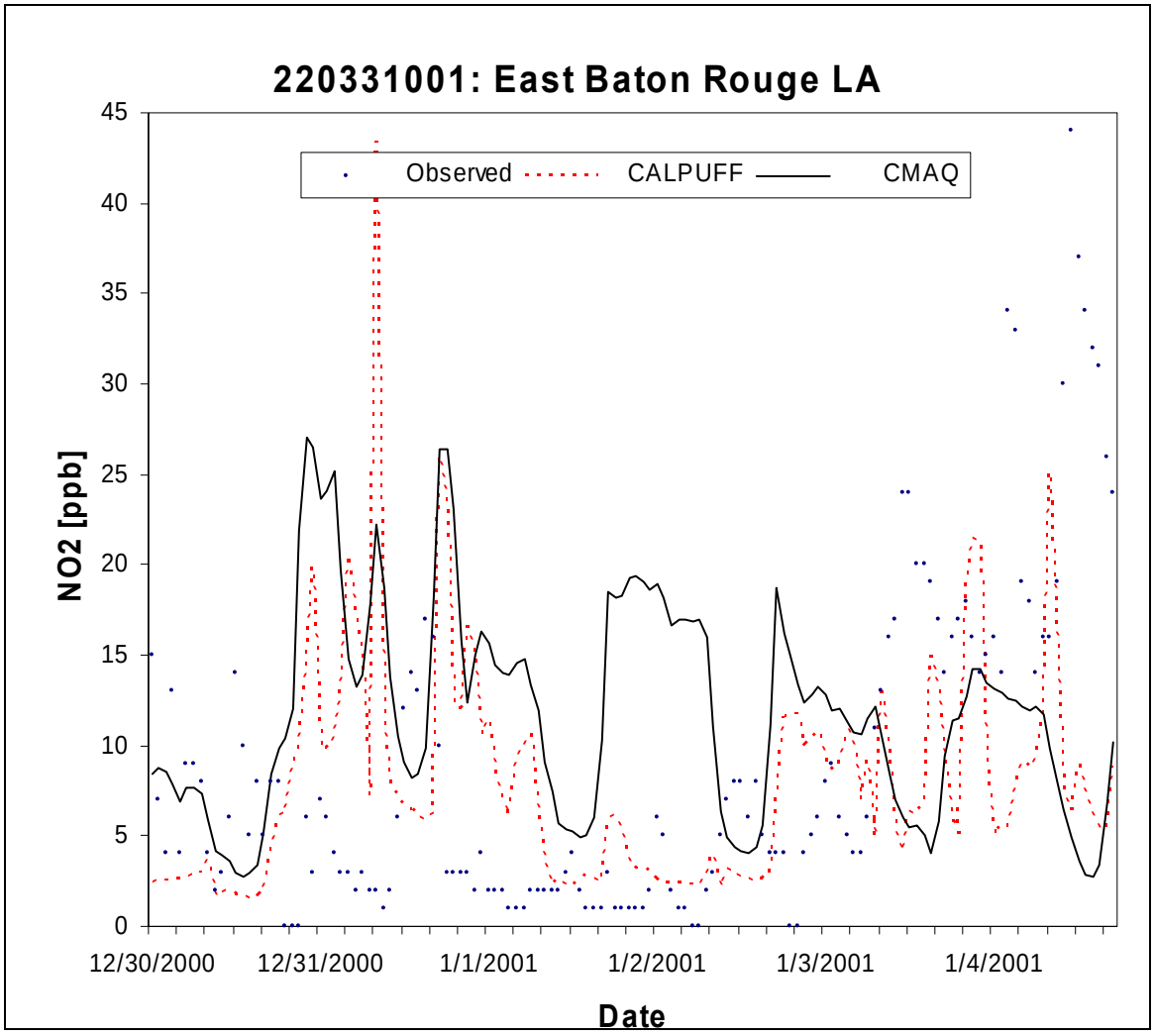

Figure E-39. Observed and predicted NO_2 concentrations at East Baton Rouge for Case 6.

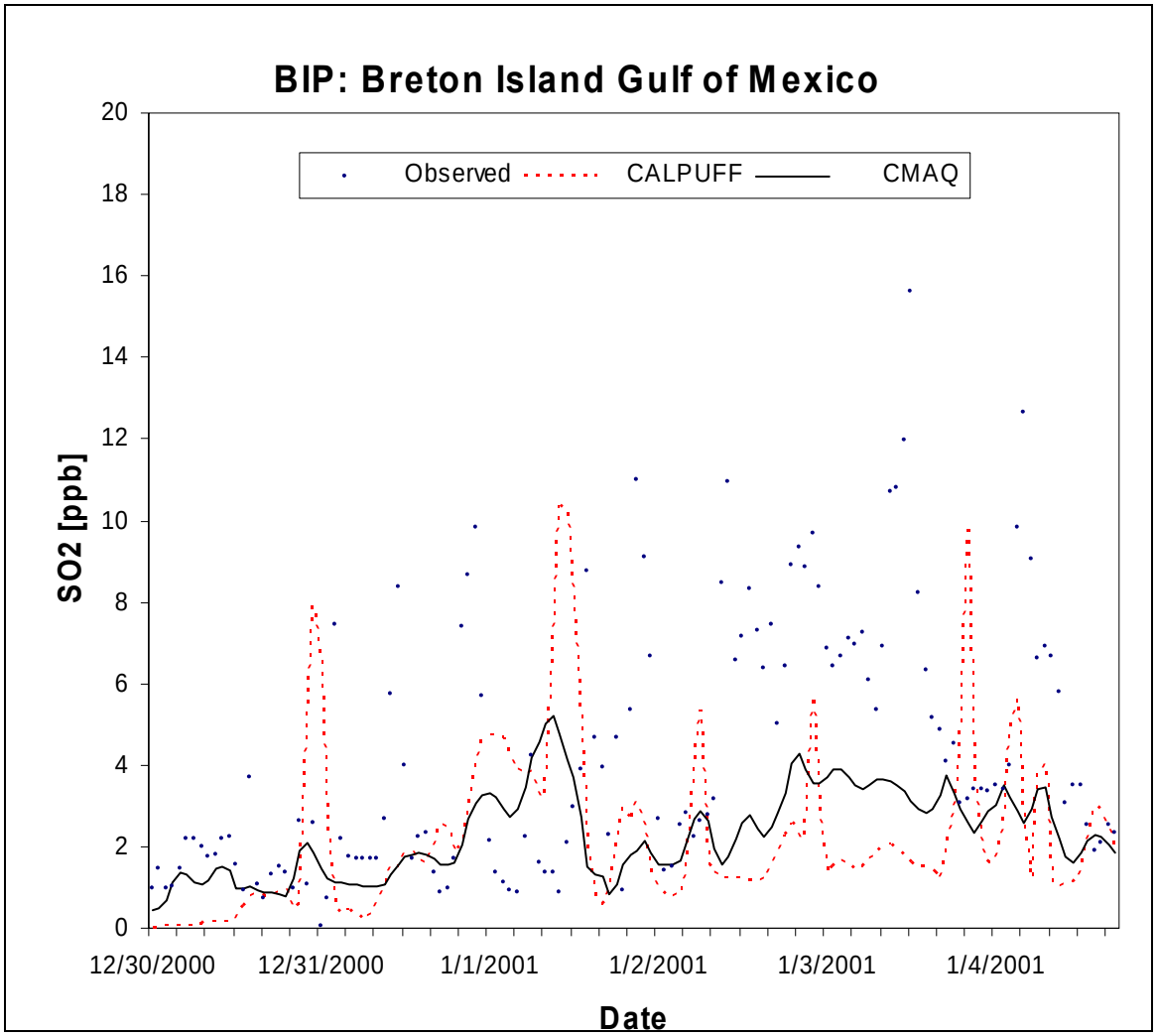

Figure E-40. Observed and predicted SO2 concentrations at BIP for Case 6.

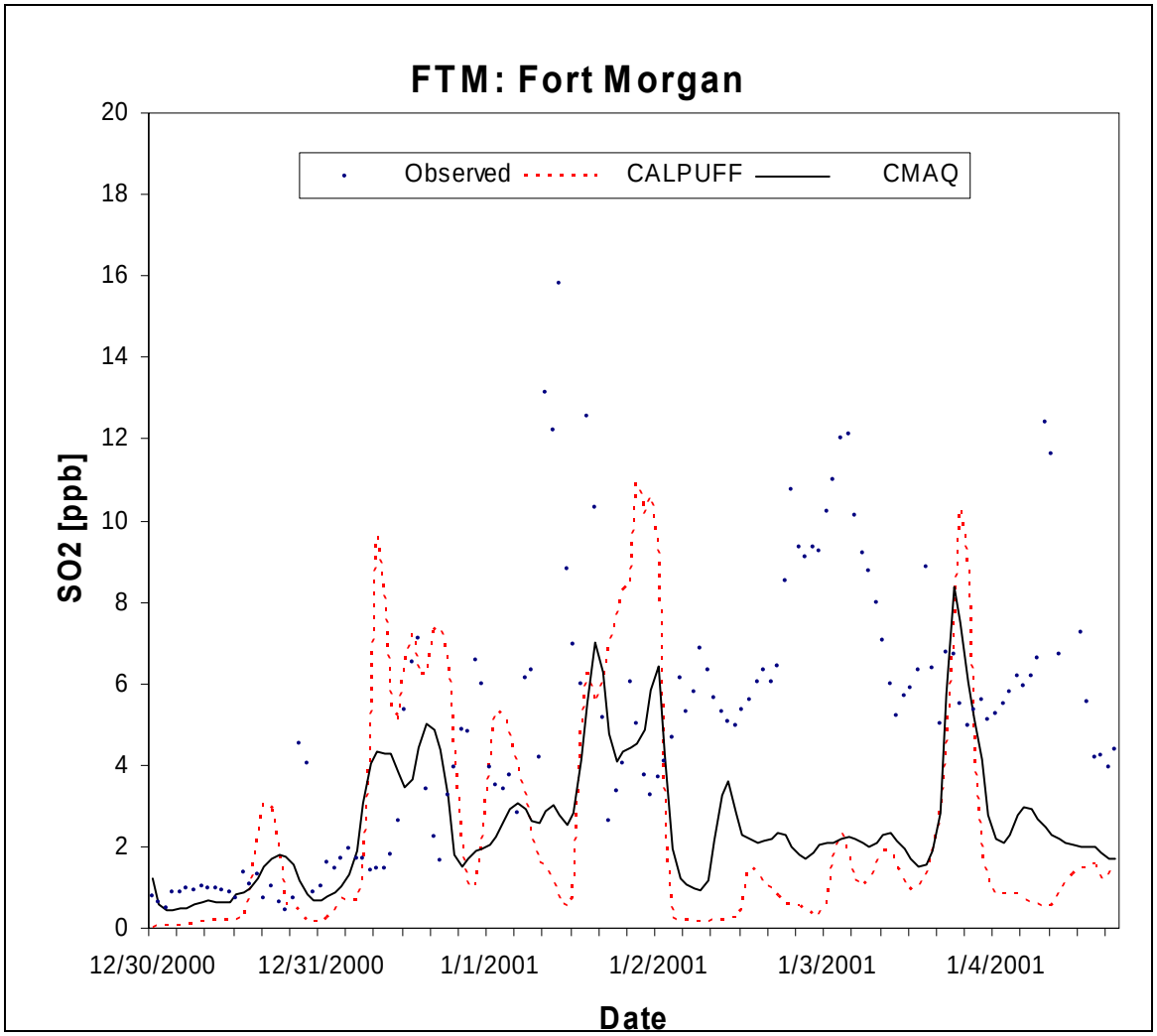

Figure E-41. Observed and predicted SO2 concentrations at FTM for Case 6.

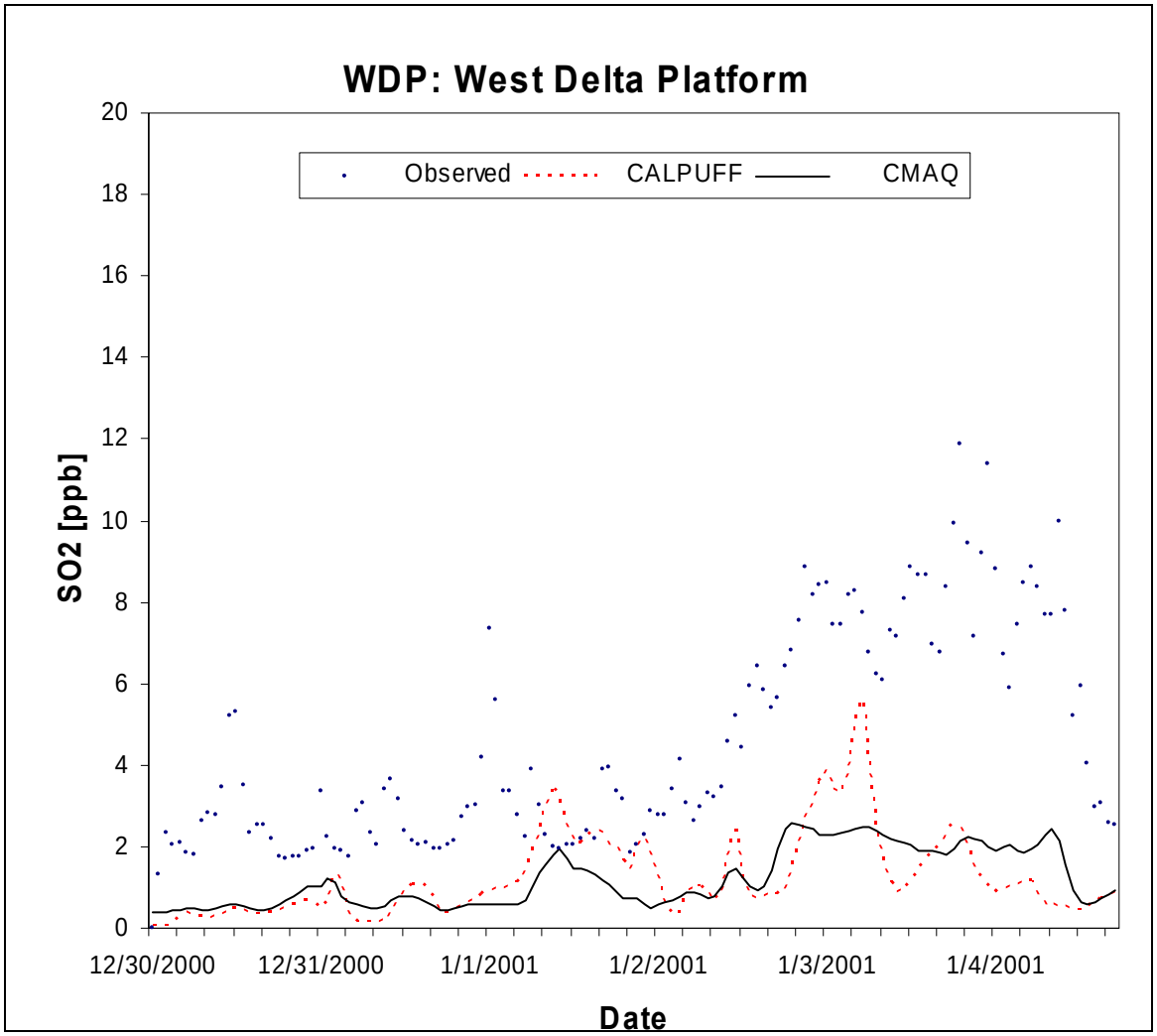

Figure E-42. Observed and predicted SO2 concentrations at WDP for Case 6.

APPENDIX F

DETAILED DESCRIPTION OF MM5 DEVELOPMENT CASE

This description of the MM5 development case was extracted from a manuscript prepared by Jeffrey R. Zielonka of the Department of Meteorology, Pennsylvania State University, State College, Pennsylvania.

The episode chosen by MMS for initial testing was defined here as Case 1, which began at 12 UTC, 1 December 2000 and ended at 00 UTC, 7 December 2000. Efforts were focused on two primary objectives: development of the most appropriate data assimilation strategy on the 12-km domain, including standard WMO and the special observational data provided by MMS, and implementation of the MODIS SST product provided by MMS into the model runs. In order to find the best possible combination of FDDA strategy and SST product, all combinations were examined (see overview of experiments in Table 4.4. A control run, i.e., no FDDA, was run using both the ETA SST (CNTLETA) and the MODIS SST (CNTLMOD). From here, both SST products were tested with additional levels of data assimilation. The addition of 3D analysis nudging (UFDA) to the control configuration was followed by 3D analysis nudging plus surface analysis nudging (USFDA), then the addition of observational nudging of standard observations (SOB), and then observational nudging of standard observations plus special observations (AOB). All observations are used to compute the statistics.

Table F-1 is a statistical comparison of all ten model experiments conducted during the development stage. Comparison of the first two sets of model statistics, which illustrate the performance of the two control simulations, indicates that statistically the CNTLMOD simulation performed equally as well or better than the CNTLETA simulation. The improvements over all layers including the surface are about 0.3 m/s, 0.1 °C, 0.1 g/kg, and 0.9 degrees for wind direction, and there are no instances when the model performs more poorly when using the MODIS SST. This is a typical winter season case, where the flow is dictated by a predominant flow from the northwest. Under these conditions, there is little influence from the GOM, even though the water temperatures are warmer than the bordering land temperatures, and it is unlikely that there would be a large difference between the model runs just by using a different SST product.

Table F-1 indicates that with the addition of more refined data assimilation techniques, the 12-km domain model simulations show subsequent decreases in model error, since more observed and analyzed data are being used to nudge the model state. Figures F-1 to F-10 show statistical curves for ready comparison of the domain-averaged MAE for each step of the FDDA development, where increasingly complex assimilation strategies are used and results are averaged over the 5-day period starting at 00 UTC, 2 December 2000 (first 12-h period is in the overlap period with previous case). The odd-numbered plots (Figure F-1, Figure F-3, etc.) each contain two time-series plots. The first plot is the MAE for the surface layer, i.e. the lowest model sigma level, and the second plot is the mass-weighted MAE averaged over all model layers. The first two curves in the time-series plots represent the model errors of the CNTLETA and CNTLMOD simulations. The time-averaged MAE values for these two cases are shown in the first row of values in the legend beneath the plot. These two values will be referred to as the "control group" (CG). The second group of statistics represents the averaged performances of the UFDAETA, UFDAMOD, USFDAETA, and USFDAMOD simulations, and is referred to as the "analysis nudging group" (ANG). The ANG consists of model simulations using 3D analysis nudging (UFDAETA and UFDAMOD), and 3D analysis nudging plus surface analysis nudging (USFDAETA and USFDAMOD). The third row of values represents the averaged performances of the USFDASOBETA, USFDASOBMOD, USFDAAOBETA, and USFDAAOBMOD simulations, and is referred to as the "observation nudging group" (ONG). The ONG includes simulations with 3D analysis nudging, surface analysis nudging, and standard observation

nudging (USFDASOBETA and USFDASOBMOD), as well as simulations with 3D analysis nudging, surface analysis nudging, and standard observation nudging plus special observation nudging (USFDAAOBETA and USFDAAOBMOD).

Some characteristics of the time-series plots should are noted. First is the reason for the apparent periodicity in the observed error curves. The model errors in these time series plots are calculated hourly, and are averaged, depending upon how many observations are available at that hourly time. Standard observations are available hourly at the surface, including wind and mass data. Special surface data with the same variables are also available 3-hourly. Every 3 hours, therefore, there are more observations to calculate statistical averages, which generally reduces the model error over the entire model domain. Above the surface layer, wind observations are available hourly, in the form of wind profiler data, which is a special data source. When these observations are not used in the data assimilation, which only occurs in the USFDASOBETA and USFDASOBMOD simulations, the only available upper air observations are 12-hourly rawinsonde observations. The time series plots clearly show lower MAE values at these 12-hour intervals when there are more observations in the error calculation. Vertical averaging for each time is mass-weighted, so the heaviest weights are from layers closest to the surface. The time average calculation is then made by weighting each time equally, and dividing by the total number of model times included in the time series.

The even-numbered plots in this range (e.g. Figure F-2, Figure F-4, etc.) are vertical profiles of MAE for each of the ten development experiments. These profile plots show the MAE at every sigma level (on the left ordinate), along with the corresponding height above ground in meters of the sigma level (on the right ordinate). The vertical average errors for the 5-day period starting at 00 UTC, 2 December 2000 are shown at the bottom of the figures, in the CG, ANG, and ONG groupings. Temporal averaging for vertical profiles is weighted by the number of observations at each time, i.e. the 12-hourly times have the largest weights, because they include the greatest number of observations. For these profile vertical means, each sigma-level is weighted equally, not mass-weighted.

Each plot provides some evidence that supports using the most detailed FDDA approach. Figure F-1 shows the VWD MAE plots for the surface layer and the all-layer average. There is a small difference between the model simulations using different SST fields (ranging from a 0.1 m/s to 0.2 m/s advantage for the MODIS products in the surface layer, and 0.1 m/s to 0.3 m/s difference in the all-layer average) but a clear pattern is evident in terms of the FDDA strategies. The addition of UFDA alone slightly decreases the errors that occurred in the CNTL runs at the surface, from 3.1 m/s to 2.9 m/s in the UFDAETA simulation and from 2.9 m/s to 2.7 m/s in the UFDAMOD simulation. Because this portion of the FDDA concentrates on the levels above the surface layer, the largest statistical improvements exist between the errors of the CNTL and UFDA runs averaged over all model layers. The UFDAETA simulation improves over the CNTLETA simulation with a decreased error from 5.3 m/s to 4.3 m/s and the UFDAMOD simulation improves over the CNTLMOD simulations, as errors decrease from 5.0 m/s to 4.1 m/s over the length of the model run.

The USFDA design shows a slight improvement over the UFDA design in the surface layer, (approximately 0.3 m/s decrease of MAE between UFDAETA and USFDAETA, and 0.2 m/s between UFDAMOD and USFDAMOD), and also shows similar improvement in the all-

layer average for both sets of experiments. It is not surprising that there is approximately an equal amount of error decrease in the surface layer statistics and the all-layer average statistics, because the times with only surface observations are given an equal weight to the model times with surface and upper-air observations. The statistics beyond this section exclude the surface from the all-layer averages statistics for this reason.

The addition of observational data appears to cause the largest decrease of model errors across the 12-km model domain. In the surface layer, the ONG consistently exhibits superior model performance, with the best results occurring with the inclusion of all observations and the MODIS SST (USFDAAOBMOD). The most noticeable improvement is in the all-layer average, where there is a slight improvement in model performance using observation nudging of standard observations from the USFDAETA to USFDASOBETA and USFDAMOD to USFDASOBMOD runs, but the use of the special data in the observation nudging in the USFDAAOBETA and USFDAAOBMOD simulations cut the model errors of the standard observation runs in half, with final average MAE values of about 1.9 m/s for both standard plus special observation nudging (USFDAAOB) simulations. In other words, this final strategy produces FDDA-assisted model results that best fit all of the available observations.

The vertical profile of VWD MAE in Figure F-2 supports the progression of decreasing model errors that is evident in the time-series plots. The CG simulations are consistently the worst, with increasing errors at higher altitudes. The ANG is slightly improved in the lower layers, but separates itself from the CG at higher altitudes, as its errors remain relatively constant with height. The ONG shows some differences, depending on what data are assimilated. The USFDASOBETA and USFDASOBMOD simulations are just slightly better than the ANG up to approximately 4000 m above ground level, before showing more separation above 5000 m. With the addition of the special data sources to the wind fields, which in this study are the wind profilers, the MAE values are consistently lower than all of the other simulations up to sigma-level 35 (approximately 5400 m). Above this height, the errors of all simulations in the ONG are nearly identical. The primary reason for this is the vertical extent of the special wind profiler observations. In this case, the wind profiler observations only recorded data as high as sigma-level 35, so that was the upper limit of the assimilation of the profilers, as well as the verification of the model fit to the profiler observations. Above this level, the only wind observations were in the form of 12-hourly radiosonde observations, which are assimilated into all ONG model runs.

The trends of the statistics for mass fields, i.e. TEMP and MIXR are somewhat different than those of the VWD statistics. In Figure F-3a, the MAE curves for TEMP in the surface layer are very similar throughout the entire length of the simulation, with the exception of the CNTLETA and CNTLMOD simulations, which tend to deviate from the rest of the simulations. The overall averages of the statistics for the ONG show reasonable improvements from the control runs since temperature is not nudged at the surface, and errors decrease between 0.2 °C for the ETA simulations and 0.4 °C for the MODIS simulations. Once again, nearly the same magnitude of MAE decrease is evident in the all-layer average plot (Figure F-3b), except for a 0.3 °C decrease in error from the CG simulations to the ONG simulations using the ETA SST. The use of observation nudging decreases model errors from approximately 2.1 °C to 1.8 °C in the USFDASOBETA and the USFDAAOBETA runs, and from 2.0 °C to 1.6 °C in the USFDASOBMOD and USFDAAOBMOD model runs. Unlike the VWD statistics, the lack of

improvement when special observations are added can be attributed to the lack of special temperature and moisture observations, and that there is no mass field assimilation in the PBL. The only temperature and moisture data that was available as a special data source is located at the surface. These data, however, are only used for verification of the model results, since assimilation of temperature and moisture observations is turned off by default below the top of the boundary layer. The vertical profile of TEMP MAE errors (Figure F-4) once again shows the increased benefits through the progression of the CG, ANG, and ONG, but the grouping of model curves is slightly different than the VWD profile. In this case, all four experiments in the ONG are grouped tightly together throughout the vertical extent of the model. The lowest errors in the ONG begin between sigma level 5 and sigma level 10 (approximately 200 m to 600 m above ground level). Because this is a winter case, the height of the PBL is much lower than if it were a summer case, where PBL heights are routinely near 1500 m during the afternoon. The low extent of the superior low model errors in the ONG is believed to be a result of the assimilation of temperature observations from radiosonde data above a relatively shallow PBL.

The MAE for MIXR displays slightly different characteristics than MAE for TEMP (Figure F-5). In the surface layer, there is little difference in model errors from the CG to the ONG, but somewhat larger differences between simulations that use the ETA vs. MODIS SST products. In all groups, there is approximately a 0.2 g/kg decrease in model error when using the MODIS SST, compared to the ETA SST (Figure F-5a), so it implies that there may be a low-level benefit of using the MODIS SST product, even when both products have comparable resolutions. The all-layer average of MIXR MAE (Figure F-5b) shows the same patterns, which may be due to the heavier weighting of surface and low-level errors; the greater number of observations at 12-hourly radiosonde times also has a large effect on the time series. In the vertical profile of MIXR MAE values (Figure F-6), however, the behavior of the errors looks similar to the TEMP MAE profiles (see Figure F-4). The overall averages here show a decrease in model error of approximately 0.5 g/kg, averaged over the depth of the profile, with the ONG once again exhibiting the superior statistical performance over the CG. Like the TEMP profiles, the lack of difference between USFDASOB and USFDAAOB strategies can be attributed to a lack of special observations that include mass field data. The special data includes mass information at the surface, which is not assimilated, and the only available upper-air observations in the special data set are wind profiler observations, which do not include TEMP or MIXR data.

The model errors for WSPD and WDIR (Figures F-7 to F-10) follow a very similar pattern to those of the VWD error plots discussed previously, with the lowest errors occurring as a result of the USFDAAOB strategy, regardless of the SST product. All-layer averages for WSPD are reduced from approximately 3.1 m/s in CNTLETA, and 3.0 m/s in CNTLMOD, to approximately 1.2 m/s with USFDAAOBETA, and 1.1 m/s with USFDAAOBMOD (Figure F-7b). The vertical profile of WSPD MAE mimics the VWD profiles quite closely, with the biggest error reduction coming as a result of the USFDAAOBETA and USFDAAOBMOD simulations. Above sigma level 35 where the special data do not exist, the errors of the entire ONG are practically identical (Figure F-8).

All-layer MAE averages WDIR are also reduced dramatically from the CG to the ONG. In the surface layer, there is an error decrease of approximately 10 degrees, from 28.3 degrees in the CNTLMOD experiment to 18.5 degrees in the USFDAAOBMOD experiment (Figure F-9a). In the all-layer average, the errors decrease by more than 20 degrees from approximately 36.0

degrees in the CNTLMOD run, to approximately 14.8 degrees in the USFDAAOBMOD run. Differences in the SST fields do appear to affect the errors, with the greatest difference between model errors with similar FDDA schemes being approximately 2.1 degrees in the UFDA runs (Figure F-9b). In the vertical profiles of WDIR MAE (Figure F-10), the grouping of error curves, however, is still similar to the VWD and WSPD vertical profiles, with the CG curves having the most error and ONG curves having the least error.

Subjective analysis of the model outputs also indicates good agreement with respect to observed surface analyses and satellite imagery. Infrared satellite imagery for 12 UTC, 2 December 2000 (t = 24 h) shows that a large portion of the weakening cold front that passed through Louisiana during the previous night is located over the GOM (Figure F-11a), corresponding with the analyzed cold front on the NCEP surface analysis map (Figure F-11b). This cold front is evident in the lowest sigma-level (surface-layer, ~15 m AGL) wind fields in the model output from experiment USFDAAOBMOD (Figure F-12). The front extends southward out of an area of low pressure located in central Alabama. Additionally, a weak trough extends to the WNW from the low, which is not evident in the surface wind fields (Figure F-13). The stronger flow of colder air from the Canadian high pressure to the northwest continues to advance southeastward over the Gulf Coast region, as is evident in the lowest sigma-level temperature field (Figure 5.14), which indicates predominantly west-east oriented isotherms over the GOM.

At the end of the simulation time, the model continues to represent the atmospheric features reasonably well. Figure F-15a is the infrared satellite imagery at 00 UTC, 7 December 2000 (t = 132 h). At this time, there is a relatively small area of clouds, associated with the precipitation over Louisiana (note the present weather observations in the Louisiana area in Figure F-15b). Also in Figure F-15b, observed wind conditions in the area of the 12-km domain are generally from the north, with a few observing stations reporting calm, or light and variable wind conditions. This wind pattern is evident in Figure F-16, which is the surface-layer (lowest sigma level) wind field. Flow along the Gulf Coast is generally light from the north, with areas of light and variable winds in a few locations over Mississippi and Alabama. The surface analysis shows a low pressure center to the south of Louisiana, with a cold front extending toward the south-southwest, and a stationary front extending toward the southeast. The modeled sea-level pressure field at this time (Figure F-17) shows the low pressure center to the south of Louisiana, with the major trough axis oriented west-east, and a secondary trough extending northward out of the low. In the modeled wind field, the circulation around the low pressure center is evident, as are the convergence and cyclonic curvature associated with the cold front and weak surface trough to the north. The stationary front lies in an east-west oriented trough, parallel to the temperature contours over the GOM in Figure F-18. Winds along the stationary front are nearly parallel to the front as expected. On the 00 UTC surface plot, there is a relatively small area of precipitation located over southeast Louisiana and southern Mississippi. Three observing stations are reporting various intensities of precipitation at this time; two stations reporting light precipitation ahead of the surface trough, and one station very close to the trough that is reporting heavy precipitation. The model produced no precipitation over Louisiana, but showed some precipitation off the southeast Louisiana coast, and the 3-hour modeled precipitation tendency field ending at this time indicates a larger area of precipitation over the GOM to the south of the border between Louisiana and Texas (Figure F-19) that is associated with the trough/frontal system convection.

Based on the subjective and statistical results of this development case, it was decided that the best possible FDDA strategy to use for the year-long study was the USFDAAOB strategy with the MODIS SST product. Not only does this USFDAAOBMOD strategy provide the best statistical results, it also successfully utilizes the additional special observation data sources that were provided by MMS.

Table F-1

Summary MAE Statistics for Each Step of the FDDA Strategy Development (Including the Control Experiment With no FDDA), Using Both SST Products

		MAE VWD (m/s)	MAE TEMP (°C)	MAE MIXR (g/kg)	MAE WSPD (m/s)	MAE WDIR (degrees)
CNTL ETA	SURFACE	3.1	2.1	1.4	2.2	28.8
	ALL-LAYERS	5.3	2.1	1.4	3.1	36.9
CNTL MOD	SURFACE	2.9	2.1	1.2	2.1	28.3
	ALL-LAYERS	5.0	2.0	1.2	3.0	36.0
UFDA ETA	SURFACE	2.9	2.0	1.4	2.1	26.0
	ALL-LAYERS	4.3	1.8	1.4	2.7	28.5
UFDA MOD	SURFACE	2.7	1.7	1.3	2.0	25.4
	ALL-LAYERS	4.1	1.6	1.2	2.6	26.4
USFDA ETA	SURFACE	2.6	1.9	1.4	1.8	23.9
	ALL-LAYERS	4.0	1.8	1.4	2.5	27.8
USFDA MOD	SURFACE	2.5	1.7	1.3	1.8	23.6
	ALL-LAYERS	3.9	1.6	1.2	2.5	26.2
USFDA SOB ETA	SURFACE	2.4	1.9	1.4	1.8	21.5
	ALL-LAYERS	3.9	1.8	1.4	2.5	26.7
USFDA SOB MOD	SURFACE	2.3	1.7	1.2	1.7	20.9
	ALL-LAYERS	3.8	1.6	1.2	2.5	25.5
USFDA AOB ETA	SURFACE	2.1	1.9	1.5	1.6	19.4
	ALL-LAYERS	1.9	1.8	1.4	1.2	15.5
USFDA AOB MOD	SURFACE	2.0	1.7	1.3	1.6	18.5
	ALL-LAYERS	1.9	1.6	1.2	1.1	14.8

a.

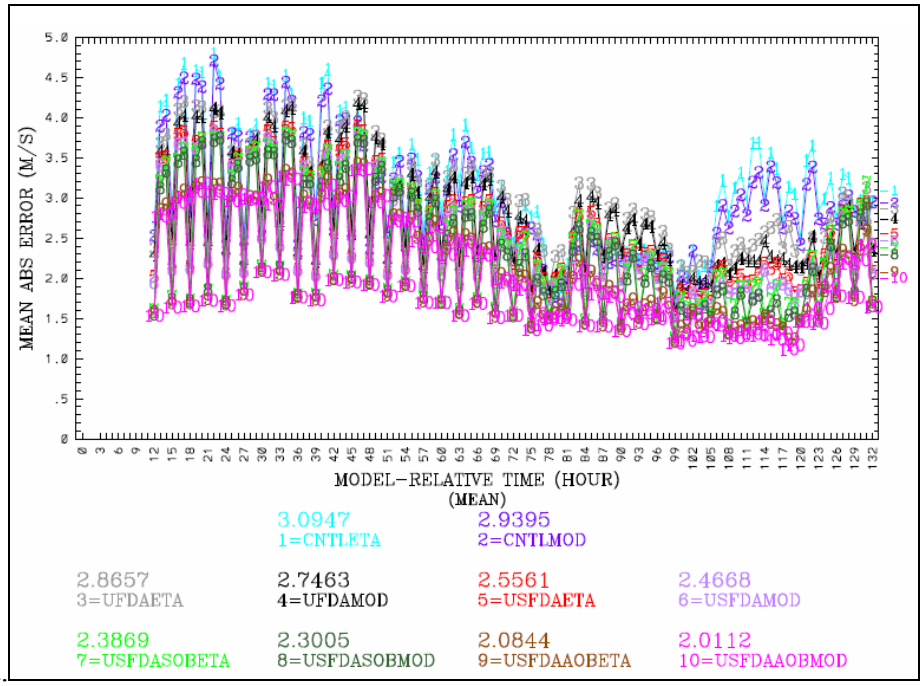

b.

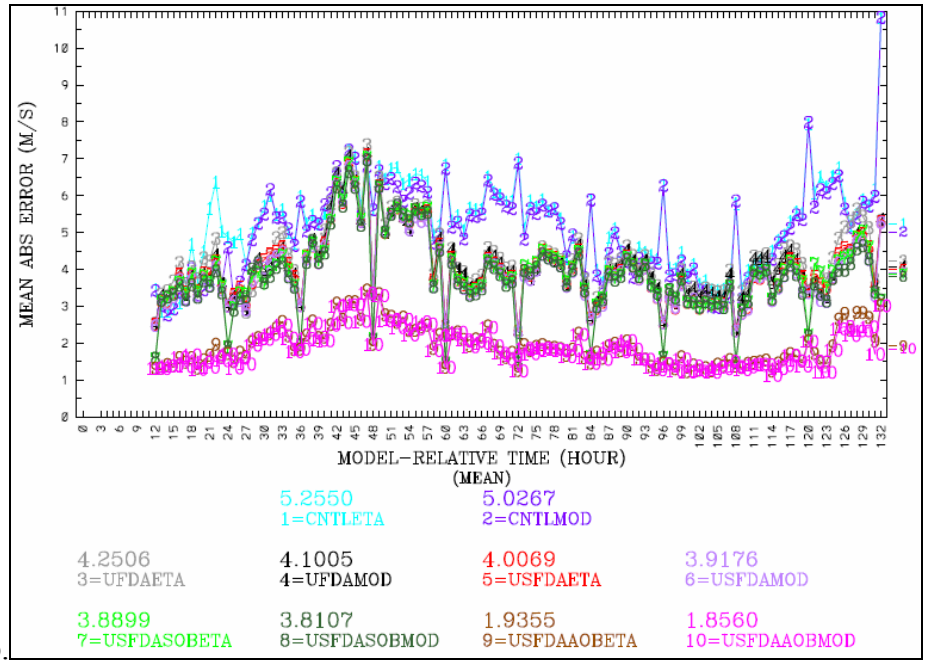

Figure F-1. MAE of model-derived VWD (m/s) for a.) the surface layer, and b.) all-layers, for the 120-hr period beginning 00 UTC, 2 December 2000 and ending 00 UTC, 7 December 2000 development case. Time-averaged MAE values are given below the time series in the colors corresponding to the error curves.

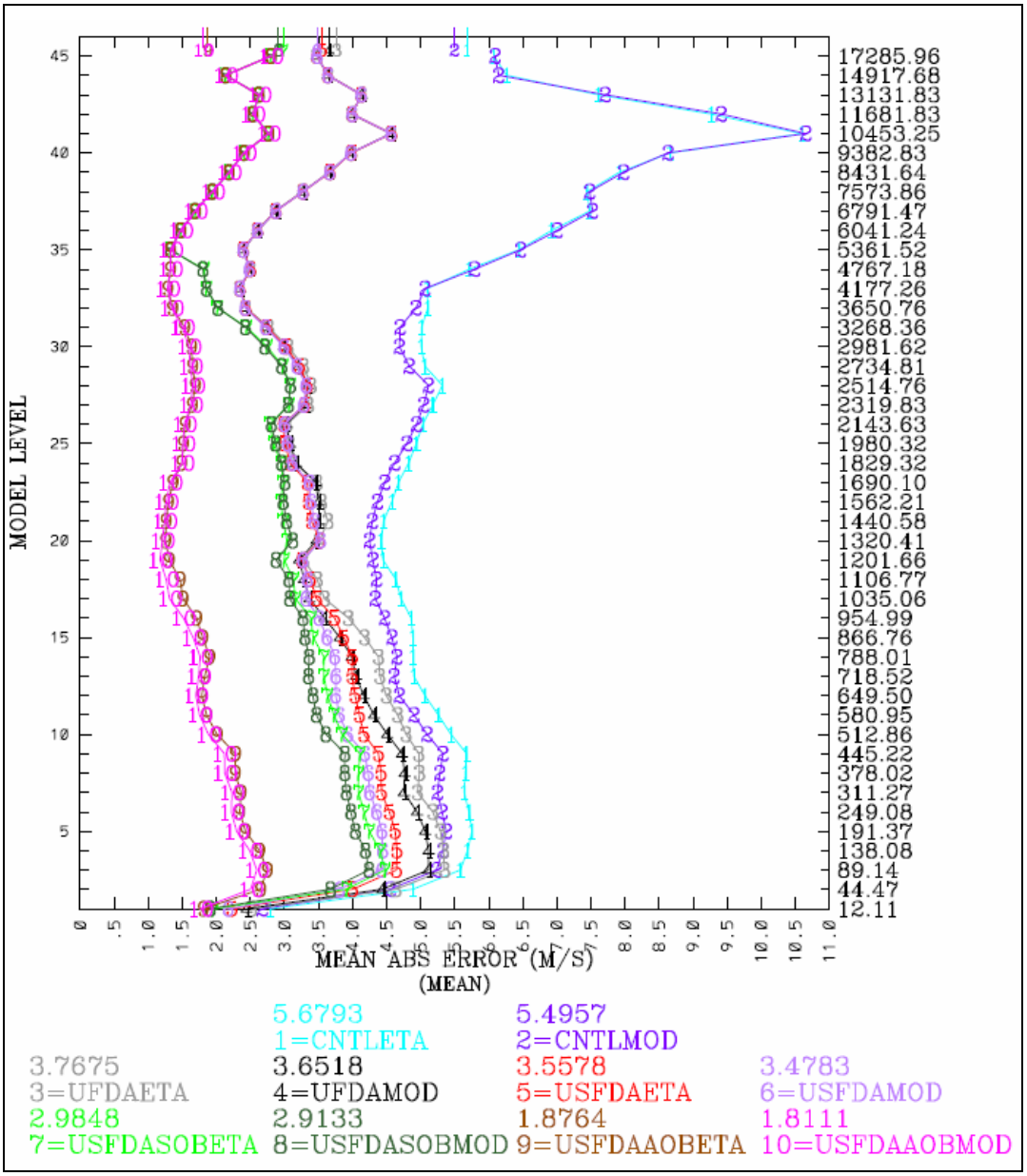

Figure F-2. Vertical profile of MAE for model-derived VWD (m/s) for the ten model development experiments. Verification is performed over the 120-hr period beginning 00 UTC, 2 December 2000, and ending 00 UTC, 7 December 2000. MAE is shown along the abscissa. On the left and right ordinates, model sigma level and model sigma level height are shown, respectively. Observation-weighted, vertical averages are given below the profile in the colors corresponding to the vertical error profile curve.

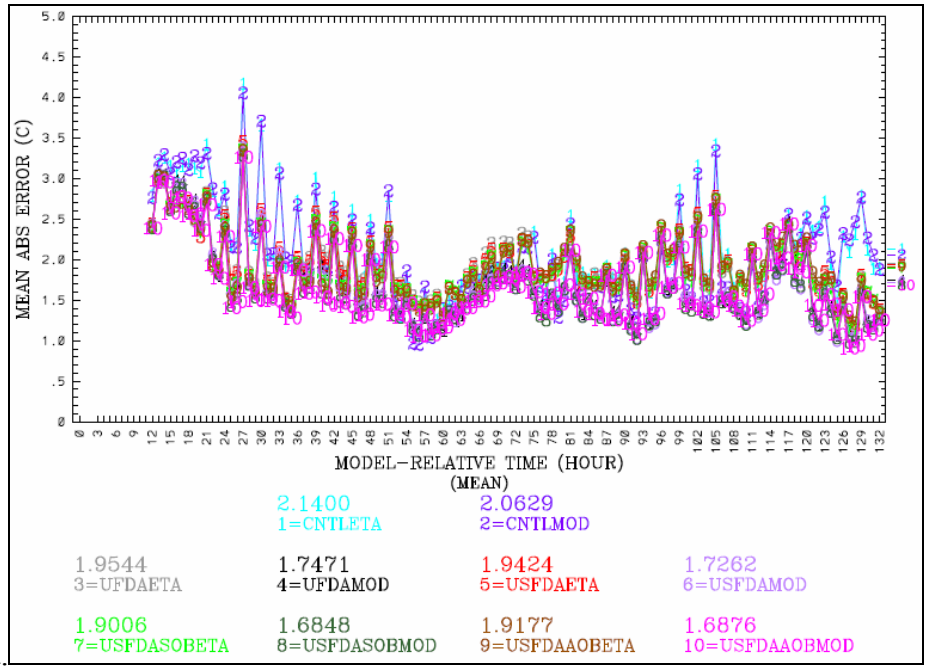

a.

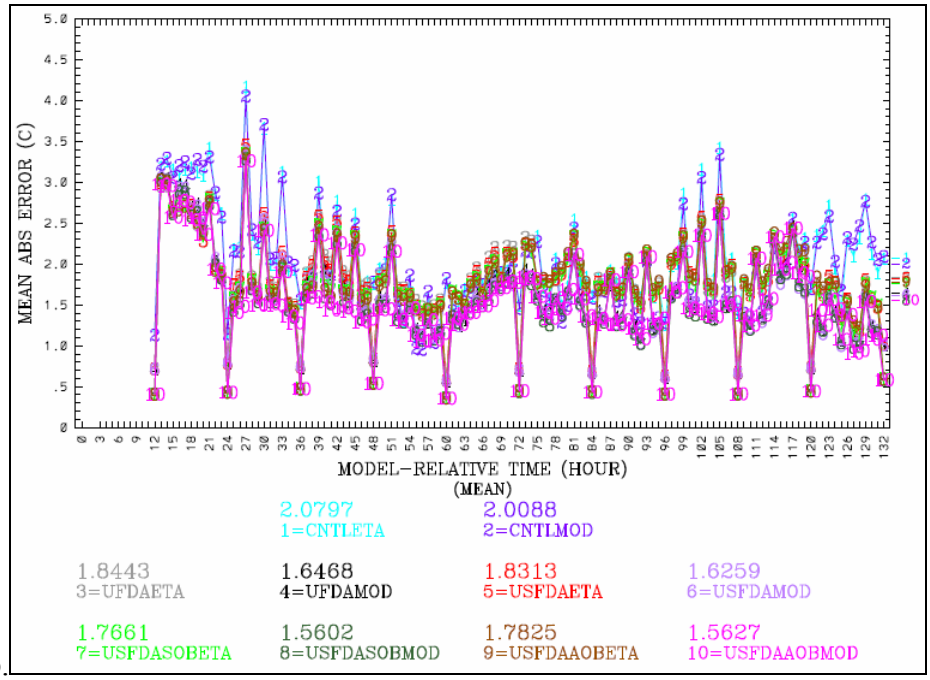

b.

Figure F-3. MAE of model-derived TEMP (°C) for a.) the surface layer, and b.) all-layers, for the 120-hr period beginning 00 UTC, 2 December 2000 and ending 00 UTC, 7 December 2000. Time-averaged MAE values are given below the time series in the colors corresponding to the error curves.

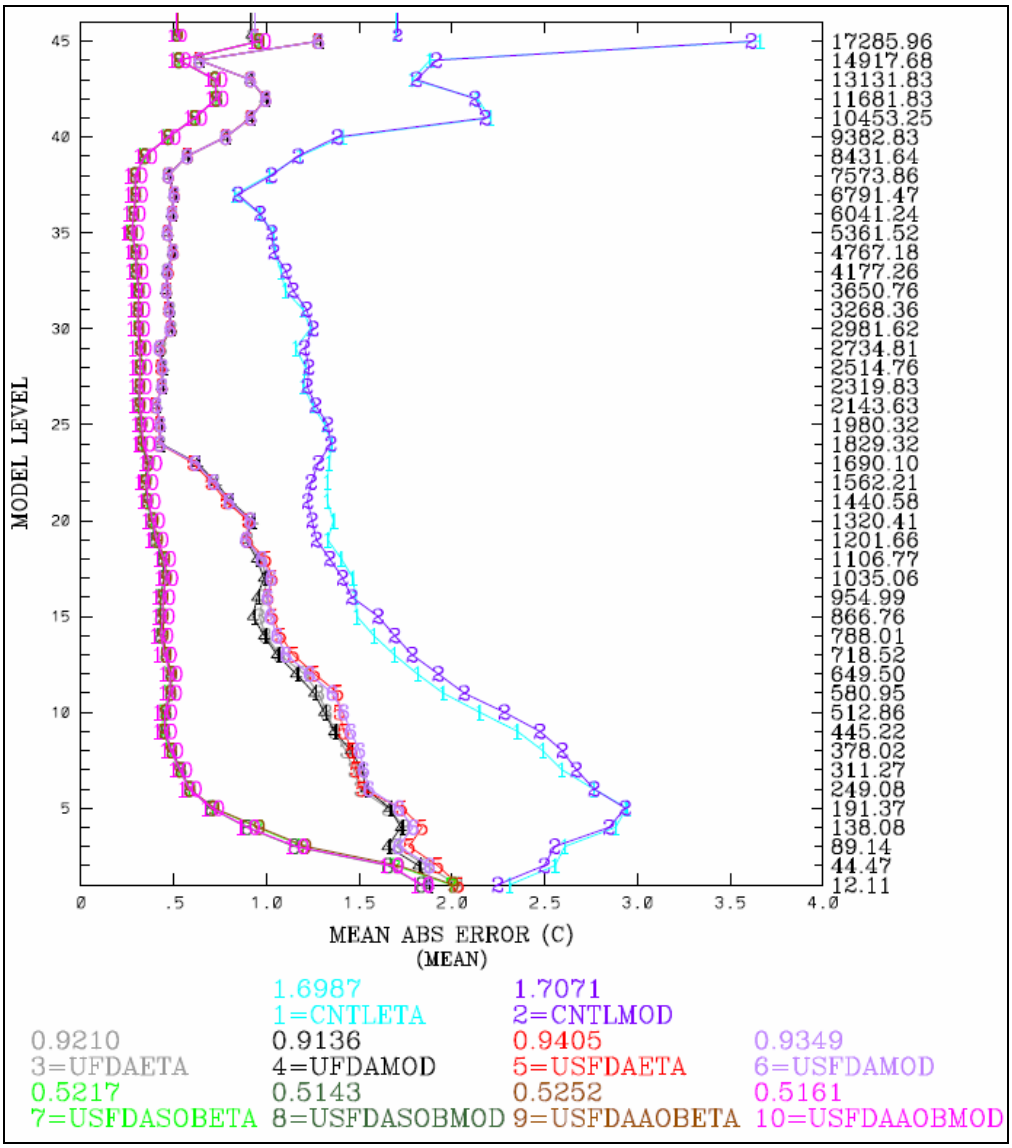

Figure F-4. Vertical profile of MAE for model-derived TEMP (°C) for the ten model development experiments. Verification is performed over the 120-hr period beginning 00 UTC, 2 December 2000, and ending 00 UTC, 7 December 2000. MAE is shown along the abscissa. On the left and right ordinates, model sigma level and model sigma level height are shown, respectively. Observation-weighted, vertical averages are given below the profile in the colors corresponding to the vertical error profile curve.

a.

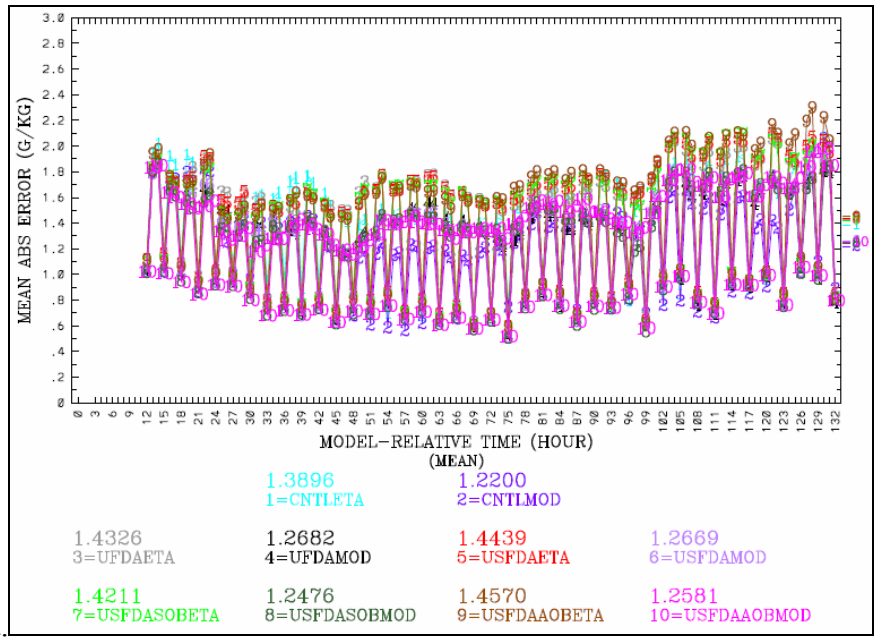

b.

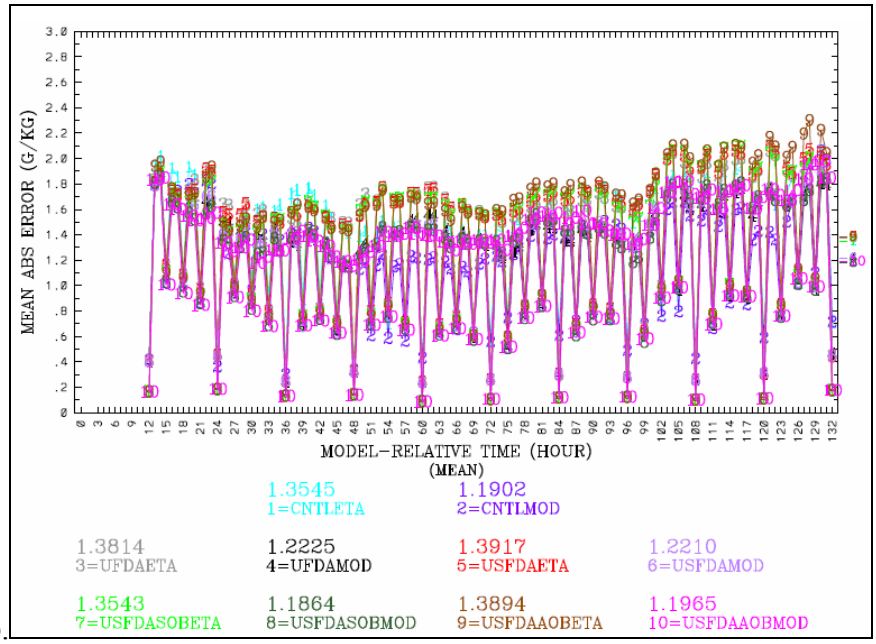

Figure F-5. MAE of model-derived MIXR (g/kg) for a.) the surface layer, and b.) all-layers, for the 120-hr period beginning 00 UTC, 2 December 2000 and ending 00 UTC, 7 December 2000. Time-averaged MAE values are given below the time series in the colors corresponding to the error curves.

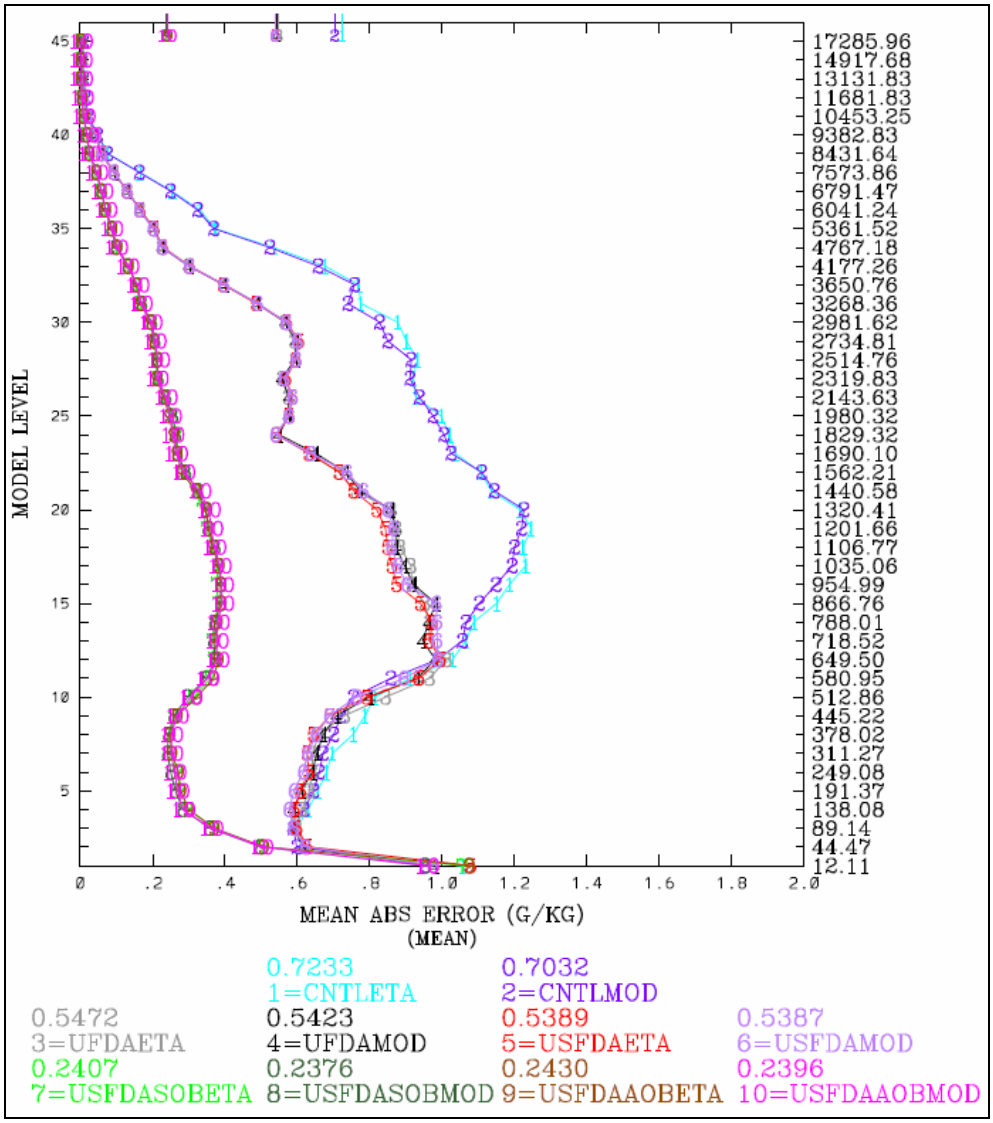

Figure F-6. Vertical profile of MAE for model-derived MIXR (g/kg) for the ten model development experiments. Verification is performed over the 120-hr period beginning 00 UTC, 2 December 2000, and ending 00 UTC, 7 December 2000. MAE is shown along the abscissa. On the left and right ordinates, model sigma level and model sigma level height are shown, respectively. Observation-weighted, vertical averages are given below the profile in the colors corresponding to the vertical error profile curve.

a.

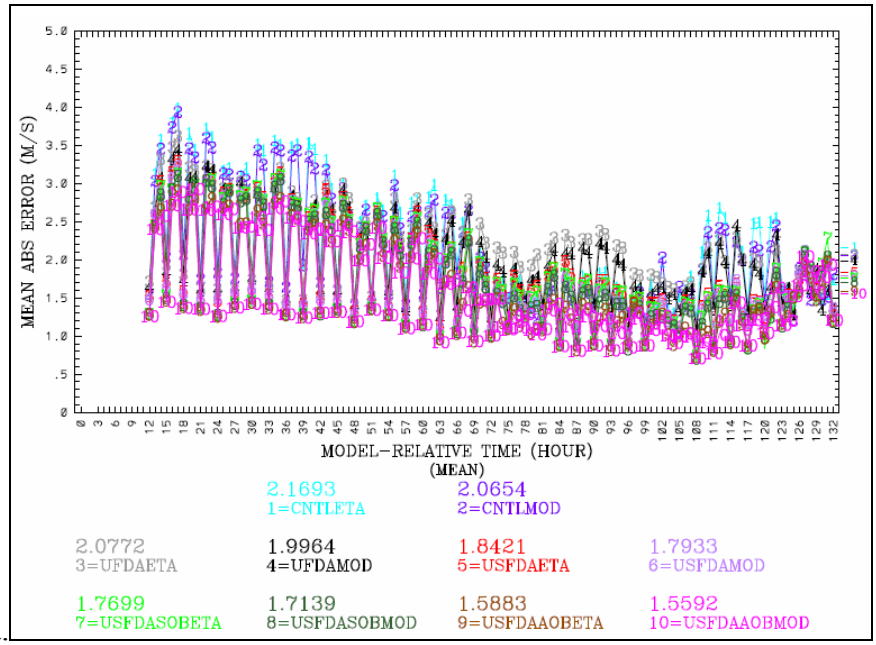

b.

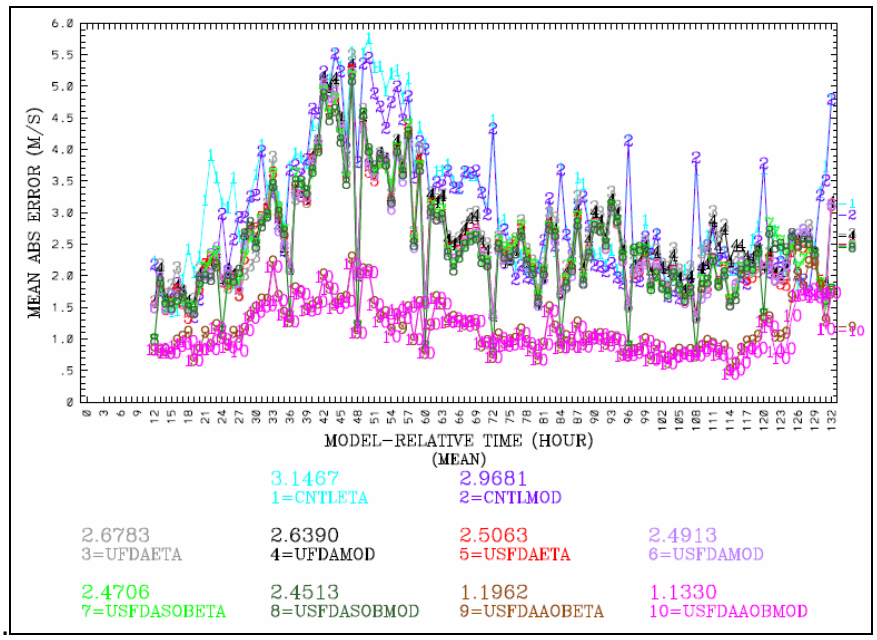

Figure F-7. MAE of model-derived WSPD (m/s) for a.) the surface layer, and b.) all-layers, for the 120-hr period beginning 00 UTC, 2 December 2000 and ending 00 UTC, 7 December 2000. Time-averaged MAE values are given below the time series in the colors corresponding to the error curves.

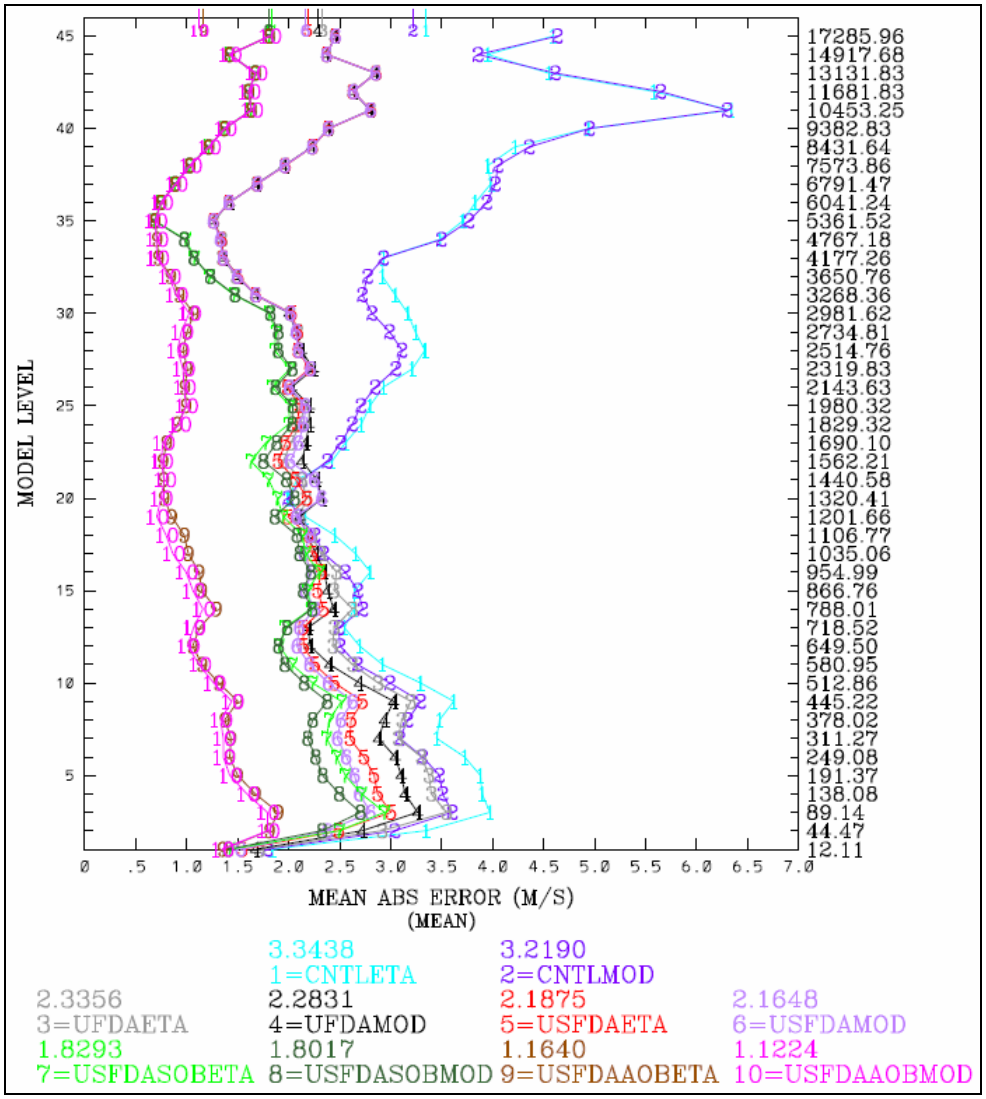

Figure F-8. Vertical profile of MAE for model-derived WSPD (m/s) for the ten model development experiments. Verification is performed over the 120-hr period beginning 00 UTC, 2 December 2000, and ending 00 UTC, 7 December 2000. MAE is shown along the abscissa. On the left and right ordinates, model sigma level and model sigma level height are shown, respectively. Observation-weighted, vertical averages are given below the profile in the colors corresponding to the vertical error profile curve.

a.

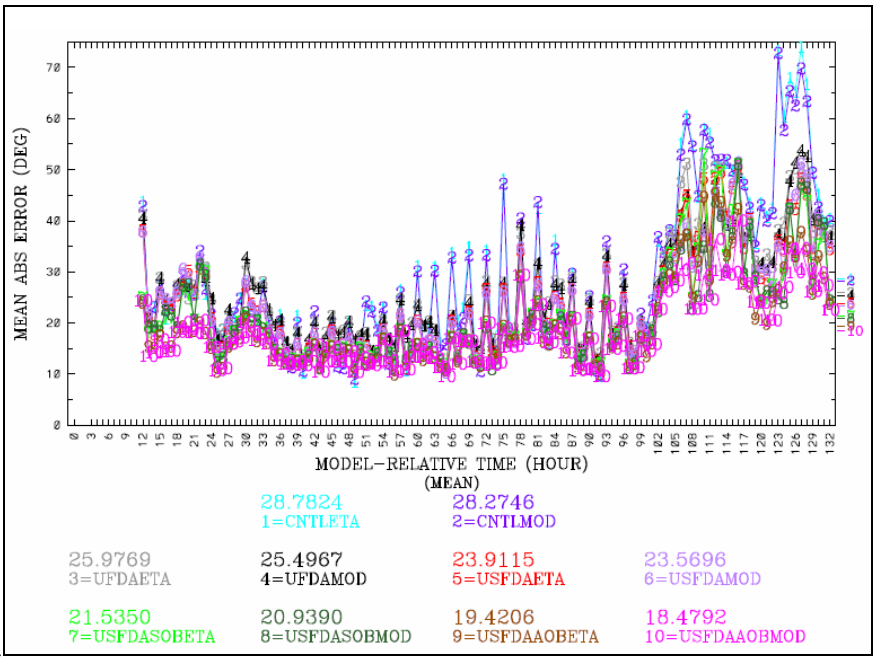

b.

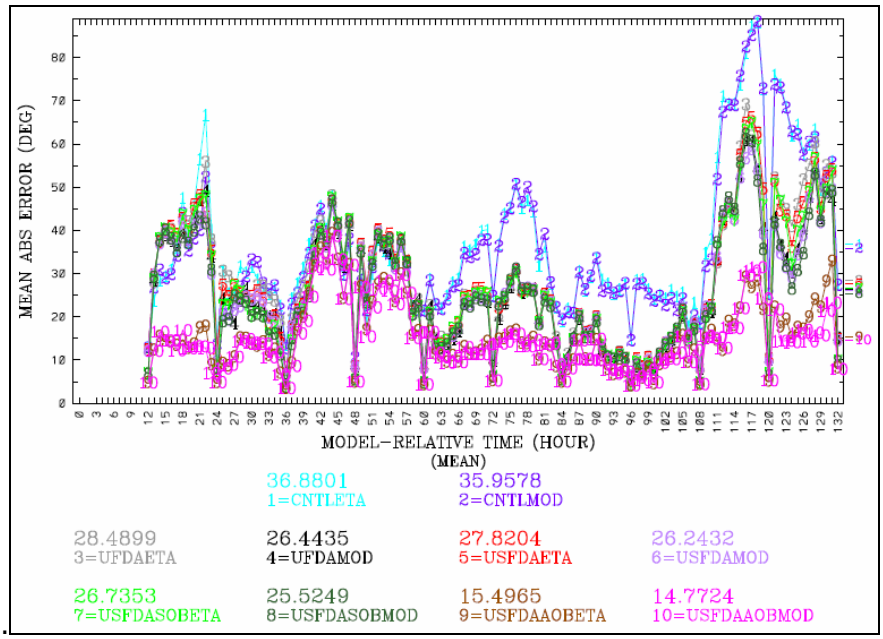

Figure F-9. MAE of model-derived WDIR (degrees) for a.) the surface layer, and b.) all-layers, for the 120-hr period beginning 00 UTC, 2 December 2000 and ending 00 UTC, 7 December 2000. Time-averaged MAE values are given below the time series in the colors corresponding to the error curves.

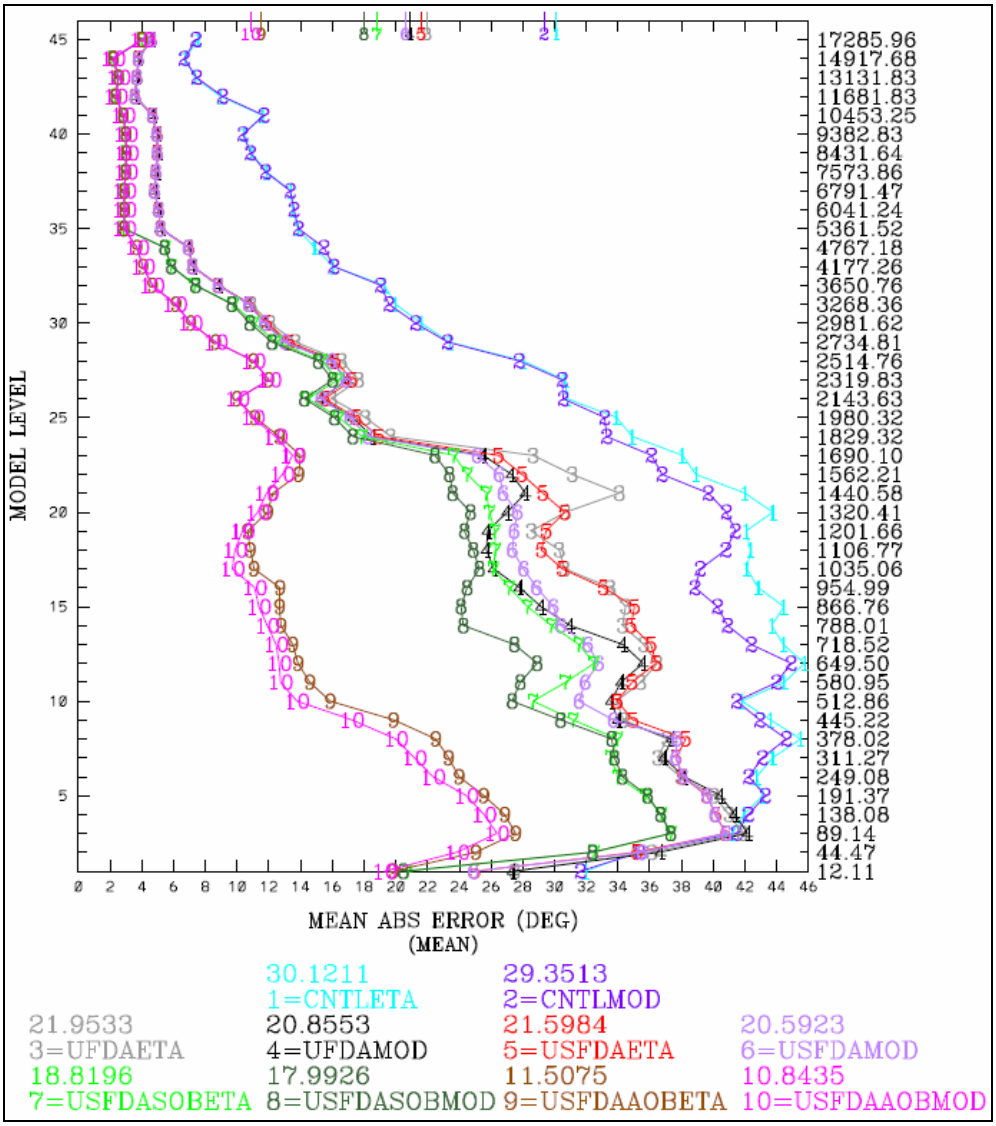

Figure F-10. Vertical profile of MAE for model-derived WDIR (degrees) for the ten model development experiments. Verification is performed over the 120-hr period beginning 00 UTC, 2 December 2000, and ending 00 UTC, 7 December 2000. MAE is shown along the abscissa. On the left and right ordinates, model sigma level and model sigma level height are shown, respectively. Observation-weighted, vertical averages are given below the profile in the colors corresponding to the vertical error profile curve.

a.

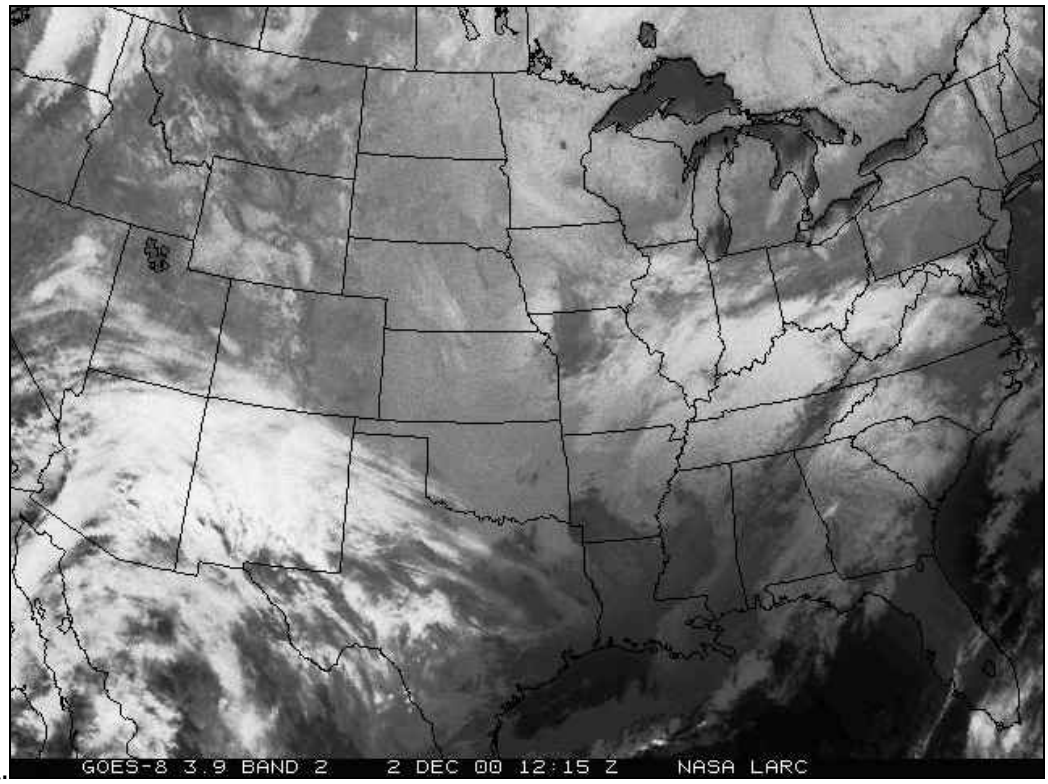

b.

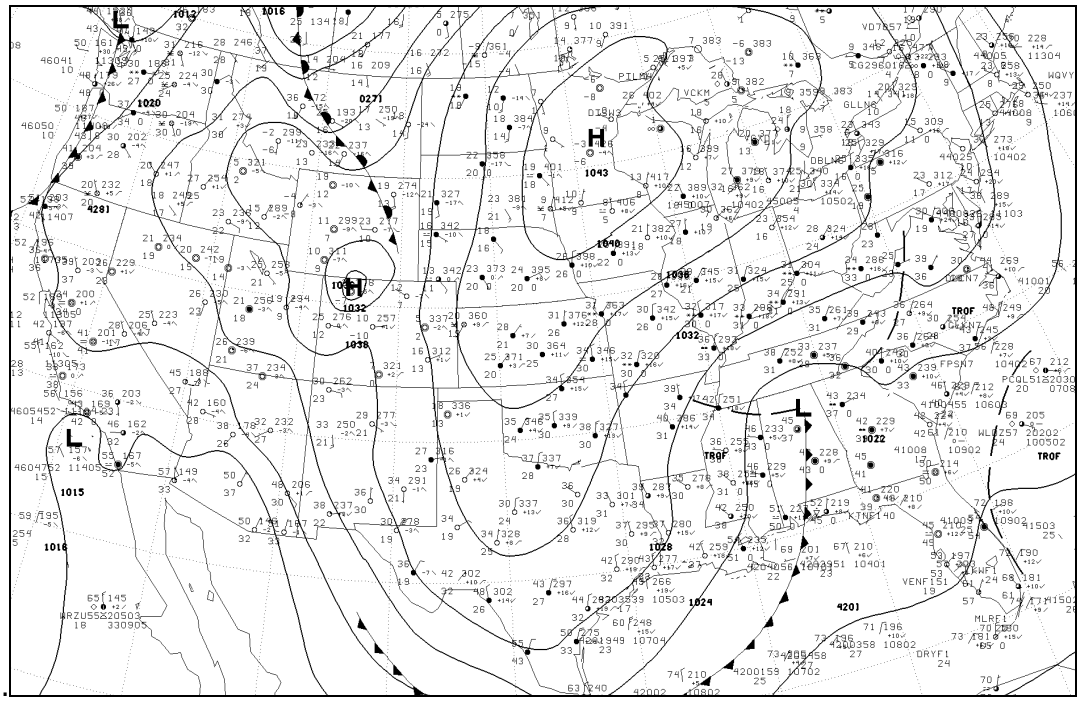

Figure F-11. Observed conditions at 12 UTC, 2 December 2000 (t = 24 h). Plot a is the IR satellite image, and plot b is the NCEP surface analysis for this time, including surface observations, fronts and isobars (drawn every 4 hPa).

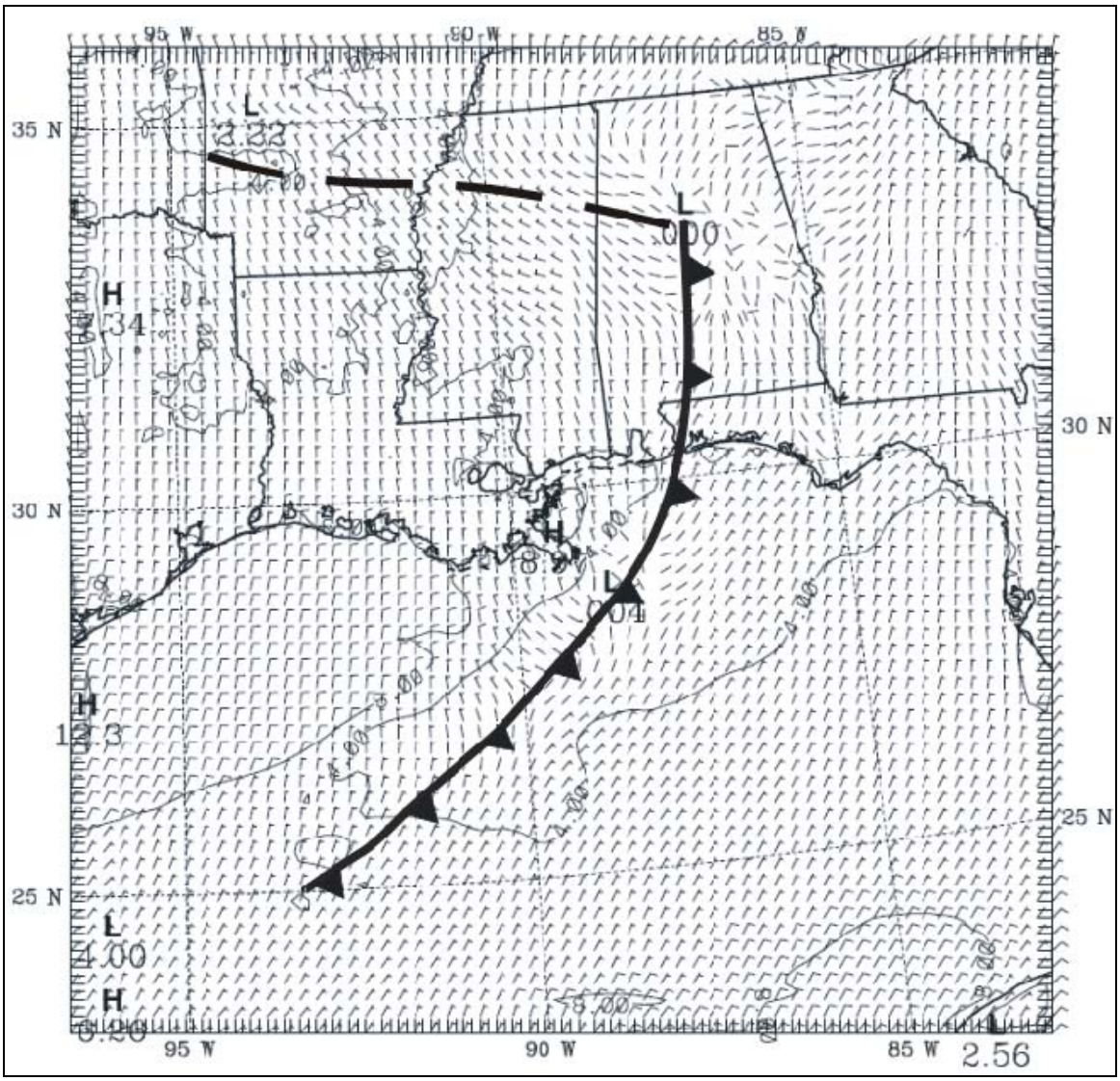

Figure F-12. Model-derived surface layer winds, and subjective frontal analysis for t = 24 h, 12 UTC, 2 December 2000. Wind barbs are plotted every other grid cell, and wind speeds are contoured every 4.0 m/s.

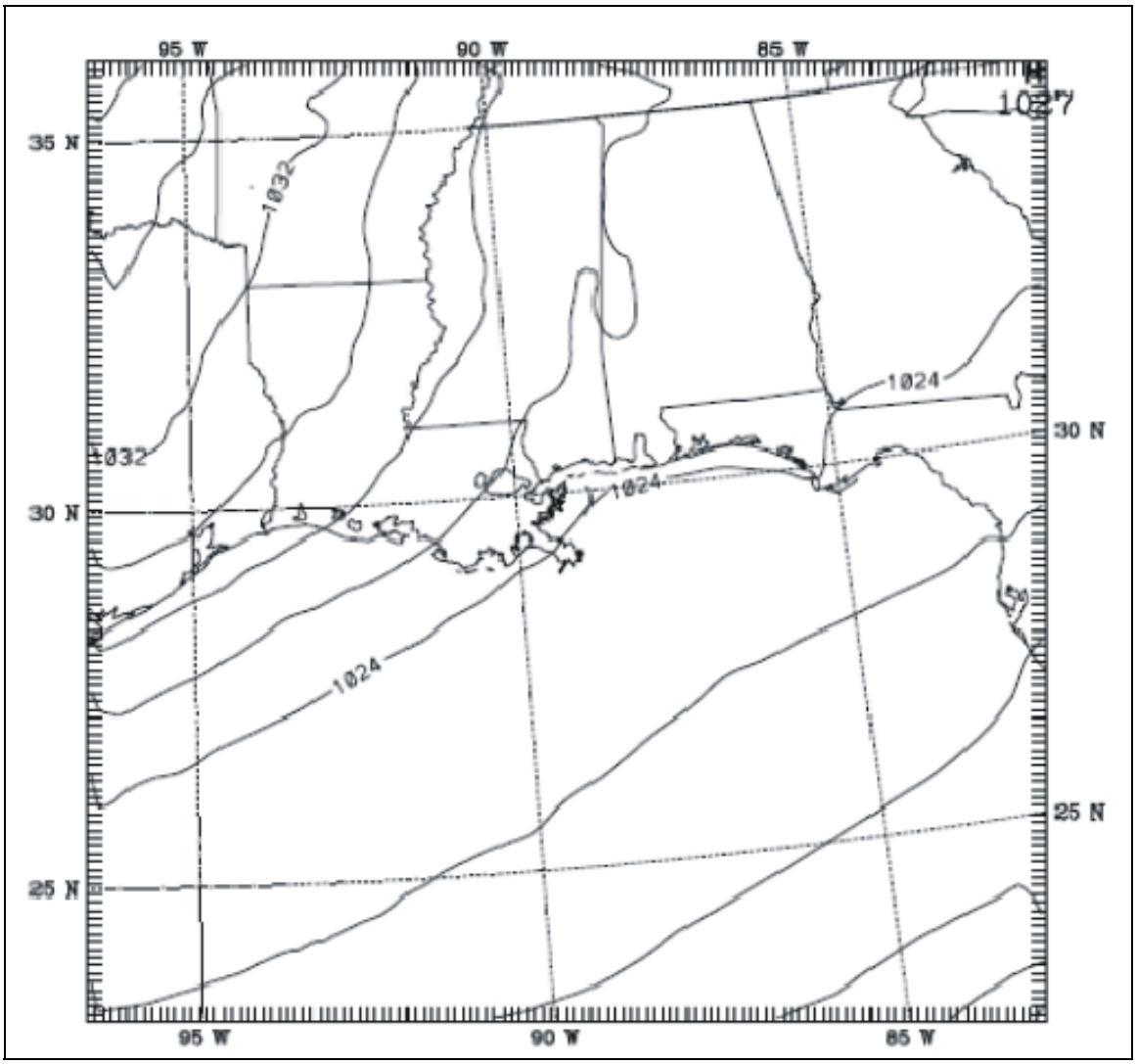

Figure F-13: Model-derived sea-level pressure field over the 12-km domain at 12 UTC, 2 December 2000 (t = 24 h). Isobars are drawn every 2 hPa.

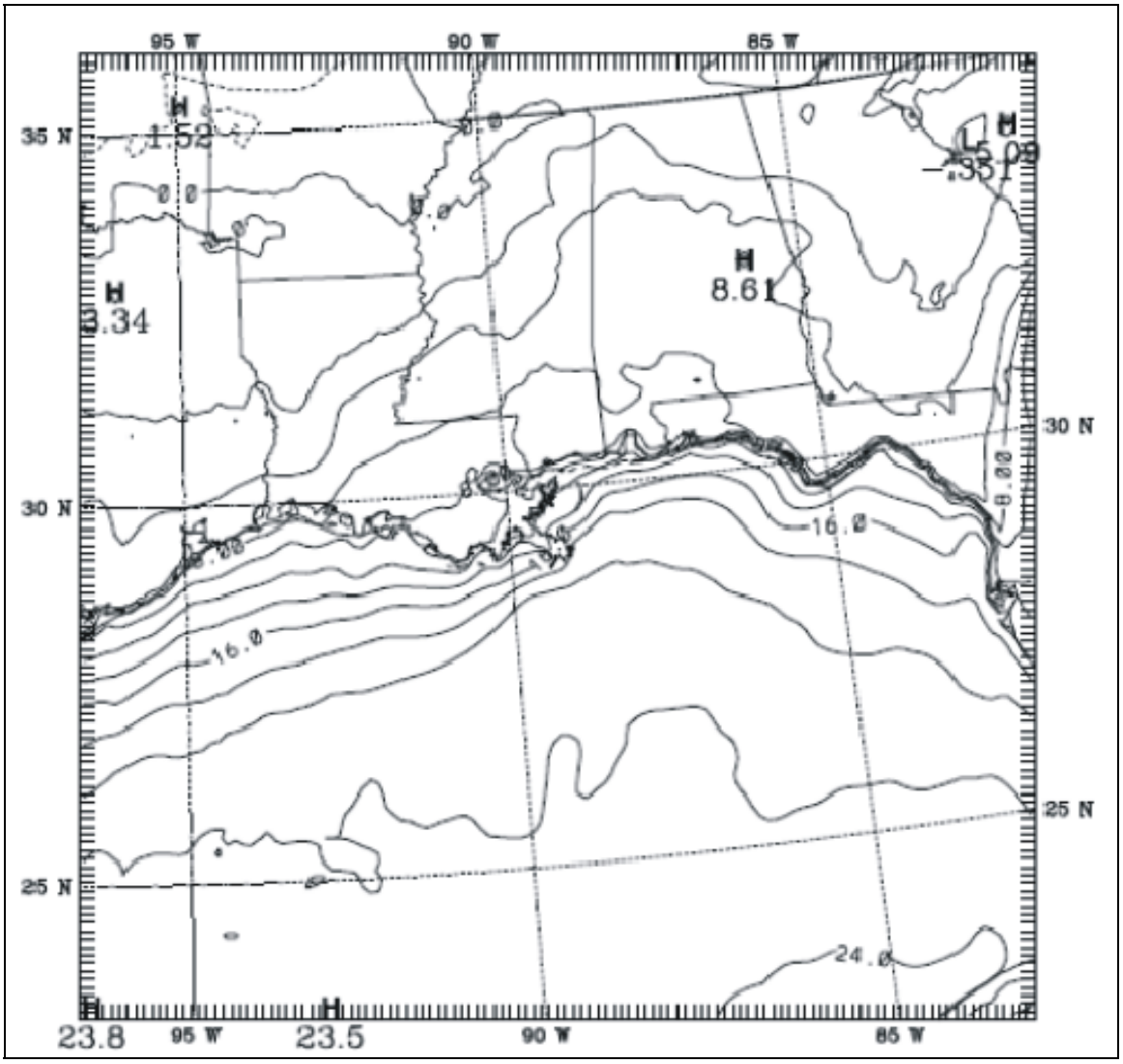

Figure F-14. Model-derived surface layer temperature field across the 12-km domain for 12 UTC, 2 December 2000 (t = 24 h). Isotherms are drawn every 2 °C.

a.

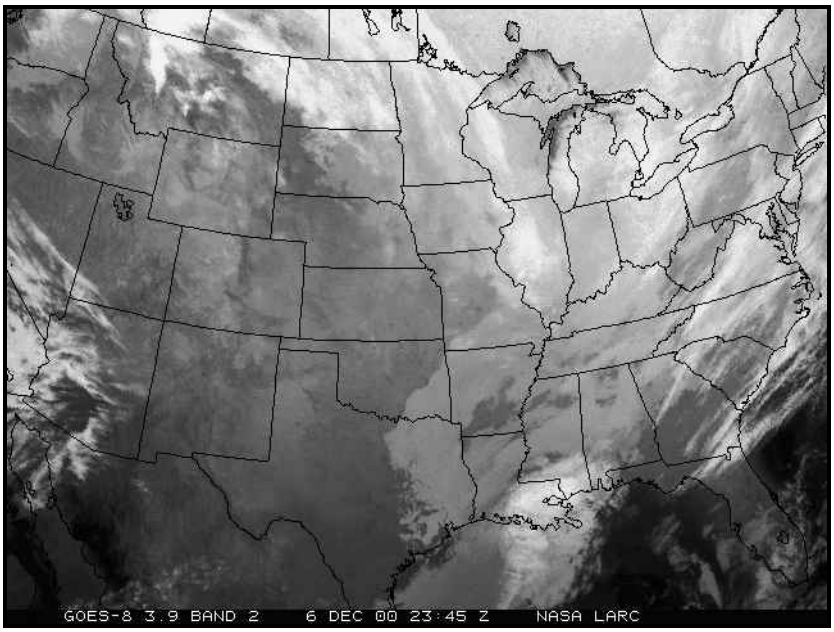

b.

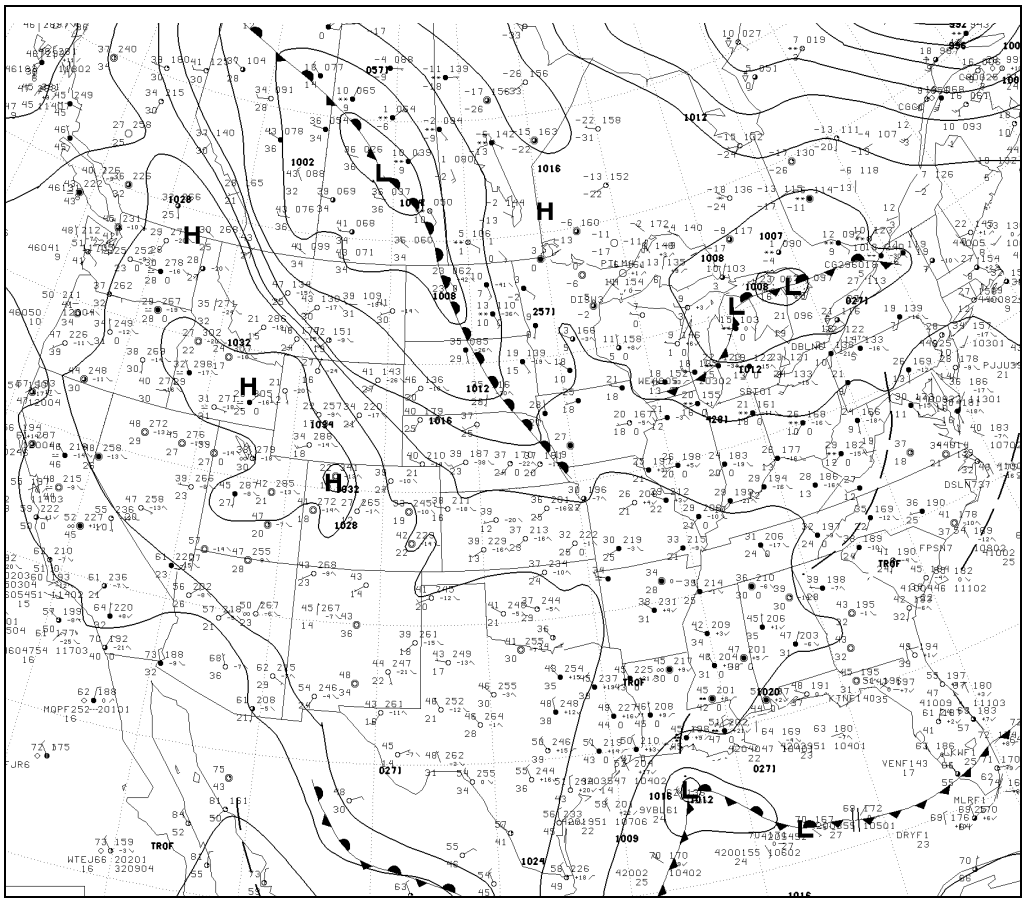

Figure F-15. Observed conditions at 12 UTC, 7 December 2000 (t = 132 h). Plot a is the IR satellite image, and plot b is the NCEP surface analysis for this time, including surface observations, fronts and isobars (drawn every 4 hPa).

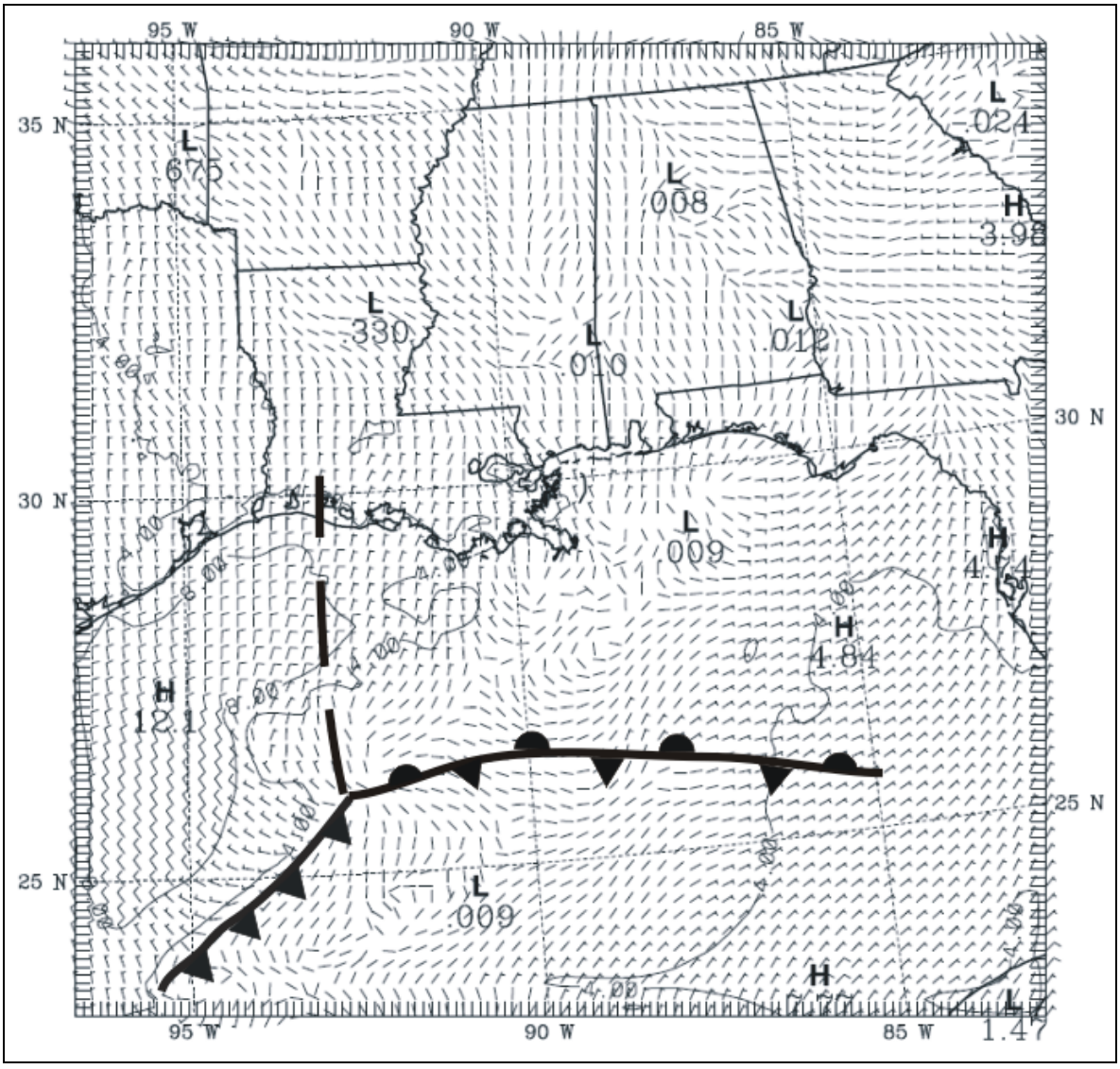

Figure **F-16**: Model-derived surface layer winds and subjectively analyzed surface fronts/troughs for 00 UTC, 7 December 2000 (t = 132 h). Wind barbs are plotted every other grid cell, and wind speeds are contoured every 4 m/s.

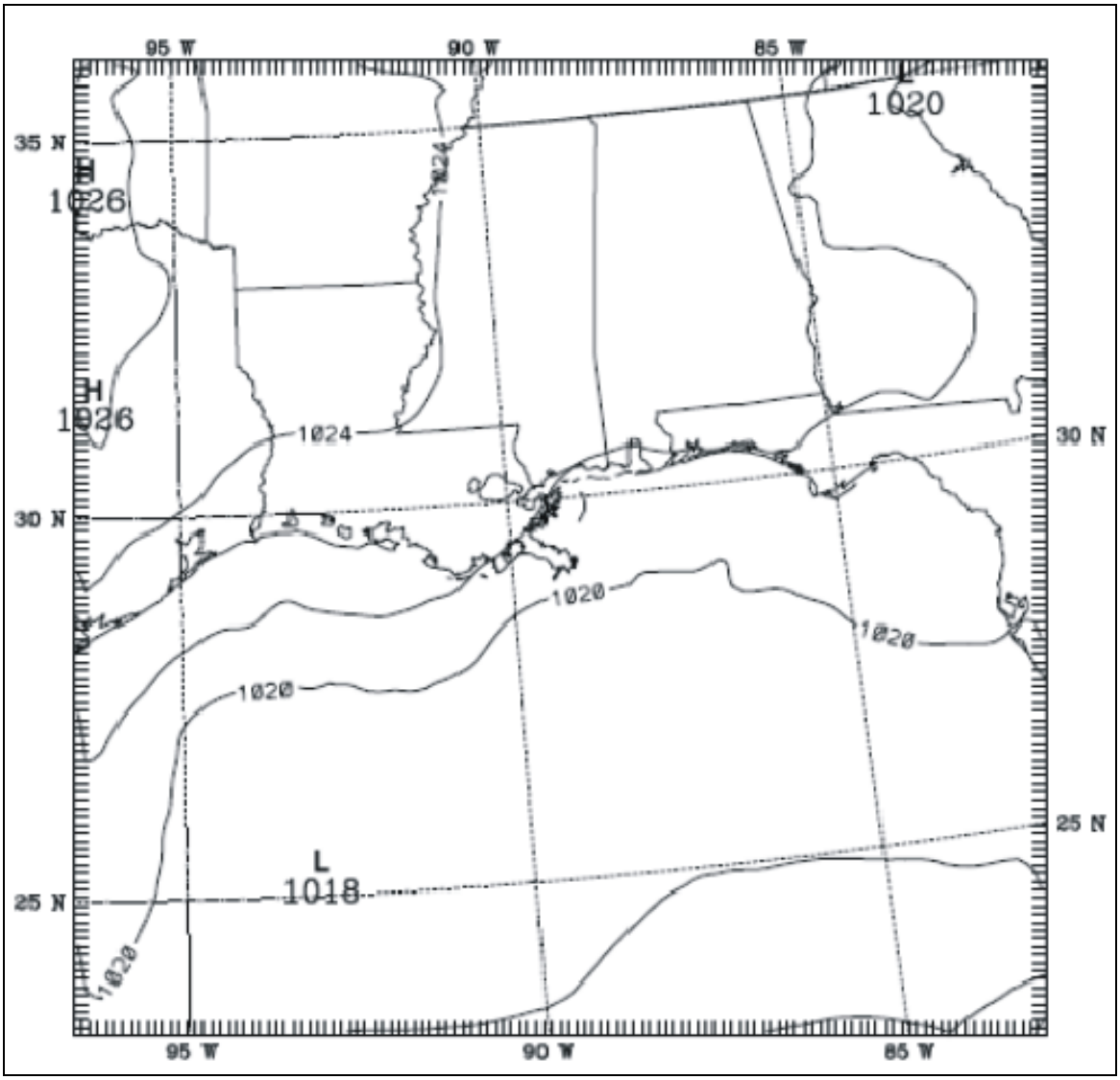

Figure F-17. Model-derived sea-level pressure field over the 12-km domain at 00 UTC, 7 December 2000 (t = 132 h). Isobars are drawn every 2 hPa.

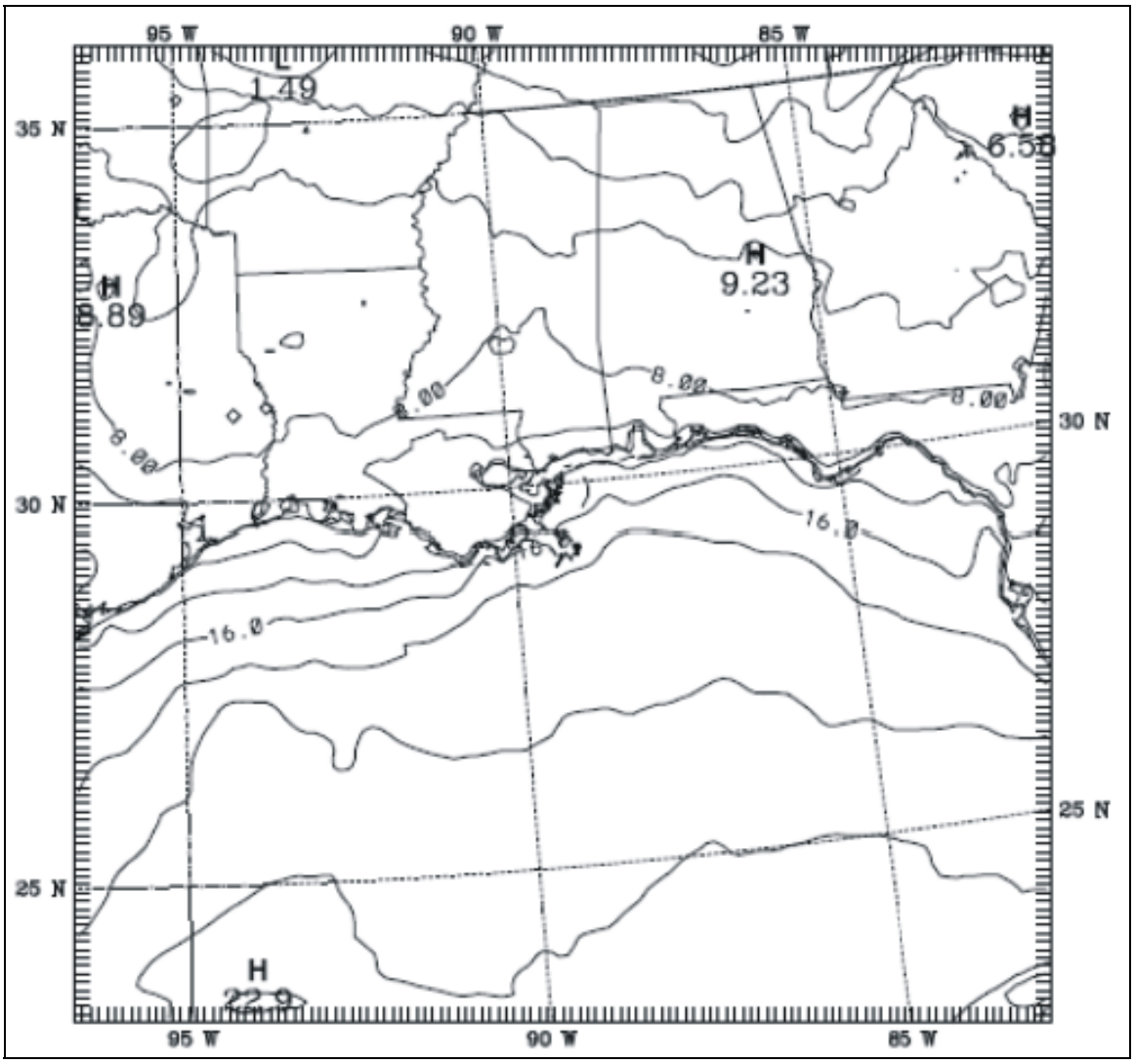

Figure F-18 Model-derived surface layer temperature field across the 12-km domain for 00 UTC, 7 December 2000 (t = 132 h). Isotherms are drawn every 2 °C.

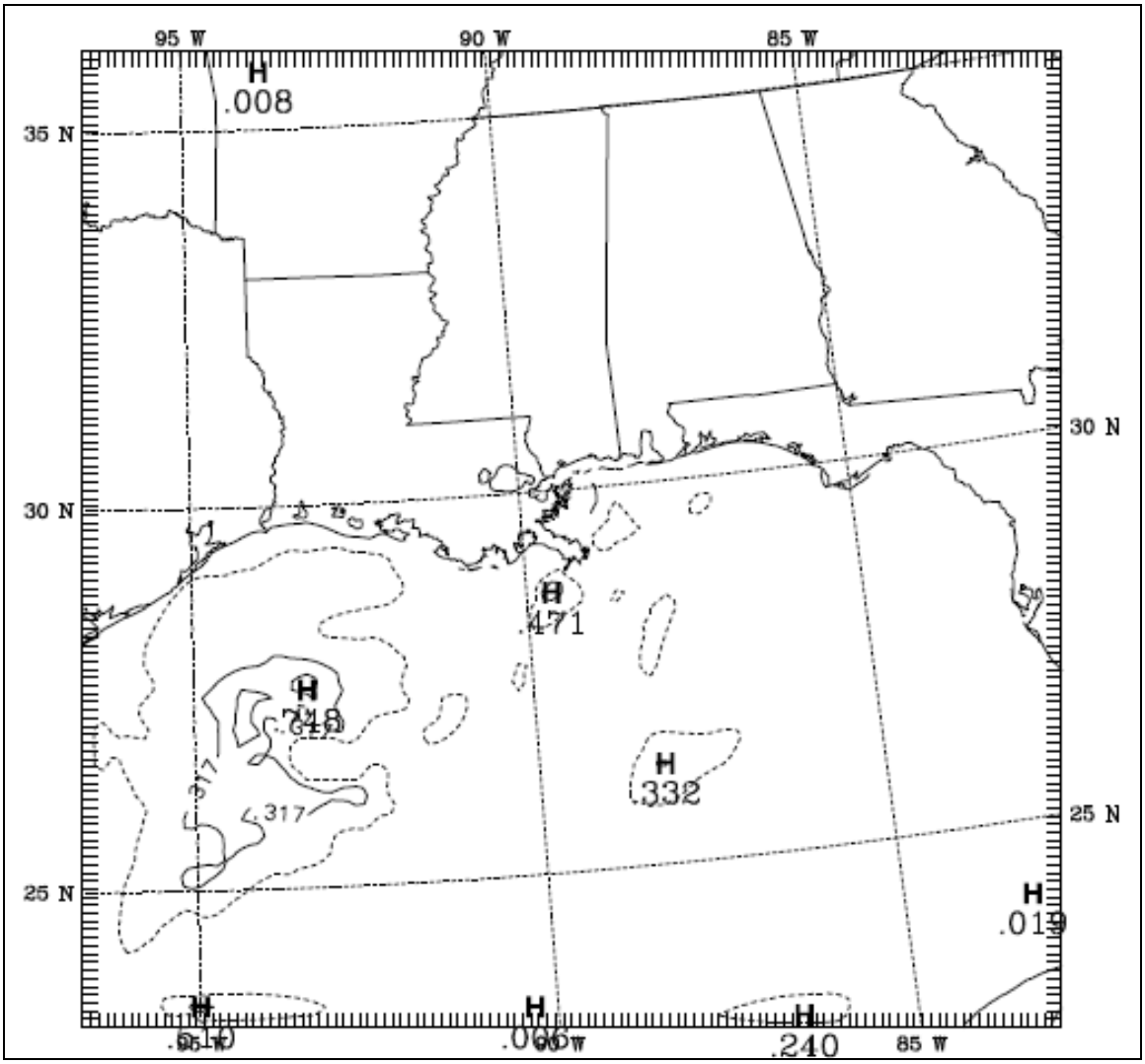

Figure F-19. Model-derived precipitation tendency (cm) for the 3 hours prior to 00 UTC, 7 December 2000. The dashed contour encloses all areas receiving measurable precipitation. Solid contours double with each successive contour, beginning with 0.317 cm (0.125 inch).

APPENDIX G

DETAILED DESCRIPTION OF 4-KM RESOLUTION MM5 SIMULATIONS

This description of the 4-km resolution MM5 simulations was extracted from a manuscript prepared by Jeffrey R. Zielonka of the Department of Meteorology, Pennsylvania State University, State College, Pennsylvania.

Air quality studies have some interesting challenges because pollutant transport in the atmosphere is inherently susceptible to small changes in horizontal wind speed and direction, as well as vertical motions. Within the three-dimensional (3D) wind field produced on say a 36-km model grid, a much more detailed wind pattern may actually exist due to mesoscale features such as convective outflow boundaries (gust fronts), or coastal thermal circulations (sea breezes). As shown in Schroeder et al. (2006), coastal circulations around the Chesapeake Bay may be resolved by a 12-km grid, but they are better resolved with complex coastlines by a 4-km resolution domain. Similarly, because the coastlines of Louisiana and neighboring Mississippi and Alabama are so detailed, a 4-km resolution mesoscale model may add value in these areas. The goal of the following section is to investigate the possible benefits of a 4-km resolution model simulation for the three different types of cases in December, March and July.

It will also be determined in later sections if any of the modeling techniques discussed previously have a positive or negative impact on the 4-km model simulations. In particular, the roles of a convective parameterization on the 4-km grid to reduce grid-point storm effects, and the use of higher-resolution MODIS SST will be investigated with these three cases.

It is hypothesized that the 4-km model-simulated meteorological fields will exhibit more detailed mesoscale structure that could enhance the performance of air-chemistry/pollutant transport models in this Gulf Coast area. In this section, the statistical and subjective differences between the 12-km simulations that were used in the year-long study for each of these cases and 4-km resolution simulations nested within the 12-km simulations are discussed. Model results for the 12-km simulations are mapped to the 4-km domain area for direct comparison with the 4-km simulation results.

G.1 CASE 1: 12 UTC, 1 DECEMBER 2000 TO 00 UTC, 7 DECEMBER 2000

Case 1 was described as a cold-season case, characterized by two primary synoptic regimes. The beginning of this case involves a FOR situation corresponding with the passage of a cold front between t = 0 h, 12 UTC, 1 December 2000 and t = 24 h, 12 UTC, 2 December 2000. By t = 48 h, 12 UTC, 3 December 2000, the cold front had pushed far enough to the south where FOR was no longer an influence within the 12-km domain. Instead, the primary synoptic influence at this time was a strong high pressure system to the north, causing northerly, offshore flow, with freezing temperatures in the northern-most quarter of the 12-km domain. This high pressure system continued to dominate the synoptic pattern until approximately t = 120 h, 12 UTC, 6 December 2000, as another cold front pushed south through Louisiana, and into the GOM. This cold front resulted in another FOR setup that was in place for the final 12 hours of the model simulation period.

At the start of the model simulation period, the approaching cold front had just entered the northwest corner of the 12-km model domain. The 12-km surface-layer (lowest sigma-level) wind field and observations over the 4-km domain sub-region is shown in Figure G-1. Since this is the model initialization time (t = 0 h), this field is representative of the 12-km domain initial conditions created from Eta model analyses and only the standard WMO observations. These initial conditions for the 12-km and 4-km simulations are created in the preprocessing steps. The

corresponding lowest sigma-level wind field and wind observations for the 4-km resolution domain are shown in Figure G-2. At this time, the cold front had not yet entered the 4-km domain, which focuses greatly on the area immediately near the Gulf coast. Here, the flow is primarily from the east and northeast, as the winds wrap around the southern edge of the retreating high pressure system to the northeast. Winds close to the northern boundary of the 4-km domain are light and variable, because these locations are closer to the center of the high and weaker pressure gradients.

The plotted observations include all observations that occur within one-half hour of the current time, so all wind speeds and directions may not be representative of conditions at exactly the time of the model plot. The observed directions and speeds show good agreement with the model winds, but note that only the standard observations are used to create these initial fields. Special data sources are only used for observation nudging and model verification. Note that one half barb on a wind observation represents a wind speed between 2 m/s and 7 m/s. With this in mind, the observed wind speeds corresponding to these half barbs all fall within the range of model wind speeds. Near the northern tip of the Breton island chain, two observations of 6.1 m/s and 6.2 m/s are reported among several observations that range from 0.0 m/s to 4.0 m/s. The wind speeds are not, however, different enough from the model background field or its neighbor observations to be removed during the QC process. The observations in the northern extent of the 4-km domain contain several 0.0 m/s winds, which support the model reporting light and variable wind conditions at this time.

As with all the cases in this year-long study, the first 12 hour period of the model simulation is reserved for spin-up time, so the model can spin up its cloud, precipitation and local circulations which are either absent or poorly resolved in the initial condition fields. During the 12 hours of model spin-up, the cold front pushed toward the southeast, and was located just to the northwest of the 4-km domain. Conditions in the wind fields remain relatively calm ahead of the cold front, which is evident in the 12-km model output and observations in Figure G-3, plotted for t = 12 h, 00 UTC, 2 December 2000. Winds over the GOM remained out of the northeast, as a weak pressure gradient existed between the Gulf coast and the central GOM. The 4-km model output and observations for the same time in Figure G-4 exhibit much of the same behavior across the GOM, with the majority of the winds blowing from the east and northeast, and the 4-km winds appear slightly faster than the 12-km winds in some coastal-zone regions in better agreement with the observations.

After the 12 hours of model spin-up is completed, statistics are computed for both the 12-km domain and the 4-km domain output fields for the rest of the model simulation. As with the subjective comparisons, the statistical comparisons between the 12-km and 4-km domain results are only calculated using observations within the 4-km domain, so the effect of grid resolution can be directly determined. The statistical comparison of the surface-layer wind fields of these two control runs, DEC12 and DEC4, is shown in Figures G-5 and G-6, where the blue and purple curves represent the hourly errors of DEC12 and DEC4 respectively. Figure G-5 shows the surface-layer MAE of VWD (m/s) for the two experiments. The values on the bottom of the figure show the average MAE for the 120-hour period during which statistics are calculated, with the corresponding experiment names. The overall average VWD MAE for these two control cases is 2.2 m/s for DEC12 and 2.4 m/s for DEC4. It appears that in the surface layer, there is little difference in statistical skill although there are regions and times when one model may have

some advantage over the other. A subjective evaluation for the entire period may reveal some more significant differences

Figure G-6 shows two plots similar to the VWD plot in Figure G-5, but instead, displays the two surface wind errors that comprise the VWD, the wind speed (WSPD) and wind direction (WDIR). In the WSPD plot, the overall average values once again slightly favor the 12-km resolution model, with a 1.4 m/s to 1.5 m/s comparison between the two simulations. Some of the same statistical characteristics are present in this speed comparison that were seen in Figure G-5, especially the lower MAE values of the 12-km simulation during the timeframe of t = 108 to 119 h. The WDIR plot presents a slightly better overall average MAE for the 12-km WDIR (21.8 degrees) than the 4-km WDIR (23.4 degrees).

For an air-quality study, the performance of the model throughout the depth of the PBL is just as important, if not more important than the performance of the model at the surface layer. .Since the transport of ground-based pollutants rarely occurs above the PBLtop without mountain upsloping or convective activity which "vents" pollutants into the free atmosphere, the PBL may contain large concentrations and is a very important atmospheric layer. The MAE of VWD for the PBL, defined here as the layer between 30 and 1000 m above ground level (AGL), gives a slightly different result for the wind errors (Figure G-7). In the PBL, the overall average MAE is still very similar, but 2.2 m/s for DEC12 and 2.1 m/s for DEC4. The largest differences between the two model PBL winds occur around t = 66 to 67 hours. At this time, DEC12 reaches its maximum MAE for the period, which is approximately 4.3 m/s. The largest hourly MAE value for DEC4 occurs around t = 28 h at approximately 3.7 m/s. This result may not be significant that the 4-km simulation performs better in the PBL, but it shows that the 12-km simulations do not always provide better objective results in all layers of the atmosphere or at all times. Since the objective analysis of the wind fields in the surface layer and the PBL offer somewhat different results, it is also interesting to examine the statistical differences in the vertical profiles, from the surface to the top of the model. This vertical profile of MAE for VWD is shown in Figure G-8, and shows that over all layers, the 4-km resolution simulation performs 0.1 m/s worse from an objective standpoint. The biggest differences between the performance of the two resolutions occurs above sigma-level 35 (approximately 5400 m). There are also some differences between the error profiles favoring the DEC12 simulation between sigma-levels 16 and 23 (approximately 950 to 1700 m AGL). Overall, the 12-km resolution simulation had an average MAE of 1.9 m/s, and the 4-km resolution simulation had a slightly worse average MAE of 2.0 m/s over the 120-hour verification period, so objective differences are again not significant. To determine whether slightly larger model errors for the wind fields in the 4-km simulations can be explained in the surface layer, the timing and placement of meteorological features such as fronts are examined and compared to observations on both model domains. For this case, the particular time periods when the model resolutions were noticeably different (see above), as well as the time periods when fronts and other features that are generally difficult to predict both spatially and temporally are studied carefully.

The most difficult scenario to forecast during the first day of model integration after spin-up is the passage of a cold front through the 4-km region between t = 12 h, 00 UTC, 2 December 2000 and t = 24 h, 12 UTC, 2 December 2000. As discussed above, the model fields from the entire 12-km domain (not shown) indicate that the front is still slightly to the northwest of the 4-km domain at 00 UTC. To follow the progression of the cold front through the 4-km domain

more accurately, 3-hourly NCEP surface analyses are used (Figure G-9). Beginning at t = 12 h, 00 UTC, the surface charts show the southeastward progression of the cold front, beginning just to the northwest of the 4-km domain. At t = 24 h, 12 UTC analysis time, the cold front has passed through the majority of the landmass in the 4-km domain, and extends southward from the area near the border of Alabama and the Florida Panhandle into the GOM. The progression of model-simulated fronts over the 4-km domain area from DEC12 (Figure G-10) appears to match the progression of surface analyses (Figure G-9) rather well. The pressure troughs and convergence zones in the wind fields are generally aligned with the analyzed fronts on the NCEP surface analyses. The nature of surface frontal boundaries, however, is such that a small horizontal displacement of a front can cause large errors, especially in the wind direction fields.

The model output for DEC4, offers a slightly different representation of the frontal positions, determined by hand subjective analysis of the wind, temperature and pressure fields. Figure G-11 shows the same 3-hourly temporal progression of the wind field and SLP for DEC4. At 00 UTC (t = 12 h), when the surface front should be just outside the 4-km domain, there is a short wind shift line that is evident in the northwest corner. The SLP and surface-layer temperature fields (not shown) indicate a trough in this area, as well as a temperature contours that are relatively parallel to this wind shift, which suggests that this feature is the cold-frontal boundary. At 06 UTC (t = 18 h), the frontal position appears to differ slightly between analyzed and modeled products. The NCEP analyses show the front to the west of Lake Pontchartrain (LP). Alternatively, the wind-shift zones, SLP field and temperature gradients (not shown) in the DEC12 and DEC4 output indicate that the frontal placement should be directly over LP. From 06 UTC (t = 18 h) to 12 UTC (t = 24 h), the surface frontal zone in the DEC12 output appears to be located slightly farther to the east. These small differences in the position of the cold front are likely the cause of the larger than average WDIR errors discussed above (Figure G-6), as there are some wind shifts present that are greater than 50 degrees across the front. In some instances, especially in the DEC4 output, there are observations that do not agree with the expected model-predicted wind patterns caused by the front. For example, it appears that the front may be slightly too slow in the DEC4 model output, but this may be a result of data density and positioning of the subjectively analyzed front in the NCEP analyses.

As is the case during most periods when there is a cold frontal passage, this case experienced precipitation ahead of the front within the boundaries of the 4-km domain. The 24-h precipitation totals from NCEP observed precipitation map, shown in Figure G-12, show widespread precipitation across the entire state of Louisiana and the southern half of Mississippi. The heaviest precipitation amount, 0.82 inches (2.1 cm), was recorded at Baton Rouge (KBTR) during this period. Since the period of precipitation matches the first 24 hours of model simulation time perfectly (including model spin-up), a direct comparison can be made to the model precipitation totals at t = 24 h, 12 UTC, 2 December 2000. The precipitation totals derived from the DEC12 output across the entire 12-km domain are given in Figure G-13, and the DEC4 precipitation totals over the 4-km domain area are given in Figure G-14. The comparison of these two images shows several differences between the depiction of precipitation totals in the simulations of different resolutions. Both resolutions produce a west-northwest to east-southeast strip of precipitation over Louisiana with the heaviest amounts to the northwest of LP, and another area of precipitation over the GOM, within the area of the 4-km domain. The east-west extent of the precipitation and the amount of precipitation, however, are quite different. DEC12 keeps the eastern edge of the 0.32-cm precipitation contour to the western edge of LP,

but the eastern extent of this precipitation contour in the DEC4 output reaches through a small portion of southern Mississippi, and into the GOM. This 4-km representation of the precipitation field seems to be much closer to the real observations, as the New Orleans observing station (KNEW), which is to the southeast of LP, still recorded 0.13 inches (0.33 cm) of precipitation. Both models had difficulty along the southern shore of Louisiana. Two stations, Acadiana (KARA) and Salt Point (KP92) both received measurable precipitation that was not present in the simulated fields (0.19 inches and 0.39 inches respectively). The DEC12 output places some measurable amounts close to the southern shore of Louisiana (denoted by the dashed contour), but no amounts as heavy as those observed at KARA or KP92. The DEC4 output predicted measurable amounts about 80 km south of the band of heaviest precipitation, but still recorded no precipitation along the southern coastline of Louisiana.

While the area of the 4-km domain is under the influence of high pressure, the model errors in the wind fields remain relatively low. Not until approximately 00 UTC, 6 December 2000 (t = 108 h), do the wind errors begin to increase again, especially in terms of WDIR (Figure G-6). At this time, a second frontal system has pushed southward toward the 4-km domain. A 3-hourly progression of NCEP surface analyses (Figure G-15) shows the fast-moving frontal system beginning to approach the region of the 4-km domain around 03 UTC, 6 December 2000. At the last time of the progression, 12 UTC, 6 December, the cold front has already crossed the land mass of the 4-km domain, a trough extends southward from the low out ahead of the cold front, and a stationary front remains across southern Mississippi. This stationary front is associated with a newly developing cyclone centered near the Texas/Oklahoma border.

This type of synoptic scenario would even be difficult for a trained human eye to analyze for a few reasons. First, the positioning and placement of the fronts within the 4-km domain are difficult, especially with the standard observation density. Second is the weak relative strength of this cold-frontal boundary. Throughout its progression southward through the 4-km domain, there are no strong winds, or noticeable directional shifts accompanying its passage. Furthermore, the modeled surface temperature fields are not much help, as the only noticeable changes are a decrease in temperatures near the shore. Because of the timing of this system, however, it is possible that the temperature changes could be a result of diurnal effects. The surface observations in the 3-hourly progressions of DEC12 and DEC4 during this period in Figures. G-16 and G-17 respectively, remain relatively calm, with variable directions even during the analyzed frontal passage. With such a weak frontal system with very subtle temperature, wind speed and direction changes typical of conditions with a very weak pressure gradient, it is not surprising to see larger than average errors in the WDIR fields during this period near the end of the simulation.

G.2 CASE 2: 12 UTC, 1 MARCH 2001 TO 00 UTC, 7 MARCH 2001

This second case is a transitional season case, complete with several different synoptic types. The first half of the case period involves some form of frontal activity near the area of interest. The second half of the case period is dominated by the weak synoptic flow associated with a CH. At the beginning of the model spin-up period, 12 UTC, 1 March 2001, a stationary front was positioned approximately west-east across the coast of the GOM, cutting through the

southern portion of Louisiana. This feature can be located in different positions, depending on the product that is used. For example, in the NCEP analyses (not shown) the stationary front cuts across a large portion of Southern Louisiana, but appears to be located just to the south of the closest observations that indicate northerly flow. This scenario is evident in the observations (WMO and special data) and the model initialization wind fields created by the Eta model analyses enhanced with only the standard WMO observations (Figure G-18) as a distinct wind shift located farther to the south, with most of the front over the waters of the GOM. Recall that the special data are used in the continuous observation-nudging FDDA throughout each model simulation.

At the end of the model spin-up period at t = 12 h (00 UTC, 2 March 2001), a frontal boundary is now located within the trough shown in Figure G-19. Although the NCEP surface analyses indicate that this frontal boundary is stationary at both analysis times, the movement of the boundary suggests a northwestward progression as a warm front between these times. The DEC12 surface wind field and SLP at this time (on the 4-km subdomain), shown in Figure G-20, have evidence of the convergence zone in the area of the surface trough at the northern edge of the 4-km domain.

Similar to the statistical results from DEC12 and DEC4, the overall differences in the MAR12 and MAR4 wind fields are also relatively small, and once again only show short periods when the two resolutions are noticeably different from an objective standpoint. Wind speed statistics in the surface layer have very little variation due to model resolution. The overall average MAE of WSPD in the surface layer for both MAR12 and MAR4 is 1.8 m/s. The only noticeable differences occur between t = 75 h and t = 80 h, when MAR4 appears to perform better, and between t = 115 h and t = 120 h, when MAR12 appears to have more accurate results (Figure G-21). In the PBL, the case-mean WSPD MAE values are slightly different, and like most fields, the difference is only about 0.1 m/s (Figure G-22). The overall MAE in the PBL for MAR12 is 1.6 m/s, as opposed to 1.7 m/s for MAR4. A few noticeable differences exist between the two error curves that warrant careful subjective attention. The MAR4 error curve shows several individual periods that have “spikes” in model error that do not correspond to errors found in the MAR12 simulation. Spikes at model hours t = 56 h, 87 h, and 116 h seem particularly large compared to the corresponding errors of MAR12. Large error spikes are also evident in the MAR12 error curves, for example, at t = 58 h. At this time the difference in the speed error between the two model resolutions is almost 2 m/s. This large anomaly may be due to differences in timing for strong vertical mixing within the PBL. In the vertical error profiles (Figure G-23), the MAE values for WSPD appear to be relatively similar between the control runs for this particular case throughout most of the depth of the atmosphere. Although there are around 0.2 m/s differences in the error curves in the PBL, the average errors for all layers over the course of the 5-day simulation only differ by approximately 0.1 m/s. Here, MAR12 has an overall average MAE of 1.4 m/s, and MAR4 has an average of 1.5 m/s.

The error curves for surface-layer WDIR (Figure G-24) show that there is once again a slight statistical advantage for the MAR12 simulation. The overall MAE for the surface layer for the MAR12 run is 17.5 degrees, and the same statistic for MAR4 is 18.6 degrees. Some interesting characteristics show up in the statistical error curves that require further subjective analysis. For example, one time when it is clear that both resolutions had difficulty correctly predicting the wind direction is at t = 48 h. This is near the time when a front began moving

through the area of the 4-km domain, so it is likely that the WDIR errors come from inexact timing and subsequent placement of the frontal boundary. In the PBL, the average wind direction errors of the two resolutions are essentially identical in value (Figure G-25). The MAE of WDIR for MAR12 in the PBL is 12.2 degrees, and the MAE of WDIR for MAR4 is 12.1 degrees. However, the differences in the errors are much larger at certain times. There are some brief model periods, when MAR4 appears to perform several degrees better than MAR12. Two examples that stand out in Figure G-25, are model hours t = 19 h to 24 h, and t = 58 h. In the first example, the differences between the two model resolutions range between 2.0 degrees and 6.0 degrees. In the second example, the difference in model errors is approximately 11.0 degrees. In the vertical, the two resolutions once again have quite similar errors. Figure G-26 shows the case-mean vertical profile of MAE values to be 7.5 degrees for MAR12, and 7.7 degrees for MAR4, which is once again only a 0.2 degree difference.

Both resolutions have marginal difficulty predicting the wind fields, especially at times when a frontal zone was moving within the 4-km domain. The first period when there were considerably higher than average errors in both resolutions at the surface was at t = 15 h (Figure G-24). At t = 15 h (03 UTC), the front is stationary, but the NCEP surface analysis shows the front located farther south than it was at t = 12 h (00 UTC) when it was classified as a warm front (Figure G-27). In both the MAR12 (Figure G-28) and MAR4 (Figure G-29) outputs, some clues regarding the spike in model error at t = 15 h are apparent. At the earlier time (t = 12 h), all wind observations in the northern portion of the 4-km domain agree rather well with the simulated wind fields. Three hours later, the model-simulated front has not significantly changed its position, but the winds near the front have changed direction suggesting a southward movement in the front... The two wind observations closest to the northern edge of the 4-km domain which showed southerly flow at 00 UTC now indicate northerly flow, which would place them to the north of the front. The modeled wind directions are still from the south in those locations, indicating that the fronts have moved, even if only by a couple grid cells. These two observations alone average two directional errors into the domain-wide statistics that are nearly 180 degrees.

The model performances seem to be relatively equal during this period, and both place the front in approximately the same location. Both capture the easterly to southerly shift in wind direction from 00 UTC to 03 UTC over LP. There are some subtle differences in the model output at these times in terms of smaller-scale structure in the wind fields. For example, the MAR4 output includes several more areas where surface convergence is more pronounced over the 4-km domain region, including an additional zone extending toward the west-northwest from the western end of LP (compare Figures G-28 and G-29). Additional circulations over the near-shore waters of the GOM also appear where MAR12 seems to have light and variable wind conditions. Statistical results (Figure G-24) and this subjective analysis of the wind patterns at 15 h (03 UTC) suggests that the model-derived circulations of MAR4 match the coastal-zone observations more closely.

The next spike in WDIR model error occurs at t = 48 h (12 UTC, 3 March 2001). At this time, another frontal boundary is oriented across the 4-km domain area (Figure G-30). From the MAR12 and MAR4 model output in Figure G-31, it is likely that the large directional errors are once again attributable to the positioning of the front. Two observations in the northwest corner of the domain have calm winds, with no discernable direction because they are in the middle of

the surface convergence zone. In this location, the variability of the wind directions in extremely light flow can cause large model errors. The 4-km model front appears be located further east near the northern boundary of the 4-km domain and further south on the western boundary. This appears to be more accurate, but on the western boundary in Louisiana, there are two observations that are reporting westerly winds, as if the front had already pushed through to the east. Both model results, however, predict southerly winds that would imply that the position of the front is still to the west. These stations would contribute an error of approximately 90 degrees to the overall average.

Throughout the remainder of the period, the two resolutions have mean surface-layer direction errors that are smaller than those at 48 h by about 50 percent (Figure G-24). There are a few periods, as noted above in Figure G-21, when the WSPD errors have slightly different values after the frontal system begins moving toward the east. Between t = 75 h and t = 80 h, the MAE curve for MAR4 implies a somewhat better performance than the MAR12 output. Later in the simulation, between t = 115 h and 120 h, the opposite is true, where MAR12 has somewhat lower errors than the MAR4 simulation. Throughout both of these examples, however, the differences in the WSPD errors between the two model resolutions are a maximum of 0.5 m/s. Differences this small are hard to discern when subjectively analyzing model wind fields and observations.

Before the frontal systems discussed above leave the area of interest for this study, they produce large amounts of precipitation throughout Louisiana and Mississippi. The stations recording the largest amounts of precipitation are located outside the 4-km domain, but some model simulation comparisons can be made using the southern edge of the west-east oriented precipitation band during the first 24 hours of model simulation. The 24-hour precipitation totals for the entire 12-km domain area are given in Figure G-32, which shows precipitation amounts ranging from 0.01 inches (0.03 cm) to 6.99 inches (17.8 cm) in Natchez, MS (KHEZ). Other high precipitation amounts that are located within the boundaries of the 4-km domain are 3.04 inches (7.72 cm) in Hattiesburg, MS (KPIB), and 1.56 inches (3.96 cm) in McComb, MS (KMCB). The stations that recorded these high precipitation totals lie in a long, narrow zone of high precipitation amounts approximately 500 km long, from west to east and 50 km wide, south to north, where the front was located throughout the majority of the period. Neither model resolution captured the large precipitation amounts that occurred, especially the amounts near the northern edge of the 4-km domain. The MAR12 24-hour precipitation totals (Figure G-33) capture the general shape of the observed precipitation, but the highest precipitation amount of 7.96 cm (3.13 inches) is located in eastern Texas. Precipitation within some areas of the 4-km domain is not representative of the observed totals. The MAR12 output shows at most, 1.27 cm (0.5 inches) of precipitation along the border of Louisiana and Mississippi. The explicit precipitation totals from MAR4 fared slightly worse than the MAR12 output in terms of precipitation coverage. The highest amount calculated over the period was 2.75 cm (1.08 inches) in Mississippi, in the northwest corner of the 4-km domain, but there is less spatial coverage by the 4-km precipitation field. The only other apparent precipitation over land in the 4-km domain is a small area in the southern extension of Mississippi, where 1.20 cm (0.47 inches) of precipitation is predicted.

During the next 24-hour period, the frontal convergence zone continued to dump relatively large amounts of precipitation across the region, as it remained practically stationary.

Observed totals in Figure G-34 once again show widespread precipitation amounts over 1.0 inches (2.54 cm), with the highest total once again at Natchez, MS where an additional 2.97 inches (7.54 cm) of rain fell between 12 UTC, 2 March 2001 (t = 24 h) and 12 UTC, 3 March 2001 (t = 48 h). As before, there are differences in the spatial precipitation coverage between the MAR12 and MAR4 simulations over the area of the 4-km domain. The precipitation totals from MAR12 reflect the precipitation coverage that is evident in the 24-hour totals in Figure G-34, as well as the totals along the southern Gulf coast of Louisiana. The predicted totals from the MAR4 output, however, lack the spatial coverage that MAR12 exhibits. While there is measurable precipitation throughout most of Louisiana, this explicit precipitation does not predict amounts nearly as large as the observed amounts or the amounts predicted by the MAR12 output. Additionally, the small areas that did receive heavier amounts of precipitation in the MAR4 output (Figure G-35) have a maximum rainfall amount of 3.63 cm (1.43 inches) that is over 1.0 inch lower than the nearest recorded observation at KHBG (Figure G-34).

As the frontal system finally began to move eastward, it continued to produce heavy amounts of precipitation, including 3.00 inches (7.62 cm) and 4.07 inches (10.34 cm) in New Orleans, LA and Mobile, AL, respectively (Figure G-36). The models appear to fare rather well in terms of spatial precipitation coverage once cyclogenesis occurs, and the system quickly exits the Louisiana Gulf Coast. The precipitation totals that are derived from both model resolutions are shown in Figure G-37. In the MAR12 model output, a maximum precipitation amount of 10.4 cm (4.09 inches) was reported in Louisiana to the west of LP, where the sparsely spaced observed precipitation amounts are all less than 1.65 inches. In southern Mississippi and Alabama, the 12-km output performed reasonably well, as it predicted more than 5.08 cm (2.0 inches) in an area that included observations of 2.03 inches (5.16 cm) and 2.27 inches (5.57 cm). Unlike the first two 24-hr precipitation periods, the MAR4 model outputs overestimated the precipitation amounts, based on the observations in Figure G-36. The maximum observed precipitation amount in the 4-km domain area is the 4.07 inches (10.34 cm) reported in Mobile, AL, which the 4-km model predicts quite well with 10.7 cm (4.21 inches). This same area is very close to the 5.1 cm (2.0 inches) contour according to the 12-km model-predicted precipitation, which is roughly half of the observed amount. The 4-km model also predicts another local maximum just east of New Orleans, LA, in the amount of 7.12 cm (2.80 inches). North of this area, however, there is much more predicted precipitation than observed, including a 15.7 cm (6.18 inches) prediction in an area where the sparse observations range from approximately 1.40 inches to 2.25 inches. Precipitation is the most difficult field to predict accurately and verify since it varies on scales much smaller than the standard measurement network. Overall, the two FDDA-assisted models produced accurate wind and mass fields and reasonably accurate precipitation results for this challenging case period.

G.3 CASE 3: 12 UTC, 8 JULY 2001 TO 00 UTC, 14 JULY 2001

Case 3 is a warm season case that has weak synoptic forcing throughout the majority of the simulation period. This weak synoptic forcing is due to a GH scenario, where the entire Gulf coast region is under the influence of high pressure. The GH persists from the model initialization time (t = 0 h), 12 UTC, July 8 2001, through the spin-up period, and ends around 12 UTC, 13 July 2001 (t = 120 h). For the last 12 hours of the simulation period, a cold front begins to push southward through parts of the 12-km domain, but does not play a role in the model

simulations in the 4-km domain, as the front remains too far to the north. Therefore, for this analysis, only the conditions relating to the GH regime will be discussed.

At the model initialization time, Louisiana is directly in the center of a high pressure system, with a 1020 hPa high located very close to New Orleans, Louisiana. As expected, the surface wind field shows light and variable winds across a large portion of the 12-km domain (not shown). In the area of the 4-km domain, many of the observations around the coastal zone show calm conditions, and variable wind directions (Figure G-38). During the period of model spin-up, the influence of the GH remains in place, while the circulations around the coastal area were driven by typical daytime convection with limited synoptic influence.

At t = 12 h, 00 UTC, 9 July 2001, at the end of the allotted model spin-up period, winds were still generally light according to the 4-km resolution model fields (Figure G-39), with 4-km domain observations ranging from 0.0 to 4.6 m/s at one reporting station on the Florida panhandle. Also evident in the model fields at this time is a convergence zone across all four states in the 4-km domain. The flows causing this convergence zone are the light and variable winds across the northern extent of the 4-km domain, and southerly flow from the GOM. With the direction of this onshore flow, and the distance inland of the convergence zone, this is most likely a thermally driven sea breeze circulation, a feature that repeats itself daily throughout the length of the simulation.

Statistically, this case brings some additional challenges that were not observed in Case 1 or Case 2. For example, no case has been under the influence of a GH synoptic regime for the entire length of the simulation. This can potentially cause higher than normal errors in terms of wind direction, but smaller errors in terms of wind speed. There is an additional level of concern for this case, because the area focuses on a coastal zone. During this summer period, during which temperatures that are routinely above 30 °C in the afternoon, there is a high probability that thermally-driven sea breeze circulations will develop under conditions of weak synoptic forcing. In addition to the sea breeze circulations, there is also a great deal of daytime convective heating. The small horizontal scales of this daytime convection are difficult to predict, and it is more difficult to determine the effects of the interaction of convection and the sea breeze circulations. While these local effects may be non-zero in other cases where there is strong synoptic forcing, the larger-scale flow typically overpowers the smaller-scale circulations.

The statistical differences between the WSPD errors of the two model resolutions are relatively small. In the surface layer, the overall average MAE values are 1.7 m/s for JUL12 and 1.8 m/s for JUL4, and the statistical curves in Figure G-40 show no sustained periods where one resolution consistently outperforms the other. In the PBL (Figure G-41), the mean statistical differences are even smaller than in the surface layer, as the MAE for JUL12 and JUL4 are both approximately 1.1 m/s. There are periods when 12-km wind speed results are slightly better than 4-km results, and there are also periods when 4-km results are slightly better than 12-km results. Figure G-42 is the MAE vertical profile comparison of the JUL12 and JUL4 simulations. Averaged over the depth of the profile for the 5-day period, the speed errors only differ by approximately 0.1 m/s (0.9 m/s for JUL12 compared to 1.0 m/s for JUL4) but the JUL12 output has slightly better directional errors throughout most of the depth of the profile, including the lowest levels of the approximate PBL.

The calculation of statistics for WDIR in a case with such weak synoptic forcing is problematic, because with daytime heating, the wind directions can change drastically, as small-scale convective activity drives the circulations, not the synoptic flow. The difficulty in predicting wind directions for low-speed winds is well-known, and is the main reason why numerical models tend to predict the direction of stronger winds aloft more accurately than weaker surface winds. Some of the difficulty can be seen in Figure G-43, where the surface layer MAE curves for both JUL12 and JUL4 have a large periodicity. During the hours when the sun is not heating the surface, the wind direction errors are relatively low. When the surface warms in the afternoon hours, however, the MAE errors climb dramatically, as the local scale differential heating drives the majority of the low-speed winds. This temporal pattern continues throughout the entire 5-day period. For these two model simulations, the average MAE for the period is 20.2 degrees for JUL12, and 23.2 degrees for JUL4, including maximum errors of approximately 65 degrees for both model resolutions. In the PBL (Figure G-44), the WDIR errors are smaller for both resolutions, but the errors for JUL12 are generally equal to or lower than those of JUL4. For JUL12, the MAE of WDIR in the PBL is 15.4 degrees, and for JUL4, the error is 17.5 degrees. The vertical profile of WDIR errors illustrates that the difficulty of predicting wind directions in weak flow is not confined to the surface layer, but is also an issue to consider throughout the depth of the PBLand troposphere. During this time of year the PBL can extend up to approximately 2000 m, so a portion of the larger model errors displayed above the surface could be due to errors mixing throughout the PBL. Including these errors, the average profile MAE of WDIR for JUL12 is 14.7 degrees, and the MAE for JUL4 is slightly larger, at 16.0 degrees (Figure G-45). These model errors are still quite acceptable compared to other modeling studies (Seaman 2000, Schroeder et al. 2006).

As discussed above, the surface wind fields are very difficult to predict in a case without the influence of a synoptic pressure gradient. The statistical fields show opposite periodicities, i.e. the wind direction is hardest for the models to predict during the day, and the wind speed is hardest for the model to predict during the night and early morning hours. After model spin-up, at 00 UTC, 9 July 2001 (t = 12 h), subjective differences in the performance of the two wind fields are already distinguishable. Additional mesoscale detail in the JUL4 simulation is easily noticeable in Figure G-46, which is a comparison of the surface wind fields at this time. The JUL12 output generally has a steady flow across the domain that contains few small-scale circulations. The higher resolution of the JUL4 output shows a number of areas where the patterns in the wind field demonstrate smaller, mesoscale circulations, especially over the GOM. There are also inland areas where localized circulations appear to be present. It also appears that at this time, there had been a sea breeze circulation penetrating inland throughout the day. Both model outputs show an onshore flow, creating a wind-shift boundary with the light and variable wind conditions typical of this type of synoptic regime farther inland. This boundary is apparent because of the contouring of wind speeds on both domains. The boundary is more pronounced on the JUL4 output, as the wind speeds in the area of the sea breeze are generally modeled to be stronger. Unfortunately, there are very few observations to verify the extent of the inland penetration of the sea-breeze front. There are several observations within 25 – 50 km of the shore that confirm that existence of the sea breeze, but very little information at about 100 km or more from the shore where the northern edge of the sea-breeze front is being simulated by JUL12 in Figure G-46. There is only one observation at this distance from shore in the northern portion of the 4-km domain in Mississippi and it reports a 2.6 m/s wind from approximately 180°. It is not clear whether this is indeed the northern boundary of the sea breeze. The isotach

gradients in the MAR12 simulation are much weaker and further north than those in the JUL4 simulation. It is difficult to say based on this one observation that one simulation is more accurate than the other. Schroeder et al. (2006) showed greater inland penetration of a sea/bay breeze with 12-km resolution, but the 4-km resolution fields showed better agreement with the satellite cloud imagery reflecting the sea-breeze front convergence zone. The scarcity of observational data in the area of the sea breeze propagation is even more problematic because of the spacing of the observations. The station in Mississippi that is discussed above, is probably too far north to consistently encounter the effects of the sea breeze circulation. The majority of the remaining observation locations are within a few grid cells of the coastline. This means that under most circumstances where a sea breeze is occurring, there is a void of observations between the near-shore sites and those that are outside the typical reaches of a sea breeze.

With these conditions, it is difficult to determine which model resolution produces the better sea breeze simulation. As this is a warm, humid case, it is also difficult to use the mass fields to locate the sea breeze because mixing ratios are high over the land and water and convection influences low-level mass and wind fields. Both model resolutions show northward propagation of cooler temperature and higher moisture fields (not shown), but the mass observations do not consistently agree with either resolution. The closest match to mass observations during a sea breeze front occurs during the afternoon of 11 July 2001 (not shown). During this period, the observations near the shore were relatively cool (approximately 23 °C) compared to inland observations (approximately 33 °C in the western portion of the 4-km domain in Louisiana). The 4-km resolution temperature field tends to represent these cooler coastal temperatures much more accurately than the 12-km resolution field. For example, the 4-km output shows a relative low temperature of 26.5 °C, very close to an observed temperature of 23.3 °C. In the 12-km output, the same observation is located between the 31 °C and 32 °C isotherms. Therefore, the 4-km model better predicted the signature of the sea breeze in the temperature field in this case.

In order to verify the position of the sea breeze front more accurately, additional data sources must be considered. Data sources with sufficient resolution to verify a sea breeze circulation are indeed difficult to obtain, so satellite imagery is often used (Schroeder et al. 2006). Satellite imagery from NOAA's Comprehensive Large Array-data Stewardship System (CLASS) provides the ability to distinguish some of the details of a sea breeze front. Unfortunately, its imagery was not available at this analysis time. Two examples for the sea breeze that developed throughout the afternoon of 8 July 2001 are given in Figure G-47, with imagery from 19 UTC, 8 July 2001 on the top, and imagery from 22 UTC, 8 July 2001 on the bottom. In the 19 UTC image, the sea breeze has not penetrated very far inland, but it is still possible to see the clear, stable region between the coast and sea breeze front, denoted by the yellow line which marks the boundary of the sea-breeze penetration. This line traces just inland of the coast, around LP, and around Mobile Bay in Alabama, with greater inland penetration on the eastern side of Mobile Bay. For reference the east-west width of Mobile Bay is around 16 km. The 22 UTC image does not give as clear a view of the sea breeze, because at that time, a relatively large convective cell has moved into the immediate Gulf coast area. The sea/lake breeze coming from LP is still visible, however, and is denoted once again with a yellow line. Maximum inland penetrations in these images are slightly less than 40 km. In the model output, the JUL12 sea breeze by 00 UTC 9 July 2001 has pushed north of 31 N and its inland penetration exceeds 100 km. The JUL4 sea breeze has its southerly winds extending north to around 31 N,

and its wind speeds and isotach gradients are greater than those in JUL12. All modeled wind fields do fall, however within the theoretical guidelines developed by Mak and Walsh (1976), who claim a maximum sea breeze intensity of 4.5 m/s, assuming a maximum land/sea temperature difference of 6.0 °C. Other results such as Schroeder et al. (2006) suggest improved inland penetration of coastal circulations with 4-km model resolution.

For the rest of the simulation period, both resolutions continue to predict the development of sea breeze circulations during the afternoon hours of each day. Model output for the remainder of the simulation period follows the same comparative trend, as the 12-km simulation consistently predicts the sea breeze to be further inland than the 4-km simulation. Much of the satellite imagery needed to subjectively analyze these sea breezes is unfortunately cluttered with deeper, more dominant convective activity near the sea breeze front, and is subsequently impossible to use for sea-breeze analysis. The only other time that can be examined due to dominance of convection and satellite imagery availability is the afternoon of 9 July 2001. During this period, a modeled sea breeze begins to develop around t = 30 h, 18 UTC (Figure G-48a) but becomes much less defined, possibly due to interference with other convective activity, during the next 3 hours (Figure G-48b). The boundary between the stronger onshore flow, and the relatively motionless air further inland is not as distinct as the observable boundary during the previous day. The satellite-observed sea-breeze circulation is also not as impressive as the previous day, and it is harder to define (Figure G-49). The second image of the pair, from 22 UTC, 9 July 2001, does not capture a distinct zone of clear, stable air, which tends to agree with the lack of definition in the modeled surface wind fields. During this period, it does not appear that either resolution has a substantial benefit over the other in terms of the surface wind fields, which was supported by the statistical results above. The sea breeze is simulated reasonably well in both the 12-km and 4-km resolution models, although there may be some advantage in the thermal fields in the 4-km model.

The synoptic scenario in this case does not allow for widespread precipitation that is the result of a frontal passage as in Case 2. The precipitation in this case is a product of convective activity, which typically occurs when temperatures and dewpoints are this high, and this precipitation regime is considerably more challenging to forecast. The 24-h observed precipitation and corresponding 24-h model-predicted precipitation outputs for each 24-h period within the model simulation can be seen in Figures G-50 through G-59. These comparisons generally show the same trends between the two model resolutions. In the observation plots, it is evident that there are no spatial patterns in the precipitation observations, except that stations directly on the coast tend to receive some precipitation on a daily basis perhaps related to sea-breeze front convergence. In the JUL12 output, it appears that the model tends to over-predict the spatial extent of the precipitation coverage, including most of southern Louisiana and along the Mississippi and Alabama coasts. Conversely, the explicit precipitation prediction of the JUL4 output tends to have more limited spatial coverage, as it did in Case 1 and Case 2. This precipitation also appears to be cellular in nature, which would be expected under these synoptic conditions, but some larger amounts of localized precipitation appear to be the result of grid-point storms (Deng and Stauffer 2006). One area where the JUL4 output tends to under-predict precipitation is along the Mississippi and Alabama coasts where precipitation is observed to some degree on each day of the 5-day period except for the 24-hour period ending at t = 120 h, 12 UTC, 14 July 2001.

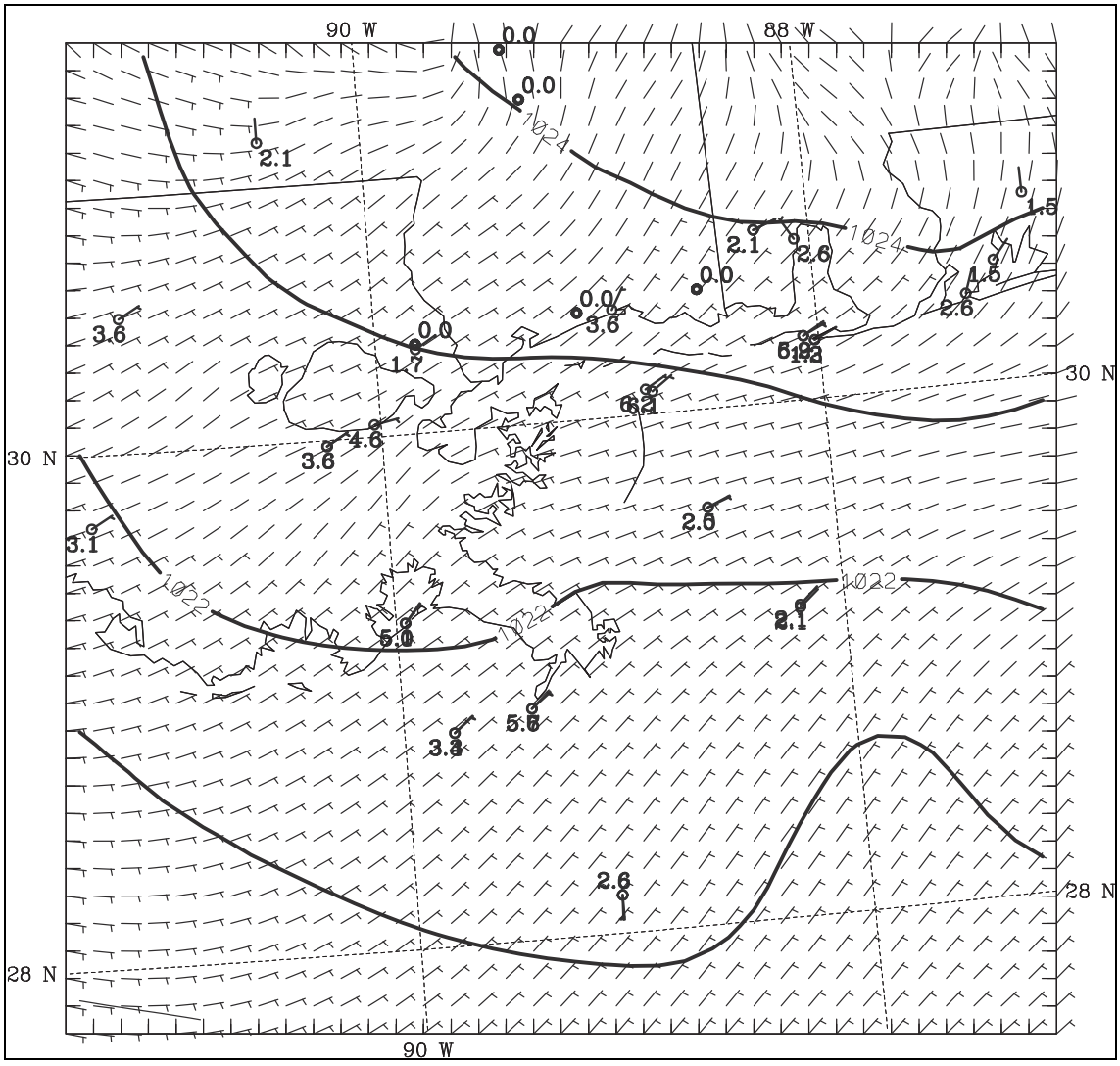

Figure G-1. 12-km resolution, Eta model-derived surface layer wind field and SLP for t = 0 h, 12 UTC, 1 December 2001 on the 4-km model subdomain. Wind barbs are plotted every grid cell, and isobars are plotted every 1 hPa. Surface wind observations within the 4-km subdomain are plotted as well, with wind speeds given in m/s.

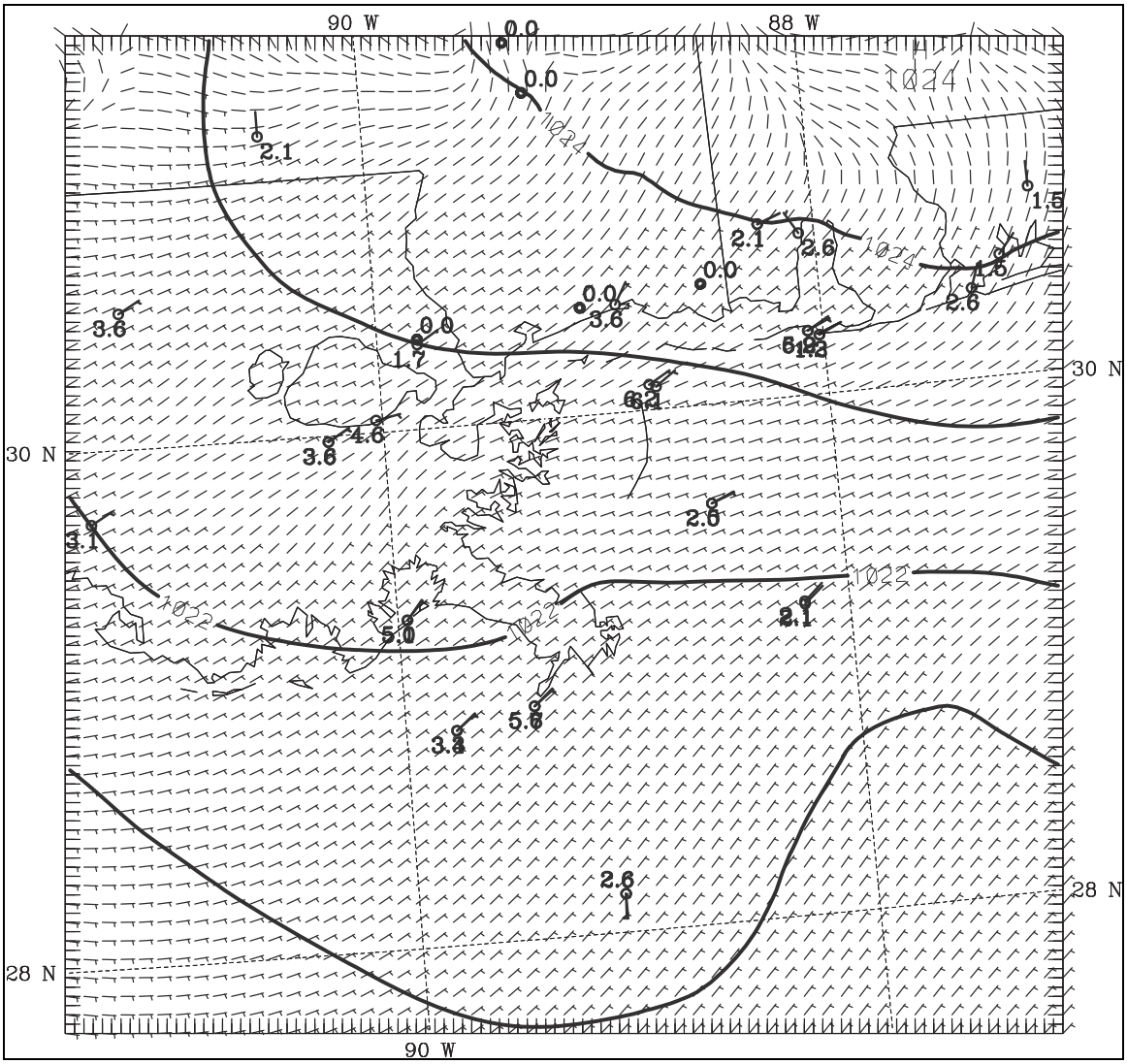

Figure G-2. 4-km resolution, model-derived surface layer wind field and SLP for t = 0 h, 12 UTC, 1 December 2001 on the 4-km resolution model domain. Wind barbs are plotted for every other grid cell, and isobars are drawn every 1 hPa. Surface wind observations are also plotted, with speeds given in m/s.

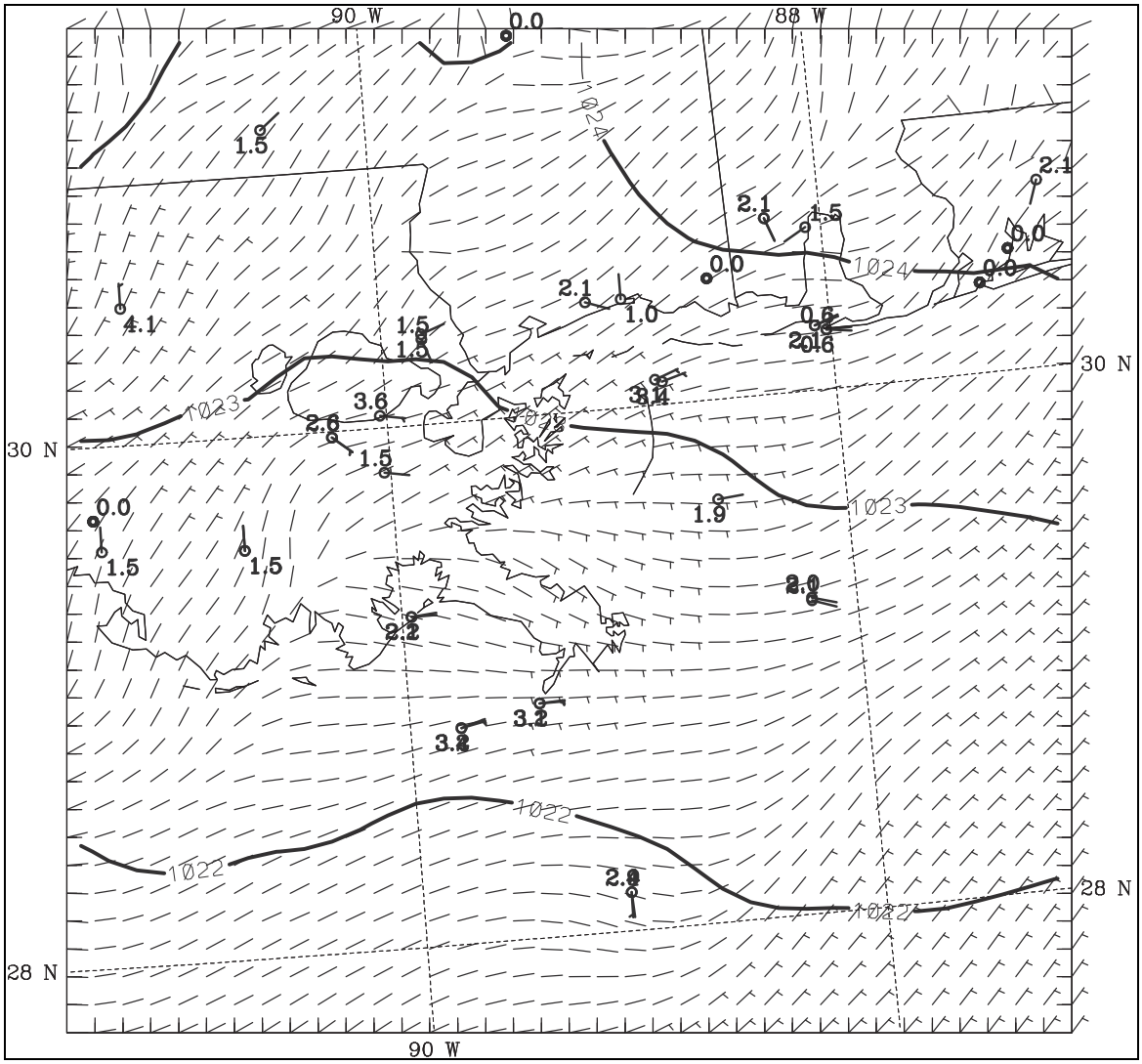

Figure G-3. 12-km resolution model-derived surface layer wind field and SLP for t = 12 h, 00 UTC, 2 December 2000 for the 12-km resolution model over the 4-km subdomain. Wind barbs are plotted for every grid cell, and isobars are drawn every 1 hPa. Observations within the 4-km subdomain are also plotted, with speeds given in m/s.

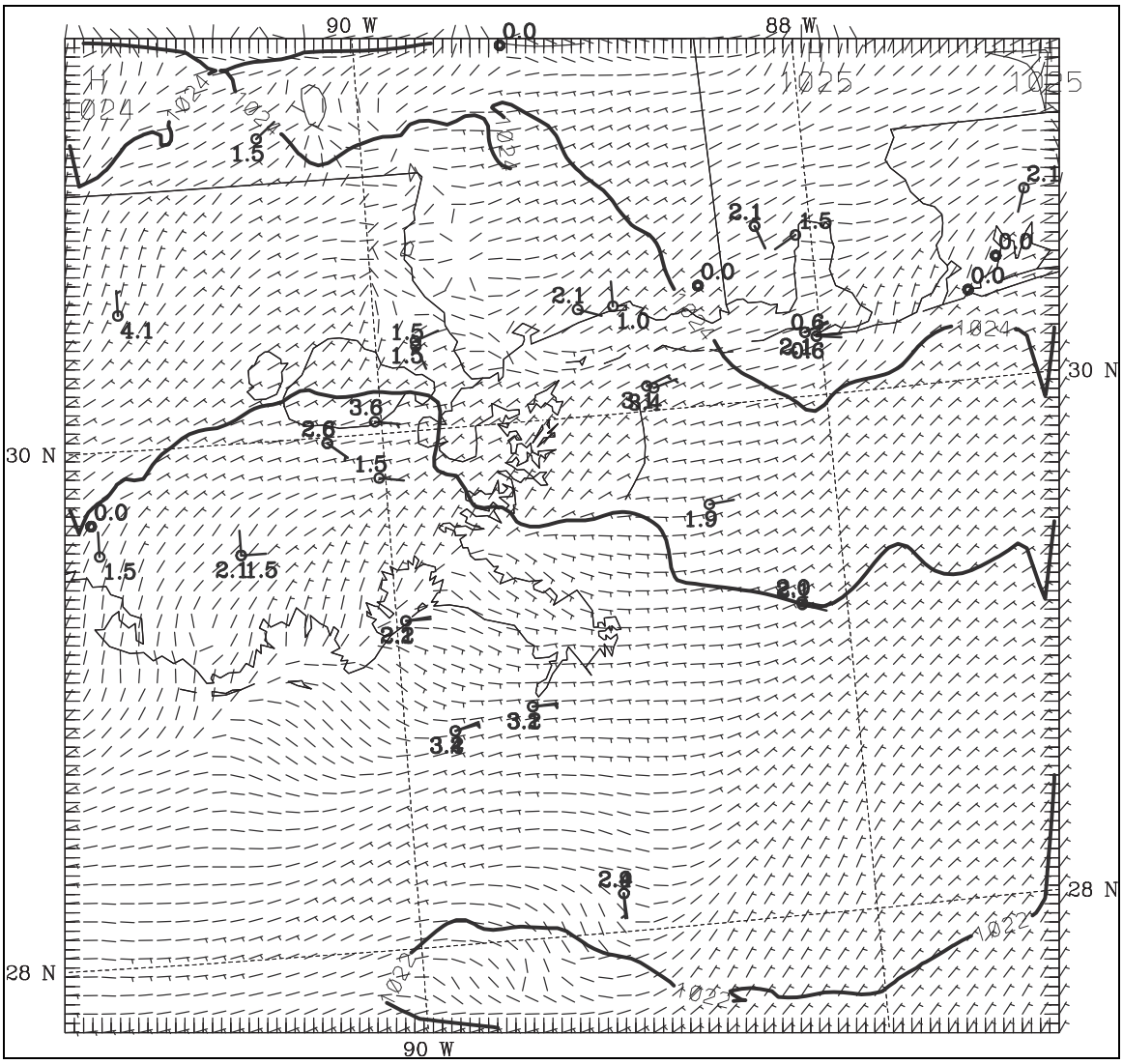

Figure G-4. 4-km resolution, model-derived surface layer wind field and SLP for t = 12 h, 00 UTC, 2 December 2000 on the 4-km resolution model domain. Wind barbs are plotted for every other grid cell, and isobars are drawn ever 1 hPa.

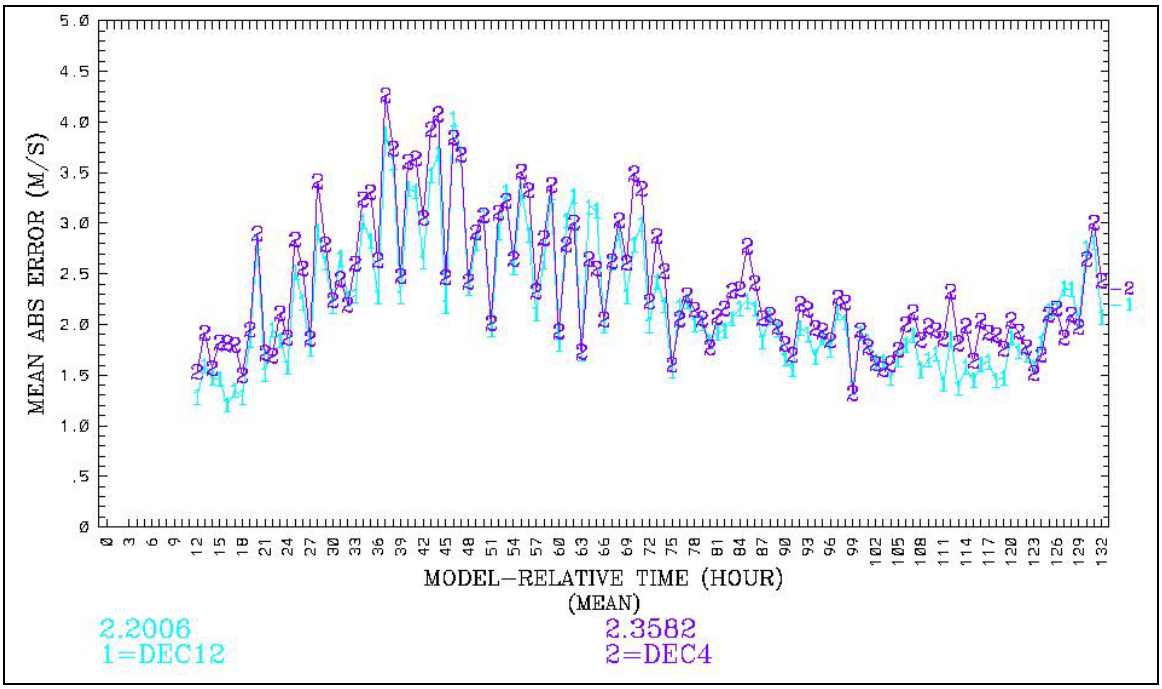

Figure G-5. Surface layer MAE of model-derived VWD (m/s) for DEC12 (blue) and DEC4 (purple) for the 120-hour period beginning t = 12 h, 00 UTC, 2 December 2000 and ending t = 132, 00 UTC, 7 December 2000.

a.

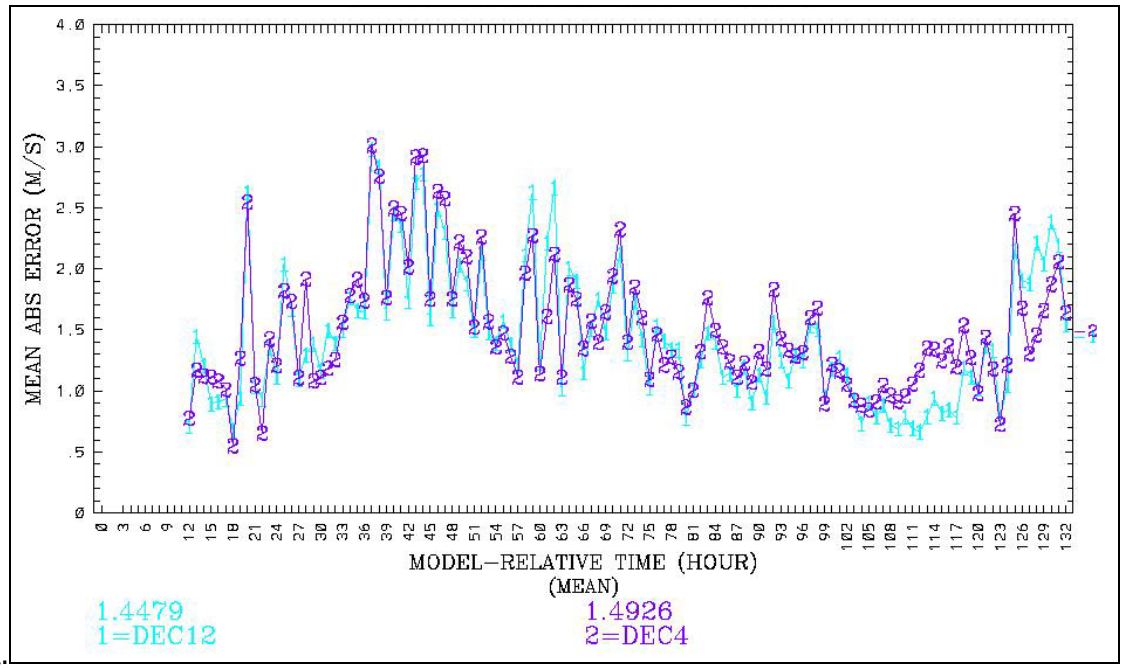

b.

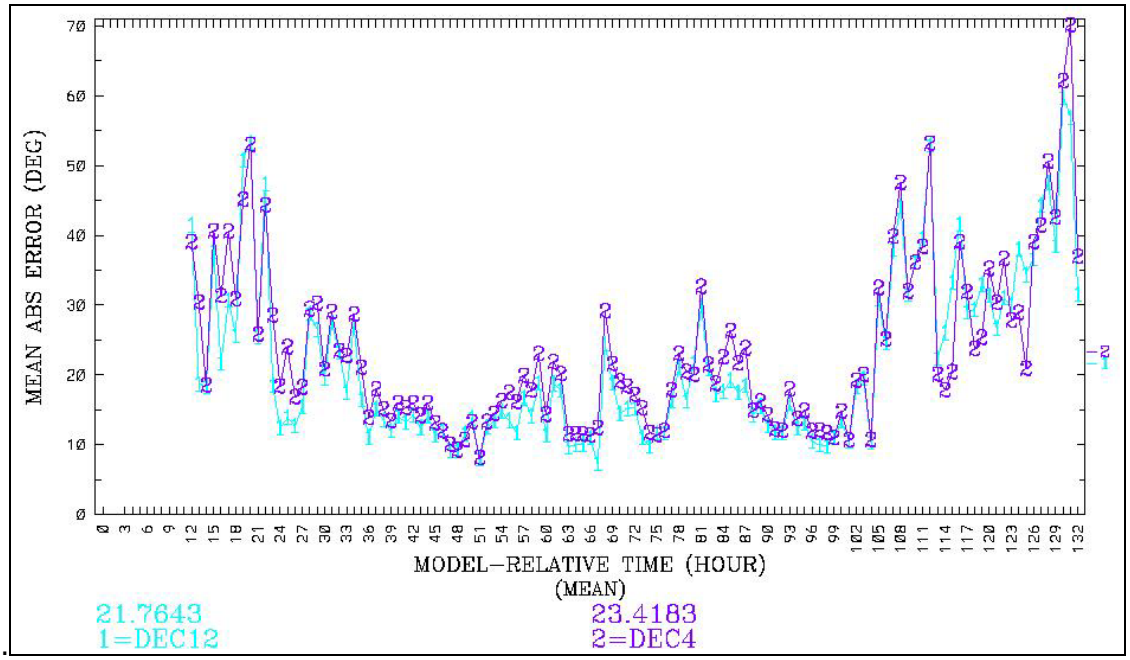

Figure G-6. Surface MAE for two model-derived wind field variables, a.) WSPD (m/s) and b.) WDIR (degrees) for DEC12 (blue) and DEC4 (purple). Both plots are for the 120-hour period beginning t = 12 h, 00 UTC, 2 December 2000 and ending t = 132 h, 00 UTC, 7 December 2000.

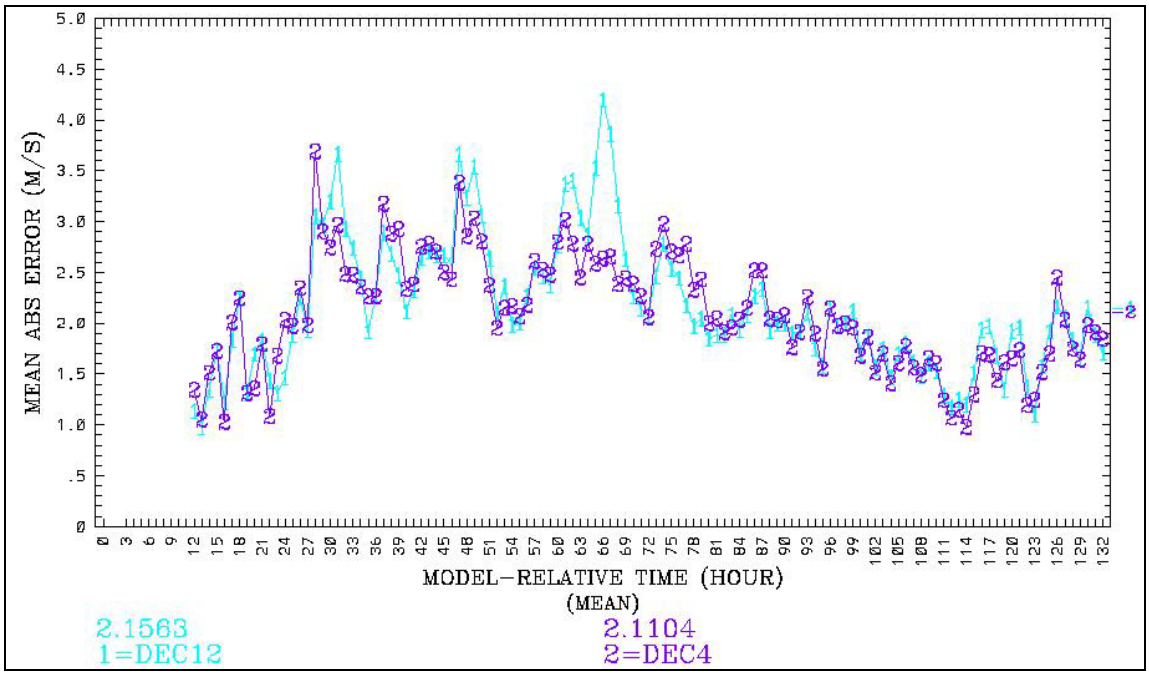

Figure G-7. MAE statistics of model-derived VWD (m/s) for the PBL (30-1000 m above ground level) for DEC12 (blue) and DEC4 (purple).

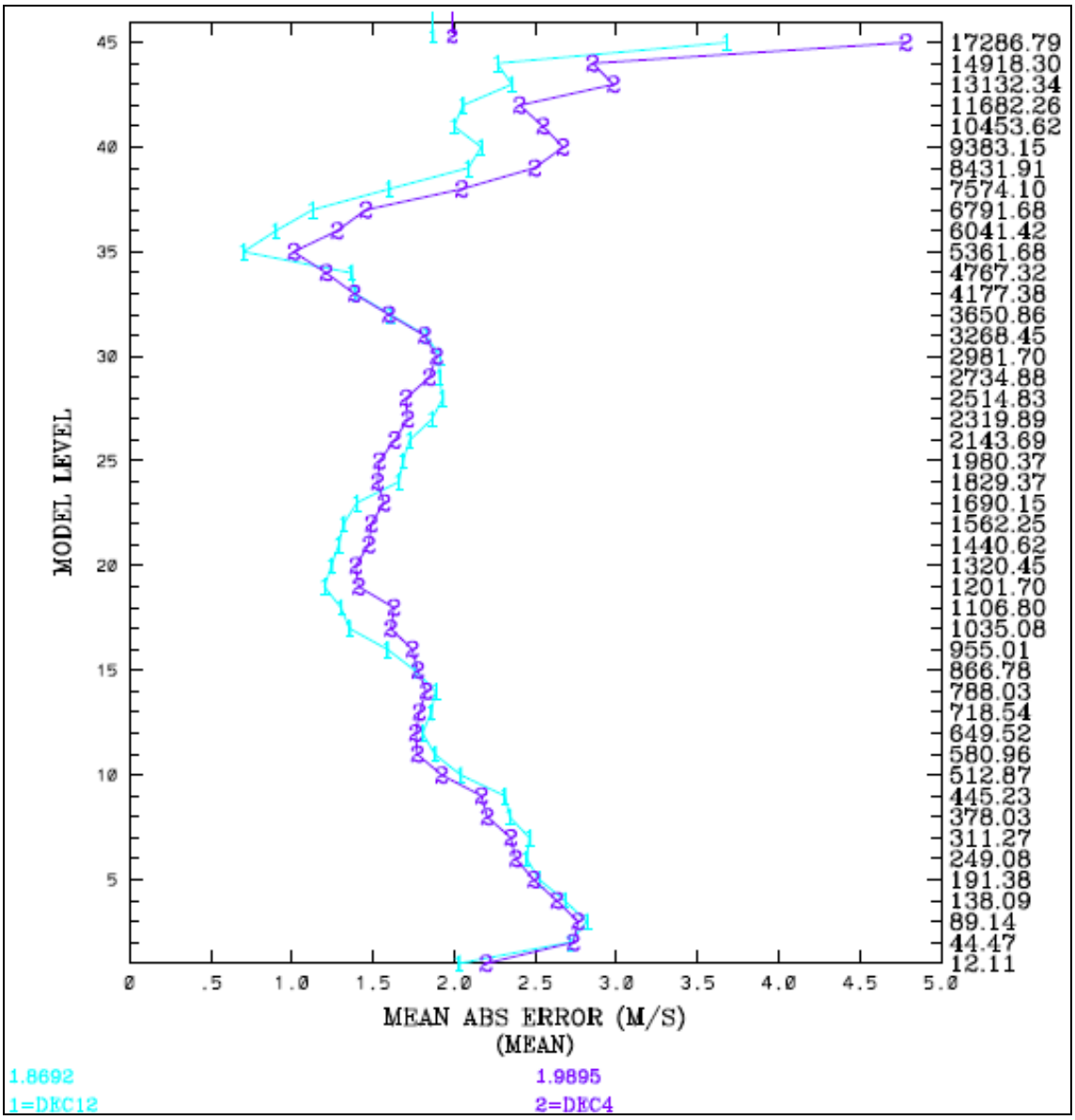

Figure G-8. Vertical profile of model-derived VWD (m/s) MAE for the all model sigma-levels, including curves for DEC12 (blue) and DEC4 (purple). MAE is shown on the abscissa, model sigma-level is shown on the left ordinate, and model height is shown on the right ordinate.

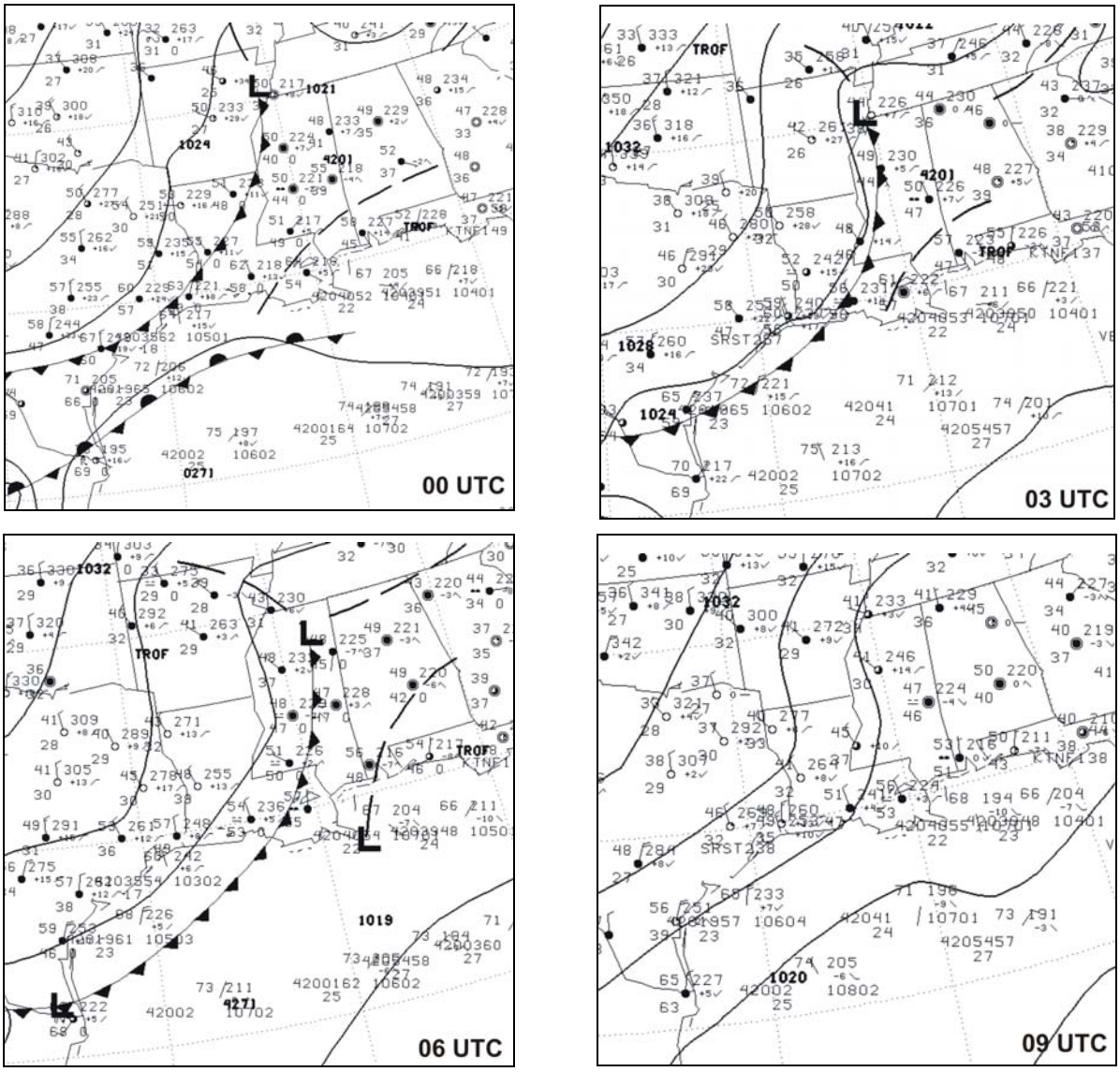

Figure G-9. Progression of 3-hourly surface analyses and observations over the approximate 12-km domain area, showing the cold front passing through Louisiana, specifically the 4-km domain. The plots are arranged from left to right, beginning at t = 12 h, 00 UTC, 2 December 2000, and ending t = 24 h, 12 UTC, 2 December 2000.

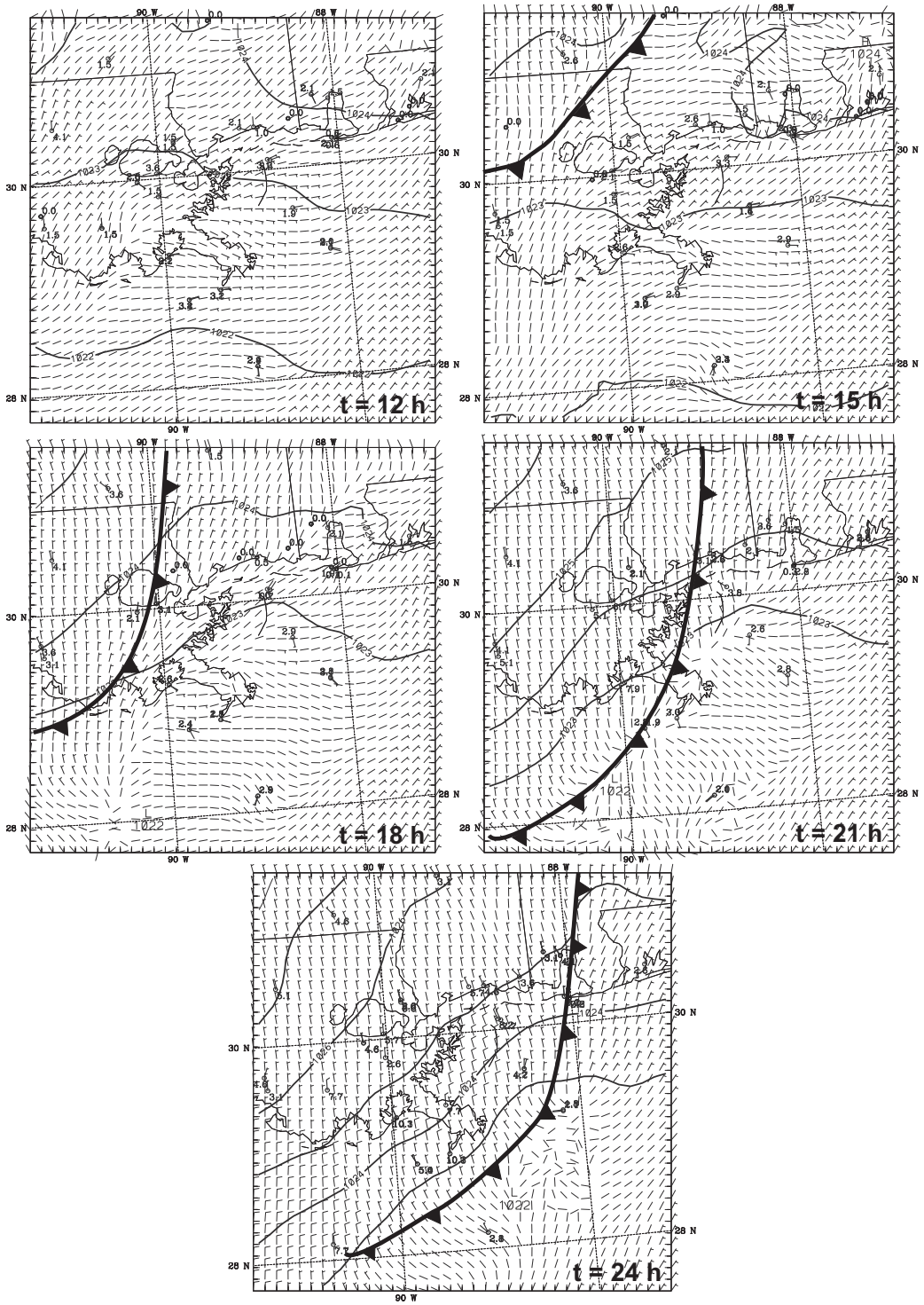

Figure G-10. Progression of 3-hourly DEC12 model output on the 4-km subdomain, corresponding with Figure **G-9**, with the surface layer wind barbs, SLP, and surface wind observations over the area of the 4-km domain. Wind barbs are plotted every grid cell, and isobars are plotted every 1 hPa.

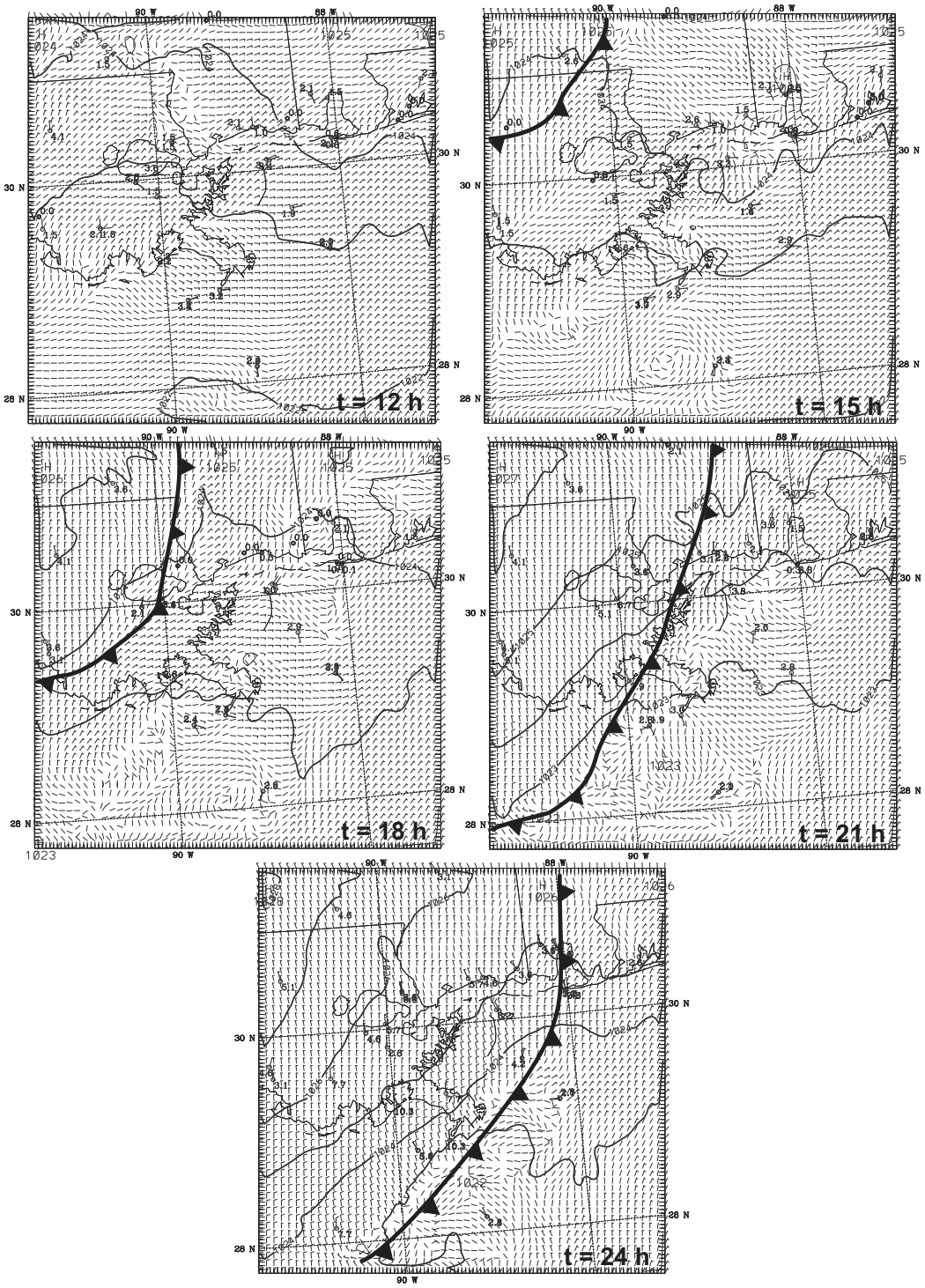

Figure G-11. Progression of 3-hourly DEC4 model output corresponding with Figure G-9, with the surface layer wind barbs, SLP, and surface wind observations. Wind barbs are plotted every other grid cell, and isobars are plotted every 1 hPa

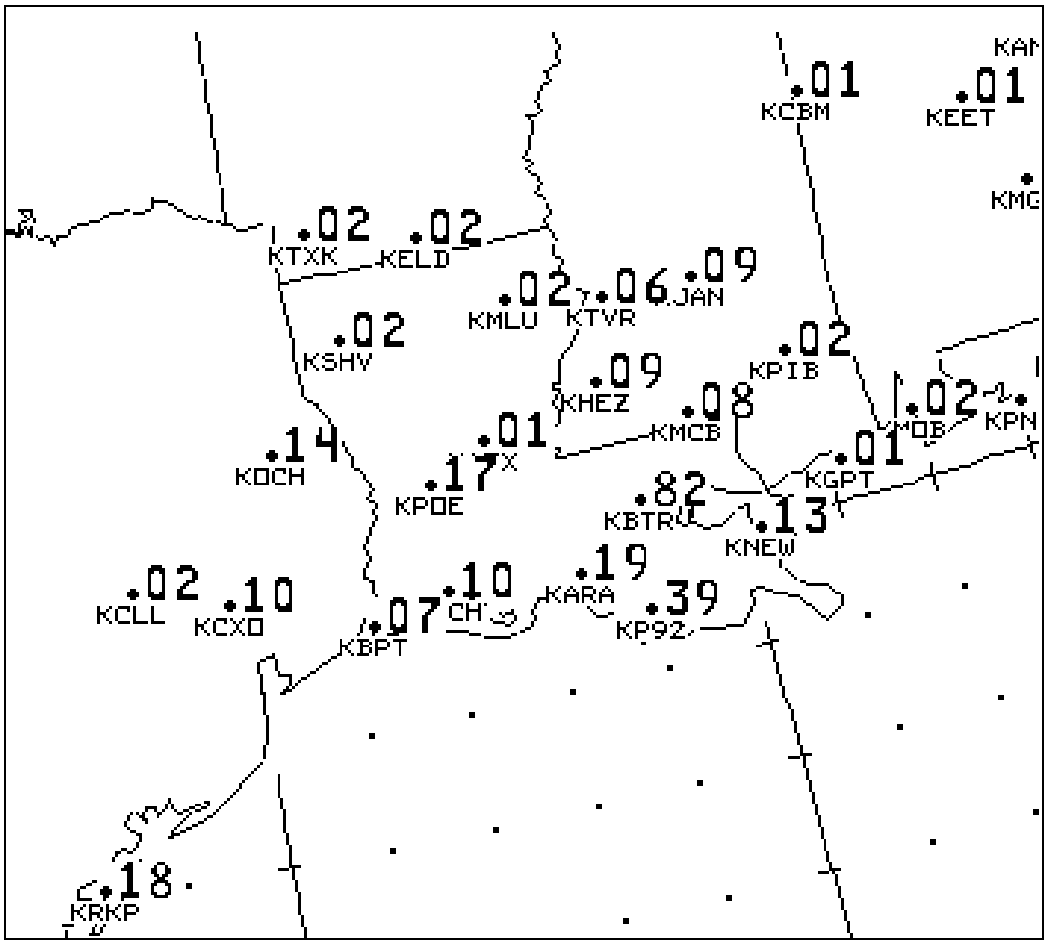

Figure G-12. 24-hour observed precipitation totals for the period 12 UTC, 1 December 2000 to 12 UTC, 2 December 2000. Precipitation totals are recorded in inches at each observation station where measurable precipitation was recorded.

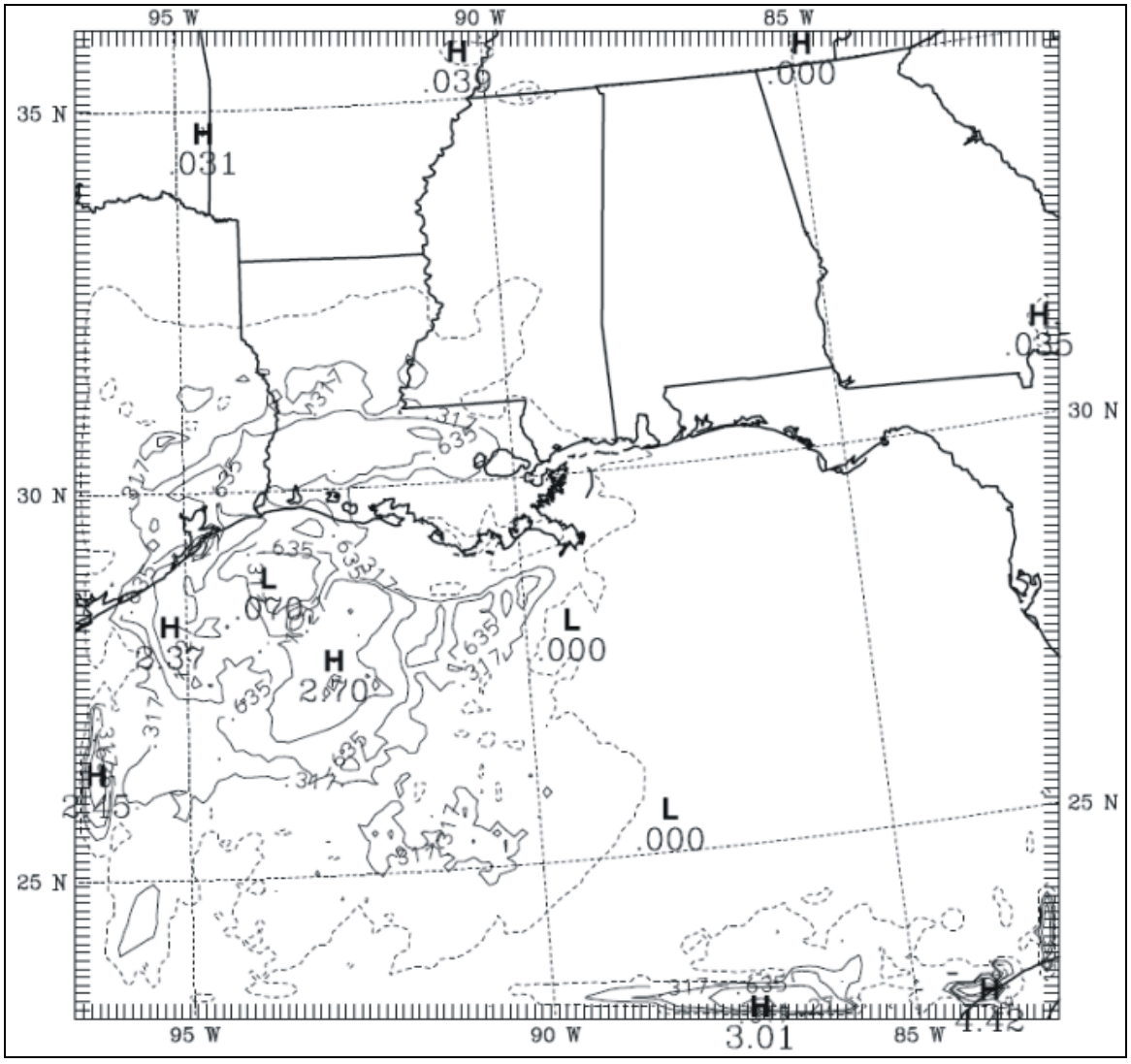

Figure G-13. DEC12 model-derived precipitation totals over the 12-km domain area for the period beginning 12 UTC, 1 December 2000 (t = 0 h) and ending 12 UTC, 2 December 2000 (t = 24 h). The dashed contour encloses all areas that received measurable precipitation during the 24-hour period. Within the dashed contour, precipitation amounts double with every successive contour, beginning with 0.125 inches (0.317 cm).

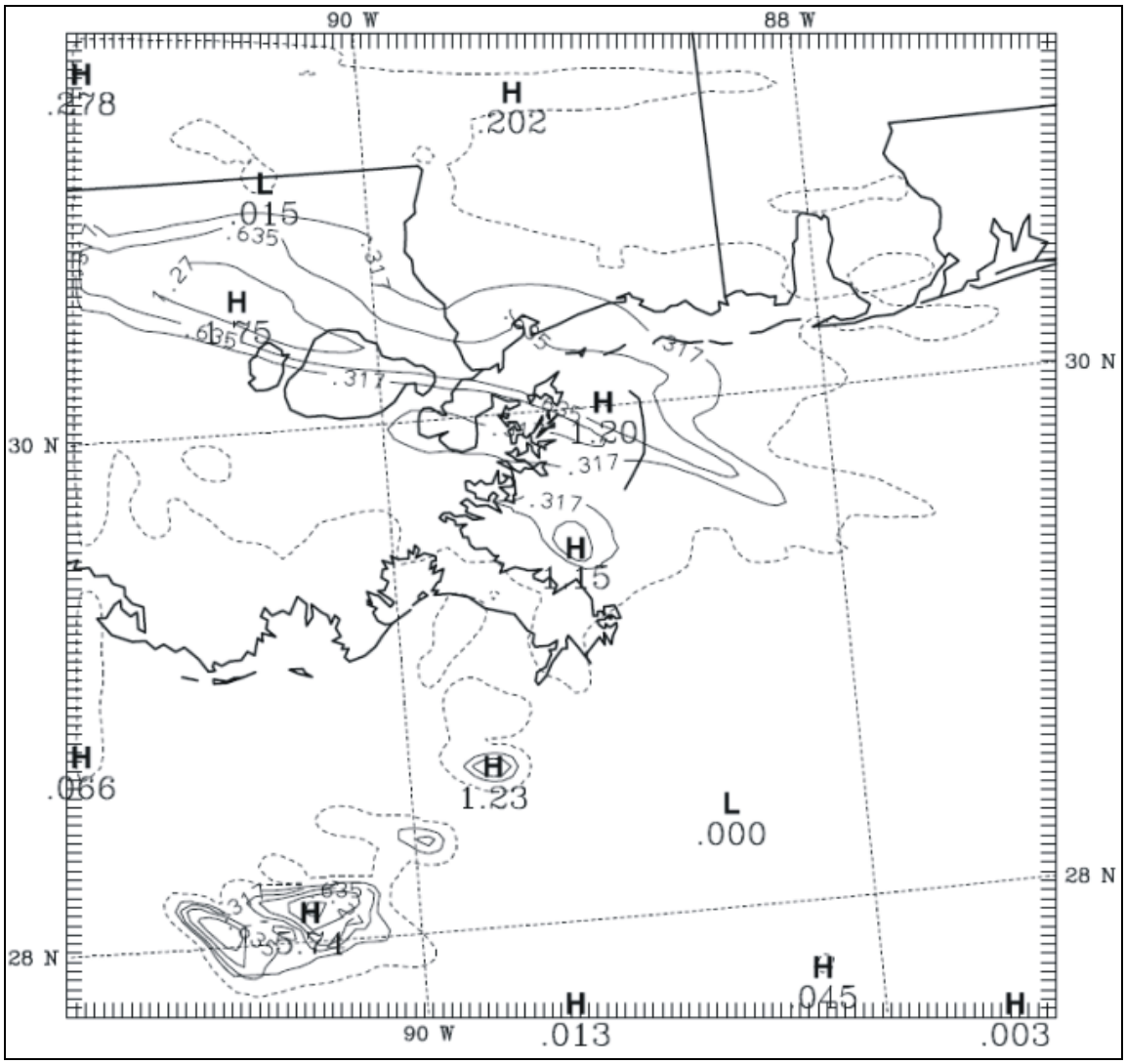

Figure G-14. DEC4 model-derived precipitation totals for the period beginning 12 UTC, 1 December 2000 (t = 0 h) and ending 12 UTC, 2 December 2000 (t = 24 h). The dashed contour encloses all areas that received measurable precipitation during the 24-hour period. Within the dashed contour, precipitation amounts are double with every successive contour, beginning with 0.125 inches (0.317 cm).

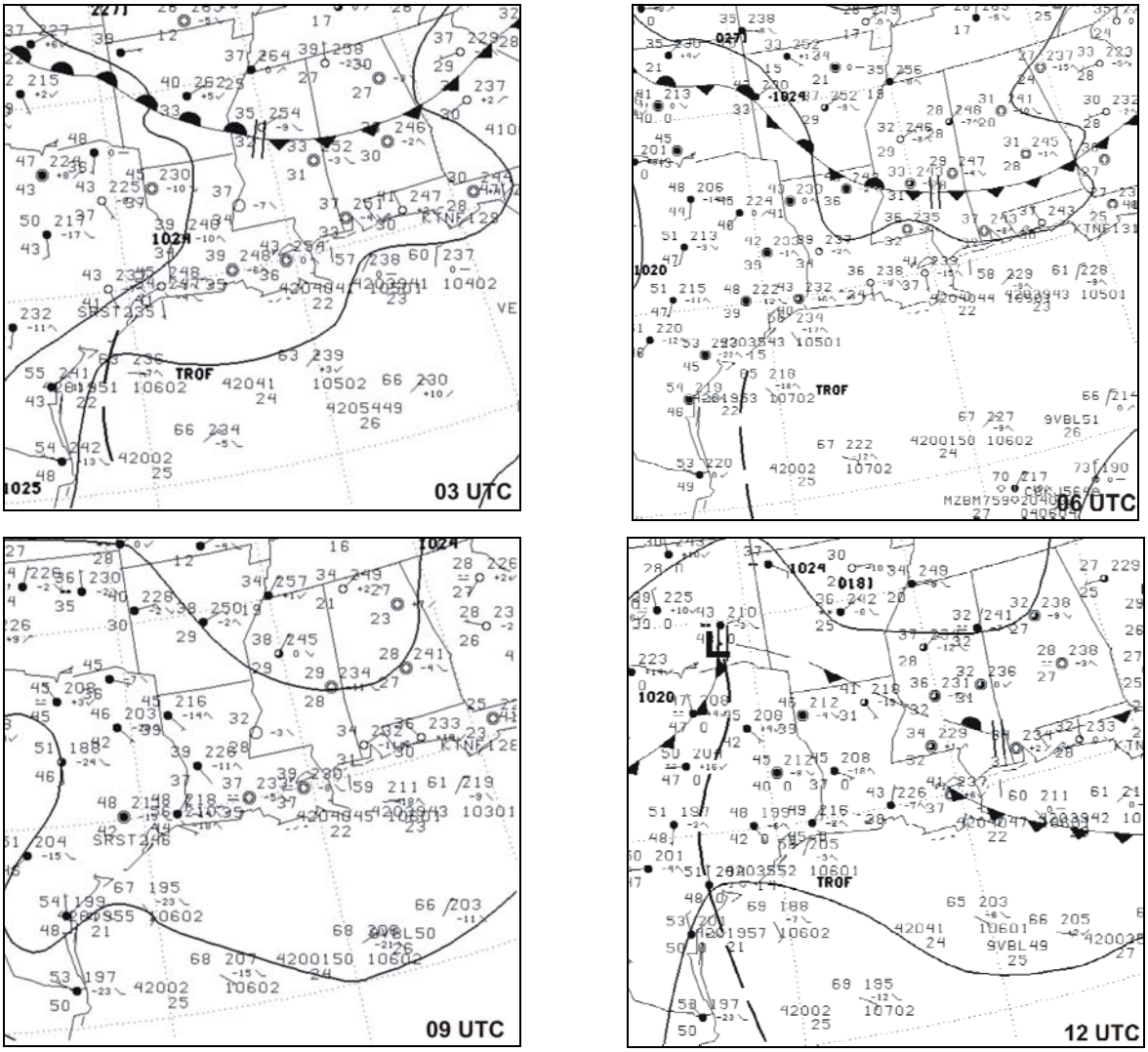

Figure G-15. Progression of 3-hourly surface analyses and observations over the approximate 12-km domain area for the period beginning 03 UTC, 6 December 2000 to 12 UTC, 6 December 2000. Included in the analyses are isobars (contoured every 4 hPa), surface observations, and hand-analyzed surface fronts and troughs.

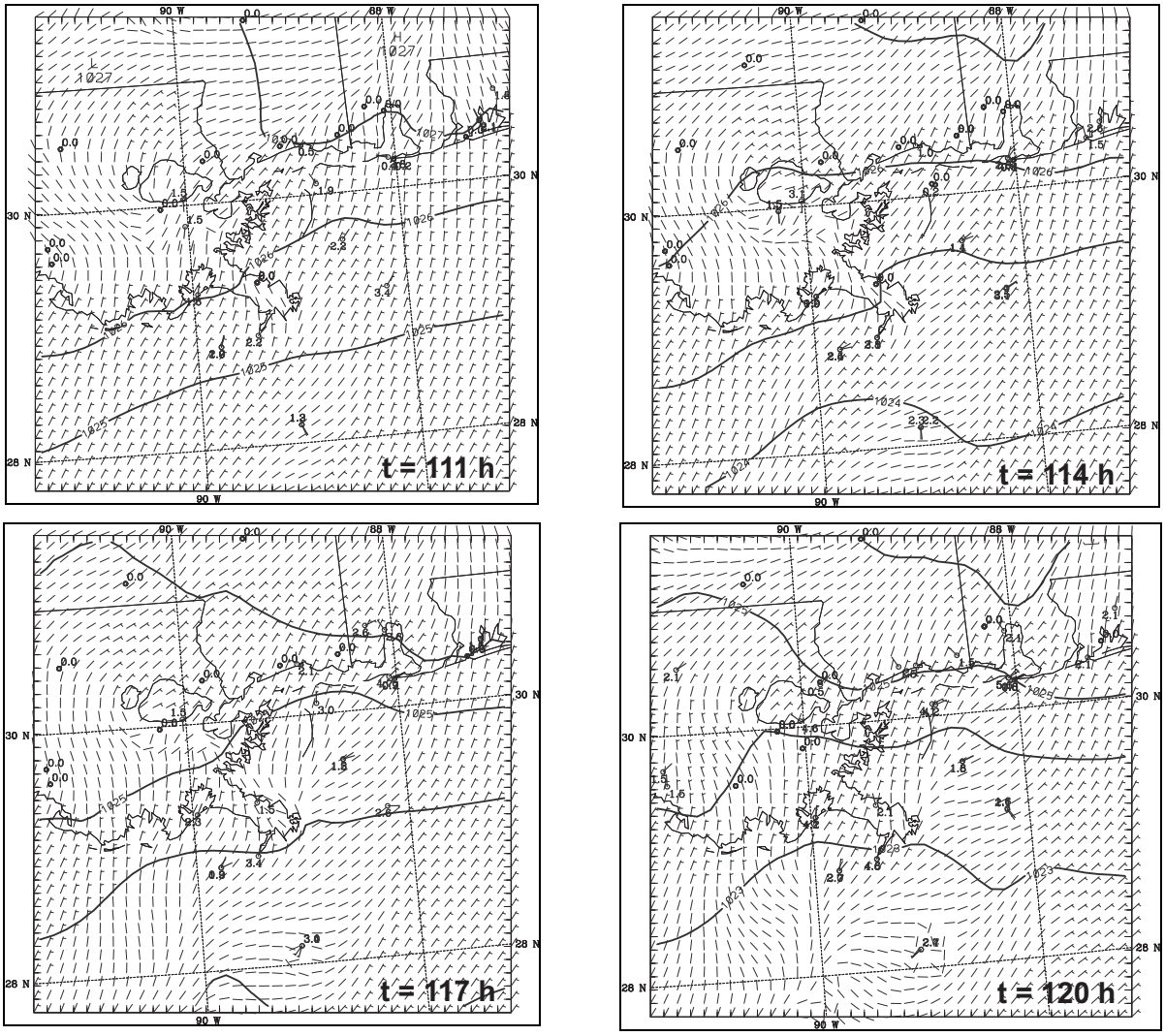

Figure G-16. Progression of 3-hourly model-derived surface wind barbs, SLP, and 4-km domain surface observations from the DEC12 simulation over the 4-km subdomain, beginning 03 UTC, 6 December 2000 (t = 111 h) and ending 12 UTC, 6 December 2000 (t = 120 h). Isobars are drawn every 1 hPa.

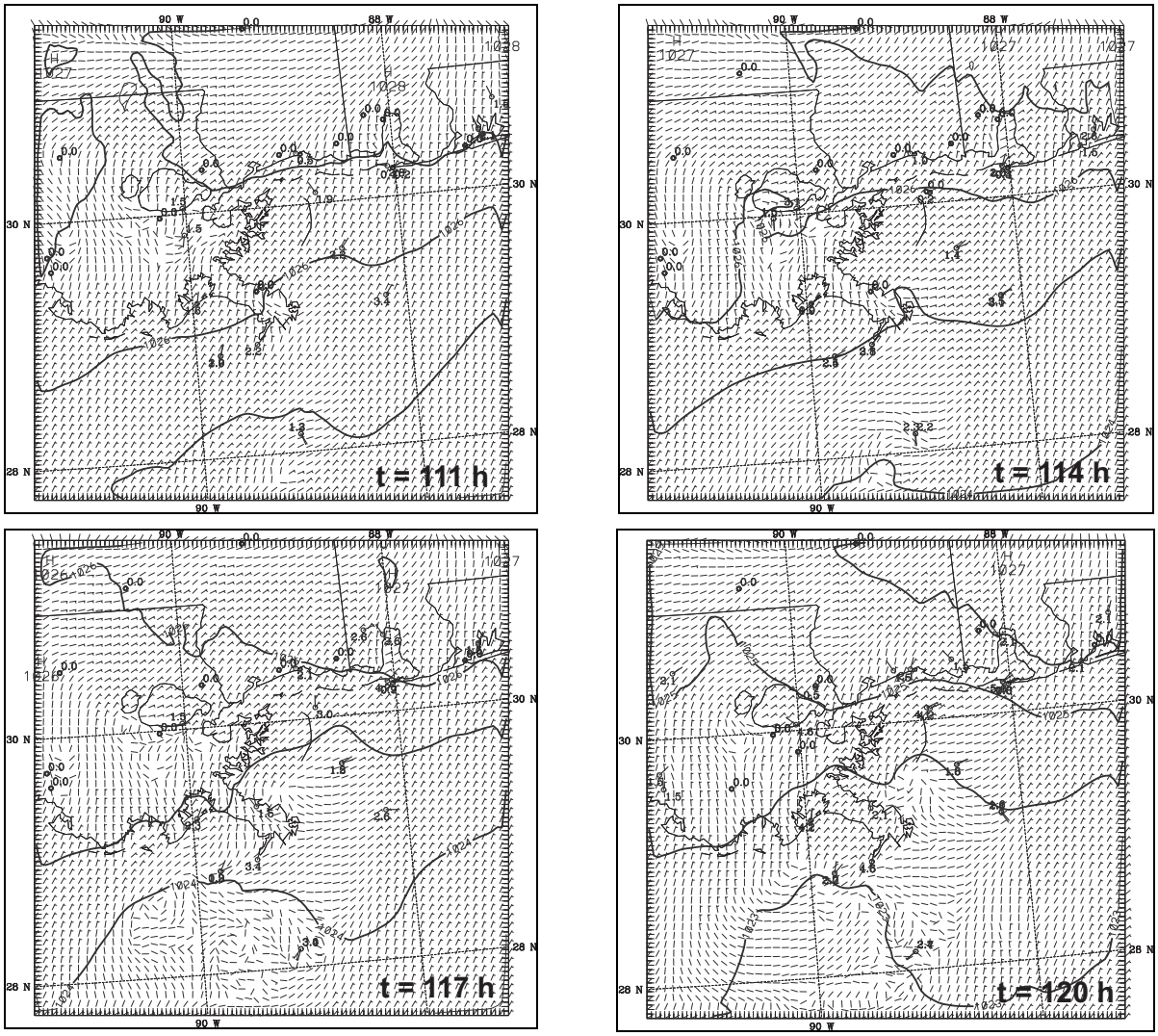

Figure G-17. Progression of 3-hourly model-derived surface wind barbs, SLP, and 4-km domain surface observations from the DEC4 simulation, beginning 03 UTC, 6 December 2000 (t = 111 h) and ending 12 UTC, 6 December 2000 (t = 120 h). Isobars are drawn every 1 hPa.

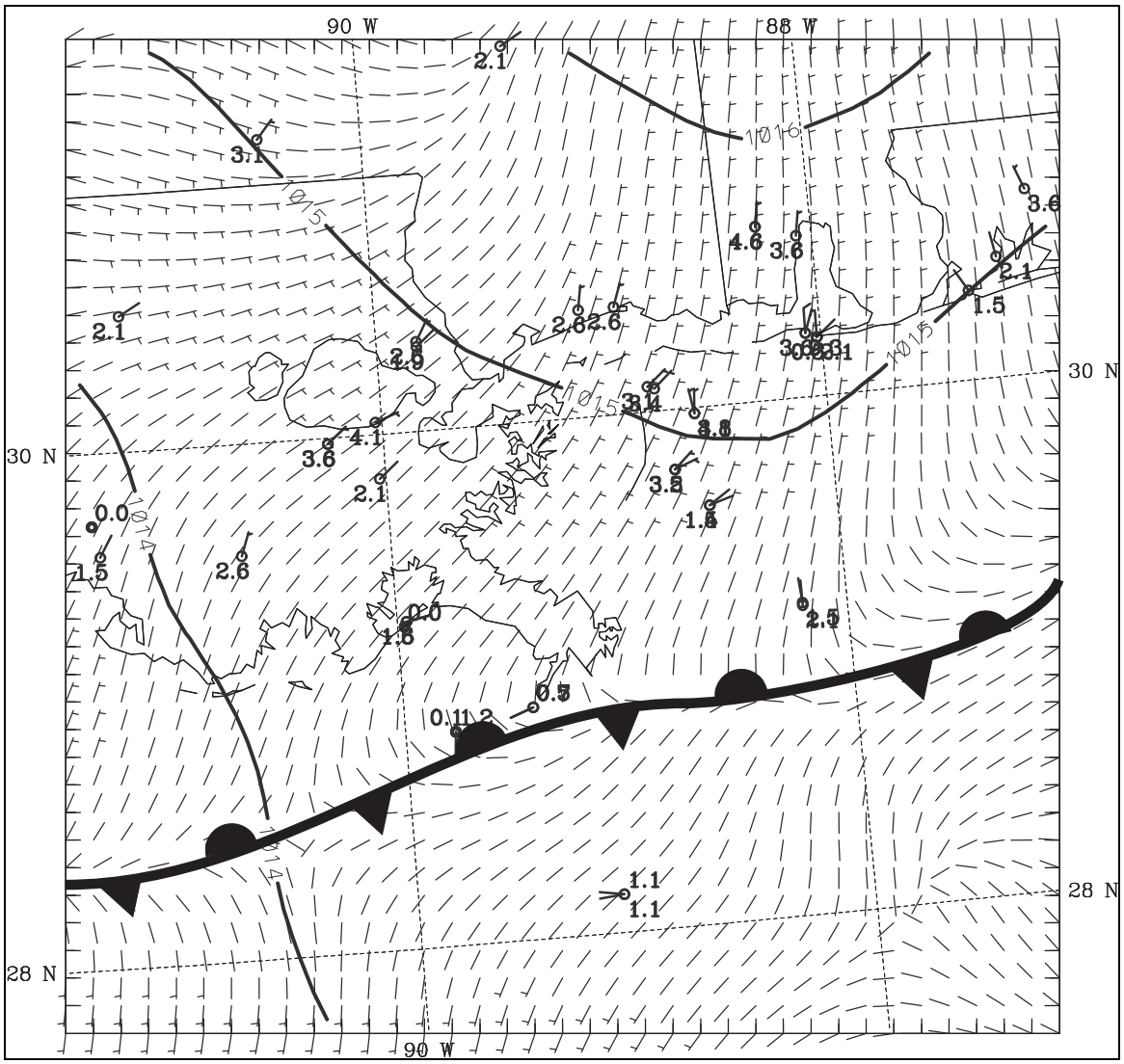

Figure G-18. Model-derived surface-layer wind barbs, SLP, and surface observations from the MAR12 model output on the 4-km subdomain, and analyzed surface front for 12 UTC, 1 March 2001 (t = 0 h). Isobars are contoured every 1 hPa.

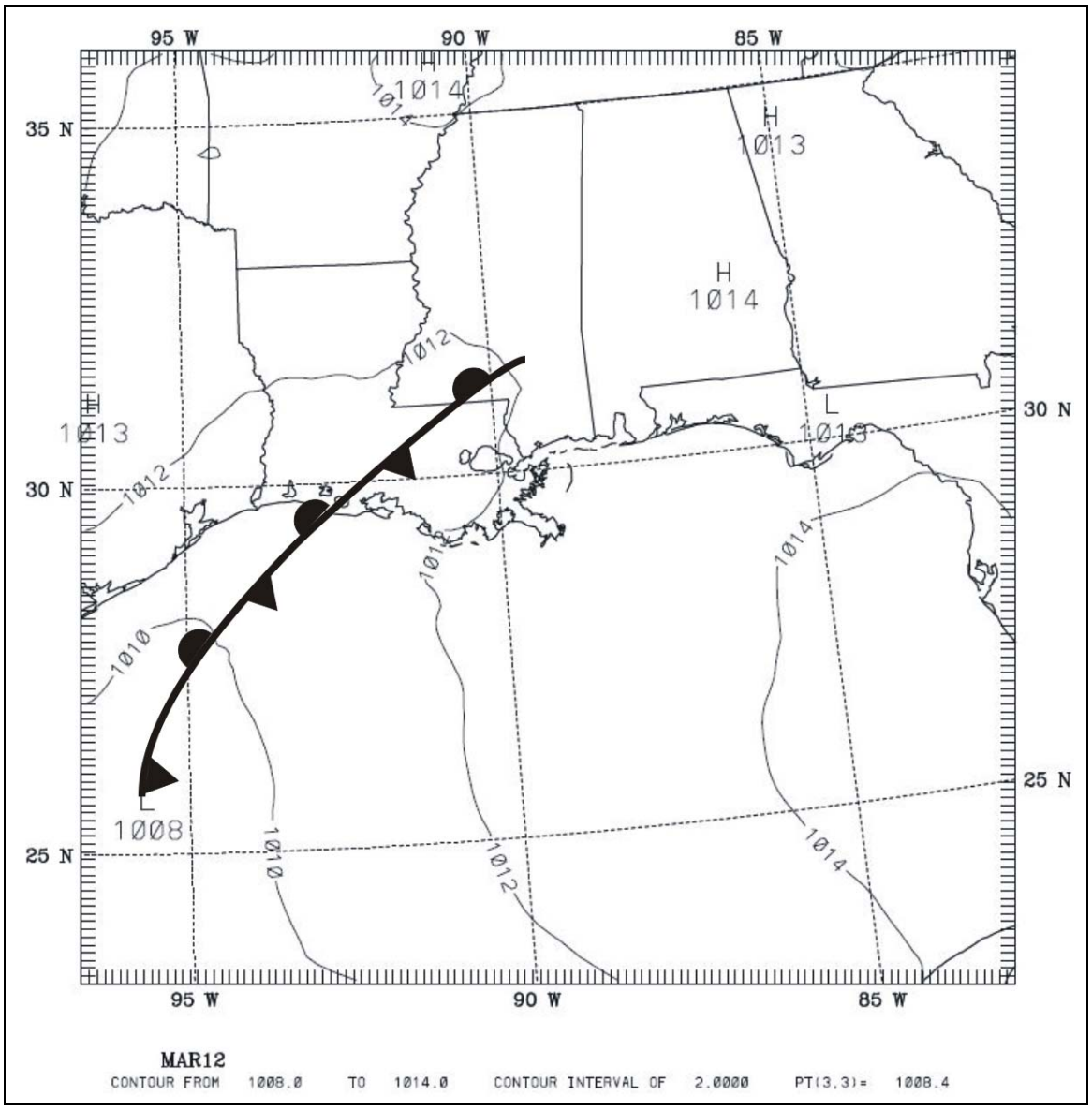

Figure G-19. Model-derived SLP (hPa) from the MAR12 model output, analyzed at 00 UTC, 2 March 2001 (t = 12 h) over the 12-km domain area. Isobars are drawn every 2 hPa.

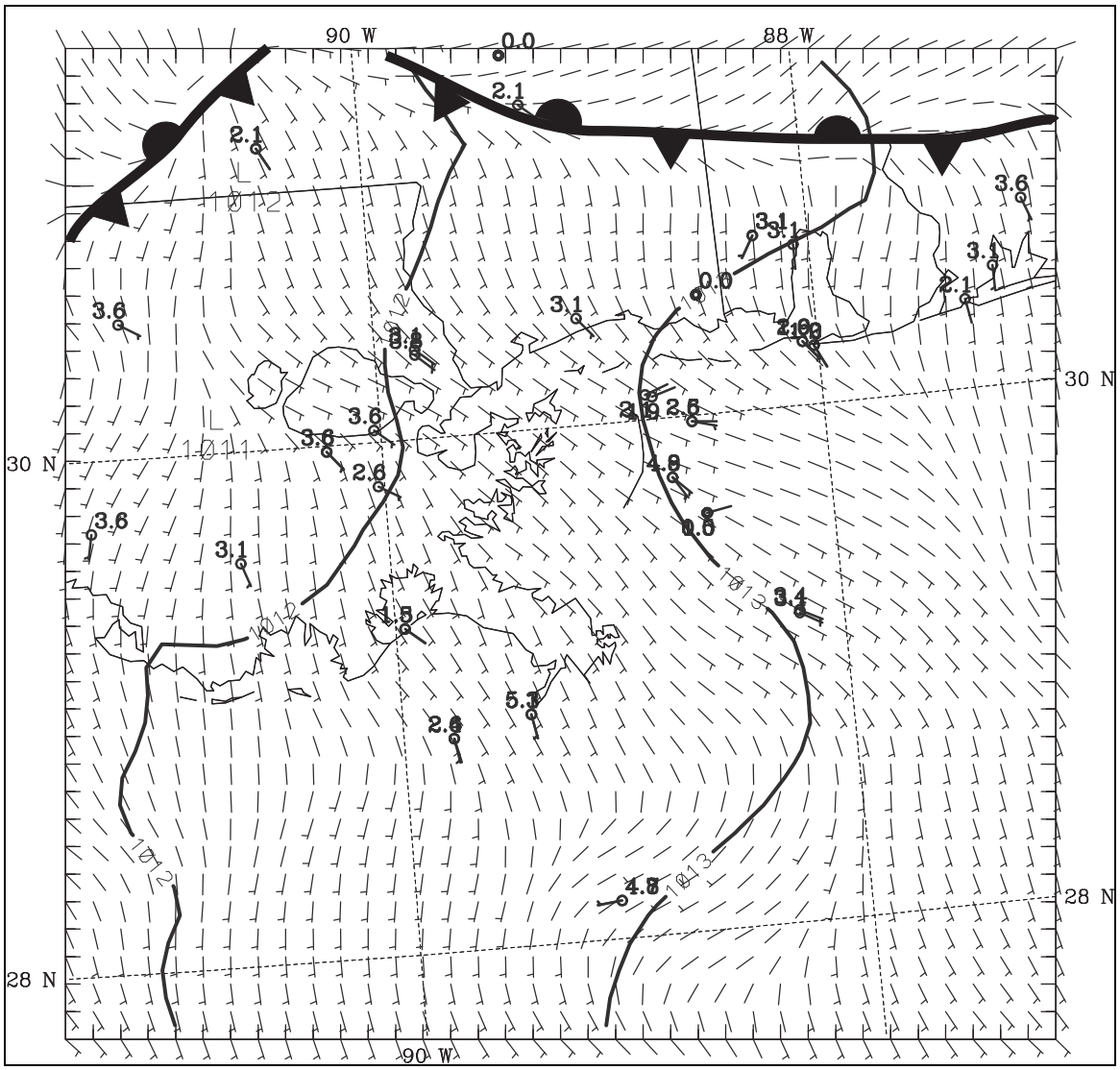

Figure G-20. Model-derived surface layer wind field, SLP, surface wind observations, and analyzed front for 00 UTC, 2 March 2001 from the MAR12 model output over the 4-km subdomain. Isobars are plotted every 1 hPa.

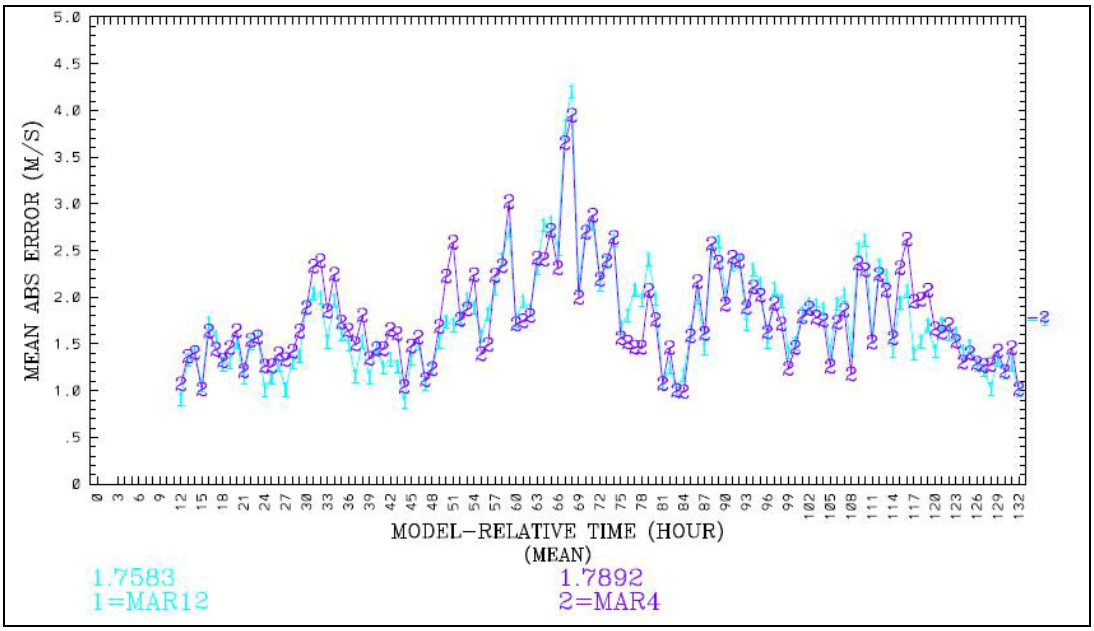

Figure G-21. MAE of model-derived WSPD (m/s) for MAR12 (blue) and MAR4 (purple) in the surface layer. Overall average MAE values for the surface layer are shown at the bottom of the figure in the corresponding colors.

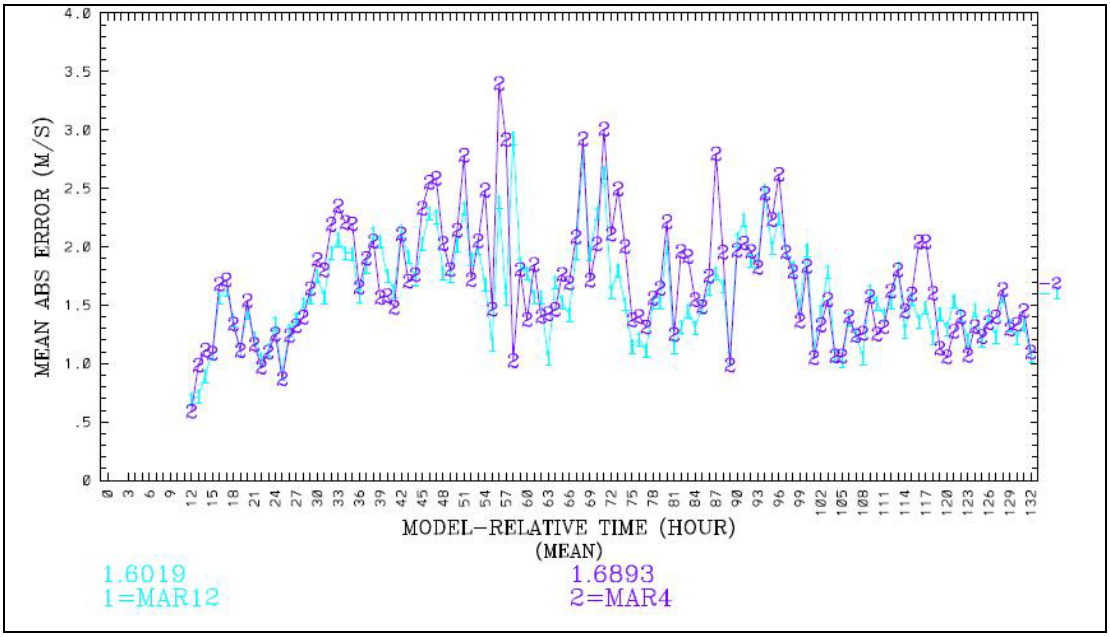

Figure G-22. MAE of model-derived WSPD (m/s) for MAR12 (blue) and MAR4 (purple) in the PBL. Overall average MAE values for the surface layer are shown at the bottom of the figure in the corresponding colors.

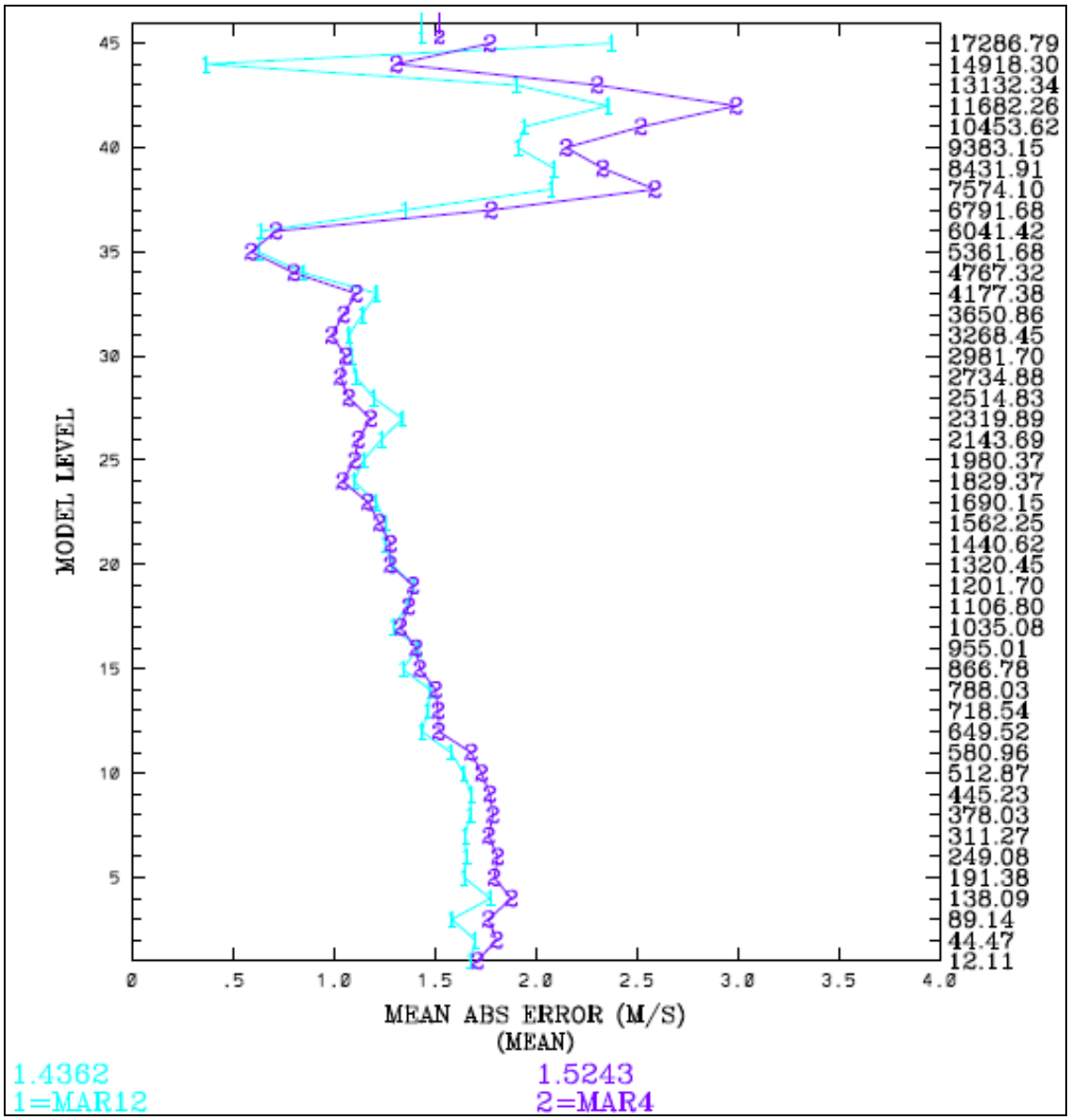

Figure G-23. Vertical profile of model-derived WSPD (m/s) MAE for the all model sigma-levels, including curves for MAR12 (blue) and MAR4 (purple). MAE is shown on the abscissa, model sigma-level is shown on the left ordinate, and model height is shown on the right ordinate.

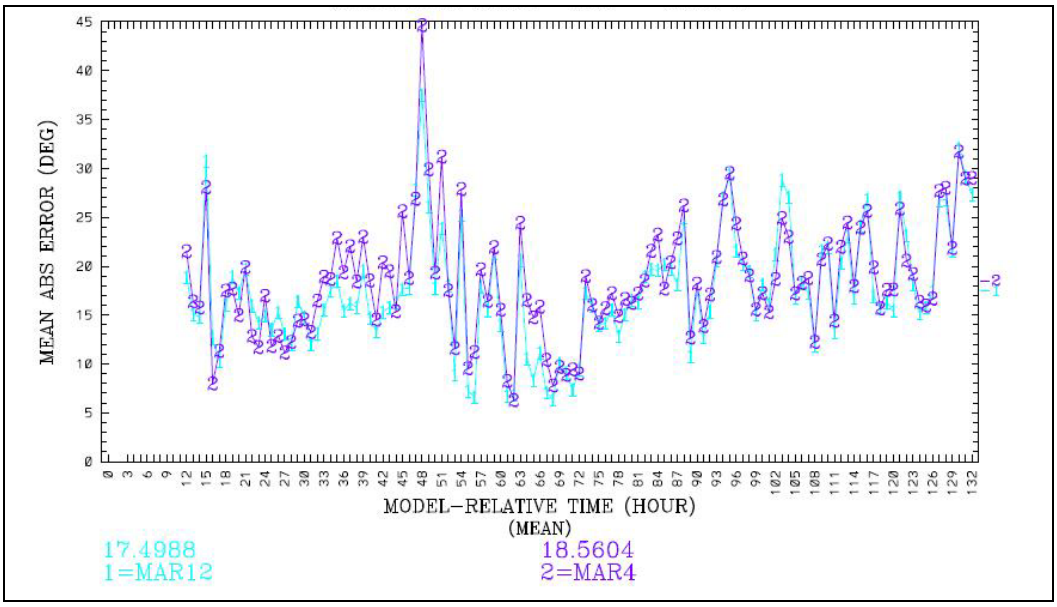

Figure G-24. MAE of model-derived WDIR (degrees) for MAR12 (blue) and MAR4 (purple) for the surface layer are shown. Overall average MAE values for the surface layer are given at the bottom of the figure in the corresponding colors.

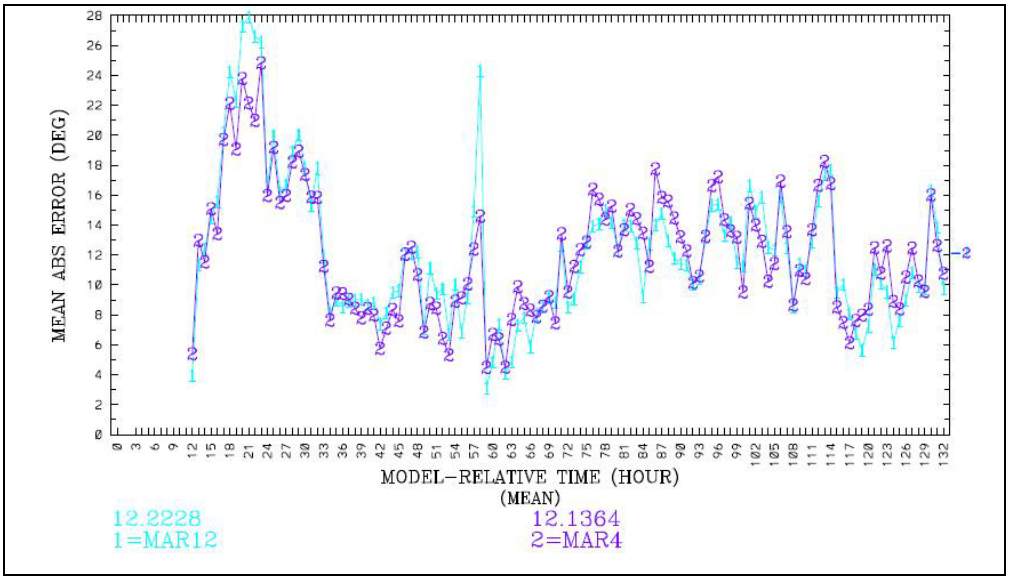

Figure G-25. MAE of model-derived WDIR (degrees) for MAR12 (blue) and MAR4 (purple) for the PBL are shown. Overall average MAE values for the surface layer are given at the bottom of the figure in the corresponding colors.

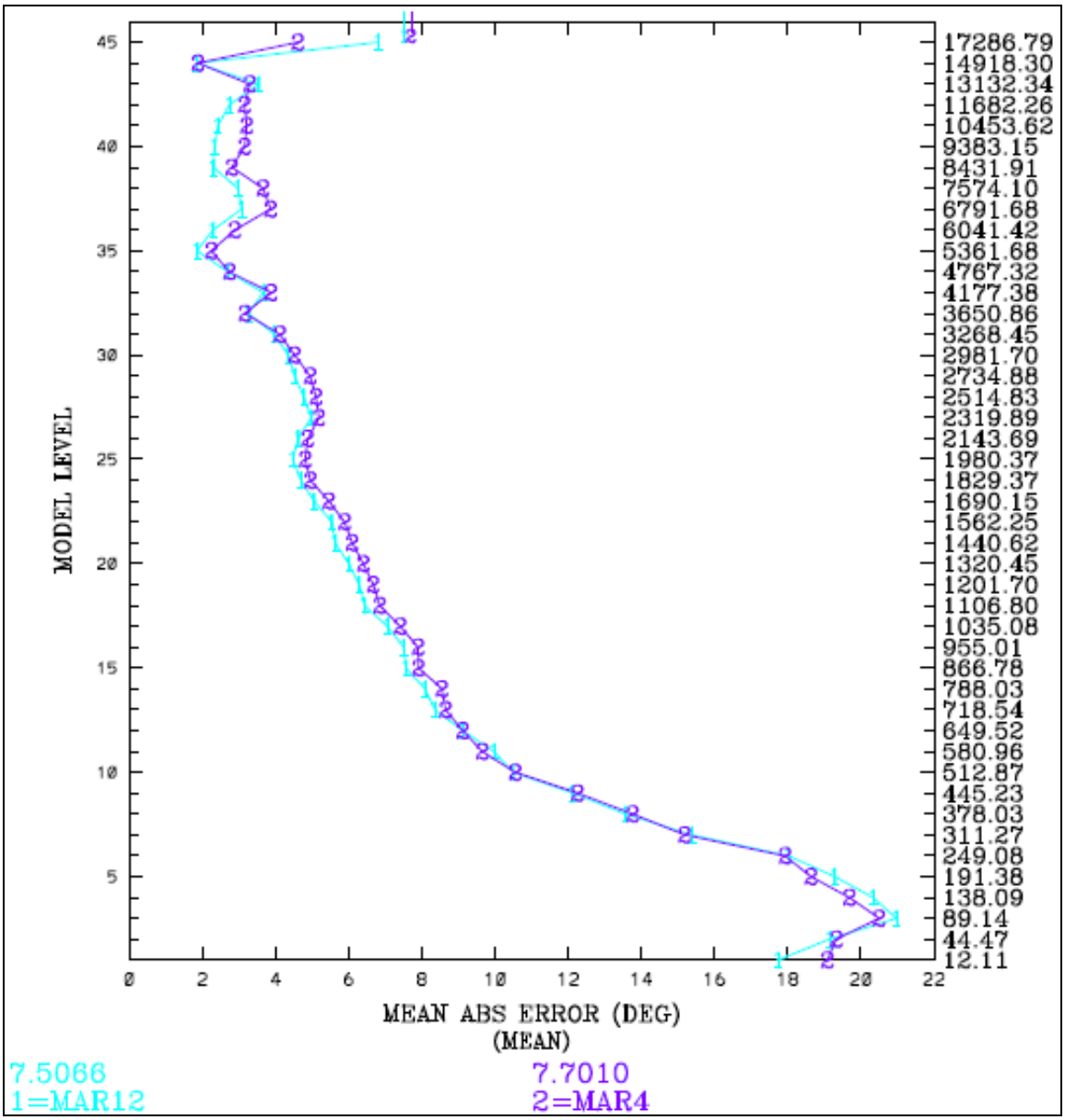

Figure G-26. Vertical profile of model-derived WDIR (degrees) MAE for the all model sigma-levels, including curves for MAR12 (blue) and MAR4 (purple). MAE is shown on the abscissa, model sigma-level is shown on the left ordinate, and model height is shown on the right ordinate.

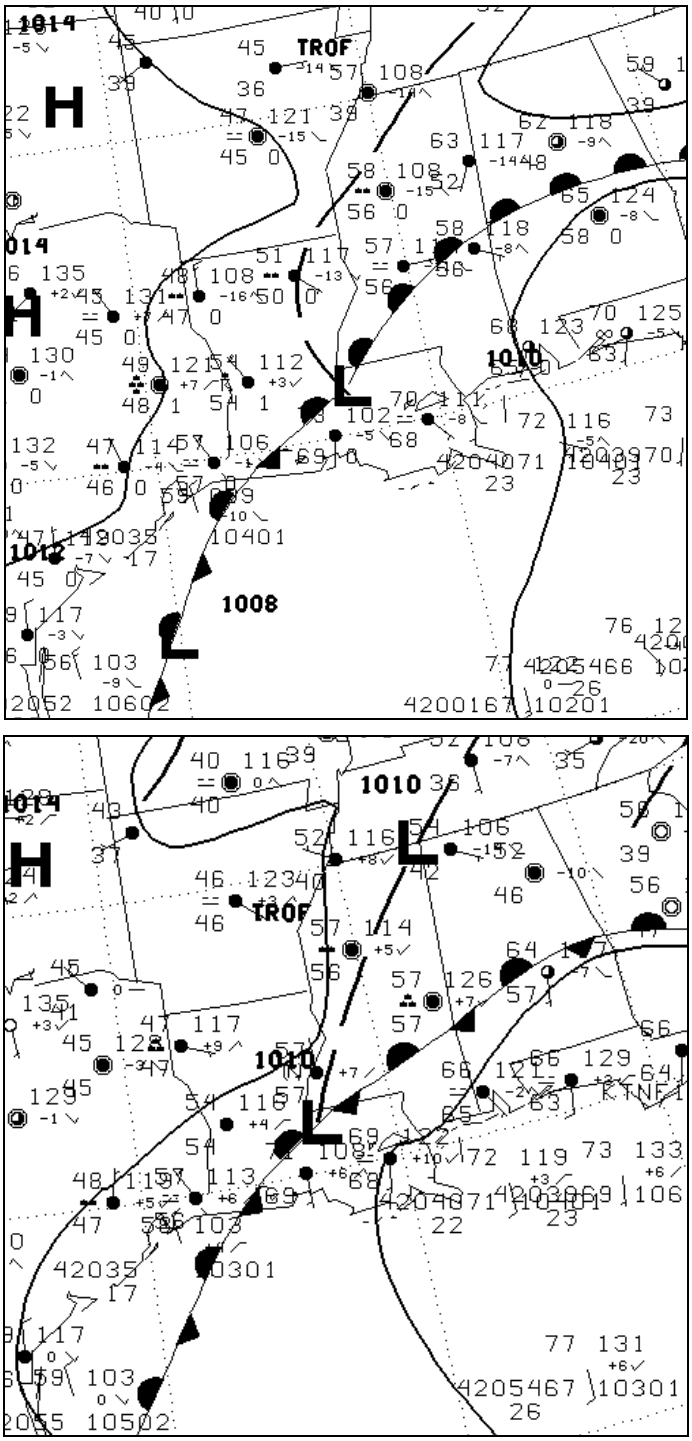

Figure G-27. NCEP surface analyses and surface observations over the approximate 12-km domain area for 00 UTC, 2 March 2001 (top) and 03 UTC, 2 March 2001 (bottom). Isobars are drawn every 4 hPa.

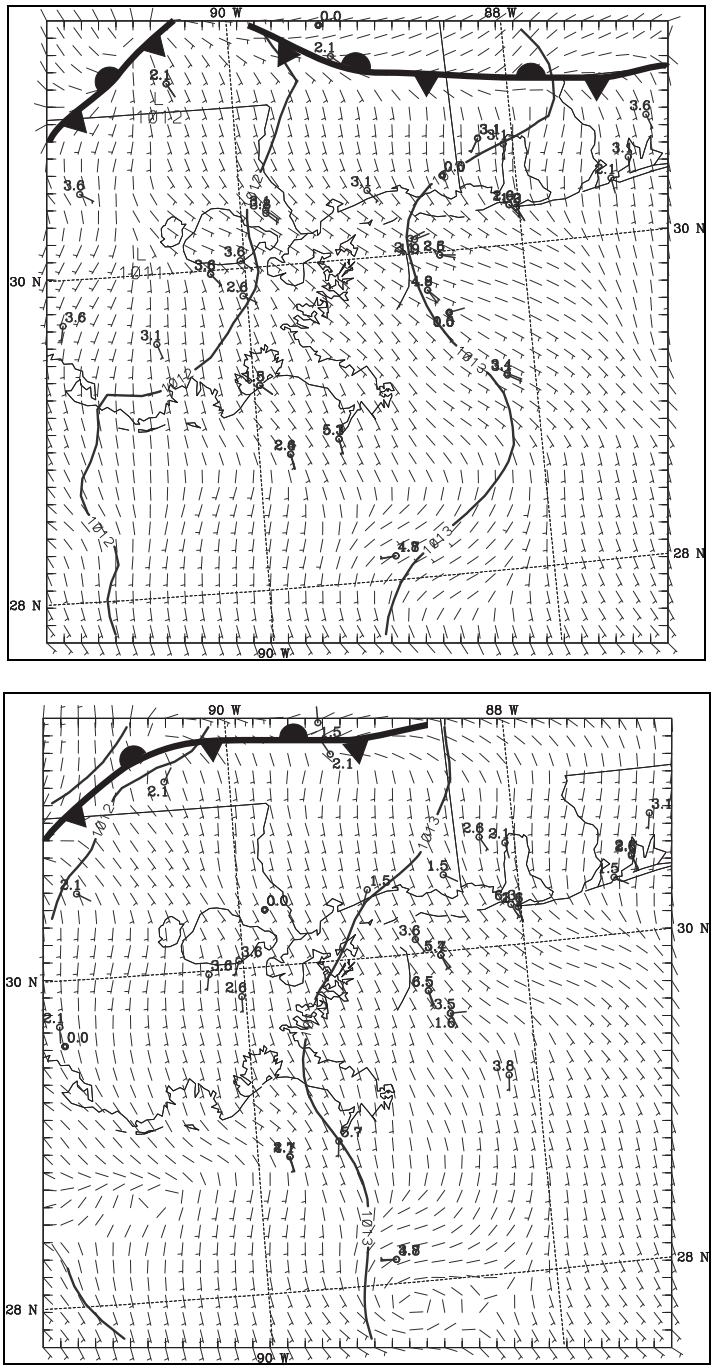

Figure G-28. MAR12 model-derived surface wind field, SLP and 4-km domain surface wind observations for 00 UTC, 2 March 2001 (top) and 03 UTC, 2 March 2001 (bottom) on the 4-km subdomain. Wind observations are plotted in m/s and isobars are drawn every 1 hPa.

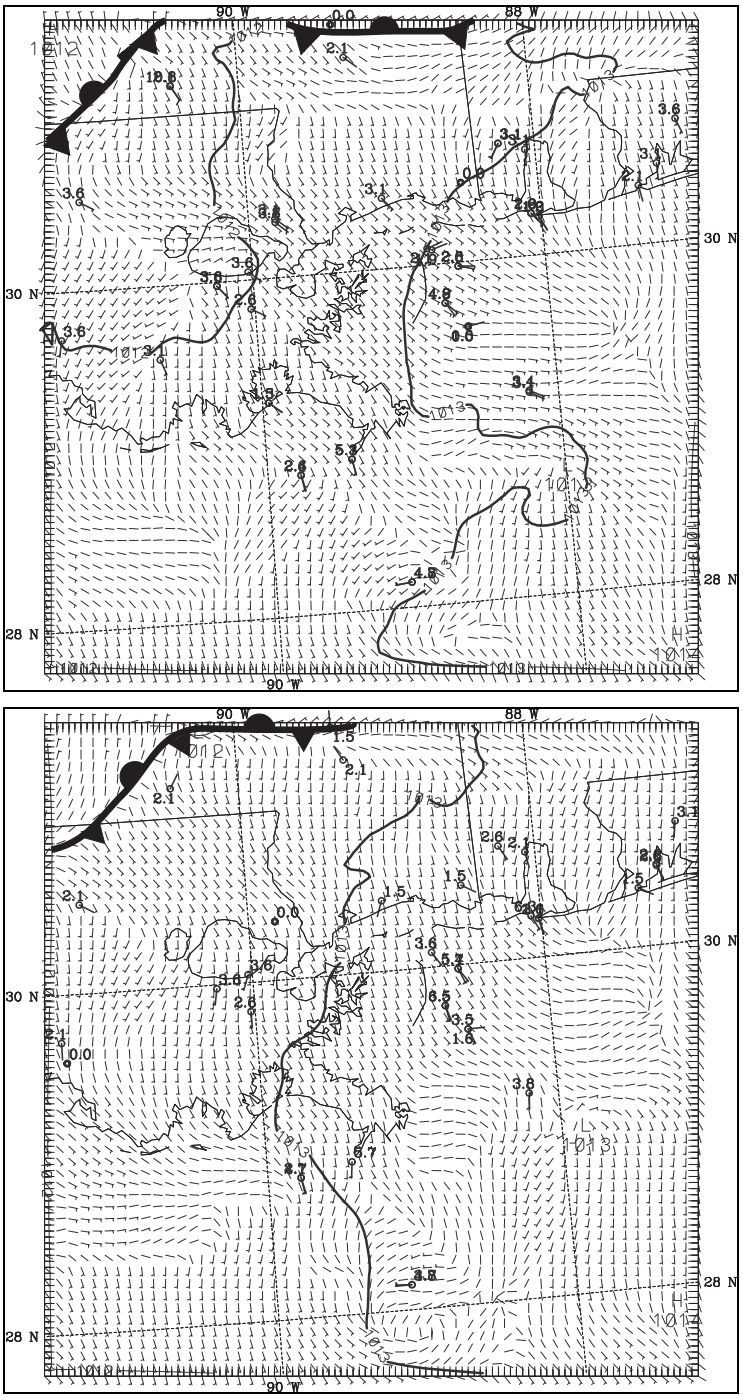

Figure G-29. MAR4 model-derived surface wind field and 4-km domain surface wind observations for 00 UTC, 2 March 2001 (top) and 03 UTC, 2 March 2001 (bottom). Wind observations are plotted in m/s and isobars are plotted every 1 hPa.

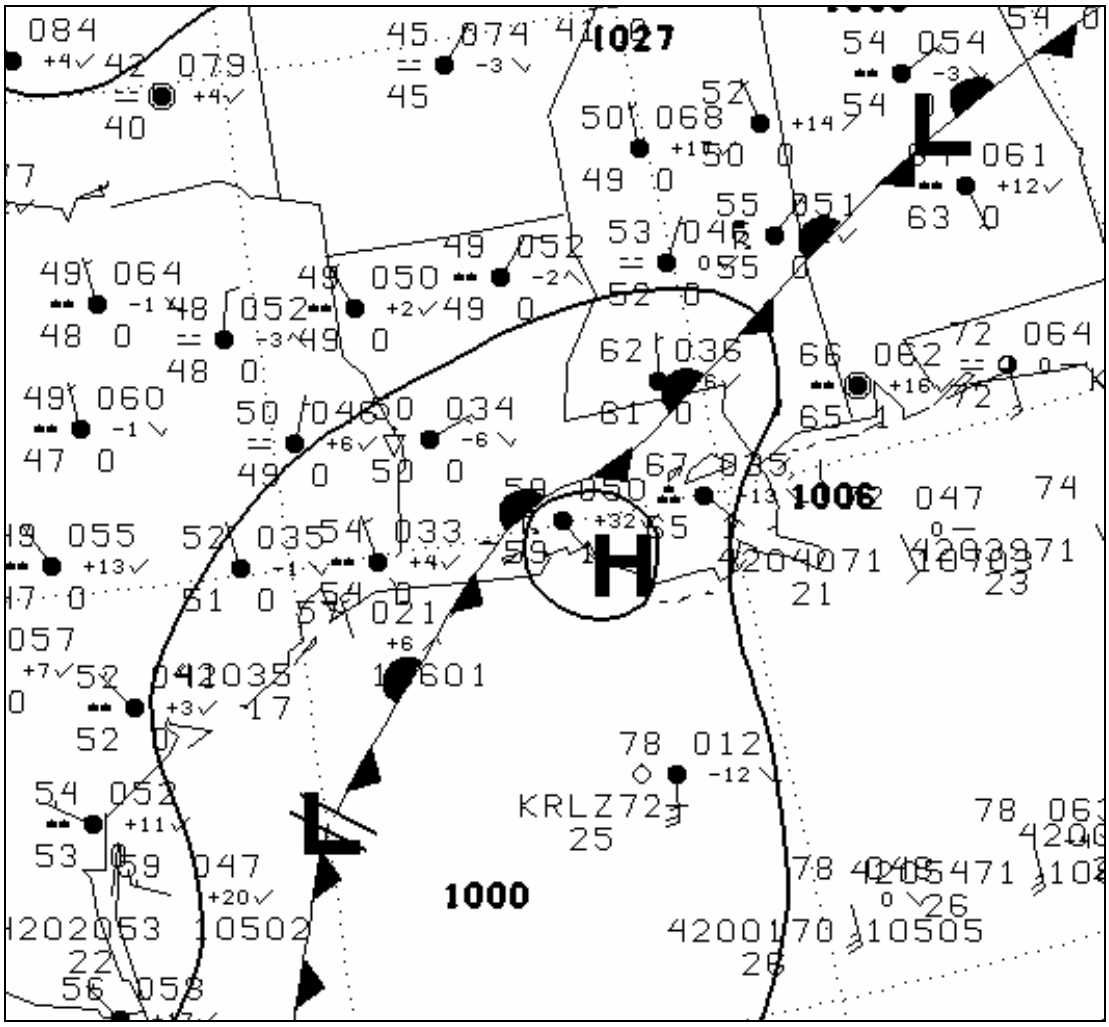

Figure G-30. NCEP surface analysis and surface observations over the approximate 12-km domain area for 12 UTC, 3 March 2001. Isobars are drawn every 4 hPa.

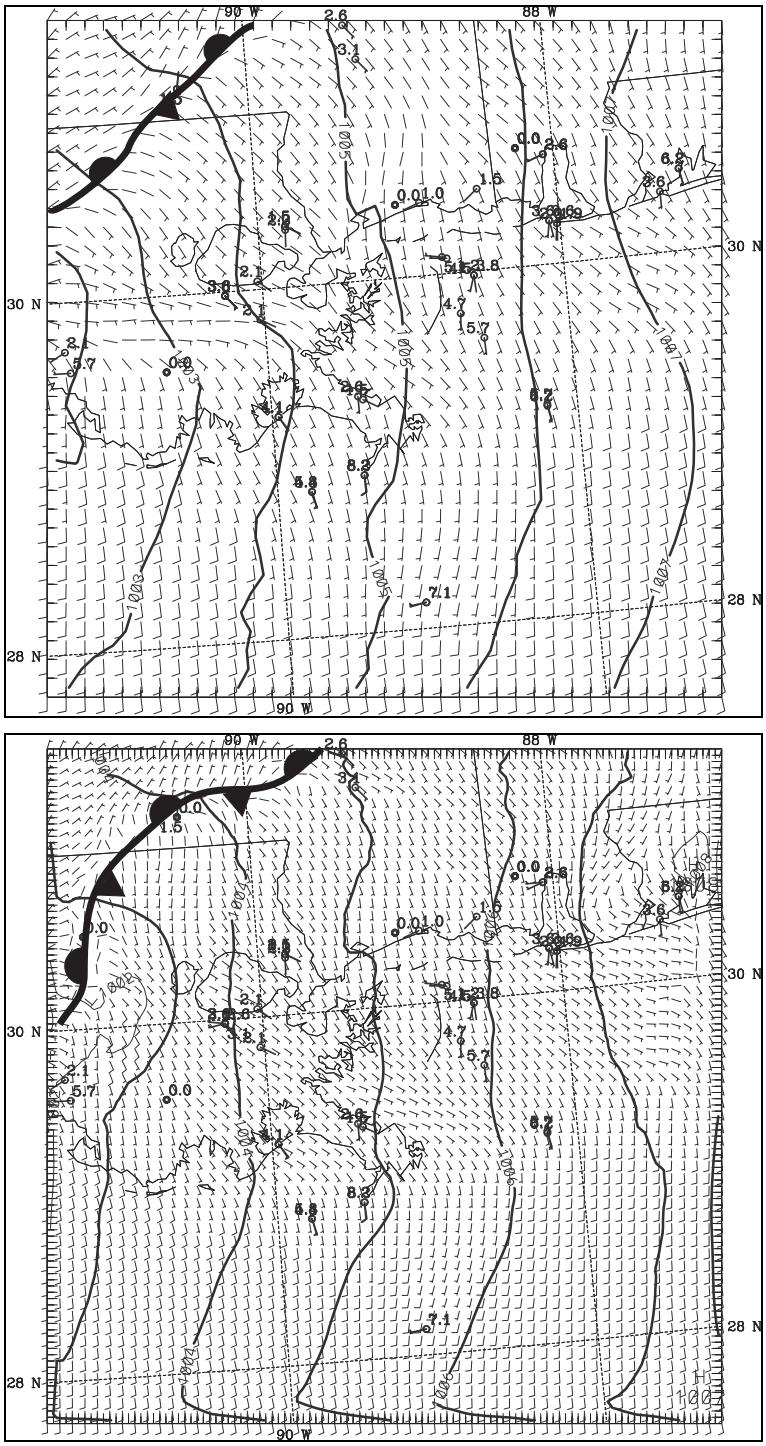

Figure G-31. MAR12 (top) and MAR4 (bottom) model-derived surface wind and SLP analyses over the 4-km domain area, for 12 UTC, 3 March 2001 (model hour 48). Wind observations are plotted in m/s and isobars are plotted every 1 hPa.

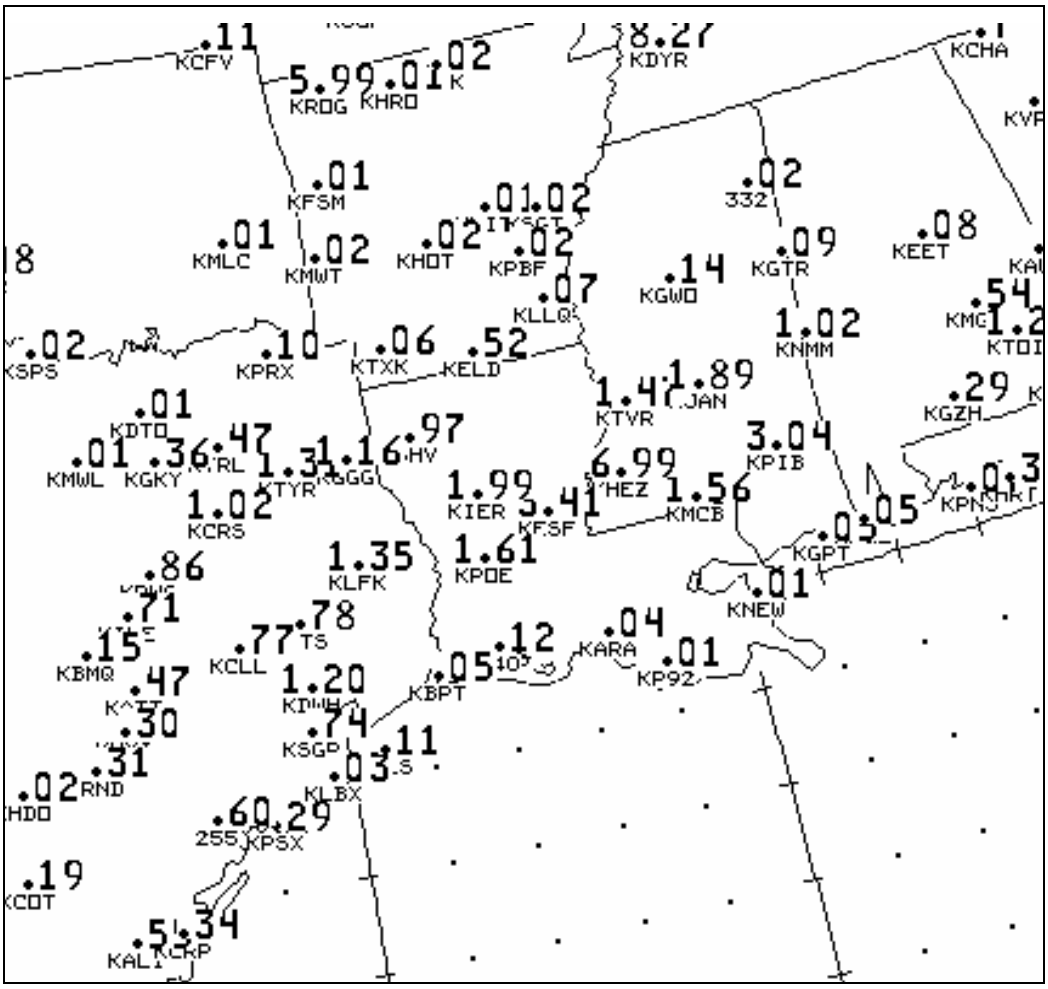

Figure G-32. Observed 24-hour precipitation totals for the period beginning 12 UTC, 1 March 2001 (t = 0 h), and ending 12 UTC, 2 March 2001 (t = 24 h). Amounts are given in inches above the station identifier.

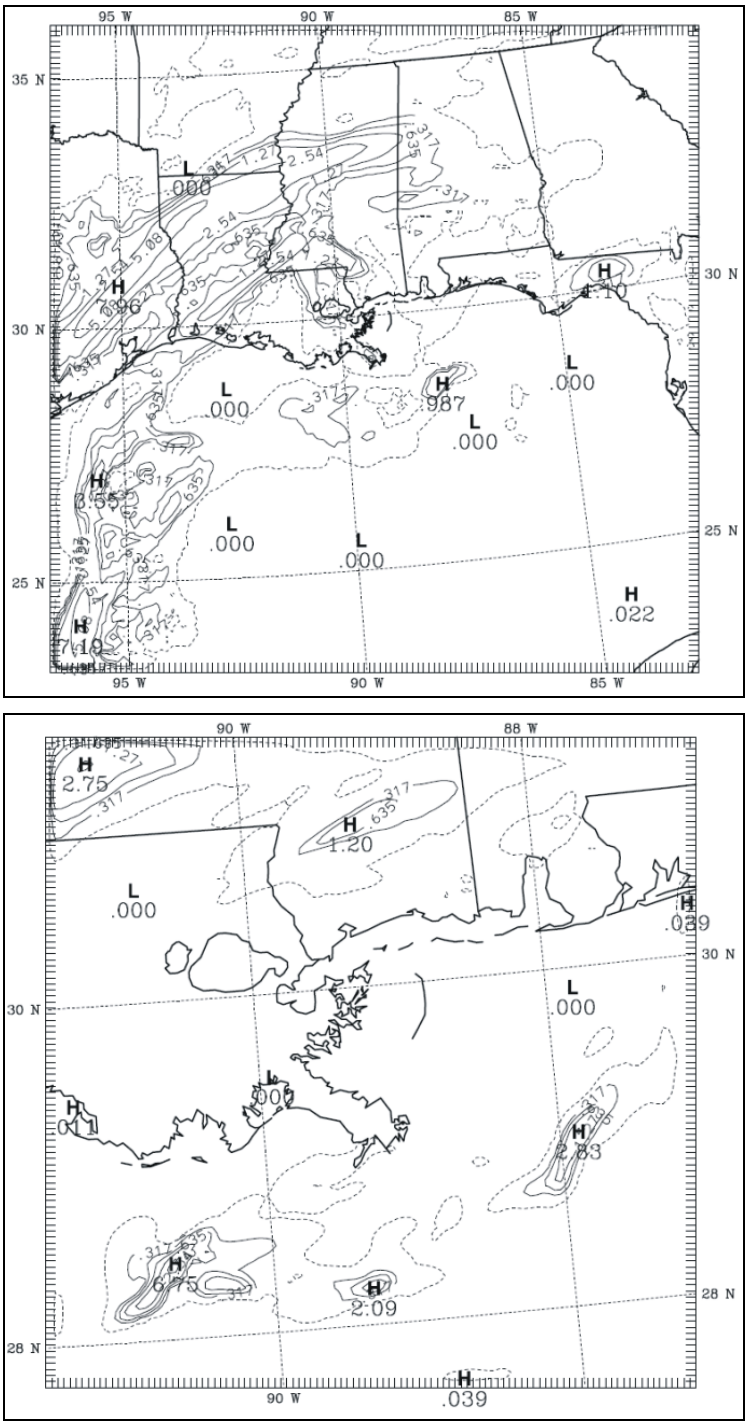

Figure G-33. MAR12 (top, 12-km domain area) and MAR4 (bottom, 4-km domain area) 24-hr model-derived accumulated precipitation for the period beginning 12 UTC, 1 March 2001 (t = 0 h), and ending 12 UTC, 2 March 2001 (t = 24 h). The dashed contour encircles all areas that have measurable model-derived precipitation during the 24-hour period. Within the dashed contour, precipitation amounts are contoured logarithmically, beginning with 0.125 inches (0.317 cm) and doubling with every successive contour.

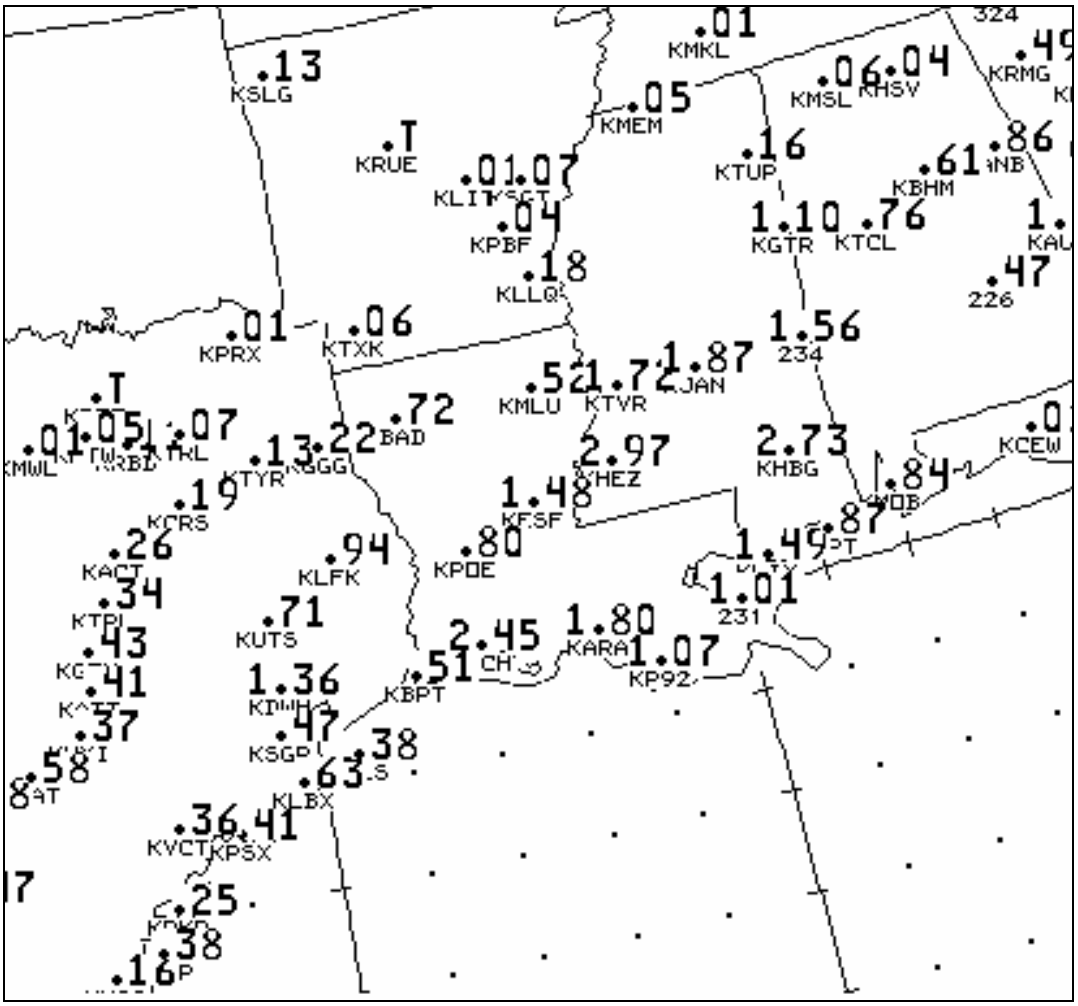

Figure G-34. Observed 24-hour precipitation totals for the period beginning 12 UTC, 2 March 2001, and ending 12 UTC, 3 March 2001. Amounts are given in inches above the station identifier.

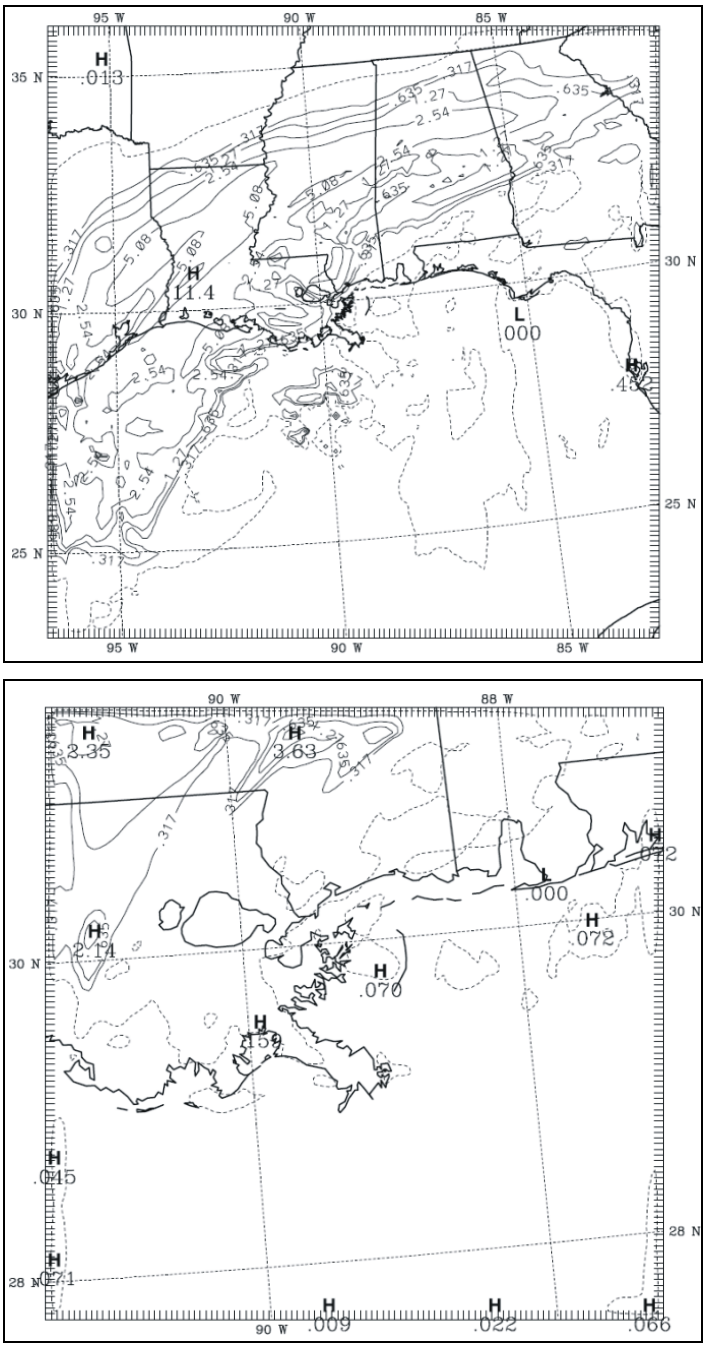

Figure G-35. MAR12 (over the 12-km domain area) and MAR4 (over the 4-km domain area) 24-hr model-derived accumulated precipitation for the period beginning 12 UTC, 2 March 2001, and ending 12 UTC, 3 March 2001. The dashed contour encircles all areas that have measurable model-derived precipitation during the 24-hour period. Within the dashed contour, precipitation amounts are contoured logarithmically, beginning with 0.125 inches (0.317 cm) and doubling with every successive contour.

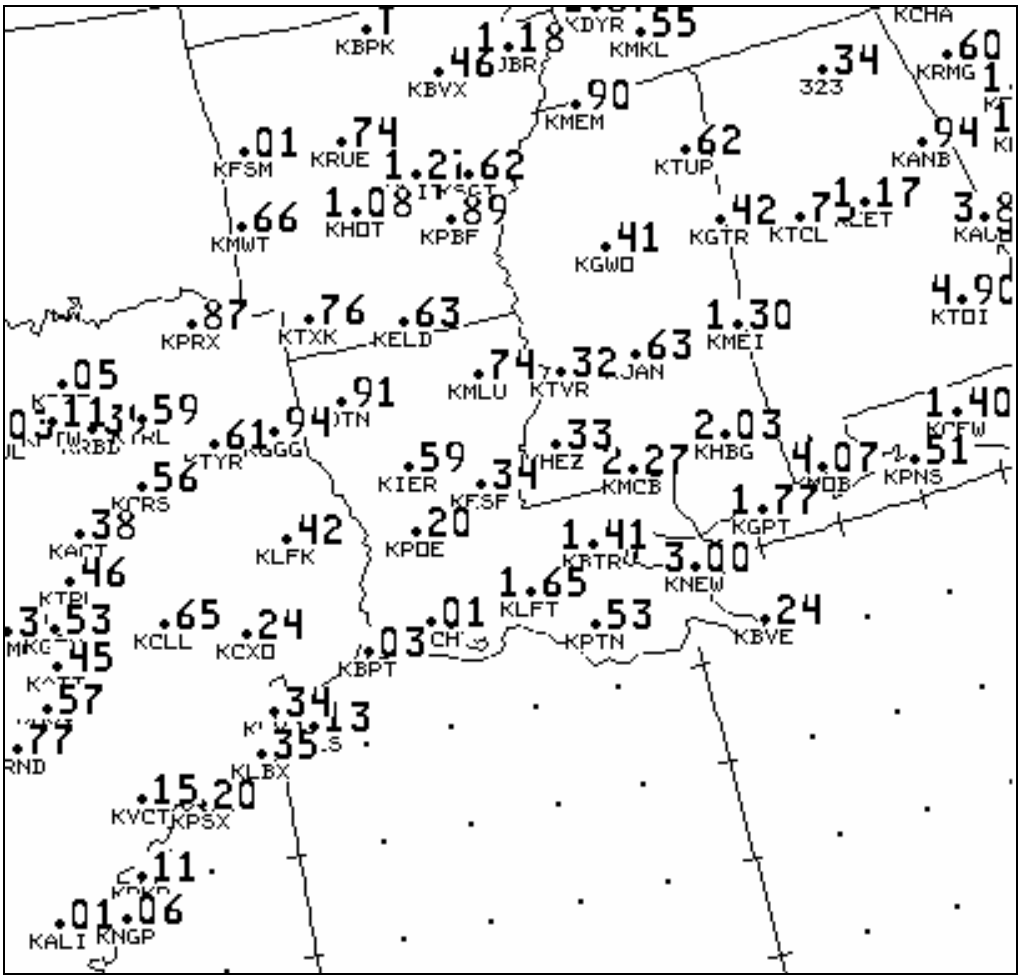

Figure G-36. Observed 24-hour precipitation totals for the period beginning 12 UTC, 3 March 2001, and ending 12 UTC, 4 March 2001. Amounts are given in inches above the station identifier.

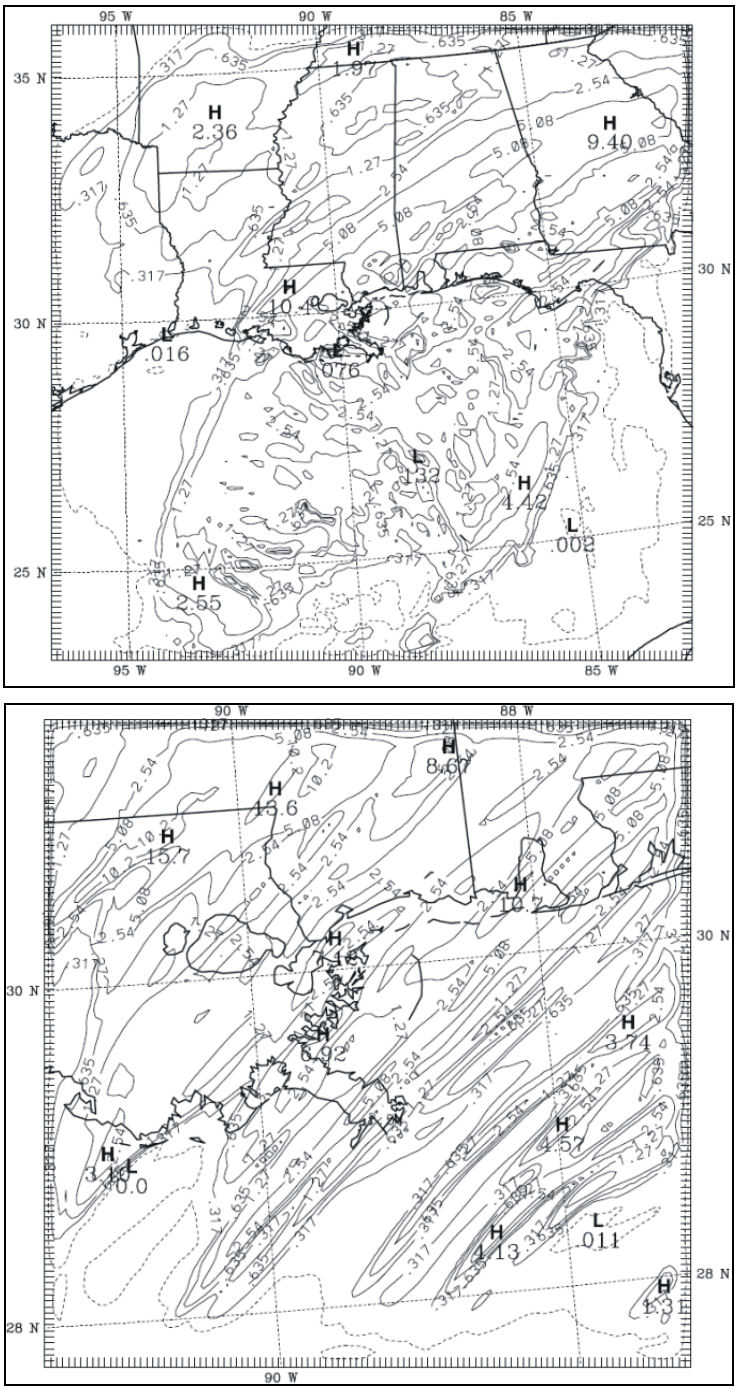

Figure G-37. MAR12 (over the 12-km domain area) and MAR4 (over the 4-km domain area) 24-hr model-derived accumulated precipitation for the period beginning 12 UTC, 3 March 2001, and ending 12 UTC, 4 March 2001. The dashed contour encircles all areas that have measurable model-derived precipitation during the 24-hour period. Within the dashed contour, precipitation amounts are contoured logarithmically, beginning with 0.125 inches (0.317 cm) and doubling with every successive contour.

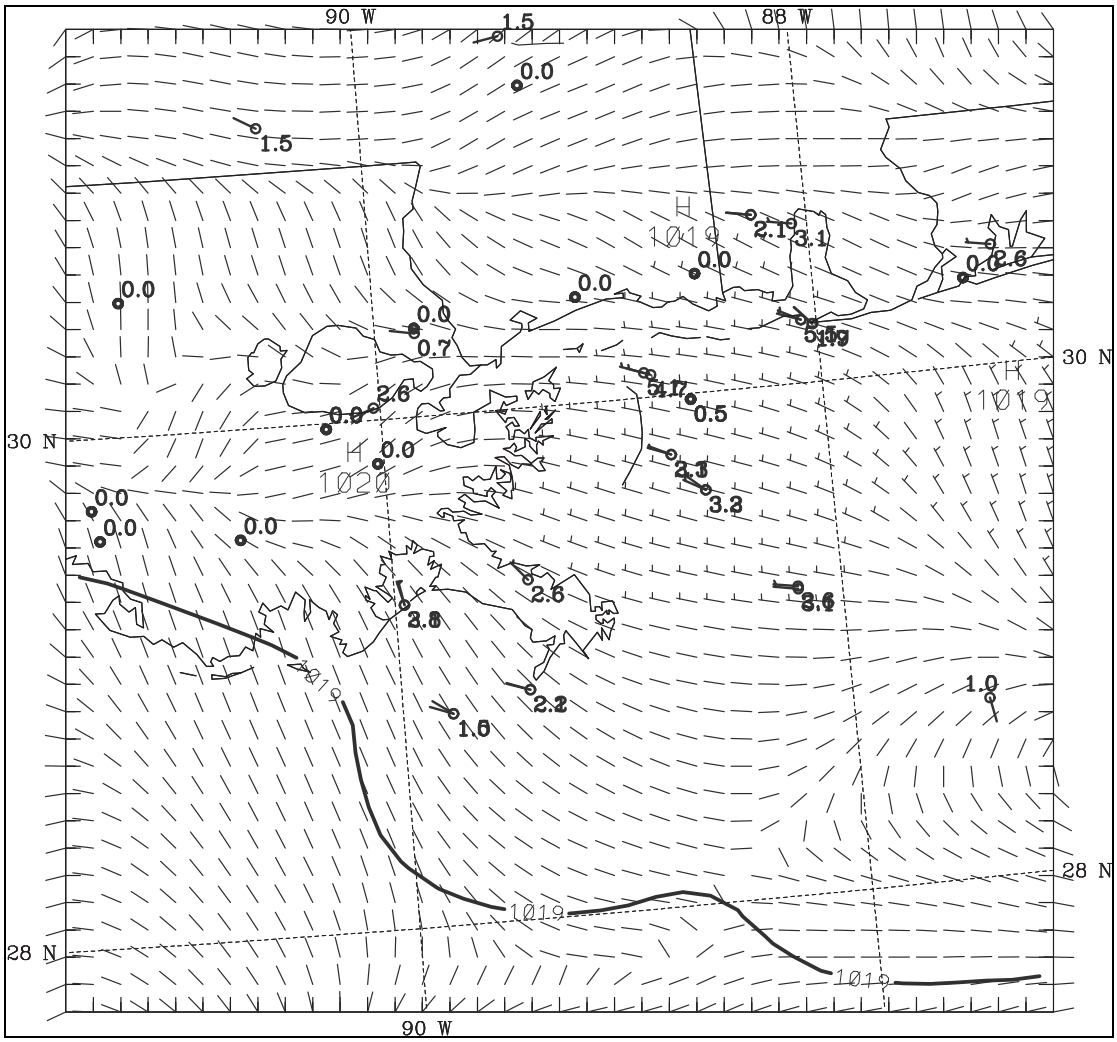

Figure G-38. JUL12 model-derived surface layer wind barbs, SLP, and 4-km domain surface wind observations are shown for the model initialization time (t = 0 h), 12 UTC, 8 July 2001 over the 4-km subdomain. Isobars are drawn every 1 hPa.

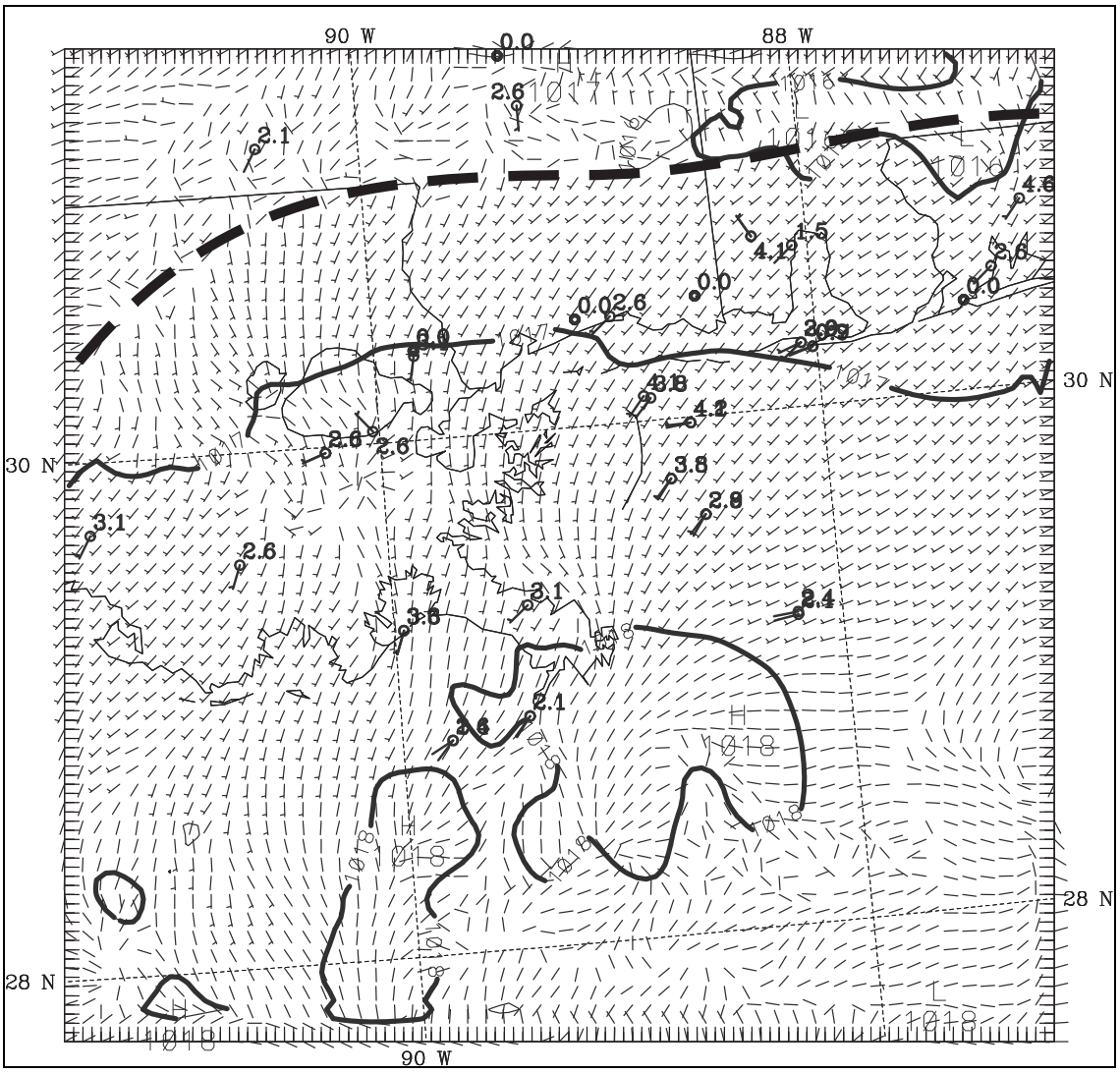

Figure G-39. JUL4 model-derived surface layer wind barbs, SLP, and surface wind observations (m/s) for the 4-km domain, at t = 12 h, 00 UTC, 9 July 2001. Isobars are drawn every 1 hPa. The boundary of the sea breeze front is denoted by the dashed line.

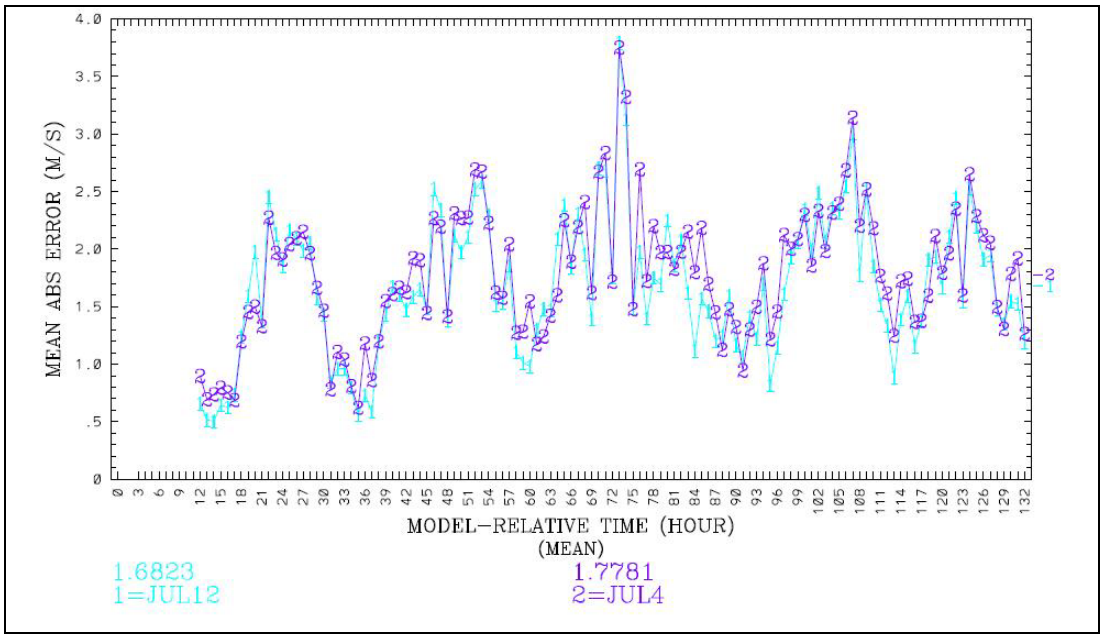

Figure G-40. MAE of model-derived WSPD (m/s) for JUL12 (blue) and JUL4 (purple) for the surface layer, beginning at model time t = 12 hours. Overall average MAE values for the surface layer are given at the bottom of the figure in the corresponding colors.

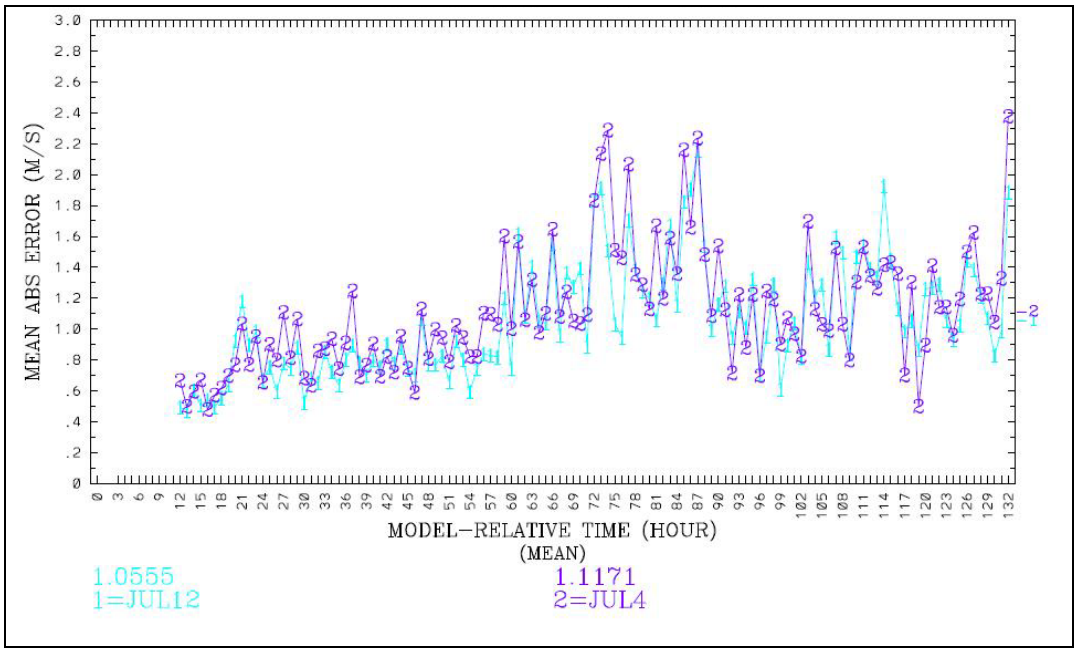

Figure G-41. MAE of model derived WSPD (m/s) for JUL12 (blue) and JUL4 (purple) for the PBL, beginning at model time t = 12 hours. Overall average MAE values for the PBL are given at the bottom of the figure in the corresponding colors.

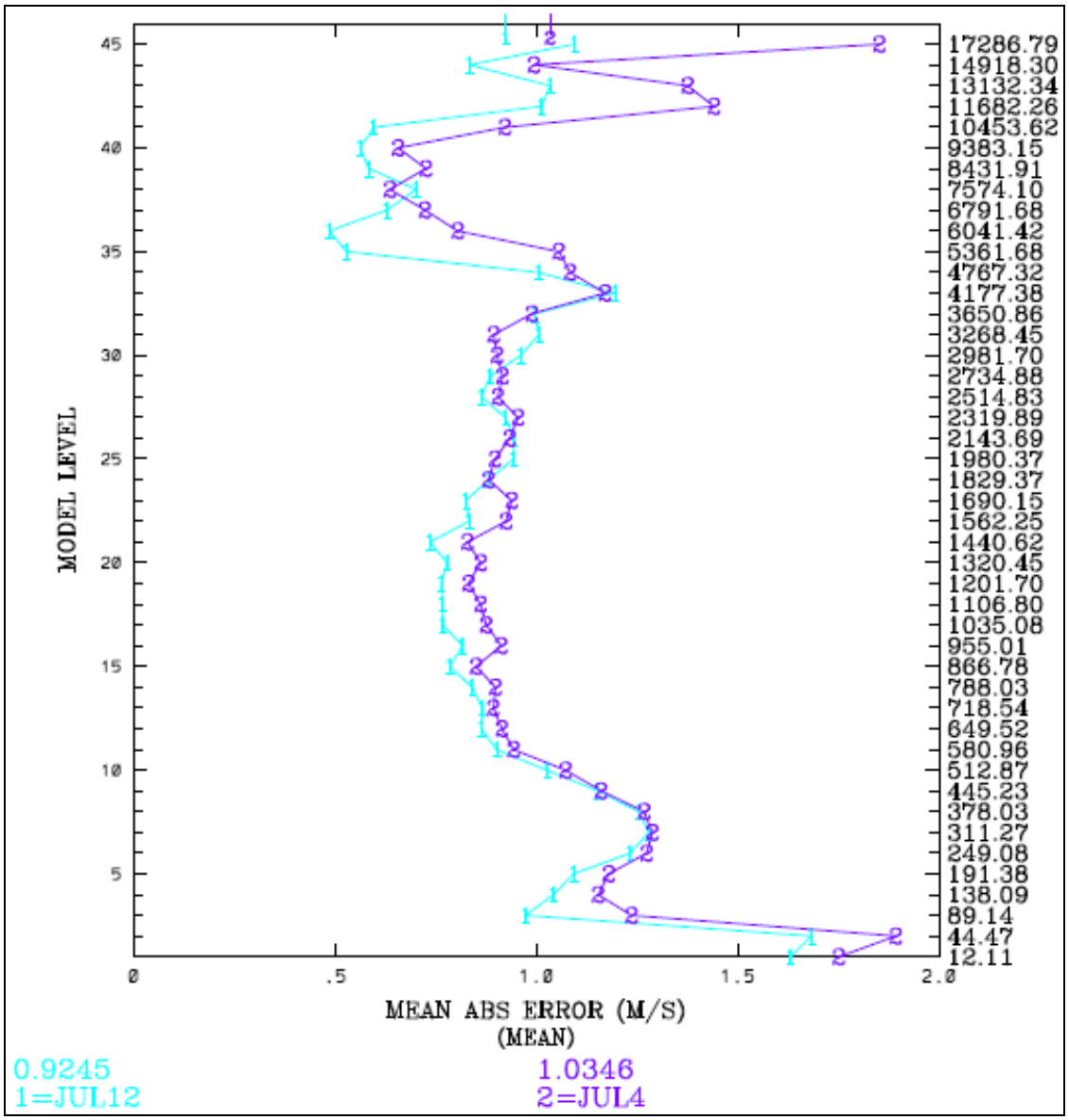

Figure G-42. Vertical profile of model-derived WSPD (m/s) MAE values for JUL12 (blue) and JUL4 (purple) for all model sigma-levels, beginning at model time t = 12 hours. MAE is shown on the abscissa, model sigma-level is shown on the left ordinate, and model height is shown on the right ordinate.

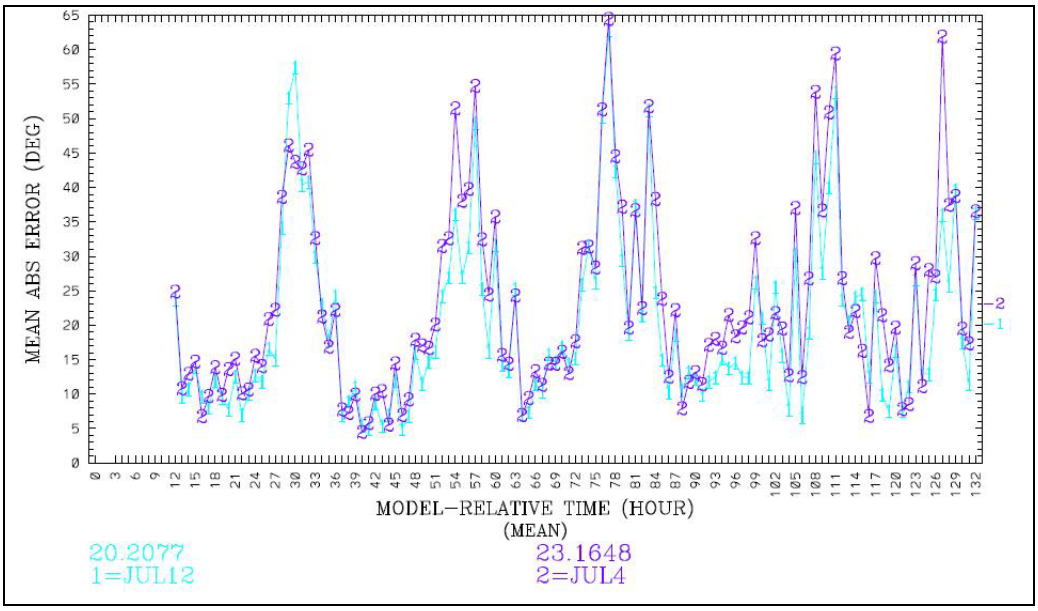

Figure G-43. MAE of model-derived WDIR (degrees) for JUL12 (blue) and JUL4 (purple) for the surface layer, beginning at model time t = 12 hours. Overall average MAE values for the surface layer are given at the bottom of the figure in the corresponding colors.

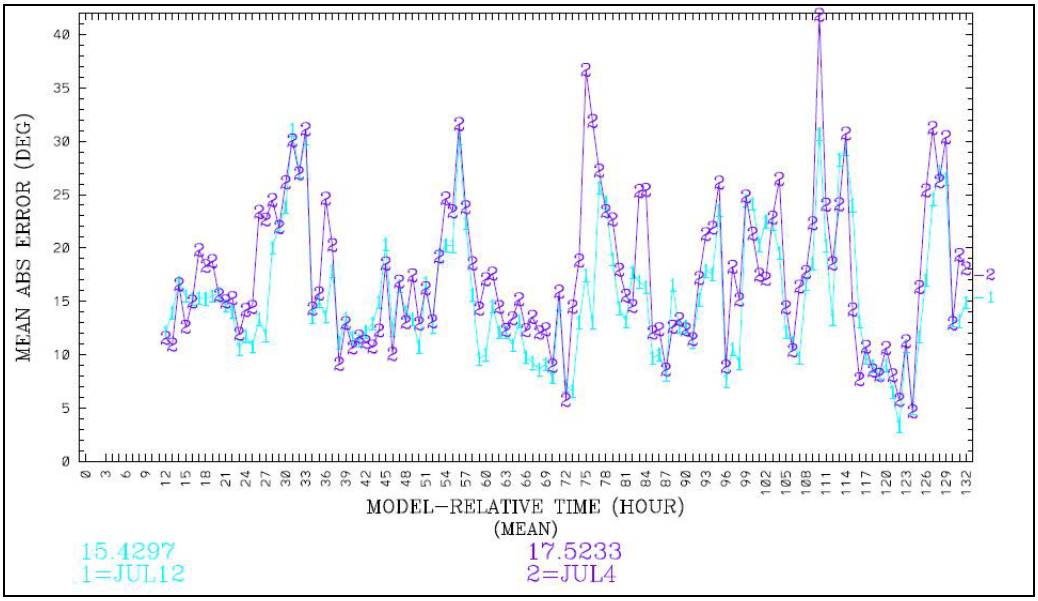

Figure G-44. MAE of model-derived WDIR (degrees) for JUL12 (blue) and JUL4 (purple) for the PBL, beginning at model time t = 12 hours. Overall average MAE values for the PBL are given at the bottom of the figure in the corresponding colors.

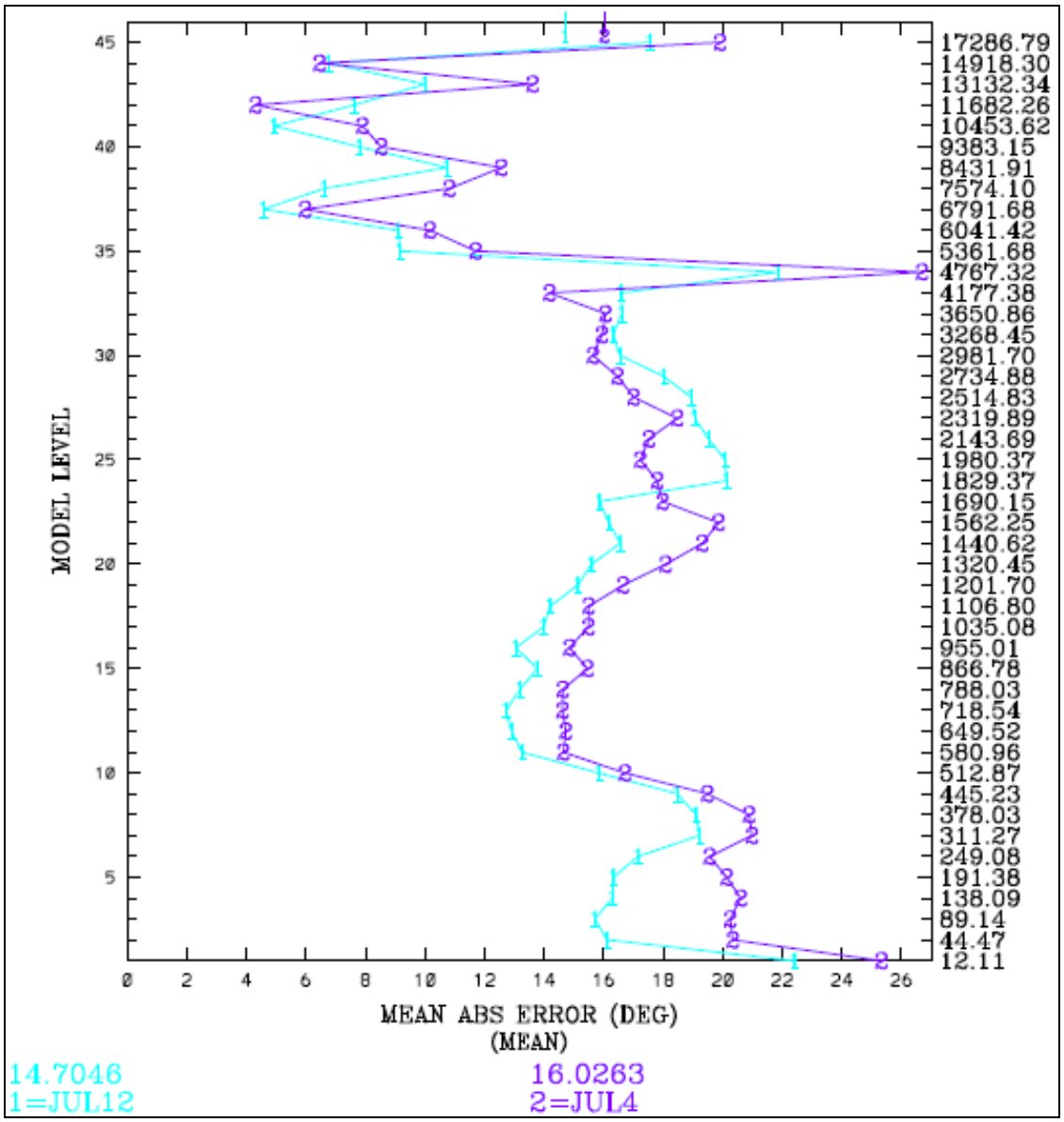

Figure G-45. MAE of model-derived WDIR (degrees) for JUL12 (blue) and JUL4 (purple) for all layers, beginning at model time t = 12 hours. MAE is shown on the abscissa, model sigma-level is shown on the left ordinate, and model height is shown on the right ordinate.

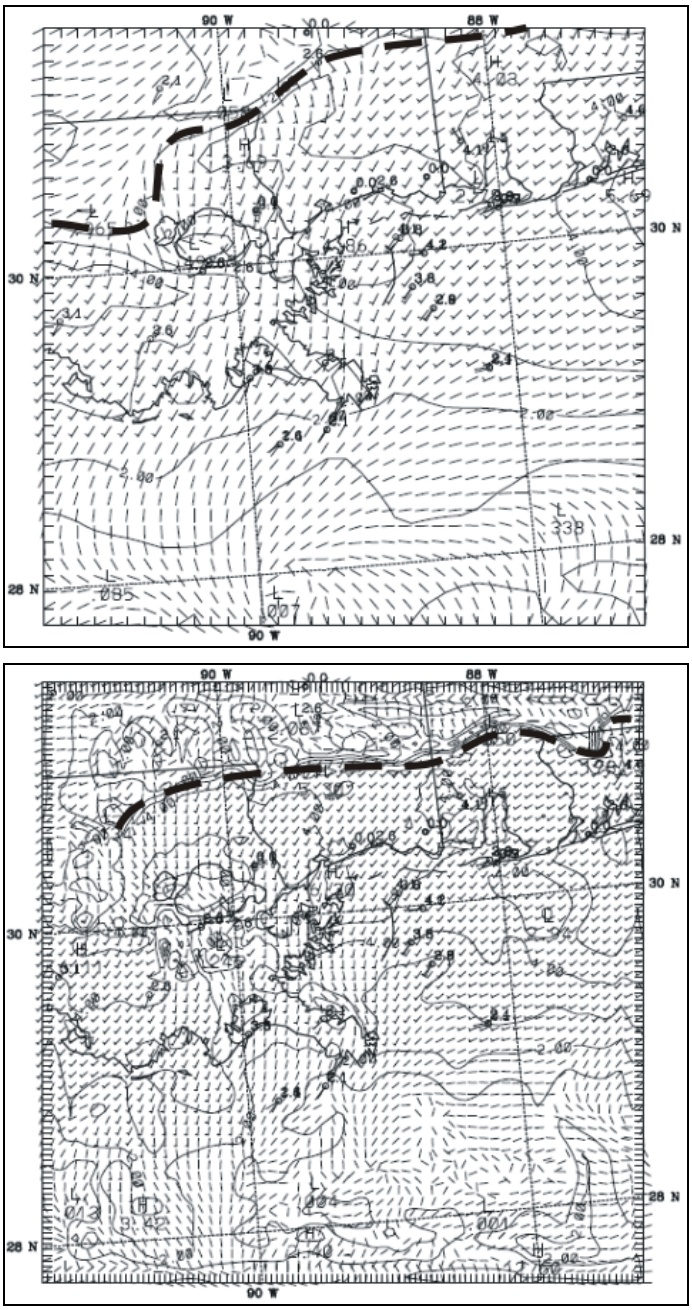

Figure G-46. Modeled surface wind field and surface observations for 00 UTC, 9 July 2001 (t = 12 h). JUL12 output over the 4-km subdomain is on the top, and JUL4 output is on the bottom. JUL12 output plots wind barbs for every grid cell, which JUL4 output plots wind barbs every other grid cell. Wind speeds are contoured every 1.0 m/s, and the sea breeze front is denoted by the dashed lines.

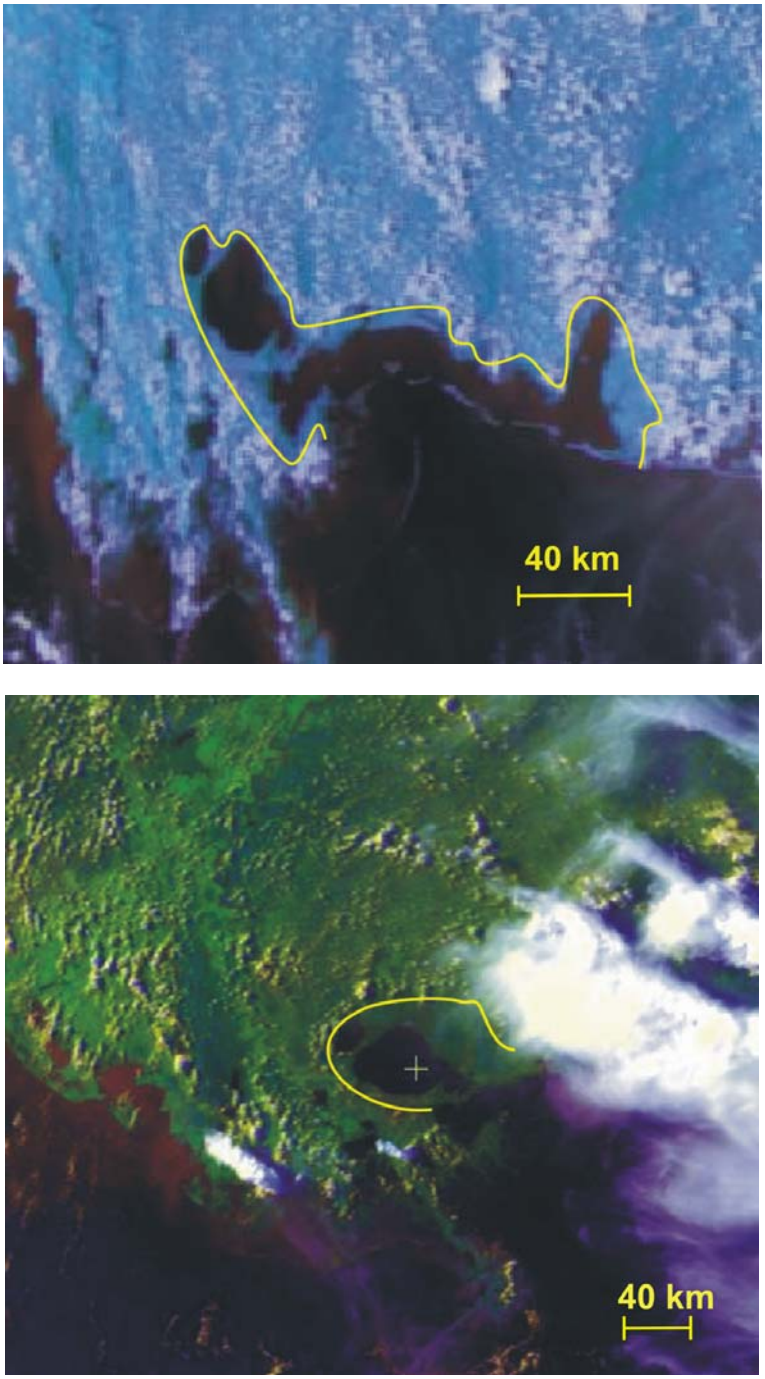

Figure G-47. Two images from the CLASS satellite imagery archive, capable of seeing the sea breeze front. The image on the top is from 19 UTC, 8 July 2001 and the image on the bottom is from 22 UTC, 8 July 2001, two hours prior to the end of model spin-up time.

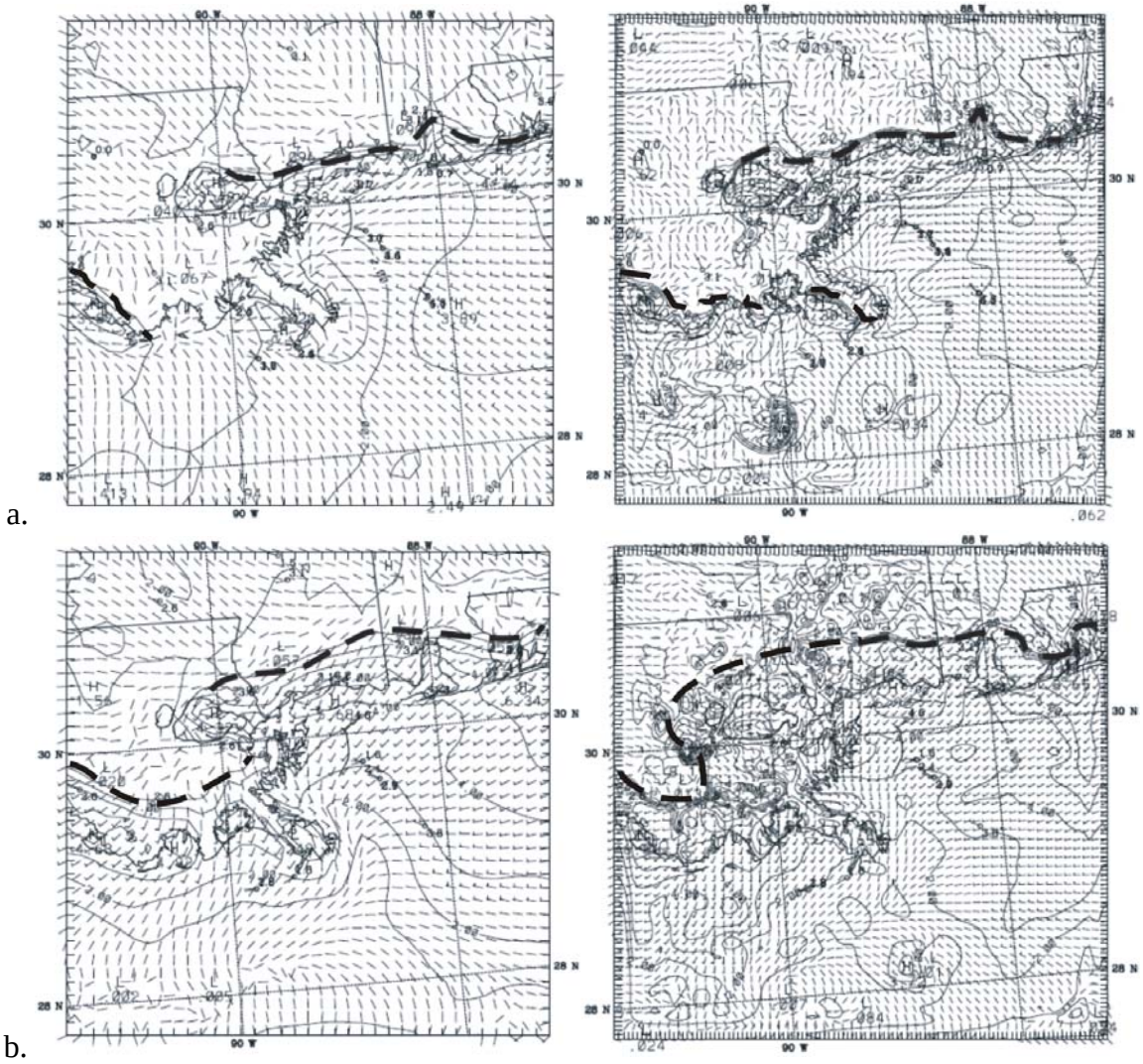

Figure G-48. JUL12 (left) and JUL4 (right) model-derived surface wind fields and observed surface winds for a.) 18 UTC, 9 July 2001, and b.) 21 UTC, 9 July 2001. Observed wind speeds are reported in m/s, and isotachs are contoured every 1.0 m/s. The sea breeze front is denoted by the dashed line.

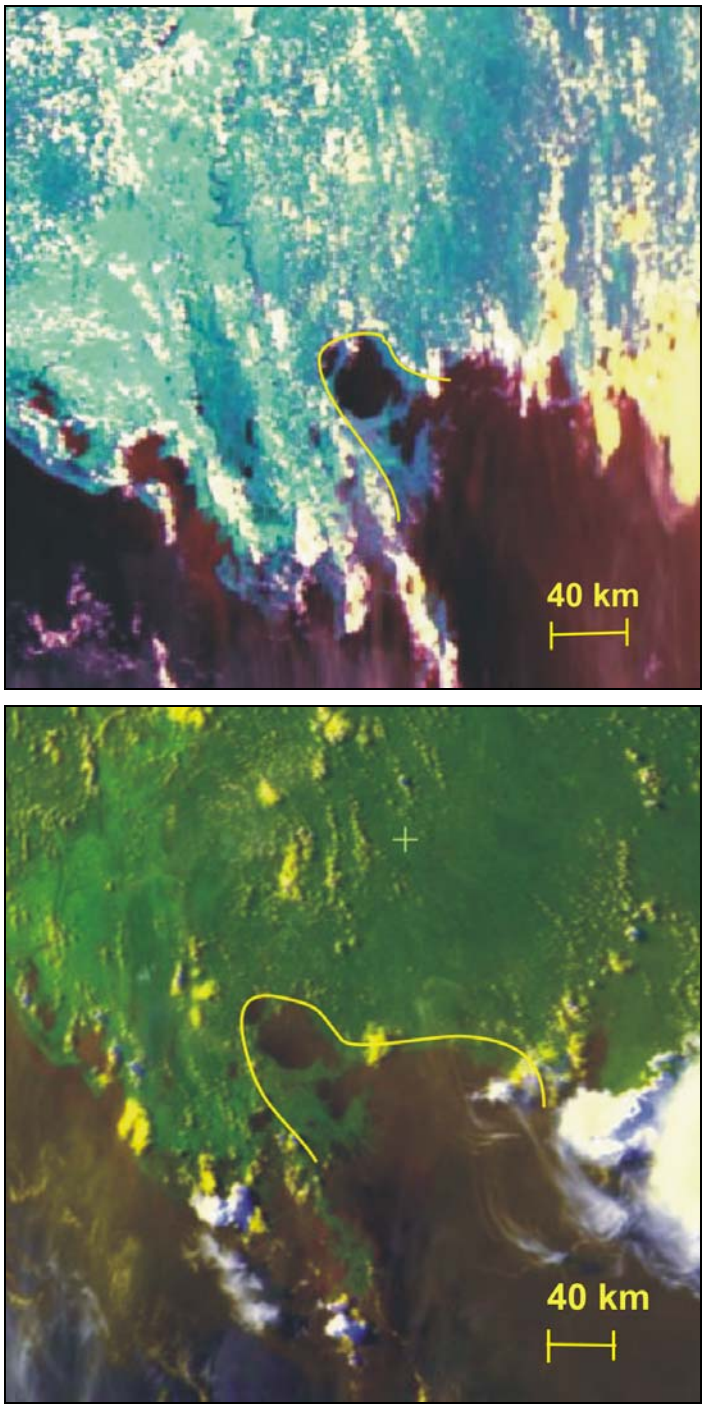

Figure G-49. Two images from the CLASS satellite imagery archive, illustrating the less-developed sea breeze front on 9 July 2001. The image on the top is from 20 UTC, 9 July 2001 and the image on the bottom is from 22 UTC, 9 July 2001.

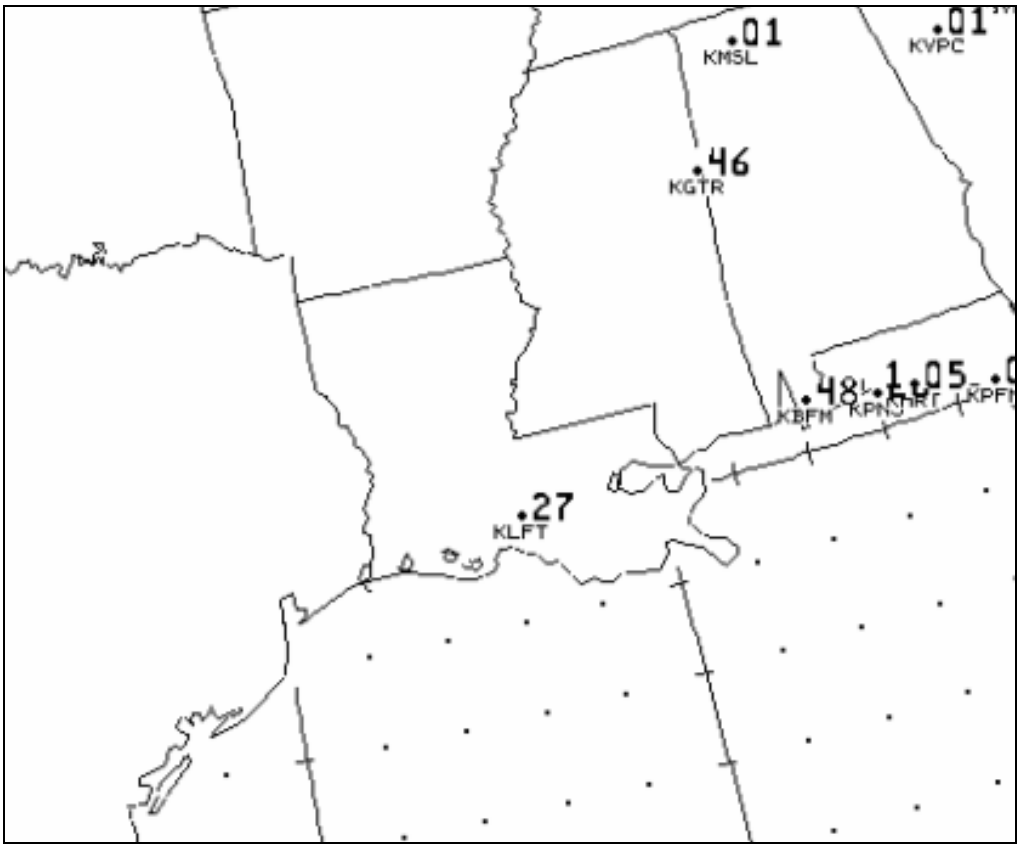

Figure G-50. 24-hour observed precipitation totals for the period beginning 12 UTC, 8 July 2001 and ending 12 UTC, 9 July 2001. Precipitation totals are given in inches, directly above the corresponding observation station identifier.

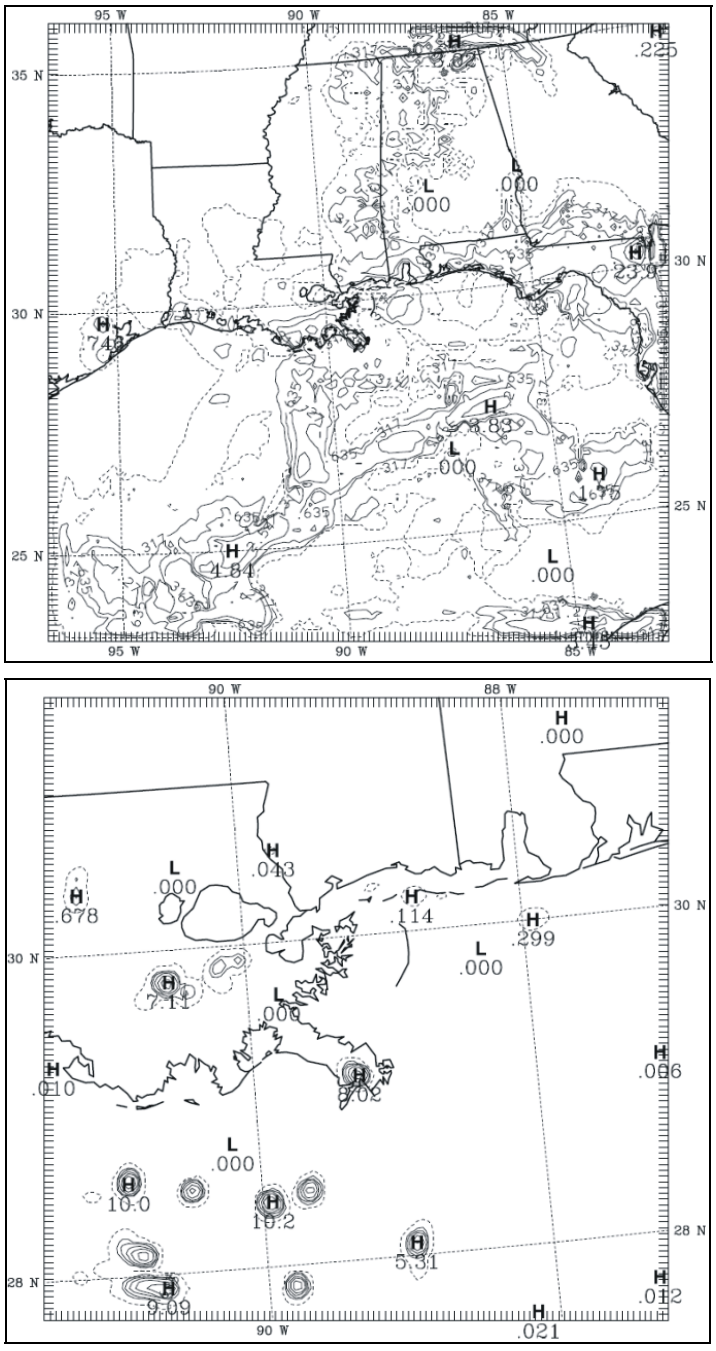

Figure G-51. Model-derived 24-hour precipitation accumulations for the period beginning t = 0 h, 12 UTC, 8 July 2001 and ending t = 24 h, 12 UTC, 9 July 2001. The dashed contour encircles all areas that have measurable model-derived precipitation during the 24-hour period. Within the dashed contour, precipitation amounts double with every successive contour, beginning with 0.125 inches (0.317 cm)

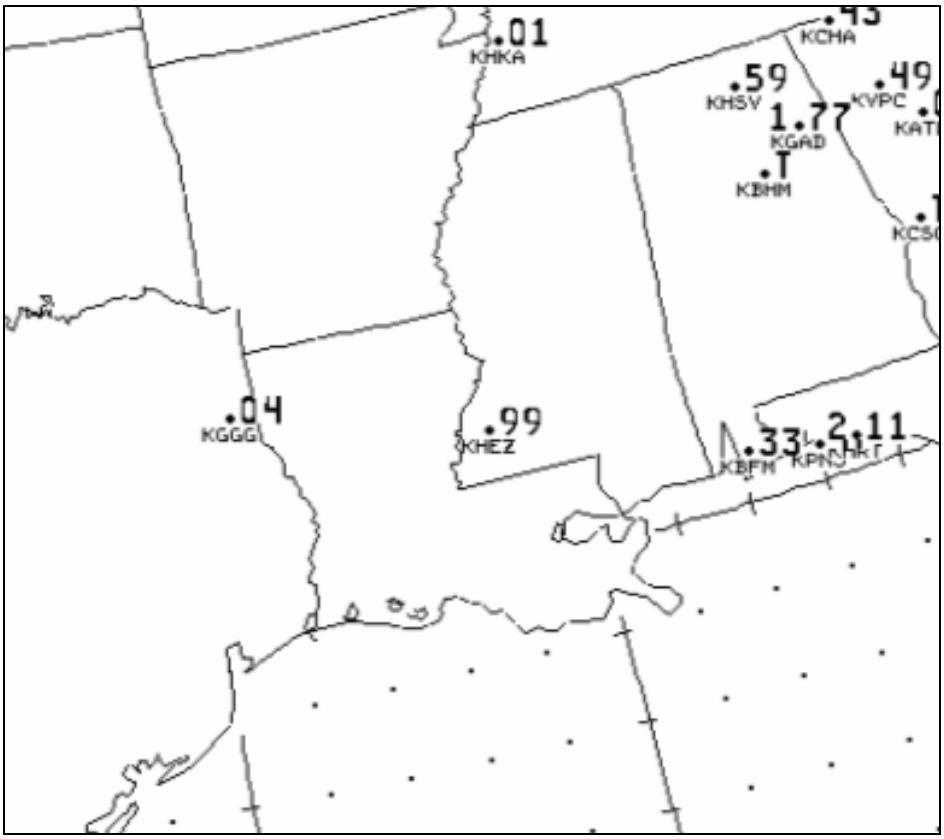

Figure G-52. 24-hour observed precipitation totals for the period beginning 12 UTC, 9 July 2001 and ending 12 UTC, 10 July 2001. Precipitation totals are given in inches, directly above the corresponding observation station identifier.

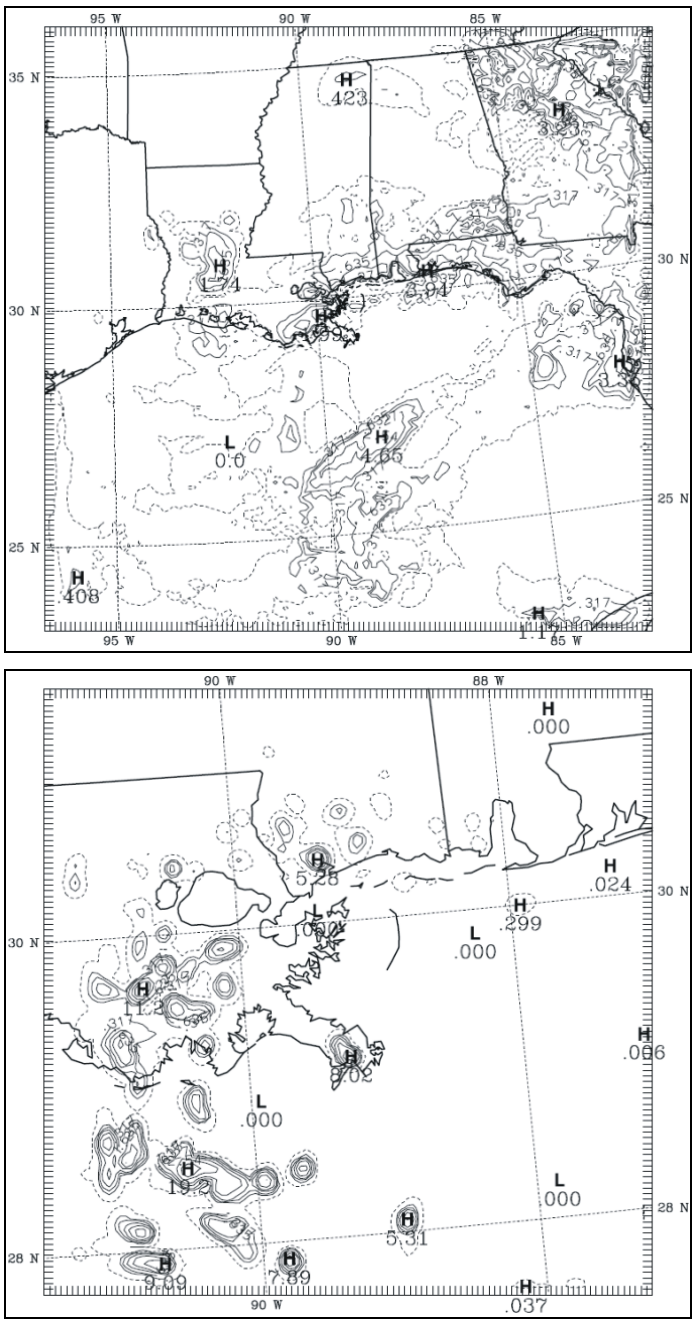

Figure G-53. Model-derived 24-hour precipitation accumulations for the period beginning t = 24 h, 12 UTC, 9 July 2001 and ending t = 48 h, 12 UTC, 10 July 2001. The dashed contour encircles all areas that have measurable model-derived precipitation during the 24-hour period. Within the dashed contour, precipitation amounts double with every successive contour, beginning with 0.125 inches (0.317 cm).

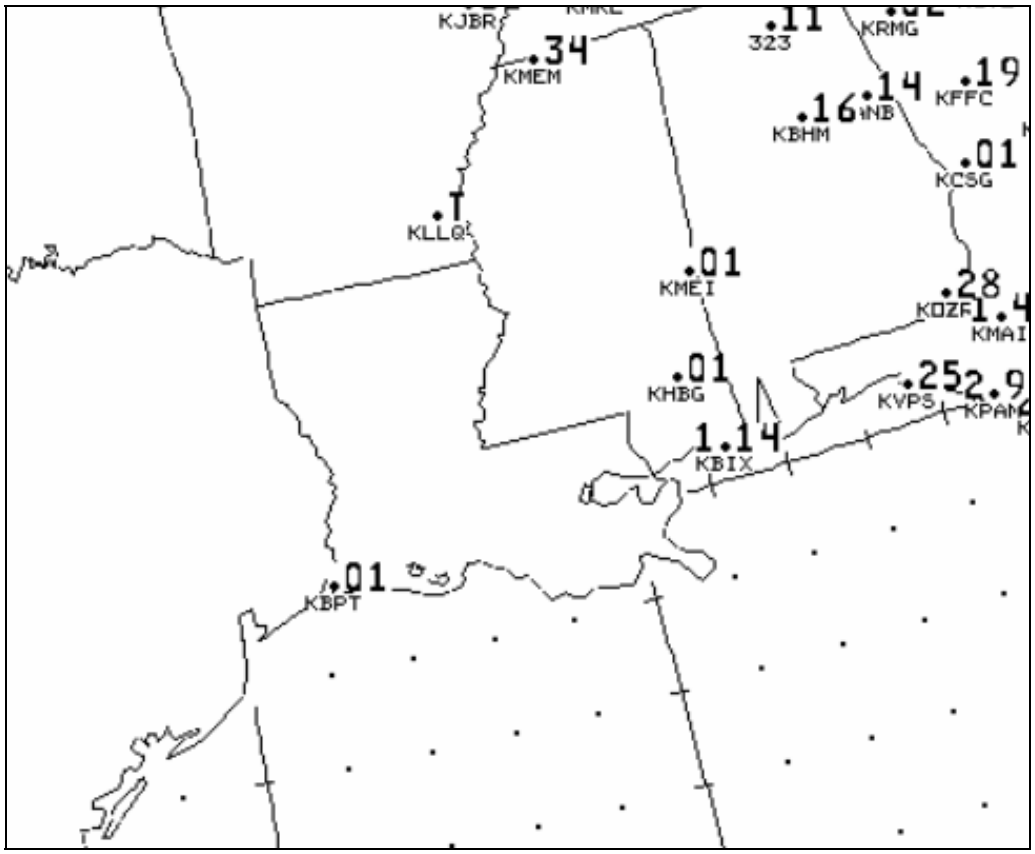

Figure G-54. 24-hour observed precipitation totals for the period beginning 12 UTC, 10 July 2001 and ending 12 UTC, 11 July 2001. Precipitation totals are given in inches, directly above the corresponding observation station identifier.

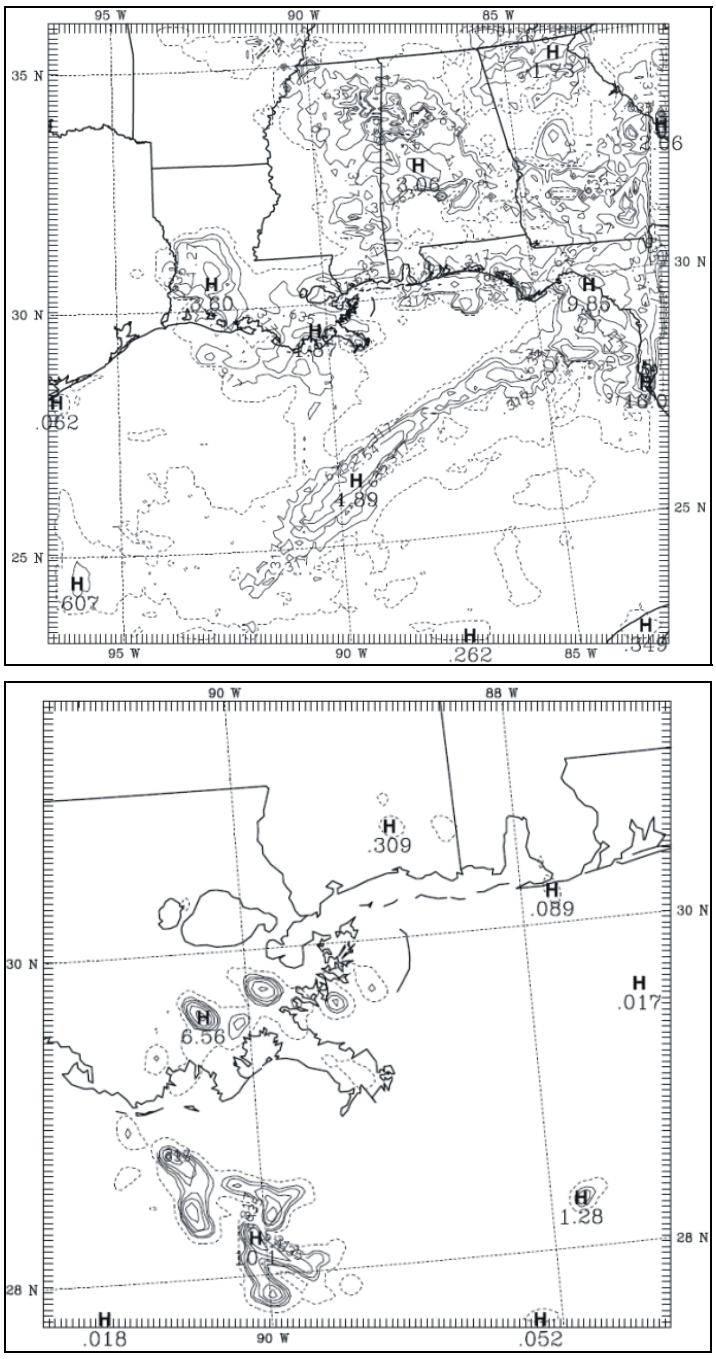

Figure G-55. Model-derived 24-hour precipitation accumulations for the period beginning t = 48 h, 12 UTC, 10 July 2001 and ending t = 72 h, 12 UTC, 11 July 2001. The dashed contour encircles all areas that have measurable model-derived precipitation during the 24-hour period. Within the dashed contour, precipitation amounts double with every successive contour, beginning with 0.125 inches (0.317 cm).

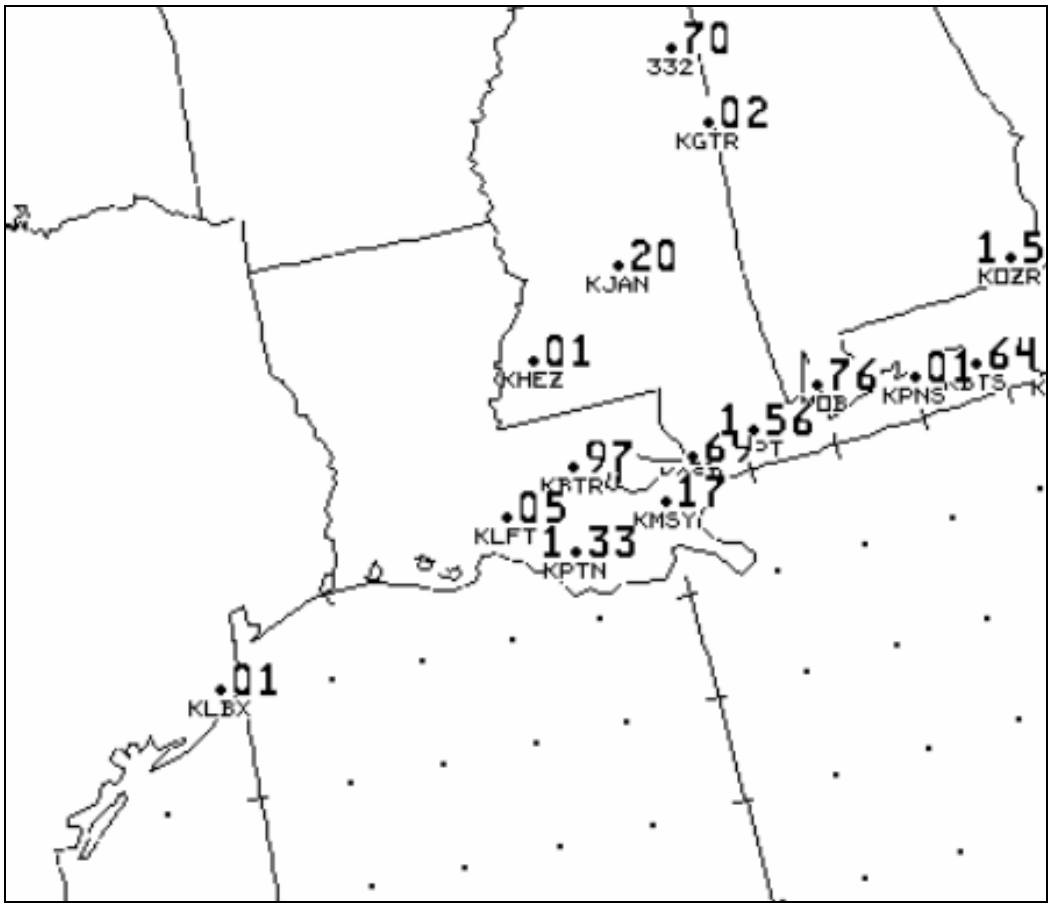

Figure G-56. 24-hour observed precipitation totals for the period beginning 12 UTC, 11 July 2001 and ending 12 UTC, 12 July 2001. Precipitation totals are given in inches, directly above the corresponding observation station identifier.

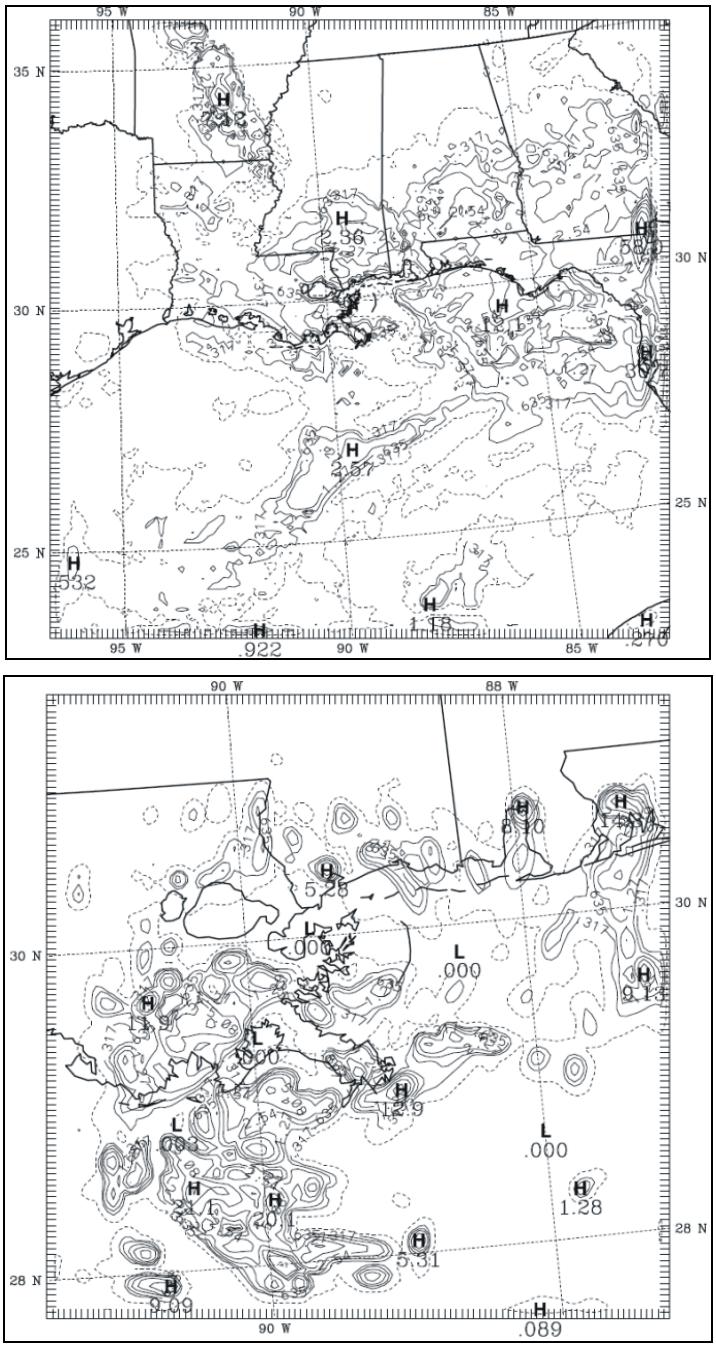

Figure G-57. Model-derived 24-hour precipitation accumulations for the period beginning t = 72 h, 12 UTC, 11 July 2001 and ending t = 96 h, 12 UTC, 12 July 2001. The dashed contour encircles all areas that have measurable model-derived precipitation during the 24-hour period. Within the dashed contour, precipitation amounts double with every successive contour, beginning with 0.125 in (0.317 cm).

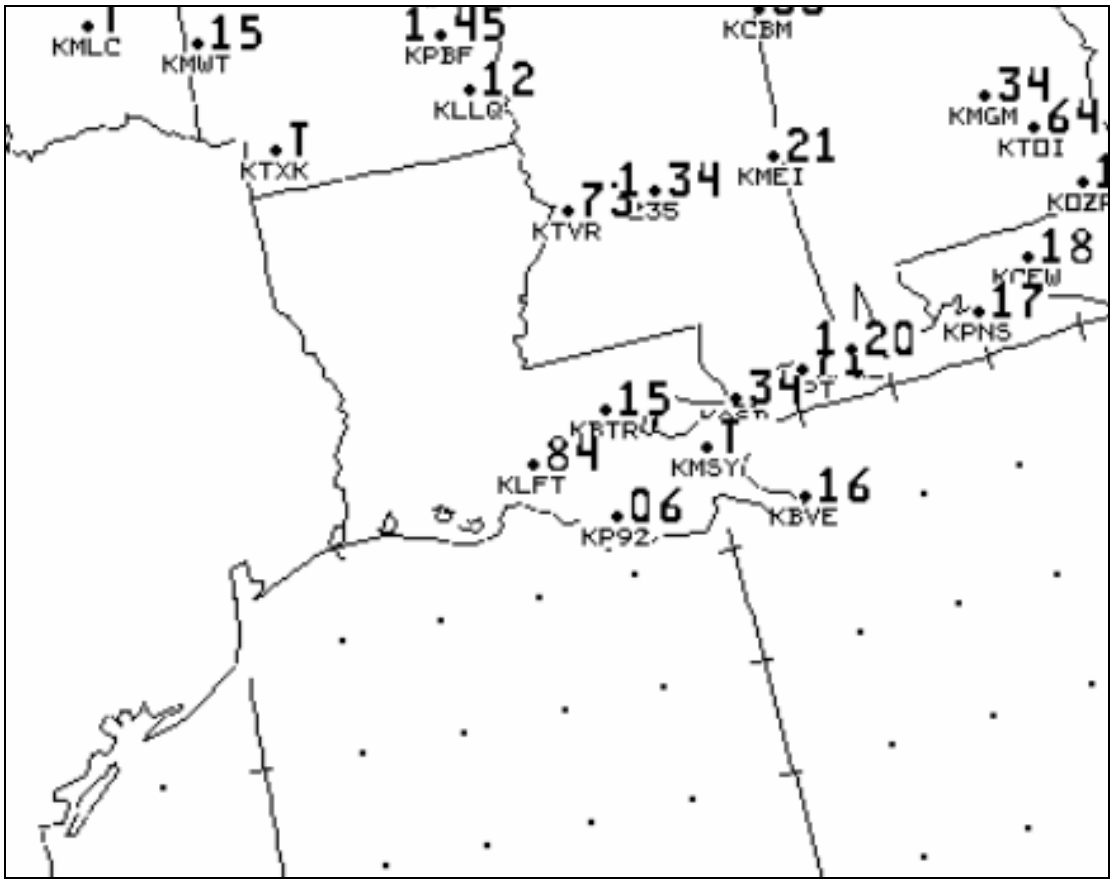

Figure G-58. 24-hour observed precipitation totals for the period beginning 12 UTC, 12 July 2001 and ending 12 UTC, 13 July 2001. Precipitation totals are given in inches, directly above the corresponding observation station identifier.

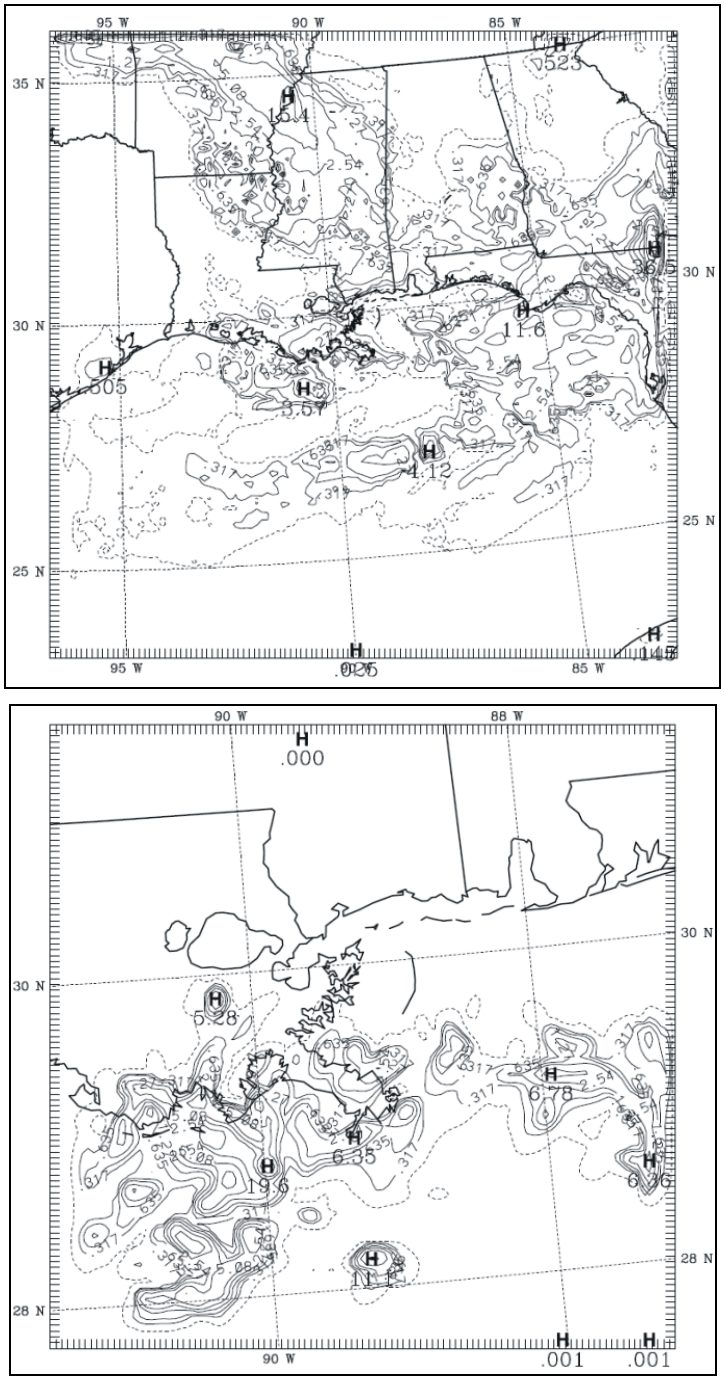

Figure G-59. Model-derived 24-hour precipitation accumulations for the period beginning t = 96 h, 12 UTC, 12 July 2001 and ending t = 120 h, 12 UTC, 13 July 2001. The dashed contour encircles all areas that have measurable model-derived precipitation during the 24-hour period. Within the dashed contour, precipitation amounts double with every successive contour, beginning with 0.125 in (0.317 cm).

The Department of the Interior Mission

As the Nation's principal conservation agency, the Department of the Interior has responsibility for most of our nationally owned public lands and natural resources. This includes fostering sound use of our land and water resources; protecting our fish, wildlife, and biological diversity; preserving the environmental and cultural values of our national parks and historical places; and providing for the enjoyment of life through outdoor recreation. The Department assesses our energy and mineral resources and works to ensure that their development is in the best interests of all our people by encouraging stewardship and citizen participation in their care. The Department also has a major responsibility for American Indian reservation communities and for people who live in island territories under U.S. administration.

The Minerals Management Service Mission

As a bureau of the Department of the Interior, the Minerals Management Service's (MMS) primary responsibilities are to manage the mineral resources located on the Nation's Outer Continental Shelf (OCS), collect revenue from the Federal OCS and onshore Federal and Indian lands, and distribute those revenues.

Moreover, in working to meet its responsibilities, the **Offshore Minerals Management Program** administers the OCS competitive leasing program and oversees the safe and environmentally sound exploration and production of our Nation's offshore natural gas, oil and other mineral resources. The MMS **Minerals Revenue Management** meets its responsibilities by ensuring the efficient, timely and accurate collection and disbursement of revenue from mineral leasing and production due to Indian tribes and allottees, States and the U.S. Treasury.

The MMS strives to fulfill its responsibilities through the general guiding principles of: (1) being responsive to the public's concerns and interests by maintaining a dialogue with all potentially affected parties and (2) carrying out its programs with an emphasis on working to enhance the quality of life for all Americans by lending MMS assistance and expertise to economic development and environmental protection.